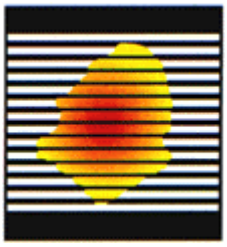
HAKONE VIII

International Symposium on
High Pressure
Low Temperature
Plasma Chemistry

Contributed Papers

Volume 1



Pühajärve, Estonia

July 21 - 25, 2002

ORGANIZER

Institute of Experimental Physics and Technology of the University of Tartu

INTERNATIONAL SCIENTIFIC AND ORGANIZING COMMITTEE

Brisset, J.-L.	France
Herbert, T.	Ireland
Ito, T.	Japan
Janča, J.	Czech Republic
Kogelschatz, U.	Switzerland
Kozlov, K.V.	Russia
Pietsch, G.	Germany
Pollo, I.	Poland
Rea, M.	Italy
Sakai, T.	Japan
Skalný, J.D.	Slovakia
Wagner, H.-E.	Germany
Yamabe, C.	Japan

LOCAL ORGANIZING COMMITTEE

Aaviksoo, J. (Chairman)	Aints, M.
Laan, M. (Vice-chairman)	Korge, H.
Haljaste, A. (Secretary)	Paris, P.
	Plank, T.

PREFACE

The HAKONE VIII Symposium hosted by University of Tartu at Pühajärve, Estonia, is the eighth in the series originated in Hakone (Japan) in 1987. It follows along the lines of the previous meetings providing the participants with the opportunity to present the progress in high-pressure low temperature plasma chemistry and physics in recent years. As the plasma chemistry is of increasing interest to industrial technologies and environmental applications, the HAKONE symposiums are appreciated as events that bridge the gap between basic research and applications. HAKONE VIII with its high number of participants (over 110) and 87 contributions testifies to that opinion.

This two-volume set of Symposium Proceedings contains the Contributed Papers, which were accepted upon the review of abstracts by the Local Organizing Committee (LOC) by the authority of the International Scientific and Organizing Committee. About 4% of the submitted abstracts were rejected, mostly on the ground that they were outside the subject area of the symposium. The authors of the accepted papers were provided with the Preparation Guide and Sample Format of Papers describing the rules of preparation. The length of the papers was limited to five pages. One of the requirements for the inclusion of the papers in the Symposium Proceedings was that at least one of the authors had to be registered. The authors were asked to submit their papers as camera ready electronic files in the PDF format. DOC files were accepted as an exception and they were formatted and converted into the PDF format by the Symposium organizers. No editorial corrections pertaining to contents were made and therefore the authors are fully responsible for the scientific and technical contents of their contributions. The papers of unsatisfactory printing quality (especially concerning the illustrations) were returned to the authors for improvements until a satisfactory material was completed. The editors thank the authors for they efforts to comply with the unified rules of preparation.

In the HAKONE VIII Symposium as well in the Symposium Proceedings, the contributions are distributed in seven different topics. Within each topic, the papers are selected for oral and poster sessions denoted by L and P in the contents of the Symposium Proceedings. Most of the contributed papers are available on the Internet under the address http://www.ut.ee/hakone8/papers/Papers.html .

The LOC hopes that you will find these five days at HAKONE VIII to be very valuable and fruitful for discussing your results hitherto, sharing experiences and exchanging new ideas. We hope the beautiful scenery of Pühajärve will create a cozy atmosphere and help you to realize your aims.

Tartu, June 2002 The Local Organizing Committee

ACKNOWLEDGEMENTS

Hakone VIII acknowledges the sponsorship and financial support of the following institutions and companies:

- E. C. Chemical Co., Ltd. (Japan)
- Estonian Science Foundation
- International Nuclear Information System
- Matsushita Electric Works Machine & Vision, Ltd. (Japan)
- Toppan Printing Co., Ltd. (Japan)
- Trailigaz (France)
- University of Tartu

Editors: Ants Haljaste, Toomas Plank

Cover design: Peeter Paris

ISBN: **9985-4-0257-X**

Contact address:

Ants Haljaste
Institute of Experimental Physics and Technology
University of Tartu
Tähe 4
51010 Tartu
ESTONIA
Phone: +372 7 375 565; +372 7 375 564
Fax: +372 7 375 858
E-mail: haljaste@ut.ee

Aiplasma
Atmospheric-pressure
Plasma Cleaning Unit

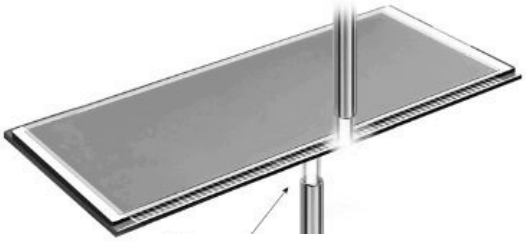
Smart Solutions by NAIS

High-speed, point-specific plasma cleaning of contacts in electronic components, under atmospheric pressure

Aiplasma **removes contaminants and improves surfaces, offering better bonding reliability, improved bonding strength, and better overall product quality**

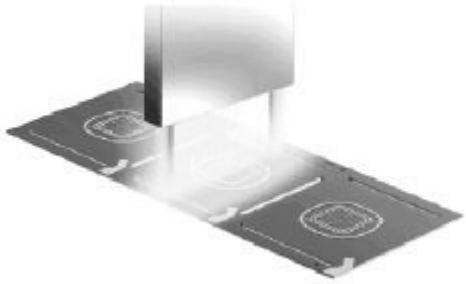
High-speed, point-specific plasma cleaning

Improves surface cleaning of organic contaminants *under atmospheric pressure*



Aiplasma nozzle

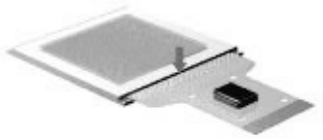
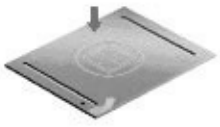
Spot: 5 to 10mm dia.



Wide: 25 to 75mm

Using propriety technology (over 60 patents pending), ***Aiplasma*** enables stable, continuous plasma flow at atmospheric pressure. Since ***Aiplasma*** works under atmospheric pressure, it can be implemented into existing manufacturing facilities for high-speed, continuous processing. With ***Aiplasma***, oxygen and hydrogen plasma are used for the removal of organic compounds on contact points of LCDs/PDPs and electronic components, and to remove surfaces and improve adhesion strength of resin substrates before sealing. These processes can all be performed in-line for improves quality, higher productivity and reduced manufacturing costs.

Applications

OLB(FOG) contact surface cleaning	BGA substrate/bonding pad cleaning	Compound chip package cleaning
		
Sections where the LCD/PDP panel bonds to the film substrate are cleaned	Cleaning the bonding pad improves the wire bonding and the peel shear strength of the sealing resin	The contact sections of compound electric components are cleaned

Matsushita Electric Works Machine & Vision, Ltd

Head Office : 1048, Kadoma, Kadoma-shi, Osaka 571-8686, Japan
http://www.aiplasma.com/
E-mail : webmaster@naismv.co.jp

Trailigaz

Ozone - Ultraviolets - Electrochloration



- **Oxidation and Disinfection technologies for Industrial and Municipal Applications**



- **Trailigaz proposes specific technical solutions well adapted to your project**



- **Compact and reliable equipments**

  Ozone generators and ancillary equipments, skids for specific applications, UV reactors, Electrochlorators…

trailigaz

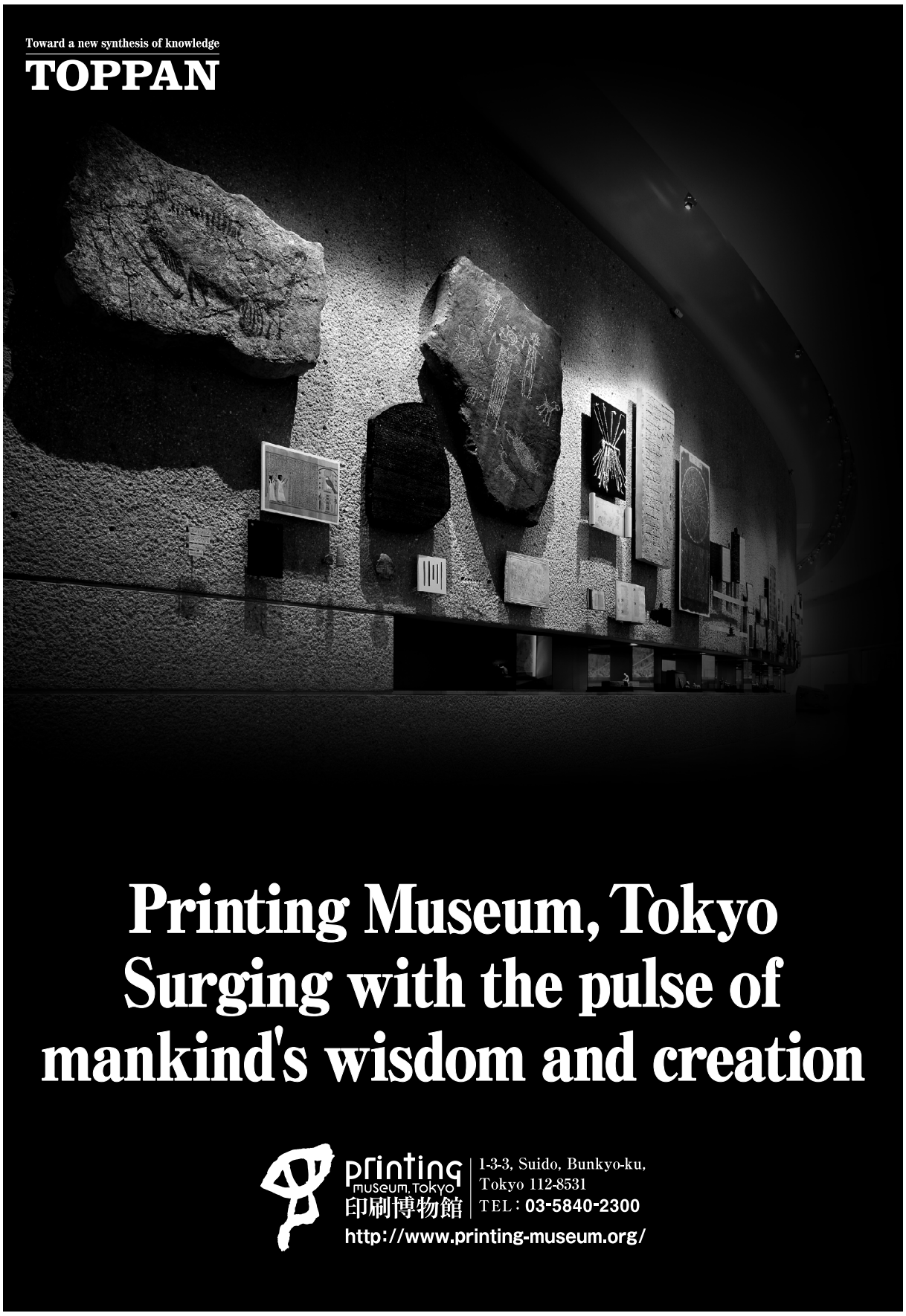
TRAILIGAZ
29-31 Boulevard de la Muette
F 95145 Garges-les-Gonesse Cedex

Tel. 33 (0)1 34 53 45 00
Fax 33 (0)1 34 53 01 96
www.trailigaz.com

VIVENDI water

Toward a new synthesis of knowledge

TOPPAN



Printing Museum, Tokyo
Surging with the pulse of mankind's wisdom and creation

printing museum, Tokyo
印刷博物館

1-3-3, Suido, Bunkyo-ku,
Tokyo 112-8531
TEL：03-5840-2300
http://www.printing-museum.org/

●ACCESS: 13 minutes walk from Iidabashi Station on the JR Chuo and Sobu lines, or the Yurakucho, Tozai, Nanboku and Ōedo Subway lines. 8 minutes walk from Edogawabashi Station.●HOURS: 10:00-18:00 (last admission 17:30) ●CLOSED: Mondays (unless Monday is a holiday, in which case it will be closed the following day); New Year period; when changing exhibitions (prior notice will be given).●ADMISSION: Adults (including junior high school students) 300 yen; Elementary school students 100 yen

E.C.

Fine Chemicals & Atomosphere Plasma Treatment

E.C.Chemical Co., Ltd.

2-28-3 Kasuganishimachi Hirakata, Osaka, JAPAN

TEL 072-850-1111

FAX 072-858-5652

E-mail : ec-chemi@rd6.so-net.ne.jp

CONTENTS

TOPIC 1:
Fundamental problems of high pressure discharges

L1.1 G. Jouve, A. Goldman, M. Goldman and C. Severac
Electrochemical phenomena at the plane electrodes of point-to-plane air corona gaps operated in glow regimes 3

L1.2 Yu.S. Akishev, A.V. Demyanov, V.B. Karal'nik, A.E. Monich and N.I. Trushkin
AC barrier pin-plane corona: similarities and distinctions to DC positive and negative coronas and dielectric barrier discharge 8

L1.3 H.-E. Wagner, K.V. Kozlov, R. Brandenburg and P. Michel
Experimental study of repetitive electrical breakdown in the barrier discharge in air 13

L1.4 P. Tardiveau and E. Marode
Effects of dielectric droplets on point-to-plane discharge dynamics and spark formation 18

L1.5 N. Gherardi, E. Croquesel, N. Naudé, P. Veis and F. Massines
Two different origins for the destabilization of a glow dielectric barrier discharge in nitrogen 23

L1.6 R. Brandenburg, K.V. Kozlov, N. Gherardi, P. Michel, C. Khampan, H.-E. Wagner and F. Massines
Spatio-temporally resolved spectroscopic diagnostics of the atmospheric pressure glow discharge in nitrogen 28

L1.7 E.M. van Veldhuizen, W.R. Rutgers and U. Ebert
Positive and negative pulsed corona in argon 33

L1.8 Y.-H. Kim, W.S. Kang, S.H. Hong and Y.-H. Song
Comparative study of pulsed corona and dielectric barrier discharges using single-streamer modeling and NO decomposition experiment 38

L1.9 M.V. Kozlov, M.V. Sokolova, A.G. Temnikov, V.V. Timatkov and I.P. Vereshchagin
Surface discharge characteristics for different types of applied voltage and different dielectric materials 43

P1.1 Yu.B. Golubovskii, V.A. Maiorov, J. Behnke and J.F. Behnke
Influence of elementary processes over an homogeneous barrier discharge in helium 48

P1.2 Yu.B. Golubovskii, V.A. Maiorov, J. Behnke and J.F. Behnke.
Townsend and glow modes of an homogeneous barrier discharge in helium 53

P1.3 A. Ignatkov, A. Schwabedissen, G.F. Leu and J. Engemann
Studies of the atmospheric pressure jet matrix plasma source: electrical properties and discharge stability 58
P1.4 D. Trunec, R. Brandenburg, P. Michel, D. Pasedag, H.-E. Wagner and Z. Navratil
Spatio-temporally resolved emission spectroscopy of the atmospheric pressure glow discharge in neon 63
P1.5 P. Slavíček, A. Brablec, M. Klíma , V. Kapička, J.F. Behnke and M. Šícha
Comparison of the barrier - torch discharge and torch discharge at atmospheric pressure 68
P1.6 N.B. Anikin, N.K. Bibinov, M. Šira and K. Wiesemann
Silent discharges in helium and helium – nitrogen mixtures 73
P1.7 J. Mizeraczyk, J. Podliński, M. Dors, M. Kocik, T. Ohkubo, S. Kanazawa and J.S. Chang
Electrohydrodynamic transport of ozone in a corona radical shower non-thermal plasma reactor 78
P1.8 T. Plank, M. Aints and A. Haljaste
Initiation probability of burst pulses 83
P1.9 Yu.I. Chutov, W.J. Goedheer, O.Yu. Kravchenko, O.A. Lavrov, T.E. Lisitchenko and G.I. Protas
Dusty RF discharges 88
P1.10 M.S. Baranchuk, T.E. Lisitchenko and M.M. Okholin
Statistical properties of electric breakdowns between glass surfaces in inert gases and their mixtures 93

TOPIC 2:
Modeling and diagnostics

L2.1 Yu.S. Akishev, I.V. Kochetov, A.I. Loboiko and A.P. Napartovich
3-dimensional model for Trichel pulses: results of numerical studies for air 99
L2.2 J.M. Park, Y.-H. Kim and S.H. Hong
Three-dimensional numerical simulations on the streamer propagation characteristics of pulsed corona discharge in a wire-cylinder reactor 104
L2.3 W.S. Kang, Y.-H. Kim, S.H. Hong and Y.-H. Song
Numerical modeling on recurrence of microdischarges in dielectric barrier discharge 109
L2.4 K.V. Kozlov, N.S. Boksha, A.M. Morozov and V.G. Samoilovich
Plasma diagnostics by cross-correlation spectroscopy in investigations of chemical activity of negative corona in air at atmospheric pressure 114
L2.5 A. Fateev, I.P. Vinogradov and A. Lunk
Dynamics of the gas temperature in dielectric barrier discharge in He/N_2 mixtures 119

L2.6 I. Radu, R. Bartnikas, G. Czeremuszkin and M.R. Wertheimer
Diagnostics of dielectric barrier discharges at atmospheric pressure in noble gases 124
P2.1 M. Madani, A. Bogaerts, R. Gijbels and D. Vangeneugden
Modelling of a dielectric barrier glow discharge at atmospheric pressure in nitrogen 130
P2.2 V. Repän, M. Laan and T. Plank
Electric field modelling for point-plane gap 134
P2.3 M. Magureanu, M. Heintze and M. Kettlitz
OES investigations of a pulsed microwave plasma used for methane conversion to C_2 hydrocarbons 139
P2.4 H. Nowakowska, J. Stańco, M. Dors and J. Mizeraczyk
Modeling of plasma chemistry in a corona streamer pulse series in air 144
P2.5 S. Baba, S. Satoh and C. Yamabe
Development of measurement equipment of ozone half life 148
P2.6 V.I. Gibalov, T. Murata and G.J. Pietsch
Parameters of barrier discharges in coplanar arrangements 153

TOPIC 3:
Molecular synthesis and decomposition

L3.1 J. Janča, M. Eliáš and V. Brožek
Low temperature reduction of tungsten precursors in RF discharge plasma reactors 161
L3.2 B. Pietruszka and M. Heintze
Plasma-promoted partial oxidation of methane to syngas over α-alumina supported nickel catalyst in dielectric-barrier discharge 166
L3.3 M. Dhainaut, E. Odic, M. Goldman, A. Goldman and C. Karimi
Dependence of the oxidation properties of a dielectric barrier discharge in air on the plasma and gas temperatures 171
P3.1 J.-M. Cormier, I. Rusu and M. Dudemaine
On a new magnetic blow out glidarc reactor 176
P3.2 K. Krawczyk, J. Ruszniak, J. Sentek and K. Schmidt-Szałowski
Acetylene from methane by gliding arc processing 181
P3.3 K. Krawczyk and M. Wieczorkowski
Studies of nitrous oxide conversion in gliding arc discharges 186
P3.4 A. Opalska, T. Opalinska, J. Polaczek and P. Ochman
Plasma-induced decomposition of chlorodifluoromethane 191
P3.5 T. Kappes, W. Schiene and T. Hammer
Energy balance of a dielectric barrier discharge reactor for hydrocarbon steam reforming 196
P3.6 M. Heintze and M. Magureanu
Efficient methane conversion to acetylene in a microwave plasma 201

P3.7 M. Miclea, K. Kunze, J. Franzke, F. Leis, K. Niemax, C. Penache, O. Hohn, S. Schössler, T. Jahnke, A. Bräuning-Demian and H. Schmidt – Böcking
Decomposition of halogenated molecules in a micro-structured electrode glow discharge at atmospheric pressure 206

TOPIC 4:
Ozone generation and applications

L4.1 S. Kaneda, M. Shimosaki, N. Hayashi, S. Ihara, S. Satoh and C. Yamabe
Ozone production by an atmospheric pulsed discharge with pre-ionization electrodes and partly covered electrode 213

L4.2 K. Yasuoka, Y. Endo and S. Ishii
Experimental study on ozone generation using DC driven micro-plasma 217

L4.3 R. Peyrous
Possibility of improvement of ozone production by using the back-corona effect 222

L4.4 A.B. Saveliev and G.J. Pietsch
On the structure of dielectric barrier surface discharges 229

L4.5 G.J. Pietsch and C. Humpert
Discharge mechanism and ozone generation by surface discharges depending on polarity 234

L4.6 J. Ozonek, K. Jahołkowski, I. Pollo and S. Okazaki
Operation conditions in an ozonizer containing a wire packing 239

P4.1 Y. Miyake, Y. Ehara, H. Kishida and T. Ito
Generation of ozonized water by surface discharge 244

P4.2 H. D. Stryczewska and T. Janowski
Reactive power of the ozone generators 249

P4.3 T. Opalinska
Cold plasma reactor with dielectric barrier discharge 254

P4.4 L. Hulka and G. J. Pietsch
On the ignition voltage and structure of coplanar barrier discharges 259

P4.5 T. Horinouchi, T. Hayashi and N. Nakajima
Development of a new type ozoniser with rotating electrode 264

P4.6 S. Jodzis
Application of surface discharges in electroplasma ozone synthesis 269

TOPIC 5:
Generation of radiation in high pressure discharges

L5.1 A. Treshchalov, A. Lissovski and E. Chikeev
Spectroscopic diagnostics of high-current discharges in UV-VUV excimer lasers 277

P5.1 M. Aints, A. Haljaste and L. Roots
Photoionizing radiation of positive corona in moist air 282
P5.2 M. Laan and J. Raud
HF capillary discharge: distribution of radiation along electrodes 286
P5.3 A. Treshchalov, E. Jalviste, A. Smerechuk, G. Gerasimov, R. Hallin and A. Arnesen
VUV emission of Kr_2 molecules under high-current sliding discharge excitation 291
P5.4 A. Khacef, J.M. Cormier, J.M. Pouvesle, O. Gorce, H. Jurado, C. Thomas, G. Djéga-Mariadassou, S. Calvo and Y. Lendresse
Plasma-catalyst system for NO_x remediation in simulated lean exhaust 296

TOPIC 6:
Environmental applications

L6.1 M. Kogoma, T. Abe and K. Tanaka
PFCs abatement system by the atmospheric pressure glow plasma 303
L6.2 D. Moussa, H. Vitrac, B.G. Chéron, E. Hnatiuc, A. Addou and J.L. Brisset
Acidity control of the oxidation reactions induced by non-thermal plasma treatment of aqueous effluents in pollutant abatement processes 308
L6.3 A.T. Appleton, P. Lukes, W.C. Finney and B.R. Locke
Study of the effectiveness of different hybrid pulsed corona reactors in degrading aqueous pollutants 313
L6.4 S.A. Nair, A.J.M. Pemen, K. Yan, E.J.M. van Heesch, K.J. Ptasinski and A.A.H. Drinkenburg
Chemical processes during biogas conditioning by pulsed corona discharges 318
L6.5 R. Rudolph, K.-P. Francke and H. Miessner
Determination of OH radical concentration in dielectric barrier discharges by CO oxidation 323
L6.6 J. Pawłat, C. Yamabe and I. Pollo
Foaming apparatus as oxidants' generator 327
L6.7 Y. Yoshioka and K. Teshima
Calculation of NO_x removal process taking pulse micro-discharge and diffusion of radicals into consideration 332
L6.8 E.A. Filimonova, R.H. Amirov, S.H. Hong, Y.H. Kim and Y.H. Song
Influence of temperature and hydrocarbons on removal of NO_x and SO_2 in a diesel exhaust gas activated by pulsed corona discharge 337
P6.1 R. Vertriest, R. Morent, J. Dewulf, C. Leys and H. Van Langenhove
Removal of trichloroethylene with a DC-excited multi-pin-to-plate plasma source 342

P6.2 G. Penghui, N. Hayashi, S. Ihara, S. Satoh and C. Yamabe
Studies on an AC/DC combination discharge mode for NO_x treatment 347
P6.3 N. Hayashi, K. Yamamoto, S. Ihara, S. Satoh and C. Yamabe
Treatment of fluorocarbon using atmospheric non-thermal plasma produced by streamer corona discharge 351
P6.4 S. Dupré, C. Deniset, A. Goldman, M. Goldman and E. Marode
Main oxidation processes and their relative contributions in the NO removal by a dielectric barrier discharge for air cleaning 355
P6.5 J. Hong, S. Kim, K. Lee, K. Lee, J.J. Choi and Y.-K. Kim
PFC decomposition with atmospheric pressure microwave plasma using resonant and non-resonant structure 360
P6.6 N. Jidenko, M. Petit and J.P. Borra
Volatile organic compounds depollution by dielectric barrier discharge in porous media 364
P6.7 M.J. Kirkpatrick, W.C. Finney and B.R. Locke
Chlorinated organic compound removal by gas phase pulsed streamer corona electrical discharge with reticulated vitreous carbon electrodes 369
P6.8 M. Sahni, W.C. Finney, R.J. Clark, W. Landing and B.R. Locke
Degradation of aqueous phase trichloroethlyene using pulsed corona discharge 374
P6.9 E. Hnatiuc, B. Cheron, B. Hnatiuc, R. Burlica and J.L. Brisset
Cold plasma electrochemical reactor with rotary discharge 379

TOPIC 7:
Surface processing and technology
(cleaning, coating, etching, modification, equipment)

L7.1 O. Goossens, D. Vangeneugden, S. Paulussen and E. Dekempeneer
Physical and chemical properties of atmospheric pressure plasma polymer films 385
L7.2 C. Penache, S. Datta, S. Mukhopadhyay, A. Bräuning-Demian, P. Joshi, O. Hohn, S. Schössler, T. Jahnke and H. Schmidt-Böcking
Large area surface modification induced by parallel operated MSE sustained glow discharges 390
L7.3 S. Vladimirov and K. Ostrikov
Nano- and micro-particles in low-temperature plasmas: occurrence, dynamic processes, and applications 395
P7.1 S. Guimond, I. Radu, G. Czeremuszkin and M.R. Wertheimer
Modification of polyolefins in nitrogen atmospheric pressure glow discharges 400
P7.2 P. Paris, M. Laan and H. Valtna
Laser ablation and aerosol particles 405

P7.3 J.F. Behnke, H. Steffen, A. Sonnenfeld, R. Foest, V. Lebedev and R. Hippler
Surface modification of aluminium by dielectric barrier discharges under atmospheric pressure 410

P7.4 Z. Rzanek-Boroch, K. Schmidt-Szałowski, J. Janowska, K.Dudziński, A. Szymańska and M. Misiak
Thin films obtained by PE-CVD method from hexamethyldisiloxane under atmospheric pressure 415

P7.5 T. Opalinska, B. Ulejczyk, L. Karpiński and K. Schmidt-Szałowski
Deposition of thin films on polycarbonates by pulse dielectric barrier discharge 420

P7.6 P. Sťahel, J. Janča and D.P. Subedi
Surface modification of non-fabricated polypropylene textile in low-temperature plasma at atmospheric pressure 425

P7.7 S. Ono, S. Teii and S. Takayama
Surface treatment of plastic film by using an atmospheric pressure corona torch 431

P7.8 K. Tanaka and M. Kogoma
Deposition of multi-layer films of hexafluoropropene - ethylene composite polymer with jet-type plasma reactor at atmospheric pressure 436

P7.9 A. Goodwin, T. Herbert, S. Leadley and F. Swallow
Atmospheric pressure liquid deposition – a new route to high performance coatings 441

Index 447

TOPIC 1:

Fundamental problems of high pressure discharges

ELECTROCHEMICAL PHENOMENA AT THE PLANE ELECTRODES OF POINT-TO -PLANE AIR CORONA GAPS OPERATED IN GLOW REGIMES

G. Jouve[a], A. Goldman[b], M. Goldman[b] and C. Severac[a]

a) Laboratoire de Physico-Chimie de l'Etat Solide (UMR 8648 du CNRS), Univ. Paris-Sud, 91405 Orsay Cedex, FRANCE

b) Laboratoire de Physique des Gaz et des Plasmas (UMR 8578 du CNRS / Univ. Paris-Sud), Equipe DEE à Supélec, 3 rue Joliot-Curie, 91190 Gif-sur-Yvette Cedex, FRANCE

Abstract. Oxido-reduction properties of positive and negative air corona discharges operated in glow regimes are investigated through their interactions with plane electrodes of different materials in point-to-plane electrode systems. An electrochemical interpretation is proposed to explain the phenomena on these electrodes surfaces: aqueous droplets as observed by scanning electron microscopy and metal oxides of high oxidation states as found by photoelectron spectroscopy.

1. INTRODUCTION

Corona chemistry has acquired its letters patent of nobility since a very long time, beginning on a industrial scale with the ozonizers and now extending more and more largely with particular reference to depollution, disinfection and sterilization purposes, without forgetting all surface treatment corona technologies. Besides this wide scope, the study of the corona induced surface effects (see for instance [1, 2]) are also interesting for the maintenance of gas-insulated equipments, and more fundamentally for the information it can bring on the gas chemistry.

Our main aim in the present paper is to give a morphological description of the surface products layers, in their macroscopic and microscopic aspects, and to analyse the chemical effects in terms of oxydo-reduction properties.

2. EXPERIMENTAL

All investigations deal with the phenomena at the plane electrode of point-to-plane electrode systems, the point electrode being energized by a dc power supply, at positive or negative voltages providing diffuse glow discharges. In all cases, this electrode receives a combined flux of ions (of the same polarity as the point electrode polarization), and, in much larger proportions, of highly reactive corona neutral products. Almost all experiments, independently of the discharge polarity, are performed with the same level of electrical charges crossing the air gap of the system: I.t ~ 0.28 C, with most generally 20 µA / 4 hours for the treatments in positive point polarity and 80 µA / 1 hour in negative point polarity. This can be done because there is a certain reciprocity between the two parameters I and t [3].

Experiments are performed in ambient air, with an air gap fixed to 8 mm. The metallic samples used for the study consist of high purity samples mechanically polished of gold, chosen for its weak sensitivity to oxidation, and of chromium and iron, chosen on the contrary for their high sensitivity. Results reported here on the transformations produced by the discharges on these samples surfaces were acquired by scanning electron microscopy (MEB) for what concerns the morphological aspects and by photoelectron spectroscopy (XPS) for the identification and quantitative measurements of the

[b] Electronic address: alice.goldman@lpgp.u-psud.fr

metallic oxides formed on them [4].

3. RESULTS AND DISCUSSION

3.1. Distribution profiles of the surface products

First, we may mention that no difference appears in dimensions, between the two areas concerned with the discharge / surface interaction, that one corresponding to the ions impact, defining the discharge current profile on the electrode [5] and that one covered with the discharge surface products, visible to the naked eye because of a surface tarnishing and the production of which is due, for a large part, to the reactive neutrals of the discharge dominating its chemistry. This shows that, contrary to the case of the chemistry induced by streamers out of their volume [6], the neutrals in glow discharges keep, through the whole gap, the directed movement conferred to them by the ions in the gas through kinetic energy and momentum transfer, so limiting their effects on the plane electrode over the same area as the area covered by the impinging ions.

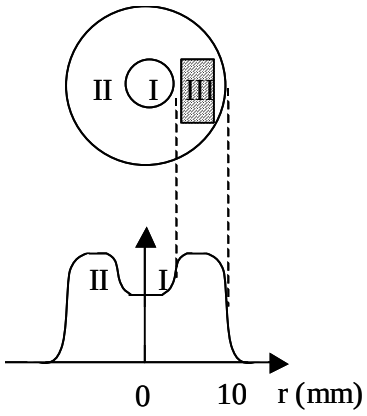


FIGURE 1. Front view and schematic distribution profile of the surface products after a corona treatment in a glow regime. I : the central region; II : "the ring" where the XPS analyses have been performed; III : the relative importance of the area covered by the analyses in "the ring".

What now with the distribution of the surface products inside this discharge / surface interaction area that has a diameter of ~ 30 mm in our working conditions? If in nature the products are everywhere the same over the whole area, their distribution profile is very different from the current distribution profile. As schematically sketched in Fig. 1 according to XPS results, the highest densities of the surface products are not found in the central region, but over a "ring" of ~ 5 mm width with an internal diameter of ~ 10 mm. This important difference between the surface products profile and the current profile should be due to repercussions on the surface chemistry of hydrodynamic effects in the gas. However this does not prevent the surface products amounts to increase everywhere in the same proportions as the current.

3.2. 3Microscopic aspects of the surface products layers

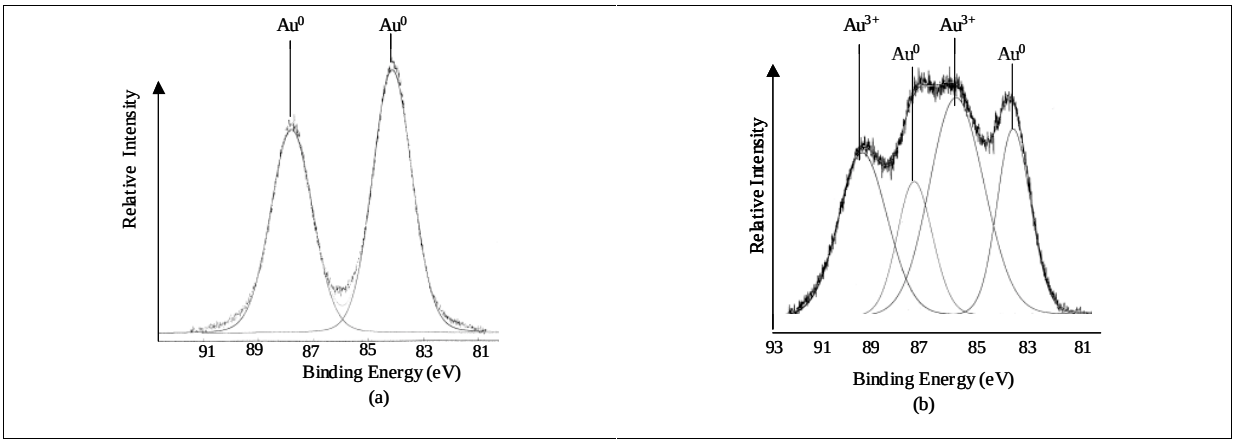
Now let us see how things evolve at a more microscopic scale, as observed by electron microscopy. In a general manner, after a given time, let say one hour, one ends with quite homogeneous oxidized layers which can present some typical aspects depending on the sample material, typically cracks that can be in particular observed on chromium and aqueous droplets of a micronic size that can be observed on any material, even on insulating ones, as soon as some water vapour is present in the discharge atmosphere. XPS resolution does not allow to get specific data on the content of these droplets, but different observations are consistent with the presence of water inside.

(i) On the three different metals studied, XPS revealed, at 232.7 eV, a O_{1s} peak suggesting [6, 7] that water was trapped inside.

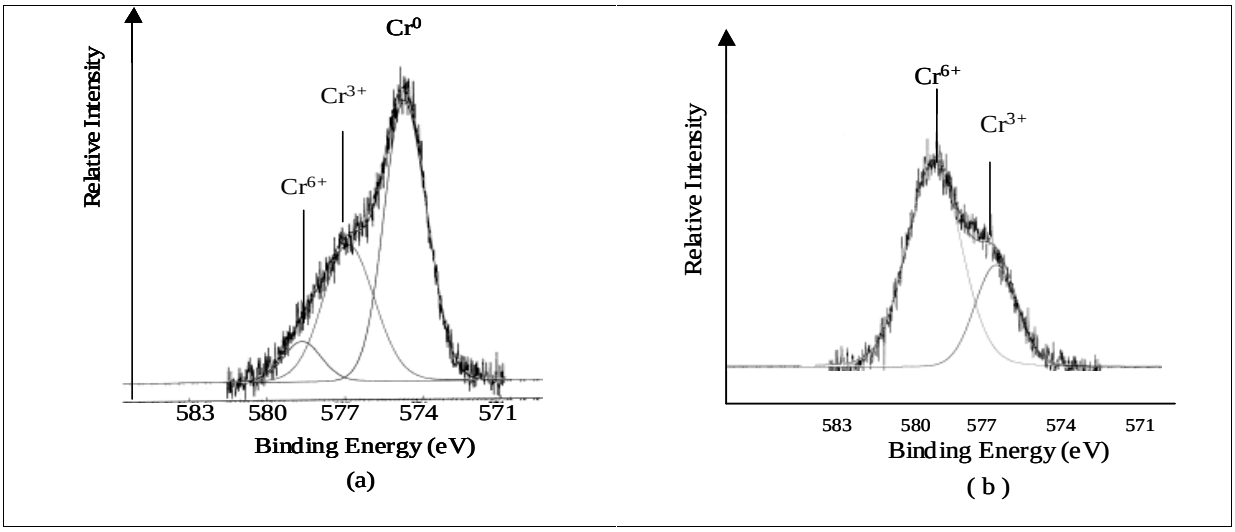
(ii) They withstand the vacuum of the scanning electron microscope (10^{-5} Pa), but not that one of the XPS apparatus (~ 10^{-7} Pa) in which they are subjected to sublimation, but keep their surface products appearing as stains when looked afterwards in the MEB.

(iii) A thermal treatment of the samples at quite low temperatures (1 hour at 395 K in a furnace) is sufficient for their elimination, that shows that they are very unstable and extrinsic to the substrate, even if containing atoms from it.

GOLD



CHROMIUM



IRON

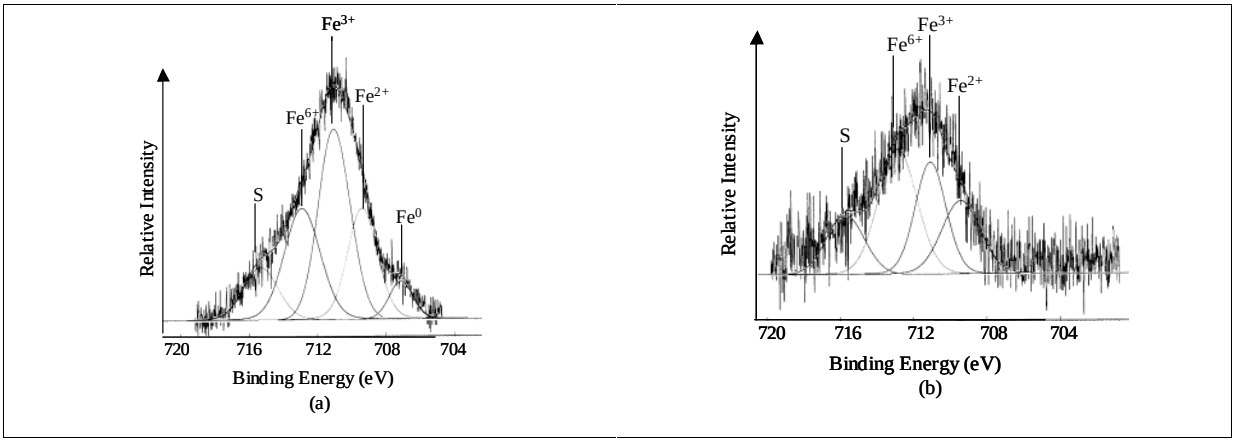


FIGURE 2. XPS spectra on the metallic low-field electrodes (a) working as cathodes; (b) working as anodes

In our opinion, the fact that water is present in the droplets is important because it allows to consider that the discharge / surface interaction proceeds through an interface chemistry in liquid phase. It brings strength to an old speculative assumption which led us to enter upon studies with an aqueous sample in place of the metallic low-field electrode, studies which helped us to establish the acid nature of the gas / surface interface [8, 9].

3.3. The surface products according to the discharge polarity

The oxidation of gold, chromium and iron has been investigated in both polarities with the discharge current and the exposure time selected so as to get a 0.28 C electrical flow of charge for almost all cases, as said ahead. Results are summarized in the XPS spectra presented in Fig. 2, which, in all cases, correspond to analyses performed on the "ring" where are found the largest densities of surface products.

- On gold, the less sensitive metal to oxidation, no oxide is found after the treatment in positive polarity while some Au_2O_3 oxide (Au^{3+} peak) is found after the treatment in negative polarity.

- On chromium, which provides peaks easy to fit, after the treatment in positive polarity, one still observes the Cr^0 metal peak, but also already a Cr^{3+} peak and even another oxide peak that should correspond to a Cr^{6+} peak. After the treatment in negative polarity, the Cr^0 peak is no more observed even with only 0.07 C instead of 0.28 C and then, the oxide peak which we suppose to correspond to Cr^{6+} is itself clearly higher than the Cr^{3+} peak obtained in the same case.

- On iron, the results are very similar to that obtained on chromium, but with spectra less easy to handle as known by the specialists of XPS analyses. As on chromium, the metallic peak, here Fe^0, is observed only after the treatment in positive polarity and again an oxide peak is found in both polarities treatments at an unusual high oxidation state attributed to Fe^{6+}, with an intensity clearly greater after the negative polarity treatment than after the positive polarity one.

All these results clearly show that oxidation prevails in all cases, on the cathodes as on the anodes, even with very high oxidation states as Cr^{6+} and Fe^{6+} observed in the two polarities. The only difference lies in the peaks intensities: for equivalent charge flows, the oxidation is always much stronger on the anodes than on the cathodes.

3.4. Putting into evidence the basic effects of the discharge positive ions in opposition to the acid effects of the negative ones [10]

A gold polished sample was first treated 1 hour at 80 µA (~ 0.28 C) with a negative polarity discharge and a XPS spectrum of the Au 4f level recorded after this first treatment. This spectrum (Fig. 3, spectrum a) exhibits two shoulders, which can be, according to the spectrum of Fig. 2 corresponding to the gold sample, identified as due to the Au^{3+} peaks corresponding to the gold oxide Au_2O_3.

Immediately after its removal from the XPS instrument, the sample was treated again, but this time with the positive point discharge (4 hours at 20 µA, i.e. with the same charge flow as in the first step, but now in the opposite discharge polarity) and a new XPS spectrum recorded (Fig. 3, spectrum b). We see on this spectrum that the shoulders which were observed on the first spectrum (spectrum a) after the negative point treatment have disappeared with the second treatment in the opposite polarity, that evidences that the Au_2O_3 oxide formed on the electrode working as an anode has been reduced by inversing the polarity for the second treatment.

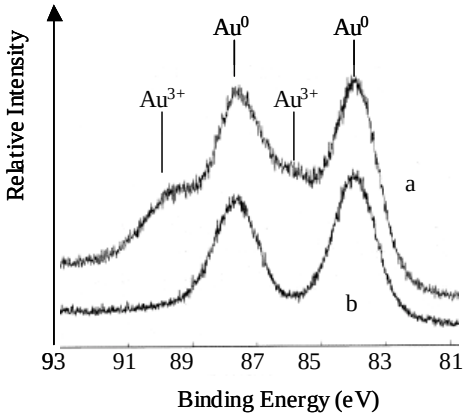


FIGURE 3. XPS spectra of the Au 4f doublet on a gold sample (a) first oxidized with a negative corona treatment; (b) afterwards treated with a positive corona for reduction of the oxide formed in step (a).

Now, we have to remember that corona chemistry is mostly a chemistry of neutral species which, in air, are almost oxidizing ones. It is in particular why oxidation effects have been seen in the present work, as in previous ones, to predominate whatever the polarity of the treatment. The experiments carried out show that a reduction process can however be obtained, thanks to the positive ions provided by the second step of the treatment. So, provided that a sufficient amount of water vapour is present in the corona gap to get water on the low field electrode, even in the form of droplets, it is possible to observe strong oxidation phenomena, but reduction ones can also be observed as in electrochemistry.

4. CONCLUSIONS

The work presented on the corona chemistry in point-to-plane electrode systems has first shown the high degree of oxidation that can be provided by air coronas in glow regimes, particularly in the negative point polarity. Secondly, the reversibility of the process has been demonstrated by achieving to reduce the Au(III) oxide to Au(0) metal through the action of the glow discharge in positive polarity over a pre-oxidized gold surface.

REFERENCES

[1] Goldman A., Goldman M., and Sigmond R. S., Corrosion and ageing mechanisms investigated by corona discharges. In: *Proc. 19 th Int. Conf. on Phenomena in Ionized Gases*, ed. by B. Perovic and D. Tosic, Beograd, Yugoslavia, Invited papers Vol., 1989, pp. 322-31

[2] Le Ny R., Boulloud A., and Labbé J. P., Influence of negative corona discharges on copper electrodes in room air. In: *Proc. 8th Int. Conf. on Gas Discharges and Their Appl.*, Oxford, U. K., 1985, pp.458-61

[3] Pinart J., Smirdec M., Pinart M. E., Aaron J. J., Benmansour Z., Goldman M., and Goldman A., *Atmospheric Environment*, **30**, 129-32 (1996)

[4] Jouve G., Goldman A., Goldman M., and Haut C., *J. Phys. D : Appl. Phys.* **34**, 218-21 (2001)

[5] Sigmond R. S., *J. of Electrostatics*, **18**, 249-272 (1986)

[6] Wagner C. D., Zatko D. A., and Raymond R. H., *Anal. Chem.*, **52**, 1445 (1980)

[7] Maurice V., Yang W. P., and Marcus P., *J. Electrochemical Soc.*, **143**, 1182 (1996)

[8] Brisset J. L., Doubla A., Amouroux J., Goldman M., and Goldman A., *Rev. Int. Hautes Temp. Réfract., Fr.*, **25**, 229-236 (1989)

[9] Goldman A., Goldman M., Sigmond R. S., and Sigmond T., Analysis of air corona products by means of their reactions in water. In: *Proc. 9th Int. Symp. on Plasma Chemistry*, ed. by R.d'Agostino, Pugnochiuso, Italy, 1989, pp. 1654-8

[10] Brisset J. L., Doubla A., Amouroux J., Goldman M., and Goldman A., *Rev. Int. Hautes Temp. Réfract., Fr.* **25**, 237-45 (1989)

AC BARRIER PIN-PLANE CORONA: SIMILARITIES AND DISTINCTIONS TO DC POSITIVE AND NEGATIVE CORONAS AND DIELECTRIC BARRIER DISCHARGE

Yu. S. Akishev, A.V. Demyanov, V. B Karal'nik, A. E. Monich, N. I. Trushkin
SRC RF TRINITI, Troitsk, Moscow region, 142190, Russia

Abstract: Alternative current (AC) atmospheric pressure corona between the sharpened pin and metallic plane covered with a thin dielectric material is widely used in applications. This kind of discharge can be classified the AC barrier corona (ACBC), because one would expect that ACBC exhibits the properties, which are close to those of both AC dielectric barrier discharge (DBD) and DC (direct current) positive and negative pin-plane coronas. Experimental and numerical study on properties of ACBC in air, nitrogen, Ar, He at atmospheric pressure was carried out. A detailed comparison between ACBC and DC positive and negative pin-plane coronas was made.

1. INTRODUCTION

AC atmospheric pressure corona between the sharpened pin (or blade) and metallic plane covered with some thin dielectric material is widely used in applications. It is clearly that presence of dielectric barrier on the metallic plane provides the similarity this discharge to a classical DBD [1] excited in narrow gaps. On the other side, an existence of the sharpened metallic pin will ensure an appearance of a corona discharge in the gap with a barrier. Indeed, as a rule, the length of inter-electrode gap and frequency of the applied voltage do not exceed several millimeters and tenths of kilohertz respectively. Under such experimental conditions, the characteristic time for ion drift across inter-electrode gap is small in comparison with a half-period of the applied sine voltage. It means the charge generated in the vicinity of a sharpened electrode fills quickly the bulk, and corona discharge has a time to be formed in a pin-plane gap during each positive and negative half-periods of alternative voltage.

Such type of discharge can be named the AC barrier corona (ACBC), because one would expect that ACBC exhibits the properties, which are close to those of both AC DBD and DC positive and negative pin-plane coronas. In such case, a spatial-temporal evolution of AC barrier pin-plane discharge at positive and negative half-periods will be controlled by evolution of quasi-stationary positive and negative coronas. From physical point of view, it is interesting to consider more particularly the similarities and distinctions of ACBC to DBD and DC coronas. We have carried out extensive experimental and numerical studies on physical properties of a pin-plane ACBC, and a detailed comparison between properties of this kind of discharge and both DBD and DC steady-state positive and negative coronas was done.

2. EXPERIMENTAL SETUP

Experimental study of ACBC was carried out with use of an acrylic plastic gas discharge chamber of 150x150x150 mm^3 in size (Fig. 1). Pin-plane electrodes were built-in the chamber. The inter-electrode gap was varied from 1.5 to 30 mm. The radius of a pin's tip equals 0.1 mm. The plane metallic electrode was fabricated in a form of a disk of 100 mm in diameter. The edges of this disk were smoothly rounded. The different polymer films like polyethylene, polypropylene, Teflon, etc. were placed on the plane electrode. A thickness of films lies in the range 30-75 of μm.

Ambient air, nitrogen (99.999% of N_2), argon (99.99% of Ar) and helium (99.99% of He) were used in experiments as process gases. To maintain the initial purity of process gases within the discharge chamber, we used a weak flow of Ar, He and N_2 through chamber (gas velocity less than or equal to

0.1 m/s), and sustained this quasi-static gas at a pressure slightly in excess of ambient. An additional series of experiments was performed with air at lower pressure (P=380 Torr).

We used two power supplies for the experiments; the first has a fixed sine frequency, 50 Hz, and voltage amplitude up to 35 kV. This power supply was used for excitation of AC barrier corona in ambient air. The amplitude U_a and frequency f of the second power supply could be varied up to 4.5 kV, and from 50 to 10^5 Hz, respectively. The latter power supply was used for excitation of ACBC in Ar, He and N_2. The waveforms of current and voltage were recorded with an oscilloscope having a bandwidth of 10 MHz. The both a charge transferred through inter-electrode gap during one half-period and active discharge power were determined from the Volt-Coulomb Characteristics (VCC). Remind, VCC is displayed on the oscilloscope screen in a form of Lissajous figure; the area outlined with Lissajous figure corresponds to active energy dissipated by ACBC over one period.

3. EXPERIMENTAL RESULTS

ACBC in all gases investigated appears in two states like to those in common DBD and DC coronas, which are named the diffusive (i.e. homogeneous) and streamer (i.e. non-homogeneous or filamentary) regimes. These different regimes can exist under the same U_a but at various (positive and negative) half-periods. In the beginning, we present therefore some discharge characteristics averaged over period of ACBC.

The most outstanding distinction of ACBC from DBD and DC coronas is an ability to expand readily over the surface of a dielectric barrier. It is well known [2], the current distribution over metallic plate for DC pin-plane corona is characterized by Warburg low. According to this low, the effective radius R_w of a corona cross-section at the plane equals nearly 0.7d (d is the length of inter-electrode gap). To a first approximation, the radius R_W depends only slightly on both the type of gas and corona current regime (diffusive or streamer). In bulk of the gap, the radius of DC corona current channel R_c increases with distance from the pin approximately like this manner: $R_c \sim R_w (x/d)^{1/2}$ ($R_w \cong 0.7d$ is the Warburg radius; x is the coordinate originated from the tip of a pin). It means DC corona current tube has a convex shape.

An existence of a dielectric barrier on the metallic plate results in both a strong spreading the pin-plane discharge over surface and modifying the shape of a corona current tube from a convex form to the concave one. The spreading of ACBC over dielectric surface is most pronounced in Ar. In this gas, the effective corona radius R_c characterizing the area occupied with surface streamers ranges up to several tens (!) of d. Helium and nitrogen are next gases in this series. The spreading of ACBC in air appears only slightly. The effective radius of ACBC in air does not practically depend on U_a, and equals almost Warburg radius R_w. It means the properties of ACBC in air at positive and negative half-periods must be close to those of DC positive and negative coronas.

The dependence of the effective corona radius R_c in Ar and He on amplitude of the applied voltage U_a is presented in Fig. 2. In the case of electropositive gases, the effective corona radius R_c has a different behavior at low and high currents (we mean an average discharge current during a single half-period of ACBC). At low average currents (i.e. under homogeneous regime), radius R_c, as in air, does not practically depend on U_a. One can state therefore that diffusive ACBC in Ar, He and N_2 exhibits itself like DC positive and negative coronas.

Once streamers occur at higher average currents, ACBC in these gases expands extremely over barrier in a form of long and branching surface streamers. In contrast to DC coronas, the effective radius R_c in this regime does not practically depend on the inter-electrode distance d. The sharpened electrode possesses a strong electric field around itself and provokes the formation of streamers under lower voltage across the inter-electrode gap than that in a classical DBD. It follows that streamers in ACBC are weaker than those are in a barrier discharge between plane electrodes. Therefore, ACBC with streamers in electropositive gases has nothing in common with DBD and DC coronas.

Typical VCCs of ACBC at lower (without streamers) and higher (with streamers) average currents are presented in Fig. 3. Once streamers occur, the charge Q transferred through gas gap during a single

half-period increases dramatically with the amplitude U_a and frequency f (Fig. 4). At the same frequencies and high amplitudes U_a, the magnitudes of Q for ACBC in Ar and He are close to each other despite the fact that effective radii of these discharges differ greatly in size (see Fig. 2). It seems, this correlates with the most density of the surface streamers observed in He in comparison with those for ACBC in Ar and other gases.

It is well known, the current waveform of a classical DBD has the same shape for the positive and negative half-periods. In the case of ACBC, this symmetry for the current waveforms is absent (Figs. 5, 6), which is to say that ACBC has different properties at positive and negative half-periods. In this connection, it is reasonably to give a detailed description of ACBC for positive and negative half-periods separately.

At positive half-period, ACBC in all gases appears in two states that are diffusive and streamer regimes. The diffusive regime is characterized by absence of sharp current splashes in oscillograms (Fig. 5a), and it exists within a narrow region of the initial corona currents no greater than tens of μA.

The streamer regime is a basic one of ACBC at positive half-period. At this regime, ACBC is non-uniform. It exhibits itself in a form of numerous non-stationary streamers (thin current filaments) spreading chaotically over the barrier surface. This regime is characterized by sharp current splashes in oscillograms. The amplitudes of these splashes range from tens to hundreds of mA (Fig. 5b). A quantity of splashes in a single half-period increases with amplitude of the applied voltage U_a. At the fixed magnitude of U_a, a number of splashes depends on a sort of the process gas. ACBC in He shows the most number of splashes (Fig. 6a). It correlates with the most density of the surface streamers in He as noted above.

At negative half-period, ACBC in all gases appears solely in a diffusive regime at low and high currents. This property is identical to that for DC negative corona, which does not show the streamer regime up to spark. The current splash of small amplitude at the beginning of a negative half-period (Figs. 5, 6) is associated with a diffusive breakdown of the gas gap (or ignition of a negative corona). After this, the diffusive quasi-stationary stage like that in common DC negative corona has been established. In the case of air, the trains of regular current pulsations (Trichel pulses) occur at the beginning and the end of a negative half-period (Fig. 6b). At small average currents, the train of current pulsations was observed also in Ar. A frequency of self-running current pulsations for DC negative corona in N_2 and He is too low, that results in absence of such pulsations for ACBC in these gases at frequencies of the applied voltage $f \geq 1$ kHz. So, the diffusive regime of ACBC at negative half-period is similar to DC negative corona rather than to diffusive DBD, because homogeneous DBD in narrow gap is sustained only at very low current densities corresponding to subnormal glow discharge [3].

4. NUMERICAL RESULTS

The numerical calculations of ACBC using the electric scheme drown in Fig. 7 were performed. The Volt-Ampere Characteristics of ACBC for diffusive regimes in <+> and <–> half-periods were taken in a parabolic form like that for common DC positive and negative coronas: $I^{\pm} = k^{\pm} \cdot U \cdot (U - U_0^{\pm})$, where k is the dimensional coefficient; in the case of electropositive gases $k^+ << k^-$, in the case of air $k^+ \cong k^-$. A value U_0^+ coincides with the inception voltage U_*^+ of a positive corona. In the negative corona, the accordance of U_0^- with an inception voltage U_*^- depends on sort of the process gas. In the case of electropositive gases, the ignition voltage of a negative corona exceeds its operating voltage: $U_*^- > U_0^-$; in the case of air at atmospheric pressure $U_*^- \cong U_0^-$. The circumstances pointed were taken into account at the modeling of ACBC under negative half-period. Besides, the model for ACBC under positive half-period incorporates the transition from diffusive regime to streamer one, if the voltage imposed across the gap reaches the critical magnitude $U_s > U_*^+$. After this transition, the discharge voltage drops down drastically. The magnitudes of $U_0^{\pm}$, $U_*^{\pm}$, U_s were taken from the experiment.

The calculations (Fig. 8) revealed one more property, which far differs ACBC from a classical DBD. In the event, a great negative charge on a barrier exists during most part of both negative and positive

half-periods. A positive charge on the surface equals almost zero at the rest of a positive half-period. An existence of different (or non-symmetrical) current regimes -diffusive and streamer- at negative and positive half-periods is physical reason of preferential accumulation of the negative charge on treated surface in ACBC. If ACBC is used in applications like surface modification, it is necessary to take this interesting property of AC pin-plane barrier corona into account.

ACKNOWLEDGMENTS

This work was supported in part by the RFBR (Project # 02-02-16913).

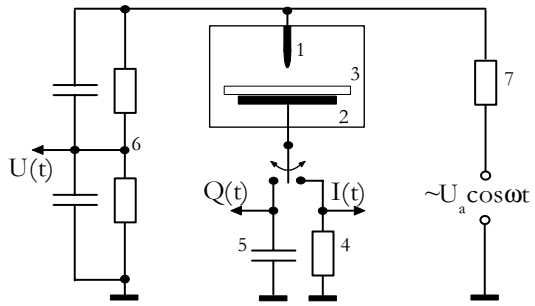


FIGURE 1. Scheme of experimental setup for ACBC investigations. 1 is a pin; 2 is the plane electrode; 3 is a dielectric film; 4 is the current shunt with a small inductance; 5 is the capacitor to measure a charge transferred by ACBC; 6 is the voltage divider; 7 is a ballast resistor.

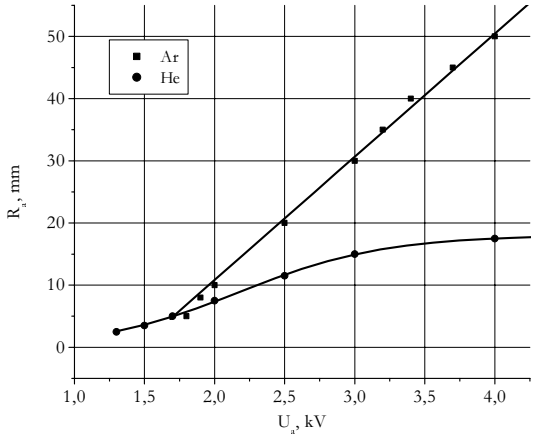
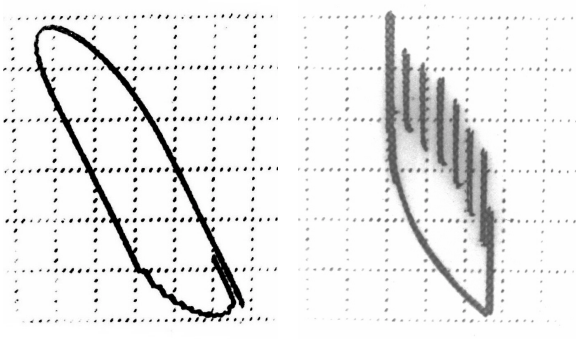


FIGURE 2. The effective visual radius R_c of ACBC occupied by this discharge on the surface of barrier vs the applied voltage amplitude U_a. Inter-electrode gap d=1.5 mm; powering frequency f=0.4 kHz for ACBC in He; f=1 kHz for ACBC in Ar.



a) **b)**

FIGURE 3. Volt-Charge Characteristics of ACBC in Ar at different current regimes. f=0.4 kHz. **a)** diffusive regimes at both negative and positive half-periods; the voltage amplitude U_a=3 kV; d=6 mm; vertical scale is 1 kV/div; horizontal scale is 1 nC/div. **b)** diffusive regime at negative half-period and streamer regime at positive one; U_a=3 kV; d=1.5 mm; vertical scale is 1 kV/div; horizontal scale is 200 nC/div.

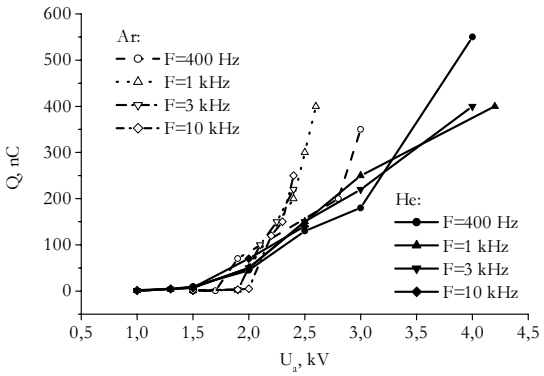


FIGURE 4. Charge Q transferred by ACBC through gas gap during single half-period vs the applied voltage amplitude U_a. Inter-electrode gap d=1.5 mm; all other experimental parameters are shown in figure.

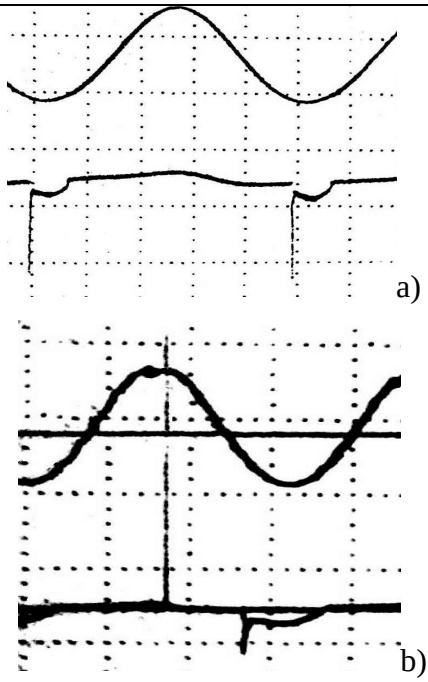


FIGURE 5. Representative experimental oscillograms of sine voltage and current (lower curves in photos) for ACBC under different current regimes. **a)** diffusive regime at both half-periods; Ar; d=6 mm; f=400Hz; [I]=0.1 mA/div; [U]=4kV/div; [t]=0.5 ms/div. **b)** diffusive regime at negative half-period and streamer regime at positive one; N_2; d = 1.5 mm; f = 3 kHz; [I] = 2 mA/div; [U] = 4 kV/div; [t] = 0.1 ms/div.

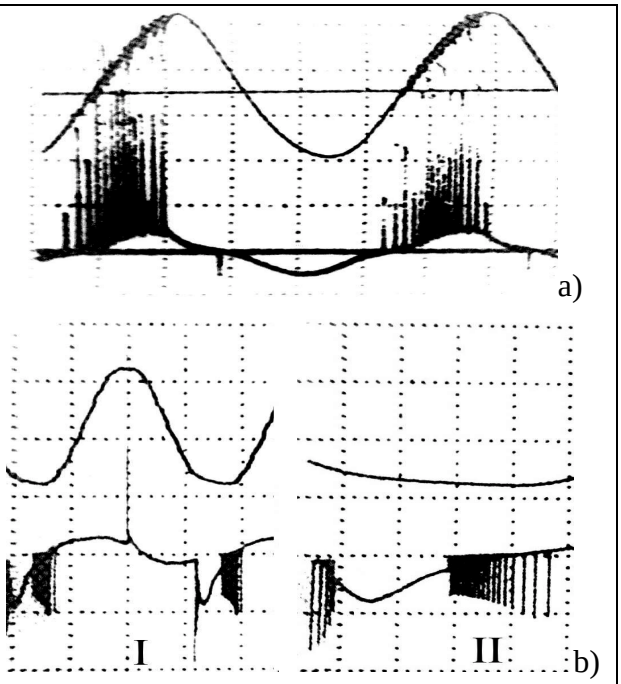


FIGURE 6. Representative experimental oscillograms of sine voltage and current (lower curves in photos) for ACBC under diffusive regime at negative half-period and streamer regime at positive one. **a)** He; d = 1.5 mm; f = 1 kHz; [I] = 4 mA/div; [U] = 2kV/div; [t] = 0.2 ms/div. **b)** air, P = 380 Torr; d = 5 mm; f = 3 kHz; [I] = 0.4 mA/div; [U] = 4 kV/div; photo I: [t]=0.1 ms/div; photo II: [t]=20 μs/div.

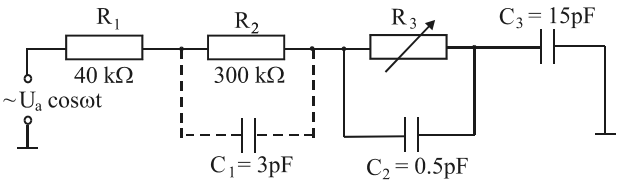


FIGURE 7. Scheme of equivalent electrical circuit that was used for modeling of ACBC. R_1 is the source resistance; R_2 is the ballast resistor; R_3 is the effective resistance of ACBC determined by its volt-ampere characteristics; C_1 is a stray capacitance of an external circuit; C_2 is capacitance of gas gap; C_3 is capacitance of barrier.

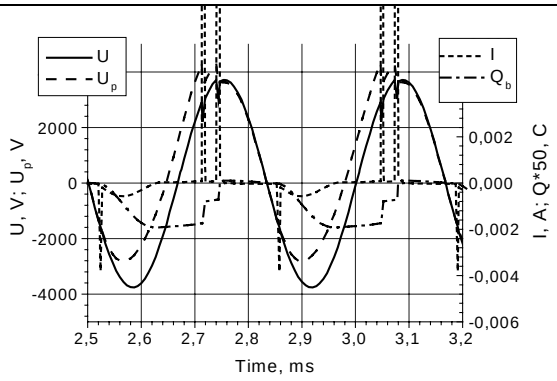


FIGURE 8. Numerical calculations of a voltage drop U_p across gas gap and current I of ACBC in N_2 under applied sine voltage U. Q_b is a charge accumulated on the surface of a barrier having a capacitance of 25 pF. Pin-plane gap is 1.5 mm. Power frequency is 3 kHz. The amplitudes of two current splashes at positive half-period equal about 70 mA.

REFERENCES

[1] B.Eliasson and U. Kogelschatz, *IEEE Trans. on Plasma Sci.*, **19**, 309-22 (1991)

[2] E. Warburg, "Ueber die Spitzenentladung", -Wied. Ann., **67**, 69-83 (1899); -Charakteristik des Spitzenstormes. In: *Handbuch der Physik*, Vol. 4, Springer Verlag, Berlin, 1927, pp. 154-155

[3] F. Massines, R. Messaourdi and C. Mayoux, *Plasmas and Polymers*, **3**, 43-59 (1998)

EXPERIMENTAL STUDY OF REPETITIVE ELECTRICAL BREAKDOWN IN THE BARRIER DISCHARGE IN AIR

H.-E. Wagner[a], K. V. Kozlov[b], R. Brandenburg[a], P. Michel[a]

a) Institute of Physics, Ernst-Moritz-Arndt University of Greifswald, 17489 Greifswald, Domstr.10a, GERMANY
b) Moscow State University, Department of Chemistry, 119899 Moscow, RUSSIA

Abstract. The technique of spatially resolved cross-correlation spectroscopy is used to carry out diagnostic measurements of the barrier discharge (BD) in flowing synthetic air (80%N_2 + 20%O_2) at atmospheric pressure. Quantitative estimates for electric field strength E(x,t) and for relative electron density $n_e(x,t)/n_e^{max}$ are derived from the experimentally determined spatio-temporal distributions of the luminosity for the spectral bands of the 0-0 transitions of the 2nd positive system of N_2 (λ = 337.1 nm) and the 1st negative system of N_2^+ (λ = 391.5 nm). These results are used to test the validity of some physical models of electrical breakdown in a BD.

1. INTRODUCTION

Experimental and theoretical study of barrier discharges (sometimes also referred to as dielectric-barrier discharges or silent discharges) has a long history [1,2] in connection with their wide industrial application in ozone generation technologies. However, despite of considerable progress in understanding the structure and properties of these discharges, that was made mostly during the last few decades, the knowledge of this subject nowadays appears to be insufficient to provide an adequate quantitative theoretical description for the BD behavior [3].

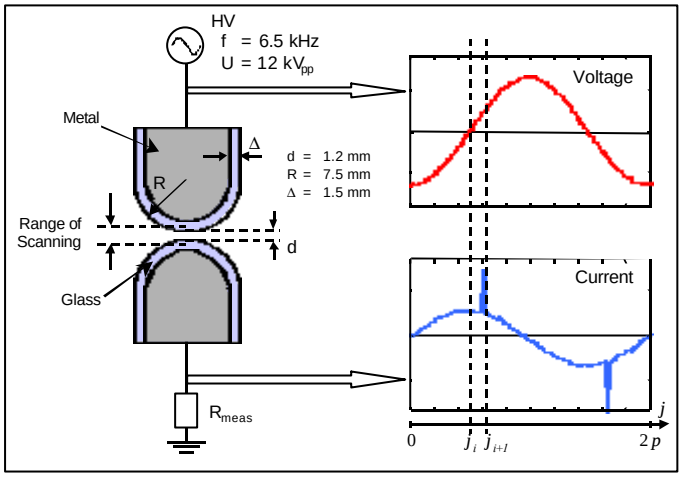
A BD in oxygen as well as in air consists of a number of microdischarges (MDs, sometimes also referred to as discharge filaments) of nanosecond duration, randomly but uniformly distributed over the dielectric surface. Under the typical conditions of the BDs operation (discharge gap width of 1 - 2 mm, dielectric: glass of 1 - 2 mm thickness and dielectric constant ε = 5 - 7, gas pressure: 1 - 3 bar), these MDs can be treated as tiny plasma-chemical reactors that act independently from one another [1,2]. That is why the study of the dynamics of a single MD is one of the most important research topics in the field of the BD physics and chemistry. It is hard to carry out any experiment with a single MD, since high temporal resolution (in a sub-nanosecond range) and spatial resolution (down to 10^{-1}-10^{-2} mm) are required. Thus, it is no wonder that a great deal of effort has been devoted to computer simulation of the MD development [3].

The potentially powerful method of quantitative estimating of electric field strength in gas discharges in air at atmospheric pressure from experimentally determined distributions of the emission intensities of both the second positive (0-0) band of N_2 and the first negative (0-0) band of N_2^+ (e.g., see [4,5]) has not been used in practice yet, since no arrays of experimental data with the required sensitivity and spatio-temporal resolution were available.

Our preliminary experiments on the BD investigation by cross-correlation spectroscopy (CCS) [6] have shown that this technique is able to comply with the requirements mentioned above. In the present paper, we report the results of an accomplished procedure of a BD plasma diagnostics by means of the spatially resolved CCS, including the quantitative estimates for electric field and relative electron density within a MD channel. All the measurements and calculations have been performed for a BD with the symmetrical electrode arrangement ("glass – glass"), discharge gap width of 1.2 mm, in flowing synthetic air (80% N_2 + 20% O_2) at atmospheric pressure.

[a] Electronic address: wagner@physik.uni-greifswald.de

2. EXPERIMENTAL DETAILS



A scheme of the used discharge cell is shown in fig.1. The BD was driven by the sinusoidal alternative voltage (frequency: 6.5 kHz, peak-to-peak amplitude: 12 kV). The voltage amplitude was adjusted so as to maintain the discharge in the "one-to-one MD" mode (i.e. a mode when the only one MD occurs per voltage half-period, as it is shown in fig. 1).

The detailed description of the used CCS-apparatus, measurement technique, as well as the procedure of the quantitative numerical analysis of the measurement data to evaluate local field strength and relative electron density, is presented elsewhere [6,7].

FIGURE 1. Electrode arrangement with the indicated range of axial scanning, and a typical example of the oscillograms of voltage and current for the "one-to-one MD" operation mode.

3. RESULTS AND DISCUSSION

Some results of the spatio-temporally resolved spectroscopic measurements are presented in fig.2.

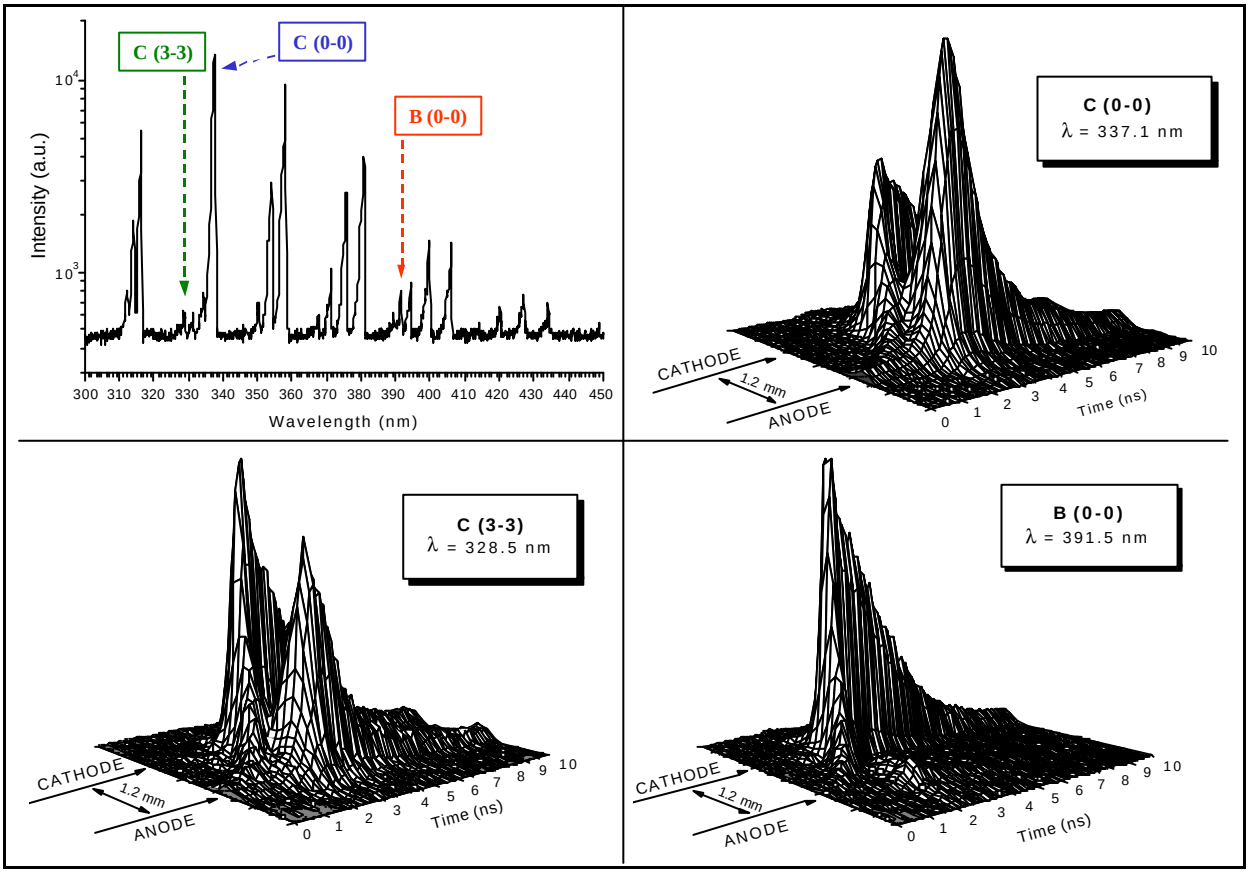


FIGURE 2. Spectrum of the BD in air (p = 1 bar, d = 1.2 mm), and spatio-temporal distributions of the emission intensities for the indicated spectral bands (measurement results).

The spatio-temporal distributions of the light emission intensity of C(0-0), C(3-3), and B(0-0) follow

the reaction rates (1,2,3), respectively [7,8]. Furthermore, these reaction rates are directly proportional to electron density, while the rate constants are strongly dependent on electric field [8].

$$e + N_2\left(X^1\Sigma_g^+\right)_{n=0} \rightarrow N_2\left(C^3\Pi_u\right)_{n'=0} + e \qquad \left(\Delta E = 11.0eV\right) \qquad (1)$$

$$e + N_2\left(X^1\Sigma_g^+\right)_{n=0} \rightarrow N_2\left(C^3\Pi_u\right)_{n'=3} + e \qquad \left(\Delta E = 11.8eV\right) \qquad (2)$$

$$e + N_2\left(X^1\Sigma_g^+\right)_{n=0} \rightarrow N_2^+\left(B^2\Sigma_u^+\right)_{n'=0} + 2e \qquad \left(\Delta E = 18.7eV\right) \qquad (3)$$

Therefore, a qualitative analysis of the results presented in fig. 2 leads to the following conclusions. The wave of light intensity, which is observed most clearly for the spectral band B(0-0) with a threshold energy of 19 eV, reveals a wave of electric field (ionizing wave, or streamer [1,3,5-7]). Two peaks of the luminosity distributions are of different physical nature, namely, there is a higher electric field and a lower electron density near the cathode, than near the anode.

The results of the quantitative analysis of the measurement data[1] are shown in fig. 3.

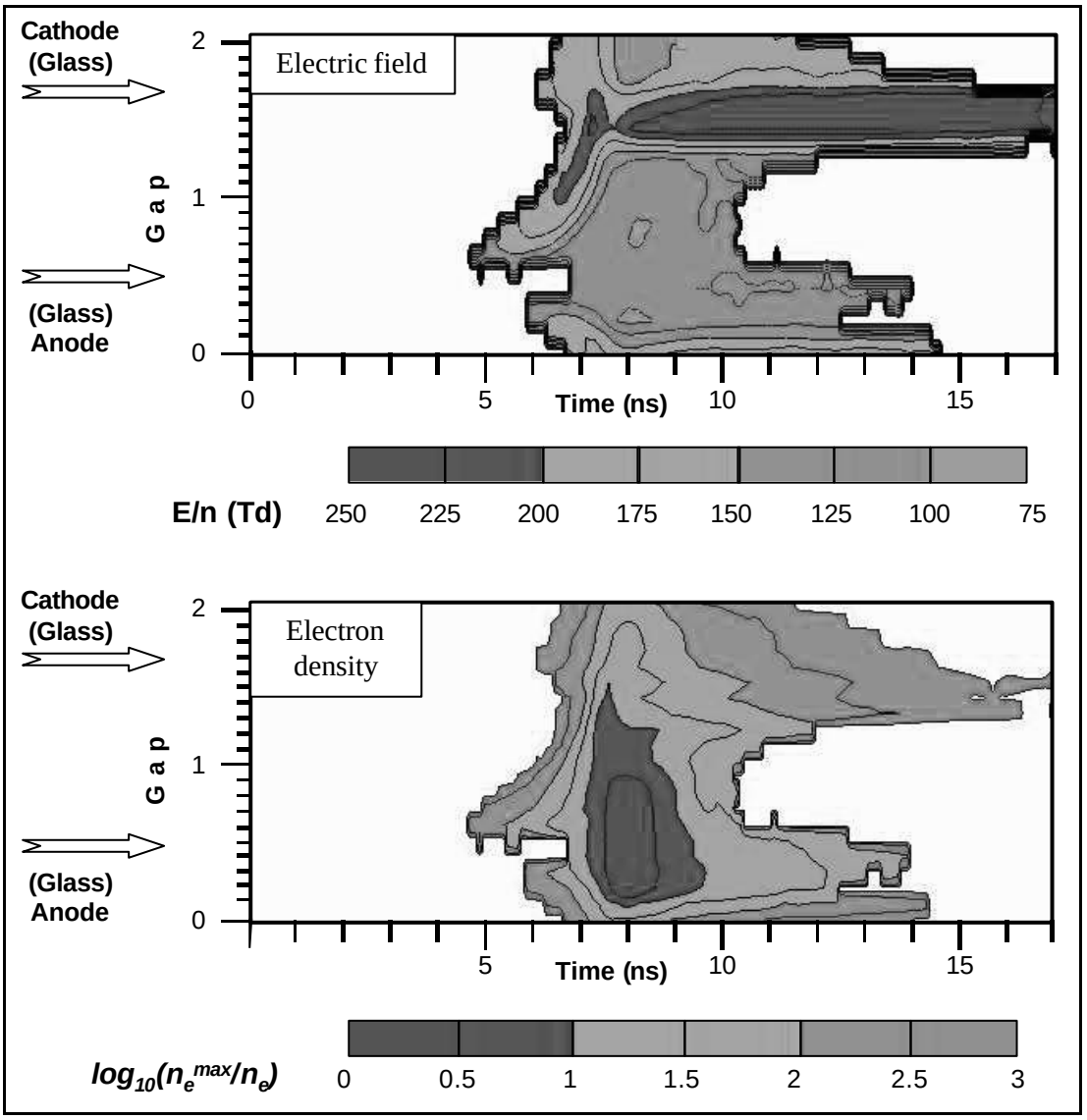


FIGURE 3. Calculated distributions of electric field and electron density. The outer boundary of these 2-D arrays is limited by the condition (I_B, I_C)>5 counts/channel. Arrows indicate the positions of electrode tips (fig.1)

[1] The detailed description of the used procedure of data processing is presented in [6,7].

Since the procedure of the evaluation of electric field strength and relative electron density from the spatio-temporal distributions of the spectral bands C(0-0) and B(0-0) includes numerical differentiation of experimentally determined radiation intensities $I_{B,C}(x,t)$ over time [6,7], it is very sensitive to the statistical noise. Therefore we carried out a careful preliminary smoothing. Furthermore, in order to avoid any artifacts, we restricted the area of our calculations by the condition (I_B, I_C) > 5 counts/channel, which was found to provide sufficient reliability and accuracy of the results. That is why the spatio-temporal distributions of electric field strength and electron density are presented in figure 3 in a smaller area than the corresponding experimental data in figure 2.

These results confirm the main conclusions derived from the qualitative analysis of the luminosity distributions. A cathode-directed wave of electric field is clearly seen in figure 10. High electric field is observed mostly near the cathode, and high electron density, on the contrary, near the anode.

It is interesting to compare quantitatively some basic characteristics of the MDs corresponding to the different models of the mechanism of electrical breakdown in BD in air. These models can be characterized briefly as follows.

Model A. Electrical breakdown of the discharge gap occurs due to accumulation of the positive space charge during initial phase of the MD development. This model has been implicitly used in a number of papers dealing with computer simulation [3].

Model B. Initial accumulation of the negative space charge within the MD channel caused by the effect of surface charges [3]. This model has been originally proposed to explain the experimentally found phenomenon of the pre-breakdown anode glow [9]. Since the initial anode glow was observed in our experiments (it is clearly seen in fig.2 for the bands C(0-0) and C(3-3)), our results are assumed to correspond to the model B.

For the comparison (fig.4), we have chosen two main parameters of the cathode-directed streamers, namely velocity and electric field strength. As a typical example of computer simulation (accomplished within the frame of the model A), we have chosen the 2-dimensional modeling of a MD development in air at atmospheric pressure for the discharge gap of 1 mm width [10]. The streamer velocities were determined from their tracks, that are clearly seen on the plots of he MD luminosity distribution for spectral band B(0-0) in the case of our results (fig.2), and on the simulated streak-photo of the MD which is presented in [10].

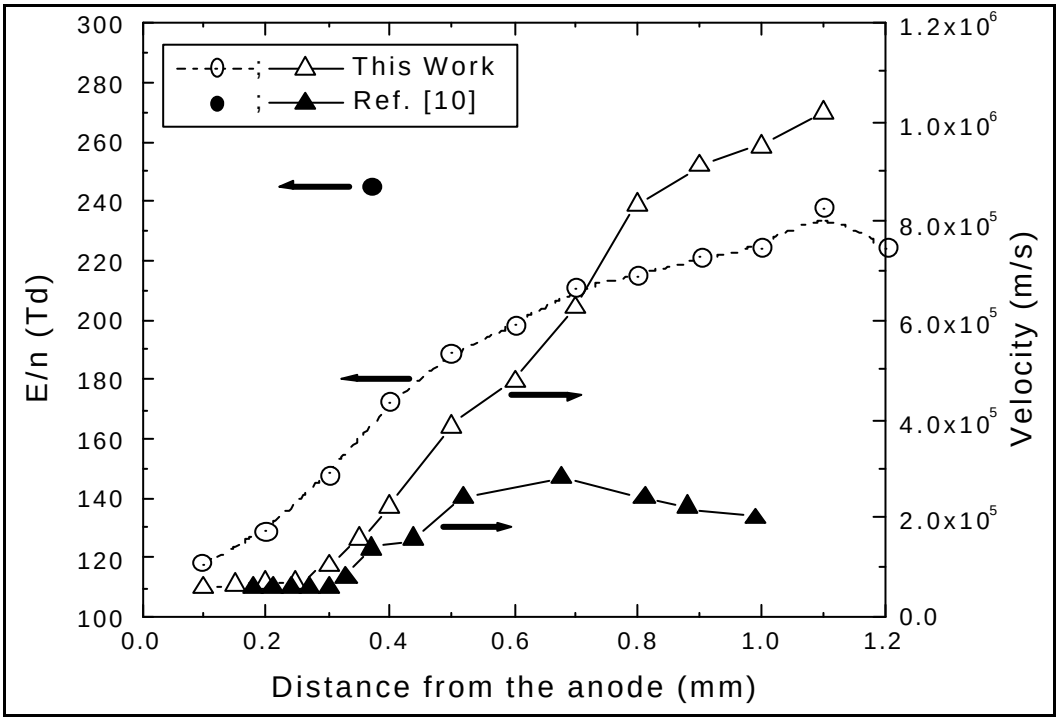


FIGURE 4. Comparison of the main characteristics of the cathode-directed streamer obtained in this work (open signs) with the corresponding results of computer modeling [10] (black signs).

Figure 4 demonstrates considerable differences between the streamers that are supposed to develop under different initial conditions assumed within the frame of the alternative models under consideration. The streamer corresponding to the model B (our experimental results) possesses a higher velocity and lower amplitude of the local electric field. It should be noted that qualitatively, such dependence of the streamer characteristics upon initial conditions of the MD development was predicted earlier in [9]. The following explanation has been proposed for this effect. When a cathode-directed streamer propagates through a media enriched by negative ions, a lower field is necessary to produce seed electrons before the streamer, because of effective detachment processes, and the velocity of streamer is expected to be higher.

4. CONCLUSIONS

There are two distinct regions with essentially different properties of plasma within the MD channel. Electric field near the cathode is higher than near the anode, and electron density, on the contrary, is considerably lower.

The streamer starts directly from the surface of the anode and crosses the gap with an increasing velocity that reach 10^6 m/s. Electric field strength of the streamer grows respectively from 120 Td at the anode to 240 Td at the cathode.

To provide a correct theoretical description of the MDs for an ordinary continuous mode, a model should be used, that takes into account an existence of initially non-uniformly charged dielectric surfaces.

ACKNOWLEDGMENTS

This work was supported by the "Sonderforschungsbereich 198, Kinetics of partially ionized gases"
The authors express their deep gratitude to Jan Schäfer for his assistance in performing spectroscopic measurements.

REFERENCES

[1] Samoilovich V., Gibalov V., and Kozlov K., *Physical chemistry of the barrier discharge,* DVS-Verlag, Düsseldorf, 1997
[2] Kogelschatz U., Eliasson B., and Egli W., *J. Physique,* **IV** C4, 47-66 (1997)
[3] Kozlov K. V., Physical models of the microdischarge in an ozonizer: classification, analysis, and comparison with the reality. In: *Proc. 7th Int. Symp. on High Pressure Low Temperature Plasma Chemistry*, ed. by H.-E. Wagner, J. F. Behnke, and G. Babucke, Greifswald, 2000, pp. 292-8
[4] Creyghton Y. L. M., Pulsed positive corona discharges: fundamental study and application to flue gas treatment, *Thesis TU Eindhoven (The Netherlands),* 1994 (ISBN 90-9007232-2)
[5] Bobrov Y. K, and Yourguelenas Y. V., Structure and radiation of streamer front. In: *Proc. 7th Int. Symp. on High Pressure Low Temperature Plasma Chemistry*, ed. by H.-E. Wagner, J. F. Behnke, and G. Babucke, Greifswald, 2000, pp. 169-73
[6] Brandenburg R., Kozlov K. V., Michel P., and Wagner H.-E., Diagnostics of the single filament barrier discharge in dry and humid air by cross-correlation spectroscopy. In: *Proc. 7th Int. Symp. on High Pressure Low Temperature Plasma Chemistry*, ed. by H.-E. Wagner, J. F. Behnke, and G. Babucke, Greifswald, 2000, pp. 189-93
[7] Kozlov K. V., Wagner H.-E., Brandenburg R., and Michel P., *J. Phys. D: Appl. Phys.*, **34**, 3164-76 (2001)
[8] Kossyi I. A., Kostinsky A. Yu., Matveyev A. A., and Silakov V. P., *Plasma Sources Sci. Technol.,* **1**, 207-20 (1992)
[9] Kozlov K. V. Mechanism of barrier discharges in electronegative gases. In: *Proc. 6th Int. Symp. on High Pressure Low Temperature Plasma Chemistry*, ed. by T. Herbert, and U. Murphy, Cork, 1998, pp. 288-92
[10] Gibalov V. I., and Pietsch G., *J. Phys.D: Appl. Phys.,* **33**, 2618-36 (2000)

EFFECTS OF DIELECTRIC DROPLETS ON POINT-TO-PLANE DISCHARGE DYNAMICS AND SPARK FORMATION

P. Tardiveau[a] and E. Marode

Laboratoire de Physique des Gaz et des Plasmas, Equipe Décharges Electriques et Environnement, Université Paris-Sud / CNRS, Supelec, 3 rue Joliot-Curie, 91192 Gif-sur-Yvette Cedex, France

Abstract. In the frame of studies on engine combustion triggered by discharges with injected droplets of gasoline, the question of the influence of dielectric heterogeneities on the discharge development mechanisms has been studied. It has been performed at atmospheric pressure in a point-to-plane gap by means of optical and electrical high-speed techniques. It has been found that the injection of oil or ethanol micrometer-sized droplets into the gap implied several effects on the streamer advancement and its transition towards the spark phase. It has been shown that a jet of dielectric droplets could attract the discharge, increase the threshold of needed applied potential and the streamer velocity and, in a certain way, promote the spark formation.

1. INTRODUCTION

The recent development of gasoline direct injection in car engines implies new studies on ignition mechanisms. Indeed, in such devices, the injection part supplies a cloud of fine fuel droplets, so that the triggering spark and the combustion are initiated in a very strong inhomogeneous medium. This two-phase air-fuel mixture is able to modify the discharge trajectory as well as the quantity of electrical energy transferred to chemical reactivity. It is thus necessary to understand the interactions between the discharge and the cloud of dielectric droplets through which the discharge propagates. For that, we start with a streamer discharge, in a point-to-plane geometry, under impulse high voltage, for which the electrical and optical properties are quite well known in air at atmospheric pressure [see for instance 1]. This choice is based on previous results [2] showing that such a discharge, followed by a controlled arc phase, could efficiently trigger combustion with less energy than it is needed with a classical spark.

The experimental protocol which has been here set up allows us to characterize the discharge path under high voltage pulses, and namely to derive an evaluation of the propagation velocities of the different streamers inside the discharge brush. This analysis, carried out at atmospheric pressure, is based on optical and electrical high-speed techniques. Injecting spherical droplets of oil or ethanol along the point-plane axis, by means of a vibrating piezo-electric generator, and comparing streamers properties with or without this jet of droplets, several effects have been found. Essentially, a guiding effect of the discharge by the droplets and an increase of streamer propagation velocities can be observed. Moreover, the spark formation seems to be promoted by the droplets in such a way that, with droplets, the energy needed to get an arc phase can be reduced and the way this energy is transferred into the mixture can be spatially controlled, increasing the probability to have a successful combustion.

2. EXPERIMENTAL APPROACH

2.1 Set-up and data processing

The experimental arrangement is shown schematically in figure 1. The measurements were made for a point-plane gap of 11 mm, with a tip radius of about 50 µm. The plane is drilled with a hole through

[a] Electronic address : pierre.tardiveau@lpgp.u-psud.fr

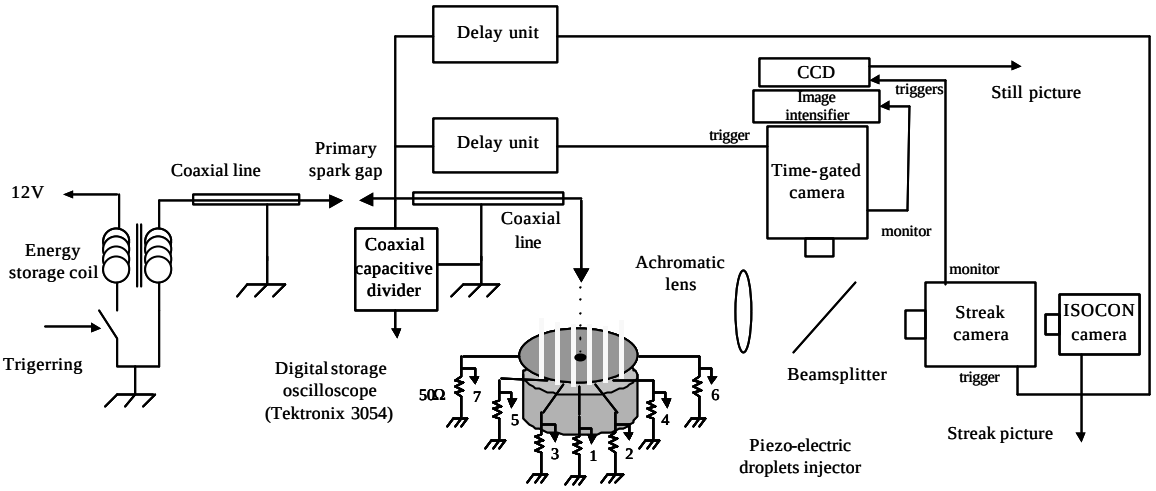


FIGURE 1. Experimental arrangement

which a jet of oil or ethanol droplets can be injected into the gap, along the axis of symmetric. A piezo-electric injector can supply mono-dispersed-sized droplets whose diameter can be adjusted between 30 µm and 70 µm. Short positive high voltage impulses were supplied to the point by a high voltage coaxial generator based on waves propagation in transmission lines and devised in the laboratory. By changing the distance between the electrodes of the primary spark gap of the coaxial generator, the voltage amplitude can be adjusted between 10 kV and 23 kV. A coaxial capacitive divider integrated in the generator line monitor the voltage. An example of high voltage pulses is shown in figure 2.

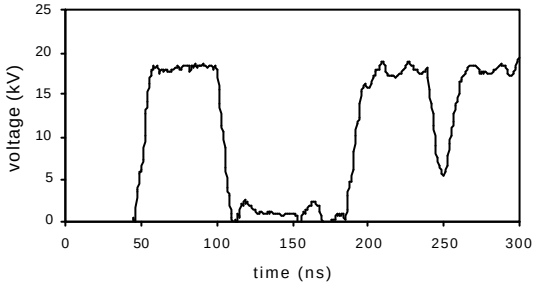


FIGURE 2. Example of voltage pulses

As several streamers simultaneously propagate to the plane when a short voltage pulse is applied to the point, each of them induces electric charges at the plane and an associated current pulse. In the case of a single grounded plane, all these pulses would merge together so that it would be impossible to distinguish a streamer from another by the analysis of the single current record. In order to separate somehow this electrical influence, the plane was divided into seven strips, as shown in figure 1, each of them being linked to the ground through a 50 Ω resistor and connected to a digital storage oscilloscope channel. By this space decoupling method, the location and the time where each streamer impacts on the plane can be roughly identified. By means of an achromatic UV lens and an optical plate beamsplitter, an image of the discharge can be directly focused on the two photocathodes of two image converter cameras. On a first optical line, a TSN506 Thomson camera is coupled with an image intensifier and a CCD camera to give a 100 ns time gated still picture of the discharge. On a second optical line, a STL high-speed streak camera, coupled with an ISOCON tube camera, gives a streak picture for a 50 ns time-resolved observation of the discharge. Both optical lines and the various devices of the equipment are triggered with the H.V. pulse front so that all electric and optical events are synchronized.

The pictures interpretation is however far to be evident since several streamers are propagating simultaneously towards the plane and are mainly off the gap axis. Figure 3 illustrates this problem. Let us consider two streamers propagating off-axis, symmetrically at left and right to the gap axis, at the same velocity, their impact locations being respectively identified by m_i and m_j on the still picture, and by m'_i and m'_j in the streak picture (algebraic values).

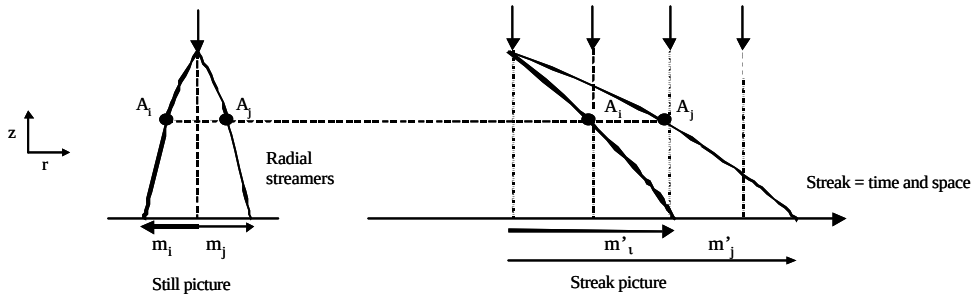


FIGURE 3. Still and streak pictures analysis

The two points A_i and A_j, correspond to the positions of the streamers heads at the same time (see still picture). The streak sweep is perpendicular to the gap axis, and on the streak picture, an axis perpendicular to the gap axis should be a time axis. However different coordinates along the sweep axis are associated to the A_1 and A_2 events, in spite of the fact that they are simultaneous. . It shows that the streak axis is not a pure time axis but contains space due to off-axis spatial movements. It follows that it is not easy to put a time parameter along the streamer trajectory on the streak photograph. To try to avoid the problem, associated current pulses allow determining the chronological order of the different streamers arrivals on the plane electrodes. However, in the case of four or even five simultaneous streamers, the situation remains inextricable. Moreover, a basic analysis is not sufficient to identify streamer velocities, the departure time t_0 of the streamers from the point being not easily determined by the current records. A special data treatment is then needed to remove these difficulties.

In order to match the paths traced by a streamer in a set of corresponding still and streak pictures and to evaluate the mean velocity of each streamers, an analytical calculation based on a mathematical representation of these paths has been performed. Each trace on the still picture can be schematically described by a function $r = f_i(z) = m_i(1-z^2)$, with r and z respectively the radial and the axial gap coordinates in a reference system where the point-to-plane distance is normalized to the unity. The matching trace in the streak picture can be expressed by an other function $r' = g(z)$ where r' is the radial coordinate on the streak axis from the point where streamers leave the positive electrode. This function introduces a sweep term, as expressed by equation (1), function of the camera sweep velocity V_b, time t(r) as a function of the radial coordinate r, and the time t_0 when streamers leave the point.

$$r' = r + V_b\left[t(r) - t_0\right] = m_i(1 - z^2) + V_b\left[t(r) - t_0\right] \qquad (1)$$

The straight traces observed on the streak record strongly suggest that even off-axis streamers propagate at a constant velocity V_{si}. Integrating the above relation until $r = m_i$, a relation between the streamer impact locations m_i and m'_i is obtained (2).

$$m'_i = m_i + \frac{V_b}{4m_iV_{si}}\left[\frac{1}{2}\ln\left[\frac{\sqrt{1 + 4m_i^2} + 2m_i}{\sqrt{1 + 4m_i^2} - 2m_i}\right] + 2m_i\sqrt{1 + 4m_i^2}\right] \qquad (2)$$

Thus, given the values of m_i, m'_i and V_b, the value of the mean streamer velocity V_{si} can be deduced.

2.2 Experimental results

Without droplets, several streamers simultaneously propagate into the gap, their velocity being estimated between 3 and 10.10^7 cm/s for voltages between 12 kV and 23 kV, and it is observed that a primary streamer, being axial in most cases (80 %), always propagates faster than other radial streamers. For our analysis, we will focus exclusively on this primary streamer. When droplets are present on the axis, several effects have been found concerning this axial streamer.

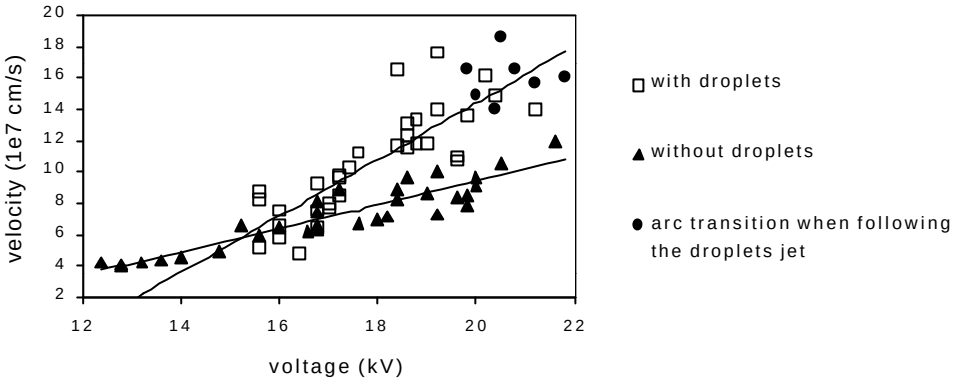


FIGURE 4. Primary streamer velocity versus voltage amplitude,
with or without a jet of ethanol droplets (droplets diameter 50 µm, droplets separation 150 µm)

A guiding effect is clearly observed when analyzing the still and the streak pictures. When the jet is slightly shifted radially off-axis (of about 1 mm), statistics about spatial location of the primary streamer show that 40 % follow the jet and only 25 % still propagates along the axis. This should be compared to the 80 % of primary streamers going on the axis without droplets. Moreover, when the jet is centered, all the primary streamers are axial. Figure 4 shows firstly that when the axial streamer propagates along the droplets jet, its velocity is quite higher, from 4.10^7 cm/s up to 18.10^7 cm/s at 20 kV. It may related to the fact that the droplets seem to increase the threshold potential where a streamer can be initiated since no streamer can be obtained below a voltage of 15,5 kV, instead of 12 kV when no droplets are present in the gap. Another effect is that the spark formation occurs from voltages above 20 kV with droplets, although such a transition is not observed without droplets even for voltages up to 23 kV. In these cases, the spark is the result of several successive axial streamers, occurring on successive voltage pulses, each of them propagating along the droplets jet.

3. DISCUSSION

To explain the changes which are experimentally observed on streamer triggering, streamer propagation and on transition towards the arc phase the following analysis can be suggested, in terms of electrostatic and electro-dynamic effects of droplets on the discharge.

3.1 Local electric field enhancement

The guiding effect of the droplets on the streamers could be due to a local increase of the electric field near the droplets, as shown by a three-dimensional simulation on Flux 3D, giving the electric field space distribution when droplets are near a sharp positive electrode. As an example where boundary conditions are closed to real engine conditions (point of 300 µm, distance gap of 0,9 mm and applied voltage of 30 kV), the figure 5 compares the electric field values on the point-plane axis with or without dielectric droplets (diameter of 35 µm and relative permittivity of 2,2).

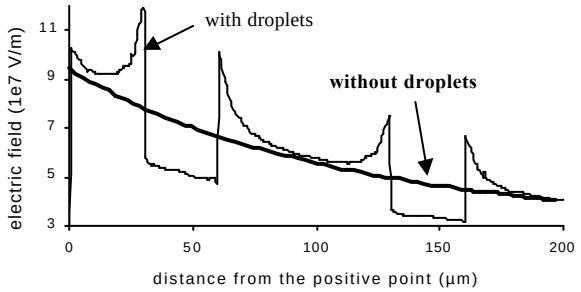


FIGURE 5. Electric field values on point-plane axis with or without gasoline droplets

However, this field increase is very limited to the region near the droplets and it remains low compared to the field created by the positive space charge of the streamer itself.
Moreover, in spite of the field enhancement between the point and the first drop on the axis, the threshold potential needed to trigger the discharge is higher with droplets because the field discontinuities induced on the axis, as shown in figure 5, reduce the ionization length needed to get a critical avalanche. Another explanation for the increase of the threshold potential could be the presence of a liquid layer on the point, inducing the same kind of effect.
Thus, the streamer guiding cannot be seen only in electrostatic terms of field enhancement and a more efficient mechanism, corresponding to the extraction of electrons from the droplets surface has to be introduced.

3.2 Ionization energy of dielectric droplets

By a theoretical study of C.F. Gallo and W.L. Lama [4], the ionization energy E_e (J) needed to extract an electron from a dielectric sphere of relative permittivity ε_r can be expressed by equation (3). In this equation x_0 is a distance beyond which no electrical forces retain an extracted electron from a dielectric surface. x_0 depends on the nature of the dielectric, and e is the elementary charge. For a sphere of polyethylene (x_0 = 1,7 Å), E_e is close to 6 eV, i.e. much lower than the12 eV ionization energy of oxygen molecule. Thus, it is easier to extract electrons from the droplets.

$$E_e = \frac{e^2}{16\pi\varepsilon_0 x_0}\frac{\varepsilon_r + 7}{\varepsilon_r + 1} \qquad (3)$$

Droplets may thus be considered as a source of electrons feeding the streamer head and influencing the streamer propagation towards them. An increase of the distance from the streamer front of secondary electrons produced at the droplet surfaces may accelerate the streamer advancement and promote the guiding of the streamers between successive droplets.

A result of this is that, when successive streamers are initiated, they always pass along the jet and the energy is always mostly deposited at the same place. The neutral density inside this channel may decrease, due the corresponding temperature increase and the spark transition is then easier due to an E/N increase within the streamer channel. This may explain the lowering of potential for spark transition.

4. CONCLUSIONS

Under impulse voltage and in a two-phase mixture at atmospheric pressure, the streamer initiation, its propagation and its transition towards the spark are modified. Streamers can be guided by the dielectric droplets, which create a preferred path rich in electrons. Once the streamers are on this path, their velocity is increased by the electrons extracted from the surface of the droplets. When successive voltage pulses are applied, each streamer deposits thus energy along the same preceding path. The energy is thus concentrated along a unique path and a reactive plasma can be obtained thus with a lower energy need. A better probability of triggering combustion in a lean air-fuel mixture may result.

ACKNOLEDGEMENTS

This work was carried out at the EDEE group of LPGP, under a collaborative work with the Renault automotive group. The authors express their thanks to this group for its scientific advise and financial support.

REFERENCES

[1] Goldman, Corona Discharges, in Gaseous Electronics, N.M.Hirsh, H.J.Oskam, (1978) 1, 219-215
[2] Jaffrezic X., Etude de l'amorçage de la combustion d'un mélange air-propane par un plasma non thermique. Application à l'optimisation de l'allumage sur un moteur. Thèse de doctorat de l'Université Paris XI (1995)
[3] Gallo C.F., and Lama W.L., IEEE Transactions on Industry Applications, **vol 1A-12**, 7-11 (1976)

TWO DIFFERENT ORIGINS FOR THE DESTABILIZATION OF A GLOW DIELECTRIC BARRIER DISCHARGE IN NITROGEN

N. Gherardi[a1], E. Croquesel[a], N. Naudé[a], P. Veis[b] and F. Massines[a]

a) Laboratoire de Génie Electrique de Toulouse, Université P. Sabatier, 118 route de Narbonne, 31062 Toulouse Cedex, FRANCE

b) Department of Plasma Physics, Comenius University, Mlynska dolina F2, 84248 Bratislava, SLOVAKIA

Abstract. Glow Dielectric Barrier Discharge generated at atmospheric pressure are studied in nitrogen in order to highlight possible reasons for its transition to a non-stable regime (filamentary-like or other). These origins can be of two types: a lack of memory effect from one discharge to the following preventing a Townsend breakdown, oscillations in the electrical circuit under specific excitation conditions reflecting itself in the gas.

1. INTRODUCTION

Glow Dielectric Barrier Discharges (GDBD) in nitrogen have been studied since a few years [1,2,3,4,5,6]. Unlike for the filamentary-like discharges, the discharge is due to a Townsend breakdown. For that, it has been shown that is necessary to have a memory effect from one discharge to the following, and that the metastable molecules of N_2 play a dominant role in this memory effect (through Penning ionisation and/or other mechanisms) [7,8]. However, several questions still remain. First, as the memory effect needs previous discharge, how does it take place during the first breakdowns? Then, the discharge can become unstable even with a high density of metastables [9]. So what mechanism is responsible for this destabilisation?

The aim of this work is to bring an answer to these questions, through the experimental study of the discharge behaviour as a function of the frequency of the applied voltage, its amplitude, and the electrode configuration. Electrical measurements and optical diagnostics are used.

2. EXPERIMENTAL SET-UP

The apparatus used is sketched elsewhere [9]. The Dielectric Barrier Discharges (DBD) are generated between two electrodes coated on ceramic plates (635µm thick), to which an a.c. high voltage is applied in the frequency range from 200 Hz to 20 kHz with a magnitude up to 24 kV peak to peak. The electrodes are rectangular, 85 mm length in the gas flow direction and 40 mm width. Two configurations of electrodes are used in this study. When not indicated, the electrodes are flat and parallel. One plane electrode in front of a slightly curved one is also used. The maximum gas gap between the surface of the two dielectrics is 1mm.

The discharge is generated in nitrogen (nitrogen C from Air Liquide society) at atmospheric pressure. A laminar gas flow is added from one side of the discharge, maintaining the atmospheric pressure by a slight pumping. The nitrogen flow velocity is 150 $cm.s^{-1}$.

Electrical measurements and light measurements, which are non-invasive diagnostics, have been chosen to study the discharge characteristics. The discharge current is measured through a 50-Ω resistor in series with the grounded electrode. The current and the voltage applied to the electrodes are

[1] Electronic address: gherardi@lget.ups-tlse.fr

visualized on a numerical oscilloscope (Tektronix 784A - 1GHz). The gas voltage really applied on the gas and the power dissipated in the discharge are calculated from these two measurements [9].

The discharge light is observed through a quartz window. A convergent lens is used to locally probe the light emitted by the plasma, and to obtain an image directly on the surface of a photomultiplier (R928 from Hamamatsu) for integrated light measurements, or on the entrance slit of a monochromator (THR1500 from Jobin-Yvon) for spectroscopic analyses. Rotational temperature measurements are done using this monochromator coupled to the photomultiplier associated to a photon-counting unit.

3. RESULTS

3.1. First steps of GDBD: need for the memory effect

The first objective of this work is to follow the developments of the first glow discharge, when the voltage is applied on the electrodes. Indeed, it has been previously shown that the glow dielectric barrier discharge (GDBD) is only obtained if there is a memory effect (via metastables in nitrogen) high enough to allow a Townsend breakdown of the gas [7]. Then, it is of interest to study how this memory effect takes place during the first discharges. Voltage-discharge current oscillograms of the cycles following the breakdown of the discharge show that only the two first discharges are actually filamentary-like. After, the memory effect becomes sufficient to induce a Townsend breakdown.

When the discharge is in the glow mode, it is characterized by electrical characteristics (discharge current and voltages) shown on figure 1. The current I_d consists of a lone pulse per half cycle. Its shape is reproducible from one discharge to another. At the beginning of the cycle, when no discharge occurs, the current is a displacement current and the gas voltage V_g rises until it reaches the breakdown voltage (≈25kV/cm). The current increases thereafter rather quickly and stops while the applied voltage V_a continues to increase. During the increase of I_d, V_g increases up to 3.5 kV and then stays almost constant until the maximum of V_a. When V_a is maximum, I_d is near zero; then V_a begins to fall and V_g follows. As described previously [9], the rise of the current (part A in figure 1) is controlled by the ionisation occurring in the discharge. On the other hand, during the time when V_g is constant (part B in figure 1), all the voltage fluctuations are applied on C_{ds}, which is the capacitance of an condenser whose plates are the two electrodes and the dielectric is the two ceramics. Then, in part B, the discharge current follows the law $I = C_{ds}dV_a/dt$ [9].

3.2. Working domain of GDBD and destabilization

As soon as the glow discharge is ignited, it is possible to determine its working domain in terms of amplitude and frequency of the applied voltage (figure 2). Indeed, the glow dielectric barrier discharge (GDBD) works only for a limited range of these two variables. The fact of being slightly apart from these limits of operation is characterized by the propagation of instabilities in the glow discharge, instabilities which lead to a pure filamentary discharge if the amplitude or the frequency of the voltage is increased even higher. These instabilities are easily visible on the discharge currents because they induce currents which are largely higher in amplitude and shorter in time than that of the GDBD (see examples on figures 3 and 4). The working domain has got two limits. The lower limit, at a given frequency, is the applied voltage to extend the discharge over the entire electrode surface. It is related to the breakdown voltage. This voltage decreases between 0.2 and 2 kHz in the conditions used in that example (electrode length and gas velocity), and is almost constant for higher frequencies. The decrease observed at low frequencies is due to the fact that at low frequency the accumulation of metastables from one discharge to the following is not optimal regarding the residence time of a gas molecule in the discharge area [10], and so the memory effect is not maximal. This shows that if two discharges are enough to establish the memory conditions necessary to have a Townsend breakdown, more discharges are needed to reach the optimum conditions. The upper limit, at a given frequency, is

the applied voltage at which instabilities appear and so defines the transition to a non-glow discharge. This maximum voltage decreases with the frequency.

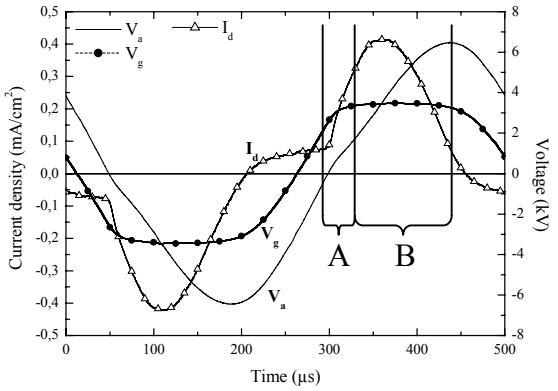


FIGURE 1. Discharge current I_d, gas voltage V_g and applied voltage V_a of a Glow DBD in nitrogen.

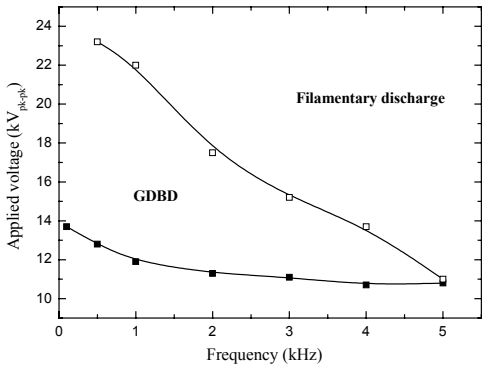


FIGURE 2. Working domain of the Glow DBD in nitrogen.

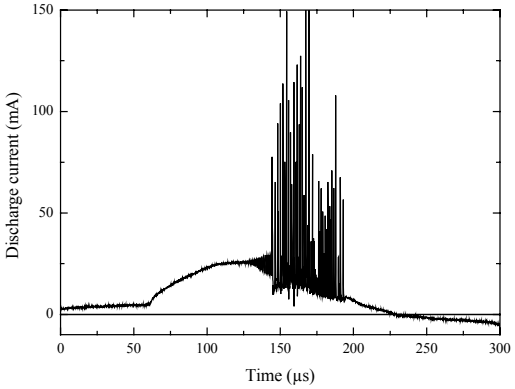


FIGURE 3. Discharge current during a destabilization with f < 3.5 kHz (V_a=21kV_{pk-pk}, f=2kHz)

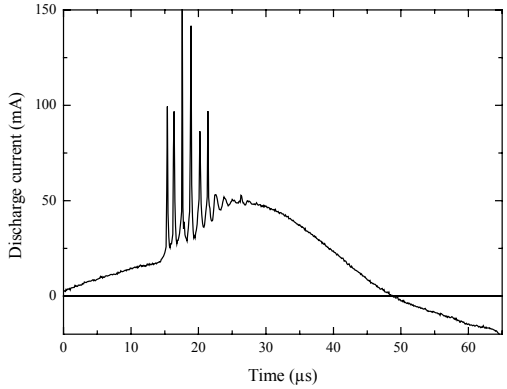


FIGURE 4. Discharge current during a destabilization with f > 3.5 kHz (V_a=13kV_{pk-pk}, f=10kHz)

We have determined that these instabilities could be of two types according to the frequency of excitation: for frequencies lower than 3.5 kHz, the microdischarges occur after the maximum of the glow discharge current (figure 3), when for higher frequencies the destabilisation occurs in the rise of the glow discharge current (figure 4). These two destabilisations look differently:

In the first case, the associated currents are clearly those of filaments (or micro-discharges) developing through the gas gap, and an optical analysis of the discharge gap (by the mean of a photomultiplier coupled to a lens) shows that this occurs everywhere in the discharge.

In the second case, the instabilities observed on the discharge current look more like oscillations, or pulses, with a time scale much longer than the development of a micro-discharge. Analysis with a photomultiplier confirms that these pulses develop too slowly to be streamers.

3.3. Cause of the high frequency destabilization

As the power dissipated in the gas increase a lot with the frequency, we measured the rotational temperature of the N_2 second positive system by optical emission spectroscopy, near the entrance of the gas in the discharge (where residence time of the gas < 5 ms) and near its exhaust (residence time of the gas > 20 ms). The two temperatures at these two positions are plotted in figure 5 against the frequency of the applied voltage, the voltage amplitude being kept constant. It can be seen that the

rotational temperature at the exhaust is more or less constant while at the entrance it increases with the frequency.

The pressure in the discharge being constant, an increase of the gas temperature will result in a decrease of the gas density. In order to see if the gas density plays a negative effect on the sustaining of the glow discharge, we measured the glow DBD working domain at 600 mbars, i.e., for a lower density. No significant difference is observed between the domains obtained at 1000 and 600 mbars. Then, the destabilisation occurring at high frequencies is not due to a decrease of the gas density.

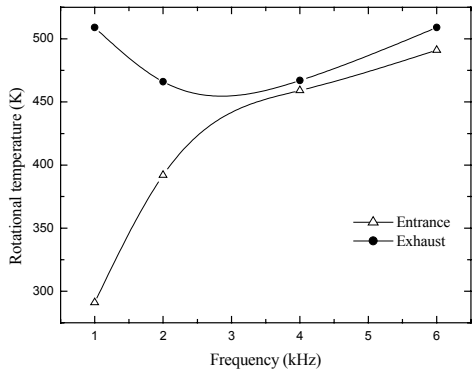


FIGURE 5. Rotational temperature of the N_2 2^{nd} positive system at different frequencies (V_a=13kV$_{pk-pk}$) near the entrance of the discharge and near its exhaust (40 mm electrode length).

As the oscillations occurs only at high frequencies, i.e., when the rise of the discharge current is fast, we tried to describe the current rise with an exponential low. The agreement is very good from the breakdown up to the V_g stabilisation. The time constant τ (in $I=I_0\exp(t/\tau)$) is given in figure 6 as a function of the frequency of the applied voltage, for the maximum value of the voltage amplitude allowing a GDGD. This was done for several gas velocities and electrode lengths. It clearly appears that the speed of the current rise allowing to keep a glow discharge without oscillations is limited for frequencies higher than 3 kHz.

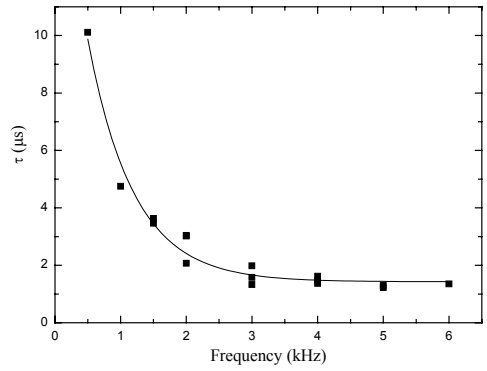


FIGURE 6. Characteristic time of the current rise speed near the destabilisation of the GDBD for different frequencies.

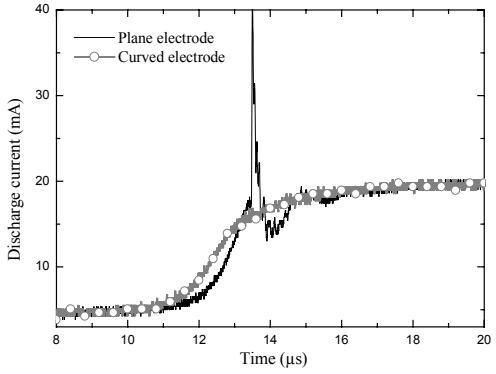


FIGURE 7. Comparison of discharge current rise using a plane and a curved electrode (V_a=12kV$_{pk-pk}$, f=10kHz).

On the other hand, we observed that the use of a slightly curved electrode in place of flat electrode pushes back the frequency at which these oscillations appear. This can be seen by comparing the discharge currents obtained at 10 kHz, for the same V_a amplitude, using the two sets of electrodes (figure 7): when in the case of plane electrode some oscillations are present, the discharge current with the curved electrode is regular. In the same time, the slope of the current is decreased (τ = 1.3 μs with curved electrode and τ = 0.8 μs with plane electrode). This is due to the fact that the discharge first

ignites where the gap is the smallest and then expands on the entire electrode. However, this is surprising that the oscillations vanish. Indeed, locally, i.e., at the place where the discharge first starts in the gas, the current density should not increase slower when the electrode curvature increases. In fact, this is only the total current which increases more slowly. Then, this let us think that this is not the discharge itself that is responsible for these oscillations but the external circuit. Indeed, several elements in the circuit can create an oscillating unit. This can be highlighted modelling the circuit-discharge unit by an electric model describes in [11]. Moreover, this is in accordance with the load network used by Roth *et al.* [12] to better match the external circuit with the discharge.

4. CONCLUSION

Glow Dielectric Barrier Discharges have been studied in nitrogen in order to highlight some of the mechanisms responsible for its destabilization. It has been first shown that the memory effect necessary to have a Townsend breakdown takes place in a few discharges. However, even when the metastable density is high enough to allow a Townsend breakdown, the GDBD has a working domain outwards of which it is not stable anymore. The first limitation seems to be due to the rise speed of the discharge current, which, if it is too fast, can induce some oscillations in the external electrical circuit. Then, these oscillations should be removed by the use of an appropriate low-pass filter, which will allow to increase a lot the working domain of the glow discharge. This will be checked soon.

ACKNOWLEDGEMENTS

The authors wish to thank the French research ministry and the Air Liquide society for their financial support.

REFERENCES

[1] Okasaki S., Kogoma M., Uehara M., and Kimura Y., *J. Phys. D: Appl. Phys.*, **26**, 889-92 (1993)
[2] Gherardi N., Gat E., Gouda G., and Massines F., About Mechanisms Leading to a Glow Silent Discharge in Nitrogen at Atmospheric Pressure. In: *Proc. 6th Int. Symp. On High Pressure Low Temperature Plasma Chemistry*, Cork, 1998, pp. 118-22
[3] Trunec D., Brablec A., and Stastný F., *Contrib. Plasma Phys.*, **38**, 435-45 (1998)
[4] Tepper J., Lindmayer M. and Salge J, Pulsed Uniform Glow Discharges at Atmospheric Pressure. In: *Proc. 6th Int. Symp. On High Pressure Low Temperature Plasma Chemistry*, Cork, 1998, pp. 123-7
[5] Monette E., Bartnikas R., Czeremuszkin G., Latrèche M., and Wertheimer M. R., Electrical and Optical Diagnostics of Atmospheric Pressure Glow Discharges (APGD) in He and N_2. In: *Proc. 14th Int. Conf. on Plasma Chemistry*, ed. by M. Hrabovský, M. Konrád, and V. Kopecký, Prague, 1999, pp. 991-6
[6] Brandenburg R., Kozlov K. V., Massines F., Michel P., and Wagner H.-E., Dielectric Barrier Discharge in Nitrogen: Transition from the Filamentary to the Glow Mode. In: *Proc. 7th Int. Symp. On High Pressure Low Temperature Plasma Chemistry*, ed. by H.-E. Wagner, J. F. Behnke, and G. Babucke, Greifswald, 2000, pp. 93-7
[7] Gherardi N., Gouda G., Gat E., Ricard A., and Massines F., *Plasma Sources Sci. Technol.*, **9**, 340-6 (2000)
[8] Golubovskii Yu.B., Maiorov V. A., Behnke J., and Behnke J. F., The Role of Emission from the Dielectric Surface in a Homogeneous Barrier Discharge in Nitrogen. In: *Proc. 15th Int. Conf. on Plasma Chemistry*, ed. by A. Bouchoule, J.M. Pouvesle, A.L. Thomann, J.M. Bauchire, and E. Robert, Orléans, 2001, pp. 3239-44
[9] Croquesel E., Gherardi N., Martin S., and Massines F., Boundary of the Glow Regime at Atmospheric Pressure in a Nitrogen Dielectric Barrier Discharge. In: *Proc. 7th Int. Symp. On High Pressure Low Temperature Plasma Chemistry*, ed. by H.-E. Wagner, J. F. Behnke, and G. Babucke, Greifswald, 2000, pp. 88-92
[10] Gherardi N., and Massines F, *IEEE Trans. on Plasma Science*, **29**, 536-44 (2001)
[11] Naudé N., Cambronne J.-P., Massines F., Modèle Evolutif de Décharge Homogène. To be published in: *Proc. 9ème Colloque Electronique de Puissance du Futur*, Montpellier, 2002
[12] Roth J. R., Tsai P. P., Wadsworth L. C., Liu C., Spence P. D., U.S. Patent 5,403,453 (1995)

SPATIO-TEMPORALLY RESOLVED SPECTROSCOPIC DIAGNOSTICS OF THE ATMOSPHERIC PRESSURE GLOW DISCHARGE IN NITROGEN

R. Brandenburg[a], K.V. Kozlov[b], N. Gherardi[c], P. Michel[a],
C. Khampan[d], H.-E. Wagner[a], F. Massines[c]

a) Inst. of Physics, Univ. of Greifswald, 17489 Greifswald, Domstr. 10a, GERMANY
b) Moscow State Univ., Dept. of Chemistry, 119899 Moscow, RUSSIA
c) Lab. de Genie Electrique, Univ. P. Sabatier, 118 r. d. Narbonne, 31062, Toulouse Cedex, FRANCE
d) CPPlA., Univ. P. Sabatier, 118 r. d. Narbonne, 31062 Toulouse Cedex, FRANCE

1. INTRODUCTION

The dielectric barrier discharge (DBD) can operate in different modes. Besides the well-known filamentary mode (typical for a DBD in oxygen or in air), a diffuse mode (also referred too as Atmospheric Pressure Glow Discharge, APGD) can be generated under special operation conditions. The APGD driven by sinusoidal voltage in the kHz-range has been originally observed in helium [1] and in nitrogen [2]. Voltage-current oscillography, short exposure photography, and time resolved optical emission spectroscopy [2] as well as numerical modeling [3-6] were used to investigate the mechanism of APGD in pure nitrogen.

In the present paper, our recent results obtained by the technique of temporally and spatially resolved optical emission spectroscopy of the APGD are compared with the corresponding data of 1-D numerical modeling [3]. In order to clarify the role of collisional quenching of the nitrogen metastables, the experiments were carried out as in pure nitrogen, as in nitrogen with the pre-defined initial admixtures of oxygen within the concentration range 40-1000 ppm.

2. EXPERIMENTAL DETAILS AND NUMERICAL MODEL

The **experimental setup** was originally developed for the investigation of single filaments in air [7,8]. The same two semi-spherical glass electrodes made of chemical test-tubes (radius of curvature 7.5 mm and glass thickness of 1.5 mm) were used to study APGD in nitrogen. The discharge gap width was about 1 mm. The discharge was driven by the sinusoidal voltage (frequency of 6.5 kHz and amplitude of about 17 kV_{pp}). The specially modified technique of cross-correlation spectroscopy [8] enabled reliable temporally and spatially resolved measurements of the light intensity distributions for selected wavelengths, and it provided the resolution $\Delta t = 2.3$ µs over time scale, $\Delta x = 0.2$ mm over space (along the discharge axis). All experiments were carried out in an open gas flow system. The flow rate of N_2 was maintained at the level of the flow rate corresponding to the linear gas velocity through the discharge gap of about $v_{gas} = 0.16$ cm s^{-1} (laminar flow). Variation of the O_2 concentration (initial admixture of oxygen) was performed using mass-flow controllers.

The detailed description of the **numerical model** is given in [3]. This 1-D numerical model is based on the solution of the continuity equations for the APGD-plasma species (electrons, ions and excited states) coupled with the Poisson equation. Secondary emission is included in the boundary conditions. Kinetic scheme of the model contains elementary reactions involving electrons, the molecules N_2 in the ground state, four types of the positive ions (N_2^+, N_3^+, N_4^+ and N^+), two lowest metastable states of

[a] brandenburg@physik.uni-greifswald.de

nitrogen (N_2(A) and N_2(a')), and the radiative state N_2(C). The kinetic coefficients of electrons and the rate constants of the elementary reactions under consideration have been calculated using numerical solution of the Boltzmann equation.

3. RESULTS AND DISCUSSION

3.1. Effect of the oxygen admixture

The entire spectrum of APGD in nitrogen has been found to consist of the second positive system (SPS) of nitrogen, NO_γ-bands, and the line of ON_2-excimer (557.7 nm). The same general structure of the spectrum was observed by the authors [2] who used bare alumina as dielectric.

N_2 (SPS): $$N_2(C^3\Pi_u)_u \rightarrow N_2(B^3\Pi_g)_{u'} + hn \quad (1)$$

NO_γ: $$NO(A^2\Sigma^+)_u \rightarrow NO(X^2\Pi)_{u'} + hn \quad (2)$$

ON_2-Excimer: $$O(^1S)N_2 \rightarrow O(^1D) + N_2 + hn \quad (3)$$

To carry out systematic emission intensity measurements, we have selected the following spectral bands: λ = 337.13 nm for SPS (1), 0-0 transition; λ = 259.57 nm for NO_γ (2), 3-0 transition; λ = 259.57 nm for ON_2-excimer. The corresponding spatially integrated intensities are presented in fig. 1a as functions of the oxygen admixture all the other parameters being constant. In fig. 1b, the emission intensities of NO and ON_2 are normalized to the intensities of N_2. Qualitatively, the curves in fig.1 demonstrate similar behavior: a steep rise followed by a slow decay. Depending on the content of oxygen, the discharge operates in different modes (diffuse or glow, filamentary, and transient). This transition can be clearly seen in the current oscillogramms (fig. 1c).

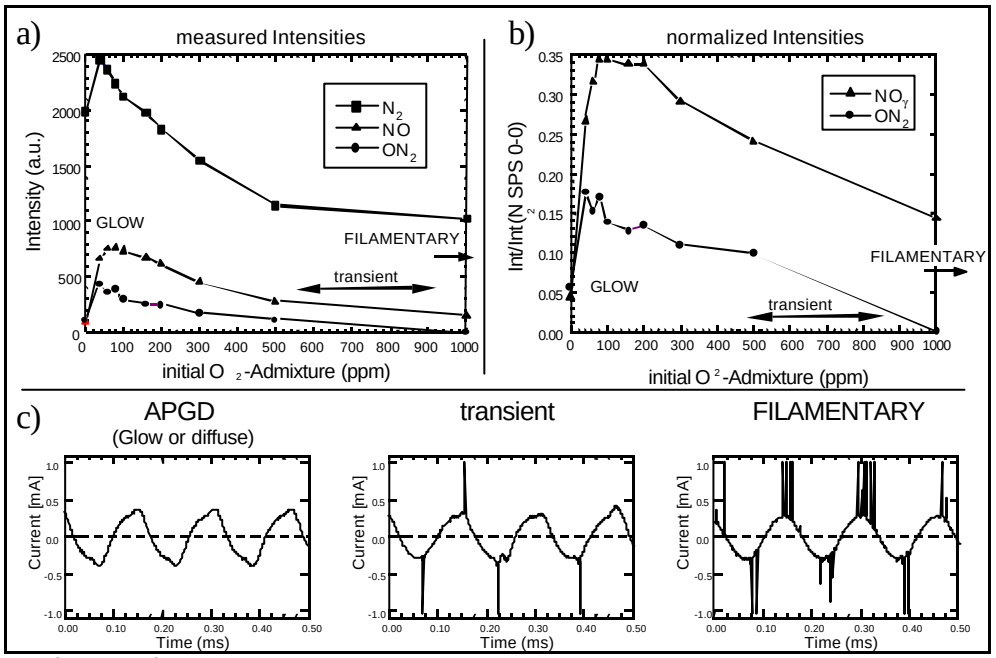


FIGURE 1. Influence of the oxygen admixture. Emission intensities (a,b) and current oscillogramms (c).

To interpret the effect of oxygen admixture (fig.1), the mechanism of the APGD in nitrogen should be considered in detail. According to the results [2,3,9], it can be explained as follows. An extremely high density of the metastable nitrogen molecules N_2(A) and N_2(a') is generated due to the excitation by direct electron impact (4a,b). In this case, the dominant ionization mechanism is the Penning-ionization (5a,b). The density of metastables depends on the rates of their formation and quenching. Their collisions with oxygen (6a,b) are very effective quenching processes. Since the rate coefficient for O_2 (6b) is about 6 orders of magnitude greater than for N_2, [10] even in the ppm-range molecular oxygen appears to be more effective quencher for nitrogen metastables N_2(A) and N_2(a').

$$e + N_2(X^1\Sigma_g^+) \xrightarrow{\Delta E=6.17eV} N_2(A^3\Sigma_u^+) + e\,; \qquad e + N_2(X^1\Sigma_g^+) \xrightarrow{\Delta E=8.40eV} N_2(a'^1\Sigma_u^-) + e \qquad (4a,b)$$

$$N_2(A^3\Sigma_u^+) + N_2(a'^1\Sigma_u^-) \rightarrow N_4^+ + e\,; \qquad N_2(a'^1\Sigma_u^-) + N_2(a'^1\Sigma_u^-) \rightarrow N_4^+ + e \qquad (5a,b)$$

$$O(^3P) + N_2(A^3\Sigma_u^+) \rightarrow O(^1S) + N_2(X^1\Sigma_g^+)\,; \qquad O_2 + N_2(A^3\Sigma_u^+) \rightarrow N_2(X^1\Sigma_g^+) + O + O \qquad (6a,b)$$

This quenching mechanism accounts for the observed drastic influence of the oxygen admixture upon the DBD behavior.

The following elementary processes can be treated as the main sources of "spectral indicators" (1-3):

N_2 excitation (SPS): $e + N_2(X^1\Sigma_g^+) \rightarrow N_2(C^3\Pi_u) + e$ (7)

NO_γ-excitation: $NO(X^2\Pi_r) + N_2(A^3\Sigma_u^+) \rightarrow NO(A^2\Sigma^+) + N_2$ (8)

ON_2-excimer: $O(^1S) + 2N_2 \rightarrow O(^1S)N_2 + N_2$ (9)

Several different effects can be distinguished, that determine the shape of the curves in fig.1a. An addition of oxygen may be expected to cause certain increase in the concentrations of NO and ON_2 (via the plasma chemical conversion), consequently some growth of the corresponding emission intensities. On the other hand, as it has been already mentioned above, molecular oxygen is an effective quencher of the N_2(A) molecules. Their density is a principal quantity, since they are needed to maintain the discharge in the APGD-mode. Furthermore, they excite the "spectral indicators" (8) and their precursors (6). Another negative effect can be caused by electronegativity of molecular oxygen. Due to electron attachment of O_2 (e.g. $O_2 + e \rightarrow O^- + O$), free electrons can be removed from the discharge zone. Therefore the concentrations of all excited species can decrease. Collisional quenching as well as electron attachment can finally result in qualitative changes of the discharge mechanism (i.e. the transition from the diffuse to the filamentary mode of the discharge).

The similarity of the intensity variations in fig.1a leads to the conclusion, that the shape of these curves is determined mainly by the influence of the oxygen admixture upon the discharge mechanism, i.e. upon the spatio-temporal distributions of electric field and electron density. In order to reveal the effects of plasma chemical conversion and collisional quenching, we have normalized the NO and ON_2 signals to the N_2 SPS (0-0) intensity (fig.1b). Here it should be noted that an admixture of molecular oxygen within the ppm-range does not affect the quenching rate of the N_2(C)-state, since the corresponding rate constant for O_2 is only one order of magnitude greater than for N_2 while the N_2 concentration is 4 or 5 order of magnitude larger than the O_2 one. Thus, the shapes of the curves in fig.1b are determined mainly by the effects of plasma chemical conversion (steep rise) and collisional quenching of the N_2(A)-states (slow decay). The highest emission intensity is reached (50-100 ppm of O_2) when these effects compensate each other. For a greater content of oxygen, the collisional quenching of the metastables dominates.

From the slopes of the rising parts of the curves in fig.1b, the offset of O_2 in "pure" nitrogen can be roughly estimated as about 20 ppm. This value appears to be somewhat greater than it can be expected from the quality of the feeding gas (total concentration of the impurities < 10 ppm).

3.2. Spatio-temporal structure of the APGD in nitrogen

Some results of the spatio-temporally resolved spectroscopic measurements are presented in fig.2. The time scale slightly exceeds the period of the driving voltage. The scale of relative intensity is color coded in logarithmic steps. The results of computer modeling corresponding to the experimental conditions (pure N_2, d= 1.1 mm; f= 6.2 kHz) are shown in fig.3. In both figures, the cathode is the upper electrode within the first half period (t= 0 ... 0.5 period numbers).

The experimentally measured SPS luminosity distribution (fig.$2a_1$) may be compared with the calculated distributions of electric field (fig.$3b_1$) and electron density (fig.$3b_2$), since the characteristic time of the collisional quenching of the N_2(C)-states by N_2 molecules is a few nanoseconds, and the

local density of $N_2(C)$ is determined by the rate of the elementary reaction (7). The maximum of the measured light intensity is observed near the anode. Although the maximum of electric field strength is located near the cathode (fig.$3b_1$), a strong increase of the electron density (fig. $3b_2$) in the direction from the anode to the cathode can dominate over the weak decay of the electric field. Thus, the experimentally observed distribution of the SPS radiation intensity (fig.$2a_1$) as well as the calculated $N_2(C)$ density (fig.$3b_2$) actually does not contradict the calculated distributions of electric field and electron density. The time shift between experimental and modelling results has to be only explained by different initial times ($\Delta t_0 \approx 0.15$ period numbers).

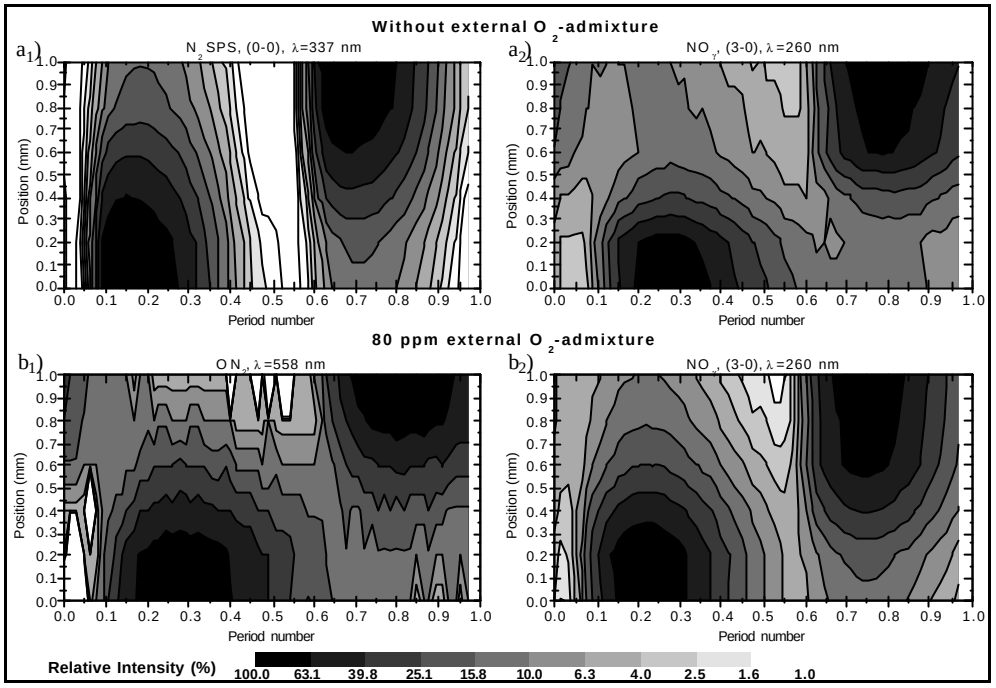


FIGURE 2. Experimentally measured space-time-luminosity distributions for N_2(C-B), NO(A-X) and O(S-D)N_2

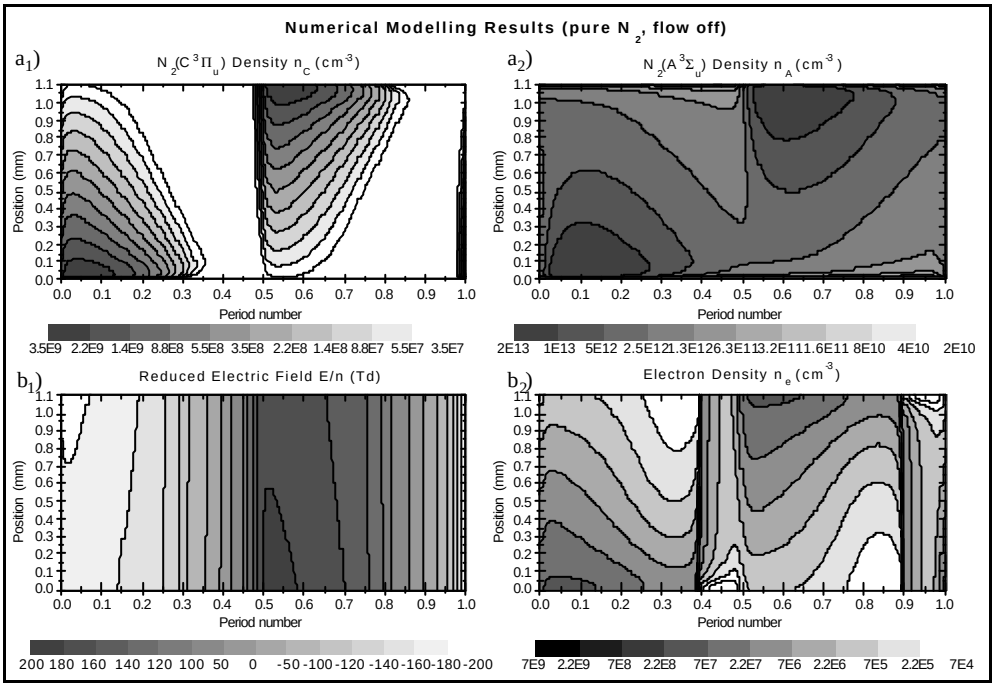


FIGURE 3. Results of numerical modeling: particle densities (N_2(C), N_2(A), e) and reduced field E/n

Following the discussion in the foregoing part of this paper and assuming a homogeneous distribution of NO in the entire discharge volume, the NO_γ radiation can be taken as an indicator for the N_2(A) metastables, i.e. the figures $2a_2$ and $2b_2$ can be compared directly with fig.$3a_2$. Due to the reactions

(6a) and (9), the ON_2 radiation intensity (fig. $2b_1$) may be related to the metastable density (fig.$3a_2$) as well. All these pictures demonstrate a reasonable qualitative agreement. The maximums are always located near the anode, but they are noticeably delayed against the SPS radiation (fig.$2a_1$), respectively against the $N_2(C)$ density (fig.$3a_1$).

The influence of the oxygen admixture on the APGD mechanism is clearly seen from the comparison of the NO_γ radiation intensity distributions, corresponding to the different levels of the background oxygen concentrations (fig. $2a_2$ and $2b_2$). In the case of "pure nitrogen" (fig.$2a_2$), the distribution seems to be smoother. The smoothest is the distribution of the $N_2(A)$ metastable density (fig.$3a_2$). The steeper decay of the experimentally observed intensity distributions over the time axis as compared to the calculated distribution of the $N_2(A)$ metastable density, can be explained by the effective collisional quenching of $N_2(A)$ by the background oxygen (20 or 100 ppm, fig. $2a_2$ and $2b_2$, respectively).

However, this explanation does not account for the steeper intensity distributions of the NO_γ radiation over the spatial axis (fig. $2a_2$ and $2b_2$), as compared to the $N_2(A)$ metastable density (fig.$3a_2$). The latter discrepancy between the modeling results and experimental data may be explained either by certain drawbacks of the model, e.g. by improper formulation of the boundary conditions (accumulation and release of the surface charges), or by some specific 2-D effects of the experimental discharge cell geometry (semi-spherical electrodes contrary to a parallel-plane arrangement implied in a 1-D model).

4. CONCLUSIONS

1. General qualitative agreement between the spatio-temporally resolved spectroscopic data and the results of numerical modeling of the APGD in nitrogen, confirm the validity of the discharge mechanism based on the dominant role played by the nitrogen metastables.
2. The variation of the oxygen admixture within the range 20-500 ppm have been experimentally found to exert a strong influence on the spectral and electrical characteristics of the discharge, that can be explained by the effective collisional quenching of the nitrogen metastables by molecular oxygen.

ACKNOWLEDGMENTS

The spatio-temporally resolved measurements has been done within the SFB-198 "Kinetics of partially ionized plasmas" of "Deutsche Forschungsgemeinschaft" (DFG).

REFERENCES

[1] Kanazawa S., Kogoma M., Moriwaki T. and Okazaki S., *J. Phys. D: Appl. Phys*., **21**, 889 (1988)
[2] Gherardi N., Gouda G., Gat E., Ricard A. and Massines F., *Plasma Sources Sci. Technol.,* **9,** 340-346 (2000)
[3] Segur P. and Massines F., *Proc. of Gas Disch. and their Applications (GD),* Glasgow, UK, 2000, pp.15-24
[4] Golubovskii Y.B., Maiorov V.A., Behnke J., Behnke J.F., *Proc. of 15th Intern. Symp. on Plasma Chem. (ISPC 15),* Orleans, France, 2001, pp. 3239-3244
[5] Golubovskii Y.B., Maiorov V.A., Behnke J., Behnke J.F., *J. Phys. D: Appl. Phys.*, (2002) accepted
[6] Massines F. and Segur P., *Proc. APP Spring Meeting,* Bad Honnef, Germany, 2001, pp. 29-38
[7] Kozlov K.V., Wagner H.-E., Brandenburg R., Michel P., *J. Phys. D.: Appl. Phys.,* **34,** 3146-3176 (2001)
[8] Brandenburg R., Kozlov K.V., Massines F., Michel P. and Wagner H.-E., *7th Intern. Symp. on High Pressure Low Temperature Plasma Chem. (HAKONE VII),* Greifswald, Germany, **1,** 2000, pp. 93-97
[9] Gherardi N., Gat E., Massines F., Lemoing S. and Segur P., *Proc. of 15th Intern. Symp. on Plasma Chem. (ISPC 15),* Orleans, France, 2001, pp. 97-103
[10] Kossyi I. A., Kostinsky A. Y.,Matveyev A.A., Silakov V. O., *Plasma Sources Sci. Technol.*, **1**, 207-220 (1992)

POSITIVE AND NEGATIVE PULSED CORONA IN ARGON

E.M. van Veldhuizen[a], W.R. Rutgers, U. Ebert

Department of Physics, Technische Universiteit Eindhoven
5600 MB Eindhoven, The Netherlands

Abstract: Photographs are obtained of corona discharges in argon at atmospheric pressure using a high resolution, intensified CCD camera. Positive and negative polarity is applied at the curved electrode in a point-plane gap and a plane-plane gap with a protruding point. Branching is observed in the positive point-plane gap but it is much less pronounced than in air probably due to the much lower energy input. The positive point-protrusion case does not show branching and it very rapidly develops into a spark breakdown. The negative corona in argon requires roughly a two times higher average applied field to develop a discharge. Its appearance is diffuse in the point-plane as well as in the plane-protrusion case. Since the inception voltage and the breakdown voltage in argon are quite close to each other it is not possible using the present set-up to obtain experimental results at the very high field condition where a new theory predicts streamer formation and branching in negative corona.

1. INTRODUCTION

Corona discharges have fascinated people for a long time. Physical research on these phenomena already started early in the twentieth century [1, 2]. In the last two decades of this century possible applications of (pulsed) corona discharge have been subject of intense research [3]. Pulsed corona here implies that the power source which creates the discharge is switched on and off on a (sub-)microsecond time scale to obtain high electric fields without sparking. Recently power supplies have become available that will enable large scale application while having a high efficiency, good reliablity and acceptable investment cost [4]. A great effort is put into advanced diagnostics and detailed simulations of the streamers which are created by the corona discharge [3]. Simulations have concentrated up to now on the single streamer discharge. In reality often strong branching is observed [1] and this will have a large impact on the distribution of active particles that are created and probably also on the energy efficiency with which they are formed. Recently this branching phenomenon is studied for positive corona in air with the use of a CCD camera with a high resolution in space and time [5, 6]. Modeling of branching has been done occasionally on the basis of stochastic processes [7-9], but the results are very limited upto now. Recently a completely different branching mechanism of streamers is found in a fully deterministic fluid model [10]. This model is derived, for the moment, for the case of negative streamers in a homogeneous electric field where photoionization can be neglected and no negative ions are present. This case is quite different from positive streamers in air. For this reason an investigation of pulsed corona in argon is made with positive polarity to compare them with previous results obtained in air, and with negative polarity to approach the predictions of the deterministic branching model.

2. EXPERIMENTAL SET-UP

The electrodes of the corona discharge are contained in an aluminium cube which is evacuated before filling it with argon of 99.999% purity. A flow of ~30 sccm is maintained, this gives a residence time of roughly 30 minutes. Figure 1 shows schematically the gap configurations that have been used for the

[a] Email: e.m.v.veldhuizen@tue.nl

experiments. Configuration (a) is a point-plane gap having a stainless steel cathode and a tungsten pin of 1 mm diameter which has a tip with a radius of ~15 μm. The same tip is used in all other configurations. In gap (b) two identical stainless steel electrodes are used but the top one contains the needle with a protrusion of 5 mm length. Corona inception is very rare with smaller protrusions. The field distribution becomes much closer to homogeneous by the introduction of the second plate as is shown in [11]. In gaps (c) and (d) a negative corona is created and the gap is made smaller to have better corona inception.

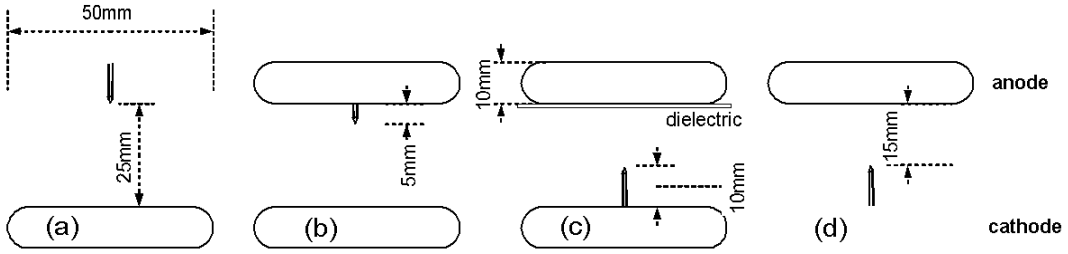


FIGURE 1. Gap configuration to create positive (a, b) and negative (c, d) corona dicharges.

The pulsed power supply is similar to the one used in [5] and [6]. Its main features are a 1nF coupling capacitor which is discharged by a fast switch giving a pulse rise time of 20 ns. The semiconductor switch (Behlke HTS-301) is used for the case of argon because at the relatively low voltages required here the available spark gap did not function reliable while the semiconductor switch retains its 0.1 ns jitter.

Photographs of the corona discharges are taken using an intensified CCD camera (Andor Technology ICCD-452). This camera has a spatial resolution of 20 μm, a minimum optical gate time of 0.8 ns and photon counting sensitivity. The complete gap is always imaged on the CCD with a 2:1 magnification using a quartz lens. The photos in this paper are taken with optical gates of several microseconds. Examples of the 0.8 ns optical gate can be found in [5] and [6].

The photographs of the CCD camera are digitized with 16 bits resolution so values from 0 to 64535 (a.u.) are possible. In reality the intensity saturates at 45000. Peltier cooling to –10 °C is always used, this gives a uniform background of ~880 with a fluctuation of not more than 10. Background substraction is not performed because it increases the noise. An intensity difference of ~10 can already be differentiated from the background. So the measurement has a very large dynamic range which cannot be represented on a printed version. In all photos the highest intensity of the optical emission is at the sharp tip and the intensity of the discharges in the gap are 10 to 1000 times lower in intensity. Breakdown channels have ~100 times higher intensity than this anode spot. Images can be reproduced in grey scale, as printed in this proceedings, or in false color pictures, as given on the Internet version of this proceedings or several other papers [5-6, 10]. The color pictures give more information because it can show more levels of intensity.

3. RESULTS

3.1 Positive corona in argon

The discharge in argon has been studied first with the point-plane gap as indicated in fig. 1a. The lowest voltage at which optical emission is detected is 3.5 kV. An example is shown in fig. 2a. One interesting feature of this picture is that is shows that the streamers bridge the whole gap. In air the first discharge is detected at 5 kV but only as a very small spot at the anode. The first, short streamers are observed at 6 kV and the lowest voltage at which the streamers reach the cathode is 12.5 kV [6]. Another interesting difference with air is that branching is less pronounced in argon. An increase of emission is seen near the cathode in the case of the two streamers that hit the cathode at the right side of the photo. This looks somewhat similar to the return stroke of lightning. The energy content of this corona pulse could not be determined because the current pulse was too weak to be detected with the equipment used. It can be remarked that the optical diameter of positive streamers in argon is more or less the same as in air [5].

(a) (b)

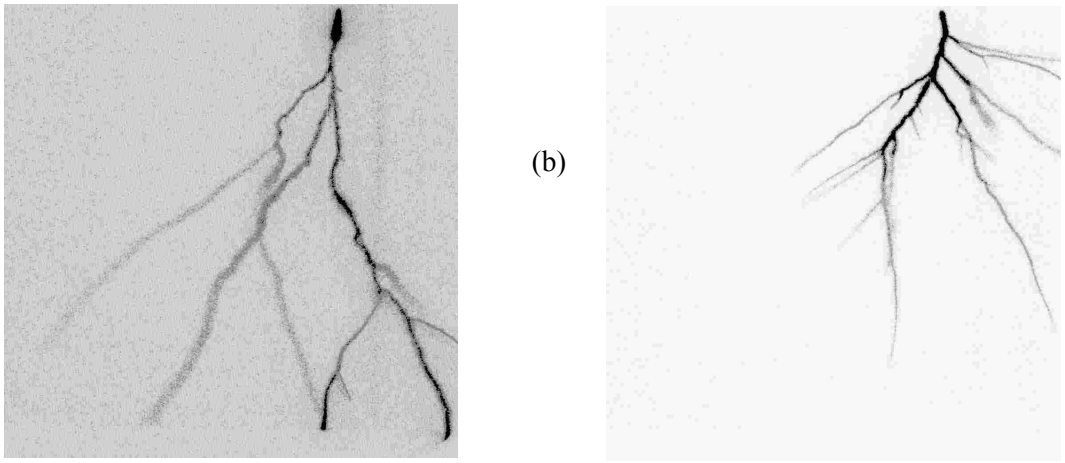


FIGURE 2. Positive corona in argon at 1 bar using electrode geometry A, voltage 3.5 kV in (a) and 5 kV in (b).

A picture as fig. 2a is a very rare occasion at the voltage of 3.5 kV. At this voltage level it was necessary, on average, to take 50 to 100 shots to obtain one photo with streamer channels. On some photos the streamers propagate only a fraction of the gap. Again this is different from air where at a certain voltage the length of the streamers is proportional to the voltage in the range of 5 to 12.5 kV. Fig. 2b shows the positive corona in argon using a pulse amplitude of 5 kV. This picture shows more branching than fig. 2a but the streamers do not reach the cathode. The central streamer attached to the anode is more intense than the other branches. Again the energy content of the pulse cannot be detected. At this voltage level one photo is obtained with on average ten high voltage pulses. At 6 kV spark breakdown occurs which is easily seen by eye.

The pictures taken with the plane-protrusion gap of fig. 1b look very different. Now the lowest voltage at which, occasionally, optical emission is observed is 4 kV. This emission is seen either as only a very small spot at the anode, fig. 3a, or as one streamer bridging the whole gap, fig. 3b-c. Intermediate shape have not been observed. At 4.5 kV a more intense streamer is observed as shown in fig. 3d. At this same voltage also a spark breakdown can occur, examples are given in fig. 3e-f. Branching has never been observed in this geometry using argon gas, this is also very different from corona in air [11].

(a) (b) (c) (d) (e) (f)

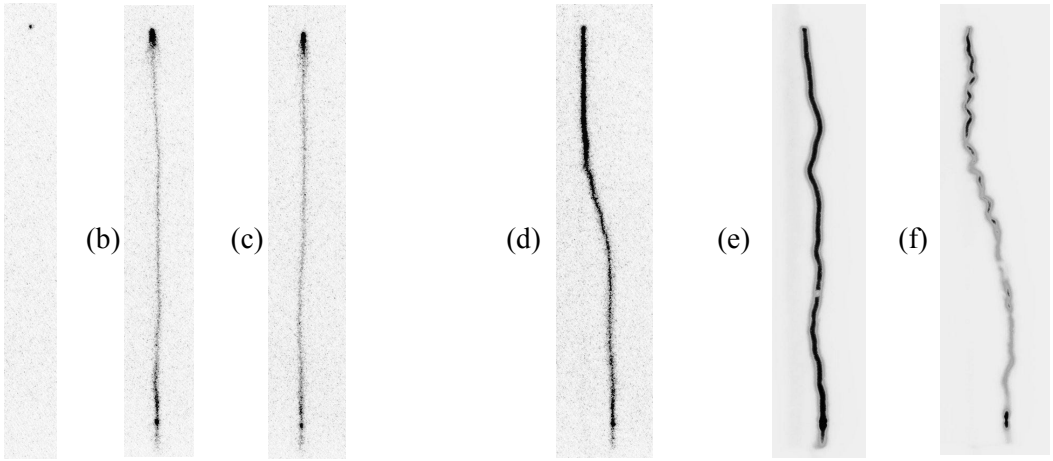


FIGURE 3. Positive corona in argon obtained with gap configuration b, a-c are at 4 kV, d-f at 4.5 kV.

3.2 Negative corona in argon

The first tests have been performed with configuration 1c with a small protrusion and an additional dielectric cover of 0.5 mm thickness on the anode since spark breakdown may occur immediately at the inception voltage. Using the larger 10 mm protrusion, optical emission is observed below breakdown voltages. Fig. 4a is obtained at a pulse amplitude of 5 kV, fig. 4b at 7 kV. In both cases the probability of

obtaining a photo is one per five high voltage pulses. The intensity at the tip is again much higher than in the gap. Photos taken with shorter optical gate times, down to 30 ns, also did not reveal any streamerlike structure. Fig. 4c is at 9 kV, but some pictures at this voltage look much more like fig. 4b. It is clear that in this case a surface discharge develops on the dielectric and it appears to be very diffuse. At 10 kV sparking occurs in few thin channels in the gas and also on the surface.

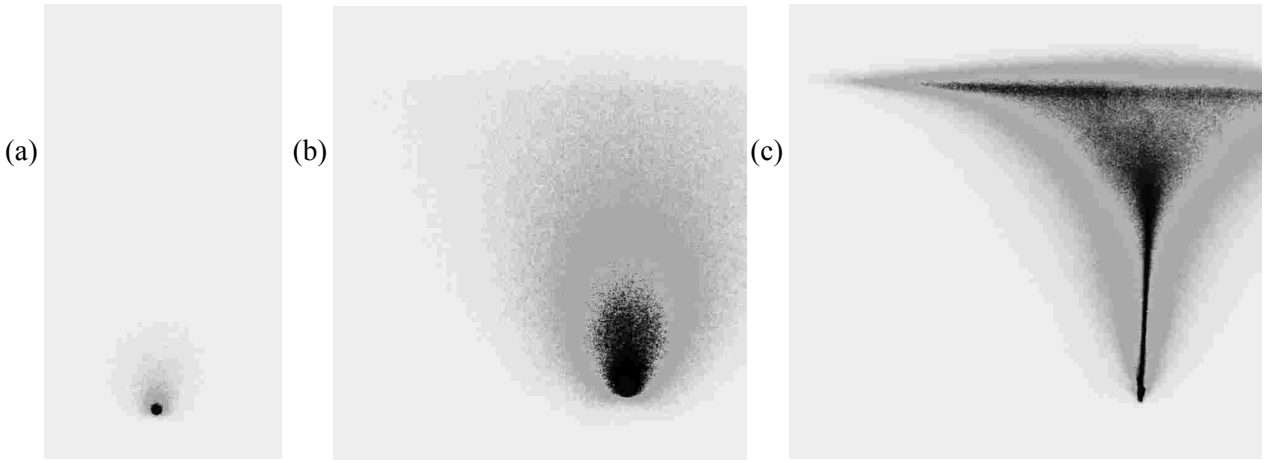


FIGURE 4. Negative corona in argon obtained with gap configuration c, a is at 5 kV, b at 7 kV and c at 9 kV.

The negative corona in a 15 mm point-plane gap with a metal anode (gap d) ignites much easier than the one between plane electrodes with a protrusion (gap c) which has a dielectric sheet on the anode. This is most likely due to the much higher field strength at the tip in the case of gap d [11]. Optical emission is observed at almost all electrical pulses of 5 kV and more, see fig. 5a-b in comparison with 4a-b. The appearance of the emission is quite similar, a diffuse cloud fills the gap. As is to be expected breakdown occurs at lower voltages now, sometimes already at 6 kV. At 7 kV almost always a breakdown occurs, a few examples are shown in fig. 5c-e.

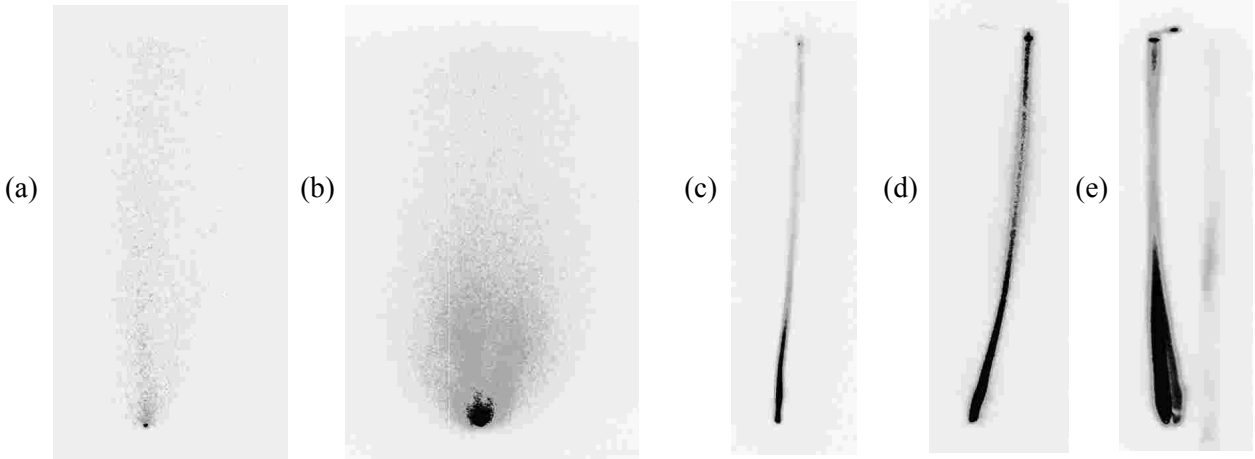


FIGURE 5. Negative corona in argon obtained with gap configuration d, a is at 5 kV, b at 6 kV and c-e at 7 kV.

4. DISCUSSION AND CONCLUSIONS

In the past it has been remarked that discharges in argon do not show prebreakdown effects [12]. In the course of our measurements it became clear that there are two reasons why it is so difficult to observe these effects. In case of the positive corona in a 25 mm point-plane gap the inception voltage in argon is 3.5 kV and in air it is 5 kV. The lowest voltage at which streamers reach the cathode is 3.5 kV in argon and 12.5 kV in air. At 3.5 kV in argon the discharge starts only sporadically, but at 5 kV in argon it starts

almost always. From these figures it can be concluded that the inception is roughly at the same voltage but the propagation in the gap is very different. This is expected from theory which says that streamers can propagate above a threshold, the "stability field" [3]. This field is 5 kV/cm for air and 0.4 kV/cm in argon [13]. This low stability field explains why corona inception and sparking are very close to each other. The second difficulty for the measurements in argon is that already at 5 kV breakdown occurs occasionally and at 6 kV regularly. So the range of voltages in which streamers can be observed is very limited. The combination of stochastic inception and very easy breakdown is probably the reason why streamers in argon could not be detected in the past. In the plane-plane gap with a protrusion these effect are even more pronounced. Inception is sporadic at 4 kV and breakdown occurs quite often at 4.5 kV. Branching is never observed in this geometry at these voltages.

The branching behaviour of positive corona in argon is also quite different from air: much less branches are observed. Since the field strength and the number of ions of a streamer head are limited, so its energy content must also be limited. Therefore one can expect that the number of branches depends on the energy input. The energy content of the corona pulse in argon could not be established but it is estimated to be 10 to 100 times less than in air. The maximum field strength at the streamer head can be estimated from the bending point of the ionization coefficient versus the electric field strength [14] using experimental data. This leads to 100 kV/cm for argon [15] and 150 kV/cm for air [16]. So because these fields a quite similar, a lower number of streamers in argon can indeed be expected.

The discharge behaviour is quite different when the cathode is strongly curved rather than the anode. Roughly 1.5 times higher voltages are required for inception and breakdown in a gap which is 15 mm instead of 25 mm. This factor is the same for argon and air. The discharge appears as a diffuse cloud which can also spread across a dielectric surface, if present. Time resolved measurements, which were possible down to 30 ns optical gate time, did not reveal any difference in shape and the cloud is present for several hundred nanoseconds. This behaviour is very different from the simulations in [10] where a much higher field is applied. In the present experiment such conditions lead to spark breakdown. The measurements can be improved by using a very short high voltage pulse to prevent breakdown, a pre-ionization trigger to overcome inception problems, and lower operating pressures to slow down the evolution so that it can be observed by the CCD camera. Then the parameter range as used in the simulations of [10] may come within reach.

REFERENCES

[1] A.M. Cravath, L.B. Loeb, *Physics* **6**(1935)125.

[2] H. Raether, *The development of electron avalanche in a spark channel (from observations in a cloud chamber)*, Zeitschrift fur Physik **112**(1939)464.

[3] E.M. van Veldhuizen (editor), "*Electrical Discharges for Environmental Purposes: Fundamentals and Applications",* Nova Science Publishers, New York, 1999, ISBN 1-56072-743-8.

[4] K.Yan, *Corona Plasma Generation*, PhD thesis, Technische Universiteit Eindhoven, 2001.

[5] E.M. van Veldhuizen, A.H.F.M. Baede, D. Hayashi, W.R. Rutgers, *"Fast imaging of streamer propagation"*, APP Spring Meeting, Bad Honnef, Germany, februari 2001, p. 231-234. (also on Internet: http://www.ilp.physik.uni-essen.de/doebele/Spring2001/pdf/116.pdf).

[6] E.M. van Veldhuizen, P.C.M. Kemps, W.R. Rutgers, accepted for *IEEE Plasma Science*, feb. 2002.

[7] S. Badaloni, I. Gallimberti, Proc. XI ICPIG, Prague, 1973, p. 196.

[8] N. Femia, L. Niemeyer, V. Tucci, J. Phys. D: Appl. Phys. **26**(1993)619.

[9] I.P. Vereshchagin, A.A. Beloglovsky, A.G. Mikheev, O.I. Kondratov, E.J.M. van Heesch, XIII Int. Conf. Gas Disch. & Appl., Glasgow, September 2000, p. 579.

[10] M. Arrayas, U. Ebert, W. Hundsdorfer, accepted for Phys. Rev. Lett. (http://xxx.lanl.gov/abs/nlin.PS/0111043).

[11] E.M. van Veldhuizen, W.R. Rutgers, submitted to J. Phys. D: Appl. Phys.

[12] J.M. Meek, J.D. Craggs, *Electrical breakdown of gases*, Clarendon, Oxford, 1953.

[13] Yu. Raizer, *Gas Discharge Physics*, Springer, Berlin, 1991.

[14] M.I. Dyakonov, V.Yu. Kachorovskii, Sov. Phys. JETP **67**(1988)1049.

[15] N. Bonifaci, A. Denat, V. Atrazhev, 12th Int. Conf. Gas Disch., ed. G. Babucke, Greifswald, 1997, p. I-244.

[16] E.M. van Veldhuizen, V.A. Bityurin, W.R. Rutgers, Plasma Chem. Plasma Procs. **16**(1996)227.

COMPARATIVE STUDY OF PULSED CORONA AND DIELECTRIC BARRIER DISCHARGES USING SINGLE-STREAMER MODELING AND NO DECOMPOSITION EXPERIMENT

Yong-Ho Kim[a], Woo Seok Kang[b], Sang Hee Hong[b], and Young-Hoon Song[a]

a) Korea Institute of Machinery and Materials, Daejeon 305-343, Korea
b) Department of Nuclear Engineering, Seoul National University, Seoul 151-742, Korea

Abstract. A single-streamer modeling is carried out to compare the characteristics of non-equilibrium plasmas in the pulsed corona and dielectric barrier discharges. The numerical simulation predicts that the pulsed corona discharge is more efficient for generating N species whereas the dielectric barrier discharge is more effective for generating O species. NO decomposition experiments are then performed in order to verify such numerical prediction and find the influence of the streamer characteristics on the generation of chemically active species.

1. INTRODUCTION

In recent years, there has been a growing interest in comparative studies between pulsed corona discharges (PCD) and dielectric barrier discharges (DBD) for the purpose of getting the more effective decomposition of toxic gases. Most of the previous work has, however, been focused on the plasma chemical reactions without paying attention to the plasma and chemically active species (CAS) [1, 2]. In this study, a single-streamer modeling makes out the characteristics of streamers in PCD and DBD in advance of NO decomposition experiments using these two discharge methods. It is then examined by comparison between numerical and experimental results how the streamer characteristics affect the generation of chemically active species, such as N and O, in each discharge.

2. SINGLE-STREAMER MODELING

A numerical model, as shown schematically in Fig. 1, includes the three modules for non-equilibrium plasma, chemically active species, and plasma interaction properties. The non-equilibrium plasma module deals with pulsed corona discharges (PCD) and dielectric barrier discharges (DBD). A wire-cylinder geometry is taken as for PCD and a parallel-plate geometry for DBD in this work. Although the generation of many streamers takes place at the same time in each discharge reactor, a single-streamer model assumes that the neighboring streamers are separated far away from each other so that their interactions are neglected and all the streamers have the same physical properties. From this assumption, only one streamer is taken into account in this numerical simulation. A time-dependent 1.5-D model for the propagating single streamer consists of Poisson's equation for the electric potential and continuity equations for the charged particle densities. The electric field strength on the axis of the propagating streamer is

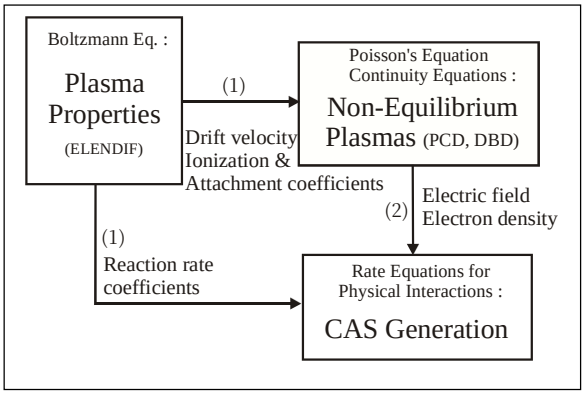


Figure 1. Three integrated numerical modules solving the streamer characteristics in PCD and DBD reactors.

[a] Electronic address: kimyh@kimm.re.kr

evaluated using the method of disk. And the charged particle densities are calculated by a flux corrected transport (FCT) algorithm with the upwind and Lax-Wendroff methods as the low- and high-order schemes, respectively. These calculated plasma variables are used in a CAS module, where the densities of several CAS are calculated by taking into account a set of rate equations for electron interactions with air molecules. Boltzmann equation solver, ELENDIF, is adopted in order to obtain the transport and collision coefficients for self-consistent calculations of the plasma and CAS modules. The electron drift velocity, ionization and attachment coefficients are used for the plasma module and then the reaction rate coefficients, representing dissociation and excitation, are also obtained for the CAS module. All the plasma properties calculated by ELENDIF can be then tabulated as a function of the electric field in the range of 5 ~ 200 kV/cm.

3. NO DECOMPOSITION EXPERIMENT

The comparative experiments are focused on the NO decomposition behavior in nitrogen(N_2) and air for both PCD and DBD reactors. Whereas the nitrogen discharge is expected to characterize the N generation efficiency, the air discharge is to the O generation efficiency. A present experimental system consists of a PCD reactor with a pulse power supply, a DBD reactor with an AC power supply, a gas supply facility, and measuring equipment for discharge and gas cleaning. The PCD processing is carried out in a wire-cylinder reactor, as shown in Fig. 2(a), which is composed of a stainless steel wire electrode of 350-mm length and a cylinder electrode of 27-mm inner diameter. Two different diameters of 1 and 2 mm are chosen for the wire electrode. The pulse power supply operated with a rotary spark-gap switch is delivering up to 40-kV voltage in a 100-ns width pulse of which repetition rate is fixed at 60 Hz. The DBD processing reactor has a coaxial-cylinder geometry as shown in Fig. 2(b). An outer cylinder electrode is made of a metal strip with a length of 240 mm wrapped on a Pyrex tube (permittivity 4, inner diameter 27 mm, thickness 1.5 mm) acting as a dielectric barrier. The 2- or 4-mm discharge gap is maintained by alternately inserting the two inner rod electrodes with different diameters inside the cylinder. This DBD reactor is operated with a sinusoidal frequency of 60 Hz. In measuring the discharge energy deposited in the plasma, two electrical methods of current-voltage and charge-voltage measurements are adopted for the PCD and DBD, respectively. Three different NO concentrations of 100-, 200-, and 300-ppm in both nitrogen and air ambient gases are initially supplied to the reactors. The decomposed gas compositions exhausted from the reactor outlet after cleaning process are monitored with a chemiluminescent NO_x analyzer.

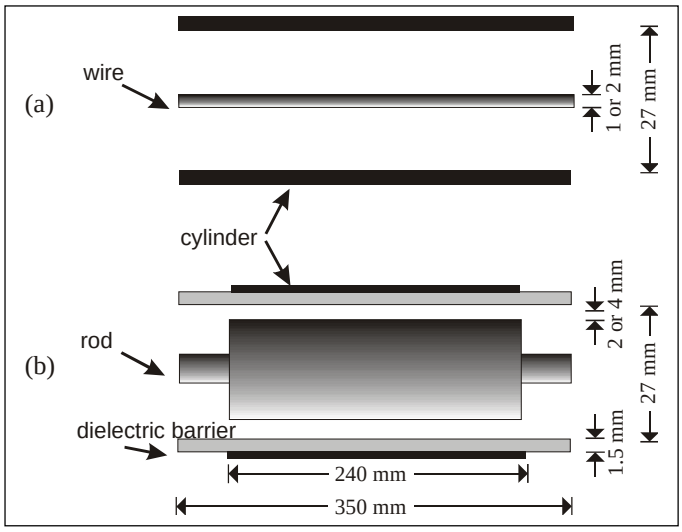


Figure 2. Cross-sectional views of the (a) wire-cylinder PCD and (b) coaxial-cylinder DBD reactors.

4. RESULTS AND DISCUSSION

4.1. Calculated Characteristics of Propagating Streamers

The single-streamer modeling is first carried out in the wire-cylinder geometry for the PCD reactor. The radii of the anode wire and cathode cylinder are 0.1 and 1.35 cm, respectively. An external pulse voltage of 30 kV is applied to the anode wire, and a spatially uniform electron distribution of 1 cm^{-3} is used as an initial condition. A grid size of 10^{-3} cm and a time step of 10^{-12} sec are taken for the

calculations. The streamer radius, which is an undetermined parameter in this 1.5-D modeling, is chosen for 700 μm because Zhukov [3] recently reported that the streamer radius increases up to 700 μm when a sufficiently high voltage is applied in the PCD reactor. Figure 3(a) shows the radial distributions of electric field in the wire-cylinder PCD reactor. The streamer propagates along its channel with the electric fields in the range of 140 ~ 160 kV/cm, which are rapidly enhanced near the anode wire region. Due to the initial non-uniform electric field of about 100 kV/cm formed near the wire electrode, the entire region along the propagating streamer path is filled with energetic electrons, of which density is around 4×10^{13} cm^{-3} as shown in Fig. 3(b).

For the simulations of a single streamer in the DBD reactor, two glass-barrier plates (permittivity 4, thickness 0.15 cm) assumed to be attached on the anode and cathode electrodes, respectively. The discharge gap distance between two barriers is 0.2 cm. The seed electrons are initially placed in front of the cathode-sided barrier with a Gaussian shape, of which peak electron density is 10^3 cm^{-3}. In the DBD modeling, a streamer radius of 200 μm is used as the other previous work. The calculated electric fields and electron densities are shown in Fig. 3(c, d) when a 12 kV is applied between the electrodes of the DBD reactor. A uniform electric field of 50 kV/cm shown in Fig. 3(c) is produced at first in the air gap and it makes the seed electrons pushed toward the anode-sided barrier. During such drift motions, electron multiplication or electron avalanche is observed until the electrons arrive at the anode-sided barrier shown in Fig. 3(d). After this moment of 9 ns, the charged particles continue to

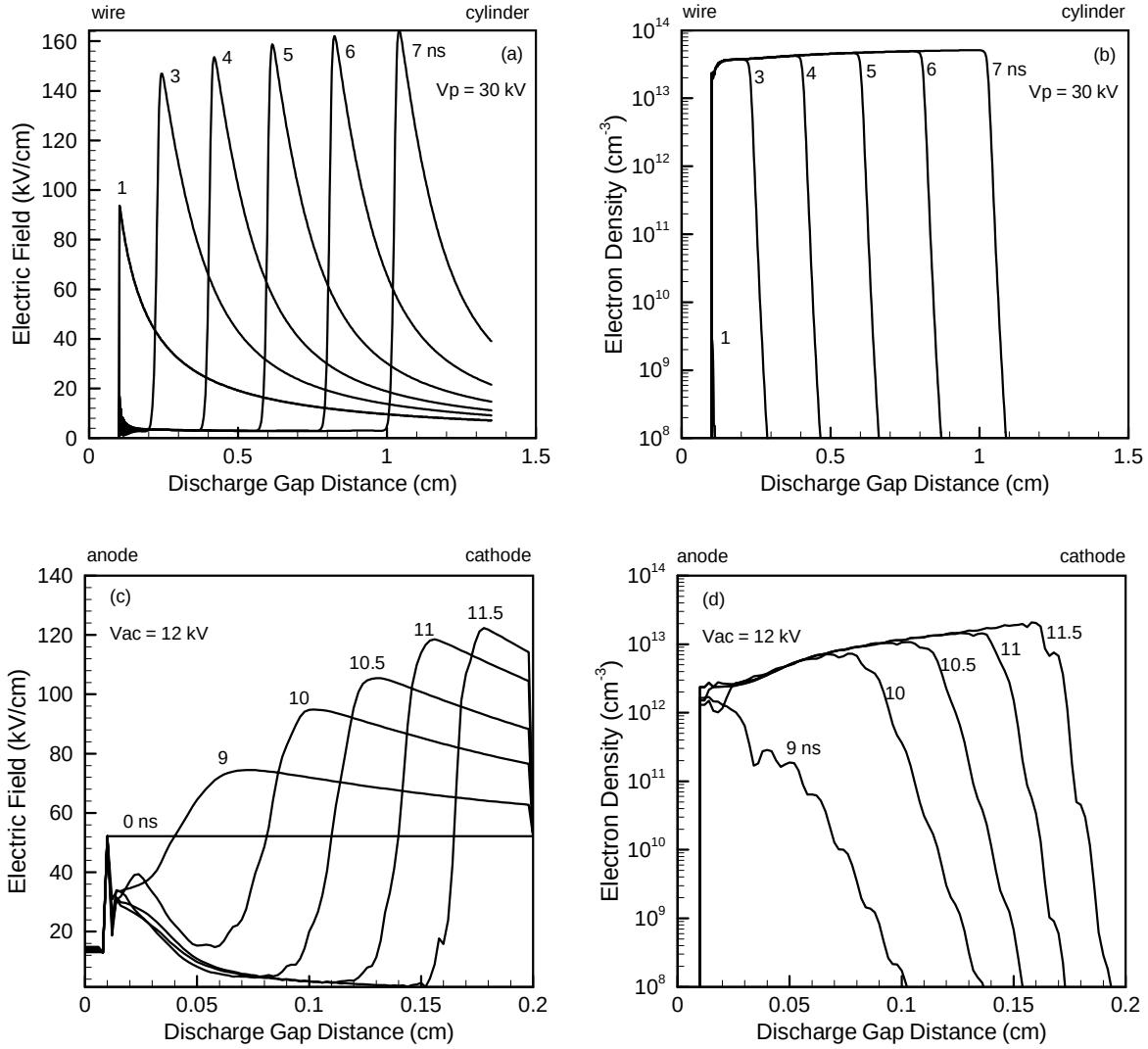


Figure 3. Temporal development of calculated distributions of electric field and electron density during the streamer propagation in a wire-cylinder PCD reactor (a, b) and in a parallel-plate DBD reactor (c, d).

build up near the anode-sided barrier and a streamer starts to be formed. The electric field distributions plotted in Fig. 3(c) show the cathode-directed streamer propagation. During this streamer propagation, the gradually increasing electric fields are observed in the range of 80 ~ 120 kV/cm before the cathode-directed streamer arrives in the vicinity of the cathode-sided barrier. The streamer in the DBD generates a relatively lower electric field due to the initial uniform electric field compared with the PCD.

4.2. Estimated Generation Efficiencies of Chemically Active Species

During the streamer propagation in either PCD or DBD, electrons in front of the streamer head are rapidly accelerated and they lose energy through inelastic collisions with background molecules. Several electron-impact interactions with air molecules are taken into account in the numerical simulation for predicting the generation efficiency of chemically active species, that is G-values. The G-values of chemically active species, such as N and O, are obtained by taking advantage of the Boltzmann solver, ELENDIF code [2]. This code calculates the electron energy distribution functions using electron-molecule collision cross sections, which are given for N_2 and O_2 by Phelps (1995) and for H_2O by Hayashi (1987). It also provides the transport and reaction rate coefficients, which depend on the gas composition and electric field. Figure 4 shows the calculated G-values as a function of electric field strength for an ambient air including $N_2/O_2/H_2O$ of 0.792/0.198/0.01. The generations of O, $N_2(A)$, and $O(^1D)$ species are efficient in the low electric field ranges, whereas N species tend to increase with the electric field. The shaded regions in Fig. 4 represent the ranges of the electric field obtained from the preceding single-streamer modeling. The simulation results predict that the PCD is more efficient for generating N species whereas the DBD is more effective for generating O species.

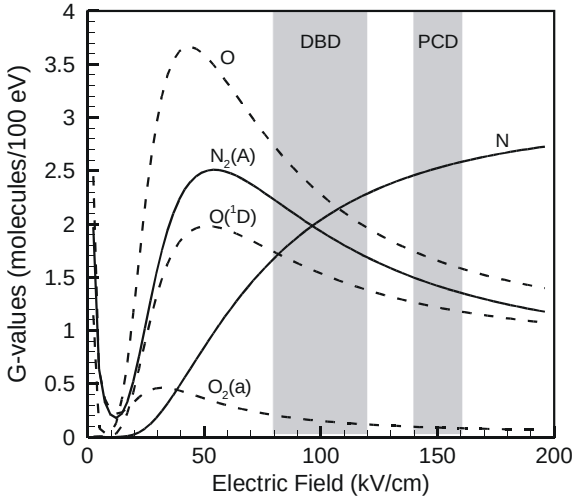


Figure 4. G-values of the CAS generated by electron collisions with air molecules.

4.3. NO Decomposition Measured in N_2 and Air

In the existence of N_2 gas, the decomposition experiments of NO molecules are first performed in the PCD reactors with two wire electrodes (r = 0.5 mm and r = 1 mm) and the DBD reactors with two different discharge gaps (d = 2 mm and d = 4 mm), respectively. Figure 5(a) presents the measured results for the degree of NO removal, $[NO]/[NO]_0$, in nitrogen as a function of input energy density in J/l in case of $[NO]_0$ of 200 ppm. As a result of NO decompositions in nitrogen, the PCD reactors show the higher efficiencies of NO removal. The NO decomposing agent in the nitrogen atmosphere is only N species, and its generation efficiency increases in proportion to the electron energy in the discharge reactor as estimated in Fig. 4. Therefore, it is experimentally proved that the PCD generates higher energy electrons than the DBD does as predicted in the single-streamer modeling. In addition, when a wire electrode of smaller radius (r = 0.5 mm) is used for the PCD reactor, it decomposes more NO molecules than the one of larger radius does. This is evidently due to the enhancement effect of electric field around the thinner wire in this PCD reactor. In case of the DBD, NO is more easily decomposed when the discharge gap distance becomes narrower. As a consequence of the NO removal experiments in nitrogen, it is found that the PCD reactor will be more efficient plasma source when decomposing pollutants with strong chemical binding energy.

Using atmospheric-pressure air as an ambient gas, the decompositions of NO are re-examined in these PCD and DBD reactors. The other experimental conditions are the same as those used in the previous experiments except for changing the ambient gas from nitrogen to air. Figure 5(b) indicates that the

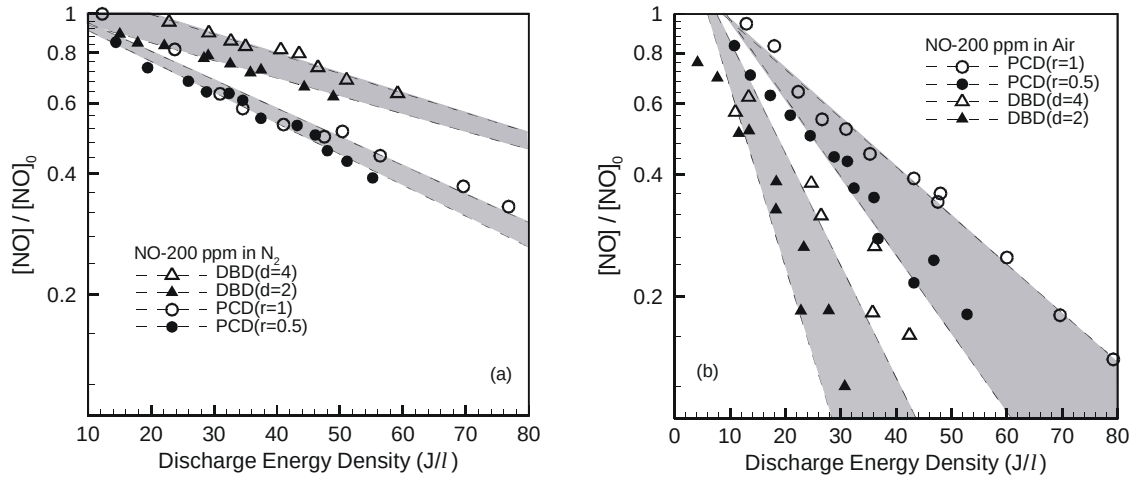


Figure 5. Measured degrees of NO removal as a function of discharge energy density in (a) N_2 and (b) air.

NO is decomposed in air with less electrical energy in both types of the discharge method. The PCD is decomposing NO in air only with consuming 50 ~ 60 % of the electrical energy compared with the decomposing energy in nitrogen. Especially, the saving of electrical energy is even greater in the DBD, which consumes about 10 ~ 20 % of the electrical energy required for the NO decomposition in nitrogen. As seen in the preceding Section 4.2, O species are the dominant agent for NO decompositions in air atmosphere and they are most effectively generated by the electric field of around 50 kV/cm. Therefore, it is also concluded that the relatively low electron energy in the DBD is more appropriate for generating O species and oxidation of chemicals.

5. CONCLUSIONS

Using the single-streamer modeling, the characteristics of the non-equilibrium plasma are compared between the pulsed corona and dielectric barrier discharges. The simulation results show that the PCD generates the energetic streamers with electric fields of 140 ~ 160 kV/cm in a wide region of the wire-cylinder reactor. On the other hand, the streamers in the DBD have relatively low electric fields of 80 ~ 120 kV/cm. The estimated G-values indicate that the PCD is more efficient for generating N species whereas the DBD is more effective for generating O species. Theoretical predictions are verified from the NO decomposition experiments that the PCD shows the higher efficiency of NO decomposition in nitrogen atmosphere, while the DBD gives the better performance in decomposing NO in air condition. In consequence, the numerical simulation on the characteristics of plasma and chemically active species turns out to be very informative for the performance comparison between different non-equilibrium plasma sources.

ACKNOWLEDGEMENT

This work has been supported by National Research Laboratory Program of KISTEP and Ministry of Science & Technology of the Republic of Korea.

REFERENCES

[1] L. A. Rosocha and R. A. Korzekwa, *J. Adv. Oxid. Technol.*, **4**, 247 (1999).
[2] B. M. Penetrante, M. C. Hsiao, B. T. Merritt, G. E. Vogtlin, and P. H. Wallman, *IEEE Trans. Plasma Sci.*, **23**, 679 (1995).
[3] S. V. Zhukov, M. V. Sokolova, and A. G. Temnikov, Proc. 7th Int. Symp. on High Pressure Low Temperature Plasma Chemistry, Greifswald, Germany, (2000).

SURFACE DISCHARGE CHARACTERISTICS FOR DIFFERENT TYPES OF APPLIED VOLTAGE AND DIFFERENT DIELECTRIC MATERIALS

M.V.Kozlov[a], M.V.Sokolova[b], A.G.Temnikov[b], V.V.Timatkov[b], I.P.Vereshchagin[b]

a) Russian Joint Stock Company "Unified Energy System of Russia" Export Dept. ul.Academica Chalomeya 5a, 117630 Moscow, RUSSIA
b) Department of Electrophysics and High Voltage Technique, Moscow Power Engineering Institute, Krasnokazarmennaya 14, 111250 Moscow, RUSSIA

Abstract. Surface discharge characteristics from multi-striped electrodes on the surface of thin dielectric plates of different kind of ceramics are presented. Experimental results obtained with voltage pulses of microsecond and nanosecond duration show significant difference of discharge structure, current impulse amplitude and intensity of ozone formation for the case when a polyaluminosilicate ceramic is used as a dielectric barrier compared with an alumina ceramic. Nanosecond voltage impulses give more dense and uniform discharge structure than long ones.

1. INTRODUCTION

The surface discharge as well as a barrier one can be used as plasma chemical reactor to produce different types of species such as ozone or atomic oxygen needed for treatment of gases containing toxic additives or in other plasma chemical technologies. Investigations of surface discharge [1,2] show that the most convenient form of the electrode is a stripe (or a wire) on the barrier surface and only initial stages of the discharge are of an interest when plasma-chemical processes are taken in view. More developed discharge stages when thermal ionisation is possible lead to a heating of the gas and of the dielectric barrier and to a decrease of the chemical species production efficiency. Although it is known that the main factors that define plasma chemical processes in a surface discharge are the electrode configuration, the applied voltage (its form and amplitude) and the material of the dielectric barrier, nevertheless for most cases the discharge structure and other parameters of the discharge such as its form (diffusive or discrete), the length, the diameter and the branching intensity of streamer channels or their number per unit length of the high voltage electrode are not known.

The aim of the present work was to investigate surface discharge characteristics for different types of ceramics because this material is one of the most advantageous for its use in a plasma-chemical reactor [2], and to analyse the influence of the material composition on the discharge development, its structure and light emission, its current characteristics and its effect on the ozone formation. The investigation is carried out using voltage impulses of different duration (this fact being significant for analysis of the mechanism of the discharge development) and using multi-striped configuration of high voltage electrode characteristic for ozone generators on surface discharge [2]. The main feature of the discharge that is analysed is its phenomenology in different conditions.

2. EXPERIMENTAL SETUP

A surface discharge developing from edges of thin metallic stripes placed on the surface of a ceramic plate was investigated. The stripe thickness is ≈ 25 μm, its width is 2 mm and the distance between the stripes from 2 to 8 mm. The dimensions of the plate are 24 x 36 mm for a single stripe case and

Electronic address: sokolova@fee.mpei.ac.ru

48 x 60 mm for a multi stripe case, the plate thickness being 1 mm. The earthed electrode is situated at the other side of the plate. The material of the plates is high frequency alumina ceramic of two types and polyaluminosilicate ceramic (policor). Volume (ρ_v) and surface (ρ_s) resistivity are given in table 1.

TABLE 1. Characteristics of the barrier materials

Ceramic material	ε	ρ_v , Ohm.m	ρ_s for 20 ^{O}C, Ohm	Electric strength, kV/mm	tg δ
Alumina, type A	9.4	10^{14}	10^{15}	54	0.0008
Alumina, type B	9.1	10^{14}	10^{15}	50	0.0001
Policor	9.9	10^{15}	2.10^{15}	50	0.00005

The high voltage pulses are formed by two specially constructed impulse generators. One of them forms pulses of microsecond duration (5-7μs) having form of a bell. The voltage amplitude can be (2-10) kV. Other generator produces rectangular pulses {full duration τ_p = 200 - 3000 ns, front duration τ_f = 50-500ns, U_m = (3-10) kV}. Additionally a series generator that forms nanosecond rectangular pulses of 5, 10, 20 or 50 ns duration with 1 ns front and amplitudes from 3 to 8 kV was used. For microsecond voltage pulses the pulse front steepness dU/dt could be made from 1 to 10 kV/μs.

Pictures of the discharge pattern were made by means of an image converter and by photo camera with high resolution and magnification. Discharge light emission was measured by means of a photomultiplier using filters that give ultraviolet and infrared parts of the light emission. To analyse the discharge current a 0.224 Ohm low inductance shunt and an impulse high-speed oscilloscope were used. Additionally ozone concentration in the gas flow was measured. The experimental procedure is given in details in [3].

3. EXPERIMENTAL PROCEDURE AND RESULTS

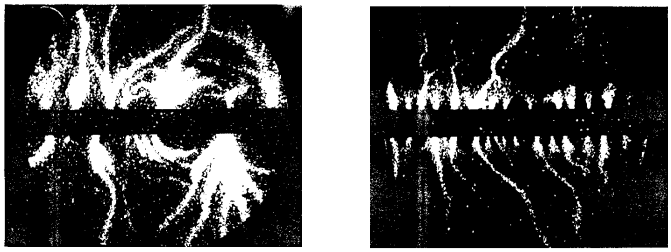
3.1. Initial voltage of the discharge

The initial voltage U_0 of the discharge appearance was measured for a series of subsequent high voltage pulses (the frequency being about 10 Hz) of microsecond duration applied to the stripped electrode. As the amplitude of the pulses is increased micro discharges appear at the edges of the electrode and the light emission of the discharges and the corresponding current pulses are measured. The U_0 values were measured for different kinds of ceramic, different electrode configuration (one stripe and multi-striped electrode with distances d = 4, 6 and 8 mm between the stripes) and different thickness of the dielectric plate δ = 0.5, 1 and 1.5 mm. Less values of U_0 for negative polarity of the applied voltage pulse for all cases are obtained as a result of photo-effect at the electrode edge. The mean values are: $U_0^- = 2.6$ kV and $U_0^+ = 2.8$ kV for all values of d and dU/dt = 1-10 kV/μs. An increase of dielectric thickness from 0.5 to 1.5 mm leads to a practically proportional increase of the initial voltage whereas there is no difference in U_0 values for different high voltage electrode pattern. The most interesting feature is a slight increase of U_0 for policor compared with other ceramic plates: 2.9 kV instead of 2.8 kV for positive polarity and 2.8 instead 2.6 kV for negative one.

3.2. Phenomenology of the discharge from a single stripe for different experimental conditions

Most experiments were carried out with alumina ceramic (type A) it being the one used as a rule in ozone generators. Photographs of micro discharges from the edges of a single stripe (its width 2mm) done by means of an image converter through a slit are given in fig.1 (a,b). The voltage range for which the structure of the discharge corresponds to ones shown in fig.1 is 3.5-12 kV. With higher voltages the discharge transforms into a creeping one that can further transform into a spark and breakdown occurs between the high voltage and earthed electrodes. With an increase of the voltage pulse an increase of the channels length and of their number per unit length of the electrode are seen.

The structure of the discharge is defined by voltage polarity. For a single stripe and positive polarity the distribution of the channels along the stripe edge is less uniform and their number per unit length is less than for negative polarity. In the last case a diffusive zone is clearly seen around each channel.



a) b)

FIGURE 1. Pictures of discharge from positive (a) and negative (b) single stripes. U_m = 9 kV. Alumina ceramic (type A).

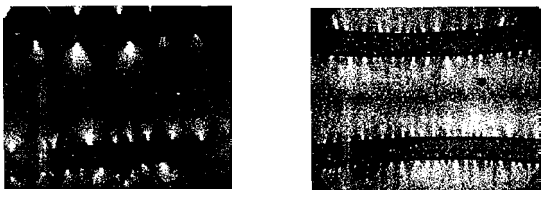
For 4-6 kV the channels are straight and their length does not exceed 1 mm. For higher voltage values the negative channels begin to overlap each other and on a diffusive background there are seen separate channels that develop more intensively and are longer. It seems that these intensive channels screen the development of nearby initial channels. The long intensive channels have very tortuous trajectory and do not branch. In case of positive polarity of the electrode the branching of the channels is seen even for (4-6 kV).

It is assumed on base of previous investigations that so called back discharges appear at the electrode edge during falling part of the applied voltage pulse. They are caused by the electric field of the charges left on the barrier surface as a result of primary discharges corresponding to the rise of the applied voltage pulse. It means that the back discharge must have the polarity opposite to the primary ones. One of the peculiarities of the discharges seen in the pictures for a single stripe is that up to U_m = 6 kV there is no special visible traces of back discharges. For U_m = 9 kV the streamer channels have bright thick parts near the electrode which can possibly be the traces of the back discharges that go along the first discharge channels.

3.3. Peculiarities of self-restricted discharge from a multi-stripped electrode

When a multi-stripped high voltage electrode is used the discharge pattern becomes more uniform. Its development in the direction perpendicular to the electrode edge becomes less intensive but the number of micro discharges per unit length of the electrode increases. For ***negative polarity*** long intensive channels do not appear at all (fig.2a,b); the channels seen have a stable form slightly enlarging as the channel develops. Near the electrode there is a short (0.2-0.4 mm) more bright part connected to our opinion with back discharge. The channel length does not exceed half distance between the stripes. The ***positive channels*** (fig.3a,b) for the same case of a multi-stripped electrode have very tortuous paths and intensive luminescence of branches that have tortuous paths as well. The luminescence of the channels near the electrode edge is very high and the diameters of the channels in this part increases. The length of the positive channels is as a rule longer than the distance between the stripes. Most channels have two or three branches.

Simultaneous development of streamers from neighbour stripes prevents the elongation of channels when voltage increases. It is a result of an opposite electric field created by channel heads. A zone without discharge appears between the stripes for negative polarity. The width of the zone filled by the discharge decreases with the increase of U_m. We call the discharge described a *self-restricted* one.

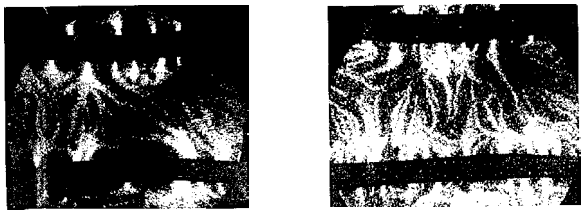


a) b)

FIGURE 2. Discharge from multi-stripped electrode. Microsecond voltage of negative polarity: a) 4kV; b) 9 kV; d = 4 mm.

To analyse the individual discharge channels a telescope with 3.5 magnifications was used. The telescope optical axis formed an angle of 8-10^O with the barrier surface and the sharpness of the picture corresponded to the middle of the stripe. Observations of the discharge pictures show that the discharge for both polarities develops along the dielectric plate surface and the dimension of the channels in the direction perpendicular to the surface does not exceed 0.2 mm. The diameter of the channels in the plane of the barrier measured by means of an image converter with high magnification can be evaluated as 0.15-0.2 mm.

An increase of the distance d between the stripes does not lead to significant qualitative differences in the discharge except an increase of the brightness of the channel base. For higher d values there is a proportional elongation of the channels.



a) **b)**

FIGURE 3. Discharge from multi-stripped electrode. Microsecond voltage of positive polarity: a) 4kV; b) 9kV.

The pictures of a self-restricted discharge for different duration τ of the applied voltage impulse (6 μs and 20 ns) are clearly different. For short impulse the discharge channels lay more closely and their length is less. The luminescence has a more diffusive character and there is no increased brightness of the channels near the electrode as it is seen for long voltage pulses. Such picture seen for short voltage impulse changes and tends to be as one for long pulse if τ exceeds 500 ns with the impulse front duration 150 ns.

.

An important fact is that the discharge pattern of a self-restricted discharge over policor is different compared with the discharge over both kinds of alumina ceramic. In a whole the discharge over policor has more bright and more infrequent channels especially for positive polarity of the applied voltage (table2).

TABLE 2. Number of visible discharge channels per 3 cm of the edge of the electrode. Multi-stripe system. U = 9 kV; 1.5/6 μs.

Polarity of the electrode	Alumina A	Alumina B	Policor
+	16	14	5
–	26	27	8

3.4. Current characteristics and plasma-chemical processes for self-restricted discharge

The full current curve includes two long parts of displacement current corresponding to the front and the tail of the applied voltage pulse and the micro discharge current impulses superimposed on the displacement current (fig.5). The first group of current impulses correspond to prime discharges, the second one - to back discharges. Current parameters for self-restricted discharge are of a very near form and amplitude. For alumina ceramic of both types and interstripe distance d=4 mm the impulse current amplitude I_m = 0.1- 0.12 A, current curve front t_f = 1.8 - 1.9 ns, current duration t_c = 9.0 - 9.2 ns. If the interstripe distance is increased (d = 6 mm) the current amplitude increases I_m = 0.2 A, but have practically the same form of the curve as for d=4 mm. As for policor the brightness of the streamer channels and the current amplitude for d = 4 mm is slightly higher than for alumina ceramic: I_m = 0.12-0.18 A with practically the same form of the current curve (t_f = 1.9 - 2.0 ns, t_c = 9.2 - 9.3 ns). All these parameters are the same for current pulses at the front of the voltage curve and at its tail. In fig.5 a) is for alumina ceramic; b) – policor.

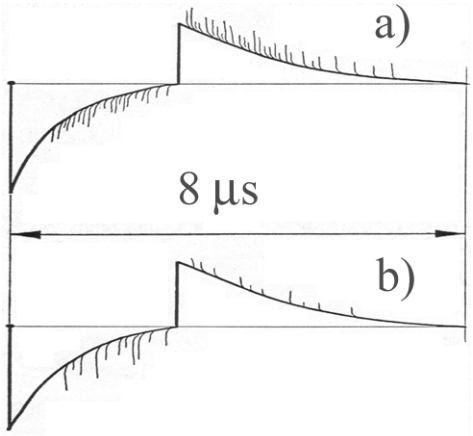


FIGURE 4. Current oscillogram. a) alumina A; b) Policor

The peculiarities of the surface discharge for different materials of the barrier are further manifested when the discharge is used to produce chemically active products (ozone). If we range the materials used according to the intensity of the discharge channels filling the discharge gap than on the first place there will be alumina ceramic of type A, then the same of type B and the last - the policor ceramic. Used as a barrier in a surface discharge ozone generator in which the high voltage electrode is a multi-stripped one with d = 4 mm and the dielectric plate thickness is 1 mm, the above materials have shown the same sequence of their ability to ozone formation (fig.7). The results presented are for high frequency of the applied voltage f = 16 kHz, oxygen and different flow rates of the gas.

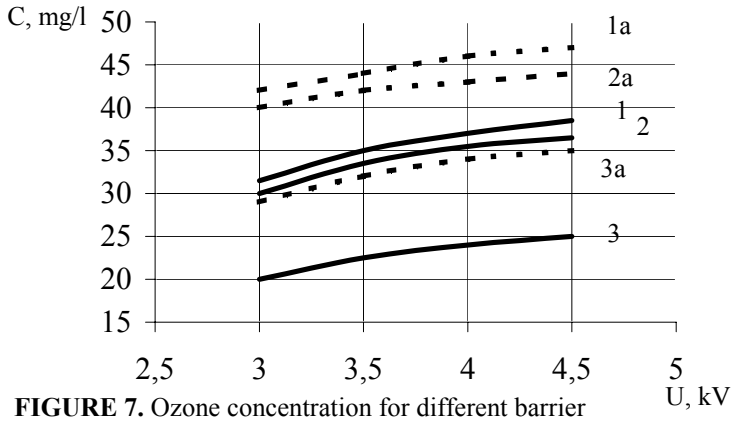


FIGURE 7. Ozone concentration for different barrier materials. Oxygen, 0.5 l/min (dots) and 1 l/min. 1 and 2 – alumina ceramic type A and B, 3 – policor.

4. CONCLUSIONS

The experimental results presented demonstrate a significant difference in the discharge characteristics with dielectric barriers of equal electric parameters but different material composition. These differences lay mainly in the number of microdischarges per unit length of the stripe electrode and are more pronounced for not too high applied voltage (overvoltage in the range 1.5-3 U_0). They are also followed by a difference in the intensity of ozone formation. A specific discharge form is seen for self-restricted discharge in a multi-stripped electrode arrangement that is different from the one developing from a single electrode.

REFERENCES

[1] Masuda S., Kiss E. On streamer discharges in ceramic-based ozoniser using high frequency surface discharge. In: *Inst. Phys. Conf. Ser. No 85 : Poster Session 2,* ed. IOP Publishing Ltd. Oxford, 1987, pp. 243-248
[2] Gibalov V.I., Pietsch G.J. *J.Phys.D: Appl. Phys.,* **33**, 2618-36 (2000)
[3] Kozlov M.V. Surface discharge investigation aimed to an increase of effectiveness of work of electro-technological devices. *Ph.D.Thesis*, Moscow Power Engineering Institute, Moscow, 1994.

INFLUENCE OF ELEMENTARY PROCESSES OVER AN HOMOGENEOUS BARRIER DISCHARGE IN HELIUM

Yu. B. Golubovskii[2], V. A. Maiorov[2], J. Behnke[1], J. F. Behnke[1]

[1] *University of Greifswald, Institute of Physics, Domstrasse 10 a, 17489 Greifswald, Germany*
[2] *University of St. Petersburg, Physical Faculty, Uljanovskaja 1, Stari Petergof, St. Petersburg, 198904, Russia*

1. Introduction

A dielectric barrier discharge is an example of the source of nonequilibrium plasma at atmospheric pressure widely used in industrial applications [1]. In many cases, it has a form of a number of transient filaments. An homogeneous state of a DBD was obtained in helium at ν=10 kHz in [2,3]. However, the simple theoretical model in pure He did not quantitatively agree with experiment [2]. In [3], the presence of a large (0.5%) addition of Ar was supposed to describe the experimental result. An assumption on the presence of N_2 [4] allowed to decrease the impurity density down to 0.05%, but it was still much larger than the maximal impurity in experiment. Therefore, a further study of the elementary processes in helium is necessary.

In the present paper, the model of a barrier discharge is constructed on a basis of fluid equations similar to [3]. The primary attention is paid to the elementary processes in helium, either pure or slightly (some ppm) impured by nitrogen. The influence of some processes over discharge characteristics is studied by the modeling of the discharge at the same conditions as in [3].

2. Elementary processes

A simplified scheme of He and He_2 states is represented in figure 1. At atmospheric pressure, some processes are much faster than the characteristic times of glow discharge development. Such processes are assumed to be instantaneous, which simplifies the reaction kinetics and reduces the number of states in the model. A list of instantaneous reactions is given in table 1.

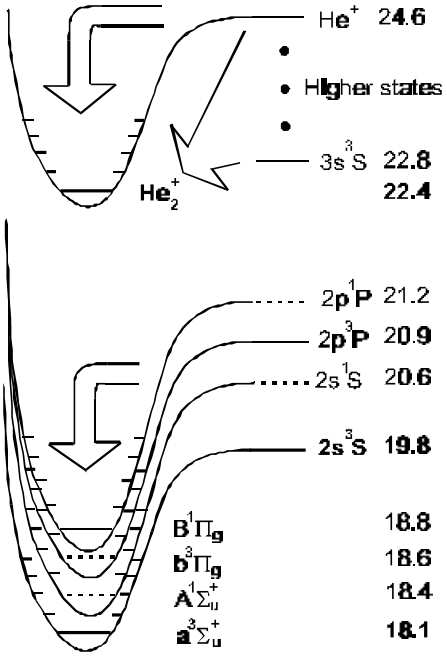


Fig. 1. Scheme of excited states in He

Process	Notation	Rate constant	n (*p*=1 atm)
associative ionization	He^* (n≥3) + He → He_2^+ + He	1.5×10^{-11} cm^3/s [5]	5×10^8 s^{-1}
He^+ conversion	$He^+ + 2He \rightarrow He_2^+ + He$	1.1×10^{-31} cm^6/s [5]	5×10^7 s^{-1}
conversion of resonance atoms	$He(2^3P) + 2He \rightarrow He_2(A^1\Sigma_u^+) + He$	1.6×10^{-32} cm^6/s [6]	10^7 s^{-1}
excimer radiation	$He_2(A^1\Sigma_u^+) \rightarrow 2He + h\nu$ $He_2(b^3\Pi_g) \rightarrow He_2(a^3\Sigma_u^+) + h\nu$	$\sim 10^9$ s^{-1} $\sim 10^7$ s^{-1}	
excimer quenching	$He_2(B^1\Pi_g) + He \rightarrow He_2(b^3\Pi_g) + He$	$k \le 10^{-11}$ cm^3/s	$\le 10^8$ s^{-1}

Table 1. Fast processes in He plasmas

According to table 1, the model of a discharge in helium must contain at least three species, molecular ion He_2^+, metastable atom (2^3S) and molecule $a^3\Sigma_u^+$. It is not necessary to consider the metastable state 2^1S separately, since its behavior is the same as the behavior of the lowest

metastable state 2^3S. In the present paper, the equations are solved for a summary density of these two metastable states. Besides the direct excitation and ionization by electron impact, the processes listed in table 2 are taken into account.

conversion of metastables	$He_m + 2He \rightarrow He_2 + He$	$2x10^{-34}$ cm^6/s [7]
chemoionization	$2He_m \rightarrow He_2^+ + e$	$1.5x10^{-9}$ cm^3/s [7]
	$2He_2 \rightarrow He_2^+ + 2He + e$	$1.5x10^{-9}$ cm^3/s [7]
dissociative recombination	$He_2^+ + e \rightarrow He^* + He$	$8.9x10^{-9}(T_e/T_g)^{-1.5}$ [5]

Table 2. Primary elementary processes in a model of He plasmas

At low currents other elementary processes seem to be inessential. It is surprising there are no effective channels of $He_2(a^3\Sigma_u^+)$ destruction. Its lifetime may reach tens of milliseconds [7]. High excimer density causes the effective chemoionization which resists the development of a glow discharge. The only destruction mechanism we can suppose is the destruction of vibrationally excited excimers,

$$He\ (2^3S) + 2e \rightarrow He_2\ (a^3\Sigma_u^+, v), \qquad He_2\ (a^3\Sigma_u^+, v) + He \rightarrow He_2\ (A^1\Sigma_u^+, v') + He$$

The rate constant of this process may reach 10^{-11} cm^3/s, whereas the vibrational relaxation, at least at low vibrational numbers, is quite slow, of the order of 10^{-17} cm^3/s [8]. In this paper, lifetime of excimers is varied in order to reach better agreement with the experimental data.
Another important question is the value of the recombination rate. The recombination rate for He_2^+ is slow relative to the rates of the dissociative recombination processes in other gases. The conversion into He_3^+ with the following recombination may be more effective, since the recombination rate of this type of ion is equal to $4x10^{-7}$ cm^3/s at T_e=300K [9]. This question requires further investigation.
When helium is impured by nitrogen (some ppm), some other elementary processes proceed efficiently in plasma. These processes are represented in table 3.

Penning ionization	$He_m + N_2 \rightarrow N_2^+ + He + e$	$5x10^{-11}$ cm^3/s [5]
	$He_2 + N_2 \rightarrow N_2^+ + 2He + e$	~ $3x10^{-11}$ cm^3/s
He_2^+ ion recharge	$He_2^+ + N_2 \rightarrow N_2^+ + 2He$	$1.4x10^{-9}$ cm^3/s [5]
N_2^+ dissociative recombination	$N_2^+ + e \rightarrow 2N$	$4.8x10^{-7}(T_e/T_g)^{-0.5}$ cm^3/s[10]

Table 3. Additional elementary processes in He with small addition of N_2

The recombination rate may be increased due to the formation of complex N_2^+-He ions.
As $[N_2]$<0.01%, the electron distribution function is not disturbed by collisions with nitrogen molecules.
The ion-electron emission, photoemission and emission by metastables are included in the model. Since the energies of species are high (20 eV) and densities are relatively low, the emission of electrons must be much higher than the desorption of adsorbed electrons. We use γ_i=0.01 and $\gamma_{ph} = \gamma_m = 0.05$. The metastable and excimer diffusion coefficients and ion mobilities are chosen as D_{He}=0.58 cm^2/s, D_{He2}=0.38 cm^2/s, $m_{He2+} = m_{N2+}$=20 cm^2/(V·s) [5].

3. Barrier discharge in pure He

Since there are some undefined parameters in the model, it is interesting to study whether it is possible to obtain a stable, periodic solution in pure helium, taking into account the chemoionization. When only direct (and associative) ionization is taken into account, the

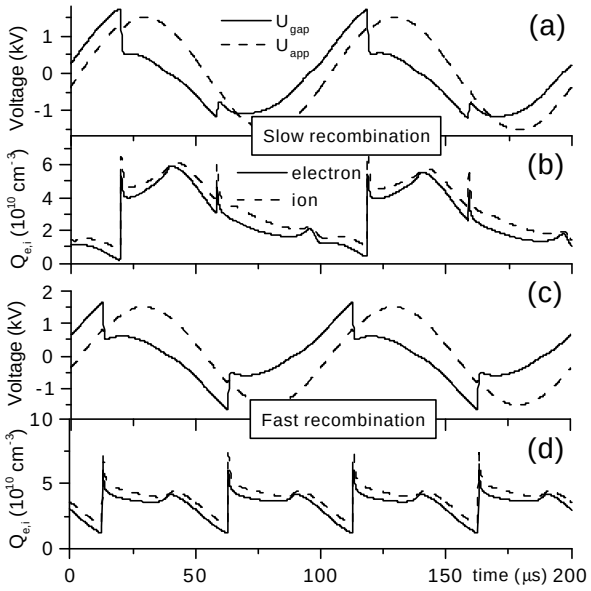


Fig. 2. Influence of the recombination rate. Voltages (a), (c); averaged electron densities (b), (d).

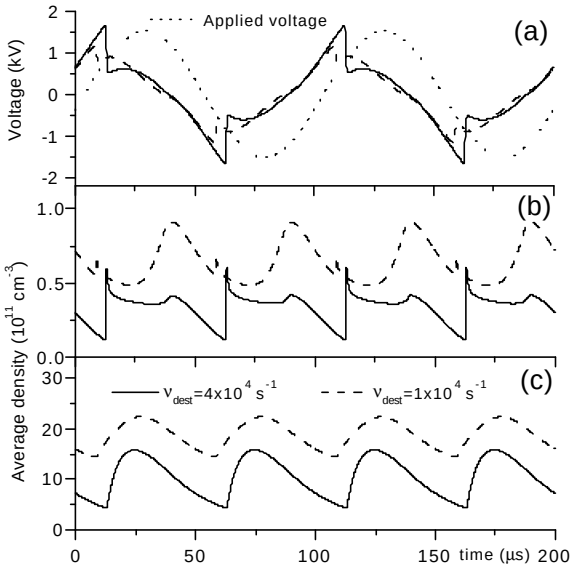


Fig. 3. Voltages (a), averaged electron (b) and excimer (c) densities for different frequencies of excimer quenching

breakdown voltage is higher than 3 kV [2]. In figure 2 the discharge characteristics are shown for two different recombination rates, corresponding to He_2^+ (a), (b) and He_3^+ (c), (d). When the recombination is weak, the electron charge cannot decrease essentially during half period [fig. 2 (b)], which causes the doubling of a period. Higher recombination rate provides the periodicity of a discharge. However, there are still many electrons before the breakdown, which are produced due to the chemoionization. Therefore, the gap does not discharge completely, as it is seen in experiment [3].

Assuming the recombination rate to be high, let us analyze the discharge behavior at different excimer destruction frequencies (Fig. 3). As $\nu_{dest} \leq 4x10^4$ s^{-1}, the solution is stable and periodic, but the electron density is always large and the gap voltage does not decrease down to zero. When $\nu_{dest} = 0$, there are no glow discharge at all, because the plasma in a gap screens the applied voltage in all phases. At higher destruction frequencies, the discharge does not burn at $U_0 = 1600$ V.

4. Influence of small N_2 addition

Since in pure helium the behavior of a glow discharge does not agree with the experiment, it is interesting to study whether the agreement is better for the impured gas. The primary difference between ionization processes in pure He and the mixture He + some ppm N_2 consists of the presence of very effective Penning ionization [2]. The processes listed in table 3 provide the solution of such the difficulties as slow recombination rate and weak ionization frequency arising in a discharge in pure helium.

In figure 4 the voltages and current densities of a discharge are shown for different admixtures of nitrogen. In these calculations, excimers are assumed to be quenched efficiently ($\nu_{dest}=10^6 s^{-1}$). At 5 ppm (0.0005%) of N_2 the discharge is stable, periodic, and the behavior of voltage and current corresponds well to the experiment [3]. Note that such purity of a gas is comparable with the experimental one.

Lower admixtures of nitrogen cause the doubling of a period and the growth of a breakdown voltage. This is due to the decrease of the Penning ionization efficiency. The discharge does not burn when the density of N_2 is lower than 1 ppm.

At higher admixture rate (20 ppm), the doubling of a period also occurs, which is very surprisingly. This is probably because the breakdown voltage decreases and the electrons drift to the electrodes less efficiently. Consequently, the plasma in a gap can not disappear during half period, and a whole period is necessary for the complete decay.

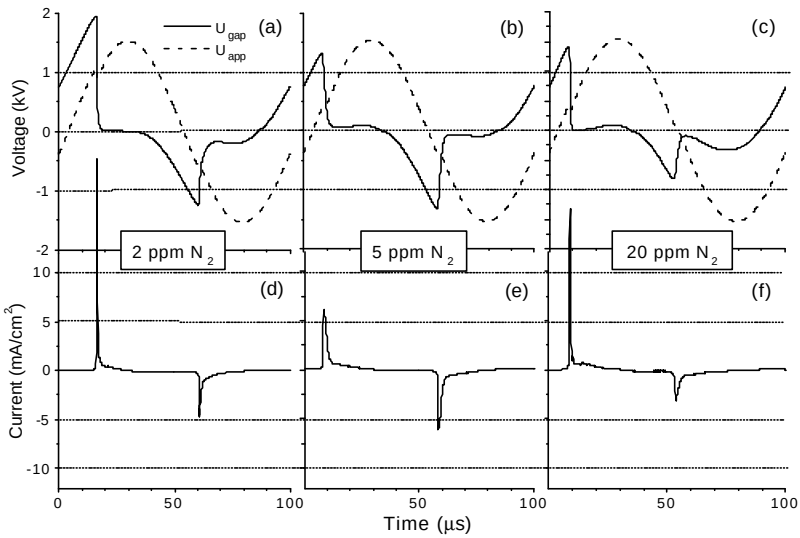


Fig. 4. Voltages (a)-(c) and discharge currents (d)-(f) for different impurity densities

Figure 5 illustrates the distributions of the electron density and electric field in a gap. It is seen that in the phase of the breakdown the distinct structure of a glow discharge is developed in a gap, which is in accordance with [3]. Before the breakdown the quasineutral region of spatial charge does not vanish completely. It is seen in figure 5(b) that this region plays the role of anode when a breakdown occurs. This causes the breakdown voltage to be different from the case when the positive column decays completely.

In figure 6 various internal characteristic of the discharge are shown. The primary type of ions is N_2^+ due to the fast recharge processes and Penning ionization. The direct ionization prevails in the phase of the breakdown, however, the Penning ionization is higher after this phase, and, which is important, before it, which decreases the breakdown voltage. The stepwise ionization is always small.

The primary emission mechanism is the photoemission, it seems even that its value is overestimated in the paper. However, the values of the emission coefficients influence weakly the discharge behavior. When they are decreased by a factor of 5, the amplitude of a current is

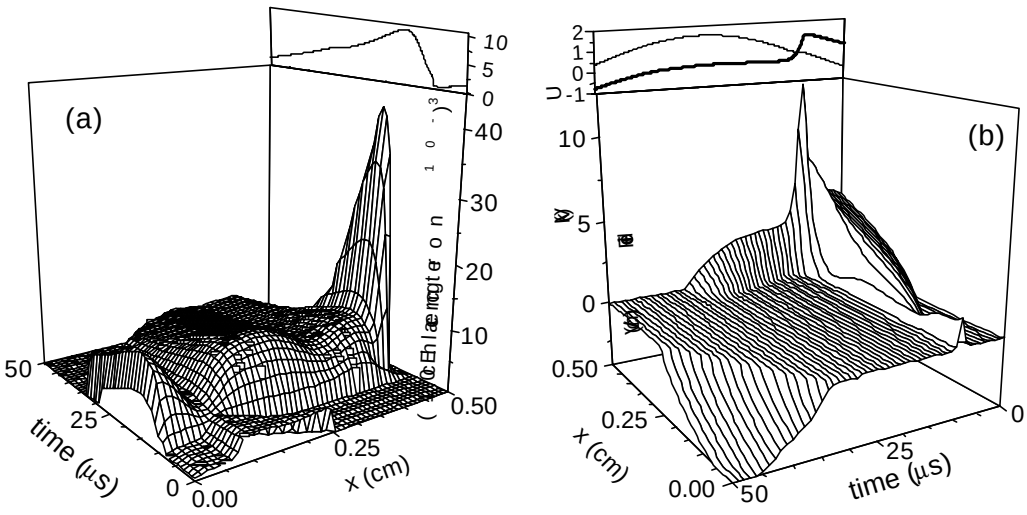


Fig. 5. Electron density (a) and electric field (b) for He + 5 ppm N_2

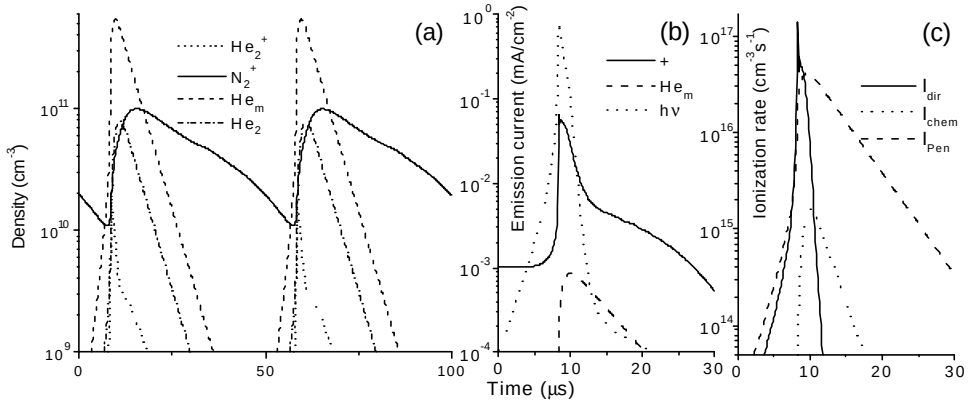


Fig. 6. (a) mean densities of different species, (b) emission currents, (c) mean ionization rates for He + 5 ppm N_2

only about 20% lower and the voltage profile does not change essentially. This is because the characteristics of a glow discharge are determined mainly by volume processes (formation of a quasineutral region and a cathode sheath), in distinction with a Townsend discharge.

5. Conclusion

The analysis of the response of the barrier discharge behavior on the changing of the rate constants improved the understanding of primary processes in helium plasma. The rigorous study of these elementary processes allowed us to obtain the characteristics of an homogeneous barrier discharge quantitatively corresponding to the experimental data available. The impurity of helium is of crucial importance.

Acknowledgments

The work was supported by the DAAD Trilateral project "Physics and Chemistry in non-equilibrium Plasmas" of the universities Greifswald, Paris-Sud and St. Petersburg.

References

[1] V. G. Samoilovich, V. I. Gibalov, K. V. Kozlov, *Physical Chemistry of Barrier Discharge* (Moscow, 1989) (in Russian)

[2] R. Ben Gadri, A. Rabehi, F. Massines, and P. Segur, Proc. XXII ESCAMPIG (Netherlands, 23-26 August 1994) p. 228

[3] F. Massines *et al*, J. Appl. Phys. **83** (1998) 2950

[4] A. Rabehi, P. Segur, F. Massines, R. Ben Gadri, and M. C. Bordage, Proc. of XXIII ICPIG (Toulouse, France, 7-22 July 1997), vol. IV, p. 44

[5] B. M. Smirnov, *Ions and Excited Atoms in Plasma* (Moscow, 1974) (in Russian)

[6] F. Emmert, H. H. Angermann, R. Dux, and H. Langhoff, J. Phys. D: Appl. Phys. **21** (1988) 667

[7] R. Deloche, P. Monchicourt, M. Cheret, and F. Lambert, Phys. Rev. A **13** (1976) 1140

[8] M. Capitelli, C. M. Ferreira, B. F. Gordiets, and A. I. Osipov, *Plasma Kinetics in Atmospheric Gases* (Berlin: Springer, 2000)

[9] J. B. Gerardo, M. A. Gusinov, Phys. Rev. A **3** (1971) 255

[10] I. A. Kossyi, A. Yu. Kostinsky, A. A. Matveyev, and V. P. Silakov, Plasma Sources Sci. Technol. **1** (1992) 207

TOWNSEND AND GLOW MODES OF AN HOMOGENEOUS BARRIER DISCHARGE IN HELIUM

Yu. B. Golubovskii[a], V. A. Maiorov[a], J. Behnke[b], J. F. Behnke[b]

a) University of St. Petersburg, Physical Faculty, Uljanovskaja 1, Stari Petergof, St. Petersburg, 198904, Russia

b) University of Greifswald, Institute of Physics, Domstrasse 10 a, 17489 Greifswald, Germany

1. INTRODUCTION

In the present time the homogeneous barrier discharge at atmospheric pressure in helium became the object of intensive experimental and theoretical studies [1-4]. The homogeneous state of the discharge exists also in other gases [5], however, only the Townsend form is stable. In helium, a glow form characterized by much higher power [1,2] or a multipeak Townsend form [3,4] can also be obtained. It is therefore interesting to study theoretically the structure of these regimes, conditions of their existence and the transitions between them.

2. MODEL

The numerical simulation of a discharge is based on a one-dimensional fluid model. Electrons, ions and excited species are described by the continuity equations

$$\frac{\partial n_k}{\partial t} = \frac{\partial}{\partial x}\left(n_k w_k\right) + S_k - D_k n_k, \qquad (1)$$

where n_k is the density of corresponding particles, S_k is the source of these particles, D_k is their destruction frequency, and w_k is their drift velocity. The latter is determined as

$$w_e = -D_e \frac{\partial n_e}{\partial x} - b_e E, \qquad w_i = -D_i \frac{\partial n_i}{\partial x} + b_i E, \qquad w_0 = -D_0 \frac{\partial n_0}{\partial x}, \qquad (2)$$

where the indices *e*, *i*, and *0* correspond to electrons, ions, and neutral excited species, *D* and *b* are the diffusion coefficient and mobility. The boundary conditions for these equations consist of the equality of the drift and thermal velocities in the sheath [6,7]. The balance equations for the surface densities of electrons and positive charges are solved simultaneously with (1).

The electric field is described by the Poisson equation. The external resistance (110 kΩ) and capacitor (35 pF) are included in the model. This external circuit describes approximately the nonideality of the power supply.

The kinetics of excitation in He, as well as the electron emission mechanisms are considered similar to [8]. The presence of a small admixture of nitrogen is assumed. The primary ionization mechanisms are the direct ionization, chemoionization, and Penning process.

To describe properly the discharge at low frequencies, the weak (1 s^{-1}) thermodesorption of electrons [6,7] is included in the model. The desorption from dielectric barriers appears to be the only source of initial electrons when the discharge period is much larger than the decay time of excited species.

3. STRUCTURE OF TOWNSEND AND GLOW MODES

The simulation is performed for two sets of conditions, when either glow discharge [2] or Townsend discharge [3] was observed experimentally. The former was obtained in the sinusoidal voltage of the amplitude U_0=1.55 kV and the frequency f_0 =10 kHz. The reduced (ε=1) barrier width d was equal to 0.08 mm and the gap width L was equal to 0.5 cm. In the latter case, the conditions were the following: f_0 =1.5 kHz, U_0 =2.5 kV, d=0.3 mm, L=0.2 cm. The electrode areas were assumed to be equal to 12.56 cm and 7.07 cm correspondingly.

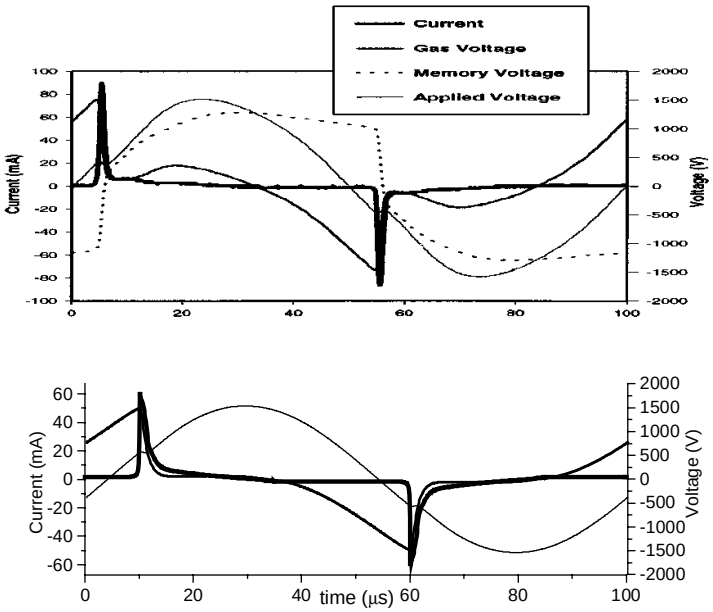


Fig. 1. Comparison between the experimental results [2] (upper graph) and theoretical description (lower graph) of a glow discharge at 10 kHz

The comparison between the experiment [2] and the present model for the glow regime of discharge is performed in figure 1. A good correspondence between experimental and theoretical curves can be seen. However, the current is slightly underestimated, which may be due to discrepancies in the external circuit and gas purity (we use 3 ppm of N_2).

The glow discharge is characterized by the following qualitative features. There is one current peak per half period, which has a large (tens of mA) amplitude. The charge transfer between the electrodes causes the essential (almost down to zero) decrease of the gap voltage. During the breakdown, a spatial structure typical for a glow discharge develops [2].

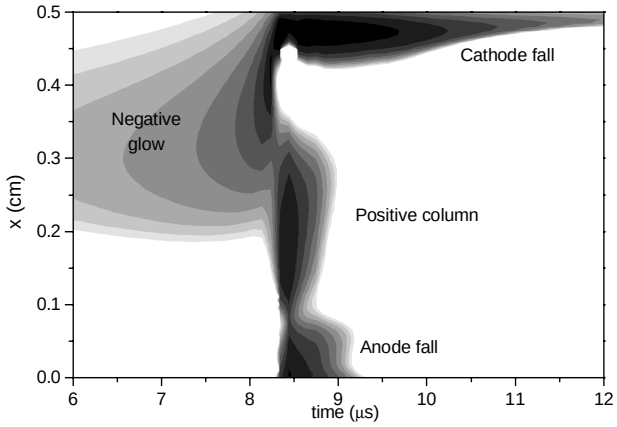


Fig. 2. Distribution of the ionization rate in the breakdown phase of the glow discharge

The spatial structure of this mode was already studied in detail in [2,8]. The diagram of the ionization rate in the discharge (figure 2) shows this structure clearly. The interesting question is the reason of the formation of a Faraday dark space between a cathode fall and a positive column. In DC discharges, this region is formed due to the intensive ionization by fast electrons from the cathode fall. A nonlocal theory must be used to describe it properly. In a local model, a cathode fall is followed directly by a positive column.

In an AC barrier discharge we use the fluid model. However, this region also occurs. The reason is that the intensive ionization in this region occurs *before* the formation of a spatial structure (figure 2).

The formation of the positive column itself may also seem to be unexpected. Indeed, there is no intensive loss of particles in a gap (the recombination loss is too slow in comparison with the time of the formation of a positive column). Therefore, the electric field might be close to zero. The large

electric field can exist due to the transiency of the breakdown. The inertia of plasma forbids the instantaneous screening of external voltage. The time lag of the screening allows the existence of a "positive column" during hundreds of nanoseconds. Therefore, the alternating of the voltage plays the primary role in the formation of a spatial structure of a glow mode.

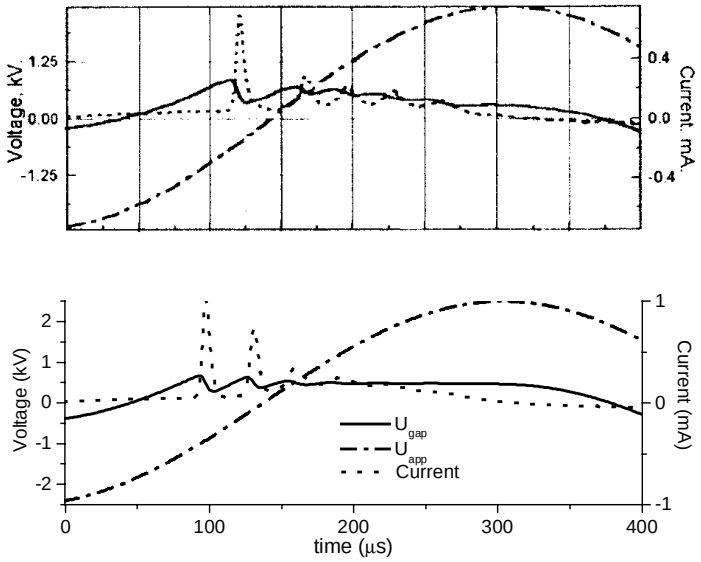


Fig. 3. Comparison between the experiment [3] (upper graph) and the calculation (lower graph) for a multi-peak Townsend discharge

A completely different mode of barrier discharge is shown in figure 3. A qualitative agreement between the simulation and the experiment can be seen. In this case, according to the data of [3], we have chosen the impurity rate to be equal to 40 ppm of N_2.

The Townsend mode of discharge differs essentially from the glow mode. The current profile has a form of several peaks of small amplitude. The gap voltage does not decrease down to zero after the passing of a current peak. The calculation shows that this mode is indeed a Townsend discharge, because the electric field in a gap is not disturbed by a spatial charge. The three-dimensional graphs of electron and ion densities are shown in figure 4. The spatial position x=0 corresponds to the cathode. It is seen that the electron density is much lower than the ion density. It increases from cathode to anode almost following the Townsend law. These are typical features of Townsend discharge [6]. However, the growth near the anode is weaker, because a sufficient spatial charge accumulates there.

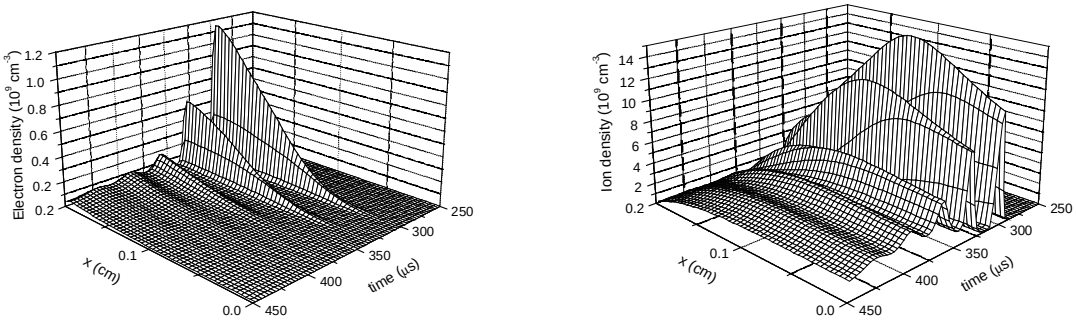


Fig. 4. Three-dimensional graphs of electron and ion densities.

Since all the excited states of He are completely quenched by nitrogen before the breakdown, the only source of electrons is the desorption from dielectric barriers. There is no desorption due to vibrationally excited molecules as in nitrogen [6]. Therefore, only the thermodesorption may take place, which is very weak (units of s^{-1}). The value of the desorption frequency influences the damping efficiency of the successive peaks. The damping increases with the growth of the desorption frequency. We must note that in absence of desorption the discharge is no more Townsend, a glow-like breakdown develops.

4. DEPENDENCE ON THE DISCHARGE PARAMETERS

It is interesting to study which form of discharge occurs under certain conditions. When the external circuit remains unchanged, the primary parameters influencing the type of discharge are the gap width L and dielectric width d. The discharge behavior can be studied with the help of the Paschen-type diagram (figure 5). In this diagram the dependence of the minimal amplitude of the voltage able to supply the discharge is shown in dependence on gap width for two fixed barrier widths. The frequency of the external voltage is equal to 10 kHz.

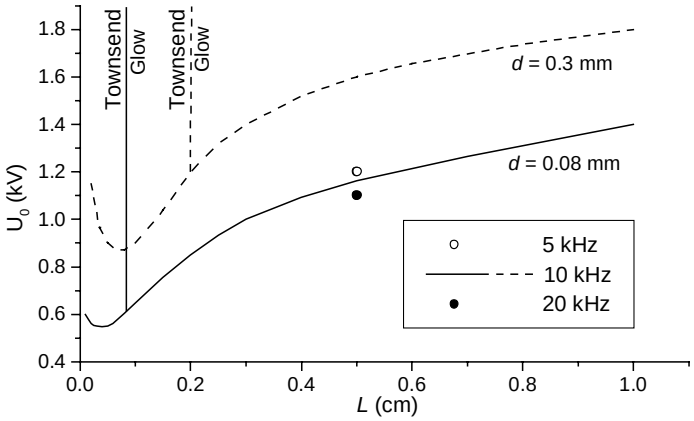


Fig. 5. Dependence of the minimal voltage supplying the discharge on gap width at 10 kHz for d = 0.08 mm and d = 0.3 mm. Vertical lines mark the Townsend-to-glow transition

The behavior of the Paschen curves is similar to that for an ordinary glow discharge. There is a minimum in a curve, which is slightly smaller than the width when a Townsend-to-glow transition occurs (vertical lines). This minimum is of the order of the width of a cathode region in a glow discharge.

The larger width of barriers corresponds to the larger external impedance. Therefore, the Townsend-to-glow transition occurs at larger gap widths. Moreover, the minimal amplitude of the supplying voltage increases.

The frequency of the external voltage influences the Paschen curve weakly. The minimal amplitudes of the supplying voltage at different frequencies are marked by circles. The factor changing with frequency is the density of the residual charge, which plays an essential role in the discharge dynamics [2]. This density grows with frequency, which decreases the minimal amplitude. As one can see, this decrease is sufficiently weak.

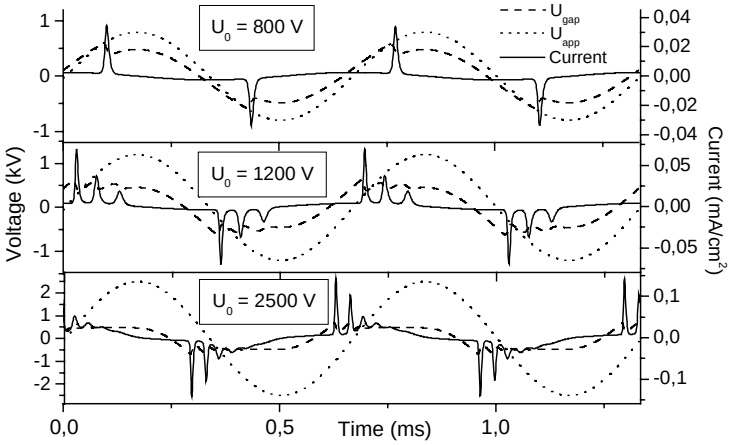


Fig. 6. Townsend discharge at different amplitudes of external voltage

The changing of the glow discharge parameters with the amplitude of external voltage is inessential. Qualitatively, only the inequality of current peaks at different halfs of period can occur. This inequality was observed in [1], its reasons are studied in [8].

The behavior of the Townsend mode in dependence on the voltage amplitude is more interesting. The characteristics of the discharge under the conditions of figure 3 at different amplitudes of external voltage are shown in figure 6. At U_0 = 800 V (the value close to the minimal supplying voltage), only one peak can be observed. When the amplitude grows, the number of peaks increases, whereas their amplitude remains almost unchanged.

These peaks are formed in the phase of the growth of the electric field. Since the number of initial electrons is low (when they are produced due to the thermodesorption, ν_{des}=1 s^{-1} corresponds to the initial current of the order of 10^{10} cm^{-2}/s, i.e., 10^{-6} mA/cm^2), a certain time is necessary to produce the number of electrons necessary for the field screening. This lag between the field growth and the screening causes the oscillations of the current. The larger is the number of initial electrons, the more effective is the damping of these oscillations. In nitrogen the desorption current is much larger due to the impact of vibrationally excited molecules [6], and no peaks is observed.

The homogeneity of the Townsend discharge observed experimentally in [3] and simulated in the present paper shows that the large number of initial electrons is not necessary to obtain a homogeneous discharge. It seems like the Townsend form of discharge is stable by its nature.

5. CONCLUSION

Using a one-dimensional fluid model, two essentially different forms of the homogeneous barrier discharge in helium are simulated. The results of modeling are compared with the experimental data of other authors. The comparison shows good agreement between the calculation and the experiment.

The glow mode of discharge is characterized by one current peak of large amplitude per half period. During the breakdown, a spatial structure typical for the glow discharge, consisting of cathode fall, Faraday dark space, positive column, and anode region, develops in the gap. The origin of the formation of this structure differs from that in a DC glow discharge. This formation is mostly governed by the dependence of processes on time. The glow mode is forming at high gap widths and thin dielectric barriers.

As the gap width decreases, the discharge transits into the Townsend mode. The primary feature of this mode is the weak disturbance of the electric field by spatial charge. The electron density, being much lower than the ion density, increases from cathode to anode. There is no quasineutrality in a discharge gap.

When the amplitude of external voltage grows, a multipeak Townsend discharge occurs. The formation of several peaks is caused by a small number of initial electrons. A certain initial current however must exist, the only mechanism of its production is the thermodesorption. The stability of such type of discharge shows that a large number of initial electrons is not a necessary condition of stability for the Townsend discharge.

ACKNOWLEDGMENTS

The work was supported by the DAAD Trilateral project "Physics and Chemistry in non-equilibrium Plasmas" of the universities Greifswald, Paris-Sud and St. Petersburg.

REFERENCES

[1] Ph. Decomps, F. Massines, C. Mayoux, Acta Physica Univ. Comenianae, vol. XXXV,№ 1 (1994) p 47
[2] F. Massines *et al*, J. Appl. Phys. **83** (1998) 2950
[3] G. Visentin, I. Mangolini, K. Orlov, U. Kortshagen, J. Heberlein, Proc. of 15th ISPC (Orleans, July 10-13 2001) Vol. VIII, p. 3251
[4] N. K. Bibinov, A. A. Fateev, K. Wiesemann, Plasma Sources Sci. Technol. **10** (2001) 579
[5] J. Tepper and M. Lindmayer, Contrib. Papers of HAKONE VII (Greifswald, Sept. 10-13, 2000) vol. 1, p. 38
[6] Yu. B. Golubovskii, V. A. Maiorov, J. Behnke, J. F. Behnke, Proc. of 15th ISPC (Orleans, July 10-13 2001) Vol. VIII, p. 3239
[7] Yu. B. Golubovskii, V. A. Maiorov, J. Behnke, J. F. Behnke, J. Phys. D: Appl. Phys. **35** (2002) (to be published)
[8] Yu. B. Golubovskii, V. A. Maiorov, J. Behnke, J. F. Behnke, Proc. of this conference

STUDIES OF THE ATMOSPHERIC PRESSURE JET MATRIX PLASMA SOURCE: ELECTRICAL PROPERTIES AND DISCHARGE STABILITY

A. Ignatkov[a], A. Schwabedissen, G. F. Leu, and J. Engemann

*Forschungszentrum für Mikrostrukturtechnik - **fmt**, University of Wuppertal, 42287 Wuppertal, Germany*

Abstract: In order to treat larger surfaces at atmospheric pressure an RF(13.56 MHz) driven plasma source consisting of a matrix of Hollow Cathode Discharge (HCD) plasma-jets has been built and investigated. The dependence of gas type, electrode distance, electrode material and discharge mode (α or γ-mode) on the discharge stability is analysed. Continuous glow discharge operation at atmospheric pressure has been obtained for the following gases and gas mixtures: He, Ar, He:O_2 (up to 40 % O_2), He:N_2 (up to 10 % N_2). The electron density is estimated from electrical measurements of discharge current and voltage. Typical electron densities are in the range of 10^{11} to 10^{12} cm^{-3}.

1. INTRODUCTION

Plasma processing of materials is a vital industrial technology in many areas including electronics, automotive and biomedical industries. The most important properties of the discharges for plasma processes are low gas temperature, high electron density and efficient production of chemically reactive species. However, for many plasma-based processes the cost of vacuum equipment is an obstacle for transfer to industry.

A possible discharge type for low pressure plasma processes in the mbar range is the hollow cathode discharge (HCD). HCDs are gas discharges between a cathode which contains a hollow structure and an anode. Under certain conditions, the hollow cathode effect (HCE) can be obtained in such discharges. The HCE is characterized by a significant increase of the discharge current density compared to a normal glow discharge. The occurrence of the HCE depends on several properties of the discharge; details can be found in [1-5]. With decreasing cathode diameter the pressure where the HCE exists increases. For dc glow discharges, as a rule of thumb the HCE occurs at pd = 1 mbar × cm, where d is the inner cathode diameter.

For dc glow discharges in the low pressure range, the HCE is well known and a lot of studies for this type of the discharge exist, e.g. [4,5]. Discharge phenomena in high pressure HCDs are not well understood. There are problems concerning the discharge stability, especially for discharges in molecular gases. Also the existence of the HCE in such discharges is difficult to prove. Studies on radio-frequency (rf, 13.56 MHz) capacitively coupled discharges at intermediate pressures (10 - 250 mbar), which have been used since the 1980's for high power gas lasers, such as CO_2 lasers [6, 7], have shown, that in general two distinctively different modes exist, the so called α and γ mode, depending on the dominant ionisation mechanism [6].

Based upon the rf driven jet matrix plasma sources which operate in the mbar range [8], we have developed similar sources which can be operated up to atmospheric pressure. In this article we give a brief overview about some experimental results concerning discharge stability using mixtures of helium with nitrogen or oxygen, and the electrical parameters. Additionally, the discharges have been characterized by emission spectroscopy, which provides information about the gas temperature and the electrode sheath thickness.

[a] Electronic address: ignatkov@fmt.uni-wuppertal.de

2. EXPERIMENTAL SETUP

A schematic of the experimental set-up is shown in Fig. 1 The discharge was produced between two planar, circular electrodes. Into both electrodes a matrix of holes was drilled. Different hole diameters from 100 to 600 μm, manufactured either by mechanical drilling or laser-drilling, were investigated. The plasma source chamber was water cooled. The active area of each electrode was 7.07 cm^2 and the gap spacing between the electrodes was varied from 0.05 mm to 3 mm using PTFE spacers. By measuring simultaneously the current and voltage across the discharge the electrical properties of the discharges were studied. The measurements were made using a high voltage probe (Tektronix P5100, bandwidth 350 MHz) and a current monitor (Pearson Current Probe 2277, bandwidth 200 MHz) and recorded with a digital oscilloscope (Tektronix TDS 520, sampling rate 500 M samples/s, bandwidth 500 MHz). The uncertainty of the electrical measurements was better than 10 %.

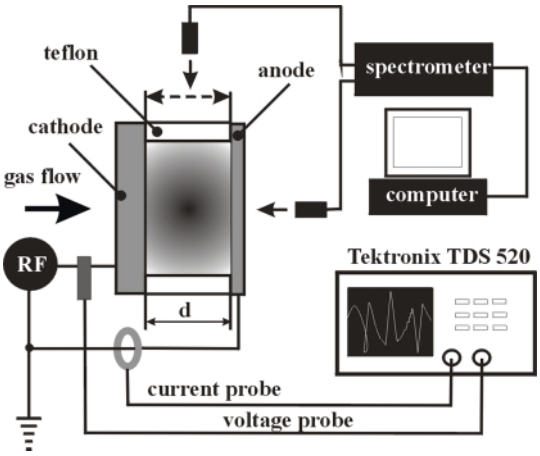


FIGURE 1. Schematic of the experimental set-up.

The light emission from the discharge was measured using a collimating slit (width 300 μm), a quartz fibre and a spectrometer with spectral resolution of 0.03 nm. By moving the collimating slit, the emission intensity profile between the electrodes was obtained.

In addition, the gas temperature of the discharge was measured spectroscopically by fitting the rotational intensity distribution of the first negative system of the N_2^+ ion at 391 nm to a Maxwell-Boltzmann distribution.

3. EXPERIMENTAL RESULTS

3.1. Effect of gas composition on discharge stability

The discharge was ignited in pure helium and afterwards the content of a molecular gas (oxygen or nitrogen) was varied. In Fig. 2 the dependency of the molecular gas content on the discharge stability is shown. Above the curves the discharge becomes unstable and turns to another mode (γ mode) in the case of aluminium electrodes (hollow circle).

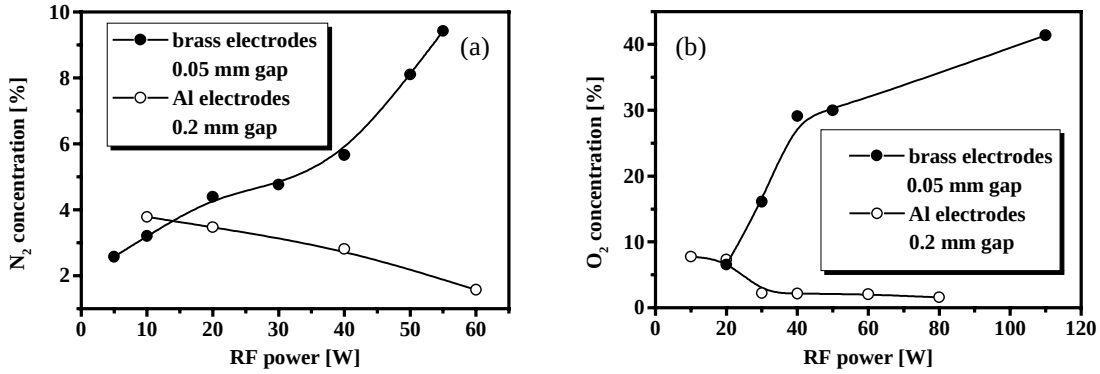


FIGURE 2. Stability properties of the discharge: below the curves are regions of stable discharge operation. (a) He:N_2 gas mixtures, (b) He:O_2 gas mixtures.

In the case of brass electrodes (solid circle) and an electrode gap separation of 0.05 mm the discharge does not cover the whole electrode surface area. If the input power reaches a critical value, the discharge turns into an arc. For electrode gap separations larger than 0.05 mm discharge properties are similar to the case of aluminium electrodes.

3.2. Current and voltage *(I-V)* characteristics

Different operating regimes can be identified and characterized using the relation between the amplitude of the rf current and the discharge voltage, the so called "*I-V* curve". The term "*I-P* curve" is used for the relation between amplitude of the rf current and the input power. In Fig. 3. an *I-V* curve and *I-P* curve are shown for pure helium discharges in the α mode (Fig. 3a) and in the γ mode (Fig. 3b). Both modes were operated in the abnormal state, when the discharge covers the whole area of the electrodes.

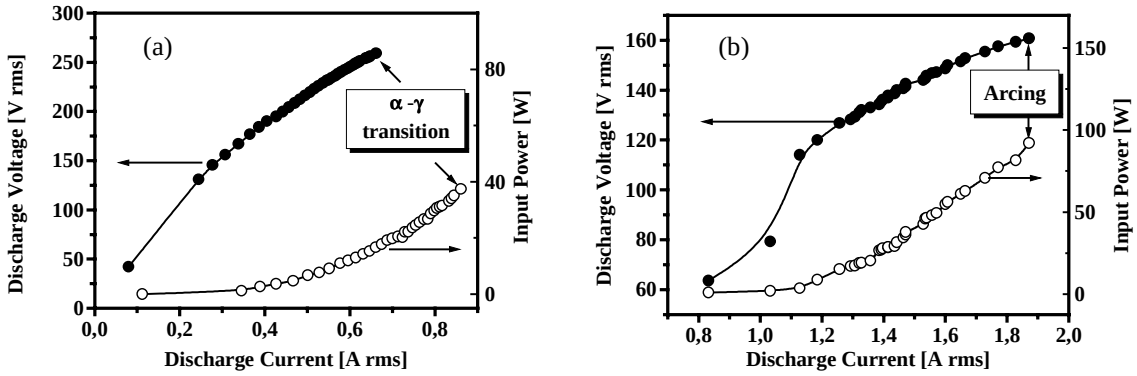


FIGURE 3. Amplitudes of discharge voltage (*I-V* curve) and input power (*I-P* curve) as a function of rf current. (a): aluminium electrodes, gap spacing 1 mm, helium flow 500 sccm, drill-hole diameter of the holes 0.6 mm. (b): brass electrodes, gap spacing 0.05 mm, helium flow 500 sccm, drill-hole diameter of the holes 0.25 mm.

With increasing input power, both the rf current and the discharge voltage increase monotonically until the discharge turns into the γ mode (Fig. 3a) or an arc (Fig. 3b).

To analyse the influence of the holes on the discharge properties the current density (Fig. 4) and ion current (Fig. 5) were measured for electrodes with bore drilled holes and without holes. No significant difference was observed for the α mode discharge operation (Fig. 4 and 5).

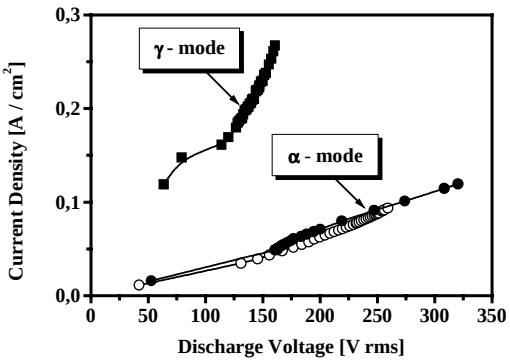


FIGURE 4. Current density amplitude as a function of the discharge voltage. Discharge parameters are: **solid square:** brass electrodes, gap spacing 0.05 mm, helium flow 500 sccm, drill-hole diameter of the holes 0.25 mm. **hollow circle:** aluminium electrodes, gap spacing 1 mm, helium flow 500 sccm, drill-hole diameter of the holes 0.6 mm. **solid circle:** aluminium electrodes, gap spacing 1 mm, helium flow 500 sccm, no holes.

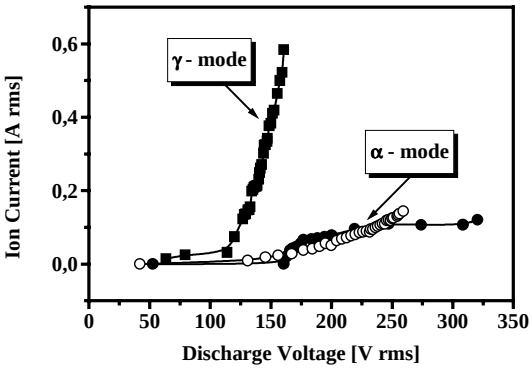


FIGURE 5. Ion **c**urrent amplitude as a function of the discharge voltage. Discharge parameters are: **solid square:** brass electrodes, gap spacing 0.05 mm, helium flow 500 sccm, drill-hole diameter of the holes 0.25 mm, **solid circle:** aluminium electrodes, gap spacing 1 mm, helium flow 500 sccm, drill-hole diameter of the holes 0.6 mm. **hollow circle:** aluminium electrodes, gap spacing 1 mm, helium flow 500 sccm, no holes.

The current density and ion current to the electrode were calculated using an electrode area of 7.07 cm^2. The ion current I_{ion} can be defined as follows [6]:

$$I_{ion} = I_{rf} \cos \phi, \qquad (1)$$

where I_{rf} is the rf current to the electrode (in our case the grounded anode) and ϕ is the phase difference between rf current and discharge voltage.

3.3. Emission intensity profile between the electrodes

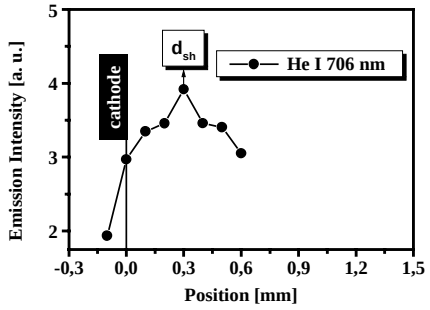


FIGURE 6. Spatial profile of emission intensity near the cathode (rf electrode) region. d_{sh} indicate the sheath thickness. Chamber is open to air.

Figure 6 shows a spatial profile of the intensity of the He I emission line at 706 nm near the cathode for a pure helium discharge. In the case shown in Fig. 6 the sheath thickness is about 0.32 mm for an input power of 50 W, a gap separation of 3 mm and a gas flow of 2000 sccm.

A measurement of the emission intensity profile between the electrodes is difficult to perform, when the discharge chamber is open to air. The He I line at 706 nm is produced by radiative dissociation of the He_2* dimer, which is formed by in a recombination process from metastable He atoms. Even small amounts of nitrogen change drastically the metastable He density by fast Penning ionisation with N_2 [9]. Thus the intensity of the He I line at 706 nm decreases if the content of air in the discharge is to high.

On the other hand, the intensity of the He line at 706 nm was high enough to detect a maximum in the emission spectrum near the cathode, which is comparable with the sheath thickness of an α mode discharge.

3.4. Gas temperature

For gas temperature measurements the anode was replaced by a metal mesh electrode. Although the discharge chamber was closed to air, small traces of N_2 are still present when operating the discharge in He. This allowed us to monitor the first negative system of the N_2^+ ion (FNS N_2^+) at 391 nm (see Fig. 7). At an electrode separation of 1 mm, typical rotational temperatures, obtained from a Maxwell-Boltzmann fit to the rotational intensity distribution, are in the range of 400 K. Because of very frequent collisions at atmospheric pressure, the gas temperature should be equal to the rotational temperature of the N_2^+ molecular ion [9]. Within the uncertainty of the measurements, the spectroscopically determined gas temperature of 437 ± 30 K (input power 40 W) is consistent with a thermocouple measurement of 410 K outside the discharge region.

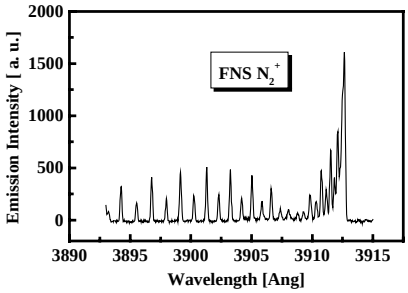


FIGURE 7. Emission spectrum of the first negative system of the N_2^+ ion at 391 nm. Discharge parameters are: gap spacing: 1 mm, input power: 40 W, 500 sccm He.

4. DISCUSSION

The measurements have shown, that it is possible to operate the jet matrix plasma source at two different, stable modes: the α and the γ mode. The discharges show similar properties as rf capacitive discharges at intermediate pressures [6, 7]. But there are some differences. One of them is the presence of finite and relatively large electric fields in the bulk region to drive the electron conduction current because of the low mobility of electrons. Park and co-workers determined an electric field strength of 300 V/cm [10] in the bulk plasma (positive column) for a pure helium discharge at atmospheric pressure. In our case the electric field can be larger because of He impurities by air, therefore we assumed electric field values in the range of 300 to 400 V/cm. The electron density n_e can be estimated as follows:

$$J_{rf} \approx J_{cond} = - n_e e \mu_e E_{bulk}, \qquad (2)$$

$$n_e \approx J_{rf} / (e \mu_e E_{bulk}), \quad (3)$$

where J_{rf} and J_{cond} are the rf current density and the electron conduction current density in the bulk region, respectively, μ_e is the electron mobility, and E_{bulk} is the electric field in the bulk region. For an electron mobility of 2.1×10^3 $cm^2/(Vs)$ [11], one obtains an electron density in the range of 10^{11}-10^{12} cm^{-3}.

At an electrode gap of 50 μm, we observe a γ mode discharge, similar to the discharge described in [6]. The discharge is characterized by a gap separation comparable of the relaxation length of the fast electrons (negative glow length). In this case the bulk plasma is the sum of two negative glows and the amount of fast electrons is much higher compared to the α mode. This results in a higher electron density of the discharge.

In our opinion the "real" HCE, characterized by a significantly higher current density compared to a normal dc glow discharge, can be obtained at in the γ mode only. For the α mode, the measured current densities are relatively low (< 0.15 A /cm^2). Additionally, the "real" HCE at atmospheric pressure can be obtained only if the cathode drill-hole diameter is much smaller than a relaxation length of the fast electrons [4]. For example, in a pure helium discharge with aluminium electrodes and a gas temperature of 300 K the drill-hole diameter should be much smaller than 38 μm.

5. CONCLUSIONS

Continuous glow discharges (in the α and γ modes) at atmospheric pressure have been obtained with rf (13.56 MHz) driven plasma sources, consisting of a matrix of hollow cathode discharges. Possible gases and gas mixtures are: He, Ar, He:O_2 (up to 40 % O_2) for the γ mode, He:N_2 (up to 10 % N_2) for the γ mode.

The study has shown, that a real hollow cathode effect (HCE) can be obtained in the γ mode only, and if the diameter of the holes drilled into the cathode is of the order of magnitude of the cathode sheath of the discharge. At atmospheric pressure, typical drill-hole diameters should be tens of μm in order to observe the HCE. Since the smallest drill-hole diameters of our cathode were at least 100 μm, we did not obtain a HCE at atmospheric pressure.

The discharge configuration can be scaled to larger areas, allowing possible applications in surface cleaning, surface modification, thin film deposition and chemical synthesis. Compared to other non thermal plasma sources at atmospheric pressure, the content of molecular gases is quite high.

ACKNOWLEDGMENTS

This work is supported by DFG under grant EN 183/12-1.

REFERENCES

[1] Moskalev B. I., *Hollow Cathode Discharge*, Energija, Moscow, 1969
[2] Little P. F., and A. von Engel, *Proc. Roy. Soc.*, **224**, 209 (1954)
[3] Kolobov V. I., and Tsendin L. D., *Plasma Sources Sci. Technol*. **4,** 551 (1995)
[4] Arslanbekov R. R., Kudryavtsev A. A., and Tobin R. C., *Plasma Sources Sci. Technol*. **7,** 310 (1998)
[5] Kolobov V. I., and Tsendin L. D., *Phys. Rev. A*, **46,** 7873 (1992)
[6] Raizer Y. P., Schneider M. N., and Yatsenko N. A., *Radio-Frequency Capacitive Discharges* (CRC, Boca Raton, FL, 1995)
[7] Yatsenko N. A., *Zh. Tekh. Fis.* **51**, 1195 (1981)
[8] Mildner M., Korzec D., and Engemann J., *Surf. Coat. Technol*., **112**, 366 (1999)
[9] Bibinov N. K., Fateev A. A., and Wiesemann K., *J. Phys. D: Appl. Phys*., **34,** 1819 (2001)
[10] Park J., Hennis I., Herrmann H. M., and Selwyn G. S., J. of Appl. Phys., **89**, 20 (2001)
[11] Huxley L. G. H., and R. M. Crompton, *The Diffusion and Drift of Electrons in Gases* (Wiley, New York, 1974)

SPATIO-TEMPORALLY RESOLVED EMISSION SPECTROSCOPY OF THE ATMOSPHERIC PRESSURE GLOW DISCHARGE IN NEON

D. Trunec[a] , R. Brandenburg[b], P. Michel[b], D. Pasedag[b], H.-E. Wagner[b] and Z. Navratil[a].

a) Department of Physical Electronics, Faculty of Science, Masaryk University, Kotlarska 2, Brno, Czech Republic

b) Institute of Physics, University of Greifswald, Domstrasse 10a, Greifswald, Germany

Abstract: In this contribution recent results on spatio-temporally resolved spectroscopic diagnostics of the dielectric barrier discharge (DBD) in neon at atmospheric pressure in combination with measurements of the discharge current are presented. The influence of small nitrogen admixtures in the 100 ppm range is studied, too. They cause a second smaller current peak in correlation with a further signal of the luminosity.

1. INTRODUCTION

The dielectric barrier discharge (DBD) at atmospheric pressure usually operates in a filamentary, non-homogeneous form. However, it was found that diffuse DBD (often referred too as atmospheric pressure glow discharge - APGD) can be generated in helium [1,2], nitrogen [3] and in the mixture of argon with acetone under specific conditions [4]. Recently it was found that APGD can be also generated in neon [5].

We used spatio-temporally resolved spectroscopy, classical optical emission spectroscopy as well as electrical diagnostics to study DBD in neon at atmospheric pressure. The results proved that this discharge is really a homogeneous (diffuse) discharge, similar to the APGD in helium [1,2]. Small admixtures of nitrogen or argon causes further discharge pulses after the main discharge during one half period of the power supply voltage.

2. EXPERIMENTAL DETAILS

The discharge was operated in a parallel plate electrode arrangement with a discharge gap of 2.2 mm. The electrode area was 2 cm x 2 cm, while the dielectric plates (Al_2O_3) were 3 cm x 3.6 cm long and 0.7 mm thick. The discharge was driven by sinusoidal voltage at a frequency of 10 kHz and amplitudes between 0.5 and 2 kV_{pp}. The specially modified technique of cross-correlation spectroscopy [7,8] enabled reliable spatially and temporally resolved measurements of the discharge luminosity for selected wavelengths, and it provided the resolution Δt = 0.5 - 1 μs over time scale, Δx = 0.2 mm over space (along the discharge axis). All experiments were carried out in an open gas flow system with a gas velocity through the discharge gap of about v_{gas}= 7.5 cm s^{-1}. Small impurities of nitrogen or argon could be admixed to the neon gas by using mass-flow controllers.

3. RESULTS

3.1. Electrical Characteristics

Oscillograms of the applied voltage and the discharge current in neon DBD are shown in fig. 1.

[a] trunec@physics.muni.cz.

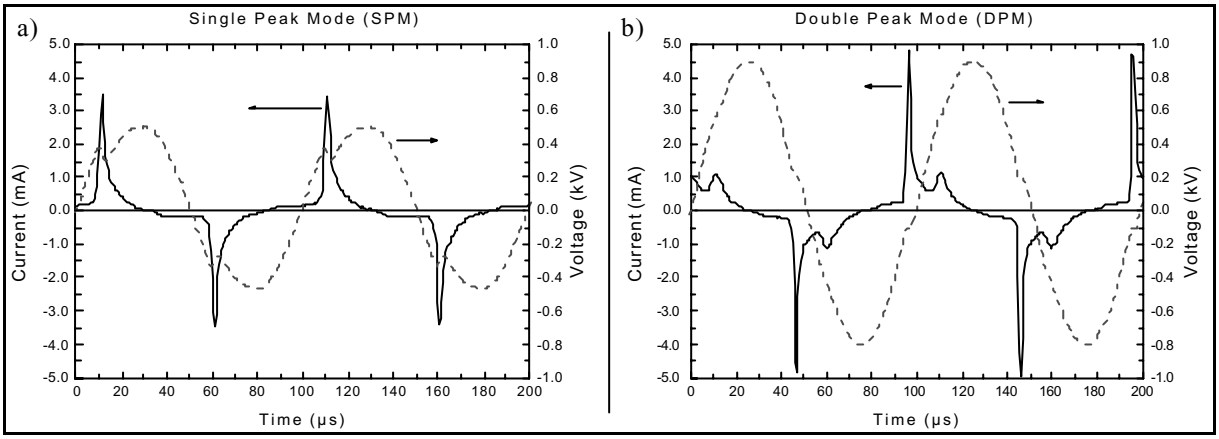


FIGURE 1. Time variation of discharge current and applied voltage in DBD in neon without (a, "SPM") and with 400 ppm (b, "DPM") external nitrogen admixture

Without any external gas admixture the current is characterized by one peak per half cycle with the same periodicity as the applied voltage (so-called Single Peak Mode SPM, fig 1a). This behavior is similar to the evolution of an APGD in helium described in [2] as well as measured with our setup. In particular, the inverse current peak is observed too (not to be seen in fig. 1a).

A small admixture of nitrogen (100 - 800 ppm) in connection with an increase of the applied voltage amplitude produces a second smaller discharge current pulse (so-called Double Peak Mode DPM; fig. 1b). Increasing the nitrogen amount more and more, further discharge peaks occurs (up to four). Then the discharge is still homogeneous, but a further increase of the nitrogen concentration above a certain level leads to the formation of filaments. A similar behavior is observed if helium is used as the working gas and/or argon is admixed instead of N_2. Similar results has been observed in [5].

3.2. Optical emission spectroscopy

The results of classical emission spectroscopy are shown in fig 2. The entire spectrum of the SPM discharge in pure neon in fig. 2a has been found to consist of the lines of excited neon atoms (almost all lines for λ= 500 - 700 nm) and atomic oxygen (e.g. λ= 777 nm), etched from dielectric surface. Emissions of nitrogen were not found in the spectrum. The difference to the helium spectrum and to the formerly observed neon spectra in [5] is a bremsstrahlung-continuum ("BC") at λ = 230-360 nm [8,9]. If nitrogen is admixed the spectrum changes as it is shown in fig. 2b. The intensities of neon and oxygen lines decrease, while molecular bands of nitrogen (second positive system and first negative system) start to occur. The continuum at λ= 230-360 nm disappears and NO_γ-system is observed.

The excitation (electron) temperature calculated from neon atomic lines was 2200 K in both cases (fig. 2a and 2b), the vibrational temperature calculated from nitrogen bands was 2300 K.

3.3. Time and space resolved emission spectroscopy

To carry out systematic emission intensity measurements, the spectral bands/lines shown in table 1 were selected. The results are shown in fig. 3 and 4. The intensity is colour coded in logarithmic steps and given in relative values (%).

	wavelength	*transition*			*exc. energy*	*char. lifetime*
Ne I	585.1 nm	3p' $[1/2]_0$	→	3s $[1/2]^0_1$	18.96 eV	15 ns
O I	777.4 nm	$3p\ ^5P^0_2$	→	$3s\ ^5S^0_2$	10.74 eV	21 ns
O II	486.0 nm	$3d\ ^2D_{3/2}$	→	$3p\ ^2P^0_{1/2}$	31.37 eV	27 ns
N_2 SPS	337.2 nm	$N_2(C^3\Pi_u^+)_{v'=0}$	→	$N_2(B^3\Pi_g)_{v'=0}$	11.03 eV	41 ns

TABLE 1. Selected spectral transitions

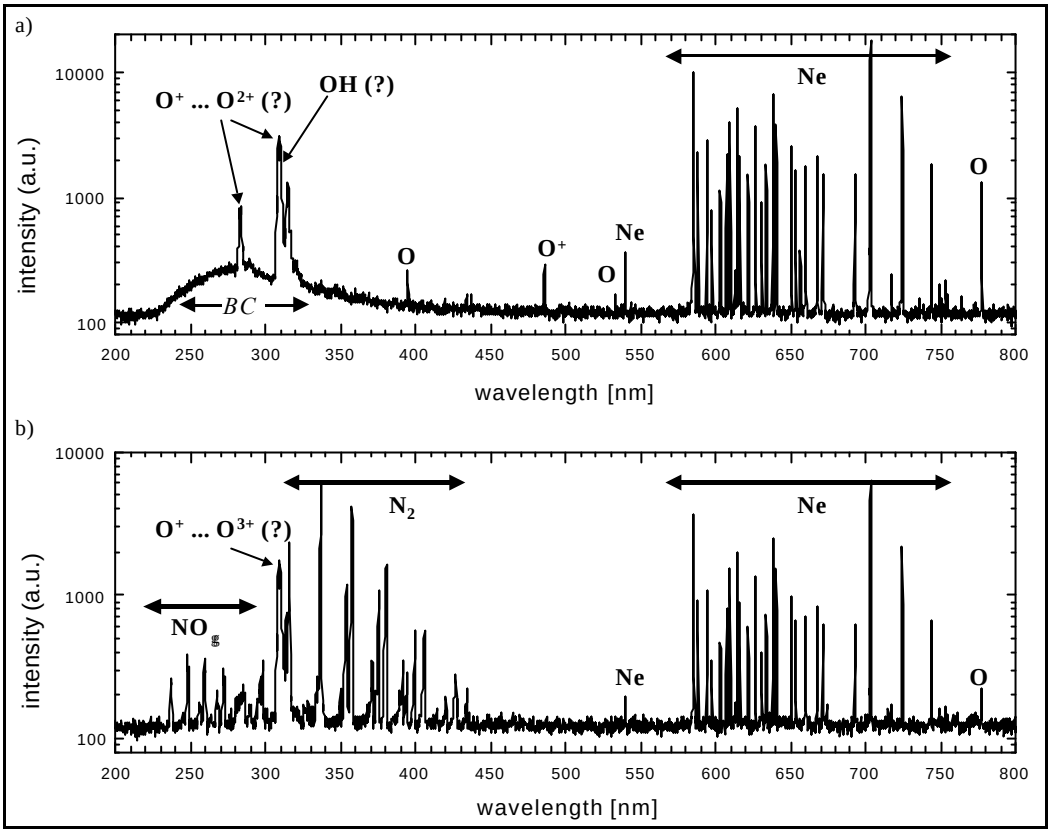


FIGURE 2. Emission spectrum of neon DBD in SPM (a) and DPM (b) with 130 ppm N_2-admixture.

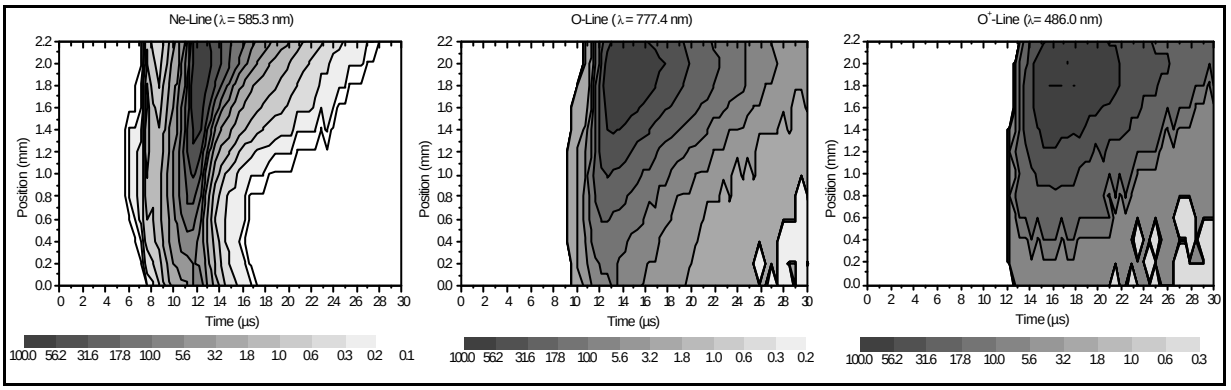


FIGURE 3. Intensity distribution for Ne I, O I and O II – lines (cathode is at the top) for SPM neon DBD

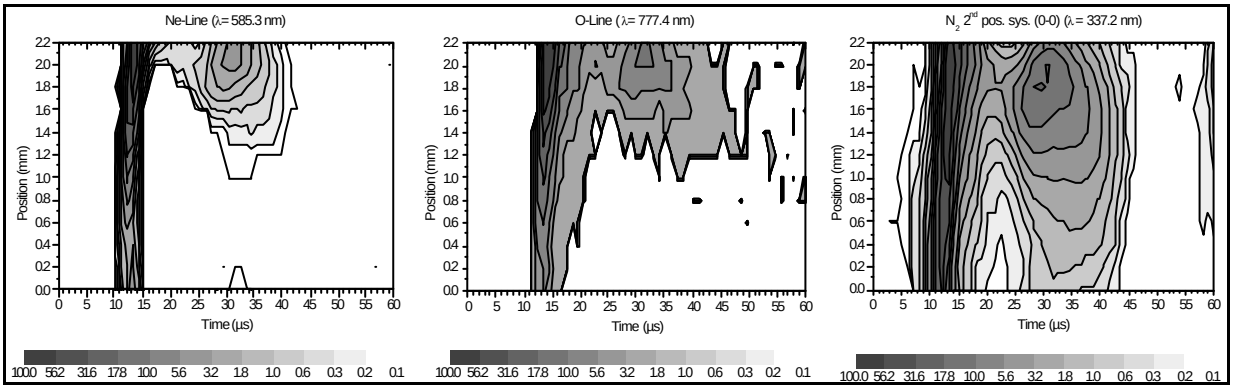


FIGURE 4. Intensity distribution for Ne I and O I – line as well as N_2 SPS (cathode is at the top) in DPM

As can be seen in fig. 3 a cathode directed discharge light, crossing the gap within a microsecond, is observed for the Ne I-line for the SPM APGD in neon. At t = 12 µs a second but much weaker local

maximum is observed directly at the anode. The oxygen intensity distributions (O I- and O II-line) shows a cathode directed intensity evolution as well, but stretched and delayed against the neon emissions. Comparing the result for Ne I-line to the intensity distribution for He I-line at 706 nm in the SPM-APGD in helium (not shown here) a small difference is observed: Just before the evolution of the cathode directed light at t = 7 µs a first weaker local maximum of the signal which develops towards the anode is observed.

As already mentioned the discharge in neon shows a great similarity to the APGD helium [2]. An APGD in helium is initiated by a slow increase of electron avalanches, which is able by the formation of electrons under a low electric field via indirect ionization processes through the interaction of metastable helium states with some impurities (Penning ionization). In neon plasmas metastable species with a sufficient life time can be formed as well. Thus one can suppose, that the APGD in helium and neon creates and develops in the same way. But to prove this suggestion a more detailed analysis of the discharge kinetic processes would be needed.

In the DPM intensity distributions in fig. 4 one can see two subsequent maxima at the cathode. The first part (up to t= 20 µs) is similar to the structure observed for the SPM, but it is shorter. Between maxima the light intensity does not decrease to zero. The two maxima correspond to the two current peaks. After reaching its maximum at the cathode, the second light decays towards the anode. The intensity distribution of NO, which has been analyzed too (not shown here) consists of one long lasting maximum, which is extended to the whole discharge space. The ratios of maximum intensities between the main and the second discharge pulse are different for every line. Compared to the main peak intensity the N_2 SPS is the most intensive band, followed by O I-line and neon radiation.

In fig. 5 light pulse evolutions for the spectral lines under consideration are shown together with the measured current pulses. The light pulses have been calculated as the corresponding sums of the spatially resolved data in fig. 3 and 4 over the entire range of axial scanning.

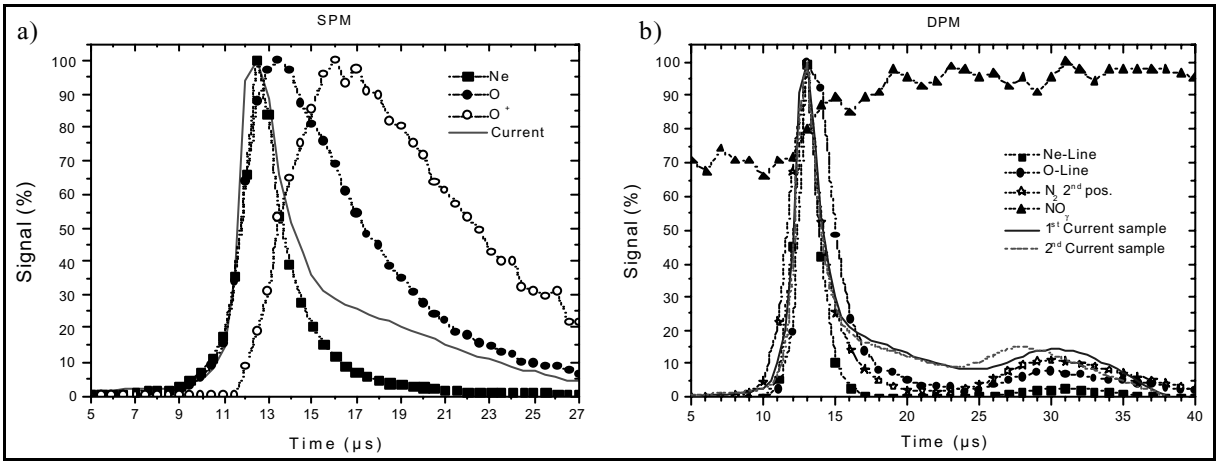


FIGURE 5. Light and current pules of the DBD in neon for SPM (a) and DPM (b)

For the SPM (fig. 5a) the rise of current and neon radiation corresponds very well. The neon signal decays faster than the current. However the oxygen emissions are delayed (1µs resp. 3.5 µs) against the current and they decay much slower than the neon light pulse. This leads to the conclusion, that neon is mainly excited due to direct electron collisions, while the oxygen species are excited in a stepwise process, including long lived species such as neon metastables, which may be produced by direct electron collisions too.

In the DPM (fig. 5b) all spectral lines under consideration except the NO signal corresponds very well with the discharge current. Only the O I-line is delayed a little. The NO radiation is always present. When the first discharge pulse occurs, the NO intensity increases. Due to the fact, that the discharge current is not stable within several hours of discharge driving, two current samples taken at the beginning resp. the end of the spectral data recording are shown in fig. 5b. The first pulse is stable but the second one is shifted about 3 µs in about 4 hours. In this second discharge pulse all species (except NO) seems to follow the current more or less immediately. Again this behavior may give information about dominant excitation processes as well as discharge formation. Thus the evolution of NO signal

leads to the assumption, that long lived species, namely nitrogen metastables $N_2(A)$ are generated and they form NO(A) [2], e.g. $N_2(A) + O \rightarrow NO(A) + N$.

The $N_2(A)$ metastables may be formed due to electron excitation and collisions with neon metastables (E= 16 eV). This would explain, why the first discharge pulse is shorter too. Due to quenching of Ne(1s3, 1s5) by nitrogen, less active, long lived species can contradict to the discharge formation.

4. CONCLUSIONS AND OUTLOOK

A dielectric barrier discharge in neon at atmospheric pressure can operate in different forms. The so-called Single Peak Mode (SPM) shows a great similarity to the APGD in helium. Results of spatio-temporally resolved emissions spectroscopy in connection with the recording of the discharge current give information about the discharge development and dominant excitation processes. The formation of a cathode fall is observed.

With admixtures of nitrogen or argon in the 100 ppm range a discharge consisting of up to four discharge pulses can be generated. The spatio-temporally resolved measurements show, that the so-called Double Peak Mode (DPM) consists of two subsequent discharge pulses. Furthermore the results let us assume, that nitrogen metastables play an important role for the formation of the second discharge pulse.

The received results were only discussed qualitatively here. To understand more of APGD formation and development as well as the transition to filamentary or multiple discharge pulse mode (e.g. DPM) in neon will be possible only in combination with a model involving an analysis of the discharge kinetics.

ACKNOWLEDGMENTS

One of us (D.T.) is grateful to the Grant Agency of Czech Republic for financial support under contract No. 202/02/0880. The investigations are further supported by Deutsche Forschungsgemeinschaft (DFG) – Sonderforschungsbereich 198 (Project A10).

REFERENCES

[1] Kanazawa S., Kogoma M., Moriwaki T. and Okazaki S.*, J. Phys. D: Appl. Phys*., **21**, 838 (1988)
[2] Massines F., Rabehi A., Decomps Ph., Ben Gadri R., Segur P. and Mayoux Ch., J. of Appl. Phys., **83**, 6, (1998)
[3] Gherardi N., Gouda G., Gat E., Ricard A. and Massines F., *Plasma Sources Sci. Technol*., **9**, 340 (2000)
[4] Yokayama T., Kogoma M., Moriwaki T. and Okazaki S., *J. Phys. D: Appl. Phys.*, **23**, 1125 (1990)
[5] Trunec D., Brablec A. and Buchta J., *J. Phys. D: Appl. Phys.*, **34**, 1697 (2001)
[6] Kozlov K.V., Wagner H.-E., Brandenburg R., Michel P., *J. Phys. D.: Appl. Phys.,* **34,** 3164 (2001)
[7] Brandenburg R., Kozlov K.V., Gherardi N., Michel P., Khampan C., Wagner H.-E. and Massines F., Spatio-temporally resolved spectroscopic diagnostics of the Atmospheric Pressure Glow Discharge in nitrogen; these proceedings
[8] Pfau S. and Rutscher A., *Beiträge aus der Plasmaphysik*, **8**, 315 (1968)
[9] Rutscher A. and Pfau S., *Physica*, **81C**, 395 (1976)

COMPARISON OF THE BARRIER - TORCH DISCHARGE AND TORCH DISCHARGE AT ATMOSPHERIC PRESSURE

P. Slavíček[a], A. Brablec[a,e], M. Klíma[a], V. Kapička[a], J. F. Behnke[d] and M. Šícha[b,c]

a) Dep. of Phys. Electronics, Masaryk University, Kotlářská 2, 611 37 Brno, CZECH REPUBLIC
b) Dep. of Electronics and Vacuum Physics, Faculty of Mathematics and Physics, Charles University, V Holešovičkách 2, 180 00 Prague 8, CZECH REPUBLIC
c) Inst. of Physic, Division of Optics, Academy of Sciences of the Czech Republic, Na Slovance, 2, 180 40 Prague 8, CZECH REPUBLIC
d) Inst. of Physics, Ernst-Moritz-Arndt University, Domstrasse 10a, D-17487 Greifswald, GERMANY

Abstract. A comparison of barrier – torches discharge (BTD) and torch discharge (TD), both driven at atmospheric pressure (RF generator, frequency 13.56 [MHz]) is presented. The BTD uses the nozzle coated with quartz and the working gas (argon) flows through the nozzle. The discharge is powered via outer electrode. In case of the TD the working gas flowing through the metallic nozzle with the sharp edge stabilizes the plasma channel. Optical emission spectroscopy, together with measurement of basic electrical parameters, was applied. It was found that vibrational and rotational temperatures in the BTD are nearly 2 times higher that in the TD.

1. INTRODUCTION

During several last years different systems with nozzle and powered by RF generator have been investigated. It was suggested, realized and studied systems working both at reduced and atmospheric pressure, in subsonic and supersonic regime, etc. (see [1-4] and references herein). It was concluded that the large variety of experimental conditions and possible modifications of arrangements allow to drive both corona and torch arc discharge and the systems working in transition regimes. Of course, there are exist another dielectric barrier discharge burning in diverse configurations, e.g. in [5].

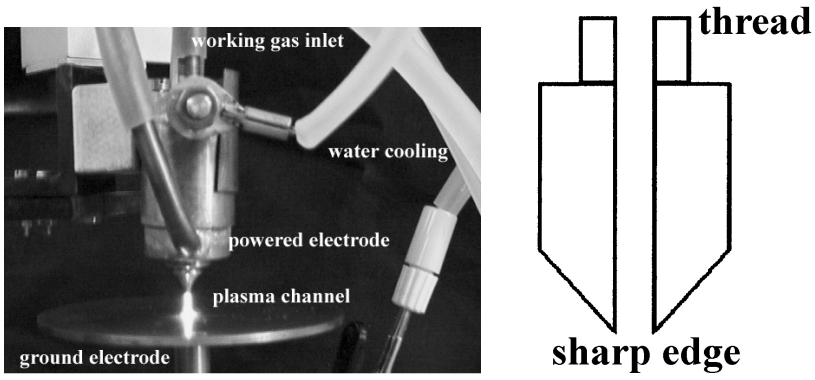


FIGURE 1. The snapshot of the torch discharge with water cooling of the powered electrode and the sketch of the simplest design of the nozzle are shown. The inner diameter is 1 [mm]. The working gas (argon) enters into the inner nozzle while the outer cover ensures the cooling.

The advantage of RF plasma discharges at atmospheric pressure consists in the fact that the torch discharge remains stable up to the atmospheric pressure for surface coating, spectral analysis, treatment of archaeological glass artifacts, fragmentation of molecules for micro-electrophoresis,

[e] Electronic address: [a] abr92@elanor.sci.muni.cz

plasma polymerization in liquids, etc. The device for hand operation has been also called plasma pencil [6]. The advantage of the plasma pencil is the possibility to work in the free atmosphere, in liquid, at lowered or increased pressures [7, 8].

Nevertheless, at present there are exist two basic configurations driven at atmospheric pressure: torch discharge (TD) and the barrier torch discharge (BTD) [9] – see Fig. 1 and the schematic block drawing in Fig. 2). While in previous contributions the individual systems and their versions were investigated separately as well as the interaction of the RF plasma channel burning at atmospheric pressure with liquid. Based on obtained results systems have been suggested for perspective industry applications. In this contribution the both fundamental versions are compared.

Especially, the application of the TD and BTD has been studied for deposition of thin films with specific properties and for treatment of various surfaces like is a plasma activation of polymer fibres at atmospheric pressure as the chemical activation is expensive and ecologically problematic.

2. EXPERIMENTAL SET-UP

The powered electrode (material: copper, iron, brass) was made from thin pipe the inner diameter of which is 1 - 2 [mm] and length several cm. The discharge was driven at 13.56 [MHz] and the power input 40 – 500 [W]. The power absorbed in the torch discharge has been adjusted in such a manner that at the electrode edge the torch discharge was created. The working gas, argon, which flows from the nozzle, stabilizes the torch discharge – see Fig. 1 where is shown the simplest version of the torch discharge (TD). In the same figure (right) there is also shown the experimental arrangement with the barrier torch discharge (BTD) where the dielectrics separates the powered electrode and the initial nozzle through which flows the working gas again. This is fundamental difference from the TD.

The electrode is connected through the matching unit to the RF generator. Optical and emission spectroscopy (i.e. the standard video CCD camera and a usage of grating monochromater [10]) and voltage and current measurements have been used as standard diagnostic methods.

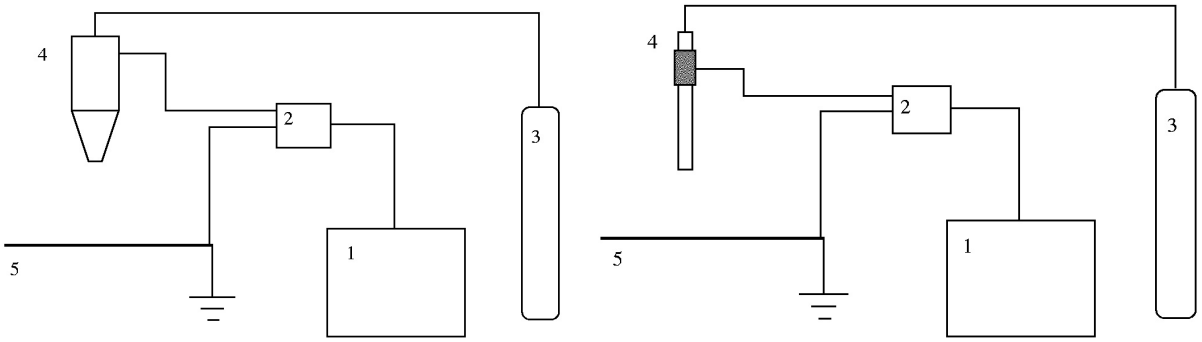


FIGURE 2. Schematic block drawing of experimental arrangements with the torch discharge with metal nozzle (a) and the barrier torch discharge (b) with the nozzle coated by dielectrics (quartz): 1 – rf genera - tor PG300, 2 – matching unit, 3 - working gas reservoir, 4- plasma nozzle, 5 – grounded electrode.

3. RESULTS AND DISCUSSION

The spectra emitted by the plasma channel were recorded by means of the Jobin – Yvon, HR640 monochromater for different parameters of the arrangements like RF power, working gas flow, material of electrodes, etc. Typical spectra emitted by the plasma are shown in Fig.3 which have been used for estimation of vibrational and rotational temperatures. Namely, rotational and vibrational temperatures were calculated from molecular bands of OH (306.4 [nm] system) and N_2 second positive system $C^3\Pi_u - B^3\Pi_g$, respectively.

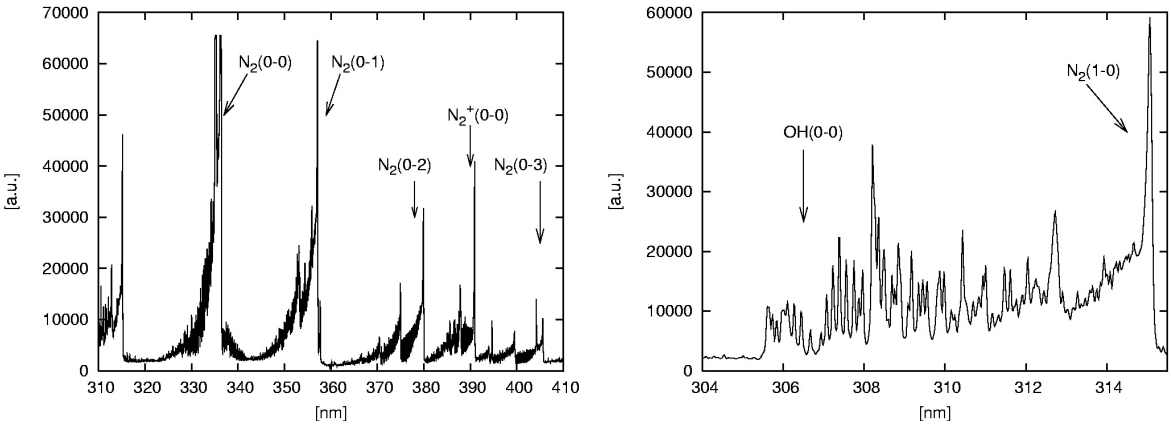


FIGURE 3. Typical spectra (left – nitrogen bands, second positive system and right – the OH band with the nearest nitrogen band) emitted by the torch discharge burning at atmospheric pressure in the configuration open system, working gas is argon.

It was found that the spectra emitted by the BTD and TD are similar with no serious differences (excluding atomic lines, which originate from the nozzle in case of the TB). Nevertheless intensities of individual bands as well as a coarse of the vibrational band taking into account its rotational structure are significant as shown in Fig. 4.

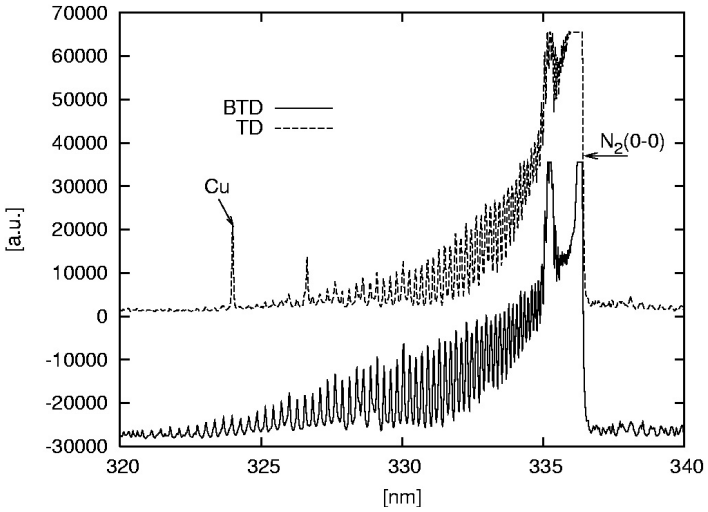


FIGURE 4. Typical spectra (left – nitrogen bands, second positive system and right – the OH band with the nearest nitrogen band) emitted by the torch discharge burning at atmospheric pressure in the configuration the open system and argon as a working. Both spectra are shifted for better reading.

The characteristic temperatures were determined as a function of input power. Results are presented in Fig. 5, errors were always less 10%. The rotational temperature approximated the temperature of neutral particles in the discharge. One can see that in general the barrier torch discharge is hotter than the torch discharge under the relative same design of the device and the same input power. This effect is important and could be used for more effective decomposition of chemical species.

Next, vibrational and rotational temperature as a function of input power for the TD is also shown in Fig. 6 for two diameters of the nozzle as mentioned before in previous contributions.

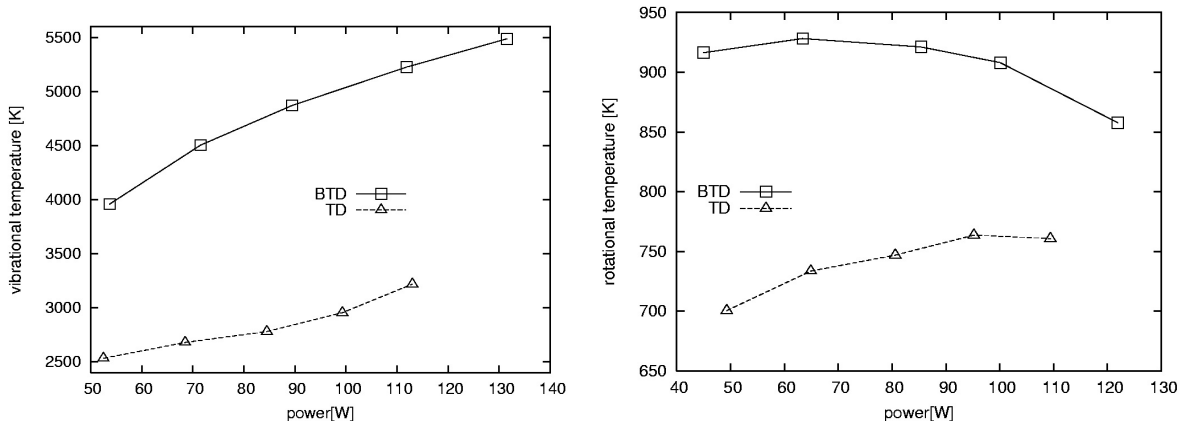


FIGURE 5. Vibrational and rotational temperature as a function of input power for BTD and TD discharge.

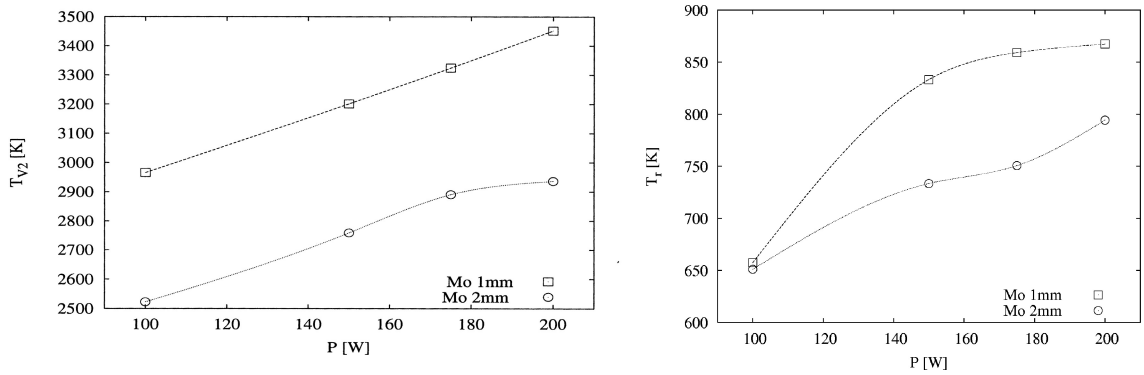


FIGURE 6. Vibrational (the band 0-2) and rotational temperature as a function of input power for the TD discharge and the same materials of the powered electrode and its different inner diameter. The argon gas flow is about 1000 sccm, the distance of the powered electrode from the grounded one is about 5 mm.

4. CONCLUSIONS

Based on the presented results one can conclude that significant differences between torch discharge and barrier torch discharge exist – in the torch discharge temperatures are practically two times lower than in the BTD. In case of the BTD the contamination of the discharge does not occur as a result of sputtered material of the nozzle. For this reason the barrier torch discharge appears now more convenient for surface treatments. In case of chemical decomposition the higher temperature could be also more needed. However, other applications require discharges with lower temperature and so the TD discharge must be used.

ACKNOWLEDGMENTS

Grant Agency, Czech Republic, financially supported the contribution (contract numbers: 202/00/D057, 202/01/P017).

REFERENCES

[1] Sicha M., Bardos L., Tichy M., Soukup L., Jastrabik L., Barankova H., Soukup R. J., Tous J., *Contrib. Plasma Phys.*, **34** (1994) 794

[2] Sicha M., Soukup L., Jastrabik L., Novak M., Tichy M., *Surface and Coatings Technology*, **75**(1995) 212

[3] Soukup L., Perina V., Jastrabik L., Sicha M., Pokorny P., Soukup R. J., Novak M., Zemek J., *Surface and Coatings Technology* **78** (1996), p.280

[4] Novak M, Sicha M., Kapicka V., Jastrabik L., Soukup L., Hubicka Z., Klima M., Slavicek P., Brablec A., *J. Phys. IV France* **7** (1977), Colloque C4, Suppl., *Journal de Physique III* d'octobre 1977, C4-331

[5] Wiesemann K., Spectroscopic Investigation of Dielectric Barrier Discharges. In *Book of Invited Lectures 20th SPIG*, ed. by N. Konjevic, Z. Lj. Petrovic, and G. Malovic, September 4 – 8, 2000, Zlatibor, Yugoslavia, pp. 307 - 325

[6] Klima M., Janca J., Kapicka V., Slavicek P., Saul P.: The Method of Making a Physically and Chemically Active Enviroment by Means of a Plasma Jet and the Related Plasma Jet, Czech patent No. 286310 (prior. 12.5.1998) or PCT/CZ99/00012.

[7] Brablec A., Slavicek P., Klima M., Kapicka V., High Pressure RF Discharge: Spectral Diagnostics and Perspective Application. In: *Proc, 11th Symposium on Elementary Processes and Chemical Reactions in Low Temperature Plasma*, ed. by M. Morvová and K. Hensel, Low Tatras, June 22 – 26, 1998, pp.188 - 191

[8] Brablec et al, *Czech. J. Phys.*, **49** (1999) 329

[9] Hubička Z et al, *Plasma Sources Sci. Technol*, in press

[10] Brablec A., Slavíček P., Kapička V., Vaculík R., Střecha M., Klíma M., *ESCAMPIG* Dublin, 1998, Ireland, p. 362-363

SILENT DISCHARGES IN HELIUM AND HELIUM-NITROGEN MIXTURES

N. B. Anikin[b] , N. K. Bibinov[a] , M. Šira[c] and K. Wiesemann[a]
[a]) Ruhr-Universität Bochum, Experimentalphysik insbes. Gaselektronik, 44780 Bochum, Germany.
[b]) Moscow Institute of Physics and Technology, Physics of Nonequilibrium Systems Laboratory, Institutskii lane, 9, Dolgoprudny 141700, Moscow region Russia.
[c]) Masaryk University, Department of Physical electronics, Brno 61137, Czech Republic

Abstract: From the molecular emission of He/N_2 silent discharges we evaluated the gas temperature as well in the micro-discharge area as in the ambient gas. Also in the case of the appearance of an APGD in pure helium we found two different temperatures in this way. From our results we estimate the average volume occupied by single micro-discharges.

For obtaining the temporal and spatial distribution of energy in He/N_2 dielectric barrier discharges (DBDs) we have measured the applied voltage, the discharge current, the absolute intensities and the rotational structures of the molecular bands in the emission spectra. If the helium pressure is high (40 – 160 kPa) and the nitrogen pressure low (< 0.8 kPa) the rotational distribution in the molecular bands corresponds to the gas temperature in the region of excitation of the corresponding molecules [1]. According to the reaction scheme and the values of the rate constants of the excitation and quenching processes one can assert that the value of the rotational temperature of the bands of the "first negative system" ($N_2^+(B^2\Sigma_u^+ \rightarrow X^2\Sigma_g^+)$) corresponds to the gas temperature in the micro-discharge area. Excited states of the transitions $OH(A^2\Sigma^+ \rightarrow X^2\Pi)$, $NO(A^2\Sigma^+ \rightarrow X^2\Pi)$ and $N_2(C^3\Pi_u \rightarrow B^3\Pi_g)$ are produced in reactions with metastable nitrogen molecules and give information on the conditions in the ambient gas [1,2].

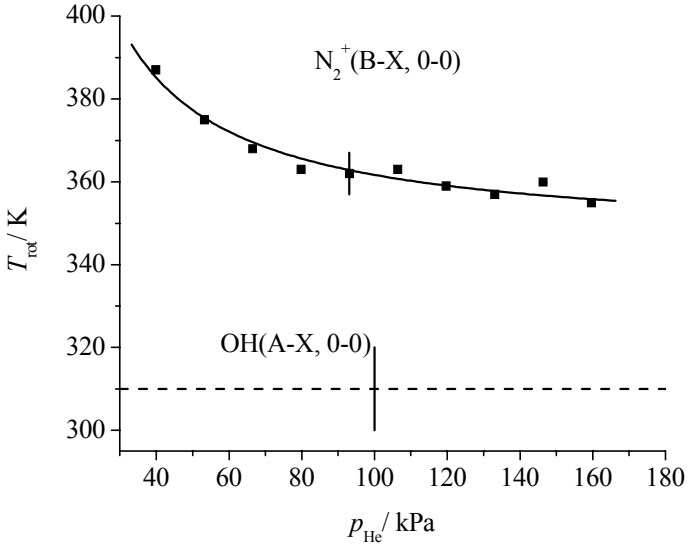


FIGURE 1. Rotational temperatures obtained from emission spectra of nitrogen ions (full curve) and OH-radicals (dashed line)

At very low nitrogen partial pressure (p_{N2} < 10 Pa) the influence of nitrogen on the discharge parameters is negligible. The bands of the "first negative system" and of the OH-radicals are observed in emission spectra of He/N_2 discharge besides intense helium "recombination"-lines near 700 nm, produced in the reactions

$$He^+ + 2He \rightarrow He_2^+ + He \quad (1)$$

$$He_2^+ + e \rightarrow He + He + h\nu. \quad (2)$$

The excited OH-radicals are produced under these conditions by photo-dissociation of water molecules the active radiation in the wavelength range 70-100 nm stemming from short living helium-dimers [3,4]:

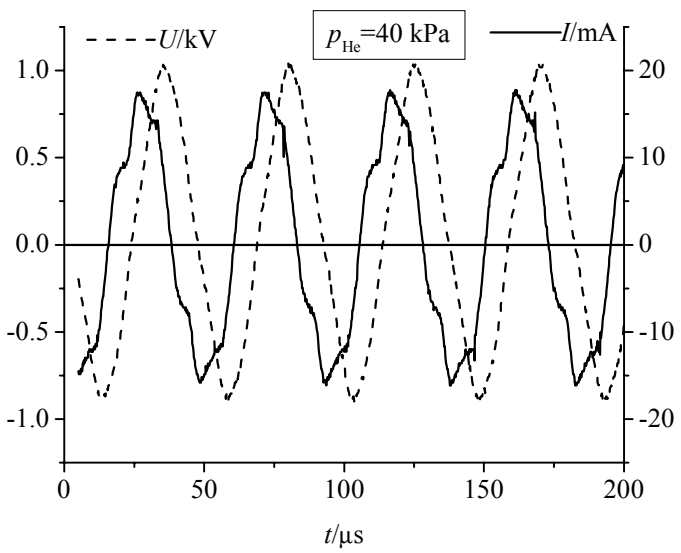


FIGURE 2. Applied voltage U (dashed curve) and discharge current I (full curve) in DBD at p_{He} = 40 kPa

$$H_2O + h\nu \rightarrow OH(A) + H. \qquad (3)$$

The emission intensity of the OH-radicals depends in this case on the square of the helium pressure, $(p_{He})^2$. The excited state $N_2^+(B^2\Sigma_u^+)$ is formed by Penning ionization.

Further the recombination rate is low and therefore the duration of the active discharge current equals the half period of the applied voltage (about 25 μs in our experiment). The discharge glow is homogeneous. For this reason this phenomenon is named atmospheric pressure glow discharge (APGD). It was intensively studied by several authors (see for example [5,6]). In these discharges one expects a constant gas temperature between the electrodes. But we have found different rotational temperatures in the emissions of nitrogen ions on the one hand and in that of the OH-radicals on the other hand - see Fig. 1. This means that the gas temperature in the range of the active discharge area (where helium atoms are excited and the nitrogen ions are produced by Penning ionization) is 50-90 K higher than the temperature of the ambient gas, where OH-radicals are produced in the excited state by photodissociation.

To estimate the dimension of the active area in this discharge we have calculated the value of the dissipated energy from the totally transferred charge during one half period (250 nC, see Fig.2) and the breakdown voltage (350V). This gives an upper limit for the energy because the gap voltage of the

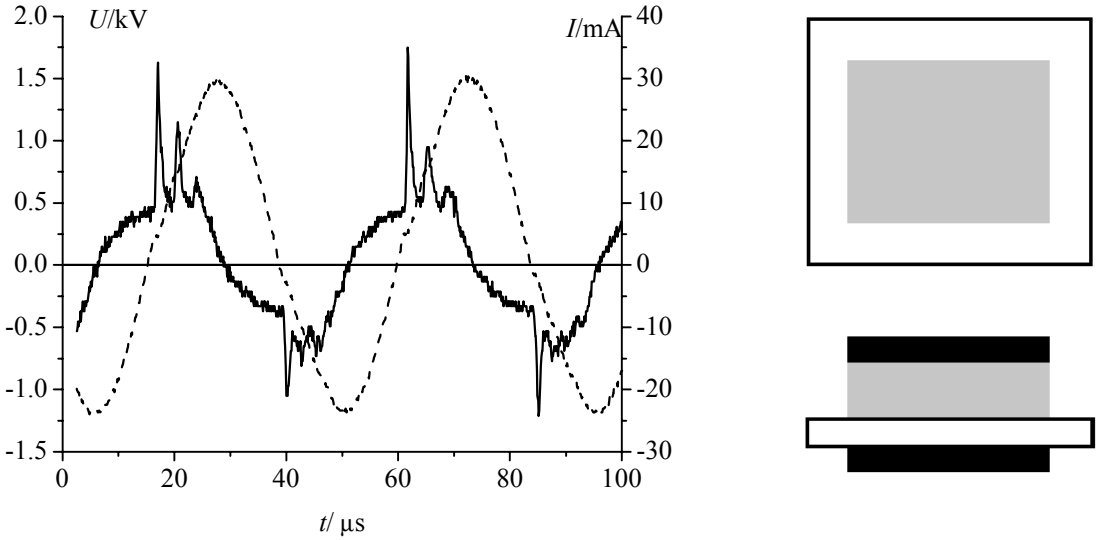


FIGURE 3. Applied voltage U (dashed curve) and discharge current I (full curve) in DBD at p_{He}= 160 kPa, p_{N2}= 0.67 kPa (T = 395 K)

running discharge pulse is smaller than the breakdown voltage and the charge transferred due to the displacement current in the gas gap capacitor was not subtracted. We obtain an energy of $8.4 \cdot 10^{-5}$ J dissipated during one half period of the applied voltage. From the heat capacity of the helium gas we

obtain an upper limit of the heated volume by assuming that the gas is heated to 90 K and all dissipated electrical energy is transformed to heat. This value ($5 \cdot 10^{-3}$ cm^3) is more than 670 times smaller than the gas volume between the electrodes (3.36 cm^3). The glow of the discharge at our experimental conditions, however, is absolutely homogeneous and fills the total gas gap volume. The He atomic "recombination"-lines are the most intensive in the emission spectrum of the DBD in pure helium. The intensity distribution in the emission spectrum evidences the excitation of the He atoms by the recombination process given in equs. (1) and (2). This process is slow and can occur not only in the active discharge but also in the afterglow.

When admixing 0.7 kPa of nitrogen the emission of gas between the electrodes is still homogeneous, though the short discharge current pulse shows that the charged particles disappear during a time much shorter than the half period of the applied voltage - see Fig.3. By decreasing the amplitude of the applied voltage at the same nitrogen partial pressure one can obtain discharges with a homogeneous glow in a bounded region. If then the nitrogen pressure increases up to 0.8 kPa (at constant amplitude of the voltage) the discharge in the bounded region in some fixed point of the dielectric surface turns into one micro-discharge in the form of a filament - see Fig.4 (in this case the gas temperature could not be determined because the emission intensity was too low).

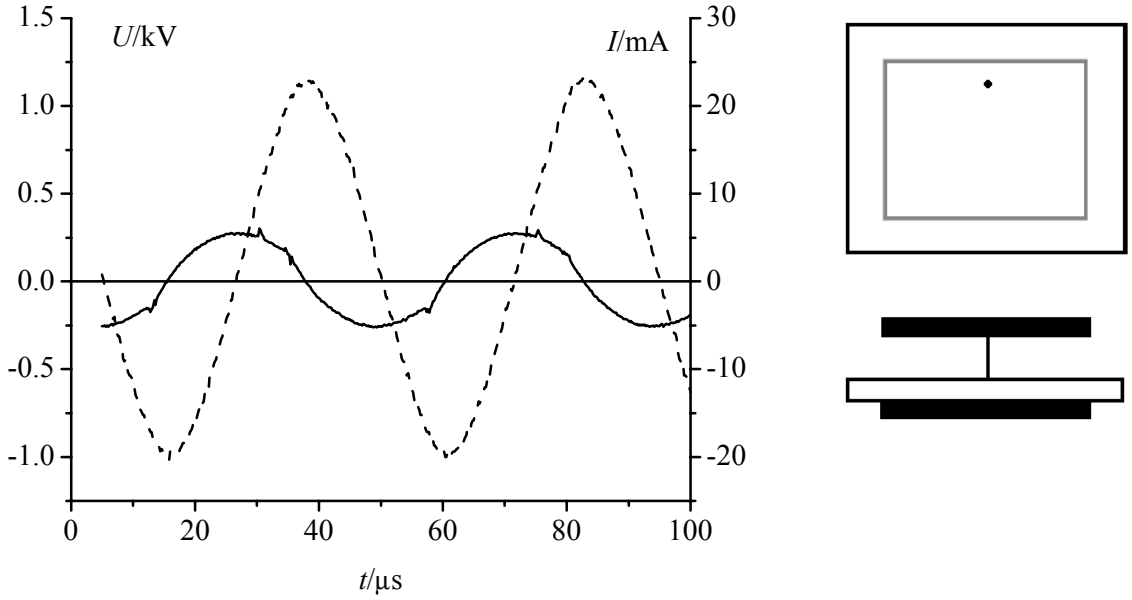
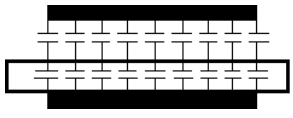


FIGURE 4. Applied voltage U (broken curve) and discharge current I (full curve) in DBD at p_{He} = 160 kPa, p_{N2} = 0.67 kPa

On the basis of these experimental findings we assume that the parallel effective capacitors in the discharge of the DBD-cell are coupled by some gas conditions not by surface effects.



If the capacitors were coupled on the surface a single filamentary discharge would ignite with higher energy content corresponding to the total energy of the combined capacitors. For proving this we have connected a number of effective capacitors by depositing a thin film of conductive ZnO:Al on the surface of the dielectric barrier. The area of this film was 10 mm^2. At low amplitude of the applied voltage a single filamentary micro-discharge appeared on the film surface. We succeeded in measuring the gas temperature (T = 410 ± 10 K), the absolute intensity of emission and the discharge current of this micro-discharge – see Fig. 5. From an estimate of the energy dissipated in the gas we obtained the volume of the discharge channel and assuming a cylindrical shape a radius r = 16 μm (upper limit). We further calculated the electron distribution function ($f_e(E)$) at our experimental conditions (E/N = 12 Td) and an average electron concentration n_e in the micro-discharge of $n_e = 3.5 \cdot 10^{13}$ cm^{-3} by fitting the absolute emission intensity to a kinetic model.

If we increase the voltage amplitude by a very small amount one - sometimes two - additional filamentary micro-discharges appear at the surface of the glass. Sometimes appears a flickering discharge area - see Figs. 6 and 7. The gas temperature at these discharge conditions is a little bit smaller than that of a single filamentary discharge from the ZnO film (T = 395 ± 5 K). The electrical energy dissipated in one micro-discharge from the glass is 4 times smaller than the energy dissipated in the micro-discharge starting from the ZnO.

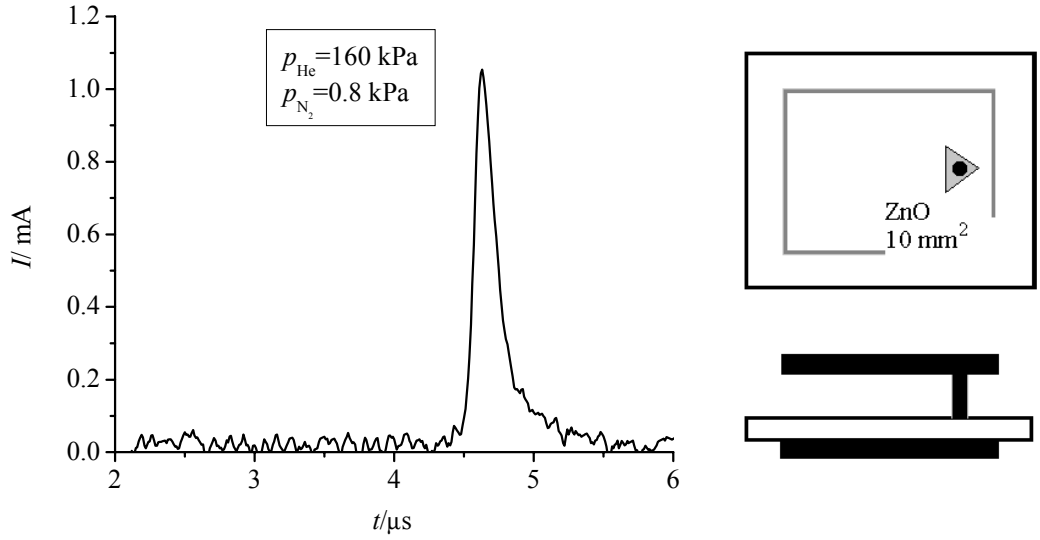


FIGURE 5. Discharge current I in DBD at p_{He} = 160 kPa, p_{N2} = 0.8 kPa. The surface area of the ZnO film is equal to 10 mm^2.

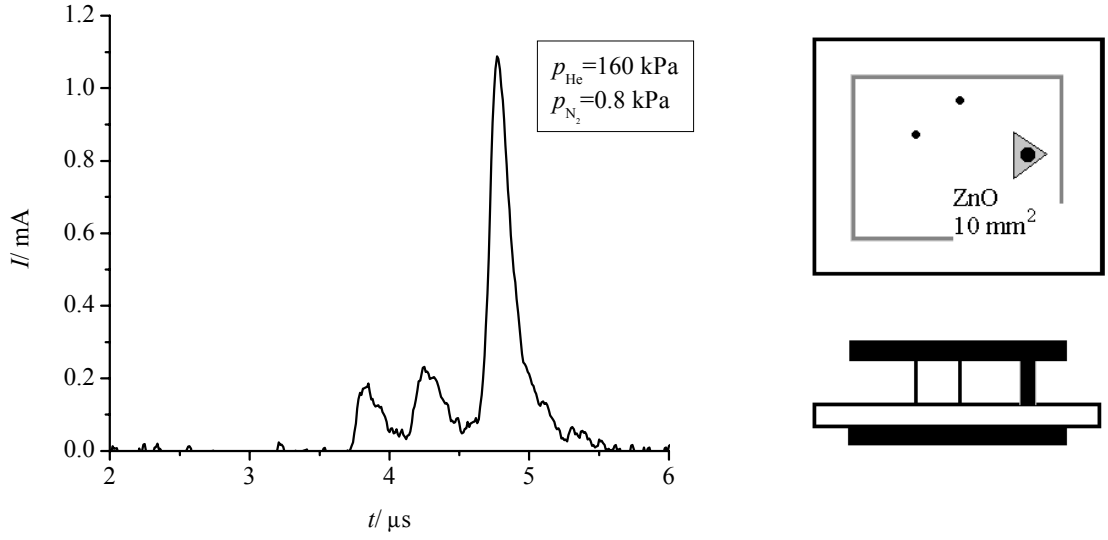


FIGURE 6. Discharge current I in DBD at p_{He} = 160 kPa, p_{N2} = 0.8 kPa
The surface area of the ZnO film is equal to 10 mm^2.

By a comparison of the emission and the dissipated electrical energy we estimated the volume and thus the radius r of a filamentary micro-discharge starting from the glass surface and the surface area S of the effective capacitor and obtained as upper limits r = 8 μm and S = 2.5 mm^2, respectively.

In conclusion we state that the phenomenon of a homogeneously glowing discharge is quite different from a discharge with the current homogeneously distributed over the entire discharge gap. A possible explanation of the apparent homogeneous glow is the presence of long living metastables diffusing into the entire gap volume and producing by Penning effect a long afterglow. The structure of the current distribution needs further investigations.

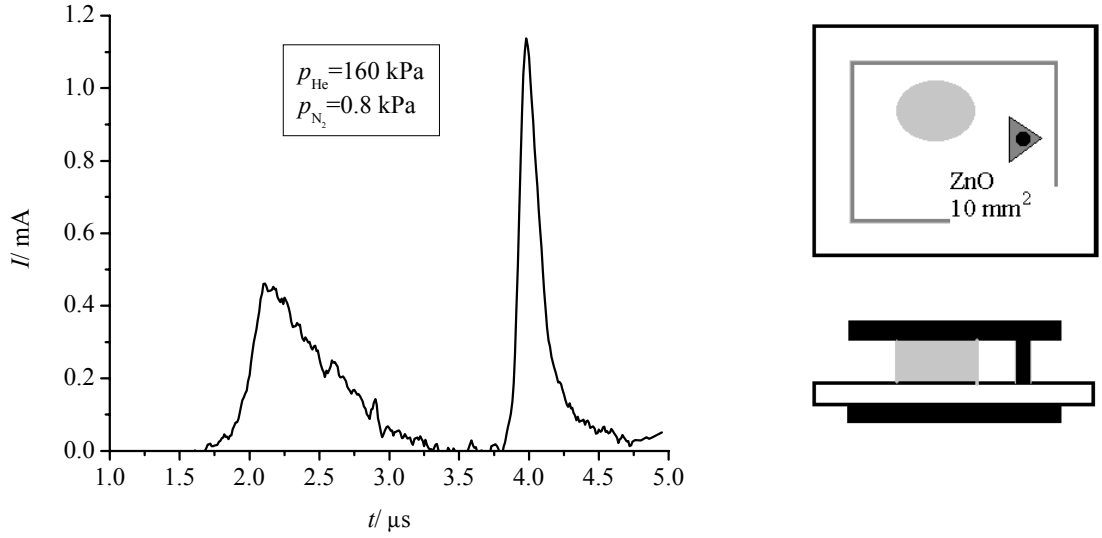


FIGURE 7. Discharge current I in DBD at p_{He} = 160 kPa, p_{N2} = 0.8 kPa
The surface area of the ZnO film is equal to 10 mm^2.

REFERENCES

[1] N. K. Bibinov, A. A. Fateev, K .Wiesemann, *Plasma Sources. Sci. Technol.,***10**, 579-88 (2001).
[2] N. K. Bibinov, A. A. Fateev, K. Wiesemann, *J. Phys. D: Applied Phys.,* **34**, 1819-26 (2001).
[3] M.Krauss, F.H.Mies, Electronic Structure and Radiative Transitions of Excimer System, In *Excimer Lasers* ed.by Ch.K.Rhodes, Springer, 1979, pp. 5-46.
[4] I.P.Vinogradov, F.I.Vilesov, *Opt.Spectrosc.,* **40**, 32-4 (1976).
[5] N. Gherardi, G. Gouda, E .Gat, A. Ricard, F. Massines, *Plasma Sources. Sci. Technol.,* **9**, 340-6 (2000).
[6] F. Massines, A. Rabehi, Ph. Decomps, R. B. Gadri, P. Segur, Ch. Mayoux, *J. Appl. Phys.,* **83**, 2950-57 (1998).

ELECTROHYDRODYNAMIC TRANSPORT OF OZONE IN A CORONA RADICAL SHOWER NON-THERMAL PLASMA REACTOR

J. Mizeraczyk[a], J. Podliński[a], M. Dors[a], M. Kocik[a], T. Ohkubo[b], S. Kanazawa[b], J.S. Chang[c]

a) Institute of Fluid Flow Machinery, Polish Academy of Sciences, Fiszera 14, 80-231 Gdańsk, POLAND
b) Dep. of Electrical and Electronic Engineering, Oita University, 700 Dannoharu, Oita 870-1192, JAPAN
c) Department of Engineering Physics, McMaster University, Hamilton, Ontario, L8S 4M1 CANADA

Abstract. In this paper results of the experimental investigation of ozone molecule transport along a corona discharge radical shower (CDRS) non-thermal plasma reactor are presented. The measured axial ozone concentration distributions along the CDRS reactor show that the ozone molecules produced in the discharge region were transported from their origin both in the upstream and downstream regions of the CDRS reactor, i.e. also against the main gas flow. The images of the flow structures in the CDRS reactor suggests that the electrohydrodynamic (EHD) flow is responsible for the ozone transport upstream.

1. INTRODUCTION

Recently, Ohkubo et al. [1] and Kanazawa et al. [2] found that the removal of NO molecules in a needle-to-plate and corona discharge radical shower (CDRS) non-thermal plasma reactors occurred not only in the streamer corona discharge and downstream regions of the reactors but also in the upstream of the discharge regions. The reason of the NO removal in the upstream region of the reactor is not clear at this moment. However, the results of the previous (e.g. [3-5]) and recent (e.g. [6, 7]) experiments on the electrohydrodynamic (EHD) secondary flow (ionic wind) in electrostatic precipitator models suggest that the EHD flow is capable of transporting long-living active species upstream of the discharge region, where they may react with other species. Hence, if the ozone molecules were transported by the EHD flow upstream of the discharge region in the experiment of Ohkubo et al. [1] and Kanazawa et al. [2], they would be long-live and active enough to oxidize NO molecules and efficiently remove them before they reach the discharge region.

In this paper we present results of the investigation of ozone molecule transport along a CDRS non-thermal plasma reactor. In addition to the fundamental interest in the transport of ozone and other species transport in the non-thermal plasma reactors, this investigation is related to the topical questions of the non-thermal plasma technology for gaseous pollutant abatement:

- how (if at all) the corona discharge itself and the no-discharge region (the part of the reactor not covered by the discharge) are involved in the reduction and/or oxidation of the gaseous pollutants in the non-thermal plasma reactors,
- how the present chemical kinetics modelling of the gaseous pollutant removal processes caused by the corona discharge (e.g. [8-10]), which neglects involvement of the no-discharge region, depicts the real phenomena in the non-thermal plasma reactors, and therefore how it can be useful for optimising the performance of the non-thermal plasma reactors.

2. EXPERIMENTAL APPARATUS

A schematic diagram of the experimental apparatus is shown in Fig. 1. The reactor was an acrylic

[a] Electronic address: jmiz@imp.gda.pl

box (100 mm x 200 mm x 1000 mm). A stainless-steel pipe (4 mm in diameter) with 18 stainless-steel nozzle electrodes (1.5 mm outer diameter, 1 mm inner diameter, 5 mm length), soldered into the pipe as shown in Fig. 2, was used as a CDRS electrode. It was mounted in the middle of the reactor, in halfway between two grounded parallel plate stainless-steel electrodes (200 mm x 600 mm). Positive polarity DC high voltage was applied through a 10 MΩ resistor to the pipe with nozzle electrodes. The operating voltage was varied from 0 to 31 kV to develop a stable streamer corona discharge from each nozzle to the plate electrodes.

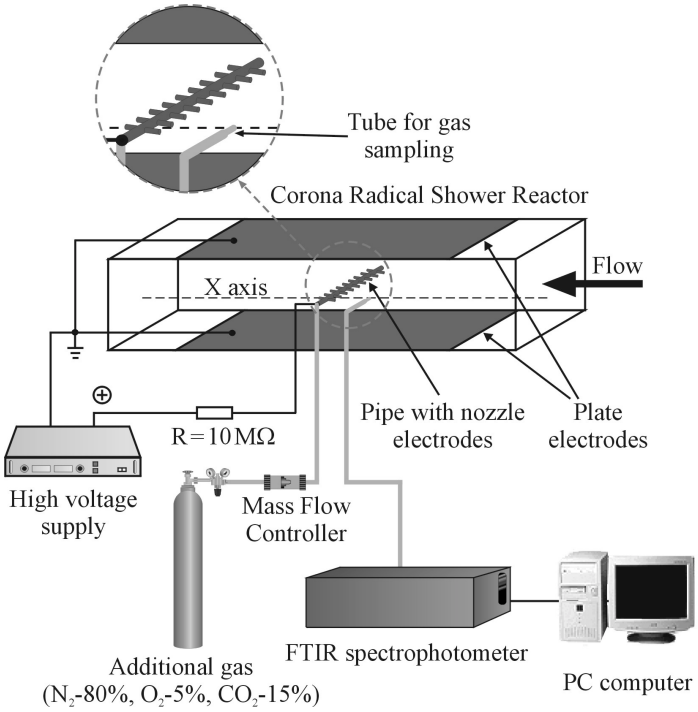


FIGURE 1. Experimental set-up.

Two gas flows, the main and the additional, were established in the reactor. The main gas (ambient air) flowed along the reactor, driven by an induced fan. The average velocity of the main gas flow was varied from 0.18 to 0.8 m/s. This is a range typical for electrostatic precipitators operations. The additional gas (N_2:O_2:CO_2=80%:5%:15%) was injected through the nozzles into the main gas flow with a flow rate varied from 0.25 to 1.5 l/min (exit gas velocity 0.3-1.8 m/s). The presence of CO_2 (15 %) stabilized streamer corona discharge mode, preventing glow and spark discharge modes [11].

Concentration of ozone, produced by the streamer corona discharge, was measured along the reactor on the x axis placed 1 cm below the discharge electrode (Fig. 1), using a cylindrical plastic sampling probe (1 mm in diameter), through which the operating gas was sucked into a calibrated FTIR spectrophotometer having a long-path measuring cell, where ozone concentration was measured. The suction was very slow (a suction rate was 2.25 cm^3/s), hence, it disturbed the flow fairly weak. As tested, a lower suction rate gave similar measuring results. The experiment was run at room temperature under atmospheric pressure.

Flow structures in the CDRS reactor were visualized to elucidate the mechanism of ozone transport into the upstream region of the reactor. Using a CuBr laser (λ=510.6 nm and λ=578.2 nm) [12], the so-called laser sheet of a thickness of 1 mm, formed by a telescope, was set along the reactor, perpendicularly to the electrode. Seed particulate (cigarette smoke), which followed the flow, was added either to the main or additional gas for scattering the laser-sheet light. The images of the particulates moving with the flow in the laser sheet were recorded with a video camera, and acquired with a computer.

3. EXPERIMENTAL RESULTS

3.1. Spatial distribution of ozone concentration

In general, the ozone molecules, produced around the electrodes during the streamer corona discharge, can be transported from their origin both downstream and upstream of the discharge region, by diffusion, the additional gas flow from all the nozzles and the electrohydrodynamic (EHD) secondary flow. They are also transported by convection of the main gas flow, but only downstream. When a steady state is established in the CDRS reactor, spatial distributions of the ozone molecules are settled as a net effect of the ozone production and transport.

Fig. 2 shows the steady-state ozone concentration distributions along the CDRS reactor for various main gas flow velocities ranged from 0.18 to 0.8 m/s. The main features of the ozone concentration axial distributions in the CDRS reactor are as follows:

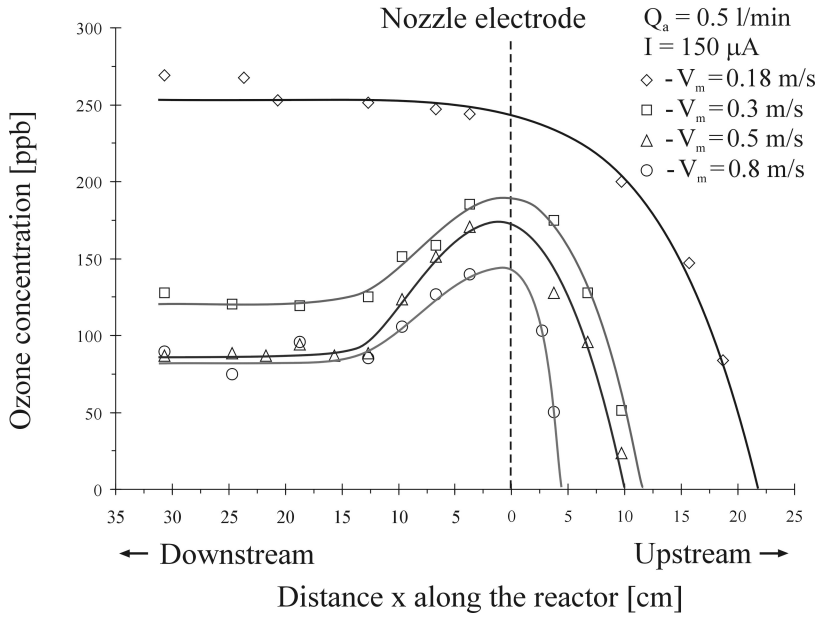


FIGURE 2. Ozone concentration distribution along the CDRS reactor during the positive DC streamer corona discharge for various main gas (air) flow velocities V_m. The ozone concentrations were measured along x axis, placed along the reactor 1 cm below the discharge electrode. Additional gas [N_2(80%):O_2(5%):CO_2(15%)] flow rate Q_a = 0.5 l/min, averaged discharge current I = 150 μA.

1. Ozone molecules are present in both the downstream and upstream regions of the CDRS reactor, assuming the position of the discharge electrode as a reference.
2. Except for the lowest main gas velocity (0.18 m/s), the ozone concentration exhibits a maximum around the discharge zone (due to the ozone production) and decreases when moving upstream regardless of main gas flow velocities. At main gas flow velocities higher than 0.18 m/s, the ozone concentration decreases downstream and then, when the convection by the main gas flow becomes dominant, is constant. At the lowest main gas flow velocity tested (0.18 m/s), the ozone concentration distribution around the discharge zone is apparently governed more or less equally by diffusion, main gas convection and EHD flow, hence, it does not exhibit any decrease downstream.
3. The ozone penetration length upstream depends on the main gas flow velocity. It is shorter at higher main gas flow velocities because the role of the main gas convection in the ozone molecule transport increases. The ozone molecules are found in the upstream region of the CDRS as deep as about 20 cm from the discharge electrode, at a main gas flow rate of 0.18 m/s. At a main gas flow rate of 0.8 m/s, the ozone molecules penetrate only a few cm upstream.

3.2. Visualization of the flows in the CDRS reactor

The image of the flow structure in the CDRS reactor when a positive voltage of 28 kV was applied is shown in Fig. 3. As it can be seen, there exists a strong secondary flow in the upstream region of the CDRS reactor, with at least two well-marked vortexes at a distance 6-12 cm from the nozzle. The flow structure observed in the upstream region results from the interaction between the gas ionic current emanating from the stressed electrode towards the collecting electrodes, and the additional and main gas flows. However, visualization of the additional flow when no voltage was applied showed that the additional gas jet does not penetrate deep upstream (Fig. 4). Thus, one may infer that the secondary flow in the upstream region of the CDRS reactor is mainly a result of the EHD forces. As measured in the similar electrode arrangements (a conventional needle-to-plate non-thermal plasma reactor [7], model of the electrode precipitator [11]), the EHD flow can be as fast as 2.5 m/s in the discharge area and about 0.6 m/s at a distance 10 cm from the discharge electrode upstream. Such velocities are higher or comparable to that of the main gas flow. Thus, the EHD flow has a momentum high enough to drift ozone molecules against the main gas flow, becoming the dominant factor of ozone molecules transport upstream of the discharge region.

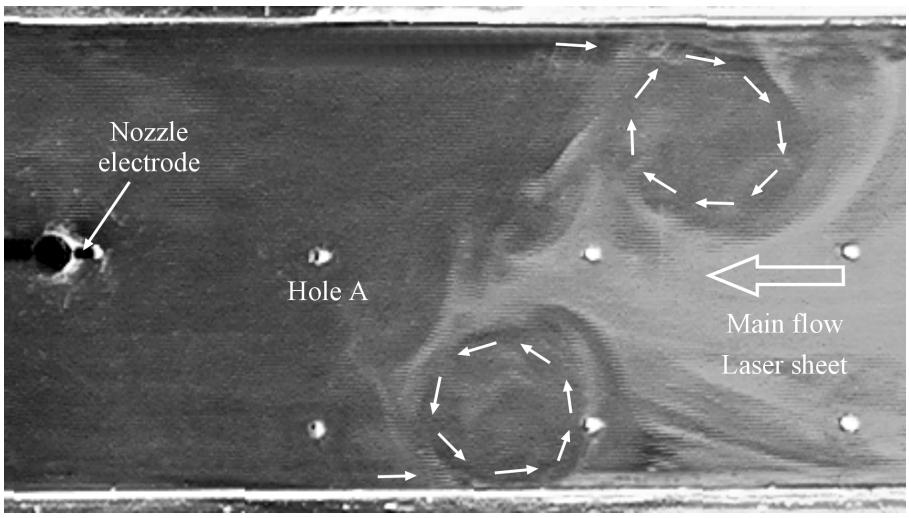


FIGURE 3. Image (side view) of the flow structure in the CDRS reactor when a positive voltage of 28 kV was applied (averaged discharge current - 150 μA). The main gas flow velocity V_m = 0.18 m/s, the additional flow rate Q_a = 0.5 l/min. The distance between the nozzle electrode tip and the hole A is 43 mm. The other holes made in the acrylic side-wall for gas sampling are seen.

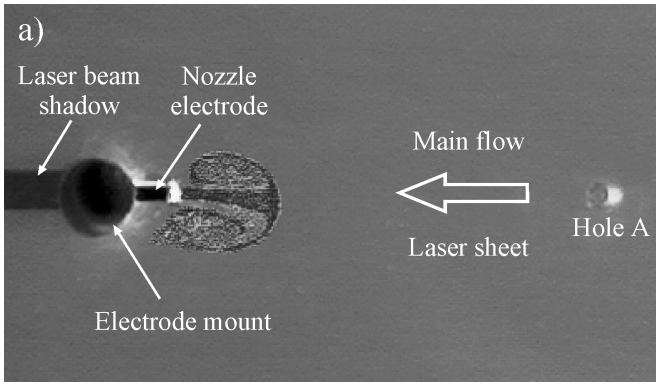


FIGURE 4. Images (side view) of the additional flow structure for additional gas flow rate of Q_a = 0.5 l/min. The main gas flow velocity V_m = 0.18 m/s. No voltage applied. The distance between the nozzle electrode tip and the hole A (made for gas sampling) is 43 mm. The main flow was air (seeded with cigarette smoke) and the additional flow was ambient air (unseeded).

4. DISCUSSION AND CONCLUSIONS

To our knowledge, this investigation showed for the first time that ozone molecules produced by the streamer corona discharge in the CDRS reactor are transported not only in the downstream region, but also in the upstream region of the CDRS reactor. The EHD secondary flow is responsible for the ozone transport upstream of the discharge region. The finding of ozone molecules (and presumably other long-living active species) far outside the discharge region may have an impact on modelling and optimising the chemical kinetics as well as design the non-thermal plasma reactors. The modelling of the chemical kinetics of species in the non-thermal plasma reactor should also comprise the processes outside the discharge region. This may require taking into consideration the gas flow and corresponding transport of the active species, which both have been neglected.

The presence of ozone molecules in the upstream region of the non-thermal plasma reactor, proved in this experiment, helps in elucidating Ohkubo et al. [1] and Kanazawa et al. [2] observation of NO removal in the upstream region of the reactor. At very low main gas velocity as in [1, 2], i.e. 2 mm/s, the concentration of ozone molecules in the upstream region of the reactor can be relatively high. As a result, the NO molecules can to be converted in NO_2 molecules already in the upstream region, showing the significant NO removal before the discharge region. Therefore, the supposition made in [7] that ozone molecules are responsible for NO molecules decomposition in the upstream region of the non-thermal plasma reactor seems to be confirmed in this experiment.

Another conclusion is that the transport of ozone molecules (and presumably other active species) outside the discharge zone can enhance the gaseous pollutant removal in the non-thermal plasma reactors. Hence, apart from the discharge zone also other regions of the reactor can be important for the processing of gaseous pollutants.

ACKNOWLEDGMENTS

This work was supported by the Foundation for Polish Science (Fundacja na Rzecz Nauki Polskiej, subsidy 8/2001), the Institute of Fluid Flow Machinery, Polish Academy of Sciences, Gdańsk (grant IMP PAN O3/Z-3/T2), the State Committee for Research and Development (grant PB 0446/T09/20/19), and the Canadian-Japanese-Polish Scientific Cooperation.

REFERENCES

[1] Ohkubo T., Kanazawa S., Nomoto Y., Mizeraczyk J., Two-dimensional Distribution of NO by LIF Technique in a Corona Radical Shower Reactor During NO_x Removal Processing, In: *35th Annual Meeting – IEEE Industry Applications Society*, Ed.: IEEE Industry Applications Society, Roma, Italy, 2000, vol. 1&2, pp. 864-867

[2] Kanazawa S., Shuto Y., Sato N., Ohkubo T., Nomoto Y., Mizeraczyk J., Chang J.S., *Submitted to the IEEE Transactions on Industrial Applications* (2001)

[3] Loeb L.B., *Electrical Coronas*, Ed. Berkeley C.A., University of California Press, 1965, pp. 402-407

[4] Yamamoto T., Velkoff H.R., *J. Fluid Mech.*, **108**, 1-18 (1981)

[5] Atten P., McCluskey F.M.J., Lahjomri A.C., *IEEE Trans., Indust. Appl.*, **23**, 705-711 (1987)

[6] Mizeraczyk J., Kocik M., Dekowski J., Dors M., Podliński J., Ohkubo T., Kanazawa S., Kawasaki T., *J. Electrostatics*, **51-52**, 272-277 (2001)

[7] Mizeraczyk J., Dekowski J., Podliński J., Dors M., Kocik M., J Mikielewicz., Ohkubo T. , Kanazawa S., *IEEE Trans. on Plasma Science*, **30** (2002)

[8] Gentile A.C., Kushner M.J., *J. Appl. Phys.*, **78**, 2074-2085 (1995)

[9] Lowke J.J., Morrow R., *IEEE Trans. Plasma Sci.*, **23**, 661-671 (1995)

[10] Filimonova E.A., Amirov R.H., Kim H.T., Park I.H., *J. Phys. D: Appl. Phys.*, **33**, 1716–1727 (2000)

[11] Yan K., Yamamoto T., Kanazawa S., Ohkubo T., Nomoto Y., Chang J.S., *J. Electrostatics*, **46**, 207-219 (1999)

[12] Kocik M., Podliński J., Dekowski J., Mizeraczyk J., CuBr Laser in Measurements of Fluids Flow Fields with PIV Method, in: *Proc. SPIE vol. 4238, Laser Technology VI: Applications, Świnoujście, Poland*, Eds.: Wiesław L. Woliński, Zdzisław Jankiewicz, 2000, pp. 246-249

INITIATION PROBABILITY OF BURST PULSES

T. Plank[a], M. Aints and A. Haljaste

Institute of Experimental Physics and Technology, University of Tartu,
Tähe 4, 51010 Tartu, ESTONIA

Abstract: The repetition rate of streamers in conditions of the combined voltage (DC + AC) is recorded for three point electrodes of different diameter depending on the humidity content of clean air. The logarithm of the repetition rate is proportional to the linear combination of fluxes of distinctive ions. The coefficients in that linear combination are proportional to initiation probabilities of burst pulses by those ions.

The ions $O_2^-(H_2O)_x$, where x = 2 ... 5, are taken into account. The initiation probability of burst pulses by the ions $O_2^-(H_2O)_x$ is determined as a function of point diameter.

1. INTRODUCTION

Experimental data about the initiation probability of burst pulses by distinctive ions are very interesting from point of view of modelling positive corona discharges.

The initiation probability $b = p_{det}\, p_{bp}$ of burst pulses is the product of two probabilities: the detachment probability p_{det} of an electron from a negative ion and the probability p_{bp} that the detached electron initiates a burst pulse. In the literature, only the data about detachment lifetime of some ions (O^- [1, 2], O_2^- [1], hydrated ions [3]) can be found. From those data, it is possible to calculate the detachment probability of an electron if the electric field strength and distribution are known.

In the present investigation, the initiation probabilities of burst pulses are determined experimentally for the ions of clean humid air as a function of humidity, for point electrodes of different diameter.

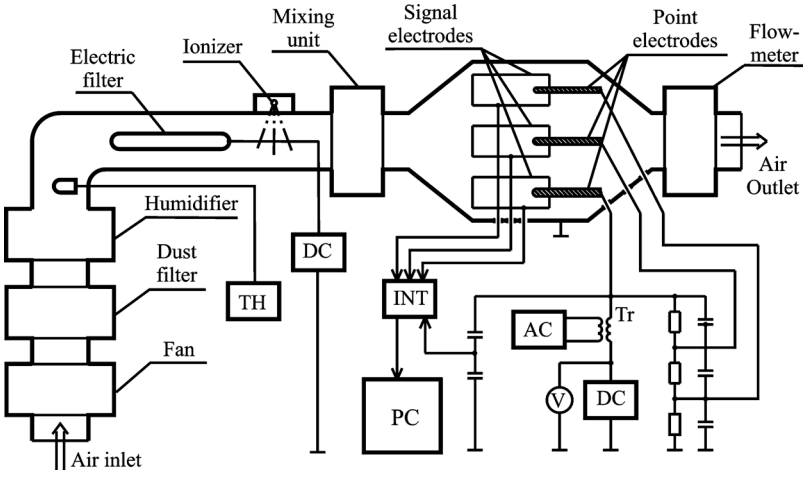


FIGURE 1. Experimental apparatus.

2. EXPERIMENTAL

The sketch of the experimental apparatus is shown in Figure 1.

Our discharge chamber includes three discharge gaps. Each discharge gap has a hemispherically tipped point electrode surrounded by a coaxial cylinder as an opposite electrode. The cylinders serve also as signal electrodes for registration of discharge pulses.

High DC and AC voltages are applied simultaneously to the point electrodes so that the resultant voltage traverses twice the voltage regions of burst pulses, streamers and that of glow corona during each positive half-cycle of the AC voltage. During the

a) Electronic address: tomas@ut.ee

negative half-cycles, there is no discharge in the gaps. The values of DC and AC voltages and onset voltages of different discharge modes for each discharge gap are presented in Table 1. Frequency f of the AC voltage is 1000 Hz.

TABLE 1. Onset voltages.

Gap number	k	1	2	3
Point diameter	d [mm]	0.13	0.25	0.50
Onset voltage of burst pulses	U_{bp} [kV]	2.34	2.91	3.89
Onset voltage of streamers	U_{str} [kV]	2.40	3.01	4.03
Onset voltage of glow	U_g [kV]	2.75	3.31	4.31
Applied DC voltage	U_{DC} [kV]	2.55	3.32	4.53
Applied AC voltage, peak value	U_{AC} [kV]	0.45	0.59	0.92

A PC equipped with a special interface INT records synchronously with the AC cycles the pulses induced by streamers on the signal electrodes.

An air stream enters the device through a dust filter. Thereafter, the desired level of humidity is adjusted by evaporation of distilled water in a humidification unit. A digital thermohygrometer TH measures relative humidity. The subsequent electric filter neutralizes primary air ions. The desired preionization level Φ is adjusted by an α-active ionizer. The age of ions reaching the discharge gaps is approximately 0.1 s. During the experiments, the preionization level was always such that the increase in preionization decreased the rise probability of streamers. Under above conditions, a burst pulse initiated in the voltage interval [U_{bp};U_{str}) transforms into glow corona eliminating streamer formation during this half-cycle.

During the experiments, the number of streamers per AC cycle (formation probability of streamer) was measured depending on the air humidity. The experiments were carried out at the pressure of 1.02×10^5 Pa, at the temperature of 304°K. The airflow rate v = 3.7 m/s.

3. DISCUSSION

3.1. Streamer formation probability

Aints *et al* show in papers [4, 5] that the formation probability of streamer in conditions of combined voltage

$$Q = \exp\left(-\Delta t \Phi \sum_i \varphi_i g_i b_i\right). \quad (1)$$

Here the factor g_i characterizes the possibility that an ion of ith type will reach the birth region of burst pulses and b_i denotes the probability that this ion undergoes detachment and initiates a burst pulse. Under the birth region of burst pulses we mean the space region near the point electrode where the detachment of an electron from a negative ion can initiate a burst pulse [6]. The probability b_i is an average one over the birth region and over the voltage interval [U_{bp};U_{str}). φ_i denotes the fractional flux of ions of a certain nature, the sum of fractional fluxes $\sum_i \varphi_i = 1$. g_i and b_i depend on the electric field distribution, which is different for different gaps. Δt is the time interval during which the combined voltage traverses the interval [U_{bp};U_{str}), and Φ (preionization level) is the ion flux reaching the discharge gaps.

3.2. Ion composition of clean humid air

For the ion composition of clean humid air, we use the model proposed by Allen [7]. Allen's model takes into account the ions $O_2^-(H_2O)_x$. The possible presence of other ions is neglected. According to Allen [7], the stationary number densities of the ions $O_2^-(H_2O)_x$ as a function of air humidity can be calculated from equation:

$$\varphi_i\left(\frac{[H_2O]}{[M]}\right)=\frac{[O_2^-(H_2O)_{i+1}]}{[e]+\sum_x[O_2^-(H_2O)_x]}=\frac{\frac{[O_2]}{[M]}\left(\frac{[H_2O]}{[M]}\right)^{i+1}\exp\left(\frac{1}{kT}\sum_{w=0}^{i+1}\varepsilon_w\right)}{1+\frac{[O_2]}{[M]}\sum_{x=0}^{5}\left(\left(\frac{[H_2O]}{[M]}\right)^{x}\exp\left(\frac{1}{kT}\sum_{w=0}^{x}\varepsilon_w\right)\right)}. \quad (2)$$

TABLE 2. Values of energy ε_x released or absorbed in different conversion reactions [7].

x	Reaction	ε_x /eV/
0	$O_2 + e + M \longleftrightarrow O_2^- + M$	0.22
1	$O_2^- + H_2O + M \longleftrightarrow O_2^-(H_2O) + M$	0.46
2	$O_2^-(H_2O) + H_2O + M \longleftrightarrow O_2^-(H_2O)_2 + M$	0.28
3	$O_2^-(H_2O)_2 + H_2O + M \longleftrightarrow O_2^-(H_2O)_3 + M$	0.18
4	$O_2^-(H_2O)_3 + H_2O + M \longleftrightarrow O_2^-(H_2O)_4 + M$	0.106
5	$O_2^-(H_2O)_4 + H_2O + M \longleftrightarrow O_2^-(H_2O)_5 + M$	0.056

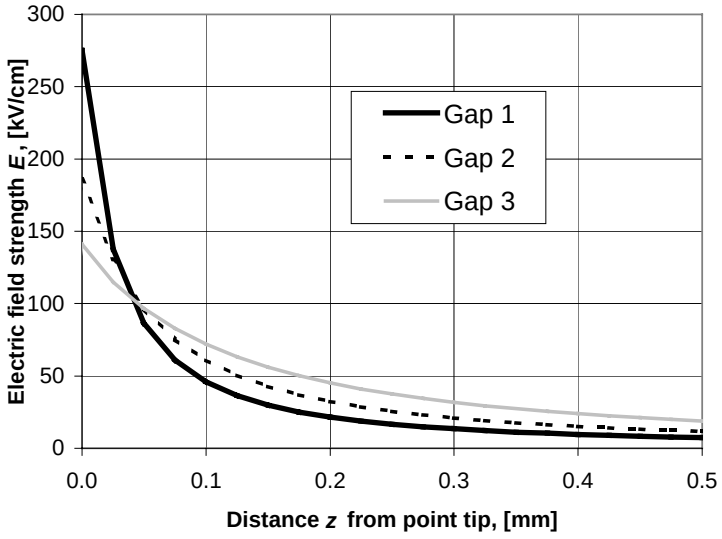


FIGURE 2. The Laplacian electric field strength along the axes of the discharge gaps as a function of distance from the point tip (U_{DC} is indicated in Table 1).

Here $[O_2^-(H_2O)_x]$ denotes the number density of complex ions with x water molecules; $[e]$, $[H_2O]$ and $[O_2]$ are number densities of free electrons, water vapour and oxygen respectively. M is a third body (oxygen or nitrogen molecule) with number density $[M]$. The values of released or absorbed energy ε_x for some reactions are given in Table 2.

In the range of air humidity used in our experiments, the ions $O_2^-(H_2O)_x$ with x = 2 ... 5 have to be taken into account because number densities of ions with $x < 2$ and $x > 5$ are too small.

3.3. Electric field strength in our discharge gaps

We calculated numerically the distribution of the Laplacian electric field strength $E(r, z)$ in our discharge gaps [8]. Here r and z denote the radial and axial co-ordinates, respectively. The Laplacian electric field strength along the axes of our discharge gaps is presented in Figure 2.

The space charge of positive ions from the previous discharge is removed before the beginning of the new AC cycle under our experimental conditions.

3.4. Trajectories of ions

We evaluate the motion of ions as a resultant drift caused by both the air flux and the electric field. The air flux is taken into account as an additional electric field $\vec{E}_{flow}(r) = \vec{v}(r)/\mu$, where $\vec{v}(r)$ is the vector of the airflow velocity, and μ is the mobility of ions. The airflow profile inside the signal electrode is calculated according to the empirical power-law equation $v(r) = v(0)\,(1\text{-}r/R_0)^{1/1.66\,\log(Re)}$, where R_0 is the coordinate of the wall of the signal electrode and Re is the Reynolds number [9].

The mobility μ of cluster ions under standard conditions we calculate according to the empirical

formula [10] $$\mu \approx \left(\sqrt[3]{\frac{1200u}{M}} - 0.2 \right) \left[10^{-4}\,\mathrm{m^2 V^{-1} s^{-1}} \right], \qquad (3)$$

where u is the unified atomic mass unit and M denotes the ion mass.

The outermost trajectories of those ions, which reach the border of the birth region of burst pulses, are indicated in Figure 3.

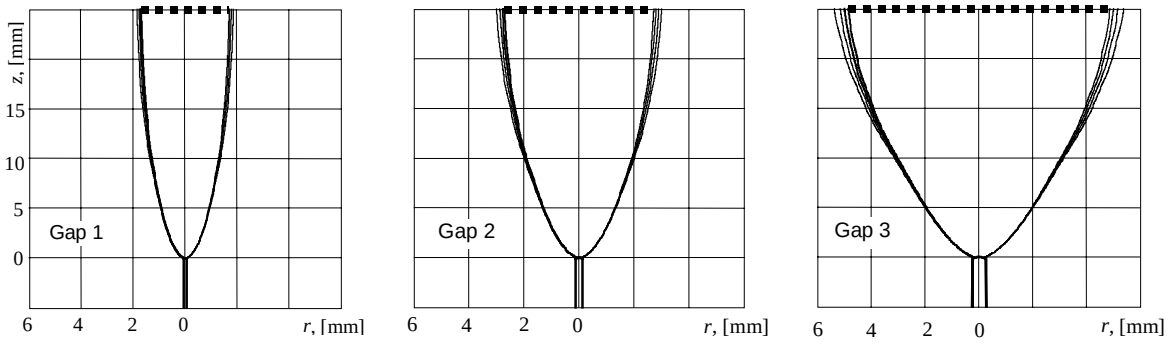


FIGURE 3. The outermost trajectories of $O_2^-(H_2O)_x$ ions, which reach the border of the birth region of burst pulses.

Coefficients g_i are determined as ratio of cross section area surrounded by trajectories (indicated by heavy dashed lines in Figure 3) to the cross section area of the signal electrode. Coefficients g_i depend strongly on point electrode diameter but are close to each other for different ion species in the case of given point electrode. Below we take g_i constant for given point electrode.

3.5. Initiation probability of burst pulses

Using the curve fitting method, we have found the coefficients b_i such that curves $f(h) = \sum_i b_i \varphi_i(h)$ with φ_i given by equation (2) fit experimental points on $-(\Delta t\, g\, \Phi)^{-1}\ln(Q(h))$ versus h plots for all three gaps (see Figure 4). The obtained values of b for above ions are presented in Figure 5.

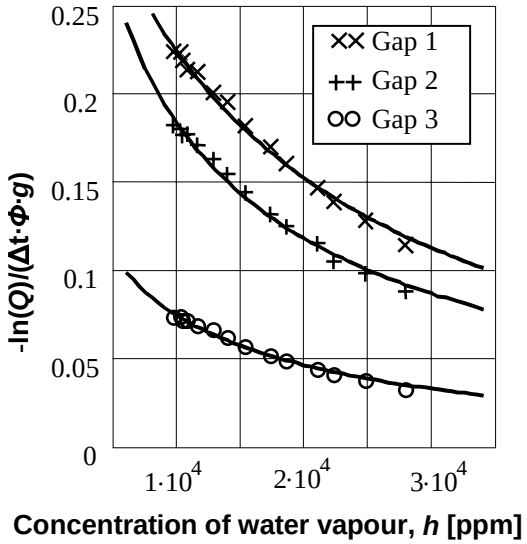


FIGURE 4. Dependence of burst pulse initiation probability of "an average air ion" on the fractional concentration of water vapour C_{H2O}.

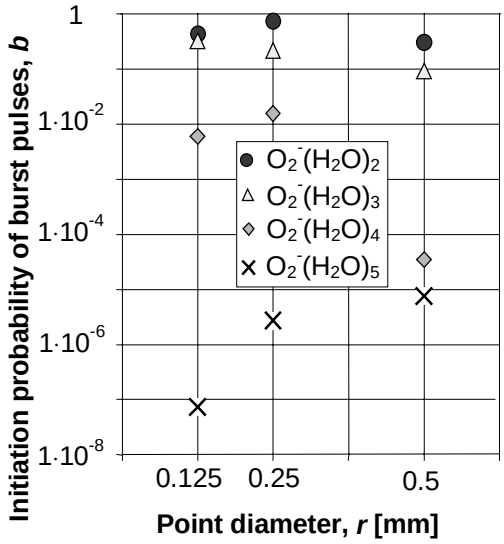


FIGURE 5. Initiation probability of burst pulses as a function of point diameter for different ion species.

4. MAIN RESULTS

The initiation probability of burst pulse by "an average air ion" is determined for three point electrodes as a function of air humidity (see Figure 4).

Assuming the ion composition of clean humid air being in accordance with Allen's model [7], the burst pulse initiation probability by $O_2^-(H_2O)_x$ ions is determined (see Figure 5).

REFERENCES

[1] Badaloni S., and Gallimberti I., *Basic data of air discharges. UPee–72/05*, Padova University, 1972, 91 p.

[2] Frommhold L., Über verzögerte elektronen in Elektronenlawinen, insbesondere in Sauerstoff und Luft, durch Bildung und Zerfall negativer Ionen (O^-). *Fortsh. der Physic*, **12**, 597-643 (1964)

[3] Gallimberti I., The mechanism of the long spark formation. *J. Physique*, **40**, C7 193-250 (1979)

[4] Aints M., Haljaste A., Kudu K., and Plank T., Corona based detector of electronegative trace gases. *Meas. Sci. Technol.*, **12**, 557-65 (2001)

[5] Plank T., Aints M., Haljaste A., and Kudu K., Corona discharge at combined voltage as a detector of trace gases. *EFS aastaraamat 2000* **XI** 40-50 (in Estonian) (2001)

[6] Plank T., Haljaste A., and Aints M., The after-effect of streamers of positive corona under combined voltage. *J. Phys. D: Appl. Phys*., **33**, 2791-7 (2000)

[7] Allen N. L., The effect of humidity on positive corona discharges in air. In: *Proc. 17th Int. Conf. Phen. Ionized Gases*, Invited Papers, Budapest, 1985, pp. 62-72

[8] Plank T., Positive corona at combined DC and AC voltage. PhD thesis, Tartu University, 2001, 163 p. http://www.physic.ut.ee/~tomas/phd_plank.pdf

[9] Miller R. W., *Flow Measurement Engineering Handbook.* 2nd edn., New York: McGraw-Hill, 1989, 1073 p.

[10] Tammet H., Reduction of air ion mobility to standard conditions. *J. Geophys. Res.*, **103**, 13 933-7 (1998)

DUSTY RF DISCHARGES

Yu. I. Chutov[a], W. J. Goedheer[b], O.Yu. Kravchenko, O.A. Lavrov, T.E. Lisitchenko, G.I. Protas

a) Taras Shevchenko Kiev University, Volodymyrs'ka 64, 01017 Kiev-17, Ukraine
b) FOM-Institute for Plasma Physics "Rijnhuizen", Edisonbaan 143439 MN Nieuwegein, The Netherlands

Abstract. One-dimensional dusty RF discharges between two plane electrodes in argon are investigated by PIC/MC simulation. Immobile dust particles of given size and density are distributed uniformly in the interelectrode gap. Spatial distributions of discharge parameters across the interelectrode gap were simulated at various densities of dust particles. Obtained results show that dusty RF discharges have non-uniform quasi-neutral central parts with low electric fields and non-stationary sheaths with strong electric fields separating the electrodes from the central parts. The dust particles essentially influence the spatial distribution of the discharge parameters, in particular an increase of a dust particle density causes an expansion of sheaths. Simulations show that electron energy distribution functions time-averaged in various points of the non-uniform quasi-neutral central parts of the RF discharges are depended on the argon pressure. At the low pressure, the functions coincide practically in the high-energy region due to a free mixing of fast electrons in the almost equipotential center region that causes non-trivial non-monotonic spatial distributions of the dust particle charge.

1. INTRODUCTION

Radio frequency (RF) discharges are very intensively investigated due to their wide application in many areas [1] including the microelectronic industry where RF discharges are used usually as sources of reactive species for plasma etching or deposition. High rates, good selectivities, and highly anisotropic profiles favor the RF plasma etching or deposition above wet methods. Argon is the dominant component in many process mixtures and therefore discharge properties is determined usually by this species [2]. The RF discharges with the argon component can be used also in analytical chemistry as a spectroscopic source for analysis of solid materials sputtered by the discharge [3].

Investigations of RF discharges shown that an interelectrode gap of the discharges is non-uniform and can be divided into two main parts, namely: the quasi-neutral central part conserved in time and non-neutral RF sheaths adjacent to electrodes and divided the electrodes from quasi-neutral plasma in the central part. The RF sheaths are very important for plasma processing because they determinate the energy distribution function of ions reaching electrodes [4] and therefore the sheaths were investigated in many works.

The RF discharges can contain dust particles, which can appear here due to an interaction of the plasma with the electrodes [4,5] or can be immersed from outside [6-9]. Dust particles can be levitated close to a RF sheath edge because the gravitational force acting on dust particles can be compensated here by a the force of the mean electric field. Of course, the dust particles can essentially influence on parameters of the RF discharges due to a collection of background electrons and ions like to the influence on the DC discharge [10] or on the pulsing barrier discharge [11].

Therefore, detailed investigations of RF discharges with dust particles including their computer simulations are very actual for understanding of the influence of dust particles on the discharges. The aim of this work is 1D-computer simulations of RF discharges in argon with dust particles, which can be considered as a physical model of processing plasmas

[a] Electronic address: yuch@mail.univ.kiev.ua

2. MODEL

It is simulated a one-dimensional RF discharge between two plane electrodes separated by a gap of $d = 2.7\ cm$ filled with *Ar* at a pressure of *0.1 Torr*. Immobile dust particles of $1\ \mu m$ radius are distributed uniformly in the interelectrode gap with a density N_d. The uniform spatial distributions of dust particles allow us better estimate their role in various regions of the RF discharge. The dust particles collect and scatter electrons and ions distributed in the discharge with a (non-uniform) density n_e and n_i, respectively. A harmonic external voltage $V_e(t)=V_o sin(\omega t)$ at a frequency $f=13{,}56\ MHz$ with an amplitude $V_o=350\ V$ sustains the RF discharge. The electrode at $x=d$ is grounded.

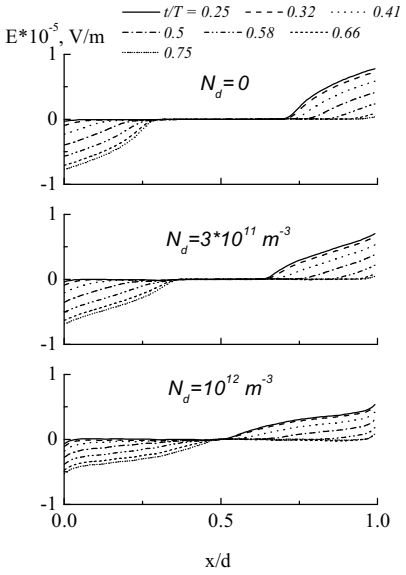


FIGURE 1. Spatial distributions of the electric field *E*.

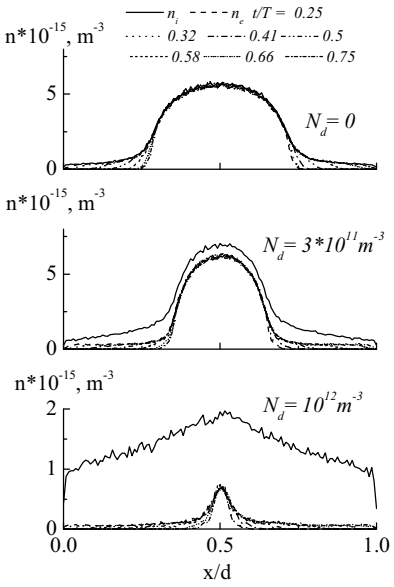


FIGURE 2. Spatial distributions of the electron n_e and ion n_i densities.

The PIC/MC method described in detail in [13] for discharges without dust particles is extended for computer simulations of the RF discharge with dust particles. The self-consistent electric field E is obtained by solving Poisson's equation using a computational grid, which is introduced by a uniform division of the interelectrode gap into 128 simulation cells. An electrode collects a " superparticle" if its center reaches the electrode surface. Each superparticle represents $8*10^7$ real electrons or ions. The size of the electrodes, needed to compute the total current, is 0.04 m^2.

The Monte Carlo technique [13] is used to describe electron and ion collisions. The collisions include elastic collisions of electrons and ions with atoms, ionization and excitation of atoms by electrons, charge exchange between ions and atoms, Coulomb collisions of electrons and ions with dust particles, as well as the electron and ion collection by dust particles. The electron-argon collision cross-sections used in the model are the same as those used in [14]. The Coulomb cross-section σ for electron and ion scattering by immobile dust particles is taken from [15]. The cross-section for collection of an electron or ion by a dust particle is taken from [16].

The simulation starts with an initial uniform distribution of electrons and ions with densities equal to $10^{15}\ m^{-3}$ and is prolonged by iterations up to a moment when the change of the discharge parameters is less than *0.1 %*. Simulations show that 400 cycles are enough to obtain the periodic steady state.

3. RESULTS

Obtained spatial distributions of the electric field E across the interelectrode gap of the RF discharge are shown in Fig. 1 for various densities N_d of dust particles for various phases t/T of the sustaining external voltage where T is the RF period. The distributions show the existence of the central quasi-neutral region and non-neutral RF sheaths close to both electrodes. The quasi-neutral part of the interelectrode gap corresponds here to $E=0$ so that the sheath edge is a point between this region and the region with $E \neq 0$. The sheath edge, which corresponds to the boundary between the charged sheath and the quasi-neutral presheath, shifts to or from electrodes depending on the phase of the sustaining external voltage. As can be seen in the Fig. 1, the sheath edge approaches the grounded electrode and is moving away from the opposite electrode between phases $\pi/2$ and $3\pi/2$ of the sustaining external voltage. Note that the size of the central quasi-neutral part is decreased with the increase of the dust particle density N_d. This is caused by the influence of dust particles on the RF sheath size. Indeed, the sheath size is determined by a condition that an applied voltage is compensated by the total space sheath charge. As can be seen later (Fig. 3), immobile dust particles have a negative charge and therefore compensate partially the ion screening of the sustained voltage in the sheath and consequently increase the RF sheath size at the same voltage.

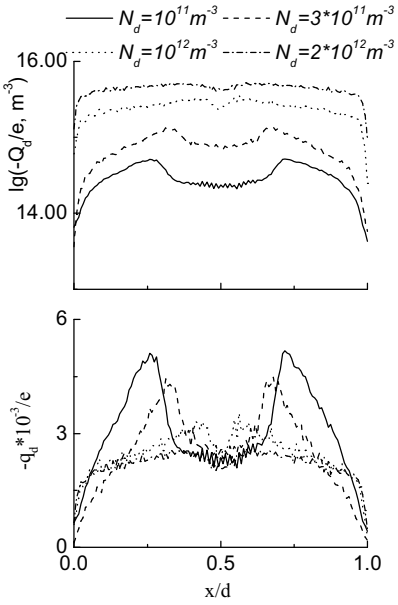


FIGURE 3. Spatial distributions of the total electric charge density Q_d of dust particles and the dust particle charge q_d.

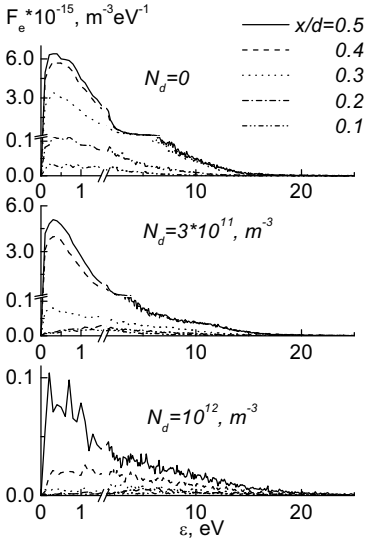


FIGURE 4 Averaged electron energy distribution functions F_e

Spatial distributions of the electron (n_e) and ion (n_i) density across the interelectrode gap are shown in Fig. 2 for conditions of Fig.1. As can be seen in Fig.2, there are stationary spatial distributions of the ion density n_i and changing spatial distributions of the electron density n_e because the sustained voltage frequency by far exceeds the ion plasma frequency and is comparable to or less than the electron plasma frequency. Note that the electron density decreases smoothly in the RF sheath, unlike the stepwise drop in the front model [17], because the Debye length is not negligable compared to the sheath size in our case.

As can be seen in Fig. 2, dust particles essentially change the spatial distributions of the electron and ion densities. First of all, a difference between these densities appears in the central part of the RF discharge with dust particles. The difference increases with an increase of the dust particle density so that the ion density by far exceeds the electron density at large densities of dust particles. The indicated difference is caused by the negative total electric charge Q_d of dust particles of which spatial

distributions are shown in the upper part of Fig. 3 for various values of N_d.

Note the non-monotonic spatial distributions of the dust particle charge q_d shown in the bottom part of Fig. 3. As can be seen here, the charge q_d in the quasi-neutral central part of the RF discharge is equal to about $2.5*10^3 e$, corresponding to a surface potential of $3.6\ eV$. The charge q_d increases towards the sheaths and then decreases in the sheaths. As a result, the charge q_d has a maximum close to the sheath edge. This maximum shifts together with the sheath edge when the dust particle density N_d changes.

The complex spatial distribution of the dust particle charge is caused by the balance of the electron and ion charging currents onto a dust particle, as usually. In our case of a non-uniform plasma with negatively charged dust particles, the ion charging current is proportional to the ion density and therefore has to decrease monotonically from the center of the interelectrode gap towards the electrodes due to the monotonic decrease of the ion density shown in Fig. 2. The electron charging current depends on the surface potential of the dust particles and the time-averaged energy distribution function F_e shown in Fig. 4 for the cases of Fig. 1. Note that the distribution functions F_e practically coincide in the energy region $\varepsilon > 3\ eV$ in the quasi-neutral central region of the interelectrode gap, due to a free mixing of fast electrons in this almost equipotential region. Therefore, the electron charging current onto a dust particle is almost the same for various points in the central region. The constant electron charging current and the decrease of the ion charging current cause the increase of the dust particle charge $|q_d|$, when moving outward from the center (Fig. 4).

Another situation prevails in the sheaths where a free mixing of electrons is not possible due to the strong voltage drop in sheaths (Fig. 1). Therefore the number of fast electrons is not constant in various sheath points (Fig. 4) decreasing towards electrodes so that the electron charging current decreases also. Obtained results show that the ratio of the time-averaged electron density $<n_e>$ to the constant ion density n_i decreases in the sheaths towards electrodes. This results in a decreasing dust particle charge q_d towards the electrodes, creating a maximum close to the sheath edge (figure 4).

4. CONCLUSION

Self-consistent 1D PIC/MC simulations of a RF discharge in argon with dust particles distributed uniformly in the interelectrode gap show that the dust particles essentially influence the spatial distribution of the discharge parameters. An increase of the dust particle density causes an expansion of sheaths.

The dust particle charge varies non-monotonously across the interelectrode gap and has maximum close to a sheath edge, due to the spatial distribution of the plasma parameters and free maxing of the energetic electrons in the quasi-neutral central part of the RF discharge.

ACKNOWLEDGMENTS

This work was partially supported by INTAS and by a grant from the Ukrainian Committee of Science and Technology.

REFERENCES

[1] Lieberman M.A., Lichtenberg A.J. *Principles of Plasma Discharges and Material Processing* (Wiley, New York, 1994)
[2] Moisan M. *et al*., *J. Vac. Sci. Technol.,. B* **9,** 8-12 (1991)
[3] Bogaerts A., Yan M., Gijbels R., Goedheer W., *J. Appl. Phys*. **86**, 2990-3001 (1999).
[4] Kawamura E., Vahedi V., Lieberman M.A., Birdsall C.K. *Plasma Sources Sci. Technol*., **8** R45-64 (1999)
[5] Tomme E. B., Annaratone B. M., Allen J E., *Plasma Sources Sci. Technol*., **9**, 87-96 (2000)
[6] Nunomura S., Samsonov D., Goree J. et al., *PRL*, **84,** 5141-4 (2000)
[7] Hayashi Y., Sawai A., In: *Frontiers in Dusty Plasmas,* ed by Y.Nakamura, T.Yakota, P.K.Shukla, ELSEVIER, 2000, pp. 83-90.
[8] Lin I. Lai Y.-J., Juan W.-T., Chen M.-H., In: *Frontiers in Dusty Plasmas,* ed by Y.Nakamura, T.Yakota, P.K.Shukla, ELSEVIER, 2000, pp. 75-82.

[9] Schabel M. Peterson T., Sinclair J., *J. Appl. Phys*. **86**, 1834-42 (1999).
[10] Boeuf J.P. *Phys. Rev. A* **46**, 7910-22 (1992)
[11] Chutov, Yu. I., Kravchenko, O. Yu., Pikozh V.V., Zuz V.M. *Ukrainian J. Phys,*. **42,** 1003-6 (1997)
[13] Birdsall C.K., *IEEE Trans. Plasma Sci*.,.**19,** 65-85 (1991)
[14] Surendra M., Graves D.B., Jellum G.M., *Phys. Rev. A* **41,** 1012-7 (1990)
[15] Trubnikov B.A., In: *Problems of plasma theory,* Gosatomizdat, Moscow, 1963, pp. 122-37
[16] Allen J., *Phys. Scr*., **45,** 497-503 (1992)
[17] Sobolewski M. A., *Phys. Rev. E* **59**, 1057-72 (1999)

STATISTICAL PROPERTIES OF ELECTRIC BREAKDOWNS BETWEEN GLASS SURFACES IN INERT GASES AND THEIR MIXTURES

M. S. Baranchuk, T. E. Lisitchenko[a], M. M. Okholin

Taras Shevchenko Kiev University, Volodymyrs'ka 64, 01017 Kiev-17, Ukraine

Abstract. In this work, an influence of a surface charge on statistical properties of the breakdown is investigated experimentally. Experiments are carried out in glass cells filled with argon or neon and their mixtures. The pulsing discharge with current impulses of the different polarity is created in the cells the meander voltage of the frequency of 100 kHz and the amplitude of 1200V. The gas breakdown takes place in some time delay measured automatically 200 times taking into account the statistical character of the breakdown. The mean statistical delay time τ is calculated from the experimental results by using the standard statistical method. The number of electrons N initiating the breakdown and the corresponding current j of the electrons are determined from the delay time τ.

1. INTRODUCTION

It is well known that a gas breakdown between dielectric surfaces delays with respect to a voltage appliance to electrodes. The breakdown delay time is of a statistical nature and depends on many factors including the amplitude of an applied voltage, the external illumination, the condition on a dielectric surface, and other ones. The investigation of these statistical properties in a dielectric cell without the deposited charges was carried out before in [1]. There are some data on the investigation of the breakdown properties for the charge that was deposited on a glass surface [2]. However these data did not take into consideration the influence of the external illumination on the electron current initiating the electric breakdown by the photoemission [3]. In this paper we have analysed the influence of the electric charge which was deposited onto the glass surfaces on the breakdown statistical properties in absence of the external illumination. The last feature took away the influence of the photoemission on the breakdown characteristics.

2. EXPERIMENTAL METHOD

The experiments were carried out in Argon, Neon, and the Neon-Argon mixture at 15 mm Hg pressure in a plane glass cell of 60 mm diameter and with 5.0 mm separation between the glass surfaces. The external sites of the cell glasses having 5.0-mm thickness each were tightly fitted with the external copper electrodes of 45-50 mm diameter. The last ones were supplied with the voltage from a special generator with the pulsing voltage of the ′meander′ type with 100 kHz frequency and up to 1200 v amplitude. A pulsing discharge was excited between the glass surfaces with the current pulses of different polarities which were running at the moments of polarity changing of the supplied voltage. While each current pulse was running, the charge in the external circuit was being carried over and at any moment it could be measured by the current integrator. According to an equivalent circuit of the pulsing discharge in a dielectric cell [4] this discharge current is uniquely connected with an electric charge that is deposited onto the internal cell walls during the single current pulse. At some point of time when the cell electrodes were supplied by the voltage equated to the maximum meander amplitude, that meander ceased and the charge Q was left on the dielectric surface. The magnitude of

[a] Electronic address: tel@mail.univ.kiev.ua

that charge was measured by the current integrator. After some delay period t_V (*0.1...5.0 s*) the probing pulse of the specified amplitude was applied onto the cell and the discharge time delay was measured. The performance of the measurements and experimental data processing were accomplished by a personal computer.

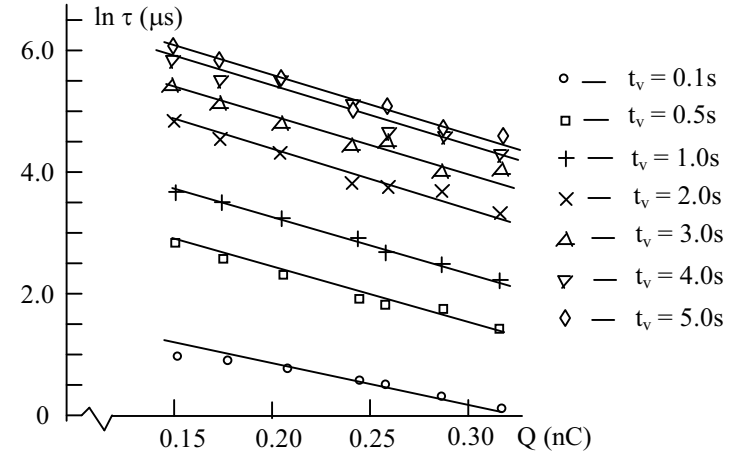


FIGURE 1.

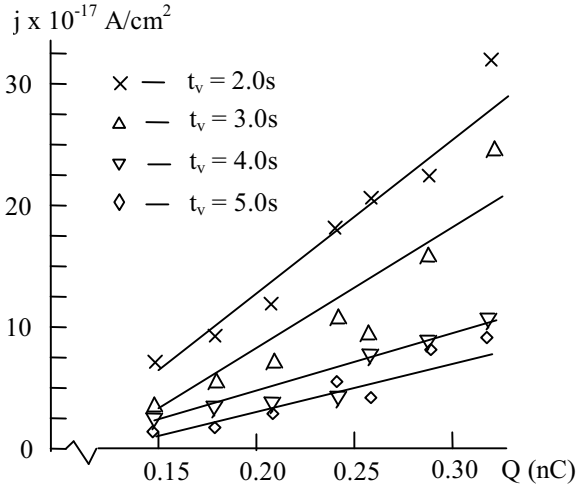


FIGURE 2.

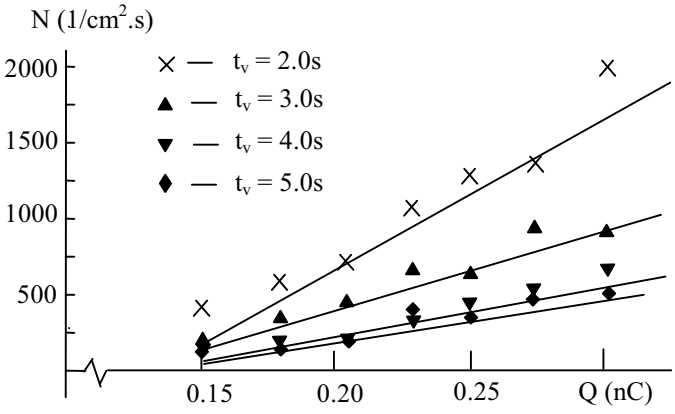


FIGURE 3

3. RESULTS

The measuring results of the mean statistical time τ of the discharge delay in Argon depending on the magnitude of the charge Q deposited on the glass surface are shown in figure 1. The parametric dependence is expressed by the delay of the probing pulse t_V with the amplitude of U=750 v. It is obvious that the charge increase on the glass surface taking place at the breakdown or the pulse delay time t_V decrease results in the practically linear decrease of τ . For the given values of the deposited charge Q and pulse delay time t_V the parameter τ was varying in 1.0 – 430 μs range. That corresponds to changing the current density j of the initiating electrons from the $8*10^{-15}$ to $2*10^{-17}$ A/cm^2 values. These functional relationships are shown in figure 2.

In terms of our experiments in the Ar agent, the number of electrons N which had been initiating the breakdown was found to be in the 120…50.000 $^{L}/cm^2.s$ range. Such data for some t_V at U_1=750 v versus Q are given in figure 3.

The pulsing discharge in the Ar agent distinctly differs by it parameters from that one in the Ne agent or the Ne-Ar mixture. In Argon this discharge was initiated in the under-test dielectric cell at 970 v and went out at 900 v. So the bistability may range 70 v. As this takes process, the discharge current pulses have the width of about 1.5 μ s at the half-height level with a short pulse front and several times slower pulse droop. In Neon or in the gas mixture the discharge was ignited at the lower voltages (770 v in the cell under consideration); the discharge current pulses were 5-10 times smaller in the amplitude and several times longer at

the half-height level. The bistability range comprised about 30 v. The mean statistical time of the breakdown delay was about 90-100 times more and N was respectively less. The number of electrons initiating the breakdown comprised only 2-3 $^{L}/cm^2.s$ at the small deposited charges (Q=0.1 nC) and the large delays of the probing pulse (t_V=5.0 s). It clearly follows from the functional relations given in figure 4.

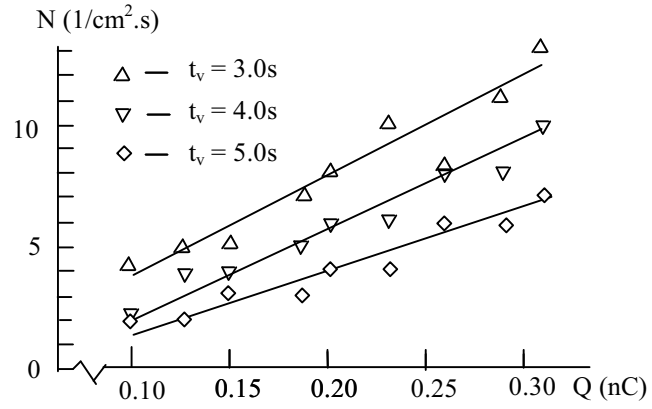


FIGURE 4.

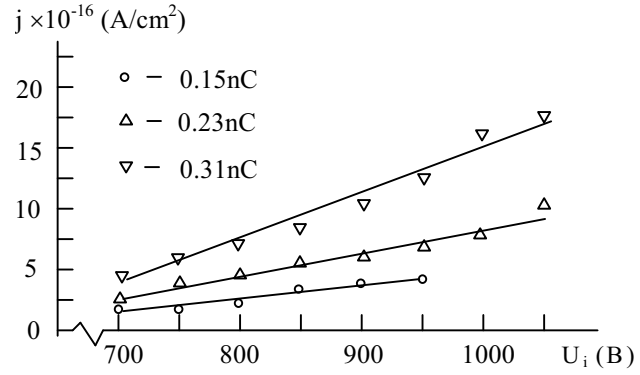


FIGURE 5

In figre 5 the j-dependence of the probing pulse amplitude U is given for the discharge in Argon. Data were obtained at t_V=1.0 s.

As these data indicate, the current density j increases arcwise with increasing of the probing pulse amplitude U in spite of the fact that the amplitude value U goes well beyond the bistability range both to the direction of smaller and larger voltages. The same measures for the Ne+1%Ar mixture under the equivalent test conditions showed that the current density j did not depend on U and was equal to $j=4.0*10^{-13}A/cm^2$.

Of some interest is the change character of the current density j of the initiating electrons relatively the delay time t_V of the probing pulse. The appropriate results for the mixture Ne+1%Ar at the probing pulse amplitude U=750 v are shown in figure 6.

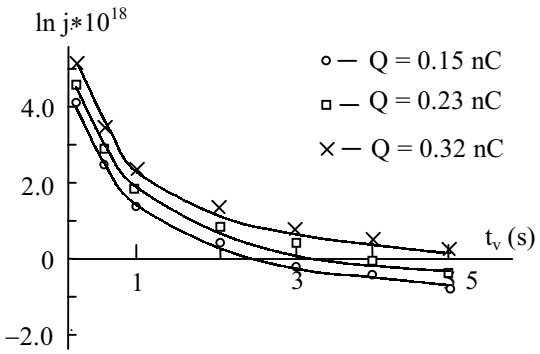


FIGURE 6.

It is obvious that j noticeably decreases for the first two seconds after the charge deposition on the glass surface. Hereafter such decrease noticeably decelerates and comes onto some fixed value with the specified amplitude of the probing pulse. The same character of changing j with time is watched for the pure Neon and Argon gases. These data are well matched in a qualitative sense with the response of the photoemission current density [3] on the probing pulse delay.

ACKNOWLEDGMENTS

This work was partially supported by a grant from the Ukrainian Ministry of Education and Science.

REFERENCES

[1] Baranchuk N.S., Chutov Yu.I., *Pis'ma JTF*, **1,** 238-242 (1975) (in Russian)

[2] Baranchuk N.S., Chutov Yu.I., The investigation of statistical properties of an electric gas breakdown between glass surfaces in rare gases mixtures. In: *Proc. 6th Union Conf. on Low Temperature Plasma Physic,* Leningrad, 1983, pp. 170-172 (in Russian)
[3] Baranchuk N.S., Chutov Yu.I., Hayoshi R., Artemov A.A., Nekhaj V.G., Ukrainian J. Physics, **37,** 1042-1045 (1992) (in Russian)
[4] Baranchuk N.S., Chutov Yu.I., Losovich M.R., Danilov V.G. *J. Techn. Phys.*, **44,** 355-362 (1974)

TOPIC 2:

Modeling and diagnostics

3-DIMENSIONAL MODEL FOR TRICHEL PULSES: RESULTS OF NUMERICAL STUDIES FOR AIR

Yu. S. Akishev, I. V. Kochetov, A. I. Loboiko, A. P. Napartovich[1]

State Science Center Troitsk Institute for Innovation and Fusion Research
142190 Troitsk, Moscow region, Russia

Abstract. It is known that an electric current in a negative corona for pin-to-plane configuration in a wide range of parameters has a form of periodic peaks, which are called Trichel pulses. Recently, authors reported about development of 3-D axially symmetric model intended for numerical simulations of Trichel pulses. In this paper authors present results of numerical simulations of a long train of pulses for pin with hemi-spherical cap to plane anode configuration in ambient air at atmospheric pressure. These calculations provide information about dynamics of Trichel pulse starting from step-wise voltage applying. Calculations clearly demonstrate that regular current oscillations are established after 4-5 pulses. Space-time evolution of electric field and charged species densities within one cycle of regular oscillations is described in detail. In particular, distributions of specific components of current density over the cathode and anode surfaces were found in dependence on time. Comparison is made with experimentally available data. In contrast to simplified 1.5-D model predicting two-peak shape of Trichel pulse, the exact 3-D model predicts single-peaked pulses when ion induced secondary emission processes are included, and photo-emission is neglected. On the anode surface, radial profiles of electric field and ion and electron current components were calculated. Variations of individual current pulse amplitude and shape with discharge voltage growth are studied, too.

1. INTRODUCTION

Since 1938 when G. W. Trichel [1] reported about observation of auto-pulsing mode in the negative corona in air, investigations into properties of pulses generated spontaneously continue for long time but not too intensively. Among attempts to give theoretical explanation for discussed phenomena the work of R. Morrow is most known [2], where the preceding theories are reviewed also. Continuity equations for electrons and positive and negative ions in a one-dimensional form were numerically solved together with the Poisson's equation computed by the method of disks. It was supposed that the electric charges occupy the cylinder of a given radius. One of electrodes, cathode, was spherical. The negative corona in oxygen at a pressure 50 Torr was numerically simulated. Only the first pulse was computed, and extension of calculations on longer time showed only continuing decay of the current. In Ref. 2 the shape of the pulse was explained while practically ignoring the ion-secondary electron emission. In the following paper [3] the step on the leading edge of the pulse was attributed to the input of the photon secondary emission, and the main peak was explained in terms of the ion-secondary emission. Present authors formulated a so-called 1.5-D model of the point-to-plane negative corona in air [4], reproducing, for the first time, in calculations periodical Trichel pulses. Predictions within 1.5-D model were in good agreement with experiments and allow for achieving some insight into the origin of the pulse mode. In particular, a two-peak shape of the pulse was associated with formation of a cathode-directed ionization wave in the vicinity of the point. However, to derive equations of this 1.5 model it was necessary to make some assumptions, the validity of which cannot be proved within the formulated theory. Moreover, most probably these assumptions (preservation of the current channel shape in time; slow variation of the current cross section area in space) are strictly false, and one could only rely on anticipated secondary role of these effects in formation of Trichel pulses. Evidently, more accurate modeling of Trichel pulses requires that 3-D model be developed.

[1] Electronic address: apn@triniti.ru

Taking into account the circular symmetry of the corona geometry, it is sufficient to make a model in two spatial variables: a distance along the discharge axis, *x*, and a radius, *r*. Such a model was developed earlier by authors [5]. However, because of complexity of computations only two first pulses were computed, and it was not clear whether regular pulses could establish. This paper reports results of comprehensive studies on Trichel pulses dynamics in ambient air for point-to-plane configuration with spacing 7 mm.

2. NUMERICAL MODEL

Transport equations for electrons, positive and negative ions (each of one sort) in combination with Poisson equation were solved in time and space. Ion diffusion was neglected, and transverse electron diffusion only was included in the equations. Electron kinetic and transport coefficients entered into equations were calculated separately from solution of the electron Boltzmann equation in two-term steady-state approximation. The current in the external circuit, *I*, is determined from the equation

$$V = U_0 - RI,$$

where V and U_0 are the discharge and power supply voltage, R is the ballast resistor. The continuity equations should be accomplished by boundary conditions. The boundary conditions for positive and negative ions are self-evident: their number density is equal to zero at anode and cathode, respectively. For electrons we, in contrast to R. Morrow [2, 3], include only the ion secondary emission with coefficient $\gamma = 0.01$.

The shape of the cathode may vary from one experiment to another. Here we, for certainty, take the cathode configuration used in many experiments: a cylinder with a spherical cap of the same radius. All calculations were made for the cap radius 0.06 mm. To limit the computational region, the additional dielectric boundary in a form of a piece of a sphere was placed closing the discharge volume. Distance between a cathode tip and an anode was taken equal to 7 mm.

Fig. 1 illustrates the discharge geometry under studies with a numerical mesh covering non-uniformly the computational region. Near the pin with the radius 0.06 mm spatial variations of the electric field and electron and ion number densities are much more rapid than far from the needle. Therefore, the mesh cell size near the cathode is very small to provide the necessary accuracy of calculations. Special measures were taken to generate the near-orthogonal mesh to reduce the errors of discretization. The problem of differential equations discretization is an important issue but goes beyond this paper frames, and is not discussed. The listed above equations were solved in space and time giving evolution of negative corona structure from a moment of step-wise applied voltage with magnitude 4.2 kV. Total number of numerical cells was equal to $n_x \times n_y = 102 \times 151$. Time step was variable changing from 0.01 to 0.1 ns in dependence on maximum over space rate of variation of charged species concentration. Computing one period takes about 36 hours of continuous operation of Pentium III-733 computer.

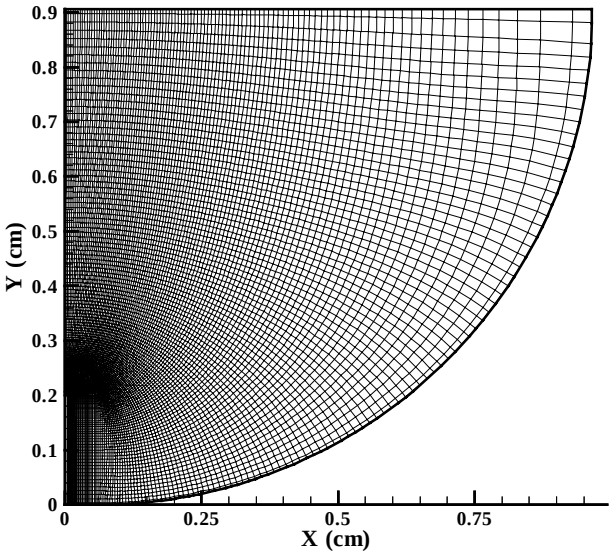


FIGURE 1. General view of the computational region and numerical grid, the minimum cell size in the cathode vicinity is 6 10^{-5} cm

3. RESULTS OF CALCULATIONS

Evolution of calculated current is shown in Fig. 2 in logarithmic scale starting from the moment of applied voltage step to more than 60 μs. The first pulse is much stronger (about 10 mA in height). The second pulse is minimum in height, and peak magnitude is established after 4 pulses. The minimum current between pulses monotonically decreases approaching steady state after about 12 pulses. Pulse repetition frequency diminishes monotonically and approaches a constant value at about pulse number 25. As a result, the average corona current is established rather late, after running of 25 pulses. Comparison with the experiment demonstrated good agreement in average current value, but the pulse period computed is shorter 2.5 times than the experimental one. This difference can be explained by taking the anode size in calculations (0.9 cm) smaller than the radius of current localization at the anode (1.2 cm). In an attempt to find compromise between accuracy of calculations (the required number of numerical mesh cells grows with anode size) and time of computing for achieving steady state, which is rather long, we restricted the computation region by a smaller radius. Experimental data for the anode with restricted area showed, in agreement with theoretical predictions, that pulse repetition frequency grows remarkably with diminishing the anode size.

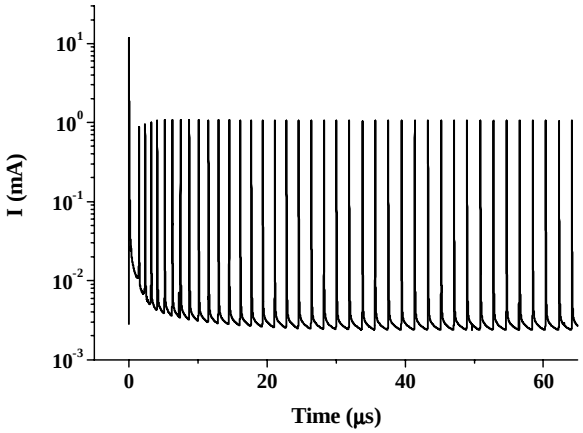


FIGURE 2. Computed electric current vs time

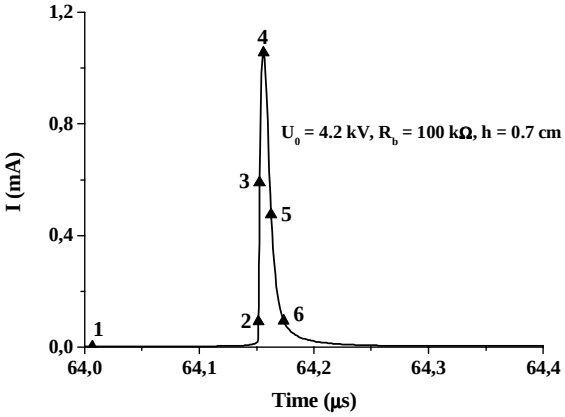


FIGURE. 3. Fine structure of an established pulse

Fig. 3 shows one of regular Trichel pulses on nanosecond scale. Duration of a peak is about 10 ns, and pulse has a smooth single-peaked shape. In contrast to prediction of the 1.5-D model [4], there is no peculiarity in pulse leading edge. To give an idea about pulse development and dynamics of electric current space distribution, a number of figures illustrate behavior of some physical quantities

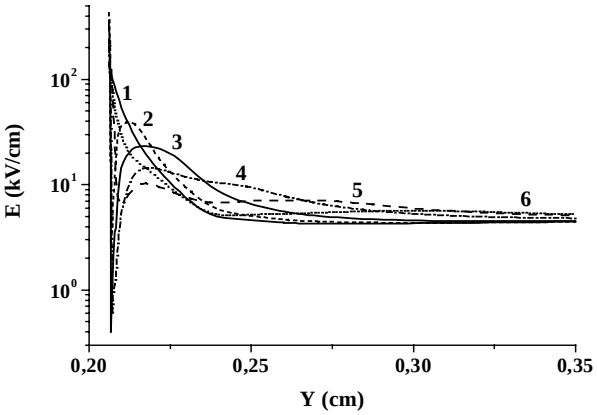


FIGURE 4. Electric field strength axial distribution for time moments marked in Fig. 3

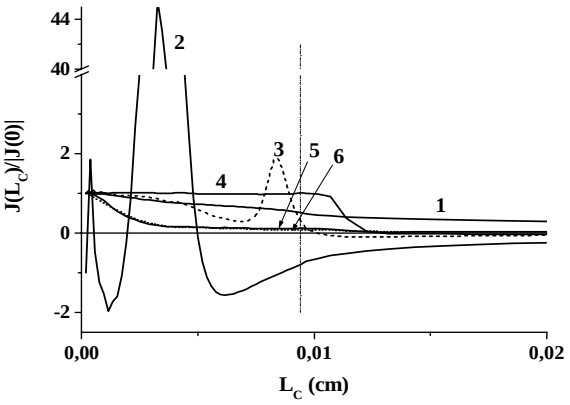


FIGURE 5. Total current density distribution over cathode surface for time moments marked in Fig. 3

along discharge axis and electrode surfaces. In particular, Fig. 4 shows variation of electric field axial

distribution starting from the moment 1 corresponding to the minimum current when the electric field is not disturbed by spatial charges and through pulse formation to its decay. Already at the moments 2 and 3 corresponding to the leading edge of the pulse, formation of low field region is clearly seen, which separates a thin cathode layer and a drift region. It is interesting that maximum electric field in the drift region is the biggest at the moment 1 then lowers and moves away from the cathode. At the pulse decay phase (moments 5 and 6) the electric field is monotonically diminishing from the cathode. Distribution of the total electric current density over the cathode surface shown in Fig. 5 has some peculiarities. To compare current density distributions at different moments, the reduced to the axial value current densities are plotted. A vertical dashed line shows boundary between spherical cap and cylinder. At the leading edge of pulse (0.1 level of peak current) a very strong peak of displacement current is seen at location about 0.035 mm from the axis. At this moment the displacement current at the axis is negative indicating that electric field at the axis is falling down. At about half of the peak current in the front of pulse (3) the current density maximum is relatively lower while moving close to the boundary between sphere and cylinder. In the moment of current peak (4), current covers evenly the surface of sphere and a small part of the cylinder. In the trailing edge the current density is maximum at the axis. Ion current density distribution over the cathode surface shown in Fig. 6 illustrates the same processes even more clear. At the leading edge of the pulse formation of the cathode layer and its propagation over the surface is clearly seen. Curves at the moments 5 and 6 demonstrate rather fast decay of the cathode layer in the trailing edge of the pulse.

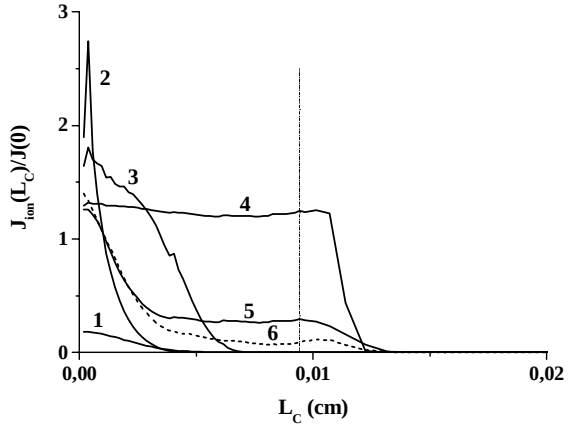


FIGURE 6. Ion current density distribution over cathode surface for time moments marked in Fig. 3

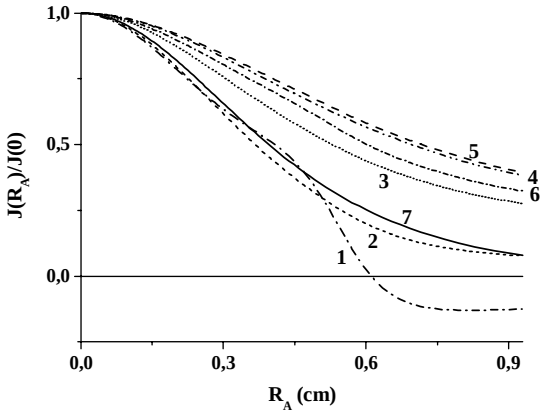


FIGURE 7. Total current density distribution over anode surface for time moments marked in Fig. 3

Time evolution of the total current density distribution over the anode is illustrated in Fig. 7. It is interesting that the current density is negative between pulses for distances from the axis larger than 6 mm. This fact reflects growth of the electric field at the anode resulting in a negative displacement current. Curve 7 shows Warburg's current density distribution over the anode. It is seen that during current pulse the anode area essentially limits the current distribution. Calculations demonstrated that negative ion density distribution suffers minor variations during the period of current oscillations. Fig. 8 shows contour plot for negative ion density in all computational region for the moment of minimum of current (1). In fact, this picture is a representative one for the negative ions at any moment.

More detailed examination of results of numerical simulations showed that most dramatic changes during the pulse took place near the cathode. In the very beginning of pulse the cathode layer with high electric fields (a couple of hundreds of kV) within distances on a scale of tens of microns is formed in a small area near the discharge axis. On the same spatial scale high fields changed to rather low fields (lower than 1 kV) while moving away from the cathode. Further evolution is development of this structure (combination of high and low fields), which looks like wave propagation along the cathode surface, approaching the boundary between spherical and cylindrical parts of the pin (see Figs. 5 and 6). In the trailing edge of the pulse this layer disappeared when discharge current fell two times. It is worth to note that the displacement current plays an important role at both cathode and

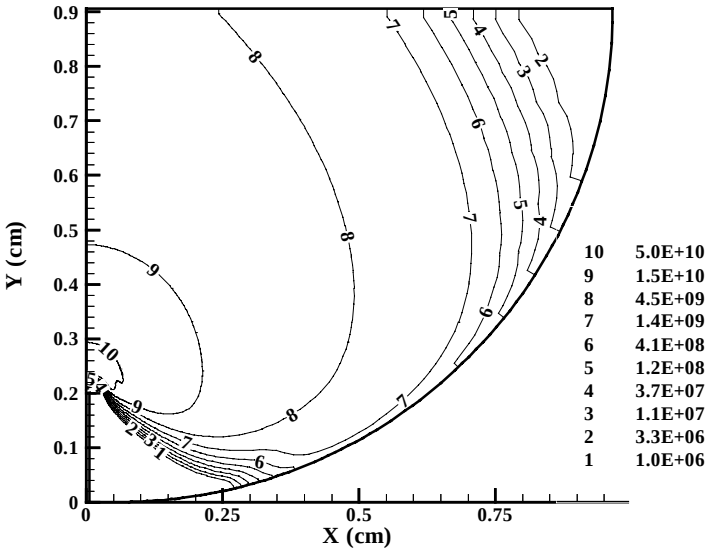


FIGURE 8. Contour plot for negative ion number density in computational region in the moment 1

anode surfaces. In particular, alternation of the total current density sign, taking place at the moment 2 in Fig. 5, is completely due to variation of electric field strength at the cathode surface. At the anode surface, negative - ion and displacement currents are the dominant components of the total current.

Fig. 8 demonstrated that negative ion number density is monotonously decreasing in space function with a peak at the axis located at about 0.5 mm from the cathode. No separate ion clouds are formed because the electron attachment length is longer than negative ion transportation length for the oscillation period.

Calculations of Trichel pulses at higher discharge voltages were performed. No significant change in pulse shape was detected. Peak current value was found to be independent of the voltage, while minimum current definitely increased and repetition rate also increased with the discharge voltage.

4. CONCLUSIONS

Comprehensive numerical simulations of negative corona in ambient air made by 3D model with axial symmetry demonstrated formation of regular sequence of Trichel pulses with parameters closely related to the experimental values. It was shown that the cathode layer is formed initially at the discharge axis with following expansion over the cathode surface filling spherical cap and a small part of the cylindrical portion. It means that the current channel shape experienced strong variations within one cycle.

ACKNOWLEDGMENTS

Authors acknowledge Dr U. Kogelschatz for initiation of this work and Dr. N. Trushkin for useful discussions.

REFERENCES

[1] Trichel, G. W., *Phys. Rev.*, **54**, 1078-1084 (1938)
[2] Morrow, R., *Phys. Rev. A*, **32**, 1799-1809 (1985)
[3] Morrow, R., *Phys. Rev. A*, **32**, 3821-3824 (1985)
[4] A. P. Napartovich, Yu. S. Akishev, A. A. Deryugin, I. V. Kochetov, M. V. Pan'kin, N. I. Trushkin, *J. Phys. D: Appl. Phys.* **30**, 2726-2736 (1997)
[5] A. P. Napartovich, Yu. S. Akishev, A. A. Deryugin, I. V. Kochetov, Final report to the Contract between ABB Management Ltd. Corporate research, Baden, Switzerland and TRINITI (1997)

THREE-DIMENSIONAL NUMERICAL SIMULATIONS ON THE STREAMER PROPAGATION CHARACTERISTICS OF PULSED CORONA DISCHARGE IN A WIRE-CYLINDER REACTOR

Jin Myung Park[a], Yong-Ho Kim, and Sang Hee Hong

Department of Nuclear Engineering, Seoul National University, Seoul 151-742, Korea

Abstract. A three-dimensional (3-D) time-dependent numerical model has been developed to simulate the streamer propagation with a more realistic description in a wire-cylinder corona reactor. Simulation results reveal that a uniform glow corona is at first generated around the wire electrode and is then transformed into a filament-like streamer during its expansion period. The spatial and temporal variations of the electric field and electron density are compared with those obtained from the 1-D corona and 1.5-D single-streamer models, respectively, to find the differences in the streamer propagation characteristics resulted from the three numerical simulation models.

1. INTRODUCTION

Pulsed corona discharge reactors of the wire-cylinder type have been widely used as a streamer generation device for the decomposition of toxic gases. Numerous efforts have been devoted to the streamer modeling to understand the physical and chemical processes occurring in these reactors. For example, either the 1-D corona model assuming the closely packed streamers radiating in the radial direction from the wire electrode [1] or the 1.5-D single streamer model based on the disk method [2] has been employed for the sake of simplifying the numerical problem and reducing the computational complexity. Although these two models have provided some physical insights and useful information on the characteristics of streamer, they predict still contradictory results specifically for the spatial distribution of the electric field strength at the propagating streamer head. In this numerical work, a 3-D time-dependent numerical simulation model has been developed and compared with the 1-D corona and 1.5-D single streamer models to get a better understanding of the streamer propagation characteristics in a wire-cylinder reactor.

2. NUMERICAL MODEL AND COMPUTATIONAL METHODS

On the basis of hydrodynamics, the densities of charged species, such as electron and ions, are calculated from the respective equations of continuity in the following;

$$\frac{\partial n_e}{\partial t} + \nabla \cdot (n_e v_e - D_e \nabla n_e) = \alpha n_e |v_e| - \eta n_e |v_e|, \tag{1}$$

$$\frac{\partial n_p}{\partial t} + \nabla \cdot (n_p v_p) = \alpha n_e |v_e|, \tag{2}$$

$$\frac{\partial n_n}{\partial t} + \nabla \cdot (n_n v_n) = \eta n_e |v_e| \ . \tag{3}$$

Here, n_e, n_p, and n_n are the densities of electron, positive ion, and negative ion, respectively, and

[a] Electronic address: myung@fusma.snu.ac.kr

v_e, v_p, and v_n are their drift velocities in the local electric field. Electron-impact ionization (a), electron attachment (h), and electron diffusion coefficient (D_e) are taken into account in the discharge conditions of atmospheric-pressure dry air [3]. The electric field is solved from the Poisson's equation,

$$\nabla^2 f = -\frac{e}{e_0}(n_p - n_e - n_n), \tag{4}$$

where f is the electrostatic potential, e is the electric charge, and e_0 is the permittivity of air.

For solving the continuity equations (1) ~ (3), a flux corrected transport (FCT) algorithm suggested by Zalesak [4] is employed, which has been successfully used in other 1-D and 2-D streamer modelings to accurately treat the very sharp gradients of charged particle densities without introducing spurious oscillation or artificial diffusion. The upwind and Lax-Wendroff methods are used as the low- and high-order schemes of the FCT algorithm, respectively. The finite difference equations resulting from the Poisson's equation are solved by using a biconjugate gradient stabilized (BiCGStab) method [5] in conjunction with an ILU(0) pre-conditioner. Since the FCT algorithm and BiCGStab method in a 3-D configuration demand the extremely time-consuming calculations, a parallel computing approach with domain decomposition is employed using a parallel supercomputer. In Fig. 1, a computational domain for a wire-cylinder reactor is represented as a shaded region, which is divided into several sub-domains. Each sub-domain is assigned to a respective processor of the parallel machine and computations of a set of sub-domains are simultaneously carried out. At the end of every time steps in the FCT algorithm and internal iterations of BiCGStab method, the data of sub-domain boundaries are exchanged between the processors using the message passing interface libraries. The developed parallel algorithm enables the 3-D streamer simulation to be successfully performed in a reasonable computational time.

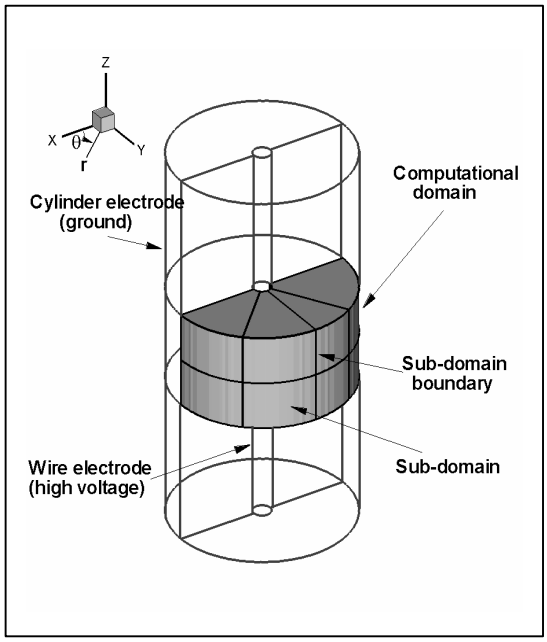


Figure 1. A computational domain and its sub-domains employed for 3-D numerical simulations in a wire-cylinder reactor.

3. RESULTS AND DISCUSSION

3.1. Three-Dimensional Simulations of Streamer Propagation

The three-dimensional simulations are carried out in the wire-cylinder reactor shown in Fig. 1. A positive pulse voltage of 46 kV is applied to the anode wire with a radius of 0.2 cm, while an outer cylinder electrode with a radius of 2 cm are grounded. The wire-cylinder reactor is initially filled with uniformly distributed electrons of 1 cm^{-3} in a natural radiation background. It is then assumed that the electron density distribution is perturbed, for example, by cosmic rays at a position of 1 mm away from the anode wire. A Gaussian profile with a peak value of 1 cm^{-3} and a width of 400 μm is used for the perturbed electrons in this numerical modeling.

Figure 2(a) shows the spatial distributions of electric field strength and Fig. 2(b) presents an iso-surface of electron density in the wire-cylinder reactor at t = 2 ns. Due to the non-uniform electrode configuration of a wire-cylinder arrangement, a positive glow corona is initiated from air breakdown at the anode wire surface and expands toward the grounded cathode tube with the cylindrical discharge volumes filled with an electron density of 10^{13} cm^{-3}. In particular, the distributions of electric field

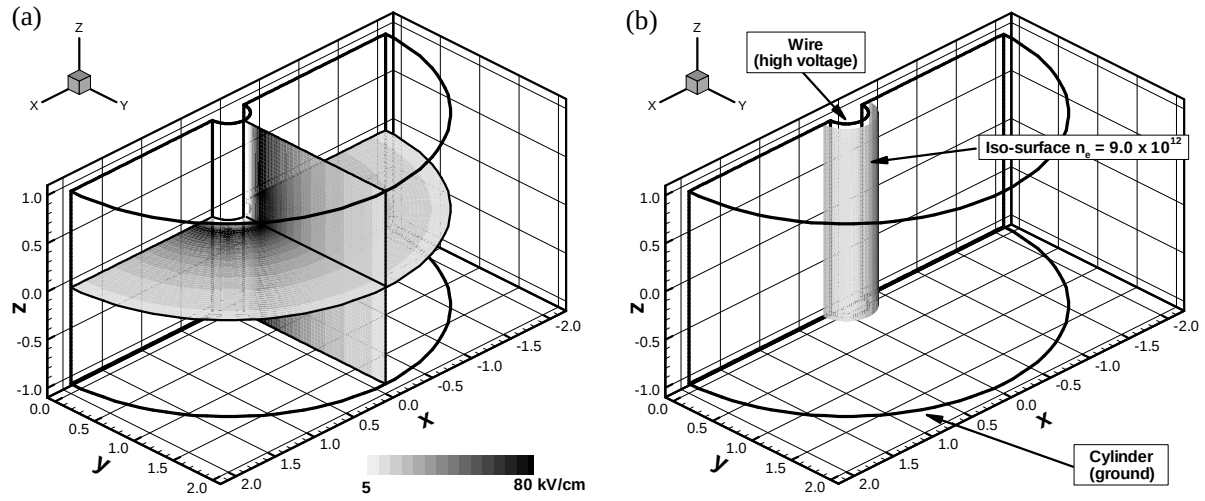


Figure 2. (a) Cutaway views of electric field distributions and (b) an iso-surface of electron density in the wire-cylinder corona reactor at t = 2 ns.

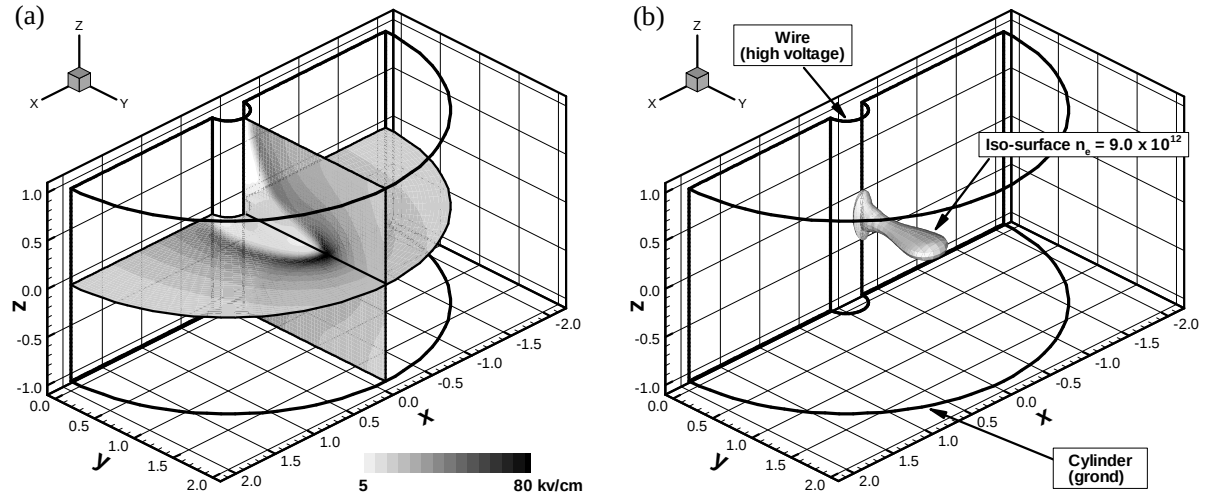


Figure 3. (a) Cutaway views of electric field distributions and (b) an iso-surface of electron density in the wire-cylinder corona reactor at t = 7 ns.

strength in the z = 0 and x = 0 planes reveal that the electric field strength depends only on the radial direction in an initial discharge phase in the wire-cylinder reactor. The 1-D approach can describe this initial phase of discharge with the same results as this 3-D simulation because the three-dimensional nature of the streamer propagation is not yet observed. However, the non-uniform perturbation of charged particles starts to grow after 2 ns and become a filament-like streamer. Figure 3 present the spatial distributions of electric field strength and their associated iso-surface of electron density at t = 7 ns showing evidently a filament-like structure. Figure 3(b) also exhibits a propagating streamer of an inherent 3-D shape with rotational asymmetry about the propagating path. If the 1.5-D single-streamer model is compared with the present 3-D approach, different results may be expected especially in the wire-cylinder reactor, because a cylindrical discharge channel with a fixed radius is commonly assumed in the 1.5-D models.

Figure 4 shows the distributions of electric field strength and electron density along the propagating streamer path during the discharge period. In the initial phase of discharge ($0 \le t \le 2$ ns), the maximum electric field of 100 kV/cm reduces to about 74 kV/cm. After the formation of filament-like streamer at t = 3 ns, electric field of the streamer head begins to increase until the streamer head is close to the cathode tube.

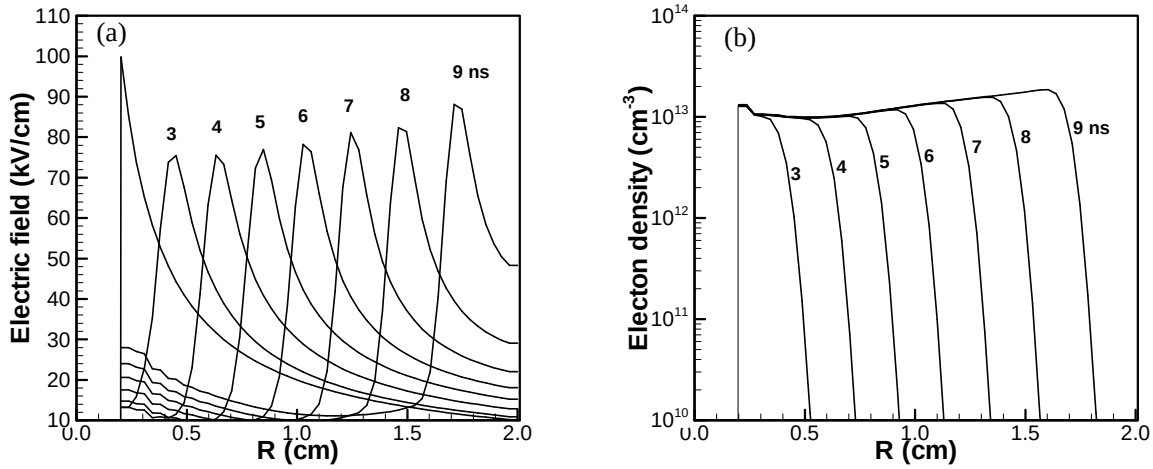


Figure 4. Temporal development of calculated distributions of (a) electric field and (b) electron density during the streamer propagation in the wire-cylinder reactor.

3.2. Comparison of 3-D Simulations with the 1-D and 1.5-D Models

In order to find the differences in the streamer propagation descriptions depending on the simulation model used, the previously known 1-D corona and 1.5-D single-streamer modelings are respectively performed. In the 1-D corona model, it is assumed that many streamers are generated at the same time and the neighboring streamers are so close to fill the whole discharge region. The governing equations (1) ~ (4) used for the 3-D simulation are also employed in the 1-D modeling except for considering the dependency of the radial component only. On the other hand, the 1.5-D single-streamer model assumes that the neighboring streamers are separated far away each other so that their interactions are neglected and a single streamer represents all the streamers with the same physical properties. The 1.5-D single streamer model uses the 1-D form of continuity equations for charged particles but calculates the electric field strength on the axis of the propagating streamer using the so-called disk method, which describes approximately the propagation of the single streamer by a cylindrical plasma column consisting of infinitesimally thin disks with a finite radius. The simulation conditions used for the 1-D corona and 1.5-D single streamer modelings are taken as the same as those for the 3-D simulation case as summarized in Table 1. The streamer radius, which is an undetermined parameter in the 1.5-D modeling, is chosen as 700 μm.

Table 1. Simulation conditions used for 1-D, 1.5-D and 3-D modelings.

numerical model	**3-D**	**1-D**	**1.5-D**
wire radius (cm)	0.2	0.2	0.2
cylinder radius (cm)	2	2	2
applied voltage (kV)	46	46	46
time step (sec)	10^{-11}	10^{-11}	10^{-11}
background density (cm^{-3})	1 + Gaussian	1 + Gaussian	1 + Gaussian
number of grid	100x100x100	100	100
disk radius (cm)			0.07

In Figure 5, the calculated results from the 3- D simulation are plotted for the traces of electric field and electron density at the streamer head during its propagation in the reactor, and they are compared with those obtained from the 1-D corona and 1.5-D single-streamer models. The 1-D corona and 1.5-D single-streamer models predict different behaviors of the streamer propagation from the 3-D model. When the streamer starts to propagate in the wire-cylinder reactor, the 1-D corona model reveals a decreasing electric field at the streamer front, while the 1.5-D single streamer model shows an increasing one. This discrepancy might come from neglect of three-dimensional nature of the streamer generation in both the models. On the other hand, the 3-D model shows a decreasing electric

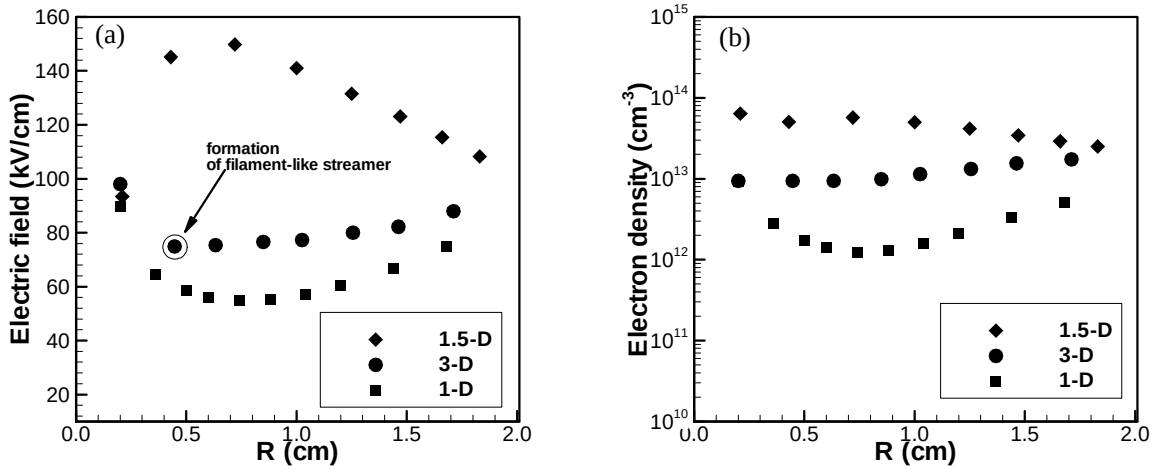


Figure 5. Time traces of (a) electric field and (b) electron density at the streamer head during the streamer propagation in the wire-cylinder reactor.

field in the initial phase of discharge and an increasing one after the formation of the filament-like structure of the streamer. The electric field strength and electron density of 3-D calculations have the intermediate values of those predicted by the 1-D corona and 1.5-D single streamer models.

4. CONCLUSIONS

The temporal and spatial variations of the charged particle and electric field distributions are calculated using the 3-D simulation model developed in this numerical work, and compared with those obtained from the 1-D corona and 1.5-D single-streamer models. At the initial phase of the discharge, the streamer propagation has the characteristics predicted by the 1-D corona model showing a decreasing electric field at the streamer front. Then the spatially non-uniform perturbations of charged particles make a filament-like streamer start to propagate. The electric field at the streamer front then increases after development of the filament-like structure. The electric field strength of 3-D calculations has an intermediate value of those predicted by the 1-D corona and 1.5-D single-streamer models.

ACKNOWLEDGEMENT

This work has been supported by the National Research Laboratory Program of KISTEP in the Ministry of Science and Technology of the Republic of Korea.

REFERENCES

[1] S. T. Chun, *J. Kor. Phys. Soc.,* **33***,* 428 (1998).
[2] Y. L. M. Creyghton, Ph.D. Thesis, Eindhoven Univ. Tech., Eindhoven, Netherland, 1994.
[3] A. A. Kulikovsky, *J. Phys. D: Appl. Phys.*, **30**, 441-450 (1997).
[4] S. T. Zalesak, *J. Comput. Phys.*, **31**, 335-363 (1979).
[5] H. Van Der Vorst, *SIAM J. Sci. Statist. Comput.*, **13**, 631-644 (1992).

NUMERICAL MODELING ON RECURRENCE OF MICRODISCHARGES IN DIELECTRIC BARRIER DISCHARGE

Woo Seok Kang [a], Yong-Ho Kim [b], Sang Hee Hong [a], and Young-Hoon Song [b]

a) Department of Nuclear Engineering, Seoul National University, Seoul 151-742, Korea
b) Korea Institute of Machinery and Materials, Daejon 305-343, Korea

Abstract: A one-dimensional time-dependent numerical modeling of dielectric barrier discharges has been carried out to get a better understanding of the recurrence of microdischarges depending on the AC voltage applied with different amplitudes and waveforms. Equations of the surface charge are modified to deal with the conduction loss of the dielectric barrier. Simulation results show that the recurrence of microdischarges is characterized by the discharge current and voltage waveforms as well as the variations of surface charges on the dielectric barriers. Comparison of the various voltage waveforms reveals that a fast rising voltage produces the electrons with higher energies while a slowly falling voltage sustains the microdischarges for a longer period.

1. INTRODUCTION

It is well known that microdischarges in the dielectric barrier discharge (DBD) take place only in a rising phase of the externally applied AC voltage and their associated streamers with a few nano second durations are recurrent. This recurrence of microdischarges is closely related with the behavior of space charge accumulation on the barrier surface. In this work, a one-dimensional(1-D) time-dependent simulation modeling has been set up with a simple modification of the surface charge equation for describing the recurrence of microdischarges. Such a new approach to the numerical analysis on the DBD opens the way for understanding the relation between the voltage rise and charge accumulation and for finding an effective voltage waveform applied to the DBD reactor.

2. NUMERICAL MODELING OF DIELECTRIC BARRIER DISCHARGE

In this modeling, the motions of electrons, positive and negative ions in the DBD are described by a set of continuity equations. A flux corrected transport (FCT) algorithm suggested by Zalesak [1] is employed in which the upwind and Lax-Wendroff methods are used as low- and high-order schemes, respectively. Electron-impact ionization, secondary emission, electron attachment, and photo ionization are taken into account in the discharge conditions of atmospheric-pressure dry air [2]. The externally applied electric fields are calculated by Laplace equation and the internally produced ones are solved using the method of disk [3]. A disk radius of 200 μm is adopted for the refined description of a highly localized streamer channel in the 1-D situation. The total electric fields are then obtained by adding the two resultant electric fields. Moreover, the discharge current profiles are obtained from an equation suggested by Sato [4].

It is assumed at the plasma-barrier interface that all the incoming electrons and ions accumulate on the dielectric barrier as surface charges. However, the accumulated electrons are then gradually submerged into the dielectric barrier because the practical barrier material is not a perfect dielectric [5]. Therefore, with considering the conducting loss of electrons to the dielectric barrier, the surface charge densities ρ_e and ρ_{ion} are described by,

[a] Electronic address : wskang@kistep.re.kr

$$\frac{\partial \rho_e}{\partial t} = \Gamma_e \cdot \mathbf{n} - \sigma E_b, \quad \frac{\partial \rho_{ion}}{\partial t} = \Gamma_{ion} \cdot \mathbf{n} \quad ,$$

where **n** is the normal vector directed from plasma to the dielectric barrier, σ is the conductivity of the dielectric barrier, and E_b is the electric field inside the dielectric barrier with the normal direction to the surface.

3. RESULTS AND DISCUSSION

3.1. Recurrence of Microdischarges

In this modeling of the DBD with two barriers placed on the electrodes, it is used that the thickness of a dielectric barrier with relative permittivity of 8 is 0.02 cm, and the discharge gap is 0.08 cm. A 100-kHz sinusoidal wave with a 6-kV peak voltage is used as an AC voltage source applied to the electrodes.

Figure 1 compares the calculated results of the discharge characteristics of the AC-DBD between two cases – with and without conductivity of dielectric barriers. In Figure 1(a) for pure dielectrics without conductivity, only a single pulse of discharge current is observed, and the discharge voltage is not appreciably changed from the applied AC voltage by the presence of the discharge. Therefore, even through the discharge voltage is maintained higher than the onset voltage of discharge in Figure 1, the microdischarge is not alive again. On the other hands, when the dielectric barriers have a conductivity of 10^{-11} S/cm as in Figure 1(b), a recurrent pattern of discharge currents appears showing a similar trend observed in the relevant experimental measurement. After the initial current pulse is appeared, the second one begins to be generated due to the loss of accumulated surface charges. Further current pulses are sequentially found with the same principles. After the onset of microdischarges, the discharge voltage is continuously increased with the applied AC voltage until reaching its highest value, and then it is gradually decreased down to a breakdown level under which the microdischarges cannot sustain any longer. A duration, from the start of microdischarges to their extinction, is called "*active period*" of microdischarges.

Figure 2 gives more detailed information about the spatio-temporal developments of electric field and electron density in the AC-DBD. In Figure 2(a), streamers are created after the onset of microdischarges with avalanche, streamer, and decay phases, and they show high electric fields toward the cathode with a recurrent trend. Moreover, the channel formations by the streamer propagation are also found with stripes in the electron density in Figure 2(b).

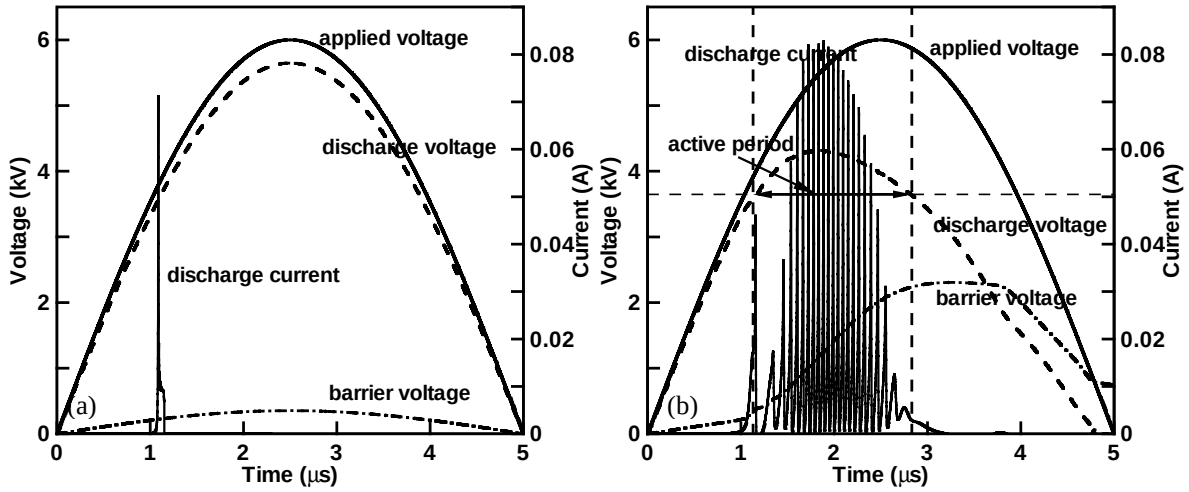


Figure 1. Discharge characteristics in the DBD with the applied AC voltage for the cases (a) without conductivity of pure dielectrics and (b) with conductivity of 10^{-11} S/cm of lossy dielectrics.

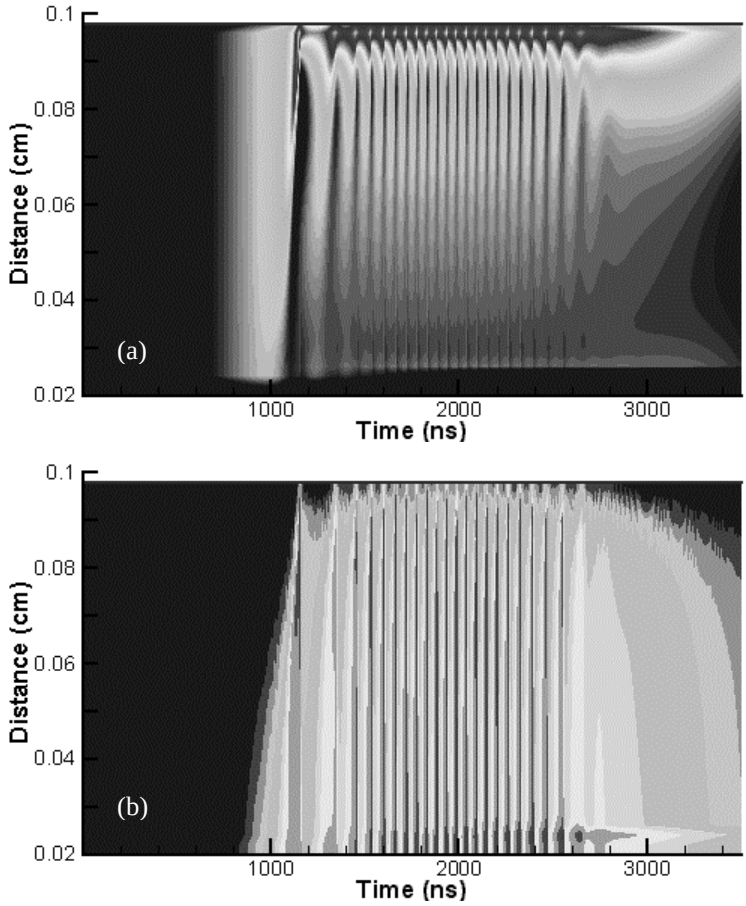


Figure 2. Spatio-temporal developments of (a) electric field and (b) electron density in the AC-DBD.

In this AC-DBD operation, the surface charges on the dielectric barriers begin to be accumulated as shown in Fig. 3(a), and the discharge energy consumption rapidly rises especially during the active period as seen in Fig. 3(b).

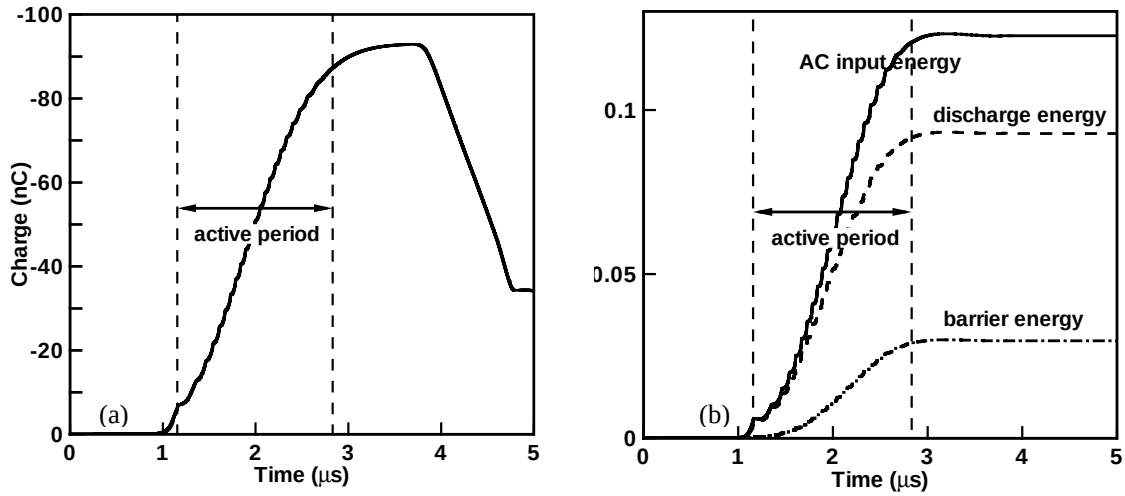


Figure 3. (a) Surface charge accumulation and (b) discharge and barrier energy consumption during the AC-DBD operation.

3.2. Effects of Amplitudes and Waveforms of AC Voltages

The effects of amplitudes and waveforms of the applied AC voltage on the generation of microdischarges are investigated. In this calculation, the 100 kHz sinusoidal waves with different voltage amplitudes of 5, 6, and 7 kV, are adopted as externally applied AC voltages. As a result of this simulation, it is clearly found in Figure 4(a) that the increase of applied AC voltage makes the microdischarge current enhanced and the active period widened. The difference depending on the AC voltage amplitude comes from the faster onset of microdischarges according to the AC voltage after all. On the contrary, in calculations of discharge energy in Figure 4(b), although the discharge energy is increased with the applied AC voltage, the energy delivery efficiency (ratio of discharge energy to AC input energy) is decreased.

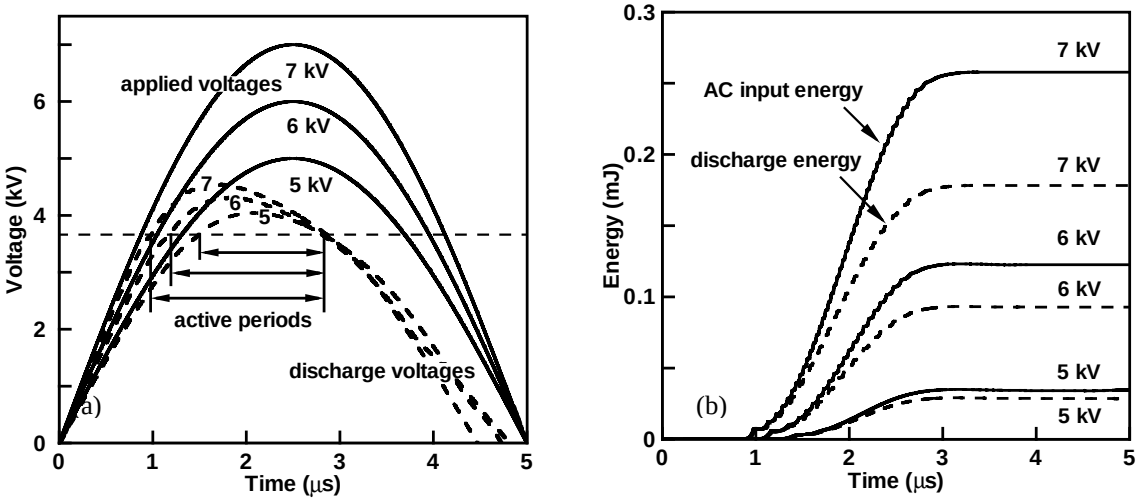


Figure 4. (a) Discharge voltage profiles and (b) discharge energy consumption for different amplitudes of the applied AC voltages.

Influences of different applied AC voltage waveforms, such as triangular and trapezoidal ones keeping with the same peak voltage value, are compared by the time evolution of discharge voltages and currents as shown in Figure 5. When a triangular voltage waveform is used in Figure 5(a), the microdischarge currents created mainly during a voltage rising period is rapidly disappeared in a voltage falling period, and therefore the active period for sustaining the recurrence of microdischarges is rather narrow compared to that obtained by the sinusoidal wave. In the trapezoidal voltage waveforms with different rising times as shown in Figure 5(b), the faster the AC voltage rise is, the higher current peaks are produced. And the microdischarges are sustained with a longer active period by a residual constant voltage of trapezoidal waveform when they are compared with the cases of triangular and sinusoidal waveforms. The discharge energies also increase with the rapid voltage rise and are eventually saturated as the discharge time elapses. In summary, the fast AC voltage rise makes the higher microdischarge current peak with higher energy electrons generated and the slow AC voltage fall sustains microdischarges with a longer active period.

4. CONCLUSIONS

Recurrence of microdischarges has been studied in the AC-DBD by a simple modification of the surface charge equations in a 1-D time-dependent numerical code with the assumption that surface charges on the dielectric barriers are consumed by electrical conduction. As a result of the AC-DBD simulations, the recurrence of microdischarges is explained by the current, voltage, and energy of the discharge as well as the calculated variations of surface charges on the dielectric barriers.

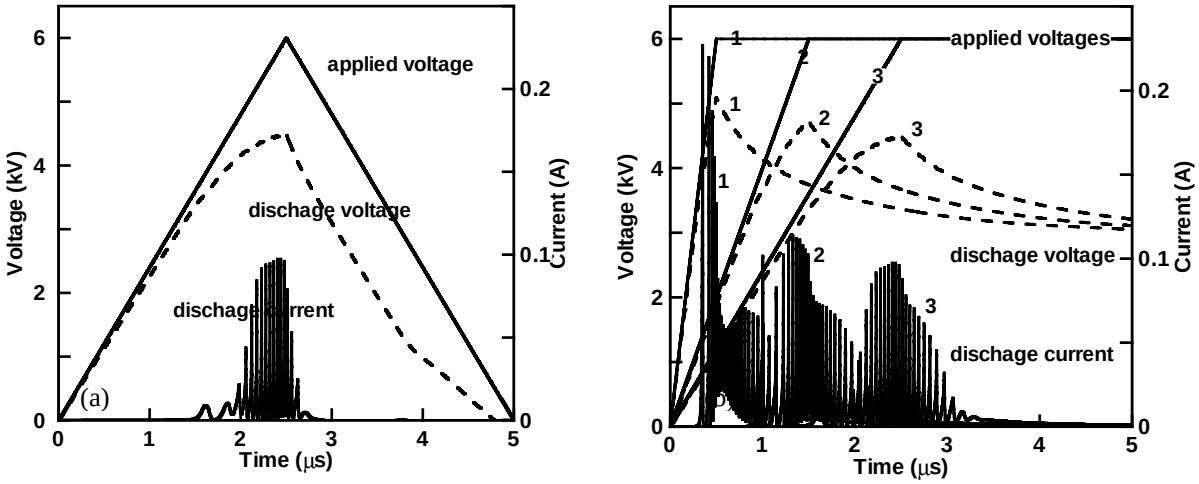


Figure 5. Microdischarge characteristics of the AC-DBD depending on the AC voltage waveforms (a) in a triangular case and (b) in the three trapezoidal cases.

The calculated results indicate that the present simulation approach apparently show a similar trend of microdischarge characteristics as the relevant experiments have done, and the electrical conduction losses of surface charges through the dielectric barriers are proved to be a key factor of generating the recurrence of microdischarges. In addition, the active period is explained by the calculated profiles of discharge voltage and surface charge accumulation during the microdischarges. It is also found that the increase of applied AC voltage amplitude enhances the discharge energy but reduces the energy efficiency of AC-DBD. The various waveforms of applied AC voltages, such as triangular and trapezoidal shapes, have been compared for finding their effects on the microdischarge characteristics. It turns out from these results that a fast voltage rise produces the electrons with high energies while a slow voltage fall sustains the microdischarges for a longer period.

REFERENCES

[1] S. T. Zalesak, *J. Comput. Phys.*, **31**, 335-363 (1979).
[2] A. A. Kulikovsky, *J. Phys. D: Appl. Phys.*, **30**, 441-450 (1997).
[3] A. J. Davies, C. J. Evans, and P. M. Woodison, *Proc. IEE*, **122**, 765-768 (1975).
[4] N. Sato, *J. Phys. D: Appl. Phys.*, **13**, L3-6 (1980).
[5] H. J. M. Blennow, Ph.D. Thesis, Chalmers Univ. Tech., Gotebörg, Sweden, 2000.

PLASMA DIAGNOSTICS BY CROSS-CORRELATION SPECTROSCOPY IN INVESTIGATIONS OF CHEMICAL ACTIVITY OF NEGATIVE CORONA IN AIR AT ATMOSPHERIC PRESSURE

K. V. Kozlov[a], N. S. Boksha, A. M. Morozov, and V. G. Samoilovich

Moscow State University, Department of Chemistry, 119899 Moscow, RUSSIA

Abstract. An attempt has been made, to use the technique of spatially unresolved cross-correlation spectroscopy for the prognosis of chemical efficiency of negative corona of the type "point-to-plane" in air. The experiments were carried out in an open gas flow system at atmospheric pressure. DC voltage was varied within the range 8.5-10.5 kV. Spatially unresolved intensities I(t) for the spectral band of the 0-0 transition of the second positive system of nitrogen (λ = 337.1 nm) were recorded simultaneously with the measurements of ozone yield and electrical characteristics of the discharge.

1. INTRODUCTION

The main idea of the method of cross-correlation spectroscopy (CCS) is to replace a direct measurement of the single pulse luminosity of a repetitive light pulse emitter by a statistically averaged determination of the correlation function between two optical signals, both originating from the same source. The first one of these signals (so-called "synchronizing signal") is used to define a relative time scale, the second one ("main signal") has to be detected with a probability at least one order of magnitude lower, than that one of the synchronizing signal. The measured quantity is actually a time delay between these two signals, and the recorded quantity is a probability density function for the light pulse intensity evolution. If the repetitive light pulses reproduce each other sufficiently exactly, and if the synchronizing signal detection is adjusted in such a way as to occur always at the same moment of a single light pulse evolution, then the recorded probability density function is proportional to the light intensity *I(t)* of the source under consideration. A detailed description of the theoretical foundations of CCS technique is given in the review paper [1], for example.

Experimental technique of the spatially resolved CCS has been demonstrated to be a powerful tool to investigate spatio-temporal structure of such filamentary discharges in air at atmospheric pressure, as the microdischarges of the barrier discharge [2-5], and the "point-to plane" coronas of both polarities [6-9]. Due to extremely high sensitivity of the CCS technique and its temporal resolution in a sub-nanosecond range, the arrays of measurement results were obtained that provided the data quality (accuracy and spatio-temporal grating), sufficient for quantitative estimating of electric field and relative electron density [3,5]. The knowledge of these basic plasma parameters allows deep understanding and complete theoretical description of the process of electrical breakdown, including discharge physics and chemistry [10].

However, even spatially unresolved CCS-measurements can provide important information concerning the properties of the repetitive filamentary discharges. As an example, we present here some results of our recent experiments with negative corona operating in the mode of Trichel pulses. In order to compare physical properties with the chemical efficiency of this discharge, we performed systematic measurements of the ozone yield simultaneously with recording of the CCS-data, the DC-voltage amplitude being used as a variable parameter. To analyze statistical behavior of the pulse sequences, we compared experimental results with two alternative semi-empirical statistical models.

[a] Electronic address: kozlov@kge.msu.ru

2. EXPERIMENTAL

The experiments were carried out in the discharge cell of typical configuration (point-to-plane, radius of curvature 0.5 mm, distance to the grounded electrode 15 mm, flowing dry air at atmospheric pressure with the flow rate of 190 l/hour). The negative DC voltage was varied within the range 8.5-10.5 kV. Under experimental conditions under consideration, negative corona has been found to operate in the mode of Trichel pulses with the frequency of 40-150 kHz.

For the CCS-measurements, we used the instrument "Fluor-99" manufactured by the company "NPO Spektroskopiya" from Belarus and equipped with the special photo-multipliers [11], combined with the monochromator "MDR-2". No lenses and optical slits have been installed between the light source (the tip of the negative needle) and the detectors (photo-multipliers), excepting the entry-slit of the monochromator. The most intensive spectral band (λ = 337.1 nm, 0-0 transition of the 2nd positive system of nitrogen) has been chosen for the systematic CCS-measurements. The time gate of the Time-to-Amplitude Converter of the instrument "Fluor-99" enable the variation of the time scale from 50 ns up to 40 μs corresponding to 1024 channels for data recording.

The measurements of the ozone yield were carried out by means of the standard KI-titration procedure. Duration of each experiment was equal to 90 minutes.

3. RESULTS AND DISCUSSION

3.1. Statistical properties of the discharge

Figure 1 demonstrates a typical example of the results of the CCS-measurements (a number of the light pulses, denoted as "Experiment" in the figure) compared to the corresponding series of the current pulses (Trichel pulses). The latter are presented in the right upper part of the figure as a drawing from the screen of the oscilloscope.

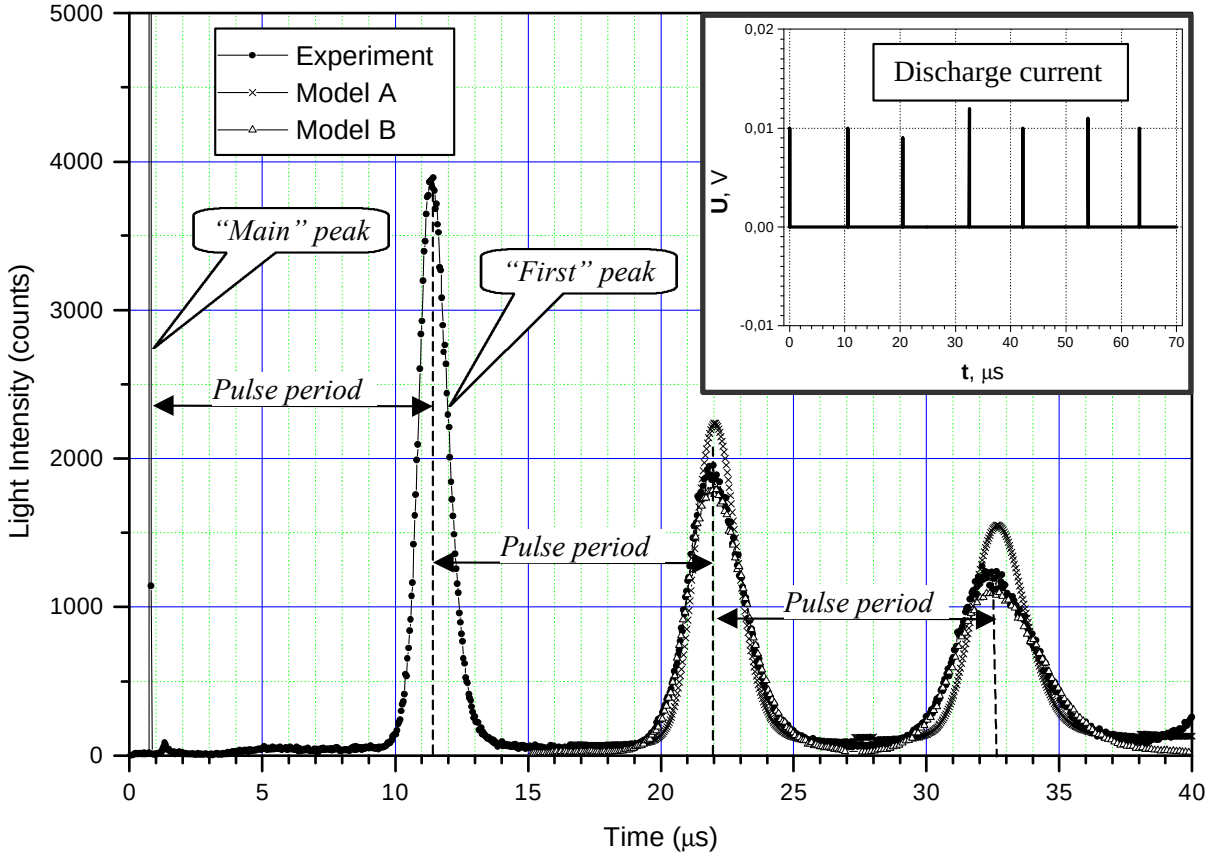


FIGURE 1. Statistical behavior of the Trichel pulses. See explanations in the text.

As it is clearly seen from the graphs in figure 1, the first light intensity peak in the sequence is very sharp, while the following ones continually decrease in amplitude but increase in half-width. To interpret these experimental results, it is essential to take into consideration the statistical nature of the CCS method. Since Trichel pulses follow one another with a fluctuation of the interval between them, the quantity measured by CCS should be treated as an auto-correlation function [1]. Only the first pulses in figure 1 can be expected to reveal a real evolution of the light intensity of the emitter under consideration, because only in these cases both optical signals ("synchronizing" and "main") originate from the same object. The shapes of the following peaks are determined by statistical distributions of the pulse repetition frequency, and the periodic structures of their series allow an evaluation of the corresponding mean frequency of Trichel pulses. The real peaks I(t) (corresponding to the first pulses in the sequences shown in figure 1) are too narrow, to be properly resolved in the 40 μs scale of the Time-to-Amplitude Converter (the corresponding time resolution is equal to about 40 ns/channel). Their half-widths have been found not to exceed 5 ns, the shape of these pulses being independent of the feeding voltage within the range 8.5-10.5 kV. A typical example is shown in figure 2.

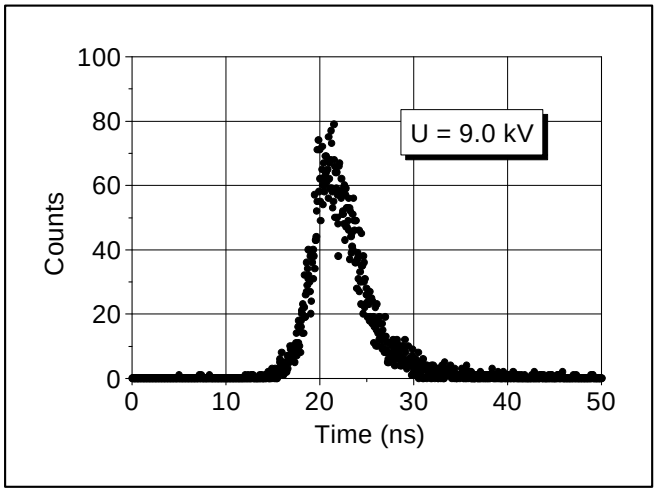


FIGURE 2. Evolution of the light emission of a single Trichel pulse from the negative DC corona.

Thus, the shapes of the peaks in figure 1 reveal certain statistical distribution of the light pulses in a sequence over time scale (compare with the corresponding current pulses at the right upper part of the figure). To analyze this distribution quantitatively, we can compare it with the results of the following alternative semi-empirical models.

Model A. (The model of "constant frequency"). This model is based on the assumption that the pulse frequency is constant, but there are some fluctuations in the times of the pulse emergence. In other words, the time period between two neighboring pulses T may be characterized by the corresponding probability density f(t–T). The extremely narrow initial peak (denoted as "Main" peak in figure 1) may be approximated by δ-function:

$$I_0(t) = \delta(t - t_0) \tag{1}$$

Therefore, the next one (denoted as "First" peak in figure 1) may be expressed as

$$I_1(t) = f(t - T - t_0) \tag{2}$$

Generally in this case, the following recurrence formula can be easily derived:

$$I_{n+1}(t) = \int I_{n+1}(\tau)\, f(t - T - \tau)\, d\tau \tag{3}$$

Model B. (The model of "frequency fluctuation"). It may be assumed that the frequency of the light pulses fluctuates as a whole, while the fluctuations of the time delays between the neighboring pulses are negligible. In this case, probability density f(t-T) characterizes statistical stability of the pulse frequency. Equations (1) and (2) are also valid for this model, but instead of (3) it should be written:

$$I_n(t) = n^{-1} f\{(t - t_0)n^{-1} - T\} \tag{4}$$

For both models, equation (2) can be used to determine the distribution function f(t–T) from the experimental data ("First" peak). After that, the light intensity distributions for the consequent peaks can be easily calculated with the help of the formula (3) or (4), within the frame of the model A or B, respectively. The results of such calculations are shown in figure 1 together with experimental data. As it is clearly seen, the model B provides noticeably better agreement with the measurement results. Therefore, the statistical behavior of the Trichel pulses is determined by the frequency fluctuations.

3.2. Radiation intensity and chemical efficiency

The CCS-measurements (carried out in a maximal time scale) enabled reliable and accurate evaluating of the period (frequency) of the Trichel pulses in the entire range of DC voltage variation. This dependence was found to be similar to the corresponding current-voltage characteristic of the negative corona (figure 3). The results shown on both plots indicate to the existence of two different modes of the discharge operation (for the feeding voltage ranges 8.5-9.5 kV and 9.5-10.5 kV).

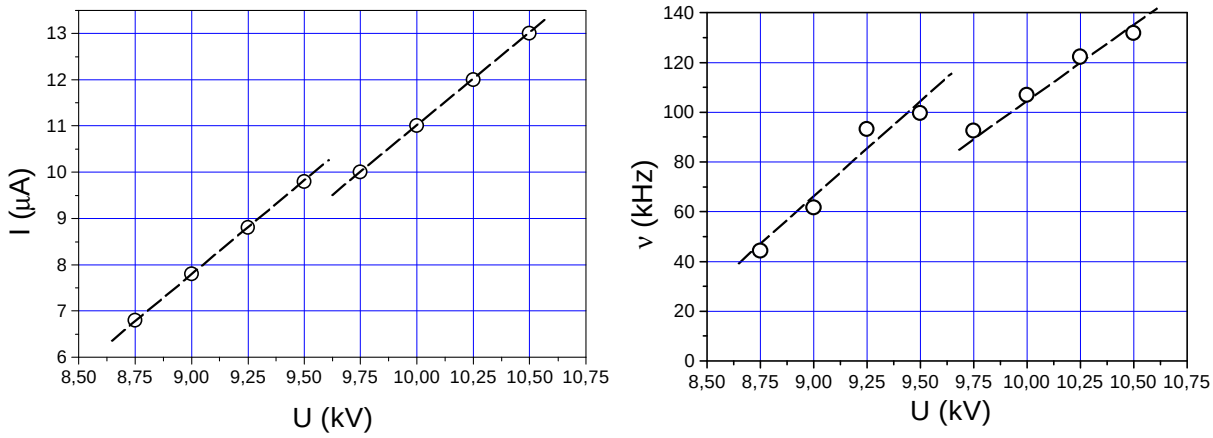


FIGURE 3. Dependence of the discharge current (left) and of the light pulse frequency (right) upon the voltage.

An efficiency of ozone generation in gas discharges in air is determined mainly by the rates of the following reactions: dissociation of molecular oxygen by direct electron impact (6-9 eV, see e.g. [12,13]) and excitation of the triplet states molecular nitrogen [10,12-14]. Since one of these states is a precursor of the observed radiation of the discharge under consideration:

$$e + N_2\left(X^1\Sigma_g^+\right)_{n=0} \rightarrow N_2\left(C^3\Pi_u\right)_{n'=0} + e \qquad \left(\Delta E = 11.0eV\right) \qquad (5)$$

$$N_2\left(C^3\Pi_u\right)_{n'=0} \rightarrow N_2\left(B^3\Pi_g\right)_{n''=0} + hn \qquad \left(l = 337.1nm\right) \qquad (6),$$

some correlation between the ozone yield and the total radiation intensity of the 2nd positive system of nitrogen can be expected. To verify this assumption, we compared these quantities within the entire studied range of the feeding voltage variation (figure 4).

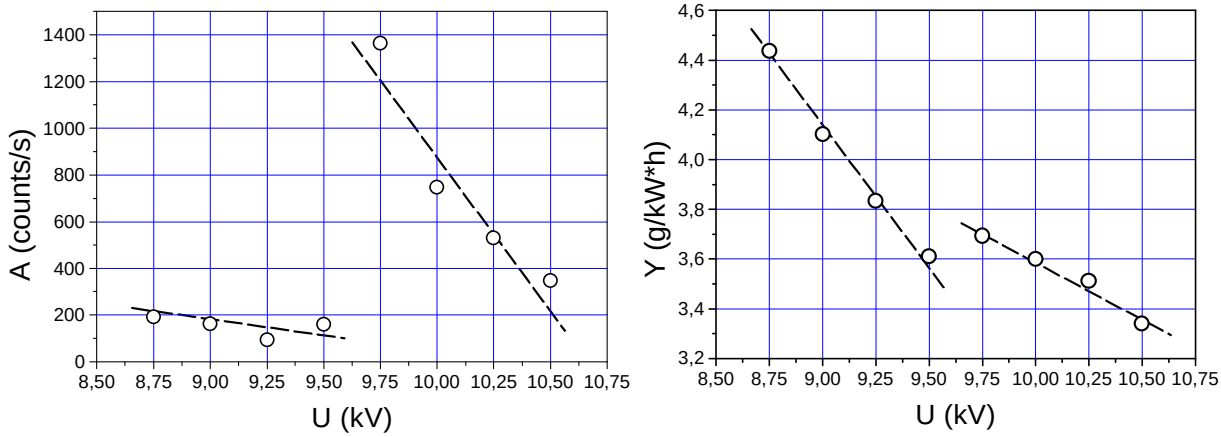


FIGURE 4. Dependence of the integral emission intensity of the discharge for the spectral band λ = 337.1 nm (left), and of the energetic yield of ozone (right) upon the feeding voltage amplitude.

As it can be seen from these results, only a weak qualitative correlation between the energetic yield of ozone and the integral light intensity can be found. This result indicates to the prevailing effect of electron density in the case of ozone synthesis, and in contrast, to the dominant role of electric field in the case of the generation of light emission via the reactions (5,6). To provide an adequate quantitative

description of the system under consideration, the complete spatially resolved CCS-diagnostics of the discharge, including systematic measurements for two different spectral bands [3-5], is necessary.

4. CONCLUSIONS

The CCS method has been demonstrated to characterize quantitatively the statistical behavior of the light pulse sequences of the negative corona (Trichel pulses). The experimentally measured distribution functions of the pulses are shown to comply with the model of variable frequency.

According to the results of the CCS-diagnostics combined with the measurements of ozone yield and electrical characteristics of negative corona, under experimental conditions under consideration, two different modes of the discharge may be distinguished, corresponding to the feeding voltage ranges 8.5-9.5 kV and 9.5-10.5 kV.

The spatially unresolved plasma diagnostics based on the measurements of the light intensity of the 2^{nd} positive system of nitrogen appears to be insufficient to provide a quantitative prognosis for the chemical activity of negative corona in air.

ACKNOWLEDGMENTS

The authors express their deep gratitude to Yu. S. Akishev for his valuable remarks on the subject of this paper.

REFERENCES

[1] Ware W.R., Technique of pulse fluorometry, In: *Time-Resolved Fluorescence Spectroscopy in Biochemistry and Biology, NATO ASI Series A: Life Sciences,* ed. by Cundall R.B. and Dale R.E., **69**, Plenum Press, New York, London, 1983, p.23-57

[2] Kozlov K.V., Shepelyuk O.S., Samoilovich V.G., Spatio-temporal evolution of the dielectric barrier discharge channels in air at atmospheric pressure, In: *Proc.11th Int. Conf. on Gas Discharges and Their Applications,* **2,** , IEE of Japan, Tokyo, 1995, p.142-5

[3] Kozlov K. V., Wagner H.-E., Brandenburg R., and Michel P., *J. Phys. D: Appl. Phys.*, **34**, 3164-76 (2001)

[4] Brandenburg R., Kozlov K. V., Michel P., and Wagner H.-E., Diagnostics of the single filament barrier discharge in dry and humid air by cross-correlation spectroscopy. In: *Proc. 7th Int. Symp. on High Pressure Low Temperature Plasma Chemistry*, ed. by H.-E. Wagner, J. F. Behnke, and G. Babucke, Greifswald, 2000, pp. 189-93

[5] Wagner H.-E., Kozlov K. V., Brandenburg R., and Michel P., Experimental study of repetitive electrical breakdown in the barrier discharge in air. In: These Proceedings

[6] Teich T.H., Determination of reaction data from corona discharge observation. In: *Proc. 3rd Int. Symp. on High Pressure Low Temperature Plasma Chemistry*, ed. by M. Lecuiller, Strasbourg, 1991, p.77-83

[7] Teich T.H., Emission spectroscopy of corona discharges, In: *NATO ASI Series, Non-Thermal Plasma Techniques for Pollution Control,* ed. by Penetrante B.M. and Schultheis S.E., **Vol. G34, Part A,** Springer-Verlag, Berlin Heidelberg, 1993, p.230-247

[8] Ikuta N., Kondo K., A spectroscopic study of positive and negative coronas in N_2 O_2 mixture. In: *Proc.4th Int. Conf. on Gas Discharges and Their Applications,* Swansea, UK, 1976, p.227-230.

[9] Kondo K., Ikuta N., *J. Phys.D: Appl. Phys.,* **13,** L33-38 (1980)

[10] Kozlov K. V., Physical models of the microdischarge in an ozonizer: classification, analysis, and comparison with the reality. In: *Proc. 7th Int. Symp. on High Pressure Low Temperature Plasma Chemistry*, ed. by H.-E. Wagner, J. F. Behnke, and G. Babucke, Greifswald, 2000, pp. 292-8

[11] Vetokhin S.S., Ermalitski F.A., Melnikov S.M., Sukhanin S.V., *Functional Materials,* **3,** p.556-61 (1996)

[12] Samoilovich V., Gibalov V., and Kozlov K., *Physical chemistry of the barrier discharge,* DVS-Verlag, Düsseldorf, 1997

[13] Kossyi I. A., Kostinsky A. Yu., Matveyev A. A., and Silakov V. P., *Plasma Sources Sci. Technol.,* **1**, 207-20 (1992)

[14] Kogelschatz U., Eliasson B., and Egli W., *J. Physique,* **IV** C4, 47-66 (1997)

DYNAMICS OF THE GAS TEMPERATURE IN DIELECTRIC BARRIER DISCHARGE IN HE/N_2 MIXTURES

A. Fateev[a] , I. Vinogradov and A. Lunk

Universität Stuttgart, Institut für Plasmaforschung, Pfaffenwaldring 31, 70569 Stuttgart, Germany

Abstract: The variation of the gas temperature and population of vibrational levels of different molecules (N_2^+(B), N_2(C)) at different discharge gaps were obtained. At small gaps the ionization rate of He atoms and the formation of He_2^+ ions are significantly increased due to a change in eedf. The rotational temperature increases also dramatically up to 800 K. Nevertheless, the gas temperature still stays equal to the rotational temperature of N_2^+(B) as is demonstrated from the modeling of the rotational relaxation.

We used the parallel plate geometry of the discharge cell. Two electrodes, 6x16 cm^2, were covered by dielectric plates made from Al_2O_3. The system allows to change continuously the discharge gap between dielectric plates in the range of 0.1 - 2 mm. A pulse generator (with discharge on/off time 4 ms/16 ms respectively, intermittent frequency, f = 40 kHz) was used as power supply. The gas flows of He and N_2 were controlled by flowmeters and total flow was kept at 2 l_n/min. Total pressure was 93.3 kPa and partial pressure of nitrogen varied from 0.4 to 3.5 kPa. Measurement of the discharge power was obtained by the Lissajous-figure method [1]. For spectroscopic measurements we used a 1 m spectrograph with CCD camera. The spectral resolution was 0.025 nm. The method of calculating rotational temperature from the emission spectra of first negative system of nitrogen ion $N_2^+(B^2\Sigma^+_u \rightarrow X^2\Sigma^+_g)$ and second positive system of nitrogen $N_2(C^3\Pi_u \rightarrow B^3\Pi_g)$ is described in detail [2].

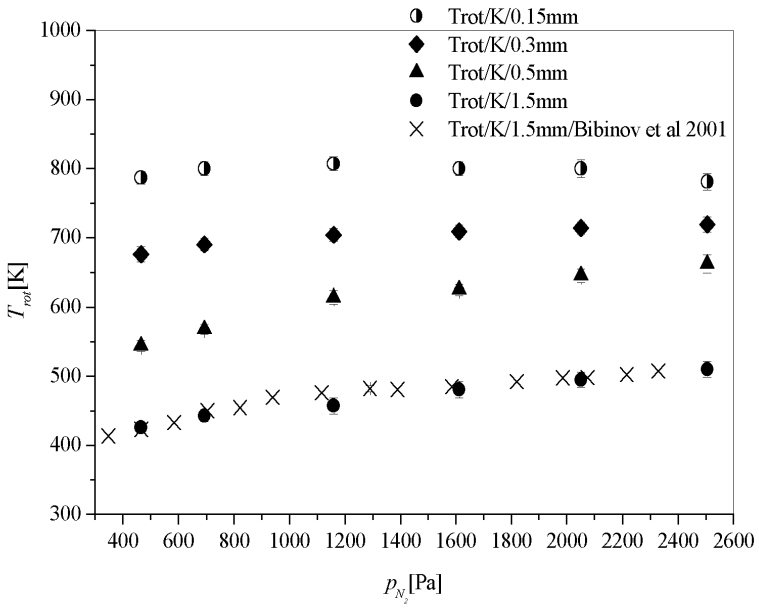


FIGURE 1. Variation of the rotational temperatures obtained from emission spectra of N_2^+(B-X) at different pressures of nitrogen and different discharge gaps.

From the emission spectra of $N_2^+(B^2\Sigma^+_u \rightarrow X^2\Sigma^+_g)$ recorded at different partial pressures of nitrogen

[a] Electronic address of the corresponding author: fateev@ipf.uni-stuttgart.de

(0.4 – 3.5 kPa) and discharge gaps (0.15 - 1.5 mm) we estimated the rotational temperatures, Figure 1. At a discharge gap equal to 1.5 mm our results confirm our previous data [2]. Rotational temperatures obtained from the spectra of $N_2(C^3\Pi_u \rightarrow B^3\Pi_g)$ were the same for all measurements and equal to (300 ± 10)K. The dependence of average concentration of metastable nitrogen molecules $N_2(A^3\Sigma^+_u)$ on discharge power has the same dependence as in [3] for a discharge gap of 1 mm. These results confirm that C-state of nitrogen is mostly populated due to 'pooling' reaction of metastable $N_2(A^3\Sigma^+_u)$ molecules. The direct electronic excitation $N_2(X) \rightarrow N_2(C)$ is negligibly small.

Population of $N_2^+(B, v=0)$ relative to $N_2(C, v=0\text{-}2)$, $N_{Bv=0}/N_{Cv=0\text{-}2}$, increases when the discharge gap decreases as seen from Figure 2 and 3 at p_{N_2} = 0.5 kPa. It is $N_{Bv=0}/N_{Cv=0}$ = 0.88 for a discharge gap 0.15 mm and $N_{Bv=0}/N_{Cv=0}$ = 0.19 for discharge gap 1.5 mm. At high pressures of nitrogen the $N_2^+(B,v=0)$ is quenching more effectively than $N_2(C,v=0\text{-}2)$. The ratio of the intensities of He emission lines to intensity of the N_2(C-B) bands at discharge gaps 0.15 mm, 1.5 mm and p_{N_2} = 0.5 kPa has the same behavior. Relatively high population of $N_2^+(B, v=0)$ at small gaps is closely correlated with the different excitation channels, namely Penning ionization ($He^* + N_2$) and charge exchange ($He_2^+ + N_2$). The relative contribution of these channels changes when the reduced field is varied.

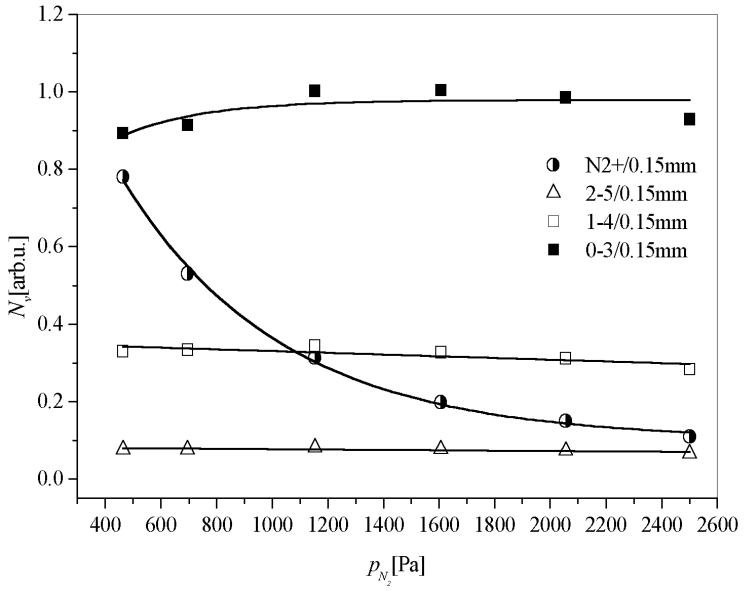


FIGURE 2. Relative population of $N_2(C,v=0\text{-}2)$ and $N_2^+(B,v=0)$ molecules at discharge gap 0.15mm.

In order to estimate the role of different channels we modeled the reaction kinetics using the code EEDF (based on solving the electron Bolzmann equation in a two-term approximation of the so-called local approximation) developed by Napartovich *et al* [4]. At high values of the reduced field (more than 40 Td) the production of the ratio He^+ relative to He^*, i.e. $He^+/(He(2^1S)+He(2^3S))$ is more 40 % whereas at lower values of the reduced field (less than 20 Td) the ratio is only 6 %, Figure 4. The high values of the reduced field for our conditions is realized at small discharge gaps 0.15 - 0.3 mm.

The high value of He^+ leads to a high amount of He_2^+ and enhances the ($He_2^+ + N_2$)-channel. As is well-known, the high initial rotational distribution (with T_{rot} = (900 ± 60) K) in the spectra of the nitrogen ion is produced by the ($He_2^+ + N_2$)-channel [5]. The other channel, ($He^* + N_2$), gives lower (T_{rot} = (360 ± 30) K) initial rotational temperature. The whole assembly of ''hot'' and ''cold'' molecules is relaxing to the ambient gas temperature if the effective lifetime of $N_2^+(B)$ is not too small. At our experimental conditions the effective lifetime, τ_{eff}, is mainly due to quenching by nitrogen and helium and equal to 5, 10, 15 ns for partial nitrogen pressures 2.4, 1 and 0.4 kPa, respectively. If the ambient gas temperature is high enough, say 650 K, then the process of rotational relaxation is relatively slow (due to effective rotational transitions with $\Delta N > 0$ and $\Delta N < 0$) and needs about 10 ns to reach steady state distribution as is shown in Figure 5 for the 10^{th} rotational level which has the

maximum population at 650 K. The same holds true also for rotational relaxation from 360 K to 650K.

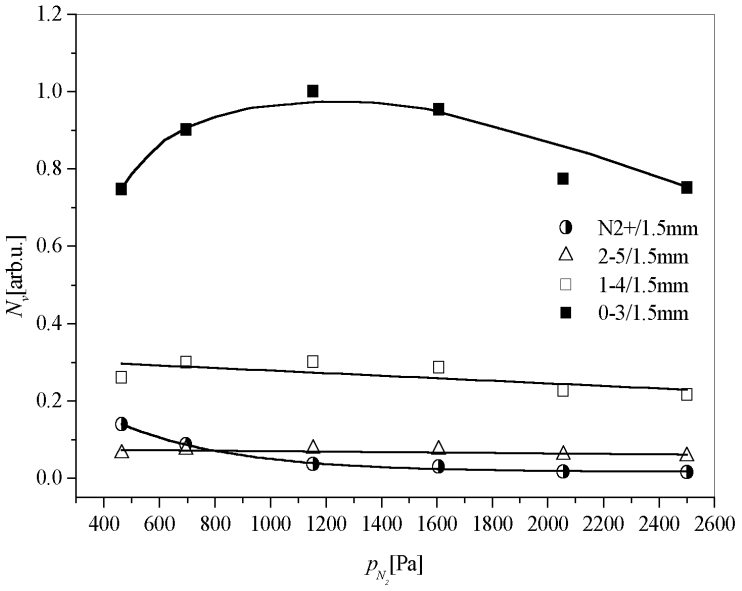


FIGURE 3. Relative population of $N_2(C,v=0\text{-}2)$ and $N_2^+(B,v=0)$ molecules at discharge gap 1.5mm.

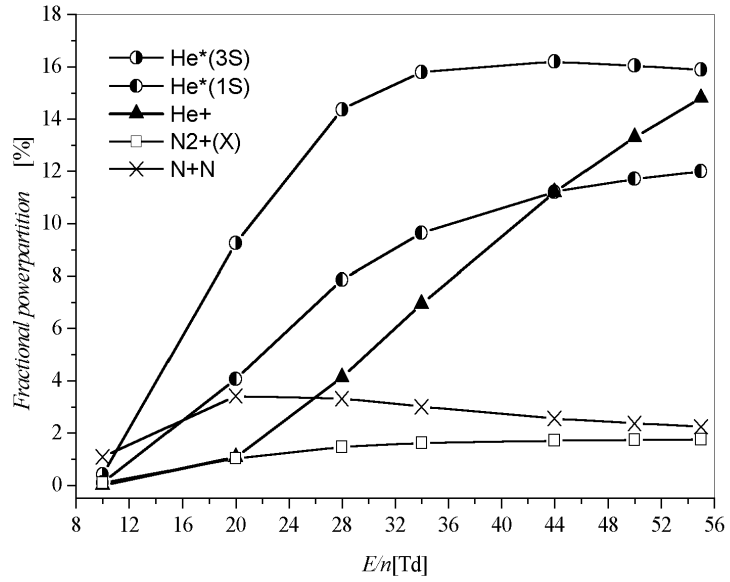


FIGURE 4. Power dissipation into different processes.

For the calculation of rotational relaxation we used the rate constants of rotational relaxation of N_2^+ in He calculated in [6]. If the ambient gas has the temperature 300 K the relaxation goes faster and the population of 10^{th} level is stabilized at 5 ns.

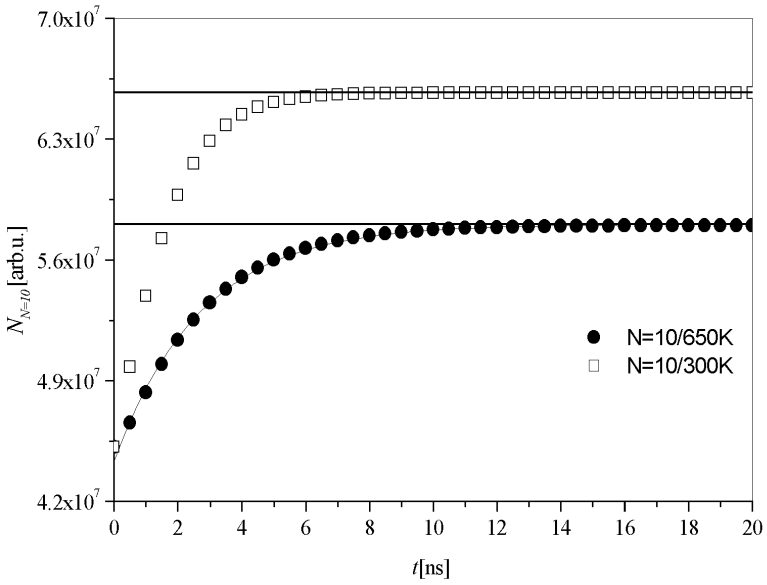


FIGURE 5. Time dependence of 10th rotational level of N_2^+(B) molecule at different ambient gas temperatures.

We obtained the rotational spectra by averaging the time variation of rotational populations during relaxation with the decay curve of excited molecule at different effective lifetimes, $\exp(-\tau/\tau_{eff})$,. Thus for τ_{eff} = 10 ns (p_{N_2} = 1 kPa) the rotational temperatures determined from the slope of the fit lines are equal (740 ± 4) K for relaxation from 1000 K to 650 K and (490 ± 6) K for relaxation from 360 K to 650 K, Figure 6. The differences between ambient gas temperature and calculated ones are 14 % and 25 % respectively. These differences occur, because we did not take into account the temperature dependence of the rate constants rotational relaxation (at high temperatures the constants are higher and relaxation is faster). Thus as is shown in Figures 5 and 6, for $\tau_{eff} \geq 10$ ns the rotational temperature will be equal to the gas temperature.

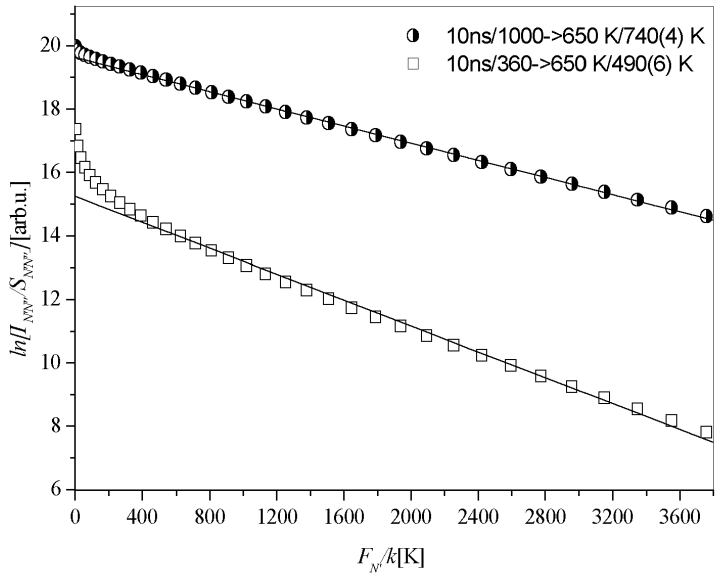


FIGURE 6. The $\ln[I_{N'N''}/S_{N'N''}]$ as function of energy of upper rotational levels of N_2^+(B) at 1 kPa N_2. The slope of the fit line gives the rotational temperature.

In our experiments we see time-averaged rotational spectra which are the convolution of rotational spectra at different times (or temperatures) and total concentration of $N_2^+(B)$ obtained from the solution of reaction kinetics in He/N_2 mixture [2]. Thus the rotational temperature of about 800 K obtained for the discharge gap 0.15 mm is an effective gas temperature in a microdischarge channel at $p_{N_2} \leq 1$ kPa nitrogen. Such high values of temperature significantly enhance the rate of gas phase processes and lead to effective formation of free radicals and excited molecules.

REFERENCES

[1] Falkenstein Z and Coogan J, *J. Phys. D: Appl. Phys.*, **30**, 817-25 (1997)
[2] Bibinov N, Fateev A and Wiesemann K, *Plasma Sources Scie. Technol.*, **10**, 579-88 (2001)
[3] Bibinov N, Fateev A and Wiesemann K, *J. Phys. D: Appl. Phys.*, **34**, 1819-26 (2001)
[4] Code EEDF, available from A.P.Napartovich, Triniti, Institute for Innovation and Fusion Research, Troizk, Moscow region, Russia
[5] Endoh M, Tsuji M and Nishimura Y, *J. Chem. Phys.*, **89**, 5368-75 (1983)
[6] Maricq M M, *J. Chem. Phys.*, **103**, 5999-6012 (1995)

DIAGNOSTICS OF DIELECTRIC BARRIER DISCHARGES AT ATMOSPHERIC PRESSURE IN NOBLE GASES

I. Radu[a], R. Bartnikas[b], G. Czeremuszkin[a] and M. R. Wertheimer[a]

a) Groupe des Couches Minces (GCM) and Department of Engineering Physics, Ecole Polytechnique, Montreal, QC H3C 3A7, CANADA

b) Hydro-Québec Research Institute, Varennes, QC J3X 1S1, CANADA

Abstract. We present experimental results of "atmospheric pressure glow discharges" (APGD) in two different electrode configurations, plane-plane and needle-plane. Although many of the phenomena we report here have been observed in different noble gases, we restrict this presentation to the case of helium, for lack of sufficient space. Discharge diagnostics have been carried out using ultra-high speed imaging (UHSI), and synchronous detection of light emission and current-voltage measurements, the former using a photomultiplier (PM). The discharge physics is discussed with reference to recent work reported by others.

1. INTRODUCTION

Scientific investigation of gas discharges at atmospheric pressure dates back to the 19th century. More recently, it has been motivated also by practical issues relating to electrotechnology and materials processing, for example. So-called dielectric-barrier discharges (DBD), of particular importance in this regard, have been reviewed by Kogelschatz and co-workers [1,2]. The DBD name derives from the fact that at least one of the electrodes of the ac-powered discharge gap is covered by a dielectric material. This facilitates the establishment of a "cold" (non-equilibrium) plasma in gases at atmospheric or near -atmospheric pressure, a fact that has opened many application areas like ozone generation, excitation of gas lasers and excimer lamps, plasma displays, surface treatment of polymers, and many others [1,2]. It was long thought that DBD occurs only in a "filamentary" mode, comprising many short (~ 100 ns), narrow (~ 100 μm) current filaments, randomly distributed in time and space over the dielectric surface. However, in 1968 Bartnikas [3] reported that ac discharges in helium can also manifest a pulseless "glow" or a hybrid "pseudo glow" regime, in which the atmospheric-pressure discharge assumes a diffuse, non-filamentary appearance. Since then, this so-called "atmospheric-pressure glow discharge" (APGD) regime has also been reported in other gases and gas mixtures, for example nitrogen [4,5], other noble gases (Ar + a few ppm of ketone [6], Ar, Ne and Kr [7,8]), and even in electronegative gases such as air [6]. Most noteworthly is the research on APGD and its applications being carried out in Japan by Kogoma, Okazaki and their collaborators [6,9], and in France by Massines and coworkers [4,10]. To distinguish APGD from filamentary discharges, the Japanese workers use Q-V measurements (Lissajous figures) [6], while the French have used the current waveform and optical measurements (high speed imaging, and spectroscopy [4,10]).

In this laboratory, we have continued using the approach of Hudon et al. [11], combining synchronous diagnostics of the discharge by electrical and optical (photomultiplier, PM) means, both capable of detecting short pulses, but the latter also able to discern pulseless glow. In the work reported here, we combine these with ultra-rapid imaging, and with measurements of Lissajous figures. Although, we have examined all of the above-named gases, we restrict this presentation to the case of helium, for reasons of space limitations.

[a] Electronic address: Michel.Wertheimer@courriel.polymtl.ca

2. EXPERIMENTAL METHODOLOGY

The experimental setup is shown schematically in Fig. 1 [5,7,8]. The chamber is a hermetic Pyrex glass cylinder with metallic end plates (1), connected to a vacuum pump and to a gas supply and flow-control unit (MKS Instruments, 8 standard litres/min, slm) with which the flowing gas (He for the present report) can be maintained at high purity and slightly above atmospheric pressure (>100 kPa).

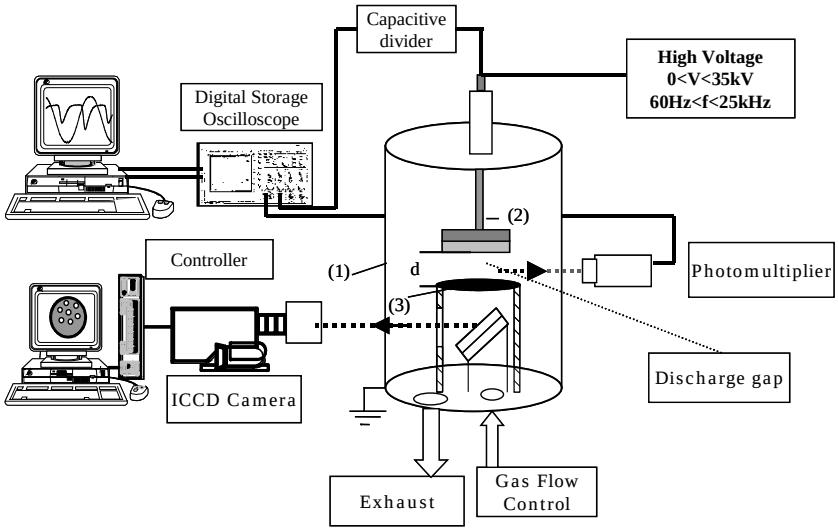


FIGURE 1. Schematic diagram of the experimental system.

The top electrode (2) is connected to the high voltage (HV) power supply, comprising a variable frequency generator (1 Hz-30 kHz), a power amplifier, an impedance matching unit, and a HV transformer. We report results obtained with four types of HV electrodes, namely:
(A) a planar, polished stainless steel (S.S.) electrode with rounded edges, 2.54 cm in diameter;
(B) the same with a thin (500 μm) plasma-sprayed dielectric layer of Al_2O_3 + 13% TiO_2 [5,7];
(C) a S.S. convex-spherical electrode with a large (10 cm) radius of curvature, 2.54 cm in diameter;
(D) a steel needle electrode with a sharp point of precisely-machined radius, 40 μm (Ogura Jewel Co.).
The electrical signal at the HV electrode is measured with a resistive divider (Tektronix P6015A) or a capacitive voltage divider built from corona-free vacuum capacitors (Jennings). The gap-spacing, d, between the upper HV electrode and the lower (grounded) electrode (3) is adjusted with a micrometer screw; the grounded, dielectric-covered electrode is either
(E) a glass plate with a transparent (indium tin oxide, ITO) conductive coating on its bottom surface, to permit observation and photography of the entire discharge zone; or
(F) a 1.6 mm thick Al_2O_3 ceramic plate, metallized on the bottom. It was used in the needle-plane experiments, to be described later; the top (Al_2O_3) surface could also be coated with an ultra-thin layer of semi-conductive graphite or metal (at floating potential), for reasons also to be explained later.

As mentioned in the Introduction, the discharges were studied by several types of diagnostics, namely:
(i) Ultra-high speed imaging (UHSI), using an intensified CCD (ICCD) digital camera (Roper Scientific PI-MAX 512RB), either parallel (plane-plane experiments) or normal (needle-plane experiments) to the gap spacing, d;
(ii) the total light emission from the gap was detected with a photomultiplier (PM, Philips 3460);
(iii) the PM signal, the applied voltage and gap-current signals were all synchronously displayed using a digital storage oscilloscope (Tektronix TDS 220, 100 MHz).

All signals, including the PI-MAX images, could be precisely synchronized and processed on a PC computer. We have studied the discharge behaviours by varying the following parameters: frequency (f) and amplitude (V) of the applied sinusoidal voltage, gap spacing (d), and electrode geometry and surface preparation (see above). Only the results for He gas are presented and discussed here, as already explained.

3. RESULTS AND DISCUSSION

3.1. Plane-Plane Geometry

Figure 2 shows electrical, optical (PM) and imaging data for discharges in He, driven by a 10 kHz, 1200 V (peak-to-peak) applied ac voltage (a). Figures 2 (a) to (i) correspond to a planar gap (d = 0.6 mm) between electrodes (A) and (E) (see Experimental section), while Fig. 2(j) shows the discharge in a gap of radially-varying spacing between electrodes (C) and (E).

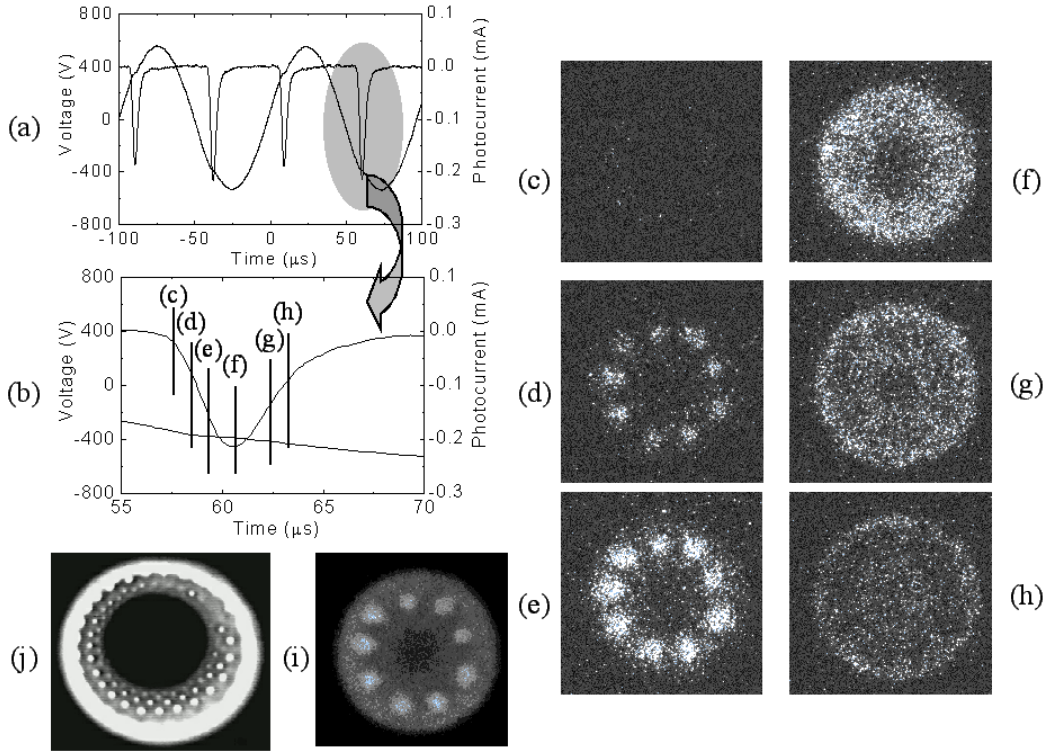


FIGURE 2: (a) Applied voltage and photomultiplier (PM) signals; (b) detail of PM peak; (c-h) time evolution (see (b)) and (i) cumulative image of a discharge in He, plane-plane geometry (d = 0.6 mm, f = 10 kHz, t_{exp} = 10 ns); (j) cumulative image with one curved electrode (He, d = 0.5 mm, f = 20 kHz).

As also reported by other workers [6,10], each half-cycle of the applied voltage is seen to display a single, relatively long-lived (~ 5 μs) breakdown event, as illustrated by the PM signal ((a), and time-expanded in (b)). However, this event is spread over the entire electrode surface area. Figures 2 (c) to (h) are a series of UHS images (exposure time, t_{exp} = 10 ns) taken with the PI-MAX camera, while (i) is the cumulative (long-duration exposure) image of the same discharge. The times corresponding to images (c) to (h) are identified by vertical lines on the expanded PM signal, Fig. 2 (b). As we have reported elsewhere [5,7,8], He discharges in short gaps, like those shown here, are often characterized by luminous "columns", which reappear in the same position in the gap over many thousands of applied voltage cycles. When the gap is widened and the voltage increased, they give way to a homogenous glow over the entire electrode area, the true "APGD" (see outer annular region in Fig. 2 (j)). The "columns" generally occur in regular (hexagonal) patterns, suggesting that electromagnetic interactive forces exist between them, as can be clearly noted in the second annular region from the periphery in (j). The same "column" patterns are also observed in other noble gases (Ne, Ar, Kr [8]), but not in nitrogen: in the APGD of this gas the single PM peak per half cycle is of much longer duration, ~ 100 μs [4,5]. From Figs. 2 (c) to (h) we note that the spatial distribution of light emission evolves in a complex manner during a single discharge event.

Figure 3 illustrates another interesting phenomenon we and others [12] have observed in connection with APGD in He: the so-called "multi-peak" effect.

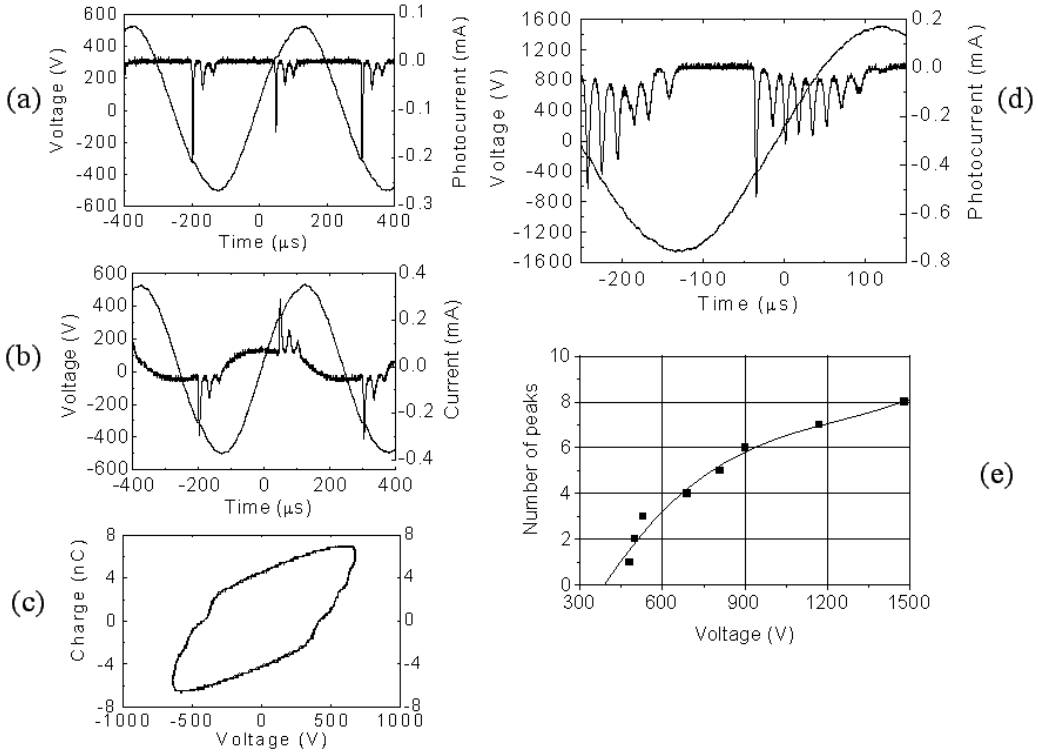


FIGURE 3. (a-e) Multi-peak effect in He as a function of voltage. (a,d) photomultiplier (PM) signal; (b) current; (c) Lissajous figure; (e) the number of peaks versus maximum voltage, plane-plane geometry (d = 0.5 mm, f = 2 kHz).

At somewhat lower f values than those in Fig. 2 (here f = 2 kHz), when the applied ac voltage is increased, a second peak appears in the PM signal, then a third (see Fig. 3 (a)), and so on. Under the particular experimental conditions represented by Fig. 3, we have observed as many as eight peaks per half cycle (see Fig. 3 (d)): their appearance with rising V is shown graphically in Fig. 3 (e). The multiple PM peaks indeed coincide with multiple discharge current pulses in perfect synchronism, as shown by Fig. 3 (b), while (c) is the corresponding Lissajous figure. Some striking features of this multi-peak phenomenon, clearly observed in (a), (b) and (d), are the facts that the peaks are very uniformly spaced and that their amplitudes follow a smooth envelope-curve, perfectly repeated from one voltage half-period to the next. Not shown here is the fact that each peak corresponds to a uniform APGD covering the entire electrode area. Akishev et al [12] have also observed this multi-peak phenomenon in He, have developed a numerical model, and attribute it to a negative differential resistance in the cathode fall region of the discharge.

3.2 Needle-Plane Geometry

In Figure 4 we portray experiments carried out in atmospheric-pressure He using electrode combinations (D) + (E) and (D) + (F) (see Experimental section), with d = 3 mm throughout. Figure 4 (a) shows a side-view of the needle-plane geometry, the lower electrode being the Al_2O_3 ceramic-covered ground plane. The discharge in (a) is a true PI-MAX image (t_{exp} = 2.5 ns) of the pulse (see (b)), 1.9 μs after its initiation, at the instant when it first contacts the Al_2O_3 surface. Coordinates "x" and "y" (see axes in (a)) represent the maximum radial and axial extent of the discharge images at any given instant. In Fig. 4 (b) we note that, like in the plane-plane configuration (Fig. 2 (a)), the discharge is characterized by a single PM pulse per voltage half-period. Due to the electrode asymmetry, however, the peak is much more intense during the positive half-cycle. Figure 4 (c) shows the time-expanded PM signal, which displays a rapidly-rising leading edge, followed by a long "tail" of total duration t ≃ 15 μs. PI-MAX images (d) to (i) show various stages of the pulse in (b,c), all taken with 2.5 ns exposure times.

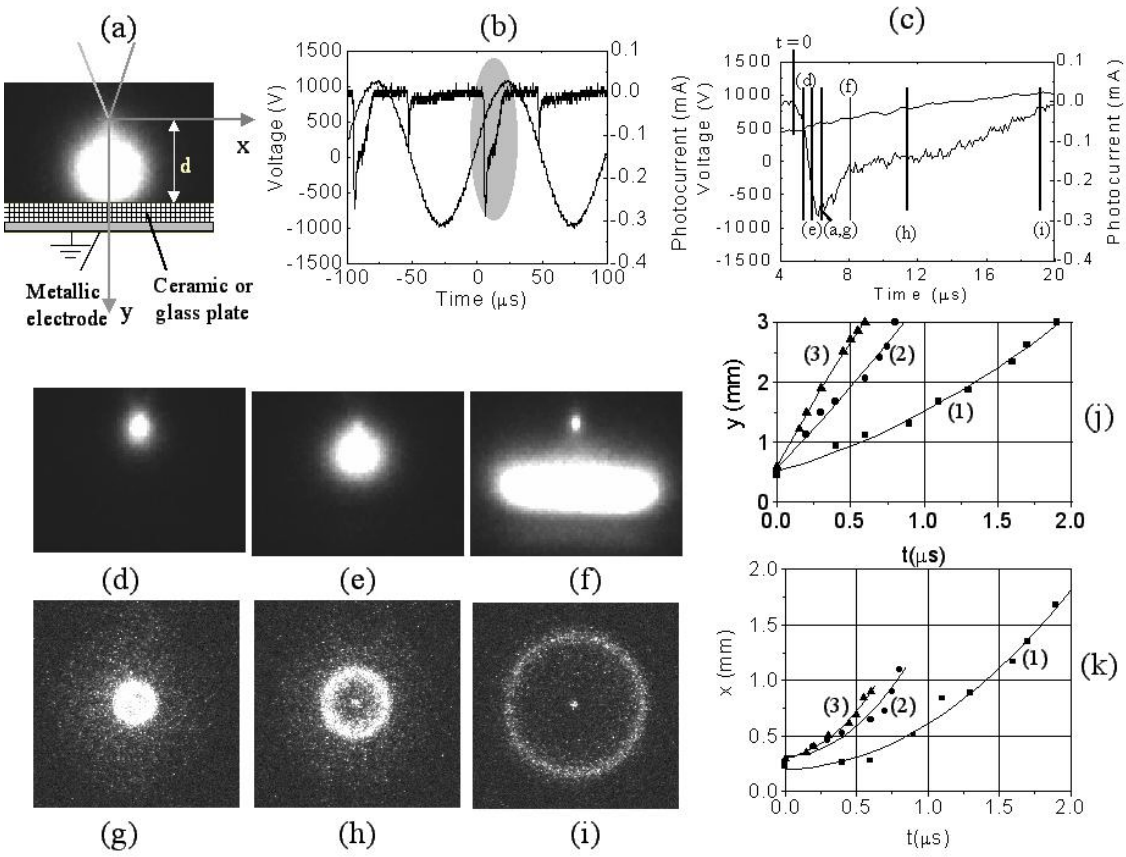


FIGURE 4. (a) Needle-plane configuration; (b) PM and applied voltage signals; (c) detail of PM peak; (d,e,f) transverse images; (g,h,i) surface images, at 2 x scale of (a,d,e,f) (exposure time, t_{exp}= 2.5 ns; t_d = 0.4 μs, t_e = 1.3 μs, $t_a = t_g$ = 1.9 μs, t_f = 2.5μs t_h = 6 μs, t_i = 15 μs); (j,k) time evolution of x and y (see (a)); for (1): bare Al_2O_3, (2): graphite – coated, (3): metal-coated Al_2O_3. (d = 3 mm, f = 10 kHz).

Images (a), (d), (e) and (f) show side views (electrodes (D) + (E)), while images (g) to (i) (note: their scale is twice that of (a) to (f)) were taken through the glass electrode (F), parallel to the discharge axis. The corresponding times (see figure caption) and positions on the PM peak are identified by vertical lines on Fig. 4 (c): Images (d), (e) and (a,g) sequentially correspond to the first 1.9 μs, during which the discharge evolves across the gap space, while (f), (h), and (i) show how the luminous region expands radially across the horizontal dielectric surface. Figures 4 (j) and (k) show the axial and radial dimensions of the discharge zone, respectively, as it traverses the He gas across the 3 mm gap: curves labelled "1", "2" and "3" correspond to the following cases: "1", bare Al_2O_3 dielectric; "2" and "3", Al_2O_3 over-coated with very thin (< 1 μm) deposits of graphite and metal, respectively, in both cases at floating potential. Clearly, Fig. 4 (j) shows that the time required by the propagating leading edge of the discharge to traverse the 3 mm gap decreases with increasing surface conductivity of the dielectric barrier, this duration being 1.9, 0.8, and 0.6 μs, for cases "1" to "3", respectively. We believe that this is the first experimental confirmation that charging/discharging of insulating or partially-conducting surfaces can strongly influence discharge kinetics in the inter-electrode gap, as predicted in a recently-published numerical model of Nikonov et al. [13,14]. If we take the slopes (propagation velocities, v) in (j) to be approximately constant, the corresponding values are v = 1.6, 3.8, and 5.0 x 10^7 cm/s, for "1", "2", and "3", respectively. As also predicted by Nikonov et al [13,14] (albeit for the case of a discharge in air), the radial dimensions of the propagating streamer are also affected by charging (or charge dissipation) on the opposite surface. This is illustrated in Fig. 4 (k), where charge buildup on the insulting surface "1" leads to a broad discharge zone (see (a)); inversely, the discharge channel is narrowed in the cases where charge spreads due to surface conduction (cases "2" and "3" in (k)), in qualitative agreement with Nikonov's findings [13,14].

4. DISCUSSION AND CONCLUSIONS

Combined experimental and numerical modeling investigations by Massines and coworkers [10] now enable quite good understanding of APGD physics in He and N_2: A necessary condition for APGD is the presence of a certain minimum "seed electron" density, n, in the gas gap between discharge events, which give rise to many Townsend-like avalanches at low electric field. These avalanches overlap, coalesce and thereby smooth the space-charge field gradients which otherwise lead to filamentation of the discharge. Palmer [15] first predicted a minimum n value $\simeq 10^4$ cm^{-3}, but Massines' model [10] indicates it to be about two orders of magnitude higher. The presence of these seed electrons, in turn, is attributable to the existence of energetic metastable states in all gases which manifest APGD, but the time between consecutive discharge periods must be short enough to ensure survival of these precursors (i.e., f in the kHz range). Beside the "memory effect" in the gas volume we have just described, there is also one associated with charge-retention on the dielectric barrier surfaces, as clearly illustrated by the experiments in Fig. 4.

Regarding the regular "column" patterns we showed in Fig. 2 and elsewhere [5,7,8], this has also been investigated by other groups [2,16]. Unlike them, however, we propose a tentative simple explanation based on the memory effect above: Analoguous to the "mixed state" of type II superconductors [17], where fluxoid filaments form a hexagonal (minimum free energy) array on account of mutual interactive forces, we believe that somewhat similar physics underlies the patterns observed in Fig. 2 (i) and (j). Under these specific conditions (relatively small d and V values), the "seed electron" volumes do not fill the entire gap, but form discrete "bubbles" or columns of space charge. Taking $n \simeq 10^6$ cm^{-3} [10] and the observed spacings (~ 300 μm), it is easy to evaluate the columns' mutual Coulomb repulsion, ~ 2nN. Returning to the fluxoid analogy, one might instead argue in terms of attractive forces between current-carrying columns, but these are 10^3 times weaker than Coulomb repulsion. For these reasons, we have coined the term "2D Coulomb crystal" to describe the regular column patterns [8].

ACKNOWLEDGEMENT

This work is being supported by grants from the Natural Sciences and Engineering Research Council of Canada (NSERC).

REFERENCES

[1] Kogelschatz U., Eliasson B., and Egli W., *Pure Appl. Chem*. **71** (1999) 1819.
[2] Kogelschatz U., *Proc. APP Spring Meeting*, Bad Honnef, Germany (2001), 10 pp.
[3] Bartnikas R., Brit. *J. Appl. Phys. (J. Phys. D.)* Ser 2, **1** (1968) 659.
[4] Gherardi N., Gat E., Gouda G., and Massines F., *HAKONE VI*, Cork, Ireland (1998), 118.
[5] Monette E., Bartnikas R., Czeremuszkin G., Latrèche M., and Wertheimer M.R., *Proc. ISPC 14*, Prague, Czech Republic (1999) 991.
[6] Okazaki S., Kogoma M., Uehara M., and Kimura Y., *J. Phys. D: Appl. Phys*. **26** (1993) 889.
[7] Miralaï F.S., Czeremuszkin G., and Wertheimer M.R., *HAKONE VII, Greifswald*, Germany (2000) 33.
[8] Radu I., Miralaï F.S., Czeremuszkin G., Bartnikas R., and Wertheimer M.R., *GEC 2001, Bull. Am. Phys. Soc*. Ser II, **46** (2001) 60.
[9] Tanaka K., Inomata T., and Kogoma M., *HAKONE VII*, Greifswald, Germany (2000) 422.
[10] Massines F., Rabehi A., Decomps P., Gadri R.B., Ségur P., and Mayoux C., *J. Appl. Phys.* **83** (1998) 2950.
[11] Hudon C., Bartnikas R., and Wertheimer M.R., *IEEE Trans. Electr. Insul*. **28** (1993) 1.
[12] Akishev Yu S., Dem'yanov A.V., Karal'nik V.B., Pan'kin M.V., and Trushkin N.I., *Plasma Phys. Reports* **27** (2001) 176.
[13] Nikonov V., Bartnikas R., and Wertheimer M.R., *J. Phys. D: Appl. Phys.* **34** (2001) 2979.
[14] Nikonov V., Bartnikas R., and Wertheimer M.R., *IEEE Trans. Plasma Sci*. **29** (2001) 866.
[15] Palmer A.J., *Appl. Phys. Lett*. **25** (1974) 138.
[16] Müller I., Punset C., Ammelt E., Purwins H.-G., and Boeuf J.-P., *IEEE Trans. Plasma Sci*. **27** (1999) 20.
[17] Huebener R.P., *Magnetic Flux Structures in Superconductors*, Springer, Berlin (1979).

MODELLING OF A DIELECTRIC BARRIER GLOW DISCHARGE AT ATMOSPHERIC PRESSURE IN NITROGEN

M Madani[a, b], A. Bogaerts[a], R. Gijbels[a]. D. Vangeneugden[b]

a) University of Antwerp (U.I.A.), Department of Chemistry, Universiteitsplein 1, B-2610 Wilrijk, Belgium
b) Flemish Institute for Technological Research (VITO), Materials Department, Boeretang 200, B-2400 Mol, Belgium

Abstract: In the last decade there is a growing interest in Dielectric Barrier Glow Discharges at atmospheric pressure. Its main advantage is the possibility to avoid the technological and economical drawbacks involved with vacuum systems, necessary in low-pressure plasma processes. Possible applications are the deposition of coatings and reactive surface treatments (e.g. cleaning, sterilisation and activation). To optimise the above-mentioned applications, it is essential to have a good understanding of the plasma discharge parameters and the processes occurring in the reactor. Some of these characteristics can be obtained experimentally, but other parameters, such as particle densities, are difficult to measure. Therefore, our objective is to obtain a better knowledge of the atmospheric pressure Dielectric Barrier Glow Discharge by means of a combination of modeling and experimental research. In this paper we will give a detailed theory of the 2 dimensional fluid model for nitrogen used for our purposes. The species taken into account are N^+, N_2^+, N_3^+, N_4^+ and some metastable states. The results that will be shown include particle density distributions and electrical characteristics such as potential and electric field distributions and time variations of discharge currents.

1. DESCRIPTION OF THE MODEL

1.1. Introduction

For modelling a Dielectric Barrier Glow Discharge at atmospheric pressure we use a 2 dimensional fluid model [1]. In this kind of model we assume that the plasma species form a continuum in equilibrium with the electric field. The different species present in the plasma, such as electrons, ions and neutrals are described by balance equations (based on conservation laws) and flux equations of diffusion and migration in the electric field. For the electrons an energy balance equation is also solved. The electric field is calculated self-consistently using the Poisson equation. The collision rates and electron transport coefficients can be obtained by solving the Boltzmann equation for the EEDF (electron energy distribution function).

1.2. Equations

In the fluid model, for each particle in the discharge a density balance is solved, given by following equation:

$$\frac{\partial n_k}{\partial t} + \overline{\nabla}.\overline{\Gamma_k} = S_{reac,k} \qquad (1)$$

where n_k and $\overline{\Gamma_k}$ are the density and flux of particle k and $S_{reac,k}$ is the source term which describes the creation or the destruction of particle k.

[a] Madani@uia.ua.ac.be, Myriam.Madani@vito.be

The flux for each particle consists of a drift term caused by the electric field and of a diffusion term caused by density gradients.

For the electrons the equation is:

$$\overline{\Gamma}_e = -\mu_e n_e \overline{E} - D_e \overline{\nabla} n_e \tag{2}$$

For the positive ions the migration under the influence of the electric field is opposite to that for the electrons:

$$\overline{\Gamma}_i = \mu_i n_i \overline{E} - D_i \overline{\nabla} n_i \tag{3}$$

The neutral species are not influenced by the electric field so the equation only consists of a diffusion term:

$$\overline{\Gamma}_n = -D_n \overline{\nabla} n_n \tag{4}$$

μ and D are respectively the mobility and diffusion transport coefficients.

For the electrons an electron energy equation is solved, which describes their energy balance and is given by:

$$\frac{\partial n_e \varepsilon}{\partial t} + \overline{\nabla}.\overline{\Gamma}_w = -e\overline{\Gamma}_e \overline{E} - k_{ion} n_e N_b H_{ion} \tag{5}$$

In this equation H_{ion} is the ionisation energy and ε is the average electron energy. The first term on the righthand side gives de Ohmic heating and the second term describes the loss of energy due to collisions. For ions and neutrals we assume that they are in equilibrium with the electric field (due to there nearly equal mass), so no energy balance is necessary.

The energy flux is again described by a drift-diffusion approximation:

$$\overline{\Gamma}_w = -\frac{5}{3}\mu_e n_e \varepsilon \overline{E} - \frac{5}{3} D_e \overline{\nabla} n_e \varepsilon \tag{6}$$

Finally the electric field is solved by the Poisson equation:

$$\Delta V = -\frac{e}{\varepsilon_0}\left(n_i - n_e\right) \tag{7}$$

1.3. The EEDF

The collision rates, electron transport coefficients and the average electron energy are obtained by solving a two-term Boltzmann equation for the EEDF. The EEDF specifies the number of electrons at a certain position, with a certain velocity and at a given time. The calculated electron impact collision rates are then used to calculate the density profiles in the fluid model. The densities of the background neutrals serve as input for the Boltzmann solver. The 2 parts of the model (the fluid and the EEDF part) are run alternately until the changes in the background neutrals at the beginning of 2 succeeding RF cycles are less than 10^{-4}.

1.4. The boundary conditions

In order to solve the differential equations mentioned above, some boundary conditions must be specified for potential and density profiles. We also have to take into account the influence of the dielectric on the discharge. Due to the accumulation of charge on the dielectrics the electric field in the plasma changes. In the model we will calculate the surface charge on the substrate at the side of the discharge and include the corresponding change in the electric field in the model calculations.

2. INPUT DATA FOR THE MODEL

2.1. Geometry

We use a parallel plate configuration, consisting of two disk-shaped stainless steel electrodes with a diameter of 150mm. Both electrodes are covered with an alumina plate of 2mm thickness. The gap can vary from 1mm to 5mm. An AC voltage is applied with amplitudes that can go up to 20kV peak and a frequency in the range of 50Hz-500kHz

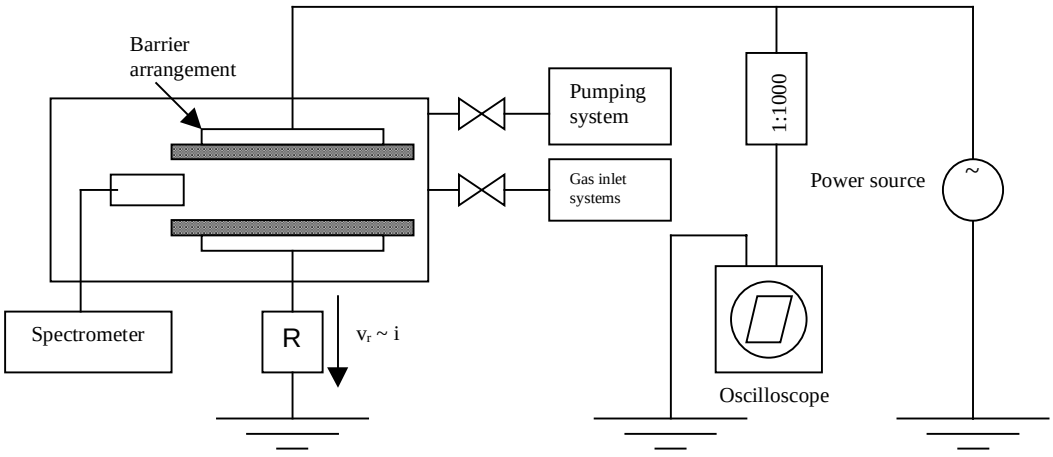


FIGURE 1. Reactor geometry used in the model and for validation experiments

2.2. Nitrogen species

The nitrogen species that are taken into account are:

The ground state $N_2\left(X\,^1\Sigma_g^+\right)$, two metastable states $N_2\left(A^3\Sigma_u^+\right), N_2\left(a'^1\Sigma_u^-\right)$, two radiative states $N_2\left(B^3\Pi_g\right), N_2\left(C^3\Pi_u\right)$, the atom $N\left(^4S\right)$ and four ions N^+, N_2^+, N_3^+, N_4^+.

2.3. Reactions

The reactions taken into account in the model are the following:

electron reactions	*Threshold energy* (eV)
1. $N_2 + e^- \rightarrow N_2^+ + 2e^-$	15.480
2. $N_2 + e^- \rightarrow N_2\left(A^3\Sigma_u^+\right) + e^-$	5.986
3. $N_2 + e^- \rightarrow N_2\left(a'^1\Sigma_u^-\right) + e^-$	8.179
4. $N_2 + e^- \rightarrow N_2\left(C^3\Pi_u\right) + e^-$	10.784
5. $N_2 + e^- \rightarrow N_2\left(B^3\Pi_u\right) + e^-$	6.992
6. $N_2\left(A^3\Sigma_u^+\right) + e^- \rightarrow N_2^+ + 2e^-$	10.790
7. $N_2\left(a'^1\Sigma_u^-\right) + e^- \rightarrow N_2^+ + 2e^-$	8.560
8. $N_2 + e^- \rightarrow N^+ + N + 2e^-$	12.000

ion – neutral reactions	*reac rate coeff* $(cm^3 s^{-1})$
9. $N_2^+ + N_2\left(A^3\Sigma_u^+\right) \rightarrow N_3^+ + N$	$3.0x10^{-10}$
10. $N_2^+ + N \rightarrow N^+ + N_2$	$7.0x10^{-13}$
11. $N_3^+ + N \rightarrow N_2^+ + N_2$	$6.6x10^{-11}$
12. $N_4^+ + N_2 \rightarrow N_2^+ + 2N_2$	$2.4x10^{-15}$
13. $N_4^+ + N \rightarrow N^+ + 2N_2$	$1.0x10^{-11}$

neutral – neutral reactions	
14. $N_2\left(A^3\Sigma_u^+\right) + N_2\left(A^3\Sigma_u^+\right) \rightarrow N_2\left(B^3\Pi_g\right) + N_2$	$1.0x10^{-11}$
15. $N_2\left(A^3\Sigma_u^+\right) + N_2\left(A^3\Sigma_u^+\right) \rightarrow N_2\left(C^3\Pi_u\right) + N_2$	$1.0x10^{-10}$
16. $N_2\left(A^3\Sigma_u^+\right) + N_2\left(a'^1\Sigma_u^-\right) \rightarrow N_4^+ + e^-$	$5.0x10^{-11}$
17. $N_2\left(a'^1\Sigma_u^-\right) + N_2\left(a'^1\Sigma_u^-\right) \rightarrow N_4^+ + e^-$	$2.0x10^{-10}$
18. $N_2\left(A^3\Sigma_u^+\right) + N \rightarrow N_2 + N$	$4.0x10^{-11}$
19. $N_2\left(C^3\Pi_u\right) + N_2 \rightarrow N_2\left(a'^1\Sigma_u^-\right) + N_2$	$1.0x10^{-11}$
20. $N_2\left(a'^1\Sigma_u^-\right) + N_2 \rightarrow N_2 + N_2$	$2.0x10^{-13}$

The cross sections used for the electron reactions are taken from Phelps and the reaction rates

coefficients for the other reactions are taken from [2-4].

3. RESULTS AND VALIDATION EXPERIMENTS

Typical results that can be obtained by numerical modelling are spatio-temporal distributions of densities, potential, electric field and mean electron energy. The fluxes of the different plasma species can also be obtained. We can also obtain information on the different ionisation processes, and the relative importance of the different loss and production processes of the species. In the figure below some of the results from the EEDF model (see § 1.3.) are given.

We wish to validate these results by means of experiments. Techniques that can be used for this purpose are Optical Emission Spectroscopy and measurement of electrical characteristics with an oscilloscope.

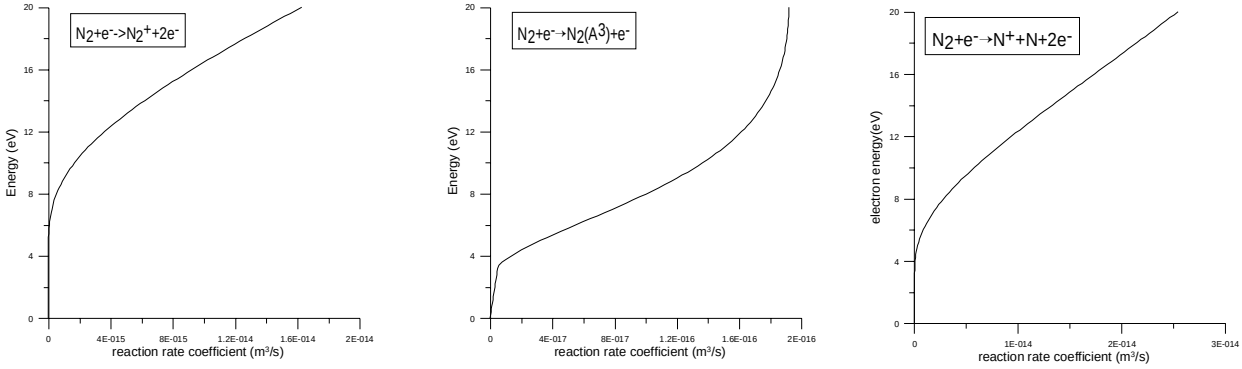


FIGURE 2: reaction rate coefficients in function of electron energy for some electron reactions.

ACKNOWLEDGMENTS

We would like to acknowledge VITO for its financial support and V.A. Maiorov, W. Goedheer and F. Massines for some interesting discussions.

REFERENCES

[1] GJ Nienhuis, Ph.D. thesis, Utrecht University 1998
[2] N. Gherardi, E. Gat, F. Massines, S. Lemoing, P. Segur, Proceedins ISPC-15
[3] A.A. Matveyev, V.P. Silakov, PSST, 1999, **8**, p.162-178
[4] Y.B. Golubovskii, V.A. Maiorov, J. Behnke, J.F. Behnke, Proceedings ISPC-15

ELECTRIC FIELD MODELLING FOR POINT-PLANE GAP

V. Repän, M. Laan[a] and T. Plank

Institute of Experimental Physics and Technology, University of Tartu, Tähe 4, 51010 Tartu, ESTONIA

Abstract. The electric field distribution for point-plane gap is modelled both for stressed point and stressed plane electrodes. In simulations, the influence of the discharge chamber walls is taken into account. The size of an avalanche and the corresponding current pulse are calculated. The results are compared with those got using other field distribution approximations.

1. INTRODUCTION

For gas discharges, the distribution of the electric field is the most important parameter, which determines the spatio-temporal development of discharges as well as the waveform of the recorded current. In the case of the modelling of corona discharges in point-plane gaps, the simplest Laplacian field approximation is the spherical one and it is widely used [1, 2]. On the basis of numerical modelling, Abou-Seada [3] presented for the ionisation zone of the gap an analytical expression of the field distribution *E(x)* along the gap axis. The approximation does not satisfy the normalization condition $U = \int_0^d E(x)dx$, where U is the applied voltage and d is the gap length. Coelho and Debeau [4] derived a formula for field distribution in hyperbolic approximation. The latter approximation satisfies the normalization condition. It should be pointed out that the approximations mentioned do not take into account the influence of the grounded walls of the discharge chamber on the field distribution.

Our experience of the modelling of non-self-sustained negative DC corona pulses confirms that the using of above-described approximations does not assure a satisfactory coincidence of simulated and recorded current waveforms. For this reason we undertook the numerical simulation of the field distribution which considers also the role of the discharge chamber walls. This paper presents the main results of the modelling and compares waveforms of avalanches calculated using different electric field *E(x)* approximations.

2. EXPERIMENTAL

We studied [5] the regularities of negative corona discharge at atmospheric pressure in air initiated by UV light pulses. UV pulses of 3.5 ms duration were formed using a deuterium lamp and a chopper and focused to the point tip. The discharge was ignited in a 4-cm point-plane gap. The point electrode was a 1-mm wire with hemispherical tip and the diameter of the plane electrode was 15 cm. The diameter of the metal walls surrounding the discharge chamber was 22 cm. Under these conditions, the onset potentials of the current pulses of negative corona (Trichel pulses) depend on which electrode is stressed. The onset potential for stressed point is ≈ 8 kV and for stressed plane it is ≈ 13 kV. Below the onset potential, the discharge was non-self-sustained, i.e. the current arises only due to the action of UV light. For a certain voltage, the maximum current recorded depends on properties of the point coating material and the intensity of UV light but in any case the current waveform has a strong dependence on which electrode is stressed. Figure 1 presents current pulses induced by UV light pulses at ≈ 20% below the corresponding onset of Trichel pulses (6.5 and 12 kV for stressed point and

[a] Electronic address: laan@physic.ut.ee

plane, respectively). The most striking difference between the current pulses is the duration of the current decay, which exists after the action of UV light. As in our time-scale the current of positive ions and electrons stops immediately, the large difference in current tail durations can be caused only by different drift-times of negative ions. It was the first reason for modelling the electric field distribution for stressed point and plane separately.

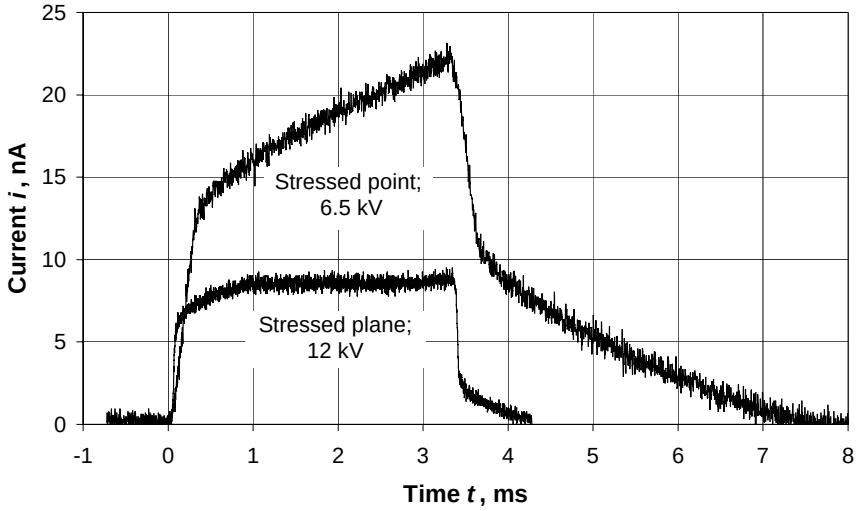


FIGURE 1. UV-initiated current pulses. The duration of the light pulse is 3.5 ms.

3. MODELLING

3.1. Procedure and data

The distribution of the Laplacian electric field $E(x,r)$, where r denotes the distance from the gap axis, is calculated numerically. The rectangular computation domain is divided first into uniform square grid having 5 nodes per millimetre. The domain is taken a little larger than the discharge gap. On the gap axis, the condition of symmetry is used. In the vicinity of the point electrode (about 1 mm around the point electrode tip), additional iterations are made. The domain is divided into a square grid having 100 nodes per millimetre.

The potential of each node is calculated using finite difference method together with the successive over-relaxation method [6]. For the convergence criterion of the iterations is taken the requirement that the relative residual in the iterative process should not exceed 10^{-14} at each interior node.

The accuracy of the computing algorithm is tested by the numerical evaluation of the well-known field distributions of coaxial cylinders and concentric spheres. The difference between analytical and numerical results is less than 0.5%.

Finally, the electric field strength is found for each node using the values of potential of that node and surrounding nodes.

To check the quality of calculation of the electric field strength, we have calculated the normalization integral. It differs from the applied voltages less than 10 V.

For the calculation of the drift times of charged particles, ionisation and attachment coefficients in air and nitrogen, the data from [7 - 11] are used. For the calculation of the current in the external circuit, the gap is split into discs. The discs size in the axial direction coincides with the grid size used in modelling. According to Ramo-Shockley theorem, the current is recorded as the sum $i = \frac{e}{U}\sum_k N_k v_k E_k$, where k is a disc number, N_k, v_k, E_k are charge carrier number, drift velocity and field strength in the disc, respectively.

3.2. Results

Figure 2 gives the distribution of the equipotential lines for the gap used in experiments (Section 2). The distributions of equipotential lines for stressed plane and point differ considerably. In the case of the stressed plate in the remarkable part of the space between the electrodes, the field is almost homogeneous both in the axial and the radial directions.

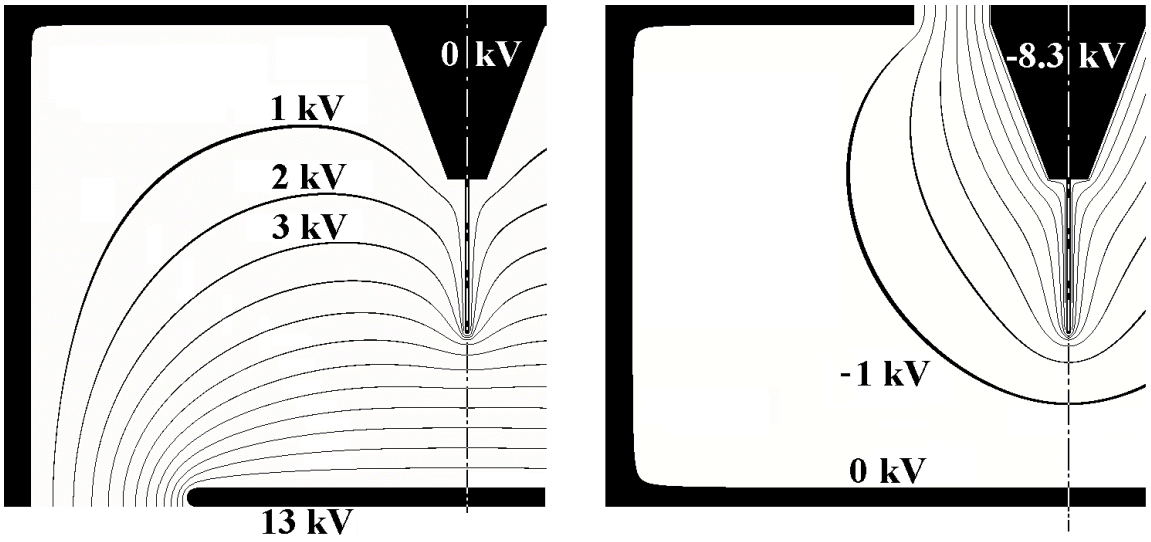


FIGURE 2. Distribution of equipotential lines at the onset of Trichel pulses: on the left - stressed plate; on the right - stressed point; the gap between the equipotential lines is 1 kV; the gap axis is presented by the dashed line; the gap length is 4 cm and the walls are at the distance of 11 cm from the axis.

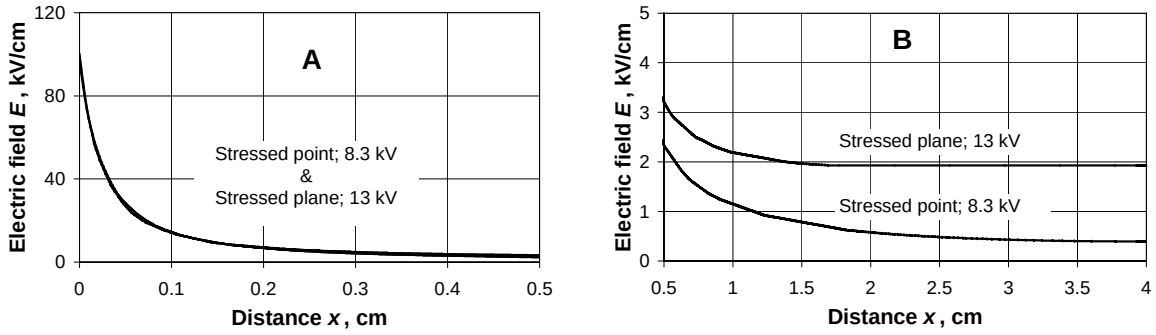


FIGURE 3. Field distributions along the gap axis at the onset of Trichel pulses: **A** - ionisation zone; **B** - drift zone.

In the ionisation zone at the onset potential of Trichel pulses, the field distributions along the gap axis demonstrate a perfect coincidence (Figure 3A). In the drift zone, axial fields have a large difference (Figure 3B): in the case of the stressed plane electrode, the field is much higher than it is for stressed point electrode. First of all, the difference in field distributions appears in drift times of negative ions. As a sample, the drift time of negative ions is calculated at voltages where curves of Figure 1 are recorded. Calculated drift times (0.9 and 3.6 ms for stressed plane and stressed point, respectively) are very close to the durations of current tails in Figure 1. Here it should be pointed out that in spite of the movement of the negative ions in low electric fields and consequent small value of the field factor in Ramo-Shockley formula, the contribution of negative ions to the total current is large. This is caused by the high concentration of negative ions in the drift zone.

3.3. Comparison with other field approximations

Figure 4 shows that Abou-Seada formula [3] gives in the ionisation zone the field distribution, which is closest to that simulated by us. There is an obvious trend: the larger is the diameter of the surrounding walls the better Abou-Seada's approximation works. Two other approximations give considerably larger deviations from our results.

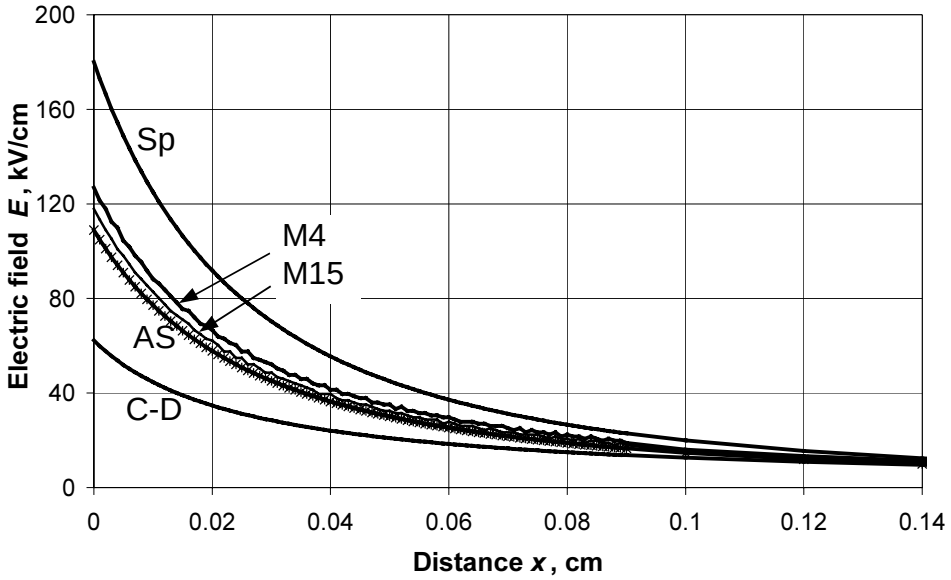


FIGURE 4. Field distribution for different approximations; applied voltage $U = 9$ kV. **Sp** - spherical field distribution; **M4** - our field modelling for stressed point (4 cm walls radius); **M15** - our field modelling for stressed point (15 cm walls radius); **AS** - field distribution according to [3]; **C-D** - field distribution according to [4].

The calculation of the avalanche size gives even more drastic difference (Figure 5): the spherical approximation overestimates the avalanche by five orders of magnitude while according to Coelho and Debeau formula the ionisation is practically missing.

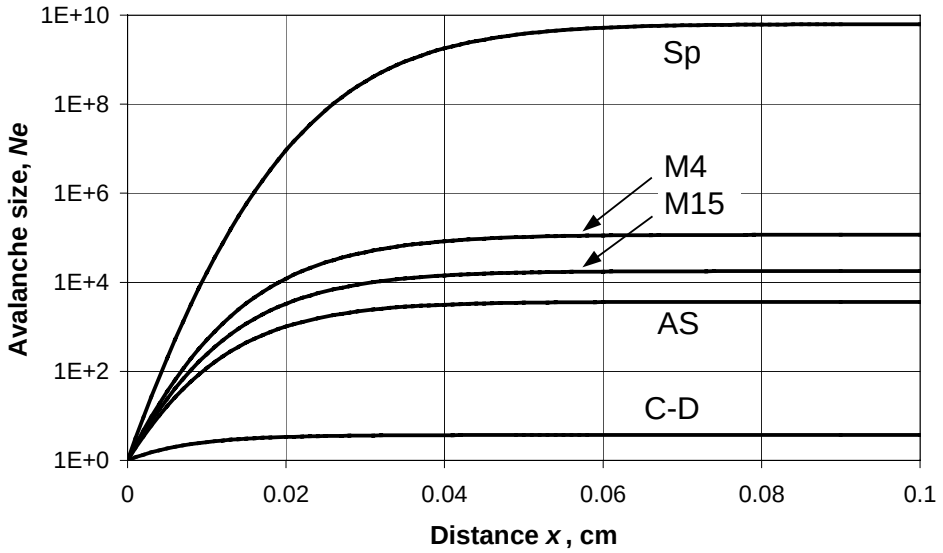


FIGURE 5. Number of electrons in an avalanche as a function of the distance from the point calculated for the stressed point in nitrogen at U = 9 kV. Explanation of the abbreviations is at the capture of Figure 3. NB! Note the logarithmic scale on the ordinate.

In spite of a huge discrepancy in avalanche sizes, the spherical and Abou-Seada approximations describe the temporal changes of the electron component of the current in nitrogen correctly. Choosing the proper fitting coefficients (inset in Figure 6), the waveforms of the current of different approximations practically coincide. In the case of Coelho and Debeau formula, the voltage as well as the effective radius of the point are varied but the current waveform does not coincide with those presented in Figure 6.

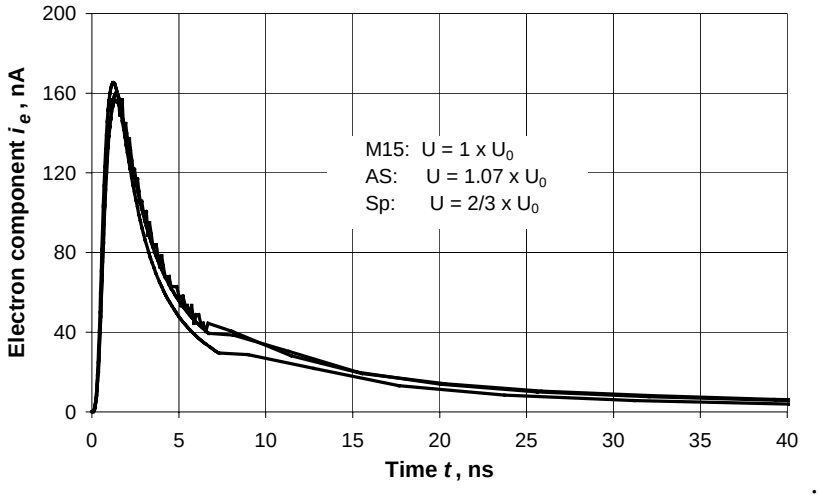


FIGURE 6. Fitting of electron components of the current for U_0 = 9 kV in nitrogen.

4. CONCLUSIONS

If we are interested only in the temporal evolution of the phenomena in the ionisation zone even the spherical approximation gives a good presentation of the reality.

Abou-Seada approximation gives quantitatively correct results for ionization zone if the ratio of the walls distance to the gap length is larger than three.

In the case of discharges in electronegative gases where the contribution of the negative ion component to the total current is large, a correctly modelled field distribution must be used.

REFERENCES

[1] Morrow R., Theory of negative corona in oxygen., *Phys. Rev. A* , **32,** 1799-1809 (1985)

[2] Sigmond R. S., The oscillations of the positive glow corona., In: *Proc. XXIII Int. Conf. Phenom. Ionized Gases, Inv. Papers*, C4-383, Toulouse, 1997

[3] Abou-Seada M. S., Calculating of high-frequency breakdown voltages of point-to-plane air gaps. In: *IEEE IAS 15th Annual Meeting*, 1980, Vol. 2, pp. 1118-22

[4] Coelho R., Debeau J., Properties of the tip-plane configuration., *J. Phys. D: Appl. Phys.*, **4**, 1266-80 (1971)

[5] Laan M., Repän V., Paris P., Waveforms of UV-induced current pulses of negative corona, In: *11thSymp. El. Processes & Chem. Reactions*, Contr. Papers 2, Low Tatras, 1998, pp 271-273

[6] Zhou P., *Numerical Analysis of Electromagnetic Fields*, Berlin: Springer, 1993

[7] Tammet H., Reduction of air ion mobility to standard conditions., *J. Geophys. Res.*, **103,** 13 933-7 (1998)

[8] Badaloni S., Gallimberti I., *Basic data of air discharges*, Upee-72/05, 1972

[9] Wen C., Wetzer J. M., Determination of swarm parameters in dry air with a fast timeresolvet swarm technique. In: *Proc. XIX Int. Conf. Phenom. Ionized Gases*, Vol. 3, 1989, p. 592

[10] Kennedy J. T., *Study of the avalanche to streamer transition in insulating gases*, Ph. D Thesis, Eindhoven University of Technology, 1995

[11] Wen C., *Time resolved swarm studies in gases with emphasis on electron detachment and ion conversion*, Ph. D Thesis, Eindhoven University of Technology, 1989

OES INVESTIGATIONS OF A PULSED MICROWAVE PLASMA USED FOR METHANE CONVERSION TO C_2 HYDROCARBONS

M. Magureanu[a,b], M. Heintze[a] and M. Kettlitz[a]

a) Institut für Niedertemperatur Plasmaphysik, Friedrich-Ludwig-Jahn-Str. 19, 17489 Greifswald, GERMANY
b) on leave from National Institute for Laser, Plasma and Radiation Physics, Bucharest-Magurele, ROMANIA

Abstract. Methane conversion into C_2 hydrocarbons, in particular acetylene, in a pulsed microwave (MW) discharge was investigated with respect to the effect of the duration and repetition frequency of the MW pulses. Optical emission spectroscopy (OES) provides qualitative information concerning the active species generated in the plasma. Their temporal evolution during the MW pulse explains the observed influence of the pulse duration on the conversion degree and distribution of the C_2 products.

1. INTRODUCTION

The decomposition of methane in MW discharges receives considerable interest both for fundamental and applicative research. Applications are the growth of diamond films and the potential conversion of methane into higher hydrocarbons. Modeling [1, 2] and experimental [3] studies conclude that pulsed discharges present clear advantages over cw excitation, one of the most important being the chemical aspect, since the production of active species may be enhanced as compared to a continuous discharge of the same average power [1, 3].

In this study a pulsed MW plasma was used for converting methane into C_2 hydrocarbons, in particular acetylene. The influence of the pulse duration and repetition frequency on the methane conversion degree and on the distribution of reaction products was investigated. For the investigation of the active species generated in the plasma OES was used.

2. EXPERIMENTAL SET-UP

A detailed description of the experimental apparatus can be found in [4]; in the following only a brief account will be given. The pulsed MW discharge was produced in a 6 mm i.d. tubular quartz reactor, positioned through a rectangular waveguide, parallel to the electric field. MW pulses with 1200 W peak power were used, with repetition frequencies of 200 Hz and 1 kHz and pulse durations between 20 - 300 μs. The experiments were performed in conditions of continuous flow (98 sccm methane and 12 sccm argon, added as internal standard) and constant pressure (30 mbar).

The analysis of the stable reaction products was done by gas chromatography and mass spectrometry [4]. For the OES measurements a 1 m spectrograph was used with 150 and 2400 groves/mm gratings, resulting in a spectral resolution of 0.011 nm at 500 nm. An intensified CCD (1024x1024 pixels) was used as detector. For the calibration a tungsten strip lamp was used. Time-resolved measurements were done by gating the image intensifier with a time window of 5 μs. An accumulation of the light over 10-10000 MW pulses was done in order to obtain a reasonably high signal.

[a] Electronic address: magu@inp-greifswald.de, monimag@alpha2.infim.ro

3. RESULTS AND DISCUSSION

The results of experiments performed in the same energy input range for two pulse frequencies, ν = 1 kHz and ν = 200 Hz and pulse durations 20 - 60 µs and 100 - 300 µs, respectively, are shown in Fig. 1.

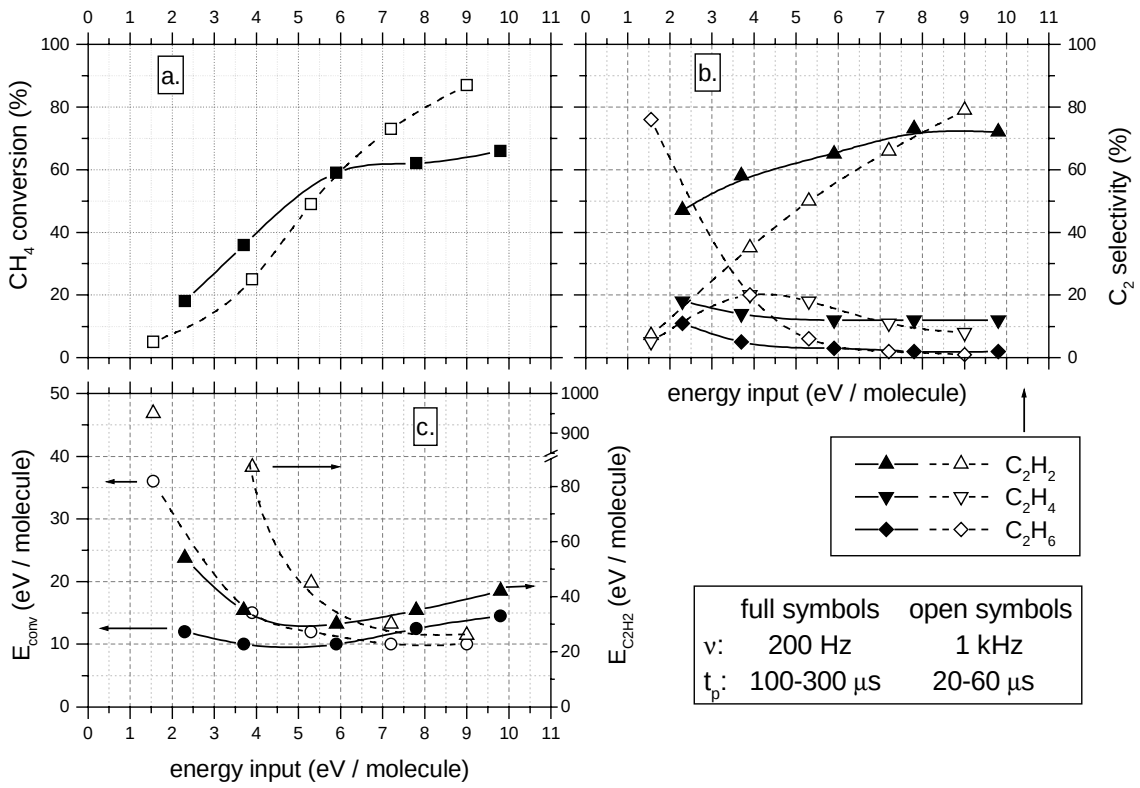


FIGURE 1. a. Methane conversion; **b.** C_2 selectivities; **c.** Energy requirement for conversion and for acetylene formation vs. energy input.

In the case of short pulses at high repetition frequency, the methane conversion shows an approx. linear increase with the energy input, reaching almost 90%. At low energy input, a higher conversion degree is achieved when using longer pulses at low frequency; by increasing discharge power in these conditions the conversion increases also linearly up to 60% and then saturates below 70%. The minimum energy cost for methane conversion in both cases is around 10 eV per converted methane molecule.

Concerning the products distribution, a considerably higher degree of dehydrogenation can be observed for the longer pulses at lower frequency. The short pulses yield ethane as the main reaction product for low energy input. With increasing discharge power, the selectivity towards ethane drops sharply, while the selectivity to acetylene increases approx. linearly up to 80%. A minimum value for the energy requirement for acetylene formation of 26 eV / molecule was obtained in these experiments. In the case of long pulse durations at low frequency, acetylene is the most abundant reaction product over the entire energy range investigated.

In order to establish if the higher dehydrogenation is only determined by the pulse length, or if an effect of the pulse repetition rate on the reaction is also involved, experiments were carried out at constant pulse length (t_p = 20 µs), with increasing the pulse frequency (ν = 1 - 3.5 kHz). The methane conversion and products distribution show a similar dependence on energy input as in the case of constant ν = 1 kHz

pulse frequency, however the dehydrogenation is less significant, resulting in a lower conversion degree (60 - 65% at 8.5 eV/molecule) and lower selectivity towards acetylene (60%).

In order to investigate the behaviour of the active species present in the discharge, the emission intensities of CH ($A\ ^2\Delta \rightarrow X\ ^2\Pi$; 431.5 nm), C_2 ($d\ ^3\Pi_g \rightarrow a\ ^3\Pi_u$; 516.5 nm) H_α ($n' = 3 \rightarrow n = 2$; 656.5 nm) and Ar ($4p \rightarrow 4s$; 750.4 nm) were monitored during the experiments. The variation of the emission intensities, normalised to their maximum value, as a function of energy input is shown in Fig. 2 in similar experimental conditions as for Fig. 1. The change in argon concentration due to the increase in total flow during the experiments has little influence on the emission intensities of CH, C_2 and H_α.

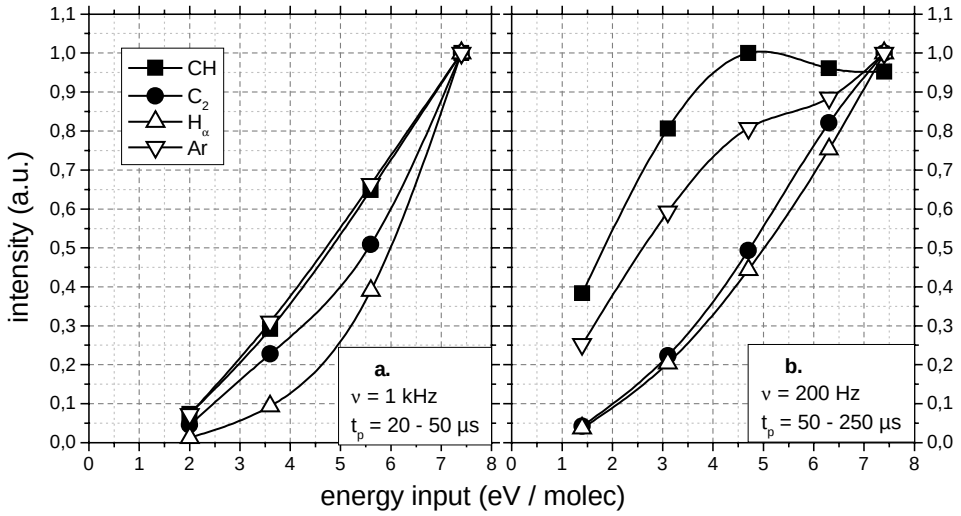


FIGURE 2. Normalised emission intensities vs. energy input.

Fig. 3 illustrates the time variation of the emission intensities of CH, C_2, H_α and Ar, along a 200 µs pulse obtained for 200 Hz repetition frequency. For short pulses at 1 kHz repetition frequency, the emission intensities have similar shapes as in the beginning of the long pulse, therefore in the following only the temporal evolution during the 200 µs pulse will be discussed.

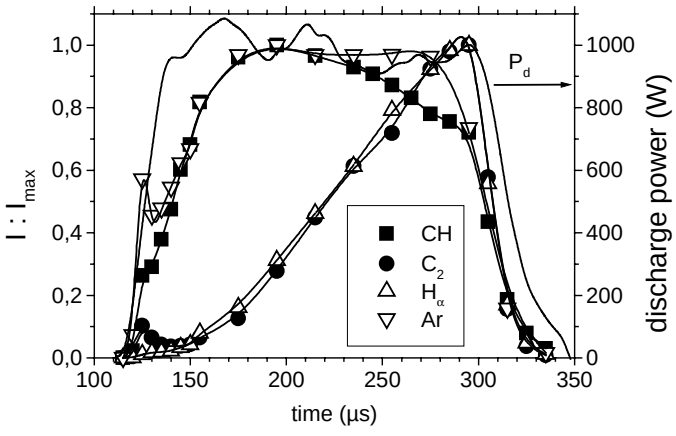


FIGURE 3. Temporal variation of the normalised emission intensities of the Ar, H_α lines and CH, C_2 bands.

The argon emission line shows a peak over the first 10-15 µs of the pulse and then increases during approx. 50 µs and reaches an approx. constant value for the remaining time of the pulse. This behaviour can be attributed to the variation of the electron density and temperature during the MW pulse. Modeling studies of pulsed MW plasmas [1, 2] predict the existence of a sharp peak in the electron temperature in the early stages of the pulse, while the evolution of the electron density is much slower. The relatively few electrons present in the ignition phase of the discharge undergo a strong and fast heating, after which, following the increase in electron density, the

temperature decreases strongly, giving rise to the temperature peak in the beginning of the pulse. The peak in the argon line intensity can be therefore explained by the correlated effect of the increase in electron density and the peak in electron temperature.

The relatively fast increase of the CH emission intensity could be due to the high electron temperature at the start of the pulse. Another possible reason for this fast increase may be the formation of the CH radical directly in the excited state by dissociative excitation of methane. After reaching a maximum, in ~50 µs from the beginning of the pulse, the CH intensity shows a slow decrease for the remaining pulse duration. This decrease is likely to be the result of both the methane depletion towards the end of the MW pulse and of the recombination of the radicals to form C_2H_x species. In view of this temporal evolution, the variation with energy input of the integrated CH emission intensity (Fig. 2) can be explained: it increases as the duration of the MW pulse increases, for pulses shorter than approx. 100 µs, and for longer pulses the decrease in the CH intensity towards the end of the pulse is reflected in the decrease of the overall CH emission.

There is a correlation between the CH emission and the degree of methane conversion, since the CH radical is obtained by subsequent dehydrogenations of methane according to the scheme: $CH_4 \rightarrow CH_3 \rightarrow CH_2 \rightarrow CH$. The linear increase in the CH intensity for pulses below 100 - 150 µs reflects the increasing methane conversion (Fig. 1a), approximately linear with the discharge power (respectively pulse duration). The saturation in methane conversion seen in Fig. 1a for longer pulses ($t_p > 200$ µs), is likely to be caused by the methane depletion during the pulse, and is observed earlier for the CH intensity (for $t_p > 150$ µs) due to the contribution of the radicals recombination to the CH loss.

Concerning the C_2 emission, spectroscopic studies in MW $CH_4 + H_2 + Ar$ plasmas typical for diamond deposition showed that a linear relation exists between the bandhead intensity of the (0-0) Swan band and the C_2 concentration in the plasma [5, 6].

The emission intensity of the (0-0) C_2 Swan band shows a similar peak as for the argon line in the early stages of the pulse. For long pulses, it shows a marked increase, starting after 40-50 µs from the beginning of the pulse. The delay in the on-set of the C_2 emission is correlated with the time needed for dimerisation and for complete dehydrogenation.

The emission intensity of the atomic hydrogen H_α line shows a continuous increase during the MW pulse, very slow in the beginning of the pulse and becoming significant after the first 40-50 µs. The delay of the on-set of the H_α emission as compared to the argon emission suggests that the H atoms are generated in the ground state by dissociation of CH_x (x = 1 - 4) and H_2 and are subsequently excited by electron impact. A similar behaviour, observed in a $H_2 + Ar$ MW plasma [7], was also interpreted as evidence that direct excitation dominates over dissociative excitation. This condition being fulfilled, a qualitative estimation of the H atoms concentration can be obtained from the variation of the actinometric ratio IH_α / IAr_{750} during the pulse, since it is known from investigations of MW discharges in $H_2 + CH_4$ mixtures [8] that the other requirements for the applicability of the actinometric method are valid in these plasmas over a relatively wide range of discharge conditions.

Fig. 4a shows the evolution of the $IH_\alpha / Iar_{750\ nm}$ actinometric ratio during the MW pulse and its variation as a function of pulse duration, for both frequencies used is plotted in Fig. 4b. The discharge power pulse shape was monitored by a fast diode detector mounted in the load in connection with an oscilloscope.

After a relatively slow increase in the beginning, the ratio IH_α / IAr_{750} was found to rise strongly during the MW pulse, reflecting the continuous increase in the concentration of atomic hydrogen due to increasing dissociation of CH_x and H_2. This shape of the temporal variation of the IH_α / IAr_{750} ratio explains the pronounced increase in the H_α emission intensity with increasing pulse duration (Fig. 2). The concentration of atomic hydrogen increases linearly with pulse duration, regardless of the repetition frequency of the pulses.

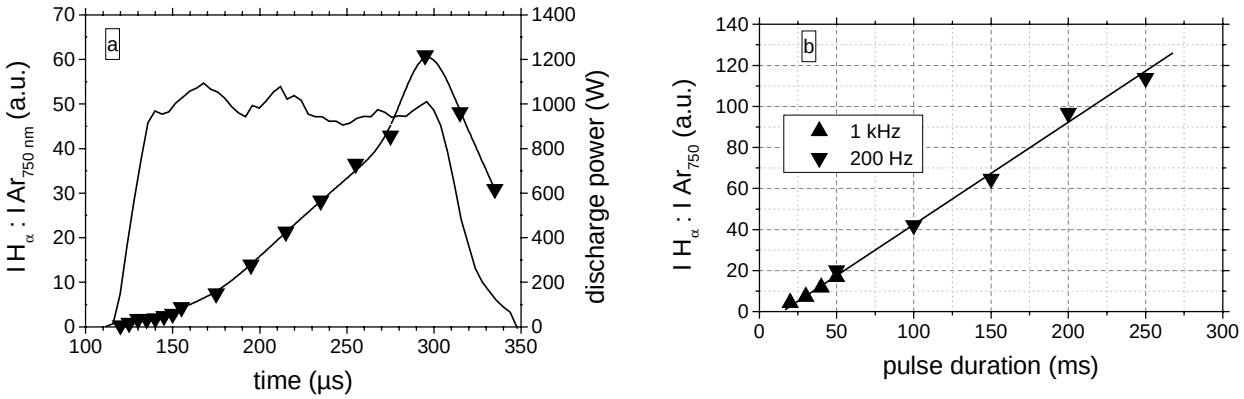


FIGURE 4. Variation of the $IH_\alpha / IAr_{750\ nm}$ actinometric ratio **a.** during a MW pulse with $\nu = 200$ Hz, $E_{in} = 6.3$ eV/molecule; **b.** as a function of the pulse duration for $\nu = 200$ and 1000 Hz.

The temporal evolution of the H atom concentration during the MW pulse suggests that the dehydrogenation reactions are relatively slow and from the similarity of the C_2 and H_α emission in time it could be assumed that dehydrogenation is the rate-limiting step in the process of higher hydrocarbons formation. The effect is seen on the distribution of stable products (Fig. 1b): the total selectivity towards C_2 hydrocarbons has similar values for short and long pulses, supporting the idea of relatively fast dimerisation reactions and a product distribution determined by the slower dehydrogenation reactions.

4. CONCLUSIONS

The experiments show that a selective conversion of methane into acetylene can be achieved under the conditions presently used. The duration of the MW pulses was found to be an essential parameter which influences the conversion degree and products distribution. The optimal choice in this respect can be made taking into account that:

1. The methane depletion that occurs towards the end of long pulses leads to the saturation of the conversion at a relatively low value and to the increase in energy requirement for conversion and for acetylene formation with increasing further the pulse duration.
2. Dehydrogenation reactions are likely to be relatively slow as compared to the dimerisation, therefore in the case of long pulses the products distribution is dominated by acetylene.

REFERENCES:

[1] Hassouni K., Duten X, Rousseau A., and Gicquel A., *Plasma Sources Sci. Technol.*, **10**, 61-75 (2001)
[2] Lieberman M. A., and Ashida, S., *Plasma Sources Sci. Technol.* **5**, 145-58 (1996)
[3] De Poucques L., Henrion G., Bougdira J., and Hugon R., *Surface & Coatings Technol.*, **146-147**, 586-92 (2001)
[4] Heintze M., and Magureanu M., Acetylene synthesis from methane in a microwave plasma. In: *Proc. I.S.P.C.-15* ed. by A. Bouchoule, J. M. Pouvesle, A. L. Thomann, J. M. Bauchire, and E. Robert, Orleans, 2001, pp. 2837-42
[5] Goyette A. N., Lawler J. E., Anderson L. W., Gruen D. M., McCauley T. G., Zhou D., and Krauss A. R., *Plasma Sources Sci. Technol.* **7**, 149-53 (1998)
[6] Khachan J., James B. W., and Marfoure, A., *Appl. Phys. Lett.* **77**, 2973-5 (2000)
[7] Rousseau A., Granier A., Gousset G., and Leprince P., *J. Appl. Physics*, **27**, 1412-22 (1994)
[8] Gicquel A., Chenevier M., Hassouni K., Tserepi A., and Dubus M., *J. Appl. Phys.* **83**, 7504-21 (1998).

MODELING OF PLASMA CHEMISTRY IN A CORONA STREAMER PULSE SERIES IN AIR

H. Nowakowska, J. Stańco, M. Dors[a], J. Mizeraczyk

Centre of Plasma and Laser Engineering, Institute of Fluid Flow Machinery, Polish Academy of Sciences, Fiszera 14, 80-231 Gdańsk, POLAND

Abstract: The aim of this study is to analyse the chemistry in air treated by a series of corona discharge streamers. Attention is focused on the conversion of ozone and nitrogen oxides. In the model it is assumed that the streamer head of relatively small geometrical dimensions propagates from the anode to the cathode, leaving the streamer channel behind. Any elemental gas volume in the streamer path is subjected first to the conditions of the streamer head, and next to those of the streamer channel. The kinetics of plasma-chemical processes occurring in the gas is modeled numerically for a single streamer and a series of streamers. The temporal evolution of 25 chemical compounds initially present or produced in air is calculated.

1. INTRODUCTION

Corona discharges have been used for about two decades as sources of non-thermal plasma, suitable for removal of dilute concentrations of pollutants, such as N_xO_y or SO_x, from gases at atmospheric pressure. The role of the discharge in pollutant elimination from air or flue gas consists in providing in the gas free electrons, which ionize, excite and dissociate the molecules, producing primary (e.g. O, OH, N) and secondary (e.g. O_3, HO_2) chemically active species. These facilitate the conversion of the polluting compounds, via a chain of reactions, into harmless components.

Modeling of plasma chemistry in a discharge can help to reduce the extent of necessary experimental investigations concerning the practical problem to be solved. Preliminary computer calculations may allow the researcher to predict the optimum experimental conditions. Also a better understanding of the chemical process kinetics may be gained.

In most papers on the plasma chemistry modeling for corona discharges the influence of a single discharge streamer only is taken into consideration. This is a far going idealization of real situations, where thousands of streamers occur at random within the reactor. Some of them develop in an almost untreated gas, some in a gas that was already subjected to the influence of streamers that crossed it earlier. It is therefore difficult to correctly relate results of modeling to experimental results.

In this report the plasma chemistry in a polluted air under the influence of a series of corona discharges is considered. This may give a better insight into the kinetics of pollutant removal under conditions closer to those actually occurring in corona discharge reactors.

2. MODEL

The model of the corona discharge plasma is a modification of that presented in earlier papers (see e.g. [1]). A discharge in synthetic air (N_2: O_2 = 4:1) polluted with NO (200 ppm) is considered. The gas pressure and temperature are taken as constant (p = 1 atm, T = 298 K). Physical and chemical processes occurring in gas volume element under the influence of streamers are considered. It is assumed that DC corona streamers are generated in a reactor with electrodes of the point-to-plate

[a] Electronic address: mdors@imp.gda.pl

geometry. The streamer head and channel have a cylindrical form. The analysis is local, and no spatial dependence (diffusion or hydrodynamic expansion of the streamer channel) is taken into account. Any gas volume element lying in the streamer path is subjected first to the conditions of the streamer head, and next to those of the streamer channel. It is assumed that the gas is at rest, so that subsequent streamers act on a gas subjected to the influence of the preceding ones. Based on the literature the time for which a gas volume element in the streamer path is subjected to the conditions prevailing in the streamer head is taken a t_h = 0.1 ns, which corresponds to the streamer propagation velocity on the order of 10^5 - 10^6 m/s. The streamer repetition rate is in the kilohertz range. Unlike in the model used previously [1] only the reduced electric field intensity E/N(t), modeling the head and channel passage, is assumed for the streamer. Both stepwise and exponential changes of E/N(t) corresponding to the streamer head passage may be modeled. It is assumed that ionization of the gas encountered by the streamer head builds the electron density up from its initial value n_{e0} to the maximum value $n_{e\ max}$, reached after time t_h.

119 primary and secondary reactions occurring between 25 species are taken into consideration. The numerical model consists of particle balance equations for those species. They form a set of stiff ordinary differential equations, which is solved by the Gear's method. PLASMAKIN [2] and ELENDIF [3] software packages are used in the numerical code. PLASMAKIN is a library designed for handling physical and chemical data used in plasma physics modeling. Its use facilitates greatly the writing of the particle balance equations. Any change in the reaction or species list, entered in the code via a namelist, results in an automatic modification of the model equations. ELENDIF, a code for solving the Boltzmann equation for the electrons in a dicharge, is used for modifying, in the course of calculations, those rate coefficients which depend on the reduced field intensity E/N or the electron temperature T_e.

3. RESULTS OF CALCULATIONS

Calculations using the model were made for an N_2: O_2: CO_2: NO = 0.8:0.2:2x10^{-4} mixture at a pressure p = 1 atm and gas temperature T = 298 K, subjected to the influence of a series of streamers (modeled with E/N(t) pulses). The initial value of electron density n_{e0} and the maximum value of E/N were

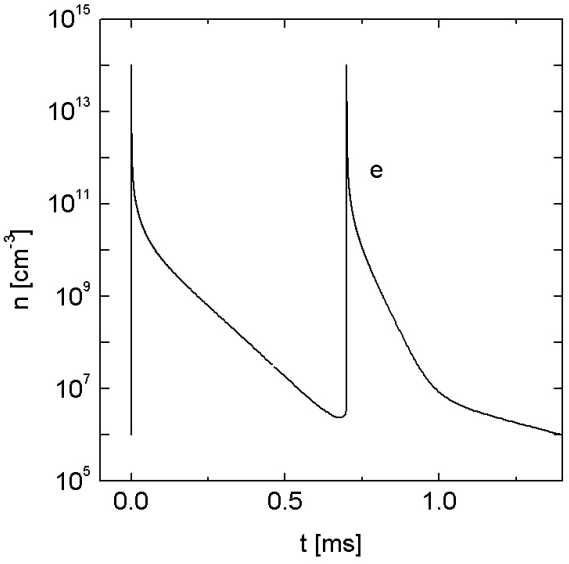


FIGURE 1. Variation of the electron number density in the gas subjected to the influence of two consecutive streamers; N_2:O_2:CO_2:NO = 0.8:0.2:2x10^{-4} , p=1 atm, T=298 K.

adjusted so as to obtain $n_{e\ max}$ on the order of $10^{14} – 10^{15}$ cm^{-3} , which is a typical value found in the literature. If an exponential rise and fall of E/N within the head were assumed, to better follow the

results of more comprehensive streamer modeling (see e.g. [4]), the peak value of E/N of about 1600 Td was needed, which is also in accord with the literature. For a rectangular pulse $(E/N)_{max}$ = 780 Td met the requirement for the maximum n_{e0}. Extensive calculations showed however, that in the streamer channel (where E/N = 20 Td was assumed, based on the literature) the kinetics of chemical reactions remained almost unaffected by the form of E/N(t) in the streamer head. Therefore, for the sake of simplicity, rectangular E/N pulses were used in most calculations. Some results of calculations of chemical kinetics in the gas under the influence of two consecutive streamers represented by such pulses are shown in Figures 1 – 4.

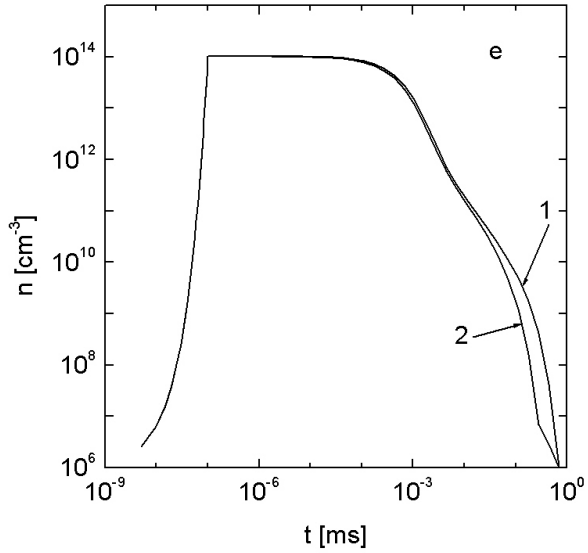


FIGURE 2. As Figure 1, logarithmic scale, the waveforms for pulses 1 and 2 shifted to overlap.

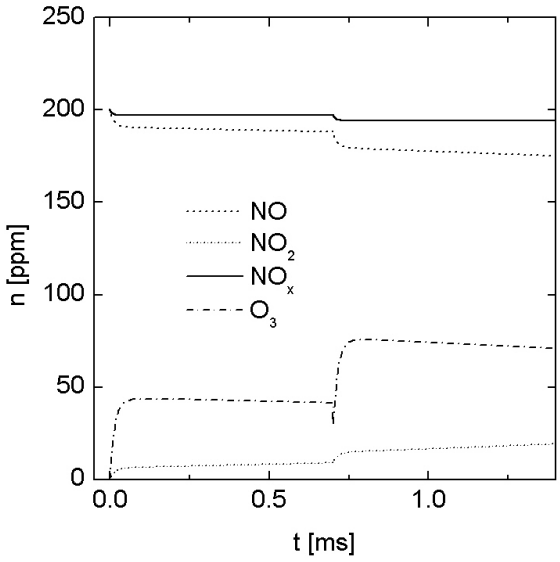


FIGURE 3. Variation of concentrations of NO_x and O_3 under the influence of two consecutive streamers; conditions as for Figure 1.

It can be seen from Figures 1 and 2 that the number density of electrons, rising in 0.1 ns from 10^6 cm^{-3} to 10^{14} cm^{-3}, remains on that level for about 1 μs, to decrease in 0.7 ms to the initial level of 10^6 cm^{-3}. The decrease of NO concentration is accompanied by a production of NO_2. However, the concentration of both those compounds together decreases (Figures 3 and 4). The decrease is fast in the streamer head, which is a region of intensive ionization and dissociation of O_2.

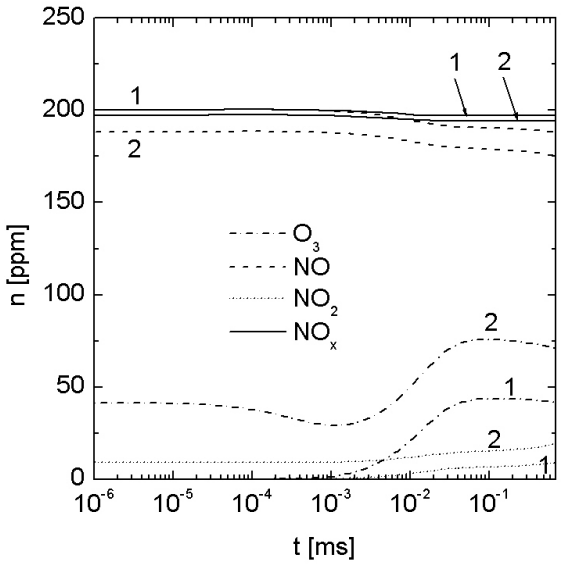


FIGURE 4. As Figure 3, logarithmic scale, the waveforms for pulses 1 and 2 shifted to overlap.

Worth noting is an accumulation of ozone in consecutive pulses. O_3 molecules begin to form in the streamer channel, about 1 μs after the passage of the streamer head, their concentration reaching a maximum in about 100 μs. Afterwards a slow decrease begins, but the next streamer causes again a large increase of ozone concentration.

The numerical model presented in this contribution may be useful for predicting the efficiency of pollutant abatement by corona discharge streamers in a more realistic way than models analyzing the effects of a single streamer only. Characteristic of this model is representation of a streamer exclusively by its electric field.

Obviously, the results of chemical kinetics modeling depend strongly on the adopted reaction rate coefficients. For that reason the authors regard the results shown as preliminary. It is planned to carry out a detailed quantitative analysis of NO conversion by corona discharge based on a new list of relevant chemical reactions, with rates updated according to recent recommendations of IUPAC, together with a full set of cross sections for the primary reactions involving electrons.

REFERENCES

[1] Dors M., Nichipor G. V., and Mizeraczyk J., Kinetics of nitric oxide removal from N_2: O_2: CO_2: NO in a point-to-plate corona discharge, In: *Proc. XXIII ICPIG*, Toulouse, 1997, pp. I-250-251

[2] Pinhão N. R., *Comp. Phys. Commun.,* **135**, 105-131 (2001)

[3] Morgan W.L., *ELENDIF for Windows 95, The Boltzmann Equation Solver,* Kinema Research & Software, L.L.C., 1999

[4] Serdyuk Yu. V., Larsson A., Gubanski S., and Akyuz M., *J. Phys. D: Appl. Phys.,* **34,** 614-623 (2001)

DEVELOPMENT OF MEASUREMENT EQUIPMENT OF OZONE HALF LIFE

Seiji Baba*, Saburoh Satoh and Chobei Yamabe

Department of Electrical and Electronic Engineering,
School of Science and Engineering, Saga University,
1,Honjo-machi,Saga-shi 840-8502,Japan

Abstract In the present research, a new measurement method and the mechanism of Ozone decay half life τ (h) is proposed Ozone is generated by such electric discharge as silent or surface discharge and has a strong oxidization power and is widely used for air or water purification. But to determine the dosage of ozone, it is necessary to know the ozone decay time [half life τ (h)] in air or water. Ozone decay is found to change in a natural logarithmic way. Through measurement the time duration τ (h) and the concentration x (g/m^3) at t ,ozone decay half life τ is calculated.
KEYWORD: Ozone purification, Ozone decay, Half life of Ozone, Ozone concentration.

1. INTRODUCTION

When the contaminated room and/or water are purified by diffusing ozone gas, quantitative analysis is necessary to know how they are contaminated. For this purpose, in general, the concentration substance is measured. However, when there are many kinds of contamination substance at the same time, it is very difficult to determine the overall contamination extent in the room or water. On the other hand ozone reacts on various kinds of contamination substances like organic or inorganic compounds at the same time. If this ozone reaction is measured overall by quantitative way like COD (Chemical oxygen demand) or BOD(Biological oxygen demand),a practical, simple and overall measurement method is established.

In our present research, we develop the ozone decay half life measurement equipment and propose ozone decay half life τ (h) as quantitative scale of the contamination of a room or water.
The principal advantages of this method are as follows:
(1) The ozone half life τ (h) is calculated by one time ozone concentration measurement value.
(2) Gaseous and liquid phase contamination is determined.
(3) The contamination extent is evaluated instantaneously.

In this paper, the theoretical formula which closely models experimental results, and determines the ozone half life τ and constitution of measurement equipment are presented.

2. CALCULATION

In case ozone gas is distributed in the room of volume V(m^3)(Figure1),the ozone concentration in the room x(g/m^3) is determined by the following differential equation.

$$dx = (Z/V)dt-(\gamma x)dt \qquad (1)$$

Here, x : ozone concentration(g/m^3)
Z : ozone distribution quantity(g/h)
V : volume of room(m^3)
γ : ozone decay ratio
t : distributing time(h)

By solving equation (1),

$$x = (Z/V)\cdot(\tau/0.693)\cdot[1-\exp(-0.693t/\tau)] \qquad (2)$$

Here, τ :ozone decay half life (h).
By equation (2), the ozone decay half life τ (h) is calculated as follows.

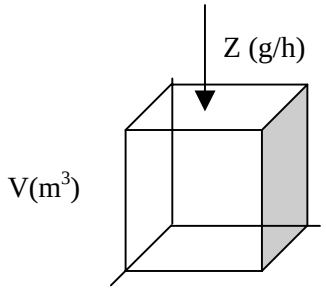


Fig.1 Room ozone distribution

*Electronic address : CYT01102@nifty.ne.jp

When $t = t_0$, $x = x_0$

$$x_0 = (Z/V)\,(\tau/0.693)\,[1 - \exp(-0.693t_0/\tau)]$$

Here, $(Z/0.693V)=C$,
then,

$$x_0 = (C\tau) - (C\tau)\exp(-0.693t_0/\tau)$$

$$1 - (x_0/C\tau) = \exp(-0.693t_0/\tau)$$

When $K = x_0/C$, $T = 0.693t_0$, $\tau_x = 1/\tau$,
then,

$$1 - K\tau_x = \exp(-T\tau_x)$$

$$\ln(1-K\tau_x) = T\tau_x$$

Here, $\ln(1-K\tau_x) = -K\tau_x+(K^2\tau_x^2)/2-(K^3\tau_x^3)/3\ldots$
When $T\tau_x = \ln(1-K\tau_x) = K\tau_x+(K^2\tau_x^2)/2$,
then,

$$-K\tau_x + (K^2\tau_x^2)/2 = -T\tau_x \qquad (3)$$

By solving equation (3),

$$\tau = X^2/2\,(X-0.693t_0) \qquad (4)$$

Here, $X = x_0/[(Z/V)\,(1/0.693)]$

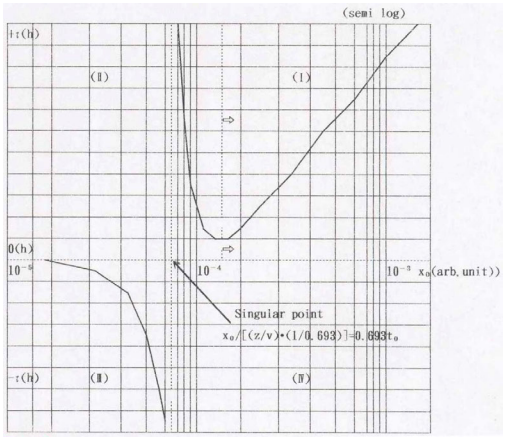


Fig.2 τ -x_0 characteristics

By equation (4) the relationship between x_0 and τ is shown in the following graph (Figure 2). When $X = 0.693t_0$, or $x_0/[(Z/V)\,(1/0.693)] = 0.693t_0$, the behavior is shown below in Figure 2.

From τ -x0 characteristics, those values Z (g/h) and V (m^3) should be chosen the proper values by which the calculated τ (h) is considered physically effective. The quadrant (1) is available and shows the practically effective range.

3. EXPERIMENTAL APPARATUS AND METHOD

To examine equation (1) and equation (4), the following experiments were performed.
The experimental apparatus, shown in Fig.3, consists of an ozone generator, reaction chamber, stir fan, ozone concentration monitor and analogue recorder.

For the control of ozone decay half life τ, several kinds of organic substances like a banana, a cigarette stub and raw fish which have a strong smell.

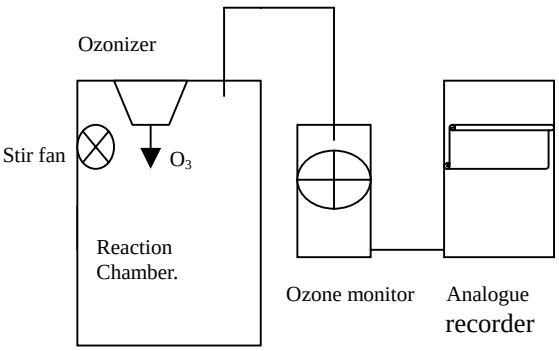
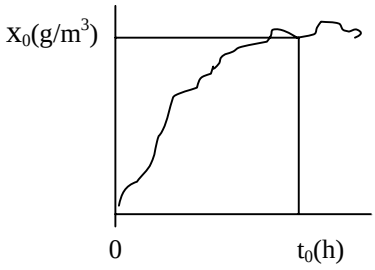


Fig.3 Experimental apparatus



$\tau = X^2/2\,(X-0.693t_0)$
$X = x_0/[(Z/V)\,(1/0.693)$

Fig 4. Ozone concentration measurement

The ozone generator in Fig.3 is an ultraviolet ray type and ozone generation is 0.3 – 0.7 mg/h. The reaction chamber is made of PVC (Polyvinyl chloride) and the volume is 1(m^3).

Experiment 1

Ozone gas is diffused into the chamber and at t_0(h) later, the ozone concentration x_0(g/m3) is measured. According to formula (4) the ozone decay half life τ (h) is calculated as,

$\tau = X^2/2\,(X-0.693t_0)$, $X = x_0/[(Z/V)\,(1/0.693)]$. Note : Fig.4

Experiment 2

Ozone gas is diffused for a long time until the ozone concentration saturates and after the concentration value saturates, ozone diffusion is stopped.

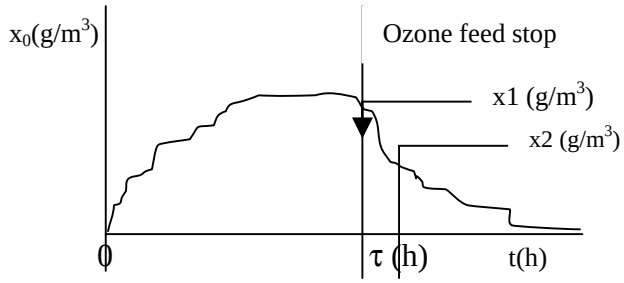


Fig.5 Ozone concentration vs time

According to the experimental result (recorded ozone concentration curve), the actual ozone decay half life τ (h) is measured.

Table 1. Ozone half life control substance

TEST No.	Half life control substance in chamber
1	Nothing (chamber vacant)
2	Banana
3	Cigarette stub
4	Raw fish

4. EXPERIMENTAL RESULTS

Experiment 1

Table 2 shows the results of experiment 1. Here, ozone concentration x_0 (g/m3) at t_0 (h) is measured and the half life τ (h) is calculated by formula (4).

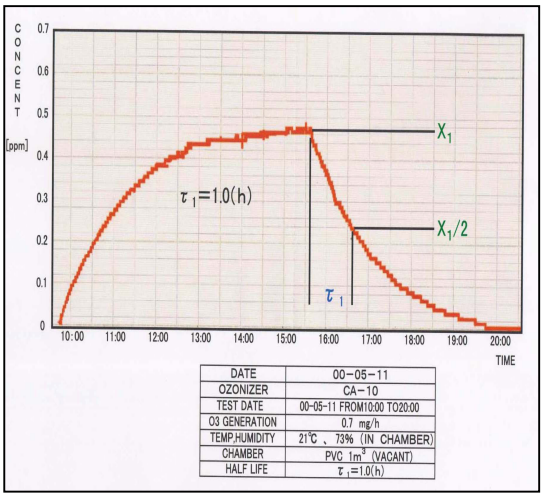
Table 2. Calculated τ by experiment 1.

Test No.	t_0	x_0	Calculated τ
1	1/4 (h)	0.31(ppm) =0.664(mg/m^3)	τ_1=0.99(h)
2	1/4 (h)	0.30(ppm) =0.685(mg/m^3)	τ_2=0.79(h)
3	1/60 (h)	0.26(ppm) =0.55(mg/m^3)	τ_3=0.48(h)
4	1/60 (h)	0.15(ppm) =0.32(mg/m^3)	τ_4=0.30(h)

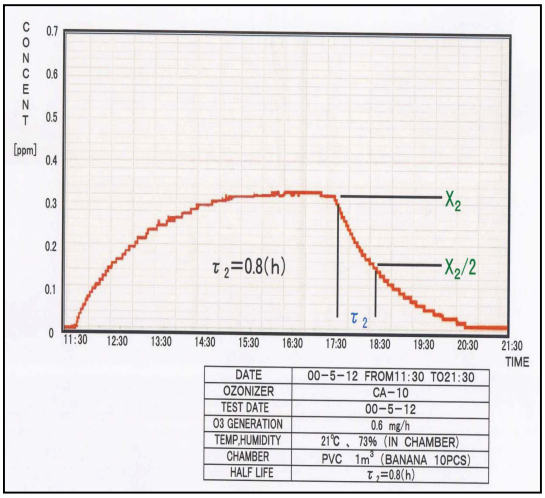
Experiment 2

Fig.6 shows the results of experiment 2 which ozone concentration is measured continuously by an analogue recorder. From the curve of ozone concentration, the ozone half life τ (h) is measured in each test.

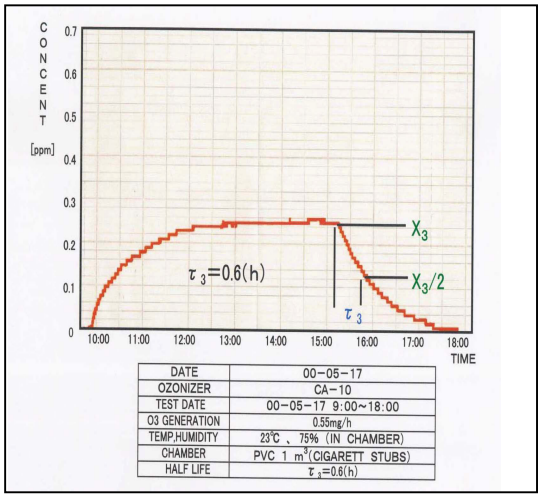
TEST 1



TEST 2

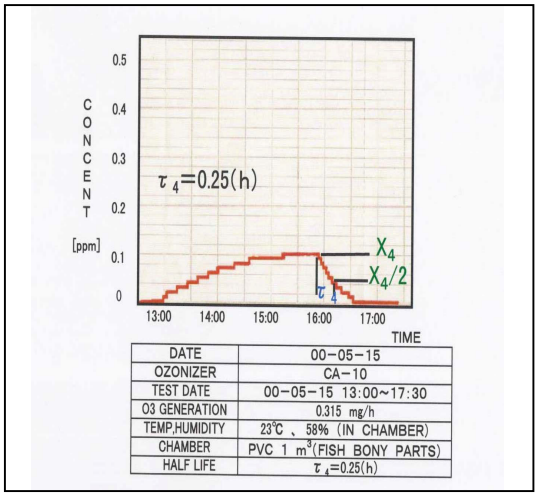


TEST 3



DATE	00−05−17
OZONIZER	CA−10
TEST DATE	00−05−17 9:00~18:00
O3 GENERATION	0.55mg/h
TEMP,HUMIDITY	23℃ 、 75% (IN CHAMBER)
CHAMBER	PVC 1 m^3(CIGARETT STUBS)
HALF LIFE	τ_3=0.6(h)

TEST 4



DATE	00−05−15
OZONIZER	CA−10
TEST DATE	00−05−15 13:00~17:30
O3 GENERATION	0.315 mg/h
TEMP,HUMIDITY	23℃ 、 58% (IN CHAMBER)
CHAMBER	PVC 1 m^3(FISH BONY PARTS)
HALF LIFE	τ_4=0.25(h)

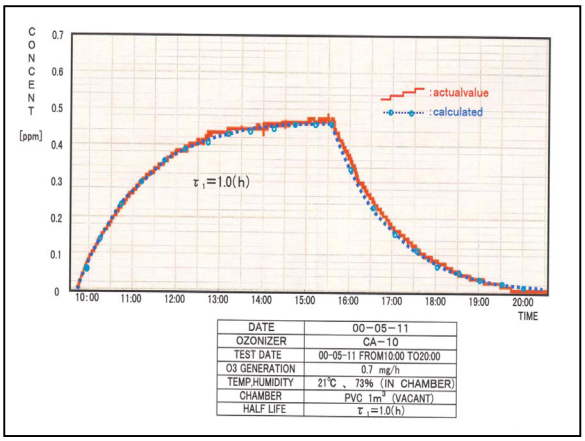
Fig.6 Ozone concentration transition

5. DISCUSSION

5.1

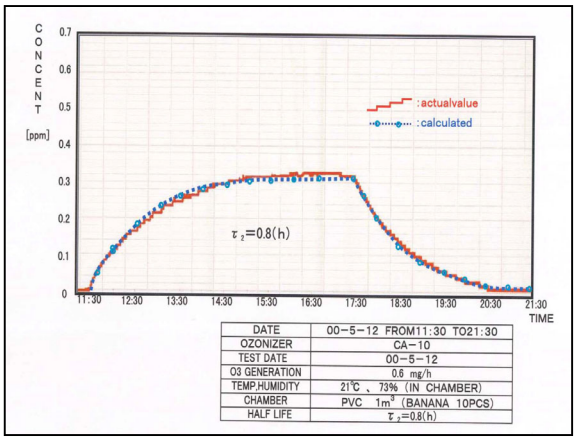
Fig 7 shows the comparison curves of measured and calculated ozone concentration in the reaction chamber. The calculated value is the results of calculation using formula (2) and very closely approximates actually measured value. The formula from differential equation (1) is considered acceptable in practical usage in the ozonation scheme.

TEST 1



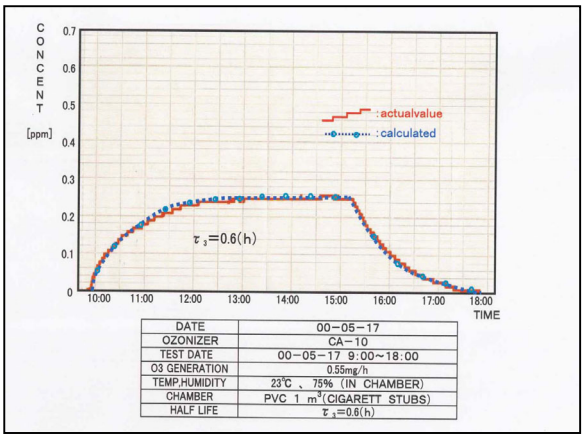
DATE	00−05−11
OZONIZER	CA−10
TEST DATE	00-05-11 FROM10:00 TO20:00
O3 GENERATION	0.7 mg/h
TEMP,HUMIDITY	21℃ 、 73% (IN CHAMBER)
CHAMBER	PVC 1m^3 (VACANT)
HALF LIFE	τ_1=1.0(h)

TEST 2



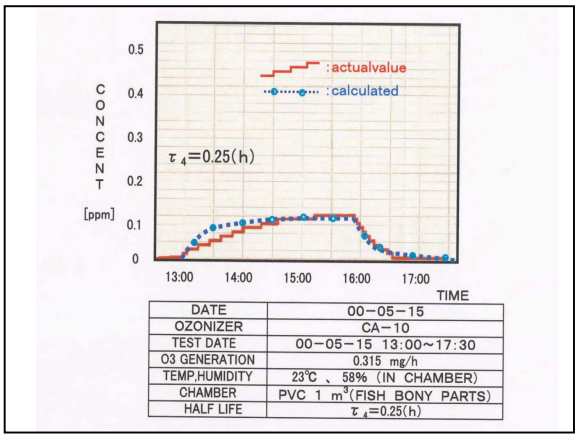
DATE	00−5−12 FROM11:30 TO21:30
OZONIZER	CA−10
TEST DATE	00−5−12
O3 GENERATION	0.6 mg/h
TEMP,HUMIDITY	21℃ 、 73% (IN CHAMBER)
CHAMBER	PVC 1m^3 (BANANA 10PCS)
HALF LIFE	τ_2=0.8(h)

TEST 3



DATE	00−05−17
OZONIZER	CA−10
TEST DATE	00−05−17 9:00~18:00
O3 GENERATION	0.55mg/h
TEMP,HUMIDITY	23℃ 、 75% (IN CHAMBER)
CHAMBER	PVC 1 m^3(CIGARETT STUBS)
HALF LIFE	τ_3=0.6(h)

TEST 4



DATE	00−05−15
OZONIZER	CA−10
TEST DATE	00−05−15 13:00~17:30
O3 GENERATION	0.315 mg/h
TEMP,HUMIDITY	23℃ 、 58% (IN CHAMBER)
CHAMBER	PVC 1 m^3(FISH BONY PARTS)
HALF LIFE	τ_4=0.25(h)

Fig.7 Comparison transition curves of ozone concentration

5.2

Table 3 shows the comparison of the calculated ozone half life τ_c (h) to the actually measured half life τ_m (h).

Table 3.Comparison of the value τ (h)

Test No	τ_c (h)	τ_m (h)
1	0.99	1.0
2	0.79	0.8
3	0.48	0.6
4	0.30	0.25

5.3

Schematic of ozone decay half life measurement equipment is shown in Fig.8.

5.4

The ozone concentration decrease calculation formula below is acceptable too, but in this case we need two times the ozone concentration measurements. We will add this algorithm in the measurement equipment.

$x = x_0 \exp(-0.693t/\tau)$,

where x_0 is the initial concentration (g/m^3) and x (g/m^3) is the concentration at after t(h).

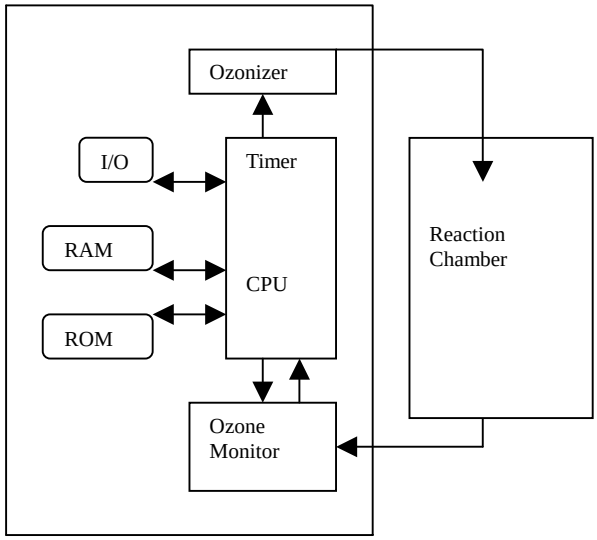


Fig.8.Schematic diagram of the half life measurement equipment.

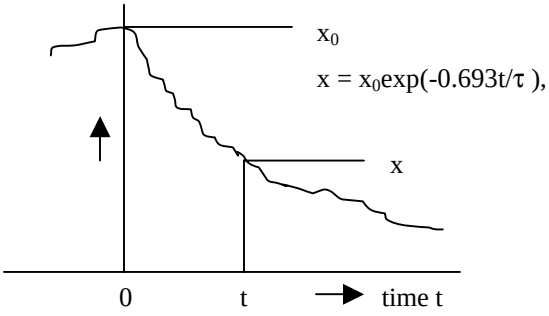


Fig. 9 Concentration decrease measurement

6. CONCLUSION

When the ozonation scheme of such deodorization, sterilization and purification of air or water is made, it is necessary to know the ozone decay half life τ (h) of object contaminated room or water for determination of necessary ozone dosage.

（1） Here, we propose a new and simple ozone decay half life τ (h) measurement method which includes a calculation formula and a schematic diagram of the measurement equipment.

（2） We confirmed experimentally that the linear reaction equation below agrees well with actual ozone concentration diffusion.

$dx = (Z/V)dt - (\gamma x)dt$

Also the τ (h) calculation formula for measurement equipment,

$\tau = X^2/2\ (X-0.693t_0)$, where $X = X_0/[(Z/V)]\ (1/0.693)]$,

is acceptable.

References

[1] Satoh S, Ihara S, Yamabe C **;** *Proceeding of the 9 th Annual Conference on Ozone Science and Technology in Japan*.2000-3.p.179-182(in Japanese)**.**

[2] Baba S, Satoh S, Yamabe C **;** *Proceeding of the 10 th Annual Conference on Ozone Science and Technology in Japan*.2000-10.p.39-42(in Japanese).

[3] Baba S, Satoh S, Nagao H, Yamabe C; *Proceeding of Electric Discharge Research Report of IEEJ* 2000-9.ED-00-114,p.55-58(in Japanese)

PARAMETERS OF BARRIER DISCHARGES IN COPLANAR ARRANGEMENTS

V. I. Gibalov[a*], T. Murata[b] and G. J. Pietsch[a]

a) Gasentladungstechnik, Aachen University of Technology, Schinkelstr. 2, 52056 Aachen, GERMANY
[*] permanent address: Chem. Dep., Moscow State University, Leninsky gory; 119899 Moscow RUSSIA
b) TOSHIBA Corporation, Kawasaki, 210-0862 JAPAN

Abstract. The parameters of barrier discharges in coplanar arrangements were obtained on the basis of a 2D numerical model. It was found that the configuration of the electrode system (distance between a pair of electrodes, electrode width and thickness of the dielectric layer above the electrodes and permittivity) determines the overall parameters of the discharge device. The ignition voltage, effective capacitances, amplitude and shape of the discharge current were obtained and are in good agreement with measured ones.

1. INTRODUCTION

Dielectric barrier discharges in coplanar arrangements differ from those in others considerably. In coplanar discharge (CD) arrangements a dielectric layer covers pair(s) of electrodes. The advantages of pure surface discharges and a fixed electrode distance are combined.

The properties of a CD element are investigated with a 2D numerical model [1]. Using the model it is possible to get detailed information about the discharge dynamics at different conditions. The aim of this paper is to study the influence of the configuration of a CD element (a pair of electrodes) on the parameters of a large discharge area arrangement with a multitude of electrode pairs in parallel. The following parameters of the configuration are taken into account, the inter-electrode distance, electrode width, the thickness of the dielectric layer and its permittivity. The feed gas under investigation is dry oxygen of 1.0 to 2.5 bar.

2. FIELD STRENGTH AND CURRENT SHAPE OF A DISCHARGE ELEMENT

The initial field strength distribution differs considerably for different configurations (Fig. 1). Increasing the inter-electrode gap the field strength maximum splits and moves to the position of the electrode edges. The field strength distribution smoothes if the thickness of the dielectric layer above the electrodes is enlarged.

During the discharge process differences in the initial field strength distributions diminish. The normal component becomes nearly zero in between the position of the electrodes, while the longitudinal one is nearly constant here with a value of about 80 to 100 Td in oxygen. The discharge process transforms finally different distributions to similar ones.

The geometrical parameters of the configuration as well as the permittivity of the dielectric has nearly no influence on the shape of the discharge current (Fig. 2), its duration is nearly constant.

The most compact discharge element under investigation has a discharge region (i. e. the inter-electrode distance plus twice the electrode width) of about 200 μm, the widest element a region of about 720 μm. The electrons need about 2 to 3 ns to drift over the furthest distance and much less for the nearest one. However, as the current duration is independent of the dimension of the discharge region there must be another reason (characteristic time), which determines the duration of the current flow.

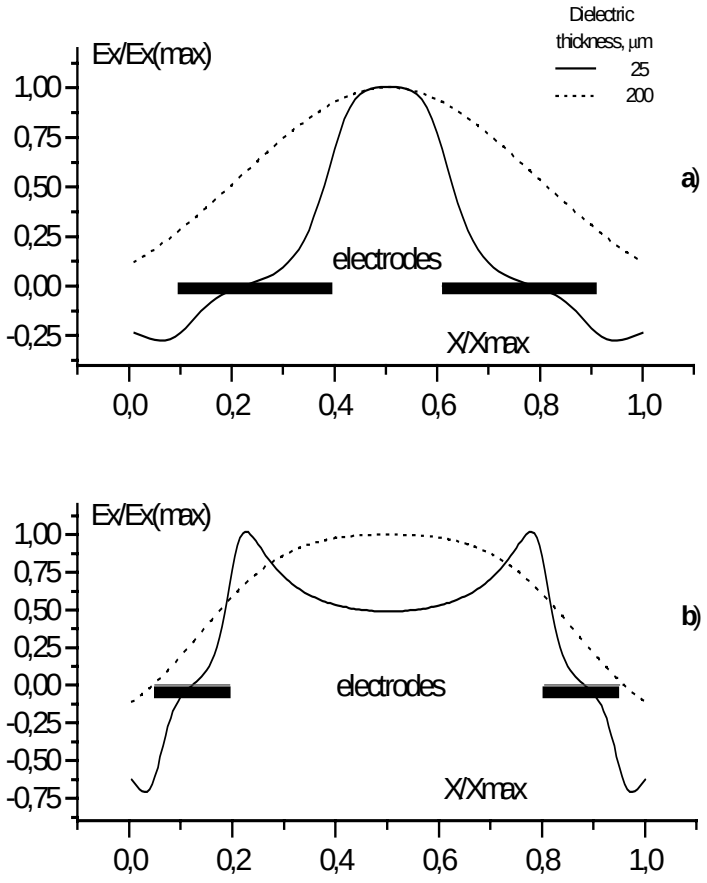


FIGURE 1. Normalized component of the initial field strength (parallel to the dielectric surface) at a thickness of the dielectric above the electrodes of 25 and 200 μm for an electrode gap of (a) 80 μm and (b) 480 μm.

This effect may result from the formation of a source of secondary electrons in the cathode region [2] (e. g. something like a normal cathode layer) and its spreading on the dielectric surface. This needs some time, which will determine the current rise. The accumulation of surface charges, which happens simultaneously, limits and finally extinguishes the current flow.

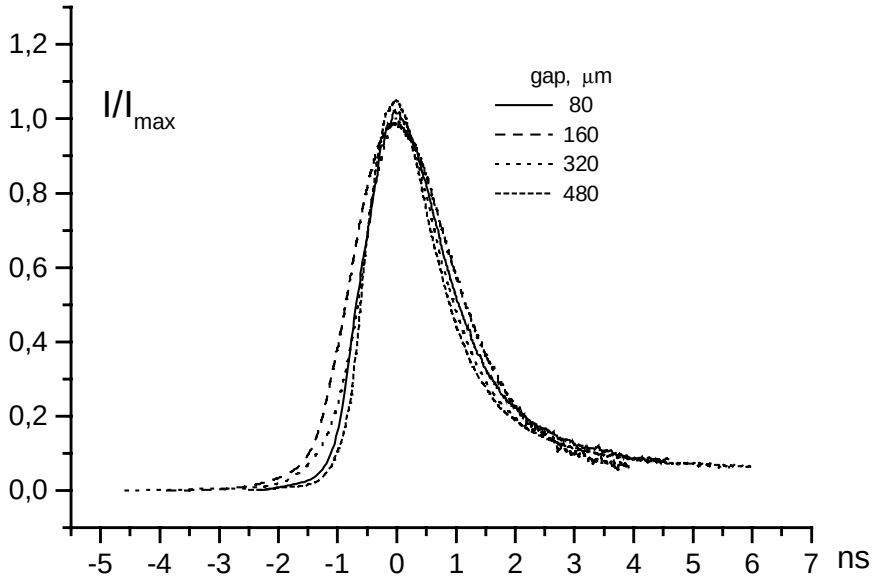


FIGURE 2. Normalized current for configurations with different discharge gaps.

The source formation and its spreading together with the charge accumulation on the surface needs more time than the time of flight of the electrons from the cathode to the anode. So the spreading of the electron source (cathode layer) on the dielectric surface determines the current rise. This spreading is driven by the local field configuration in the cathode layer and is independent on the dimensions of the configuration. The properties of the cathode layer are determined by the gas characteristics and the interaction with the dielectric surface, only.

3. IGNITION VOLTAGE AND CAPACITIES OF LARGE AREA CD-ARRANGEMENTS

The ignition voltage and the capacities of arrangements are some of the parameters, which determine the electrical properties of a device. There exist two capacities of the discharge system, one without discharge (C“off”) and a second effective one, when the discharge is on (C“on”). All these parameters can be derived from Lissajous figures. To calculate the Lissajous figure of the system the model has to be modified. The 3D structure of the CD (discharge channels, their size and number density) is included in the model. This allows obtaining more realistic values of the overall parameters of large area CD-arrangements.

The influence of the value of the relative dielectric constant on the ignition voltage of a large system is presented in Table 1. The ignition voltage is defined as the voltage at which the active discharge power starts to rise. The experimental value in the table belongs to a relative permittivity between 10 and 11.5. As expected, the higher the permittivity the lower the ignition voltage. The agreement between the calculated and measured values of the ignition voltage is rather good.

TABLE 1. Calculated and measured ignition voltages for different relative permittivities.

ε	5	10	15	Experiment [3]
Ignition voltage, kV	2.4	1.9	1.8	1.9

The electrode distance, the electrode width and the thickness of the dielectric layer above the electrodes influence the ignition voltage furthermore. An enlargement of the electrode distance and of the thickness of the dielectric layer increases the ignition voltage; an enlargement of the width decreases it.

The rise of the ignition voltage with pressure is non-linear (Table 2). A pressure increase of 240 % causes an ignition voltage increase of about 180 %. This can be explained by the non-linear behaviour of the Paschen curve in the pd-range under investigation (5 to 10 mbar·cm).

TABLE 2. Influence of the pressure on ignition voltage (simulation values).

Pressure, bar	1.0	1.7	2.4
Ignition voltage, kV	1.3	1.9	2.4

The values of the capacities of a discharge arrangement are presented in Table. 3. C“off” is simply the capacity of the system without discharge. In the case of discharges the situation becomes more complex.

The C”on”-value is determined by the charge transferred between the conductive electrodes. The charge, however, is influenced by the dynamics of the discharge within single channels on one side and by the interaction of the multitude of channels during the voltage cycle on the other side. Both processes are modelled. This means that the final value of the transferred charge is obtained using a complicated model, which includes a set of equations, swarm parameters, rate constants and the interaction of the discharge with the dielectric surface. Taking into account the complexity of the process,

the agreement of the calculated and measured values is more than satisfactory (Table 3).

TABLE 3. The capacities of a discharge system with an area of 0.04 m^2 (oxygen of 1.7 bar).

ε	5	10	15	Experiment [3]
C“off”, nF	4.5	10.7	14.2	9.7
C“on”, nF	7.3	16.6	22.2	13.9

The accuracy of the simulation depends on the configuration; it is better for compact discharge elements and less for wider ones. The maximum error was found for the largest inter-electrode distance and the widest electrode (discharge region of about 750 μm) with a value of 18 % for C”on”.

4. CURRENT OF LARGE AREA CD-ARRANGEMENTS

The amount of charge, which is transferred in a period of the applied voltage and by this the current of the device can be found from Lissajous figures. Furthermore the current is proportional to the frequency. 10 kHz is used for all results presented in the following.

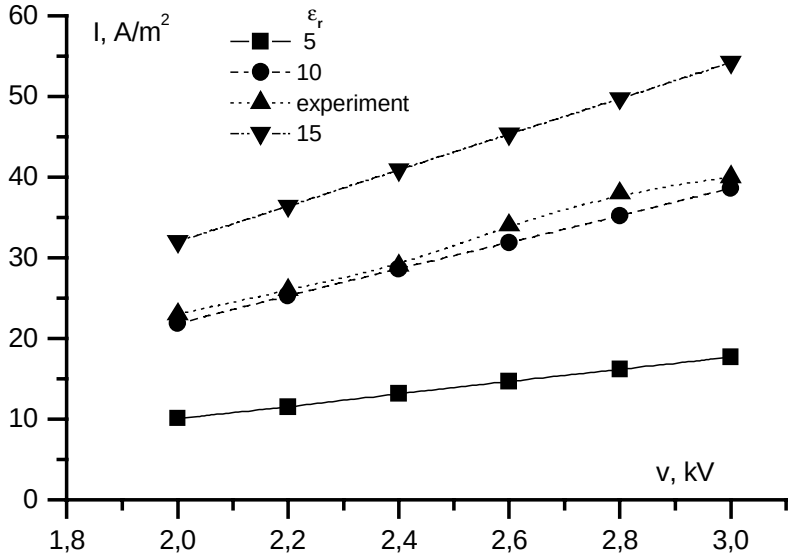


FIGURE 3. Current density of the discharge system (oxygen of 1.7 bar, 10 kHz).

In Fig. 3 the current density at different values of the relative permittivity is depicted. As expected, the higher the permittivity the higher is the current density. The experimental value (belonging to an ε-value between 10 and 11.5) is about 10 % higher than the calculated one. The current densities for other frequencies can be derived from the data in the figure.

The dimensions of the discharge element have an effect on the current (density) of the whole device as well (Fig. 4). The larger the inter-electrode distance, the lower the current. However, one has to have in mind that the ignition voltage increases with distance.

At equal inter-electrode distance and different electrode widths, the current is enlarged for the wider electrodes. In Fig. 4 this effect is about 10 % (in A/m^2). However, one has to take into account that the electrode length per unit area depends on the configuration of the element. The smaller the electrode width, the longer is the total length of the electrode pairs per unit area. The difference in the total lengths is about 20 % so that the current per unit length of the electrode pair differs about 30 %. As a result a 100 % increase of electrode width (at constant electrode gap) causes a 30 % increase in the

transferred charge.

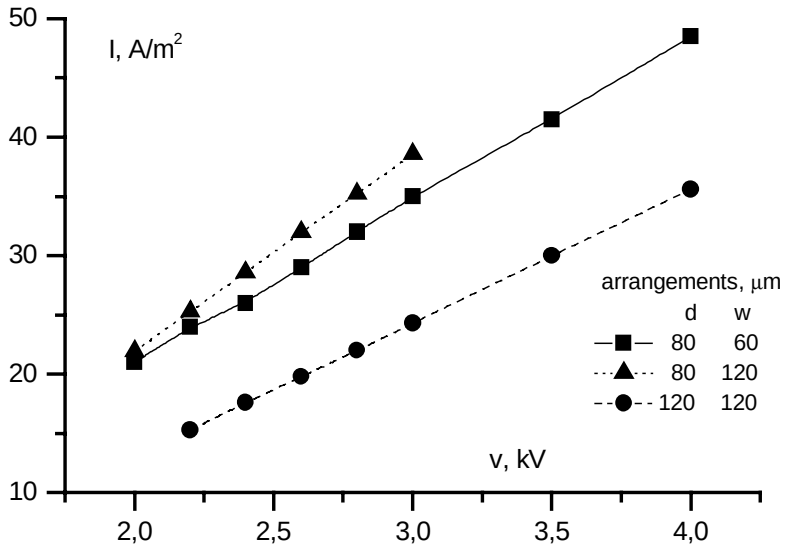


FIGURE 4: The influence of the dimensions of the CD element on the current of large area CD-arrangements (*d* is the inter-electrode distance and *w* the width of the electrodes).

5. CONCLUSIONS

A 2D model of a CD element has been used to investigate the influence of the configuration on the field strength and the current shape. The electrode gap, its width, the thickness of the dielectric layer on the electrodes as well as the permittivity has been varied. Although the initial field strength distributions differ considerably, they become more similar during the discharge process. The current shape is not influenced by different discharge element configurations.

With a modification of the model it was possible to simulate Lissajous figures of large area CD-arrangements. From Lissajous figures the ignition voltage, characteristic capacities as well as the current have been obtained for different configurations. The ignition voltage decreases with permittivity and increases with pressure. The capacities of CD-arrangements (with and without discharge) determine the power of the discharge and by this the current. The current is proportional to the applied voltage and permittivity. The smaller the electrode width and the larger the inter-electrode gap the lower the current.

The simulation results are in good agreement with measurements in general.

REFERENCES

[1] Gibalov V. I., Murata T. and Pietsch G. J., Productivity and Efficiency of Ozone Synthesis in Coplanar Discharge Arrangements. In: *Proc. 15th World Congr. of the Int. Ozone Ass.,* London, 2001, Vol. III, pp. 1-14

[2] Gibalov V. I., and Pietsch G. J., *J. Phys. D: Appl. Phys*., **33,** 2618-36 (2000)

[3] Murata T., Okita Y., Noguchi M. and Takase I., Basic Parameters of Coplanar Discharge Ozonizer. In: *Proc. 15th World Congr. of the Int. Ozone Ass.,* London, 2001, Vol. III, pp. 39-54

TOPIC 3:

Molecular synthesis and decomposition

LOW TEMPERATURE REDUCTION OF TUNGSTEN PRECURSORS IN RF DISCHARGE PLASMA REACTORS

Jan Jančа[a], Marek Eliáš[a] and Vlastimil Brožek[b]

a) Department of Physical Electronics, Faculty of Science, Masaryk University, Kotlářská 2, CZ-611 37 Brno, CZECH REPUBLIC

b) Institute of Chemical Technology, Technická 5, CZ-16628 Prague, CZECH REPUBLIC

Abstract. The new plasmachemical reduction techniques of tungsten precursors were investigated with the aim of producing a tungsten powder with high sinterable activity, enabling to rise the density of tungsten compact products above the hitherto technological limit. The application of non-isothermic hydrogen plasma enables iniciation of reduction processes at low temperature of neutral gas. The high electron temperature makes possible the increase of atomic hydrogen concentration entering into the reduction process.

1. INTRODUCTION

The influence of tungsten reduction parameters on the nucleation and crystal growth has been described from different points of view [1-4]. The tungsten metal powder production by hydrogen reduction usually proceeds in some temperature steps in the furnace between 600 - 1100°C. The input reactants are WO_2 - WO_3, resp. WO_{3-x} oxides obtained by thermal breakdown of precursors on the tungstate salts basis. The reduction process does not represent the simple conversion of oxides to the metals according to often cited reaction

$$WO_3 + 3\ H_2 = W + 3\ H_2O \qquad (1)$$

but there occur the simultaneous reduction and chemical transport reaction which influence in a decisive manner the morphology, the physical and chemical properties of the final product. Creation of volatile tungsten oxide-hydroxide $WO_2(OH)_2$ resp. WO_3H_2O in the W-O-H system plays an important role. The complicated transport reaction connected with its condensation influences the morphology and grain size of final product - tungsten metal powder. In addition the thermal cycle represents a refinement process, too. Impurities in reactants affect not only the thermodynamics but also the kinetic conditions of mass transfer.

The industrial and laboratory reduction process of tungsten metal powder production passes in two different types of devices, static (push furnace) or rotating tube furnaces. The modern furnaces with rotation tube reflects the new findings about diffusion controlled process with lowered aerodynamic resistance of powdered reactants and about generated water vapor motion through the layers of the reactant and product mixture.

In the macroscale of reduction furnace the reduction time or retention time of reactants in zones with changeable temperature is pursued. The motion of powdered mass throughput compared with the flow of gaseous reactants is given by the mentioned conditions. From the stoichiometric standpoint for the reaction course the input H_2/H_2O ratio is decisive, which results from initial moisture and changes of this ratio during proper reduction. The part of primary present or by reduction created water vapor is consumed for the $WO_2(OH)_2$ formation. Powdered reactant can in the course of reduction include all known forms of tungsten oxides. Their relations depend on previous processing of various forms of

[a] Jan92@physics.muni.cz

[b] vlastimil.brozek@vscht.cz

ammonium tungstates. Thus the density, porosity and grain size of reactant layer is influenced.

From the gaseous reactants only a small quantity passes through the moving powdered layer under non-isothermal conditions. In the layer, with few centimeter thickness, the laminar flow of gaseous reactant can change into a turbulent one. The flow change follows also from the increase of the quantity of water vapor. The controlling diffusion process takes place not only by the hydrogen diffusion through the surface, but also into the reactant pores. The water vapor diffuses out of the pores and its desorption plays an important role.

This complicated system was in our study complemented by a further dominating factor, i.e. atomisation and ionisation of molecular hydrogen by means of inductive RF discharge. It is impossible to predict the success of this affect of such technical arrangement because the number of moles of atomic hydrogen increases and changes the diffusion conditions. At the same time the reactivity grows and influences the formation of volatile products. Another important matter is that through this modification the hydrogen from cracked ammonia in situ can be utilized.

The diffusion of necessary amount of atomic hydrogen into individual grain pores of solid phase becomes more complicated, however the surface reactions are simplified due to recombination effects.

2. EXPERIMENTAL

2.1. Plasma chemical reactor

For the reduction of dihydrogen-decaammonium-dodecatungstate tetrahydrate (ammonium para-tungstate, APT) we used two a barrel shaped quartz reactors, in which the reduction was carried out under reduced pressure (0.1 - 1.2 kPa). First was used the capacitively coupled barrel reactor. Central part of discharge tube made of quartz (inner diam. of 4.2 cm, length of 90 cm) was inserted into electrically heated cylindric oven. Vacuum tightness of the tube was accomplished by means of two stainless steel flanges. The inner quartz cylinder (outer diam. 3.9 cm, length 30 cm) may be rotated. Both edges of the inner cylinder were bent inside by 2 mm to prevent possible escape of pulverised APT during the rotation. We used hydrogen as the working gas with possible admixture of argon. The discharge was maintained by means of two cylindrical electrodes, placed in the exterior of discharge tube near the ends of the oven. The rf power (max. 500 W) was fed from generator (13.56 Mhz) through an impedance matching network. Due to a capacitive character of the discharge, the plasma was strongly non-isithermic.

A complete description of a plasma discharge requires a choice of heating mechanisms and a geometric configurations that sustain these mechanisms. In the capacitively coupled RF plasma reactor the currents in the main body of the plasma lead to ohmic heating, while the voltage across the sheath leads to stochastic sheath heating. With the external coupling the power is transmitted to the plasma through the capacitance of the dielectric wall of a tubular reactor. Since RF generators are characterized by a purely resistive internal impedance, the scope of matching network is to balance the capacitive part of the reactor impedance with an inductance contribution. If the external capacitive coupling is used, then approx. 90% of the total output power can be lost in the matching network and power feedthrough. In the inductively coupled reactors the power coupling is not uniform unless the operating pressure is increased at values higher than 100 Pa. At higher pressures the energy transfer is more incorporated in the plasma chemical process and the energy loses in the matching network and power feedtrough are approx. 20%. With inductive coupling, there is no high energy ion bombardment of surfaces in the plasma and high density plasmas are easily achieved.

The second barrel shaped quartz reactor in which the reduction of APT was investigated was inductively cpoupled and consists of outer quartz tube (inner diam. 8.6 cm, length 50 cm) and inner quartz cylinder (outer diam. 8 cm, length 30 cm) - Fig.1. Vacuum tightness of the reactor was accomplished by means of two brass flanges. Output flange besides being connected to a pumping system contained also a removable cover with feedthough for turnable rod. Using this rod the inner quartz cylinder may be rotated. Feeds of the working gases as pressure gauges were placed in input brass flange. The working pressure and flow rate of gases were controlled by mass flow meters and by

system of needle valves. The pumping speed during the reduction process was reduced by the throttle valve. High frequency power from generator (27 MHz, max. power 4 kW) was fed through the marching network to the coil with the inner water cooling.

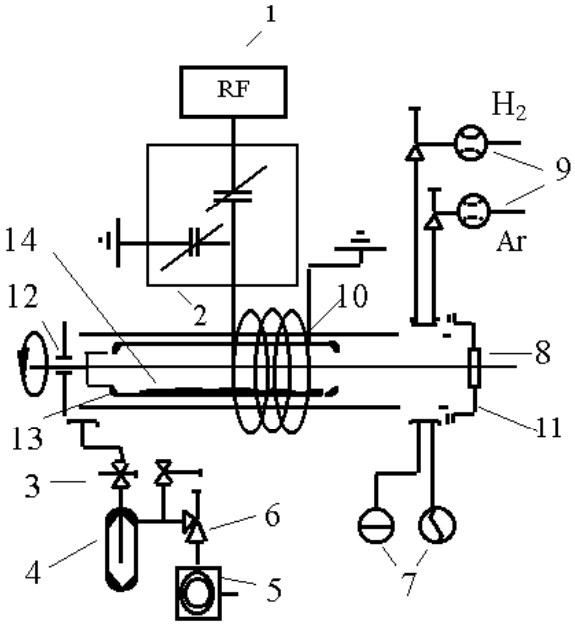


FIGURE 1. RF barrel reactor with inductive coupling.

1 - RF generator (27 MHz, 4 kW), 2- matching network gas inlet flange, 3- throttle valve, 4-cold trap, 5-vacuum pumping system, 6-valve, 7-vacuum gauges (membrane, Pirani), 8 - quartz observing window, 9 - mass flow meters, 10 - outer quartz reactor tube with coil (inductive coupling), 11 - inlet flange, 12 - outlet flange, 13 - inner quartz rotating cylindrical tube, 14 - pulverized APT sample.

Light irradiated from the rf discharge was continuously recorded by monochromator Jobin-Yvon HR 320 with CCD. Recorded atomic and molecular spectra were used for the monitoring of the plasma reduction APT process.

2.2. Reactants

Experimental investigation of plasma chemical reduction were performed with ammonium para-tungstate from OSRAM Bruntal Ltd, produced by used cemented carbides recyclation. The hydrogen purity was 99,8% with 0,2% oxygen, the purity of argon was 99,996%.

2.3. Analytical methods

Diffractograms of reactants and products were made on Diffractometer System XRD 3000 (Seifert, Germany) (CoK_α) device. Powder diffraction data were compared with database PDF 2. The density, porosity and pore surface were stated on mercury porosimeter Autopore 8200 Micromeritics and helium densitometer Accupyc 1330 Micromeritics. The images of microstructure were made with electron scanning microscope CamScan 4DV, Cambridge UK. For the thermal analysis Derivatograph Q-1500 D, MOM Budapest was used.

3. RESULTS AND DISCUSION

According to differential thermal analysis (Fig.2), $(NH_4)_{10}[H_2W_{12}O_{42}].4H_2O$ dehydrates in the range 20 - 100°C to anhydrous salt. In the interval 180 - 225°C transformation according to eq.(2) occurs:

$$(NH_4)_{10}[H_2W_{12}O_{42}] \rightarrow (NH_4)_6[H_2W_{12}O_{40}].\ 2H_2O + 4\ NH_3 \qquad (2)$$

The created dihydrogen-hexaammonium-dodecatungstate dihydrate by another name ammonium meta-tungstate (AMT). In relatively wide temperature interval 230°C to 325°C, ammonia and water vapor are released and ammonium metatungstate transforms into anhydrous diammonium dodecatungstate according to eq.(3).

$$(NH_4)_6[H_2W_{12}O_{40}]\ 2H_2O \rightarrow (NH_4)_2[W_{12}O_{37}] + 4\ NH_3 + 5\ H_2O \qquad (3)$$

The tungsten oxide is formed at temperatures over 400°C with further release of ammonia and water vapor (eq.4).

$$(NH_4)_2[W_{12}O_{37}] = 12\ WO_3 + 2\ NH_3 + H_2O \quad (4)$$

Under certain conditions non stoichiometric tungsten bronze $(NH_4)_xWO_3$ can arise. In most cases however ammonia dissociates and hydrogen partially reduces the tungsten trioxide to lower oxides. Most known is the blue oxide (TBO) $WO_{2,9}$ resp. $W_{20}O_{58}$ with a density 7,15 g cm^{-3}. Another oxide $WO_{2,72}(W_{18}O_{49})$ which has a violet colour and a density 7,78 g cm^{-3} is formed.

The crystallographic features and extraordinary stoichiometry are caused through partial replacement of common octahedral edges which form by interlayer shift (so-called Crystal Shear Structures - CSS). The partial reduction of intermediate products by cracked ammonia in our apparatus was supported by capacitive/inductive RF discharge, eventually by flow of generated hydrogen plasma.

The experimental conditions are summarized in Table 1.

TABLE 1. Conditions of reduction experiments

Capacitive (CC) or inductive (IC) coupling	Temperature (^{o}C)	P total (Pa)	H_2 flow (sccm)	P (W)
CC	500 - 700	1000	270 - 540	100
IC	700 - 800	150 - 300	200 - 500	2 200
IC	700 - 850	400 - 500	650 - 700	2 200

The kinetics of the reduction process was monitored by NH, OH, N_2 and H_2 molecular spectra.The results are summarised in Fig. 2.

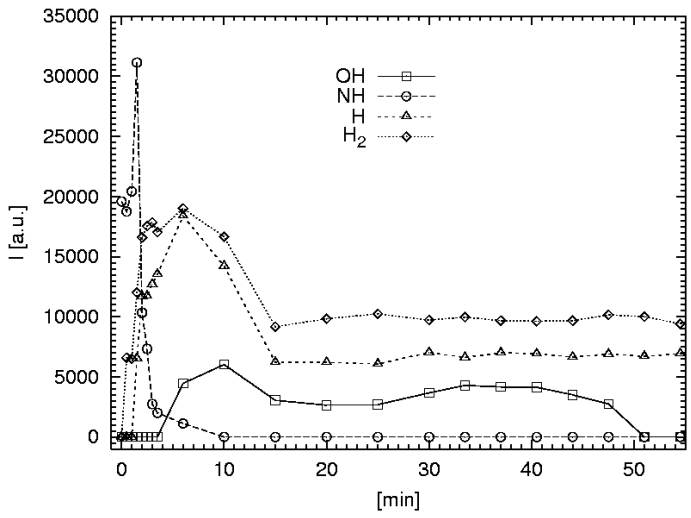


FIGURE 2. Time dependence of selected molecular band intensities used for the monitoring during the plasma reduction process.

The moisture influence on nucleation conditions of powdered metal is of primary interest. Besides the reduction temperature the dynamic moisture in the reactant layer attributes to nucleation and tungsten grain growth. In the presence of hydrogen above 420°C the reactant is only WO_2. The presence of WO_2 as main intermediate product is documented on the diffractogram of APT sample reduced at 600°C. The low moisture during further reduction of $WO_2 \Rightarrow W$ at low layer thickness results in high degree of nucleation and therefore to finer grain size. These products are expected to prove increased reactivity (sinterability). On the contrary high moisture suppresses the nucleation rate and leads to a coarser grain size.

The input amount of APT determines the water vapor quantity released during the reduction process. The powdered layer call forth the resistence to gas phase motion. The water vapor retention (local moisture of powder) influences the nucleation and the conditions of metallic particle growth. Therefore a direct proportion exists between layer thickness and final grain size of product.

The overall porosity of powdered layer and its permeability is given by superposition of macroporosity (the space between grains) and microporosity of individual oxide grains. For this measurement the 80 – 100 μm APT fraction was selected. The specific surface was 0,527 m^2g^{-1}, average pore size was 244 nm.

From the loose volume and density it follows that the porosity of free poured layer of APT is about 20%, the porosity value of tungsten oxides prepared by APT thermal decomposition increased to 75%. To this value it is necessary to add the internal porosity of individual grains, which is characterised not only by the increase of average pore size to 447 nm but also a remarkable growth of specific surface to 2,76 $m^2 g^{-1}$.

High porosity of powdered layer, in which better flow of gas mixture H_2-H_2O during reaction, leads to creation of tungsten with finer grain size. The mixing then lowers the value of hydrodynamic and aerodynamic resistance to a minimum. For the diffusion flow the porosity of proper reduced precursor is decisive. Increased hydrogen flow lowers the value of H_2O/H_2 ratio and shifts the equilibrium in the direction of finer products. The dew point, which is connected with temperature and H_2O/H_2 ratio, is a parameter pursued in the production as a qualitative indicator of reduction direction. The hydrogen which has high moisture leads to coarse tungsten grains.

4. CONCLUSIONS

Introductory experiments with applying the hydrogen plasmachemical activation for tungsten reduction from oxygen containing precursors indicate the possibility of further lowering the reduction temperature in comparison with conventional technologies.

Direct decomposition of precursors in the system, which allows hydrogen recyclation, appears economical for taking advantage of hydrogen reuse which raises through ammonia thermal dissociation. This breakdown to hydrogen and nitrogen can be activated in a different manner. Preferentially it occurs on the solid phase surface. For metallic tungsten the zero-order reaction starts at about 850°C [5,6]. This temperature complies with kinetics of reduction under industrial conditions. The lowest limit for atmospheric hydrogen pressure the temperature 600°C can be considered.

The plasma presence brings the temperature of ammonia decay from APT precursor down to 500°C and contributes according to stoichiometric proportions to the hydrogen enrichment in the system of about 25%. The comparison of theoretical calculations with experimental results [7] is not reliable yet because of the low value of the statistical significance coefficient due to relatively high scatter of individual results. The experiments performed show that in the inductively coupled plasma reactor is the RF energy more effectively consumed in the reduction process.

As the next supporting argument for plasmachemical technology application a better sinterability of tungsten powder is expected, which will be investigated successively through evaluation of sintering tests.

ACKNOWLEDGMENTS

This work was supported through the NATO SfP 972379 Program and by the Ministry of Education Czech Rep., contracts ME 301 and MSM 143100003.

REFERENCES

[1] Haubner R., Schubert W.D., Lassner E., Schreiner M., Lux B., J. Refract. Met. Hard Mater., **2**, 108-15 (1983)
[2] Lassner E., Schubert W.D., *Tungsten,* Cluwer Academic/Plenum Publishers N.Y. 1999
[3] Agte C., Vacek J., *Tungsten and molybdenum*, SNTL Praha 1954.
[4] Benesovsky F., *Pulvermetallurgie und Sinterwerkstoffe*, Metallwerk Plansee 1980.
[5] Šarman L., Hák L., Janča J., Dufek V., Brožek V., Proc. International. Conference on Tungsten, Hard Metals and Refractory Alloys, Sept. 25-27, 2000, Annapolis, Maryland, Sess.7/3. , pp. 151-8
[6] Janča J., Eláš M., and Brožek V., Proc. 15th ISPC Orléans 2001, vol. I, pp. 59- 64
[7] Tsvetkov Yu.V., *Plasma Metallurgy - Current State, Problems and Prospects,* Proc. 14th ISPC Prague 1999, Vol.I, pp.11-3

PLASMA-PROMOTED PARTIAL OXIDATION OF METHANE TO SYNGAS OVER α-ALUMINA SUPPORTED NICKEL CATALYST IN DIELECTRIC-BARRIER DISCHARGE

B. Pietruszka and M. Heintze[1]

Institute of Low Temperature Plasma Physics (INP) Greifswald,
Friedrich-Ludwig-Jahn-Strasse 19, 17489 Greifswald, GERMANY

Abstract. The combination of a dielectric barrier discharge and an α-alumina supported nickel catalyst for the synthesis gas (H_2 and CO) production was studied. Two processes - partial oxidation of methane and combined steam-oxygen reforming of methane were investigated. It was found that the presence of a catalyst in the discharge zone enhanced plasma selectivity. The methane conversion and product distribution were functions of oxygen concentration in the feed gas and the input power energy. Selectivity to hydrogen as high as 90% was obtained.

1. INTRODUCTION

Currently the utilization of natural gas to synthesis gas (or hydrogen) or directly to liquid hydrocarbons production becomes one of the most investigated chemical processes [1-3]. Synthesis gas production is mainly realized *via* steam reforming of methane ($CH_4+H_2O=3H_2+CO$, $\Delta H^o=229$kJ/mol) over a nickel catalyst at temperatures above 1000°C. Such high temperatures result in high costs of syngas production (above 60%) and forces to look for an economical technology [1]. Partial oxidation of methane ($CH_4+{}^1/_2O_2=2H_2+CO$, $\Delta H^o=-59$kJ/mol) or combined steam-oxygen reforming of methane have been investigated as promising processes for CO and H_2 production. As an alternative way to chemical processes the combination of plasma and catalysis has been widely investigated during recent years [4-8]. Different types of discharges i.e. dielectric-barrier discharge, corona discharge, gliding arc, microwaves, etc., also with the combination of a catalyst in the plasma zone (or behind it), are used as an effective way to activate the reagents mixture (CH_4 and O_2, CO_2 or H_2O). Caldwell et al.[6] have investigated syngas production via partial oxidation of methane in an AC corona reactor. It was found that the oxygen enhances the activation of methane and changes the product distribution. An increase of oxygen in the feed gas caused significant enhancement of methane conversion and the selectivity to carbon oxide whereas the selectivity to hydrogen was almost constant. The best results of methane conversion and selectivity towards syngas were found for a CH_4:O_2 ratio of 2 (stoichiometric value), no matter if pure oxygen or air were used. Also, operating at low discharge power and increasing reaction pressure were found to improve the efficiency of methane conversion. Kogelschatz et al. [7] have investigated methane dry reforming ($CH_4+CO_2=H_2+CO$, $\Delta H^o=247$kJ/mol) to syngas in a dielectric-barrier discharge (DBD) reactor up to 230°C at atmospheric pressure. It was found that increase of the electric input energy enhanced the syngas production whereas the H_2:CO ratio depended strongly on the CH_4:CO_2 ratio in the feed gas. No influence of temperature, pressure and specific input energy on the syngas composition was detected. High amount of CH_4 in the feed mixture and higher temperature promoted wax formation and carbon deposition. The further investigation of the combination of a DBD reactor with a catalyst in the plasma zone [8,9] for the CO_2 reforming of CH_4 led to conclusion that the catalyst in the discharge zone can significantly improve the efficiency of the plasma chemical reactions. The nickel catalyst was found active (much more than a rhodium one), showing clearly interactions between discharge-activated feed gases and the catalyst surface.

[1] Electronic address: heintze@inp-greifswald.de

As an alternative way to syngas production we have investigated the partial oxidation of methane and combined oxygen-steam reforming of methane over an α-alumina supported nickel catalyst in a DBD reactor at temperatures up to 500°C and atmospheric pressure.

2. EXPERIMENTAL SET-UP

In Fig.1 the scheme of the reactor is shown.

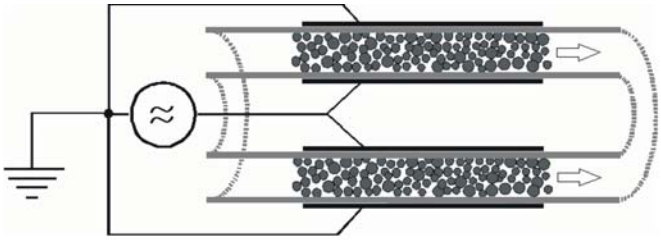


FIGURE 1. The schematic view of a packed bed reactor filled with catalyst grains.

The reactor consists of an outer quartz tube with an outer diameter of 20 mm and the wall thickness 1.5 mm. The inner tube has an outer diameter of 15 mm, giving the discharge gap of 1.5 mm. The inner electrode (high voltage) is formed by a thin metal coating inside the inner tube. In the outer tube a metal heating band is wound, which serves also as the outer (grounded) electrode. The catalyst is placed in the discharge gap between the tubes. The length of the catalyst bed is 10 cm, resulting in the reaction volume approximately 7 cm^3. To drive the discharge an AC high voltage (frequency: 27.8 kHz) was generated with a maximum of 10 kV. The discharge power was calculated from the time averaged product of discharge voltage and current. The electric power in the performed experiments was changed up to 40 Watt.

The catalytic measurements were carried out using an α-Al_2O_3 supported nickel catalyst (Süd-Chemie). The catalyst sample with grains between 710-1000 μm was calcinated in air at 700°C for 4 hours. The BET-surface was 6 m^2g^{-1}. The amount of the catalyst in the reactor was 6.4g. Before the catalytic measurements the catalyst was reduced in 6.7% H_2 in Ar at the flow rate of 150 sccm, at the temperature range between 200-450°C with the slope of 5 $Kmin^{-1}$ and kept at the final temperature for 1 hr. The reaction was conducted at the temperatures up to 500°C, at total flow rates of 150 and 170 sccm. Air containing 20% of O_2 was used as an oxidation mixture. A small amount of argon was added to monitor the total volume flow at the reactor outlet and the volume variations during the reaction. For the partial oxidation of methane the total flow rate was 150 sccm and the reagents ratio was CH_4:Air:Ar=40:100:10 giving a CH_4:O_2 ratio of 2:1. For the combined oxygen-steam reforming of methane the gas (flow of 170 sccm, CH_4:Air:Ar=50:100:20) was passing through the bubbler (heated at 60°C, p_{H2O}=19.92%) giving the final reagents composition CH_4:O_2:H_2O=2.5:1:1. Product analysis was done using NDIR, MS and GC/FID connected on-line.

3. RESULTS AND DISCUSSION

A series of experiments was performed to study the effect of the electric power, methane/oxygen ratio and addiction of steam on the partial oxidation of methane to synthesis gas. The product distribution, mainly H_2, CO, H_2O and CO_2, was investigated as a function of the discharge power and the reagents (CH_4:O_2) ratio.

3.1. The discharge power.

In Fig. 2 the CH_4 and O_2 conversions and product distribution versus temperature for the catalyst and increasing power input are presented.

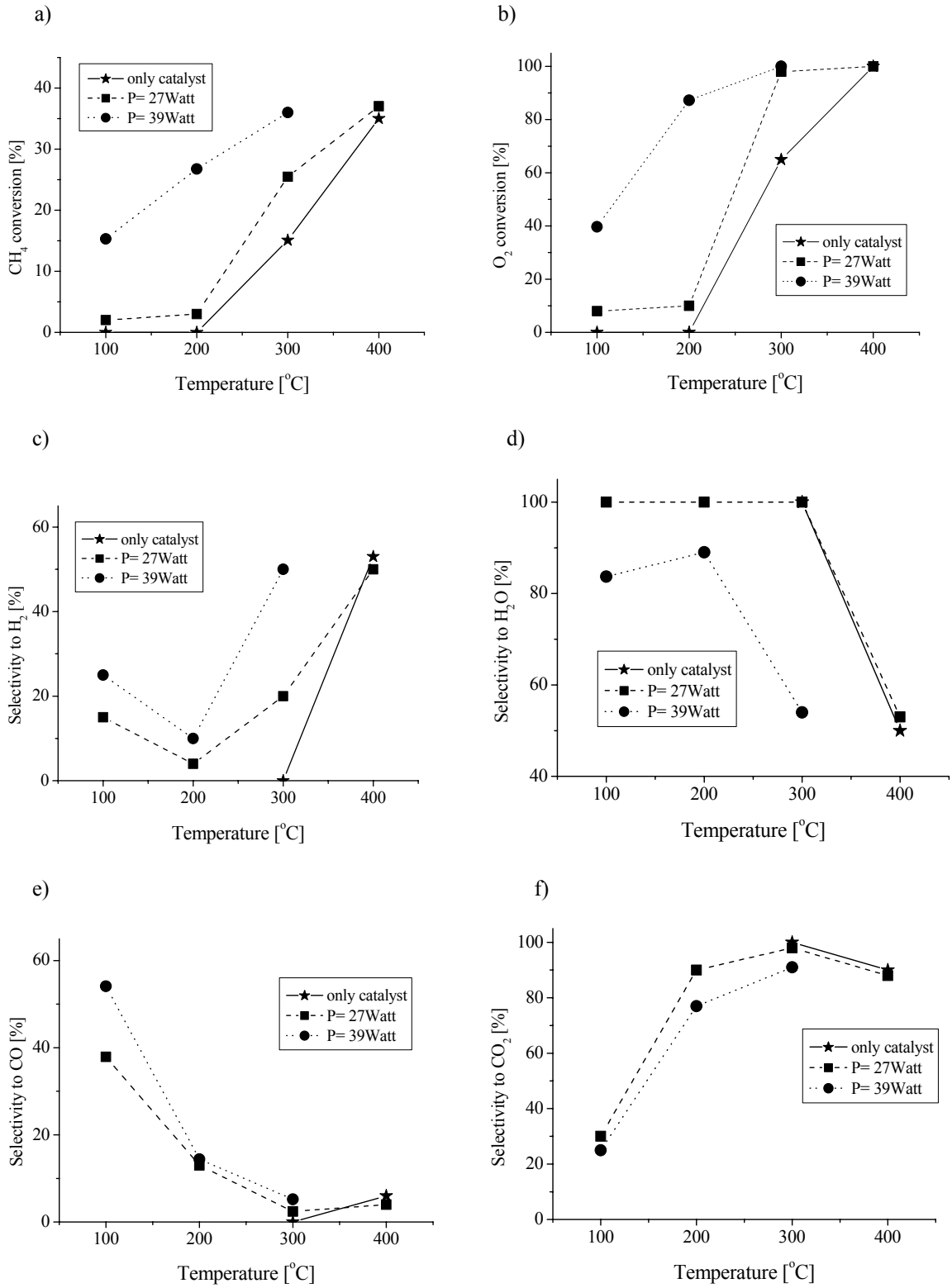


FIGURE 2. The CH_4 and O_2 conversions (a,b) and selectivity to H_2, H_2O, CO and CO_2 (c,d,e,f) versus temperature for the catalyst and increasing power input.

As shown in Fig.2, the increasing input power enhanced methane and oxygen conversion as well as the selectivity to hydrogen and carbon oxide. At lower temperatures up to 200°C some traces of methanol and C_2-C_3 hydrocarbons (C_2H_2, C_2H_4, C_2H_6 (mainly), C_3H_6 and C_3H_8), no more than 0.1% were detected as by-products. The catalyst was not active up to 200°C and even with the plasma

assistance the process was selective mainly to H_2O and CO_2. At 300°C the catalyst was active but selectivity only to H_2O and CO_2 was detected. At 400°C the catalyst became active and the plasma assistance had no major influence on the product distribution. At that temperature the oxygen conversion reached 100% and at the top of the catalyst bed some sparks were observed. The reason is due to the total combustion process ($CH_4+2O_2=2H_2O+CO_2$ ΔH^o=804 kJ/mol) which started to dominate. The produced heat promoted probably the water gas shift reaction ($CO+H_2O=CO_2+H_2$ ΔH^o=-40kJ/mol), which leads to higher selectivity to H_2, as it was observed. The increase of reaction temperature promotes the H_2 production whereas CO becomes less. It is important to notice that oxygen conversion was always higher than methane conversion even for total combustion of methane. Under such conditions (low temperature) the catalyst surface was oxidized (Ni to NiO) causing further oxidized of CO to CO_2. This can be also an explanation of low CO production.

3.2. The CH_4:O_2 ratio

In Fig. 3 the influence of the oxygen concentration on the methane conversion and product distribution in the presence of plasma are presented. At 300°C the catalyst was selective to H_2 and CO only for the lowest oxygen concentration (CH_4:O_2=4:1).

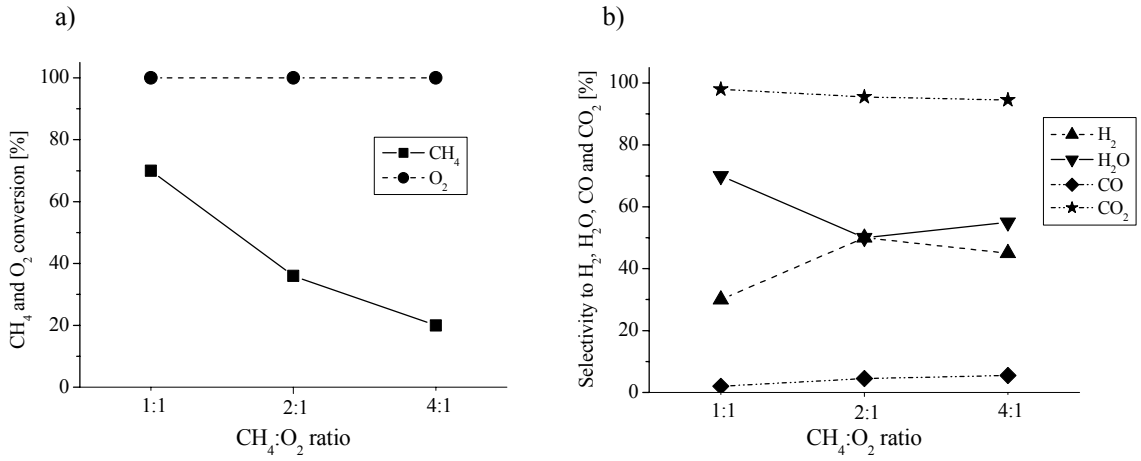


FIGURE 3. Methane and oxygen conversion (a) and product distribution (b) versus the CH_4:O_2 ratio in the reagent mixture (temperature of 300°C, P=15Watt, reagent flow rate of 150 sccm).

As seen in Fig.3, the methane conversion was strongly dependent on the oxygen concentration in the feed gas. In the presence of discharge for all the investigated CH_4:O_2 ratios the oxygen conversion always reached 100% and its increase in the feed gas caused increase in CH_4 conversion. The product distribution, mainly H_2, H_2O, CO and CO_2, was controlled by oxygen concentrations. The process was selective, in all the cases, to H_2, even for the ratio of CH_4:O_2=1:1, where the selectivity to H_2 was about 30%. The highest selectivity to hydrogen (46%) was obtained for a CH_4:O_2 ratio of 2:1. At the lowest oxygen concentration (CH_4:O_2=4:1) the results obtained with and without plasma were similar, only the selectivity to H_2 was about 10% higher for the plasma process. For all the cases the selectivity to CO was very low, up to only 5%. For the lowest oxygen concentration some traces of C_2-C_3 hydrocarbons (mainly C_2H_6), no higher than 0.2%, as by-products were detected.

3.3. Oxygen-steam reforming of methane

In Fig.4 the CH_4 and O_2 conversion and product distribution versus increasing temperature for the input power P=27Watt are presented.

When steam was added to the reagent mixture the only reaction was observed when the plasma was sustained in the reactor. The detected products were H_2, H_2O, CO and CO_2. The detected amount of water was always higher than the amount added to the reagent mixture. Thus, we consider, that water did not react with CH_4 and was a product in the process. To calculate the selectivity to H_2O the difference between its output and input concentrations was taken.

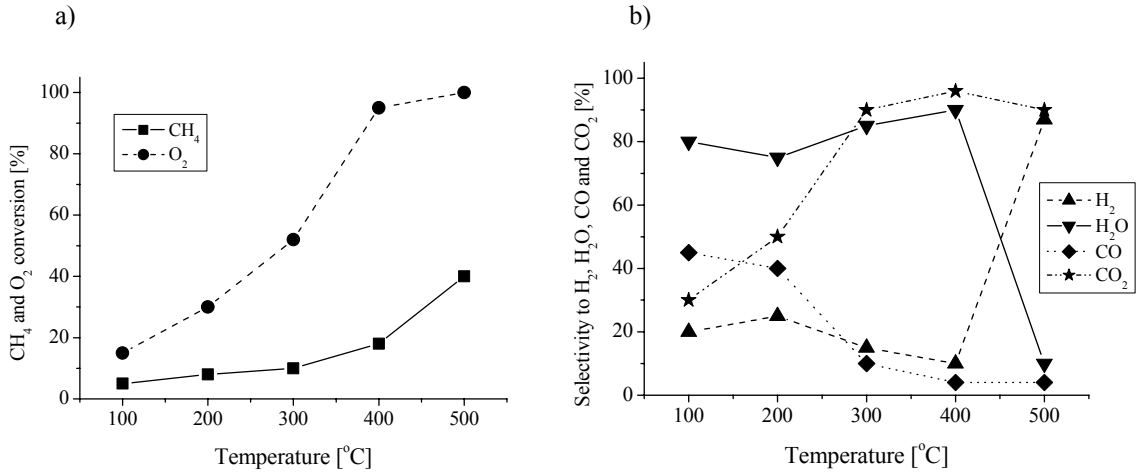


FIGURE 4. The CH_4 and O_2 conversion (a) and product distribution (b) versus temperature (P=27Watt).

As seen in Fig.4 with increasing temperature an increase in the CH_4 and O_2 conversion and changes in the product distribution are observed. The changes in CH_4 and O_2 conversions and selectivity to CO and CO_2 were very similar to the results for partial oxidation (Fig. 2). The selectivity to H_2 was decreasing up to 400°C and selectivity to H_2O was increasing whereas for the partial oxidation the tendency was opposite. The highest selectivity to H_2 was 90% for the reaction with water whereas for the partial oxidation it was only below 50%. For the increasing power input some changes in conversion and selectivity as for the partial oxidation were found (results not shown). The increase of power input enhanced selectivity to H_2 and CO and decreased the selectivity to H_2O and CO_2. The observed selectivity to CO was higher only at temperatures 100-200°C, whereas for the higher temperatures mainly CO_2 was produced. In the presence of steam no sparks in the catalyst bed were observed. Some changes in the catalyst properties were observed (XPS, PTR/O, SEM/EDS, BET), especially for the partial oxidation process, resulting in the total catalyst deactivation due to coke deposition.

ACKNOWLEDGMENTS

Thanks are to Dr Kui Zhang for the helpful discussion.
Kirsten Anklam and Dr Mario Hannemann for the technical assistance.
This research was supported by the E.U. (contract number ICA2-CT-2000-10004)

REFERENCES

[1] Sundset T., Sogge J. and Strom T., *Catal. Today*, **21**, 269-283 (1994)
[2] Dietz A.G., Schmidt L.D., *Catal. Lett.*, **33**, 15-27 (1995)
[3] Pietruszka B., Najbar M., Litynska-Dobrzynska L., Bielanska E., Zimoowska M., Camra J., *Studies in Surface Science and Catalysis,* **136**, 471-477 (2001)
[4] Lesuer H., Czernichowski A., Chapelle J., *Hydrogen Energy,* **19**, 139-144 (1994)
[5] Cormier J.-M. and Rusu I., *J.Phys.D., Appl. Phys.,* **34**, 2798-2803 (2001)
[6] Caldwell T.A., Le H., Lobban L.L., Mallinson R.G., *Studies in Surface Science and Catalysis,* **136**, 267-273 (2001)
[7] Zhou L.M., Xue B., Kogelschatz U., Eliasson B., *Energy and Fuels*, **12**, 1191-1199 (1998)
[8] Kraus M., Eliasson B., Kogelschatz U., Wokaun A., *Phys.Chem.Chem.Phys.,* **3**, 294-300 (2001)
[9] Kraus M., *Catalytic CO_2 reforming of methane in a dielectric-barrier discharge,* Ph.D. Thesis, Swiss Federal Institute of Technology, Zurich, 2001

DEPENDENCE OF THE OXIDATION PROPERTIES OF A DIELECTRIC BARRIER DISCHARGE IN AIR ON THE PLASMA AND GAS TEMPERATURES

M. Dhainaut[a], E. Odic[b], M. Goldman[a], A. Goldman[a] and C. Karimi[b].

a) Laboratoire de Physique des Gaz et des Plasmas (Université Paris Sud - CNRS), Equipe Décharges Electriques et Environnement, SUPELEC, F-91192 Gif-sur-Yvette Cédex, FRANCE

b) Service Electrotechnique et Electronique Industrielle, SUPELEC, F-91192 Gif-sur-Yvette Cédex, FRANCE

Abstract: Investigations were carried out on atmospheric pressure dielectric barrier discharges, in a point-to-plane geometry energized with ac or pulsed high voltage power supplies of variable frequency (from 3.5 to 50 kHz). Electrical / chemical coupling processes on the one hand, and thermal / chemical coupling processes on the other hand were studied through ozone production. Correlations based on these properties were established, using emission spectroscopy measurements for the determination of the plasma gas temperature. The temperature in the active gas volume, i.e. the volume in which the ozone three body formation reaction takes place, was evaluated thanks to comparisons between experimental data and calculations based on a simple model for the ozone formation.

1. INTRODUCTION

The chemical reactivity of Non Thermal Plasmas produced at atmospheric pressure in oxygen containing gaseous mixtures by electrical discharges is mainly based on oxidation processes. The specific oxidation properties principally lay on the generation, through direct electron impact with molecular oxygen, of short life primary species such as atomic oxygen O (ground state ^{3}P and excited state ^{1}D) and excited molecular oxygen O_2 ($^1\Delta_g$). For gas phase depollution purposes, these highly reactive species can directly react on target molecules (VOC, NO), or on the background gas (molecular oxygen) to form ozone. The two chemical pathways can be considered as competitive [1], and according to the required reactor chemical behavior, one or the other should prevail. Moreover, ozone itself is widely used as an oxidizing agent for drinking water treatment but also for gas treatment (odor treatment) and consequently is considered as an efficient reactant for environment protection industry. However, at a laboratory scale and according to its strong temperature dependent formation / destruction kinetics, ozone monitoring can also be used as a diagnostic tool highlighting the electrical / chemical and thermal / chemical couplings phenomena. The aim of this paper is to characterize these coupling effects studied with a dielectric barrier discharge reactor, in which the discharge input power, but also the medium temperature, can be increased through an increase either of the high voltage peak amplitude or of the ac voltage signal frequency (the pulsed voltage repetition rate in the case of a pulsed high voltage).

2. EXPERIMENTAL SET-UP

2.1. Experimental set-up general description

The discharge reactor consists of a point-to-plane electrode system. The high field stainless steel electrode (point ≈ 50 µm of curvature) is connected to an ac or pulsed high voltage supply. The

[a] Electronic address: marielle.dhainaut@lpgp.u-psud.fr

[b] Electronic address: emmanuel.odic@supelec.fr

grounded brass plane electrode is covered with a dielectric barrier (alumina-silicate ceramics) of 3 mm thickness. The gas gap length d between the high field electrode and the dielectric barrier surface is fixed to 2 mm. The gas flow is introduced along a direction parallel to the point-to-plane revolution axis directly in the vicinity of the point electrode. A more detailed description of the complete experimental set-up can be found in [2]. Three measuring devices are used, allowing a simultaneous monitoring of (i) the applied voltage and discharge current signals, (ii) the plasma temperature and (iii) the reactor outlet gas phase analysis. Experiments are carried out with synthetic dry air (water vapor content < 3 ppm) with a variable gas flow rate fixed between 0.03 and 0.1 Nm^3/h. Gas temperature is controlled and measured from 272 to 295 K using a cryo-cooling circuit (Huber) and a temperature probe (Hanna 253-323 K range).

2.2. Electrical measurements

Electrical measurements are carried out using a Lecroy LC347A 500 MHz – 2 GS/s numerical oscilloscope. The high voltage applied to the point electrode is acquired through a Lecroy 100 MHz 1:1000 voltage probe, providing the $v_1(t)$ signal. The low field electrode is connected to ground through a 50 Ω resistor; the discharge current signal is monitored through the resistor voltage rises and drops $v_2(t)$. Averaged power P measurements are performed by means of instantaneous current/voltage values multiplication as follows:

$$P = \frac{1}{nT} \times \frac{1}{R} \times D \times \int_0^{nT} v_1(t).v_2(t).dt \qquad (1)$$

where T is the applied voltage signal period, n the number of complete periods taken into account for the area calculation, R the measuring resistor value (50 Ω) and D the high voltage probe ratio. The input energy density J is defined as the ratio of the injected power P by the gas flow rate. For the study of the discharge current signal itself (stored by the oscilloscope and transferred to the computer), an accurate electrical analysis is realized using a numerical data treatment. The capacitive current is compensated. The constitutive components of the discharge current (pulsed current I_p and pseudo continuous current) are then distinguished, identified and quantified. Such measurements and numerical treatment are reported and discussed in details in a previous paper [3].

2.3. Temperature measurements

Temperature measurements are performed, using emission spectroscopy for the study of the $0 \rightarrow 1$ band of the second positive system, i.e. the transition:

$$N_2(C^3\Pi_u) \rightarrow N_2(B^3\Pi_g) + h\nu \qquad (2)$$

used to determine the rotational temperature of the $C^3\Pi_u$ state, and by identification, the rotational temperature of the fundamental state, i.e. the neutral gas temperature. These measurements thus provide an evaluation of the temperature of the plasma gas itself, so called plasma temperature T_{pl}, in the filamentary discharge [2].

2.4. Gas phase chemical measurements

Chemical gas phase measurements are carried out by means of absorption spectroscopy. Ozone is identified and quantified thanks to its 253.7 nm Hartley absorption band observed with a UV Perkin-Elmer Lambda 18 spectrophotometer (10 cm optical pathway UV gas cell, detection threshold value : 500 ppb). In all experiments, the UV gas cell temperature was checked and maintained to constant room temperature (295 K).

3. RESULTS AND DISCUSSION

For a given reactor geometry, if one wants to evaluate chemical reaction yields (ozone production for

this study) for different gas flow rates, the input energy density J ($J.l^{-1}$) is a suitable parameter as shown in Figure 1 (note that for the considered reactor geometry, residence time and gas flow rate are actually disconnected) which exhibits a strong dependence of the ozone production energy cost on the applied voltage frequency and waveform (i.e. pulsed and ac 3.5 – 50 kHz high voltage signals). Differences observed on the chemical reaction kinetics may be attributed to dominant (i) electrical processes (current signal shape) or (ii) thermal processes.

3.1. Electrical / chemical coupling processes

It is now well admitted that, for a given discharge regime, ozone production is mainly linked to the discharge current [4], independently of the gap length and of the applied voltage. In Figure 1, we distinguish two separate curves for the ac and pulsed 15 kHz applied voltage signals. If we now turn to another representation, plotting ozone concentration as a function of the pulsed current integral summed up over a high voltage period Q_p (as reported in a previous paper [5]), we observe that the two 15 kHz curves of Figure 1 merge into a unique linear curve. In order to extend the study to different frequency values F, we introduce the pulsed discharge current I_p defined as $I_p = F.Q_p$. In Figure 2, we can see that linear relationships are in fact obtained for all frequencies, but with different slopes. Increasing energy yields of Figure 1 correspond to increasing $[O_3] = f(Ip)$ linear slopes of Figure 2, and so to decreasing frequency values.

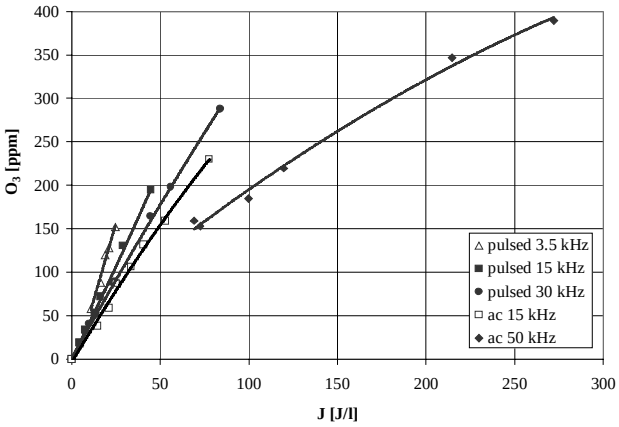


FIGURE 1 Ozone concentration vs. J for different voltage frequencies (feed gas at room temperature)

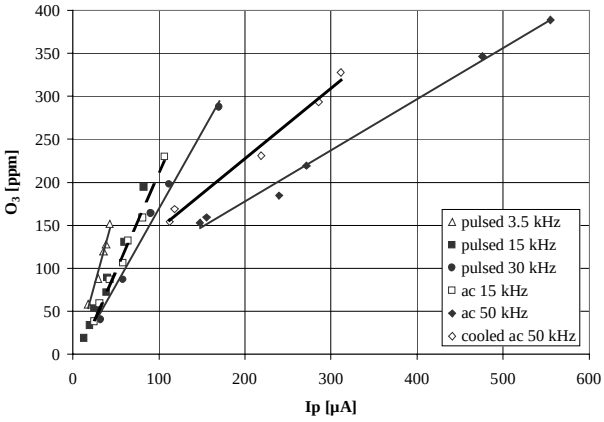


FIGURE 2 Ozone concentration vs. pulsed current I_p for different voltage frequencies (feed gas temperature : thin and dotted lines = room temperature, bold line = 272 K)

The better energy yield observed at 15 kHz for the pulsed voltage in comparison with the case of an ac voltage comes from the different energy levels required to obtain a same given I_p value. But, while the current pulses have similar characteristics in both cases, on contrary, different frequencies mean, for a same I_p value, completely different pulses characteristics (see Table 1), i.e. different production rates of atomic oxygen and thus O_3 production rates as long as there is no significant increase of the plasma and gas temperatures, which is not the case for the 50 kHz ac voltage.

TABLE 1 Current pulses characteristics corresponding to a same pulsed current I_p (40-42 µA) for three different pulsed voltage frequencies

	Number	Amplitude (mA)	Duration (ns)	Charge (nC)
3.5 kHz	2	412/49	95/50	10.05/1.89
15 kHz	1	172	80	2.69
30 kHz	1	82	85	1.46

3.2. Thermal / chemical coupling processes

On the whole range of investigated frequencies, in only one case (50 kHz ac voltage), the plasma

temperature T_{pl} exceeds 450 K, reaching in this particular case 740 K (for I_p maximum value). In order to modify the heat transfer processes in the reactor, an attempt was made by cooling the feed gas from 295 to 272 K. This did not change neither the pulsed current characteristics, nor the plasma temperature T_{pl} (740 K), but increased the $[O_3] = f(Ip)$ slope (see the bold line in Figure 2). This result can be attributed to the cooling of the filamentary discharge surrounding volume, i.e. the gaseous volume where ozone formation / destruction reactions take place [6, 7]. At this stage, a complementary thermal parameter should be introduced : the temperature T_g of this gaseous "active" volume. This peculiar parameter, submitted to important space and time gradients, and of crucial importance for the chemistry, cannot, in our case, be measured.

Nevertheless, simple calculations allow us to determine its averaged value in the "active" volume, using the following reactions for ozone formation and thermal destruction

(i) formation: $e + O_2 \rightarrow e + O + O$ $\quad k_1 = 2.0\times10^{-9}\ cm^3s^{-1}$ (3)

$O + O_2 + N_2 \rightarrow O_3 + N_2$ $\quad k_2 = 5.58\times10^{-29}\ T^{-2}\ cm^6s^{-1}molec^{-2}$ (4)

$O + O_2 + O_2 \rightarrow O_3 + O_2$ $\quad k_3 = 8.6\times10^{-31}T^{-1.25}\ cm^6s^{-1}molec^{-2}$ (5)

(ii) destruction: $O_3 + O_2 \rightarrow O + O_2 + O_2$ $\quad k_4 = 73\times10^{-11}exp(-11400/T)\ cm^3s^{-1}molec^{-1}$ (6)

Ozone formation reactions and thermal destruction reactions are considered successively and treated independently. The residence time is fixed to 15 µs for the formation reactions, in agreement with the literature for air [8], and incremented from 15 µs up to 2.5 ms for the thermal destruction reaction. For reactions (5) and (6), the atomic oxygen net concentration values come from low temperature ($300 \leq T_{pl} \leq 380$ K) experimental data, assuming that in these conditions the ratio O radical/ozone is equal to 1. Attention is drawn on the fact that the calculated temperature values T_g remain averaged, time and space gradients concerning the gas temperature, its dimensions and its absolute and relative densities being not taken into account at this stage.

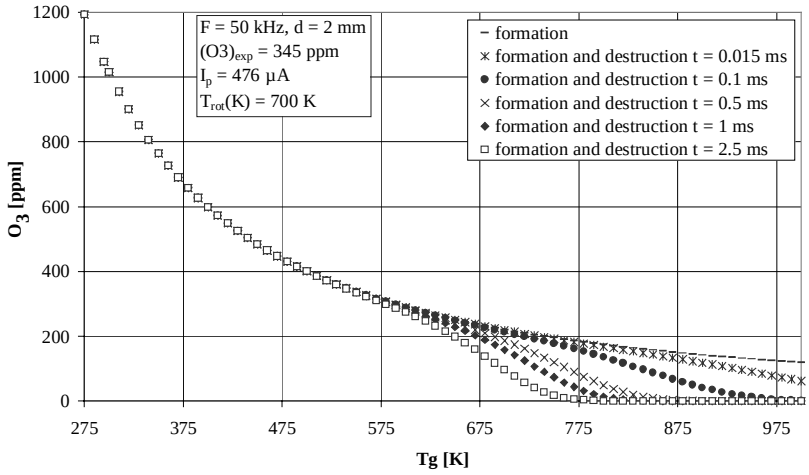


FIGURE 3. Evolution of the ozone calculated concentration versus the gas temperature T_g

Calculated results are proposed in Figure 3 for a set of working conditions detailed in the figure itself. Each value of the O_3 production provides a T_g value, without any influence of the destruction processes in the range 275-600 K for the T_g values. Thermal destruction of ozone begins to be active only beyond this temperature range which corresponds in energy densities to a 0-300 $J.l^{-1}$ range. In order to experimentally extend this energy density range (300-600 $J.l^{-1}$), we decrease the gas flow rate down to 0.03 Nm^3/h. A first result is that the ozone concentration no more linearly increases with I_p: ozone thermal destruction can no more be neglected. The same curve shape is observed when cooling the feed gas (down to 272 K), but with higher ozone concentrations, while the discharge current characteristics and the plasma temperature T_{pl} are not affected. This suggests that cooling the feed gas only modifies the "active volume" temperature T_g, (in this specific case promotes the ozone formation reaction kinetics and lowers the destruction one) and demonstrates that these reactions actually take place out of the plasma volume.

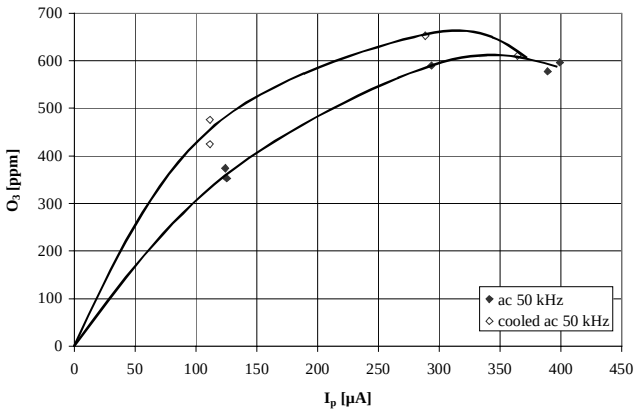


FIGURE 4. Ozone concentration vs. pulsed current I_p with and without cooling.

4. CONCLUSION

Using the $[O_3]$ vs. I_p representation allows to

- get ride of the geometry factors and applied voltage shapes inducing different energy costs for a same I_p value
- put in light a single electrical/chemical coupling process for low plasma temperature conditions
- distinguish the thermal/chemical coupling process for higher plasma temperature conditions
- distinguish the ozone formation and destruction reactions kinetics when thermal/chemical coupling processes are predominating
- provide a new evidence that ozone formation reaction takes place outside of the filamentary plasma channel.

A better insight on the influence of the plasma and gas temperatures respectively on the formation and on the destruction of ozone has been gained experimentally, and by our simple model which helped us, through the calculated "averaged temperature" values, to get a better knowledge about the notion of an active gaseous volume surrounding the plasma channel, the dimensions of which will be strongly dependent on the discharge characteristics.

REFERENCES

[1] Falkeinstein Z., *J. of Appl. Physics*, **Vol. 85**, pp. 525-9, 1999.
[2] Parissi L., Odic E., Goldman A., Goldman M., Borra J.-P., *Electrical Discharges for Environmental purposes : background and application*", Nova Science Publishers, New York, 2000,chapter 11, pp. 279-313.
[3] Petit M., Jidenko N., Goldman A., Goldman M., and Borra J.-P., accepted for publication in Review of Scientific Instruments, 2001.
[4] Borra J.-P., Goldman A. , Goldman M., *Chemical Processes and Reactions under extreme and non classic conditions*, COST Action D6, Comission Européenne, Chambéry, 1996, pp. 43-9.
[5] Odic E., Dhainaut M., Petit M., Karimi C., Goldman A. and Goldman M., "Towards a better understanding of the electrical parameters monitoring the chemical reactivity of dielectric barrier discharges at atmospheric pressure" in *International Symposium on Non Thermal Plasma Technology for Pollution Control -3*, ed. by J. S Chang and S. J. Kim, Cheju Island, Republic of Korea, 2001, pp. 62-7.
[6] Marode E., Djermoune D., Samson S., Deniset C., Modelling of the chemical dynamics in a streamer induced discharge, *11th Symp. on Elementary Processes and Chemical Reactions in Low Temp. Plasma*, Bratislava, Slovakia, 1998, pp. 93-108.
[7] Odic E., Parissi L., Goldman A., Goldman M., Koch S., Chemical by-products in air with admixtures in correlation with the gas temperature enhanced by non equilibrium discharges in *International Symposium on Nonthermal Plasma Technology for Pollution Control –2,* ed. by J. S. Chang and J. L. Ferreira, *Salvador*, Brazil, 1997, pp. 107-12.
[8] Eliasson B., Kogelschatz U. and Baessler P., *J. Phys. B: At. Mol. Phys.*, **Vol 17**, pp. L797-L801, 1984.

ON A NEW MAGNETIC BLOW OUT GLIDARC REACTOR

J.M. Cormier[a], I. Rusu[b] and M Dudemaine[a]

a) GREMI, Université d'Orléans, 14 rue d'Issoudun, BP 6744-45067, Orléans Cedex 2, France, Tél : (33) 2 38 49 46 09, fax : (33) 2 38 41 71 54

b) Technical University "Gh. Asachi", Faculty of Industrial Chemistry, Bd. Dimitrie Mangeron 71, Iasi 6600, Romania

Abstract: This work is dedicated to the presentation of a new glidarc reactor, which was used to perform the methane steam reforming reaction. The conversion efficiency is described by means of the following parameters: power input, conversion rate of methane and the production cost energy of hydrogen. Experiments clearly demonstrated the ability of magnetic blowing discharges to increase the conversion of chemical reactions at low temperatures.

1. INTRODUCTION

There are several methods to produce syngas but most of it (40%) is obtained by steam reforming (SR) [1]. The conventional catalytic technology presents several shortcomings as: the large size of the equipment, the high investments and exploitation costs, the limitations on rapid response, the catalyst sensitivity to poisons, the extreme operating conditions that limit the lifetime of reactors, etc. [2, 3].

Plasma is known to be a very high energy density media and gives an attractive alternative for the production of hydrogen and synthesis gas. In this approach, the plasma replaces catalysts and accelerates chemical reactions due to both temperature and active species effect. Plasma reactors represent an incisive approach by their simplicity, compactness and low price.

Gliding arc reactors are the subjects of multiple possible applications to a variety of chemical processes. The gliding discharges allow high specific throughputs in the reaction zone, which generally largely exceed other chemical methods, including electrochemical and thermal ones. However, previous studies on the methane steam reforming indicated that these types of reactors must be improved in order to obtain better conversions [2-5].

The aim of this paper is to present a new three-phase reactor which has been proposed with good results, the conversion increasing up to 50% [6]. The reactor uses a rotating effect, produced by a magnetic field, on the ionised gases.

2. EXPERIMENTAL

2.1. Magnetic blowing arc reactor

The new reactor design is shown in Figure 1. The plasma reactor consists of three anodes that are arranged around of a single cathode. The cathode is a tungsten rod with a diameter of 6 mm. The anodes are fixed at the output of the inlet tube, which is made on ceramic. A magnet is surrounding the inlet tube. Discharges are ignited at the outlet of this tube and then pushed by the flow. The discharge column is a plasma string with a visible diameter less that one millimetre that glides in the gas flow and the magnetic field. At the same time the voltage increases and the length of the discharge grows up. Due to the magnetic field a rotating effect of the plasma strings is produced.

[a] e-mail : jean-marie.cormier@univ-orleans.fr

The discharge behaviour in a magnetic field is quite different than the usual gliding discharges. The first effect is the increase of the mixing properties of the reactor [6]. The plasma string performs a helix movement and looks like a wrapped wire around the cathode. As a result the plasma can sweep a large part of the inlet gas. The second effect is the maintaining of the non-equilibrium behaviour of the discharge. For usual gliding discharges, the transition to the arc must be avoided using external current limitation (resistors, reactors, etc). In the case of magnetic blow out, the force acting on the lengthening discharge column is proportional to the product between the current and the magnetic-field strength. This force produces a very rapid lengthening of the discharge column. The deionisation occurs much faster, leading to the mixing of the discharge gases with the cold gas through which the core is forced to pass in its rapid motion. Due to the magnetic field, a self-limitation of the current intensity is produced.

The reactor also contains a special device conceived in order to keep catalyst sieves for catalytic tests. The distance between the support and the plasma strings can be regulated in order to verify the influence of this parameter on the reaction's evolution. The contact time between the gas reagents and the catalyst can also be regulated.

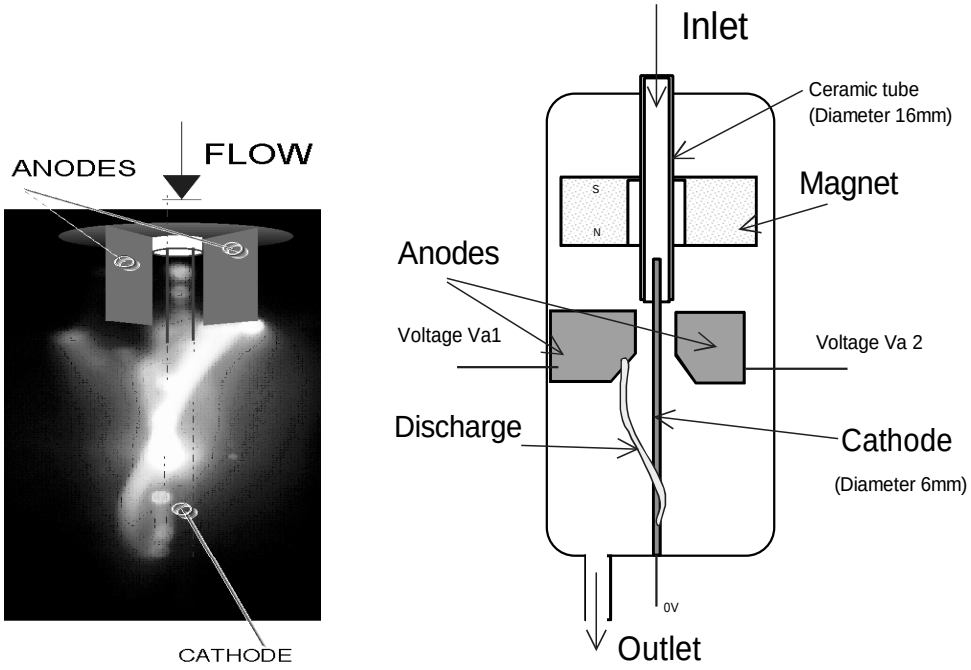


FIGURE 1. Photo and scheme of the new reactor.

2.2. Electric supply and electrical measurements

The electrical supply is a three channels one, which is used to power up the three cascading discharges. One channel (Figure 2) consists of two transformers with rectifiers that allow two running phases: the ignition at high voltage and low current intensity and a complementary energy supply with higher current [7]. Due to the magnetic field there is no need of additional resistance for current limitation.

Figure 3 shows the variation of voltage current and power for one of the three discharges as a function of time. In order to clarify the diagram from Figure 3 we have to mention that the voltage is plotted as a negative signal. As can be seen on this figure, the discharge behaviour is not definitely periodic due to the instabilities in the growing discharge. The electrical power is obtained by averaging results over a large number of periods. High voltages peaks are corresponding to a larger length of the plasma column and to a non equilibrium regime.

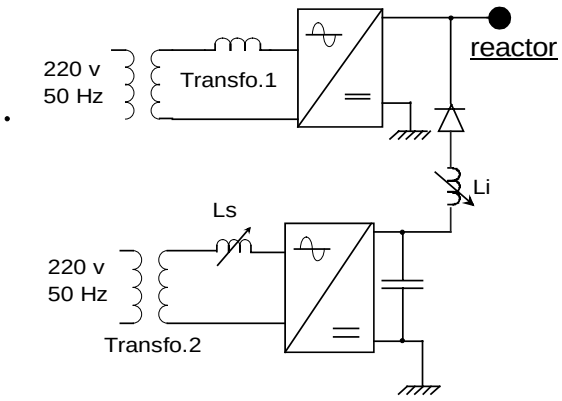


FIGURE 2. Simplified electric scheme of the power supply.

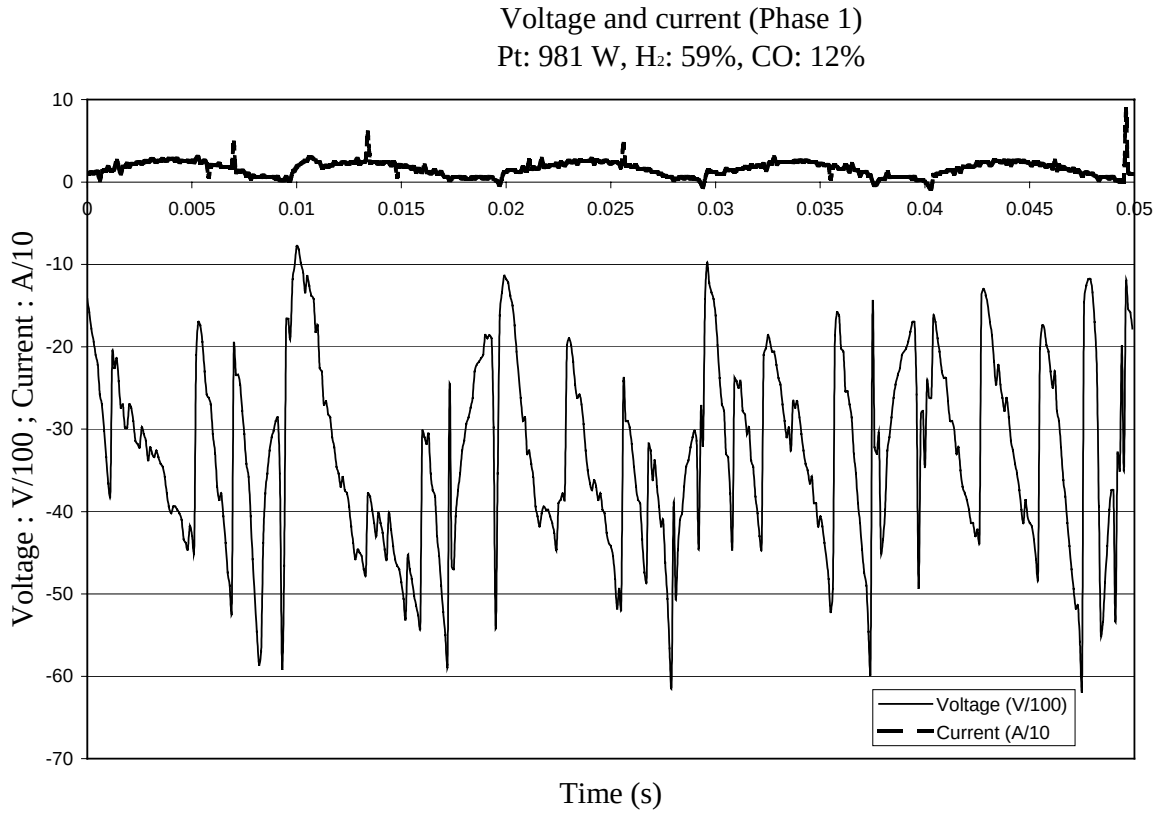


FIGURE 3. Variation of voltage and current for a one-phase discharge.

2.3. Chemical tests

All experiments were conducted at atmospheric pressure. The water and methane are mixed before injection in a heating tube. The inlet temperature was fixed at about 150°C for all the experiments. The exhaust gas from the reactor was passed through a condenser and then through a desiccant column. The major gaseous components were analysed on-line and quantified by chromatography (H_2 using a TCD detector/ HP5890, respectively CO, CO_2, CH_4 and C_2 with a FID detector/Varian 3400CX).

The final results were expressed by means of the following parameters: the total flow rates, the methane/water molar ratio (M), the conversion and the hydrogen production energy cost for one litter of hydrogen (Wh/Nl).

3. RESULTS AND DISCUSSION

One of the main characteristics of a traditional gliding discharge reactor is the power variation as a function of the inlet flow: this one is increasing as the arc length and the total flow are increasing. Magnetic blow out reactor is quite different due to the additional magnetic force on the discharge core. At low flow rates the input power is approximately constant, and lower electrical powers are observed in high flow rate regimes (Figure 4). The lengthening of the discharge at low flow rate regimes is mainly determined by the magnetic field strength. For high flow rates the turbulence is producing higher heat exchanges and higher values of the discharge resistance. Therefore, as the maximum powering voltage is limited the input power is decreasing.

The following values present the best results obtained in our experimental conditions: methane conversion = 50% for M < 0.67 and a hydrogen production energy cost of 1-2 Wh/Nl of H_2 for M > 0.67.

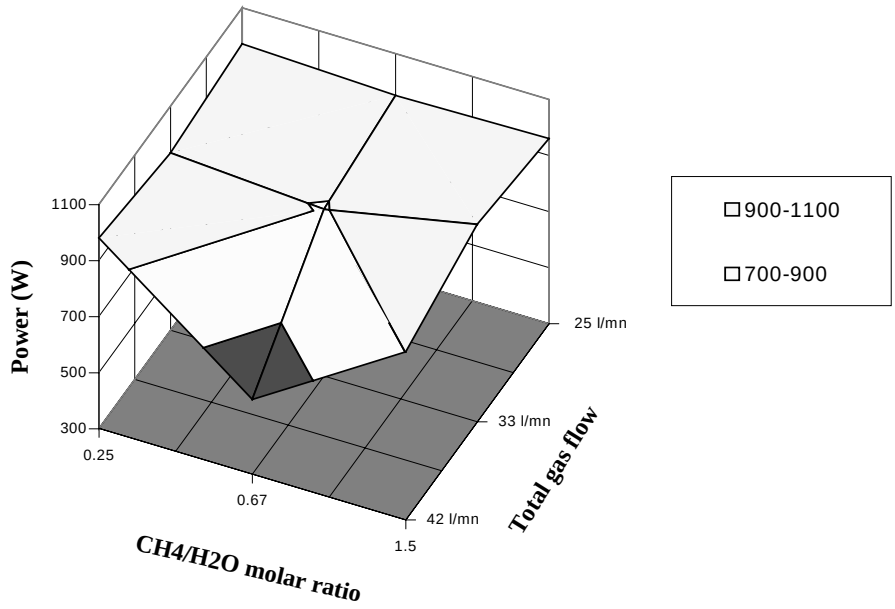


FIGURE 4. Power variation as a function of the feeding parameters of the reactor.

4. CONCLUSIONS

The new magnetic blow out glidarc reactor has reached its main aim – the increase of the methane conversion. On the other hand the system is well suited for plasma catalytic reactions. Further tests must to be performed, in order to determine the best feeding parameters of the reactor and the effect of plasma catalysis and/or classic catalysis on hydrogen production.

ACKNOWLEDGMENTS

The authors would like to acknowledge the support of the European Community - Access to Research Infrastructure action of the Improving Human Potential Programme.

REFERENCES

[1] Liu C., Mallison R. and Lobban L., *J. Catal*., **179**, 326-34 (1998)

[2] Cormier J. M., Rusu I. and Apostolescu N., Hydrogen production via methane steam reforming. Plasma reactors vs. chemical reactors, In: *Proc. ISPC 15*, ed. A. Bouchoule, J.M. Pouvesle, A.L. Thomann, J.M.Bauchire & E. Robert, International Plasma Chemistry Society, Orléans, 2001, pp. 3295-301

[3] Cormier J. M. and Rusu I., *J. Phys. D: Appl. Phys.*, **34**, 2798-803 (2001)

[4] Cormier J. M., Rusu I. and Kaminska A., *High Temp. Mater. P-US*, (2002) in print

[5] Rusu I. and Cormier J.M., *Chem. Eng. J.*, (2002) in print.

[6] Cormier J. M., Rusu I., Dudemaine M. and Sibiescu D., On the Optimisation of Glidarc Reactors by Means of Electric Discharge Frequency Analysis, In: *Proc. OPTIM 2002*, Brasov, 2002, pp.151-6

[7] Reveau N., Nikravech M., Martinie O., Lefaucheux P. and Cormier J.M., Methane decomposition to hydrogen and carbon in rotating discharge reactor, In: *Proc. HAKONE VII*, ed. H.E. Wagner, J.F. Behnke and G. Babucke, Greifswald, 2000, pp. 252-6

ACETYLENE FROM METHANE BY GLIDING ARC PROCESSING

Krzysztof Krawczyk, Joanna Ruszniak, Jan Sentek, and Krzysztof Schmidt-Szałowski[a]

Faculty of Chemistry, Warsaw University of Technology,
Noakowskiego 3, 00-664 Warszawa, POLAND

Abstract. Basing on thermodynamic data, the equilibrium composition of products formed from the mixtures CH_4+H_2 was examined within a wide temperature range at pressure of 1 and 10 bar. The limits of solid carbon stability were indicated and temperature of the maximum acetylene concentration was found. In the experiments with methane processing by gliding arc discharges, the influence of CH_4/H_2 ratio on methane conversion and selectivity of the acetylene production was investigated.

1. INTRODUCTION

Among a number of studies on methane processing under plasma conditions, promising results were obtained using the gliding arc (Glid-Arc) discharges at atmospheric pressure [1-4]. Czernichowski [1] studied the methane Glid-Arc assisted pyrolysis at atmospheric pressure in a flat metal-and-glass reactor of capacity 0.11 l and in a tubular steel reactor of capacity 1.35 l. The gas flow rate was up to 2.3 m^3/h STP, and temperature was kept up to 500°C. The methane conversion reached 34%, acetylene and hydrogen being the primary products. The formation of some carbon was also observed, but the reaction selectivity into acetylene was generally high: 70 to 90 %. The Glid-Arc reactor was successfully used [2,3] for the conversion of NG into syngas in studies of methane processing in mixtures with steam, carbon dioxide, and oxygen at moderate temperature about 1000^0C. Interesting results were also obtained investigating the partial oxidation of methane with oxygen enriched air (containing 45% O_2). A complete conversion of methane into hydrogen and carbon monoxide (H_2/CO = 2) has been attained at rather low energy cost. Conversion of methane in Glid-Arc was also investigated by Czech [5]. To sum up, it may be concluded that up till now the most favourable conditions for methane conversion were obtained using non-equilibrium plasma generated in Glid-Arc discharges.

Under conditions of non-equilibrium plasma, as that being generated in gliding-arc discharges, stable methane molecules may be activated at relatively low temperatures owing to the high energy of electrons. The kinetics of the reactions thus initiated, as well as the generated products, depend mostly on the discharge conditions, because the E/n value (electric field strength E divided by the total gas density n) determines the average energy of electrons. However, it should be taken into account that the reactions initiated by the electron impact may be accompanied by many other transformations which can lead the reacting gas mixture toward the thermodynamic equilibrium state. Generally, the equilibrium state is not attained under the discharge conditions, but nevertheless the latter group of reactions may affect the final product yields, particularly in cases where the residence time of gas reagents in the reaction zone is sufficiently long. When converting methane by pyrolysis, and also in electrical discharges, carbon soot formation is often observed. As it is an undesirable reaction, if the process is aimed to produce hydrocarbons or other organic compounds, this problem should be taken into consideration.

[a] Electronic address: kss@ch.pw.edu.pl

2. EQUILIBRIUM IN THE CH_4+H_2 MIXTURES

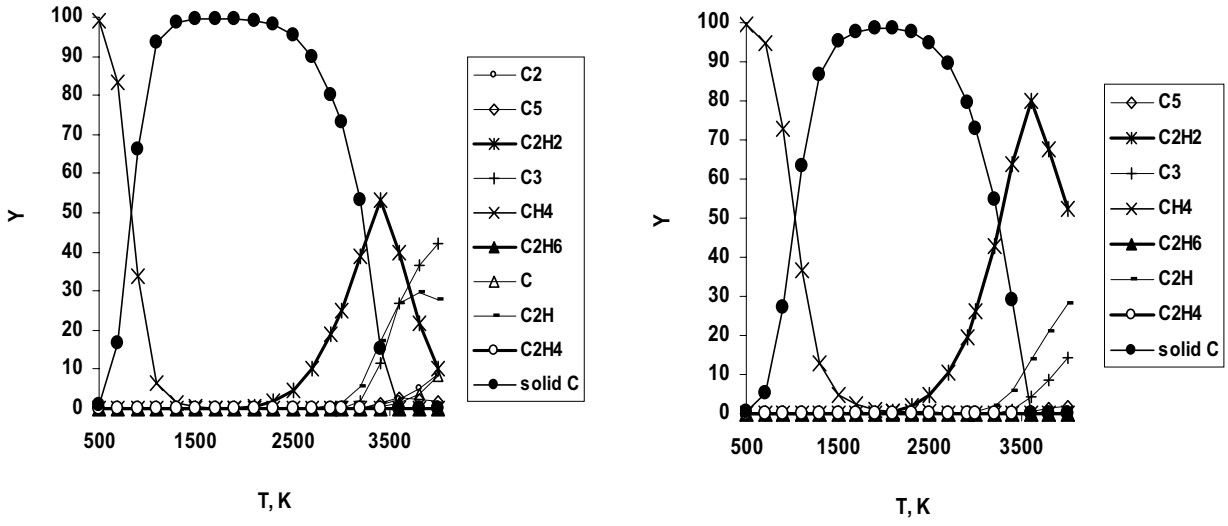
Basing on the available thermodynamic data, methane conversion values in the equilibrium state, involving main reaction products, have been calculated. Use was made of a computer program “Astra” developed by Russian Centre of Physicochemical Modelling CVD. The equilibrium state for the initial gas mixtures CH_4+H_2 of different molar ratio of C/H (from 1:4 - like in methane, up to 1:32) were examined within the temperature range 500-4000 K at pressures 1 and 10 bar. It was found that methane, solid carbon and acetylene are the only components in the equilibrium state within the wide temperature range of up to 3000 K, with negligible amounts of other products (Fig. 1 and 2). At the pressure of 1 bar carbon forms a solid phase thermodynamically stable in temperature range 700 – 3500 K for the molar ratio C/H = 1:4 (pure methane) and for C/H = 1:32 in temperature range 1100 – 2700 K. It is hence evident that the initial contribution of hydrogen in the reaction mixture has a substantial influence on the equilibrium composition. The presence of hydrogen has also a strong bearing on the maximum equilibrium methane conversion to acetylene (Y_A) being calculated from the formula:

$$Y_A = \frac{2n[C_2H_2]}{n_0[CH_4]} \qquad (1)$$

where: $n[C_2H_2]$ – moles C_2H_2 generated
$n_0[CH_4]$ – moles CH_4 introduced.

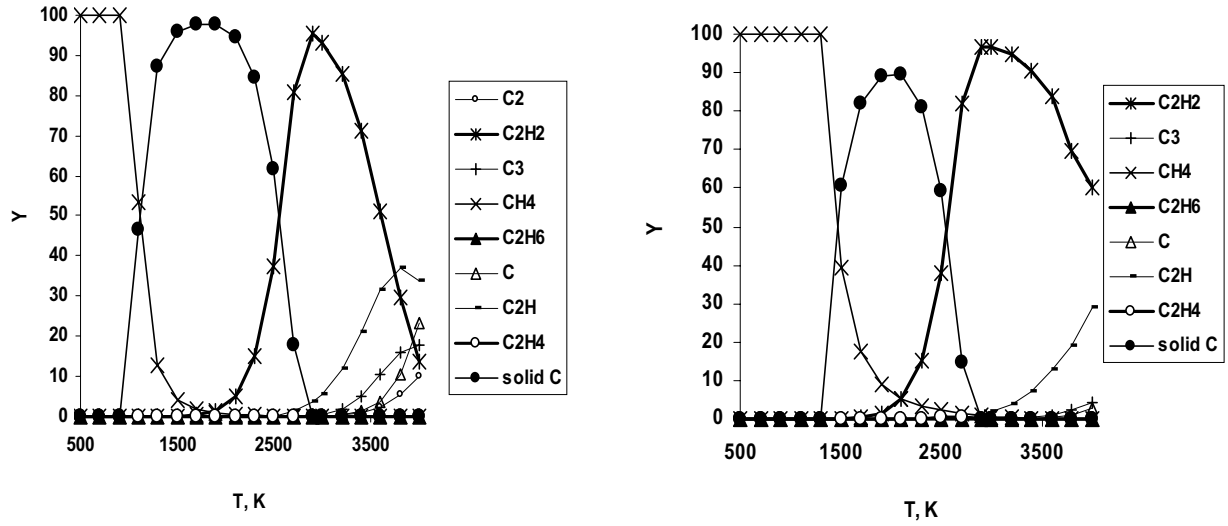
The maximum value of Y_A is 53.2% for molar ratio of C/H = 1:4 (at 3400 K) and 95.6% for C/H=1:32 (at 2900 K). Hence, in the mixtures CH_4+H_2, the equilibrium methane conversion to acetylene Y_A can reach large values, but only in a narrow range of process parameters (temperature and hydrogen concentration). The solid carbon, being the main product of the methane conversion, occurs in a much wider range of parameters. However, it should be noted that the temperature range of solid carbon occurrence is evidently diminished by the increase of pressure to 10 bar. For example, at C/H = 1:32, carbon is stable between 1300 K and 2900 K. On the other hand, a pressure increase extends the range of temperatures at which considerable values of Y_A are attained (up to maximum 97% at 2900 K). Hence, it may be concluded that:

1. In the equilibrium state of products formed from the mixtures CH_4+H_2, methane, acetylene, and solid carbon are the main components in temperatures <3000 K.
2. In such mixtures solid carbon is stable within a wide temperature range <3000 K .
3. The equilibrium methane conversion to acetylene (Y_A) attains large values (>90%) at temperatures 3000 – 3500 K.



1.a. **1.b.**

FIGURE 1. The equilibrium state for the initial gas mixtures CH_4+H_2 of molar ratio of C:H=1:4 within the temperature range 500-4000K at different pressures: **a** – 1bar, **b** – 10 bar.
Y – methane conversion into C_2H_2, C_2H_4, C_2H_6, C_2H, C_3, solid C and other products (and contribution of remaining CH_4),
(Y values were calculated in the same way as Y_A).



2.a. **2.b.**

FIGURE 2. The equilibrium state for the initial gas mixtures CH_4+H_2 of molar ratio of C:H=1:32 within the temperature range 500-4000K at different pressures: **a** – 1bar, **b** – 10 bar.

3. EXPERIMENTAL

The experiments were carried out in a reactor (Fig. 3) made of quartz glass tube 4 of diameter 40 mm and length 260 mm, comprising two knife-shaped stainless-steel electrodes 2 [6]. The row gas mixture was introduced to it through a nozzle 1 of diameter 0,75 mm disposed at the axis of the tube. The process was carried out under atmospheric pressure. The temperature in the reactor (Table 1) was measured by means of thermocouple 5 located 4 cm under the electrodes. Electric current of frequency 50 Hz was supplied to the reactor by means of a system consisting of autotransformer, resistors, and high voltage transformer. The voltage, current, and power were measured in the primary, low voltage circuit of the transformer. The gases of commercial grade: methane, hydrogen, and argon were applied with the overall flow rate 300 Nl/h. The reaction products were analysed by means of 2 gas chromatographs: 1) Chrompack CP 9002 supplied with a column Poraplot Q and detector FID, and 2) a Willy Giede chromatograph supplied with a column Carboxen 1000 and detector TCD.

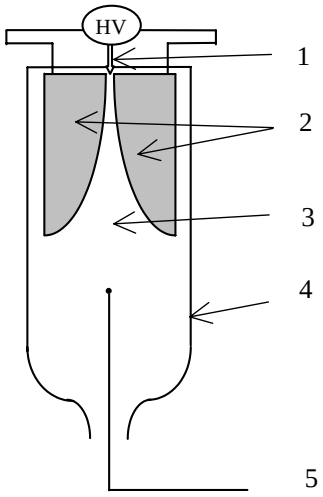


FIGURE 3. Scheme of Glid-Arc reactor: HV-high voltage, 1-nozzle, 2-electrodes, 3-discharge zone, 4- glass tube, 5-termocouple.

4. RESULTS

Acetylene was the main reaction product in the experiment performed, although small amounts of ethylene were also found. Carbon deposits were observed in reaction products of CH_4+H_2 mixtures with initial methane concentration exceeding 20% by vol. At constant current value (in the low voltage circuit) the discharge power was scarcely influenced by the initial CH_4 concentrations. The methane conversion to C_2 hydrocarbons ($\mathbf{Y_{C2}}$) and the total methane conversion ($\mathbf{Y_M}$) depended on the discharge power and on initial methane concentration ($\mathbf{C_o}$) in the initial mixture CH_4+H_2. A maximum value of $\mathbf{Y_{C2}}$ (0.27 - 0.36) was observed at $\mathbf{C_0} \cong 20\%$, whereas $\mathbf{Y_M}$ was still increasing within the higher range of $\mathbf{C_o}$, because of the higher methane conversion into solid carbon.

TABLE 1

Initial methane conc. / %	**2,11**	**2,67**	**4,04**	**4,31**	**8,76**	**13,46**	**14,51**	**25,92**	**36,21**
10A, Temp. / °C	320	320	310	320	300	280	280	250	230
20A, Temp. / °C	390	380	380	380	390	410	400	360	340

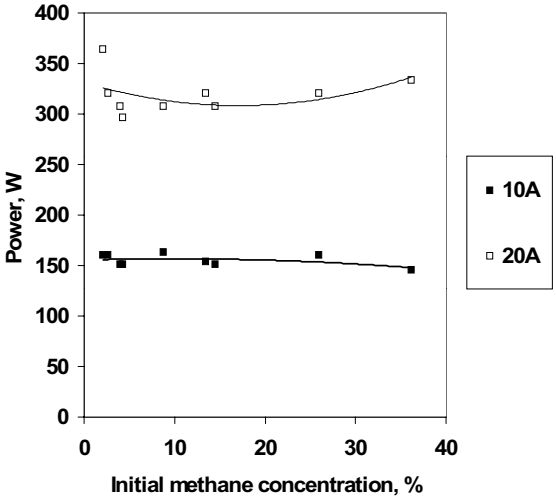


FIGURE 4. Discharge power vs. methane conc. in the initial mixture CH_4+H_2. Overall flow rate – 300 Nl/h, current in low voltage circuit – 10A and 20 A.

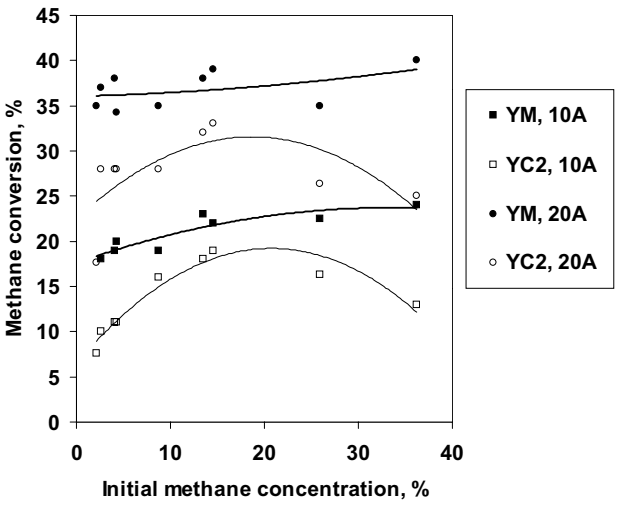


FIGURE 5. Methane conversion vs. methane conc. in the initial mixture CH_4+H_2. Overall flow rate – 300 Nl/h, current in low voltage circuit – 10A and 20 A.
$\mathbf{Y_M}$ – total CH_4 conversion
$\mathbf{Y_{C2}}$ – conversion into C_2 hydrocarbons

ACKNOWLEDGMENT

The work was granted by the State Committee for Scientific Research;
Project Nr PZB/KBN/018/T09/99

REFERENCES

[1] Czernichowski A., Czernichowski P., and Ranaivosoloarimanana A., Plasma Pyrolysis of Natural Gas in Gliding Arc Reactor. In: *Proc. 11th World Hydrogen Energy Conference*, Stuttgart, Germany, 1996, pp. 661-666

[2] Czernichowski A., *Karbo-energochemia-ekologia,* **11,** 359-369 (1998)

[3] Czernichowski A., Electrically Assisted Conversion of Natural Gas into Syngas. In: *Gas To Liquids Processing*, San Antonio, Texas (1998)

[4] Fridman A., Nester S., Kennedy L.A., Saveliev A., Mutaf-Yardimci O., *Progr. Energy Comb. Sci.*, **25** 211-231 (1999)

[5] Czech T., Doctor Thesis, Institute of Fluid Flow Machinery, Polish Academy of Sciences, Gdansk (1997)

[6] Schmidt-Szałowski K., Krawczyk K., Ruszniak J., Processing of Methane by Gliding Arc Discharges. In: *Proc. 15th Int. Symp. on Plasma Chemistry*, Orleans, France, 2001, 2933

STUDIES OF NITROUS OXIDE CONVERSION IN GLIDING ARC DISCHARGES

K. Krawczyk[a], and M. Wieczorkowski

Warsaw University of Technology, Faculty of Chemistry, ul. Noakowskiego 3, 00-664 Warszawa, POLAND

Abstract. The aim of this work was develop, design and check new type of the reactor for N_2O conversion to NO, nitrogen and oxygen in gliding arc discharge. The reactor was made of stainless steel. Experiment were carried out using the nitrous oxide and oxygen mixtures. It has been shown that both the nitrous oxide conversion to NO and overall conversion of nitrous oxide depend on the linear flow rate of gas mixture passed through a nozzle. The obtained results showed a clear effect of applied arrangement of discharge space on the conversion of nitrous oxide to NO.

1. INTRODUCTION

High concentrations of nitrogen and sulphur oxides, methane, carbon dioxide, and freons are responsible for the occurrence of the so-called greenhouse effect and for the destruction of the ozone layer. Also nitrous oxide belongs to the group of stable compounds having a negative effect on the natural environment.

Much research work is being done to reduce the emission of nitrous oxide to the atmosphere. Thermal and catalytic decompositions to nitrogen and oxygen are among the methods most often used for destruction of nitrous oxide [1]. The method has been utilised commercially for purification of waste gases in the manufacture of adipic acid [2]. Conversion of N_2O to NO is the most desirable method used. NO obtained in this process can be oxidised to NO_2 and used in the manufacture of nitric acid.

In recent years studies have been carried out on the use of gliding arc discharge (Glid-Arc) for decomposition of nitrous oxide. This type of discharge is characterised by a low temperature of the gas mixture, as compared with the temperature of the electrons, and a high productivity of the oxidizers. The Glid-Arc reactors enable to carry out the reaction under high flow rates. Another advantage of using this type of discharge for decomposition of N_2O is the possibility of obtaining large quantities of NO.

The studies of nitrous oxide decomposition in gliding arc discharge were carried out in a reactor fitted with three pairs of electrodes and in a two-electrode system. The studies enabled to obtain high conversion of N_2O to NO, which was of the order of 20 – 37% in the system with two electrodes. Such results were obtained with flow rates of 150, 200, 300 or 400Nl/h of gas mixtures having initial concentration of nitrous oxide of 2.5, 5 or 10% by vol. The overall conversion of N_2O reached about 80% max [3, 4].

The conversions of nitrous oxide were also studied with the use of phenomena of heterogeneous catalysis [4]. The packing materials used were TiO_2, SiO_2, γ-Al_2O_3 and metal oxides deposited on a γ-Al_2O_3. It has been found the use of a solid packing material in the reaction space increases the conversion of N_2O. The highest activity of the nitrous oxide conversion was observed in the processes in which nickel, iron, or copper oxides deposited on γ-Al_2O_3 were used. A clear increase of the overall conversion of N_2O was observed with all the catalysts used. The highest conversion of nitrous oxide (90%) was obtained with the use of CuO. However, no significant effect of the catalysts used on the conversion of N_2O to NO was observed.

[a] Electronic address: kraw@ch.pw.edu.pl

The influence of the gliding arc discharge space organisation on the conversion of nitrous oxide was also investigated. The conversion of N_2O to NO about 50% was obtained in a reactor with reduced reaction zone and two electrodes forming an acute angle. The overall conversion of N_2O was about 80%. These results were much higher than those obtained under identical conditions in a reactor of much larger cross-section and knife-shaped electrodes. These results have shown that the process of conversion of nitrous oxide depends on the layout and organisation of the reaction space, in which the electric discharge is effected, and on the hydrodynamic conditions of gas flow through the plasma generation zone.

The aim of this work was to study the parameters influencing the conversion of nitrous oxide in gliding arc discharge and to determine the effects of interelectrode gap width, linear gas flow velocity, volume of reaction space, and electric power applied on the kinetics of conversion of nitrous oxide.

2. EXPERIMENTAL

The studies on conversion of nitrous oxide were carried out in a stainless steel reactor with two electrodes. The electrodes were connected to 50 Hz AC supply (see Fig. 1) from a high voltage transformer (6). An oscilloscope (8) enabling the observation of voltage runs in the discharge and evaluation of performance of the reactor was connected to the transformer through a voltage probe (7).

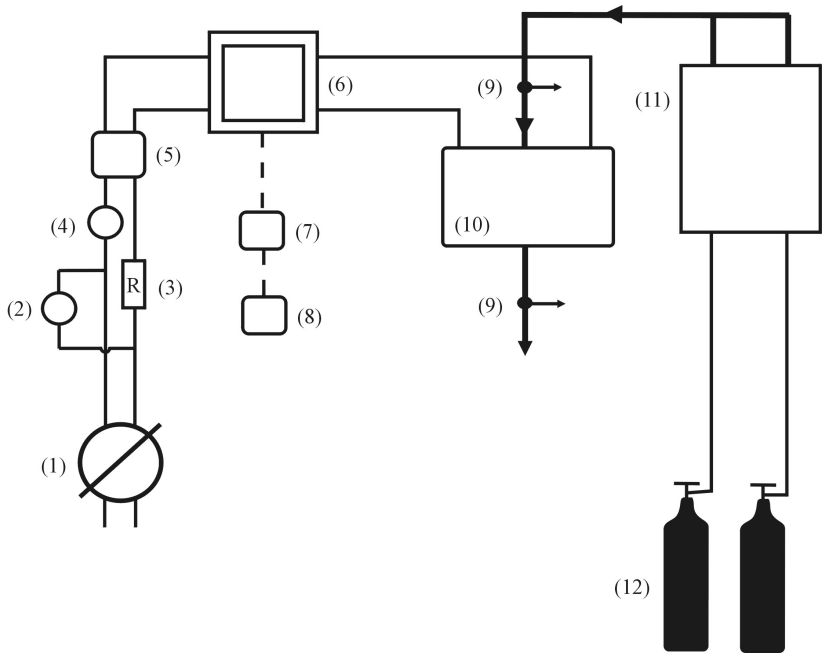


FIGURE 1. Setup of apparatus for studies on conversion of nitrous oxide. 1 – autotransformer, 2 – voltmeter, 3 – resistor, 4 – ammeter, 5 – electric energy meter, 6 – high voltage transformer, 7 – voltage probe, 8 – oscilloscope, 9 – gas sampling fittings, 10 – reactor, 11 – gas flow control , 12 – oxygen and nitrous oxide.

The conversion of nitrous oxide was studied in oxygen atmosphere. Nitrous oxide was introduced to the reactor through a system of gas flow controlling instruments (11) and a quartz nozzle. The body of the reactor (Fig. 2) was made of stainless steel. Knife-shaped stainless steel electrodes were mounted inside the reactor. A quartz glass nozzle was installed within the stainless steel body. The distance between the nozzle outlet and the narrowest interelectrode separation was 5 mm. The volume of the reaction space was reduced by placing ceramic elements on both sides of the electrodes.

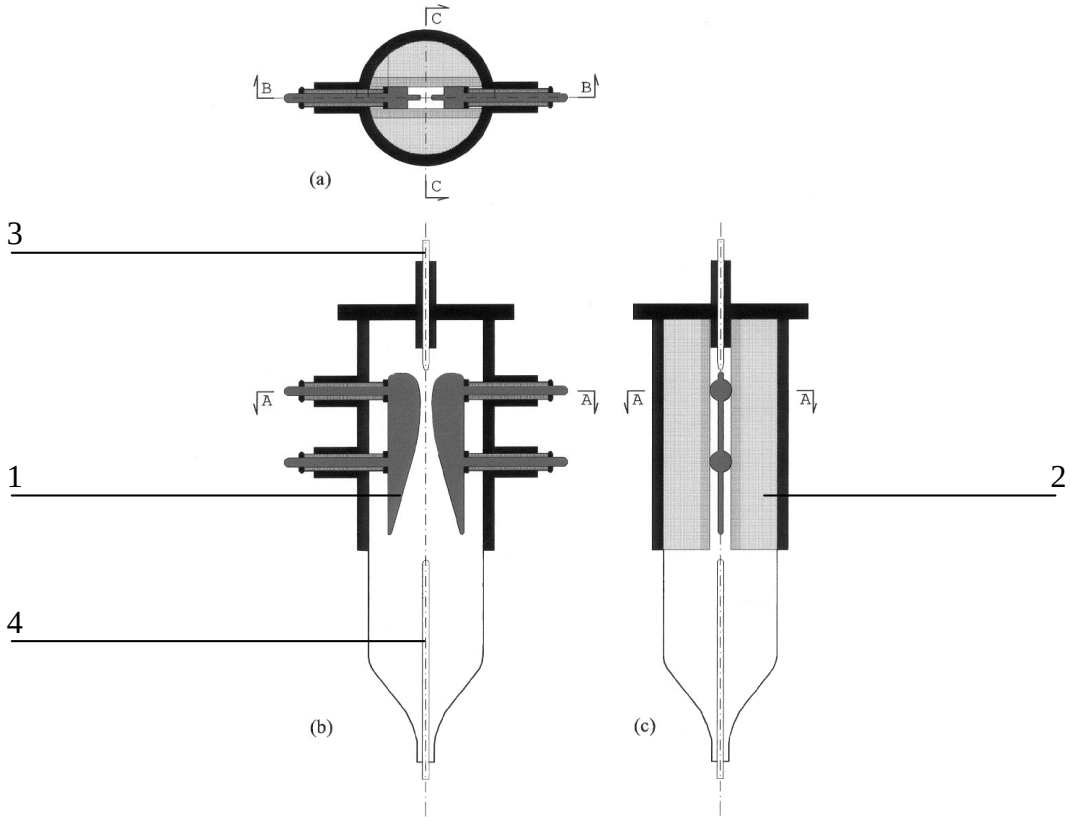


FIGURE 2. Stainless steel reactor for the study of nitrous oxide conversion in gliding arc discharge. a) A-A – cross-section view from above, b) B-B – cross-section of face view, c) C-C – cross-section of side view. 1 - electrodes, 2 – ceramics, 3 – quartz nozzle, 4 - thermocouple

The studies were carried out with constant nitrous oxide and oxygen flow rates equal 200 Nl/h. The initial N_2O concentration was 5% by volume. Three linear velocities of gas at the outlet from the quartz nozzle were applied: 45, 70 or 125 m/s by using nozzles with inner diameter of 1.25, 1 or 0.75mm, respectively.

The width of the interelectrode gap was 1, 1.5, 2.25, 2.75, or 3.25mm. Studies with a reactor with modified reaction space volume were also performed using the same interelectrode distance and nozzle diameter of 0.75 or 1.25mm. The conversion of N_2O to NO and the overall conversion of N_2O were determined as a function of the electric power applied.

The composition of the gas mixture was monitored throughout the experiment. The concentration of nitrous oxide before and after the reaction was determined by gas chromatography. The amount of nitric oxide formed was determined by titrimetric and gravimetric methods [5].

3. RESULTS AND DISCUSSION

The width of the interelectrode gap had no significant effect on the overall conversion of N_2O and on conversion of N_2O to NO. At higher gap widths the arc initiation occurred at higher voltage values. At the highest value of interelectrode gap width (3.25 mm) the overall conversion was higher by 10% than that observed at the other gap widths. It should be pointed out, however, that the 80%

conversion was obtained for the discharge power of about 470 W, which was by 170 W higher than that applied in the other experiments.

The course of the process was much more influenced by the linear velocity of the gas mixture entering into the reactor (Fig. 3).

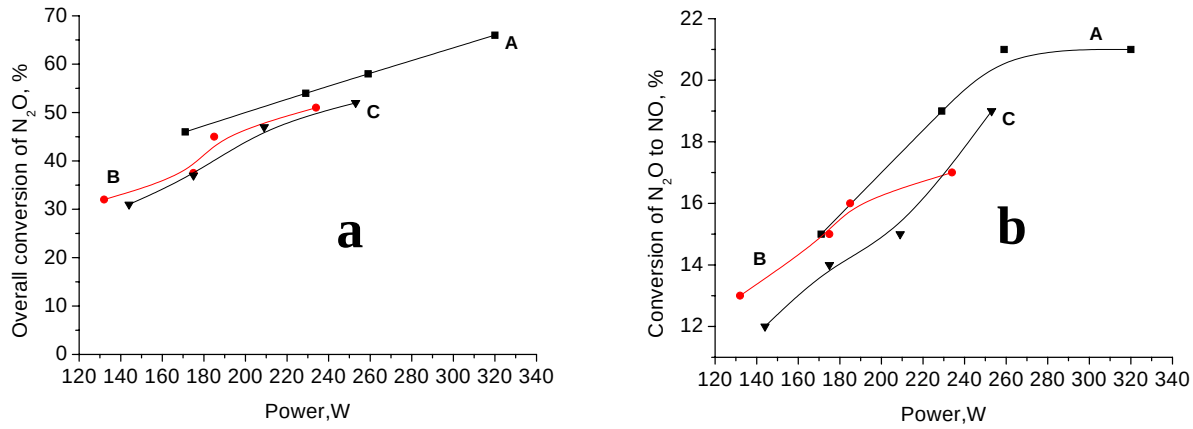


FIGURE 3. Effect of discharge power on overall conversion of nitrous oxide (a) and on conversion of nitrous oxide to NO (b). Interelectrode gape width 1 mm, initial nitrous oxide concentration 5% by vol. Nozzle with inner diameter: A – 0.75, B – 1, C – 1.75mm.

The overall conversion of nitrous oxide increased when the linear gas flow velocity was changed from 45m/s to 125m/s (quartz nozzle diameter from 1.25 to 0.75 mm, respectively). The change of the nozzle diameter (and the resulting change of linear gas velocity) changes the hydrodynamic conditions of gas flow through the plasma of gliding arc discharge and that could have increased the overall conversion. of nitrous oxide and conversion of N_2O to NO. The maximum conversion of N_2O to NO was about 22%, and the overall conversion of N_2O was about 70% (Fig. 3).

The studies carried out in the reactor with modified reaction space (with ceramics – Fig. 2) were performed at constant interelectrode gap width (1 mm). Two nozzles used had the inner diameter of 0.75 mm or 1.25 mm, respectively. The decrease of the reaction space volume resulted in a change of hydrodynamic conditions of gas flow through the plasma formation zone. The conversion of nitrous oxide to NO was smaller than that in experiments with original reaction space volume (Fig. 4). The fact may be due to the higher temperature in the reactor with modified reaction space, resulting from the increase of power density within the reactor. In the reactor with modified reaction space the temperature was several dozen higher than in the reactor without ceramics. The increase of temperature can accelerate the decomposition of the NO formed. The observed values of overall conversion of N_2O are only slightly smaller than those obtained in the reactor before the modification of the reaction space.

The disclosed effect of discharge power on the overall conversion of nitrous oxide and on the conversion of N_2O to NO (Fig. 4) shows that the linear gas flow velocity has a bearing on both the conversion of N_2O to NO and the overall conversion of nitrous oxide.

For lower powers applied the values of conversion of N_2O to NO and overall conversion of nitrous oxide were higher in experiments where the linear gas velocity was 125m/s (quartz nozzle diameter 0.75 mm). For higher powers identical values were obtained for overall conversion of nitrous oxide and for conversion of N_2O to NO.

The results of the experiments performed have shown that in decomposition of nitrous oxide maximum amounts of NO are obtained when the process is carried out in a reactor with higher cross-section area. When high linear gas flow velocities were applied maximum conversion of N_2O to NO was about 22%. The conversion of N_2O to NO decreased by about 5% when the volume of the reaction space was reduced.

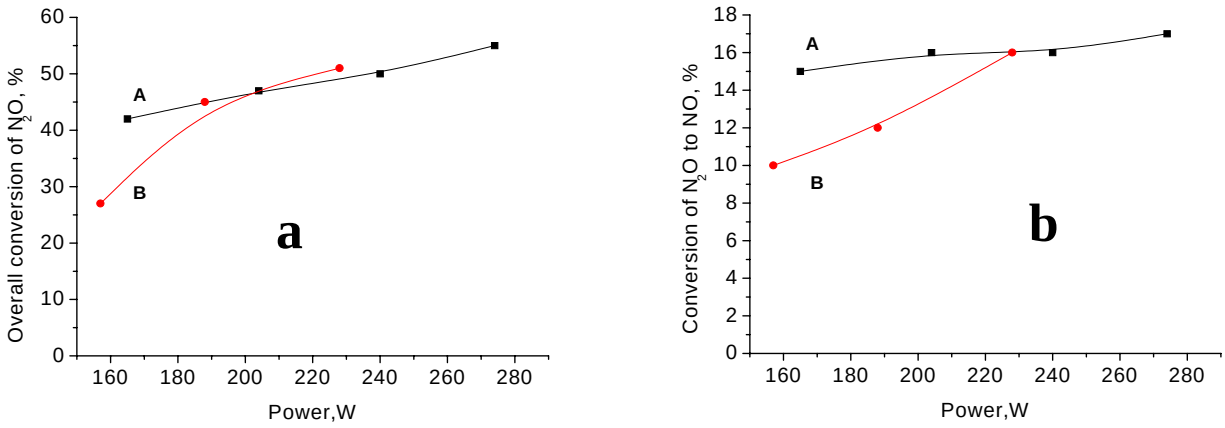


FIGURE 4. Effect of discharge power on overall conversion of nitrous oxide (a) and on conversion of nitrous oxide to NO (b). Reactor with modified reaction space. Interelectrode gap width 1 mm. Initial concentration of nitrous oxide 5% by vol. Nozzle with inner diameter: A – 0.75, B – 1.75mm.

REFERENCES

[1] Kapteijn F., Rodriguez-Mirasol J., and Moulijn J.A., *Appl. Catal. B: Environ.*, **9**, 25-64 (1996)

[2] Reimer R.A., Slaten C.S., Seapan M., Koch T.A., and Tomlinson P.E., Development of Technologies for Control of N_2O Emission Associated with Adipic Acid Manufacture, In: *Proc. of the 6th Int. Workshop on Nitrous Oxide Emission*, Turku, 1995, 515-538

[3] Krawczyk K., Ruszniak J., Młotek M., Czernichowski A., and Schmidt-Szałowski K., *Pol. J. Appl. Chem.*, **XLII**, 151-157 (1998)

[4] Krawczyk K., and Młotek M., *Appl. Catal. B: Environ.*, **30**, 233-245 (2001)

[5] Krawczyk K., Petryk J., and Schmidt-Szałowski K., *Appl. Catal. A: General*, , **175**, 147-157 (1998)

PLASMA-INDUCED DECOMPOSITION OF CHLORODIFLUOROMETHANE

Anna Opalska, Teresa Opalinska[1], Jerzy Polaczek, Pawel Ochman

Instytut Chemii Przemyslowej, Rydygiera 8, 01-793 Warsaw, POLAND

Abstract. Decomposition of chlorodifluoromethane ($CHClF_2$, Freon R22) was studied under nonequilibrium oxidizing plasma conditions. The decomposition was carried out in a plasma reactor in which a high-voltage gliding arc discharge was generated. The overall decomposition degree of the Freon and the composition of the outlet gases were studied in relation to oxygen concentration and plasma power. The maximum decomposition degree of the Freon (0.99) was attained in a gas mixture composed of Freon (0.96 mol/h), argon (27.97 mol/h) and oxygen (34.54 mol/h) at an input power of 1.44 kW. Carbon dioxide, chlorine and fluorine were the main products of the process.

1. INTRODUCTION

Chlorodifluoromethane ($CHClF_2$, R22) belongs to the group of fluorinated and/or chlorinated paraffin hydrocarbons (chlorofluorocarbons, CFCs) known as Freons. The compounds are the main source of chlorine atoms in the stratosphere. Chlorine atoms initiate and participate in ozone-depleting reactions. Therefore, in November 1992, the Montreal Protocol was revised to phase out CFCs by 1 January 1996. The present ban on the use of Freons in new refrigerating machines and air conditioners is the result of internationally concerted legislative actions. At present, scientists are looking for efficient and environmentally friendly methods to decompose the large reserves of Freons. Thermal oxidation [1], biodegradation [2], and chemical [3, 4] and catalytic [5, 6] decomposition methods have been reported. The process of Freon decomposition has also been studied under the conditions of equilibrium and nonequilibrium plasmas generated by various types of discharge [7, 8]. Plasma is a source of high temperatures (equilibrium plasma) and yields active species such as free electrons, ions, atoms, particles, and radicals (non-equilibrium plasma). The active species present in the discharge space react with neutral molecules and cause destruction of stable bonds in the molecules. As a result, low-molecular-weight compounds like CO_2, H_2O, HCl and HF are formed.
The aim of this work is to study the decomposition of chlorodifluoromethane (R22, $CHClF_2$) in high-voltage gliding arc discharge. This type of discharge was generated in a plasma reactor at atmospheric pressure under oxidizing conditions (Ar + R22 + O_2).

2. EQUILIBRIUM CALCULATIONS

Thermodynamic calculations [9] were performed for the $CHClF_2$/Ar equilibrium system within a temperature range of 500–2500 K and at a pressure of 1 atm. Two cases, A and B, were taken into consideration:
A) elementary carbon is present, and
B) elementary carbon is absent in the mixture of Freon decomposition products.
The calculations were carried out for a (1:10 by moles) chlorodifluoromethane-argon gas mixture. The equilibrium conversion of the Freon into organic and inorganic products was calculated from equations (1) and (2).

[1] Electronic address: Teresa.Opalinska@ichp.pl

$$U_X = \frac{a \times n_X}{n_{R22}} \quad (1)$$

$$U_Y = \frac{b \times n_Y}{c \times n_{R22}} \quad (2)$$

where: X – organic products; Y – inorganic products; a – number of carbon atoms in X; b – number of chlorine and fluorine atoms in Y; c – number of chlorine and fluorine atoms in the reactant; n_X – number of generated mols of X [mol/kg equilibrium mixture]; n_Y – number of generated mols of Y [mol/kg equilibrium mixture]; n_{R22} – number of introduced mols of R22 [mol/kg equilibrium mixture]

Tetrafluoromethane and elementary carbon or unsaturated CFCs (C_2Cl_2, C_2F_2, C_2ClF, C_2Cl_4, C_2HCl_3, $C_2H_2Cl_2$, and C_2H_3Cl) are the main products of thermal decomposition of Freon R22 (Figs. 1 and 2)

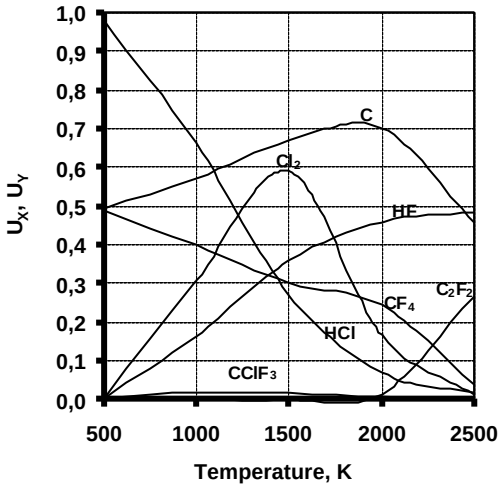


FIGURE 1. The degree of Freon R22 decomposition in relation to equilibrium temperature, case A

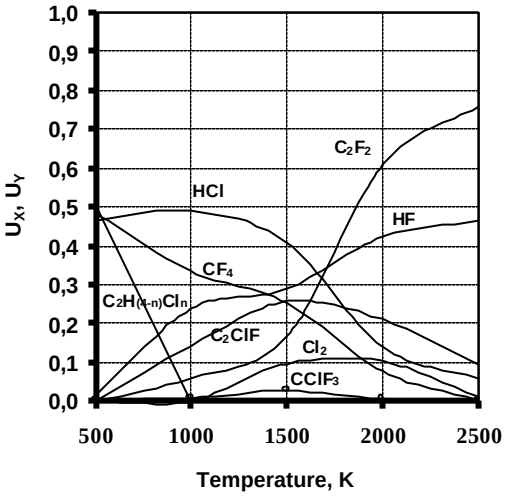


FIGURE 2. The degree of Freon R22 decomposition in relation to equilibrium temperature, case B

The thermodynamic calculations carried out to yield chemical equilibrium data in the $CHClF_2$/Ar system show pyrolysis of the Freon to be an ineffective process because the products of decomposition are stable and hazardous compounds. As regards pyrolysis of CF_4, the thermodynamic calculations show CF_4 to decompose totally at a temperature as high as 3500 K (Fig. 3). Therefore, decomposition of the Freon should be carried out so as to avoid the formation of hazardous stable compounds like CF_4. Addition of an oxidizer (O_2) makes CF_4 decompose totally to yield CO_2 and a minor amount of CO already at 2500 K (Fig. 4). Thus, the Freon should be decomposed in an oxidizing medium.
Therefore, in this study, we used non-equilibrium plasma generated in an argon-oxygen gas mixture in a gliding arc discharge. Plasma of this type is a source of high-energy electrons and active oxygen atoms, which take part in the reactions with stable molecules of the reactant.

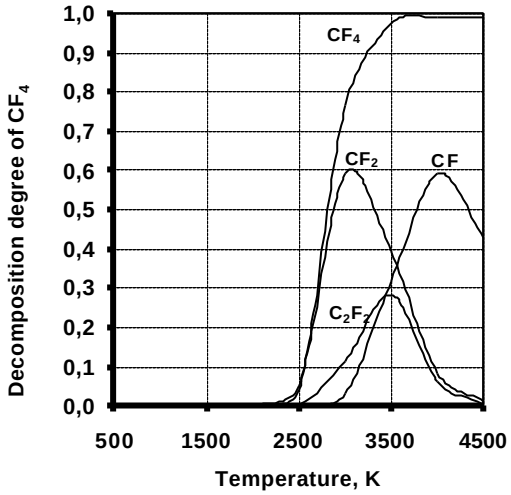


FIGURE 3. The degree of CF_4 decomposition in relation to equilibrium temperature

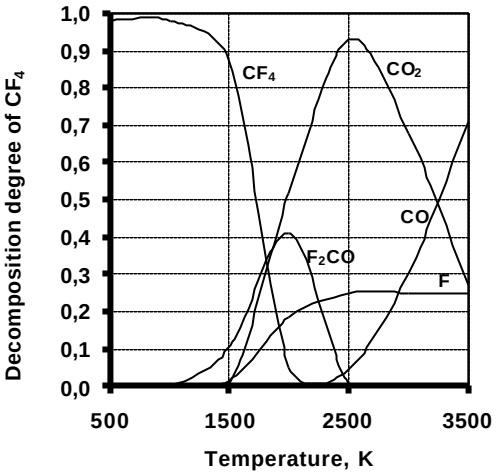
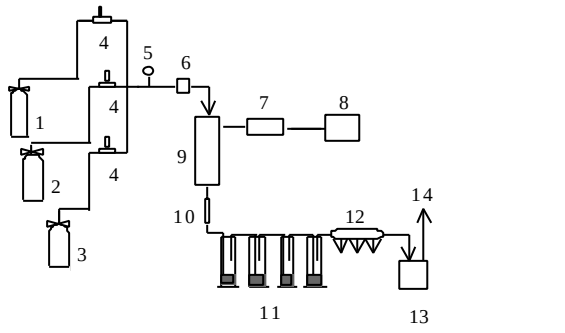


FIGURE 4. The degree of CF_4 decomposition in relation to equilibrium temperature, in the presence of oxygen

3. EXPERIMENTAL

3.1. Experimental set-up

Figure 5 shows a scheme of the experimental set-up. Its main part of the set-up is a plasma reactor (Fig. 6) in which the gliding arc discharge is generated. The plasma reactor consists of a quartz tube comprising three knife-shaped working electrodes and an ignition electrode. The plasma reactor was fed with a by high-voltage alternating current (50 Hz). The three-phase current meter was installed in the electric circuit and it was used for measuring the electric power and the elementary energy consumption. The reactant gas was introduced into the plasma reactor through a mixer and then through a nozzle. The unit supplying the gas included the line of the carrier gas (Ar), the line of the oxidizing gas (O_2), and the line of Freon R22. The outlet gases were cooled and delivered to an absorption unit (four glass washers filled with a potassium iodide solution). Three glass burettes formed part of the sampling device. The composition of the outlet gases was determined by gas chromatography with the aid of external standards. Freons (CCl_2F_2, $CHClF_2$ and $CClF_3$) were determined by using a flame ionization detector and a Fluorocol column. Carbon dioxide, carbon monoxide and tetrafluoromethane were determined by using a katharometer and a Carboxen-1000 carbonaceous molecular sieve column. The flow rate of the outlet gases was measured by a gas flowmeter installed behind the supplying unit.



1, 2, 3 - gases, 4 - mass flow control, 5 - manometer,
6 - mixer, 7 - power supply unit, 8 - power measurement systen
9 - plasma reactor, 10 - cooler, 11 - absorption unit,
12 - gas sampler, 13 - gas measurment system, 15 - vent

FIGURE 5. Scheme of the experimental set-up

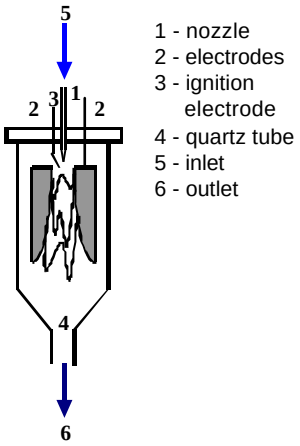


FIGURE 6. Scheme of the plasma reactor

3.2. Process parameters

The total flow rate of the inlet gases was kept constant during an experimental series (63.9 mols/h). The argon and oxygen concentrations were changed in the stream of the inlet gases. The concentration of Freon R22 was kept constant in each experiment (1.5 vol. %, 0.97 mol R22/h).
The overall Freon decomposition degree and the degrees of Freon decomposition into individual products were calculated from gas-chromatography results by equations (3) and (4).

$$U = \frac{W_E[R22] - W_Y[R22]}{W_E[R22]} \tag{3}$$

$$U_X = \frac{a \times W_Y[X]}{W_E[R22]} \tag{4}$$

where: $W_E[R22]$, $W_Y[R22]$ – flow rates of inlet and outlet gases, resp., [mol/h]; $W_Y[X]$ – flow rate of outlet product X [mol/h]; a – number of carbon atoms in molecule of product X

The input reactor power was measured on the primary winding by a three-phase current meter

4. RESULTS

The results of the present study are presented in figs. 7 and 8. The degree of plasma-induced decomposition of Freon R22 is seen to be related to the composition of the inlet gas stream and to the input reactor power (Fig. 9). Discharge conditions were found to have been affected by changes in the inlet gas composition. Under established electrical energy supply conditions, the input reactor power increased as the oxygen concentration was increased. The elementary energy consumption varied (1.23÷1.68 kWh/mol) over the examined range of oxygen concentrations (10÷80 vol. %) and discharge powers (1.1÷1.6 kW). The decomposition degree of Freon R22 achieved a maximum, *viz.,* 0.99, in an $O_2/CHClF_2$ mixture at a mole ratio of 36 (Fig. 9). Carbon dioxide was the main carbon-containing product of the decomposition. The concentration of CO_2 in the outlet gas increased as the discharge power and the oxygen concentration in the inlet gas were increased. Minor amounts of carbon monoxide and of few other Freons (CCl_2F_2, $CClF_3$) were found in the outlet gas. No tetrafluoromethane (R14, CF_4) was found to occur in the outlet gas.

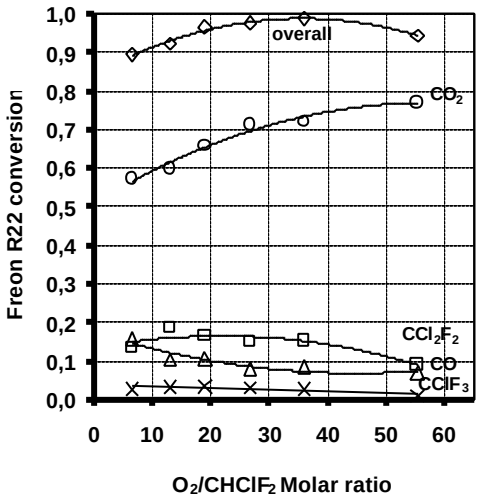


FIGURE 7. The degree of Freon R22 conversion in relation to reaction gas composition

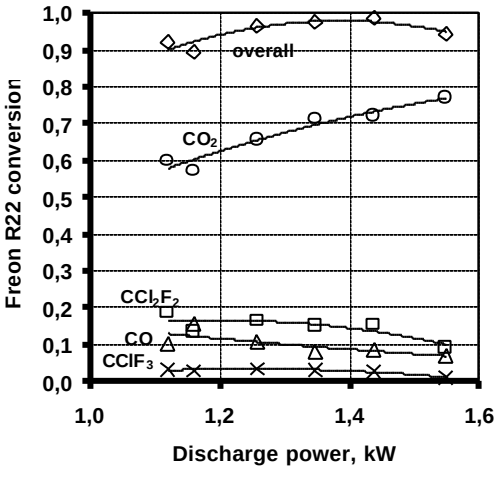


FIGURE 8. The degree of Freon R22 conversion in relation to discharge power

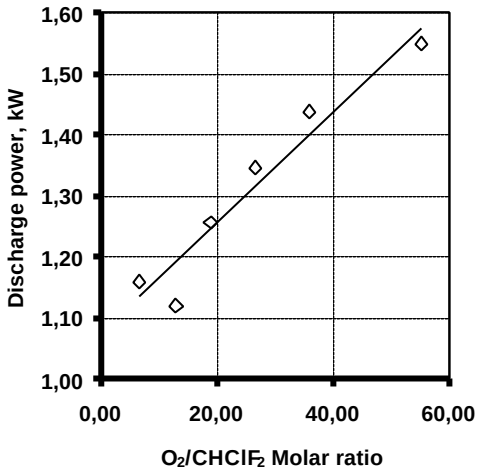


FIGURE 9. The discharge power in relation to reaction gas composition

5. CONCLUSIONS

- Plasma-induced conversion of Freon R22 was found to be related to the reaction gas composition and discharge power.
- High degrees of Freon R22 conversion were achieved. The maximum conversion degree was 0.99.
- Low-molecular-weight chemical compounds (mainly CO_2) were the main products of the decomposition.
- R12 and R13 (CCl_2F_2, $CClF_3$) and carbon monoxide were by-products of the conversion.
- The reaction products were found to contain no Freon R14 (CF_4).

REFERENCE

[1] – EU Pat. 0 212 410 (1986)
[2] – Susanna A.,Braus-Stromeyer, Alasdair M. Cook, and Leisinger T. *Environ. Sci.Technnlogy*, **27**, 1577-9, 1993
[3] – US Pat.5 110 364 (1992)
[4] – US Pat. 5 414 200 (1995)
[5] – Rosin J. A. and Farris M. M., *Ind. Eng. Chem. Res.* **32**, 1024-9, (1993)
[6] – Juszczyk W., Malinowski A. and Karpinski Z., *Appl. Catal.* **166**, 311-9 (1998)
[7] – Czernichowski A., Opalinska T. and Potapkin B. V., International Flame Days, Clean Combustion of Waste and Non-Conventional Fuels, Compromise Press, Biarritz, 1994, paper no. 46
[8] – Sekiguchi H., Honda T. and Kauzawa A., *Plasma Chem. Plasma Process.* **13,** 463-478 (1993)
[9] – Fridman A., Potapkin B. and Petrusev A., Program ASTRA, Moscow, 1992

ENERGY BALANCE OF A DIELECTRIC BARRIER DISCHARGE REACTOR FOR HYDROCARBON STEAM REFORMING

Thomas Kappes[a], Wolfgang Schiene, and Thomas Hammer

Siemens AG, Corporate Technology, CT EN 3, Erlangen, Germany

Abstract. In the future, hydrogen is supposed to play an important role in the worldwide energy supply. It allows a more efficient utilization of fossil fuels and the reduction of noxious emissions, e. g. by fuel cells or the use of hydrogen enriched fuels in combustion engines or gas turbines. Plasma methods are expected to allow low temperature and fuel flexible on-site hydrogen generation. They are also favorable in terms of a dynamic behavior at load changes, which is particularly important in mobile applications. However, one has to ensure an efficient plasma generation. Experiments on methane steam reforming for hydrogen generation with a dielectric barrier discharge (DBD) reactor were performed. A strong temperature rise of the reactor was observed when the plasma was ignited. To investigate the source of this heating effect, the DBD reactor was furnished with a series of temperature sensors and a constant power electrical heating to determine and quantify the input and output heat fluxes of the reactor. It was possible to strike an energy balance over the reactor including both thermal heat fluxes and the reaction enthalpy. It appears that more than 60 % of the electrical energy input is spent for heating of the dielectric barrier. This effect is independent of the gas type or the presence of chemical conversion, since similar results are obtained when pure nitrogen is fed to the DBD reactor. Nevertheless, it has been demonstrated that steam reforming reactions can be induced by DBD at temperatures below 400 °C, which is not possible with purely catalytic methods.

1. INTRODUCTION

Methane or natural gas reforming is widely used in industry to obtain hydrogen or synthesis gas (H_2+CO), which are utilized in industry for example as source materials for the production of raw chemicals like methanol and ammonia, as hydrogenation agents in oil refinery and as reducing gases in steel industry. Recently hydrogen gains in importance as fuel in fuel cell applications, combustion engines or gas turbines with the goal to achieve a more efficient exploitation of energy sources and to reduce noxious emissions.

The main reaction in steam reforming of methane is the oxidation with steam, yielding a mixture of hydrogen and carbon monoxide:

$$CH_4 + H_2O \rightleftharpoons CO + 3\,H_2 \qquad \Delta H° = 206\ \text{kJ/mol}$$

This strong endothermic reaction is industrially carried out using a nickel based catalyst at about 800 °C and 25 bar. To further increase the hydrogen yield and to remove carbon monoxide from the product gas, the exothermic water shift reaction can be applied in an additional stage at temperatures between 190 °C and 260 °C over a copper-zinc based catalyst.

$$CO + H_2O \rightleftharpoons CO_2 + H_2 \qquad \Delta H° = -41\ \text{kJ/mol}$$

The need to use a catalyst causes great demands on the process management and on the purity of the reactants to avoid coke formation or poisoning of the catalytic material.

[a] Electronic address: thomas.kappes@erls.siemens.de

Plasma based processes have fast response time, so they are more suitable for mobile applications with a fast changing load, and they are uncritical in terms of fuel impurities. Plasma-induced steam reforming has been investigated before using thermal arc discharge [1] or microwave discharge [2].

Non-thermal dielectric barrier discharge has already proven its applicability to gas conversion processes like ozone production, flue gas cleaning and destruction of volatile organic compounds [3, 4]. Some recent publications discuss the influence of dielectric barrier discharges on pure methane [5] and mixtures of methane with air, oxygen [6] and carbon dioxide [7], and aim mainly on the production of methanol or higher hydrocarbons. Also some basic studies dealing with methane steam reforming using DBD have been performed [8, 9]. However, the water conversion was low compared to the methane conversion, and the main reaction path has shown to be the formation of ethane and hydrogen. The energy demand relative to the hydrogen yield was substantially higher than reported for arc or microwave induced steam reforming and a strong heating of the dielectric barrier was observed.

In order to investigate this behavior in more detail, a thermally controlled test bench allowing the determination of heat fluxes was set up and an assessment of the energy balance was performed for the DBD steam reforming process, supported by the results of numeric modeling calculations.

2. EXPERIMENTAL

Plasma-chemical reactions were carried out in a coaxial DBD reactor, which was made of a alumina ceramics tube with 46 mm inner diameter and 5 mm wall thickness coated with a vapor deposited metal layer as the outer electrode. The inner high voltage electrode consisted of a metal rod equipped with 30 metal disks of 38 mm diameter with serrated edges. The disks were lined up on the tube in a distance of 5 mm to each other. This results in a discharge zone of about 19 cm length and a reactor volume about 450 ml. Both ends of the tube were closed with metallic caps containing the gas inlet and outlet tubes. One of the caps had a feed-through insulator for the high voltage connection of the inner electrode. To perform calorimetric measurements, the reactor was equipped with a set of thermocouples: inside the gas flow at the inlet and at the outlet, at the outside of each of the two metal caps as well as at three points along the barrier tube. A 5 cm thick layer of mineral wool provided a good thermal insulation. A drawing of the reactor is shown in Fig. 1.

The electrical discharge inside the reactor was induced by a pulsed high voltage power supply with a pulse rise time of about 15 V/ns. The discharge power was adjusted by the pulse voltage with a pulse frequency of 15 kHz. A four-channel digital storage oscilloscope (200 MS/s) together with a high voltage probe (1:1000, 100 MHz bandwidth, max. 40 kV) and a pulse current transformer (10 ns square pulse rise time) was used to record voltage and current waveforms and to calculate the pulse energy and the average discharge power, which was adjusted to be 180 W, corresponding to a specific energy of 3.6 kJ/l (STP).

After leaving the reactor, the gas was conducted to the analysis part through lines, which were heated to 180 °C in order to prevent condensation of water and other reaction products. The analysis was carried out with two gas chromatographs to determine the concentrations of CH_4, H_2, O_2, N_2, CO, CO_2, methanol and hydrocarbons. A Fourier transformed infrared (FT-IR) spectrometer was used for H_2O, CH_4, CO and CO_2 quantification. While the product gas was injected into the gas chromatographs without any pre-treatment, it was 6-fold diluted before FT-IR analysis with nitrogen preheated to 180 °C.

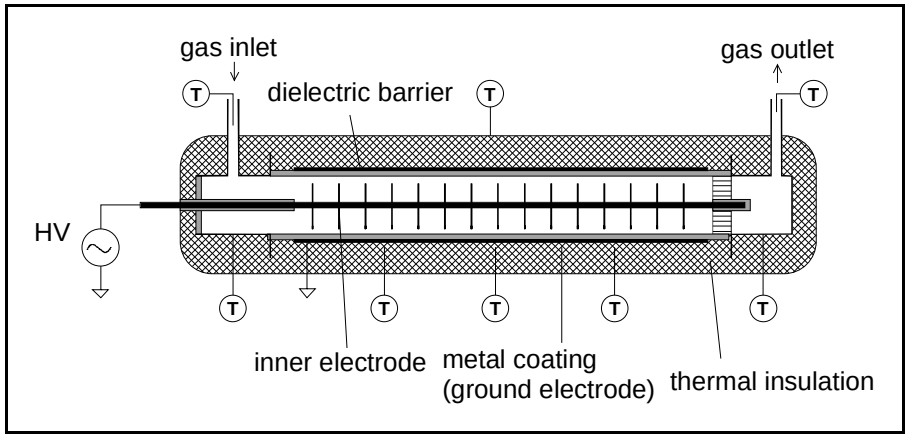


FIGURE 1. DBD reactor with calorimetric equipment

3. RESULTS AND DISCUSSION

DBD reactors in earlier experiments [9] were designed for isothermal operation with a temperature controlled electrical heating. Attention was focused rather on the chemical conversion of the gas under different conditions than on the energetic behavior of the system. However, when applying a high plasma power, a reduced heating energy requirement was observed, which indicates a heat dissipation caused by the plasma activity.

In order to investigate and to quantify these heating effects, the DBD reactor system was modified to operate in adiabatic mode or with a constant heating power, including a good thermal insulation and a series of thermocouples regularly spaced over the reactor for localized temperature measurements. The aim was to establish a complete heat balance over the reactor system considering the electrical, thermal and chemical energy fluxes.

A methane water vapor mixture (1:2) at a total gas flow of 3 l/min (STP) was prepared using mass flow controllers for methane and liquid water, the latter being evaporated in a heated tube before mixing with the methane. The mixture was preheated to 400 °C and then piped to the reactor inlet. The reactor was heated with a constant heating power of 80 W. The temperatures at the various measuring points in thermal equilibrium are shown in Fig. 2 for $t < 0$. At time $t = 0$ plasma generation was switched on with a mean plasma power of 180 W, and a sharp increase of the barrier temperature was observed, especially in the center, were the temperature rise at the beginning was 16 K/min. After 470 s, the plasma generation was switched off and the temperatures measured at the barrier tube decreased again. The wall temperatures of the metal caps as well as the gas outlet temperature rose slowly with a delay and continued rising after the plasma had been switched off due to heat transfer from the barrier tube.

Neglecting the heat transfer to the reactor caps, in a first approximation, and the losses to the environment, one can estimate the power spent for the barrier heating from the heat capacity of barrier tube and the temperature gradient, averaged over the whole length. About 113 W heating power is spent to the barrier corresponding to 63 % of the plasma power.

The fraction of the plasma power which is stored chemically in the reaction products can be estimated from the yields of the chemical species formed during the plasma induced reforming reaction. The conversion of methane and water were 5.9 % and 1.1 % respectively. The reaction products (with the yields in %) were H_2 (3.95), C_2H_6 (1.96), CO (1.46), C_2H_4 (0.69), C_2H_2 (0.55), C_3H_8 (0.42), CH_3OH (0.29), CO_2 (0.27), C_3H_6 (0.13), C_4H_{10} (0.12). From a balance of the formation enthalpies we found that the overall reaction was endothermic with a reaction enthalpy rate of 5 W which corresponds to 3 % of the plasma power.

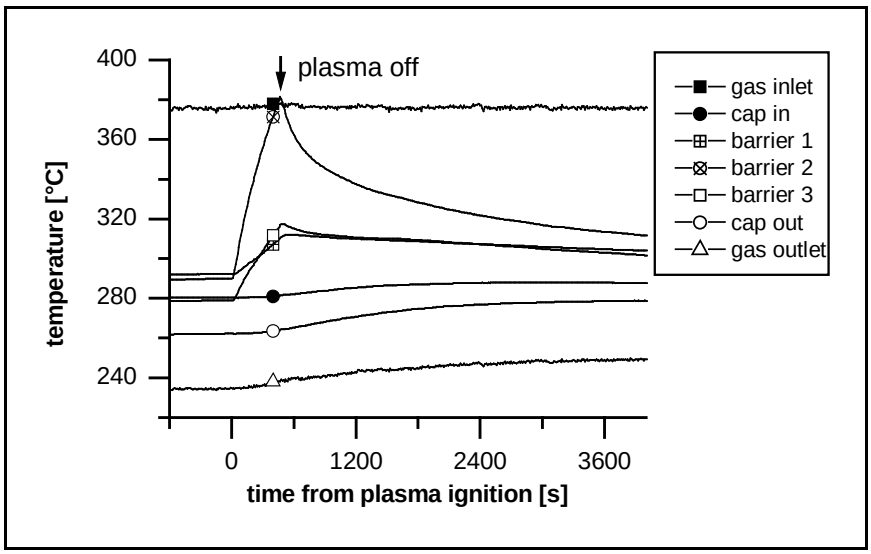


FIGURE 2. Temperature records at various point of the DBD reactor during a plasma run. (cap in/out = outside of the metal caps at the gas inlet/outlet; barrier 1/2/3 =outside of the ceramic tube at ¼, ½ and ¾ of the plasma zone length; plasma power 180 W; CH_4:H_2O 1:2; flow rate 3 l/min (STP)).

The complete heat balance over the reactor system is given in Tab. 1. Since a direct measurement of the gas temperature in the discharge gap was not possible, it remained unclear from the experimental results, whether the barrier itself is heated, e.g. by dielectric losses in the barrier material, or the gas is heated by the discharge nearby the barrier surface. The heat released in the gas discharge zone will rapidly be transferred to the reactor walls, so that it is not possible to get information about this problem from the gas temperature at the outlet.

Kinetic considerations and numerical simulations can help to clarify the origin of the heat dissipation and the low energy efficiency of the DBD steam reforming process: Because of the low water conversion it can be assumed that most of the reactions were induced by the highly endothermic electron collision dissociation of methane:

$$CH_4 + e \rightarrow CH_3 + H + e \qquad \Delta H_{673K} = 446 \text{ kJ/mol} \qquad (1)$$

Because of the small reaction enthalpy this reaction will very likely be followed by the formation of H_2 from another methane molecule reacting with the H-radical:

$$CH_4 + H \rightarrow CH_3 + H_2 \qquad \Delta H_{673K} = 5.2 \text{ kJ/mol} \qquad (2)$$

The two methyl radicals may react in a highly exothermic reaction with each other forming ethane:

$$CH_3 + CH_3 + M \rightarrow C_2H_6 + M \qquad \Delta H_{673K} = -381 \text{ kJ/mol} \qquad (3)$$

where M is a third molecule.

TABLE 1. Energy balance over steam reforming DBD reactor.

Energy sources		Energy sinks	
heat of the incoming gas	30 W	heat of outgoing gas	-17 W
plasma power	180 W	reaction enthalpy	-5 W
electrical heating	80 W	heating of the barrier	-113 W
		heat loss to the environment	-93 W
		rest (heating of caps, electrode etc.)	-62 W
total	290 W	total	-290 W

Thus the product yields can very roughly be explained by a set of three reactions with the methane dissociation being the rate limiting step. An estimation of the energy requirements for the plasma induced reforming reaction can be given under the assumptions, that

- every single H_2 formation reaction requires one electron collision methane dissociation reaction,
- the electrons do not undergo other processes than methane dissociation,
- the heat dissipation of reaction (3) cannot be utilized to initiate further reforming reactions.

The reaction enthalpy of reaction (1) corresponds to a plasma power of about 19 W, of which 16 W are dissipated as heat during the formation of ethane (3). These values do not yet take into account the heat dissipation caused by the reverse reaction of (1).

It is further known from numerical simulations of DBD steam reforming process [10], that only 34 % of the energy coupled into the gas discharge is spent on dissociative electron collisions with methane, while the vibrational excitation of water absorbs 47 % and of methane 7 % of the plasma energy, which corresponds to a total power of 97 W under the given experimental conditions. This energy is likely to be dissipated as heat during the relaxation of the excited molecules.

These mechanistic estimations indicate, that the observed reactor heating rather arises from the gas itself than from the barrier material.

4. CONCLUSIONS

DBD steam reforming of methane for hydrogen production has been investigated with a particular focus on the energetic behavior of the process. A thermally controlled reactor allowed to trace the energy fluxes to and from the system and to make an assessment of the energy balance. A very fast heating of the dielectric barrier was observed coinciding with the initiation of the discharge, more than 60 % of the plasma power is spent to this barrier heating. The main reaction products were ethane and hydrogen formed by the decomposition of methane, while the water conversion was low. The global reaction enthalpy was positive corresponding to about 3 % of the plasma power.

Mechanistic considerations and numerical simulations show, that on the one hand most of the plasma energy which is spent on the dissociation of methane is reemitted as heat during the recombination of the intermediate species, and that on the other hand more than 50 % of the plasma energy is absorbed by vibrational excitation of water and methane and does not contribute substantially to the formation of the desired reaction products. A more efficient activation of the steam reforming reaction would be possible by increasing the ratio of dissociative collisions to vibrational excitation, which requires a higher mean electron energy than it is obtained in DBD.

REFERENCES

[1] Bromberg L., *Energy & Fuel*, **12,** 11-18 (1998)
[2] Babaritskii A. I., *High Energy Chemistry*, **33**, 404-408 (1999)
[3] Eliasson B., *IEEE Transactions on Plasma Science*, **19**, 1063-1077 (1991)
[4] Hammer T., *Contributions to Plasma Physics*, **39**, 441-462 (1999)
[5] Mallinson R. G., *AIChE Journal*, **44**, 2252-2257 (1998)
[6] Kogelschatz U., *Plasma Chemistry and Plasma Processing*, **18**, 375-393 (1998)
[7] Kogelschatz U., Zhou, L. M., Xue, B. and Eliasson, B., In: *Greenhouse Gas Control Technologies,* ed. by B. Eliasson, P. Riemer and A. Wokaun, Elsevier, Amsterdam, 1999, pp. 385-390
[8] Okazaki K., *Thermal Science & Engineering*, **7**, 109-114 (1999)
[9] Schiene W., Kappes T. and Hammer T., *Proc. 15th International Symposium on Plasma Chemistry,* Orléans, pp. 701-706 (2001)
[10] Schiene W., Nichtthermische Plasmaverfahren zur Erzeugung von Wasserstoff aus Kohlenwasserstoffen, Ph.D. Thesis, University of Bochum (2002)

EFFICIENT METHANE CONVERSION TO ACETYLENE IN A MICROWAVE PLASMA

M. Heintze[a], M. Magureanu[a,b]

a) Institut für Niedertemperatur-Plasmaphysik, Friedrich-Ludwig-Jahn-Str. 19, 17489 Greifswald, GERMANY
b) on leave from National Institute for Laser, Plasma and Radiation Physics, Bucharest-Magurele, ROMANIA

Abstract. The optimisation of the parameters of a microwave discharge used for methane conversion into acetylene was intended with the aim of increasing the efficiency of the process. As a result, acetylene was obtained with high selectivity (70%) and energy expenses of 10 eV/molecule.

1. INTRODUCTION

Acetylene could become an attractive feedstock for the chemical industry if it is produced at reduced cost and at the point of use. Recently many attempts have been made to use plasma activation of methane in different types of non-equilibrium discharges (dielectric barrier discharge [1, 2], corona [3-5], rf [6], microwave [7-9]) for methane conversion into acetylene. Due to the non-equilibrium character, it is hoped to substantially reduce the energy spent for gas heating, resulting also in diminishing the decomposition of the reaction products to undesirable by-products and therefore in a more selective and less energy consuming conversion of methane.

Microwave discharges, due to the high electron densities, are characterised by high production rates of reactive species [10], which are expected to promote the further methane activation by chain reactions and indeed promising results were already reported in the literature [11, 12].

The experiments presented in this paper were aimed at minimising the energy costs for acetylene formation in a microwave discharge in methane thus increasing the process efficiency.

2. EXPERIMENTAL

A schematic view of the experimental arrangement is shown in Fig. 1. The discharge is generated in a quartz tube, 30 mm diameter, which is positioned along the axis of a cylindrical resonant cavity and through the wide faces of a rectangular waveguide. The resonant cavity has a radius of 44 mm and a height of 86 mm. The specific resonant mode is determined by the geometry of the cavity and in this case is the transverse magnetic mode TM_{010}. Due to the high quality factor of the cavity at resonance, leading to significant field enhancement, the discharge can be ignited in principle up to atmospheric pressure.

The microwave generator used is a cw magnetron which can supply up to 1600 W at 2.45 GHz operating frequency. The power measurements were done by inserting a waveguide section equipped with directional couplers for both the forward and reflected power, coupled to a power-meter (Anritsu ML2438A with MA2442A High Accuracy Sensors). The power absorbed by the discharge is the difference between the forward and reflected powers, considering that the other power losses, in the dielectric and the waveguide are negligible as compared to the absorbed power. An E-H tuner was used for the minimisation of the reflected power, having the advantage of simpler operation as compared to a three-stub tuner.

[a] Electronic address: heintze@inp-greifswald.de

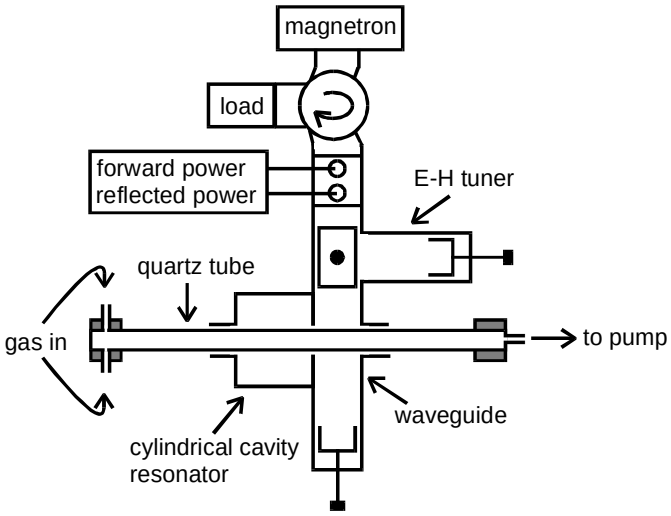


FIGURE 1: Experimental set-up.

The experiments are carried out under continuous flow of methane, the rate being regulated by flow controllers. Two tangential gas inlets are used in order to create a vortex for the stabilisation of the plasma. The pressure in the reactor is adjusted by a pump controlled by a valve and is measured by a pressure gauge at the exit of the tube.

The discharge ignites in the cavity and by proper tuning it is made to propagate also inside the waveguide so that the plasma extends downstream up to the end of the quartz tube.

The reaction products, mainly C_2 hydrocarbons, were analysed by mass spectrometry, using a QMS 200 spectrometer (Balzers), placed after the pump, so that sampling of the products is done at atmospheric pressure, regardless of the operating pressure. The following gases were monitored: hydrogen (m/z 2), methane (m/z 14) and C_2 hydrocarbons (m/z 26, 27). Since only very small amounts of ethane and hydrocarbons with more than two carbon atoms were detected in these experiments, their contributions to the MS signals at m/Z 26 and 27 were neglected and only the dominant reaction products, ethylene and acetylene, were followed. The calibrations were done using test gases containing 1% C_2H_4 and 1% C_2H_2, respectively. The C_2H_4 concentration is determined from the signal at m/Z 27. The signal at m/Z 26, corrected for the C_2H_4 contribution, shows the C_2H_2 concentration.

Optical emission spectroscopy was used in order to determine the gas temperature in the discharge region. The radiation emitted from the plasma is collected by an optical fiber and detected by an AH6130 diode-array spectrometer with a resolution of ~ 3 nm. The optical fiber was placed perpendicular to the narrow face of the waveguide, so that the direction of observation is perpendicular to the tube axis.

3. RESULTS AND DISCUSSION

3.1. Effect of the pressure

In order to study the influence of the total pressure in the plasma reactor on the CH_4 conversion degree and products distribution, experiments were performed in the range 50-300 mbar at constant energy input. The results for 1500 W discharge power and 28 slm CH_4 flow rate, resulting in an energy input of 0.8 eV/molecule, are shown in Fig. 2.

With increasing pressure from 50 to 100 mbar the conversion degree increases strongly, reaching a maximum value of 19%. Further increase of the pressure above 100 mbar has less influence on the CH_4 conversion degree, which shows a slow decrease towards higher pressures. The energy cost for conversion shows a minimum of less than 4 eV per CH_4 molecule converted. Over the entire pressure range, C_2H_2 is the main reaction product. Its selectivity increases with pressure to approx. 60% at 100-200 mbar and decreases slightly towards higher pressures. The corresponding energy required for C_2H_2 production reaches a minimum value of 13 eV per C_2H_2 molecule formed for 120 mbar. The selectivity towards C_2H_4 decreases from 26% to 11% with increasing pressure in the range 50-150 mbar and then remains constant at this value.

The optimum pressure range for CH_4 conversion to C_2H_2 is therefore 100-150 mbar. The slight decrease of the conversion degree observed at higher pressure could be due to soot formation, favoured with increasing total pressure, which is likely to absorb a part of the MW power, resulting in lower power available for the discharge.

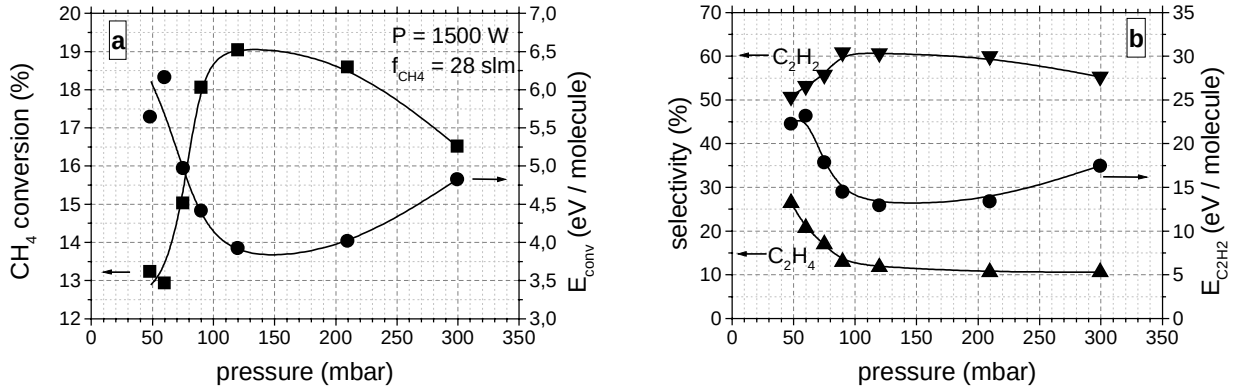


FIGURE 2: a. CH_4 conversion and energy required for conversion; **b.** Selectivities towards C_2H_2 and C_2H_4 and energy requirement for C_2H_2 formation vs. total pressure.

Since the reaction rate of CH_4 dissociation by electron impact is expected to decrease dramatically with increasing pressure [13], the observed pressure dependence of the conversion degree suggests that the mechanism of CH_4 dissociation in the plasma is not based solely on electron-neutral collisions, but active species produced in the discharge contribute also to the dehydrogenation reactions. As most of these reactions are thermally activated [14], the increase in conversion with pressure is likely to be due to the increase in gas temperature, which is expected to occur with increasing pressure [15].

3.2. Effect of the energy input

The energy provided to the discharge per CH_4 molecule was varied by changing the CH_4 flow rate in the range 18-35 slm, while maintaining a constant input power of 1500 W. The pressure in the plasma reactor was kept constant at 120 mbar, this value being in the optimum range for CH_4 conversion into C_2H_2.

Fig. 3a shows the CH_4 conversion degree and the energy requirement for conversion and in Fig. 3b the selectivities towards C_2H_2 and C_2H_4 and the energy costs for C_2H_2 formation as a function of input energy are presented.

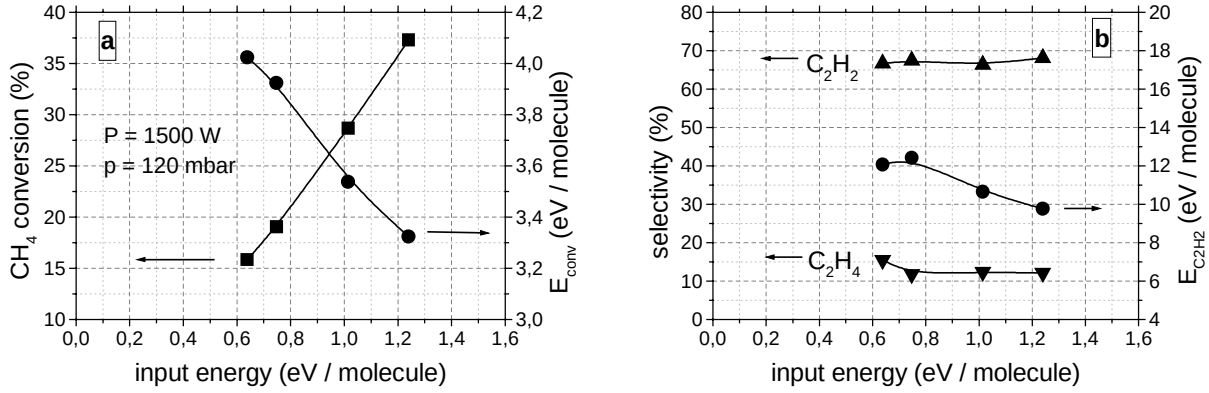


FIGURE 3: a. CH_4 conversion and energy required for conversion; **b.** Selectivities towards C_2H_2 and C_2H_4 and energy requirement for C_2H_2 formation vs. energy input.

The CH_4 conversion degree increases with the energy input, reaching approx. 37% at 1.25 eV/molecule. The conversion energy decreases continuously and a minimum value of 3.3 eV per CH_4 converted was obtained in these experiments, corresponding to the maximum conversion. The selectivity towards C_2H_4 decreases slightly with increasing energy input and the selectivity to C_2H_2 is 67-68%. The energy cost for C_2H_2 production shows a slight decrease towards higher energy, reaching a minimum value of approx. 10 eV per C_2H_2 molecule formed at the maximum energy input delivered to the discharge. A further increase of the energy input is likely to result in a higher efficiency, however, in these experiments, lower flow rates could not be used due to the instabilities that appeared in the discharge.

Preliminary experiments performed in pulsed mode showed that soot formation can be successfully suppressed. However, the results were similar to those in cw operation, most likely due to the long duty cycles available (15-50%), where the enhancement of the dissociation degree characteristic for short-pulse discharges does not occur [16].

3.3. Temperature determination

A typical spectrum observed in the low pressure range used (40-60 mbar) is shown in Fig. 4-1. The main features of the spectrum consist in the CH bands corresponding to the B $^2\Sigma \rightarrow$ X $^2\Pi$ and A $^2\Delta \rightarrow$ X $^2\Pi$ transitions, C_2 emission belonging to the Swan system (d $^3\Pi_g \rightarrow$ a $^3\Pi_u$) and atomic hydrogen emission of the Balmer H_α line. As the pressure is increased (Fig. 4-2), the C_2 Swan bands show a strong increase, while the CH bands suffer a decrease in intensity. In addition, a continuum emission is observed, underlying the atomic and molecular lines. This continuum radiation can be attributed to the incandescence of the hot carbonaceous particles produced in the discharge. Similar continua were observed from particulate carbon produced by laser vaporisation of graphite [17] and from soot particles in hydrocarbon flames [18] and can be used for the temperature diagnostic.

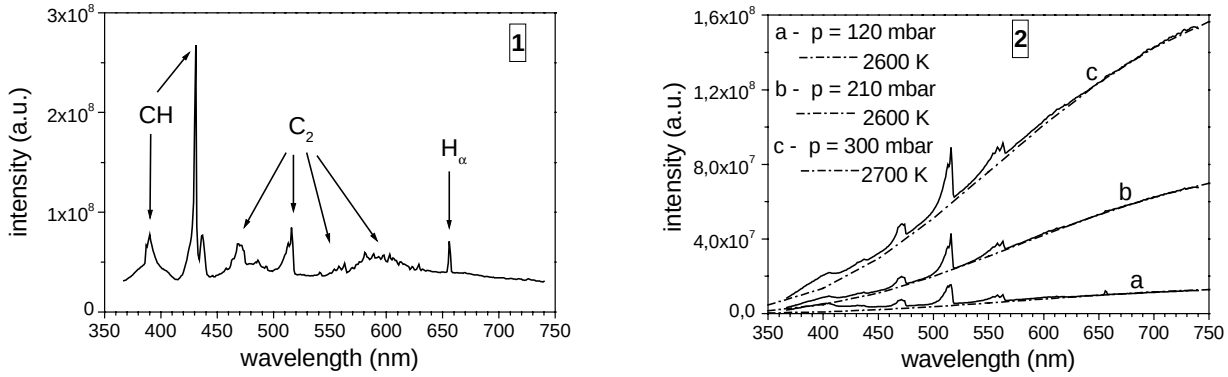


FIGURE 4. Emission spectrum obtained for power = 1600 W, flow = 28 slm, **4-1:** p = 60 mbar; **4-2:** p = 120, 210, 300 mbar and the fit to the blackbody radiation curve.

Following the approach applied in [17], the continua are fit to the Planck blackbody distribution function modified by the spectral emissivity of the particle. The emission intensity from a blackbody radiator at a wavelength λ depends on the temperature, the emissivity and the size of the radiating particle: $I(\lambda, T, a) = \varepsilon(\lambda, a) P_\lambda(T)(4\pi a^2)$, with a – the particle radius, $\varepsilon(\lambda, a)$ - the particle emissivity and P_λ - the Planck function. In the visible wavelength range, the emissivity of the soot particles is not sensitive to particle size [Roh88] and its variation can be approximated to be proportional to $1/\lambda$, assuming that both the Rayleigh criterion and the wavelength independence of the refractive index of the particles are satisfied at the long wavelength of incandescence. In this case, the radiation intensity from the hot particles is expressed by:

$$I(\lambda, T) = \frac{2\pi c^2 h}{\lambda^6 \left[\exp\left(hc / \lambda k_B T\right) - 1\right]}. \quad (1)$$

The temperature is determined by fitting the experimental spectra with the blackbody radiation curve given by equation (1), normalised to the emission intensity at 650 nm. The curves corresponding to temperatures of 2600-2700 K show a good fit to the shape of the experimental spectra in the long wavelength range. The slight discrepancies visible for short wavelengths can be due to the wavelength variation of the refractive index of the particle in this spectral region, which were not taken into consideration. The increase in the overall emission intensity which accompanies the increase in pressure is likely to be the result of a higher amount of soot particles present in the discharge at higher pressure.

5. CONCLUSIONS

An efficient conversion of methane into acetylene was achieved in the MW discharge under study, with high selectivity towards acetylene and minimum energy costs of only 10 eV per C_2H_2 molecule.

Besides electron impact, neutral-neutral collisions with active species generated in the plasma have an important contribution to the methane dissociation and the subsequent hydrogen abstraction reactions. Therefore the high gas temperature obtained at relatively low energy input is essential for the increased dehydrogenation and the low energy requirement achieved.

Lower energy costs are likely to be obtained when increasing further the energy input. A pulsed discharge with short pulse duty cycles is expected to reduce even more the energy expenses.

REFERENCES

[1] Rutkovsky J., Drost H., and Klotz H.-D., Kinetics of the nonthermal plasmachemical conversion of methane in barrier discharge. In: *Proc. ISPC-5*, ed. by B. Waldie, and G. A. Farnell, Edinburgh, 1981, pp.765-70

[2] Thanychotpaiboon K., Chavadej S., Caldwell T. A., Lobban L. L., and Mallinson R. G., *Reactors, Kinetics and Catalysis*, **44**, 2252-7 (1998)

[3] Gong W., Zhu A., Zhou J., Shi H., Ruan G., and Zhang B., The catalytic coupling of methane under pulse corona plasma. In: *Proc. ISPC-13*, ed. by C. K. Wu, Beijing, 1997, pp. 1578-83

[4] Kado S., Sekine Y., and Fujimoto K., *Chem. Commun*., 2485-6 (1999)

[5] Zhu A., Gong W., Zhang X., and Zhang, B., *Science in China*, **43**, 208-14 (2000)

[6] Hsieh L.-T., Lee W.-J., Chen C.-Y., Chang M.-B., and Chang, H.-C., *Plasma Chem. Plasma Process.*, **18**, 215-39 (1998)

[7] Oumghar A, Legrand J. C., Diamy, A., and Turillon, N., *Plasma Chem. Plasma Process.*, **15**, 87-107 (1995)

[8] Onoe K., Fujie A., Yamaguchi T., and Hatano Y., *Fuel* **76**, 281-2 (1997)

[9] Kopytko N., and Barronet F., *Can. J. Chem.* **76**, 1875-85 (1998)

[10] Wertheimer M. R., and Moisan M., *J. Vac. Sci. Technol. A*, **3**, 2643-9 (1985)

[11] Fridman A., Babaritskyi A., Jivotov V., Dyomkin S., Nester S., Rusanov V., Methane conversion in acetylene in the nonequilibrium MCW-discharge. In: *Proc. ISPC-10*, ed. By U. Ehlemann, H. G. Lergon, and K. Wiesemann, Bochum, 1991, pp. 1-6

[12] Babaritskyi A., Cheban'kov F., Jivotov V., Dyomkin S., Nester S., Rusanov V., and Fridman A., *VDI Berichte*, p. 541-7 (1995)

[13] Mechold L., Röpcke J., Duten X., and Rousseau A., *Plasma Sources Sci. Technol*., **10**, 52-60 (2001)

[14] Baulch D. L., Cobos C. J., Cox R. A., Esser C., Frank P., Just Th., Kerr J. A., Pilling M. J., Troe J., Walker R. W., and Warnatz, J., *J. Phys. Chem. Ref. Data*, **21** (1992)

[15] Chen C.-K., Wei T.-C., Collins L. R., and Phillips, J., *J. Phys. D: Appl. Phys*., **32**, 688-98 (1999)

[16] Hassouni K., Duten X, Rousseau A., and Gicquel A., *Plasma Sources Sci. Technol*., **10**, 61-75 (2001)

[17] Rohlfing E. A., *J. Chem. Phys*., **89**, 6103-12 (1988)

[18] Flower W. L., *Comb. Sci. Tech*., **33**, 17-33 (1983).

DECOMPOSITION OF HALOGENATED MOLECULES IN A MICRO-STRUCTURED ELECTRODE GLOW DISCHARGE AT ATMOSPHERIC PRESSURE

M. Miclea[1a)], K. Kunze[a)], J. Franzke[a)], F. Leis[a)], K. Niemax[a)], C. Penache[b)], O. Hohn[b)], S. Schössler[b)], T. Jahnke[b)], A. Bräuning-Demian[b)], H. Schmidt – Böcking[b)]

a) Institute for Spectrochemistry and Applied Spectroscopy (ISAS), Bunsen-Kirchhoff-Str.11, D-44139 Dortmund, GERMANY

b) J.W.Goethe University, Institut für Kernphysik (IKF), August-Euler-Str. 6, D-60486 Frankfurt am Main, GERMANY

Abstract. A Micro-Structured Electrode (MSE) discharge operating at 1 bar is applied as a detector of halogenated hydocarbons. Due to its physical properties (T ~ 2000 K and high electron number densities of about 10^{15} – 10^{16} /cm^3) this microplasma has comparable performances as classical plasmas used in analytical spectroscopy. The small size (µm range) and a low power consumption makes it suitable for integration in miniaturized devices for chemical analysis.

1. Introduction

In the last years, the trend in analytical spectrometry was directed to the miniaturization of analytical instruments and the creation of portable lab-on-a-chip devices with similar properties like large scale laboratory instruments. Besides the goal of reducing size and weight, miniaturization offers additional advantages such as the possibility to bring the laboratory to the sample which may increase the analytical performances, portability for personal use and personal dosimetry, lower the cost and reduces the needed quantities of analyte samples.
Plasma sources are efficient atomisation and excitation devices. In combination with different analysis techniques (emission spectroscopy, absorption spectroscopy or mass spectrometry) they can be employed for the analysis of solid, liquid and gaseous samples [1].
In the category of non-thermal plasmas, the interest in using MSE discharges recently increased due to their multiple application possibilities (surface treatment, reduction of pollutants and generation of UV and VUV radiation) using high pressure operation and low power consumption [2-5]. The micro-dimensions of the discharge combined with convenient plasma parameters make it very attractive also for analytical applications.
In this paper we demonstrate, by applying atomic emission spectroscopy technique, the efficiency of a MSE atmospheric pressure discharge for the measurement of halgogenated hydrocarbons.

2. High pressure MSE discharge operation

The MSE is a multilayer system consisting of two metallic foils (Cu, Ni, Pt or W) separated by an insulator (Kapton, mica or ceramic). A hole with a diameter varying from tens to hundreds of µm is drilled through the structure. Applying direct current (DC) or alternative current (AC) a weekly ionized plasma is produced between the electrodes in pure noble gases, gas mixtures or air. The operation of the discharge depends mainly on the ratio between the hole diameter and the distance between the electrodes, the gas pressure and the current density. Due to the reduced dimensions of the holes, high pressure can be applied for the generation of a stable discharge according to the Paschen law. The discharge can be operated in the pressure range from a few tens of mbar up to 2 bar.

[1] Miclea@isas-dortmund.de

Recently, spectroscopy has been applied to determine the discharge parameters [6]. Diode laser atomic absorption measurements performed on a MSE discharge operating in Ar revealed an increase in the gas temperature from room temperature at 50 mbar to 1200 K at 400 mbar. The electron density increased with the pressure up to $5\times10^{15}/cm^3$ at 400 mbar. Scaling these values to atmospheric pressure, we can expect that the gas temperature and the electron density should be close to 2000 K and $10^{16}/cm^3$, respectively. Knowing that the ionisation energy is different, the values for He as plasma gas should be within one order of magnitude smaller than those obtained in Ar. The discharge has a strong non-homogenous distribution of the electrons and the excited atoms following the change of the cathode fall length with the increase of the pressure. In Fig.1 the schematic view of the microstructure and a CCD recorded image of the plasma in Ar at 400 mbar are presented.

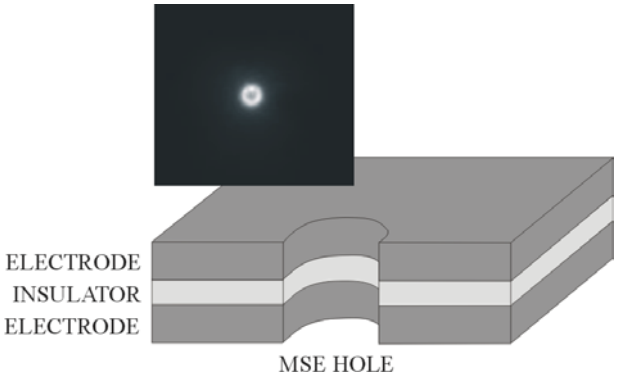


FIGURE 1 Schematic view of the structure and an end-on CCD recorded image of the plasma in Ar at 400 mbar

In the present experiment a structure with 30 µm Pt electrodes and Al_2O_3 as insulator was used. The diameter of the hole was 100 µm and the distance between electrodes 250 µm, respectively. Due to the reactivity of the halogens, noble metal electrodes with a low erosion rate were applied. Attempts to use a system with copper electrodes and Kapton as insulator failed due to the fast erosion of the cathode and the Kapton. The discharge was operated in He as well as Ar with reduced admixtures (less than 50 ppm) of halogenated hydrocarbons (CCl_2F_2, $CHClF_2$) in the pressure range of 0.7 – 1.4 bar. The presence of the added analytes had almost no influence on the plasma operation conditions.

The discharge works in a stable mode for currents ranging from 4 mA to 8 mA. The input power density is about 1 MW/cm^3 at a current density of 60 A/cm^2. The voltage-current characteristics of the discharge measured in He and Ar are presented in Fig. 2. The gas voltage is constant and does not exceed 250 V for any of the pressure values, corresponding to a normal glow discharge operation.

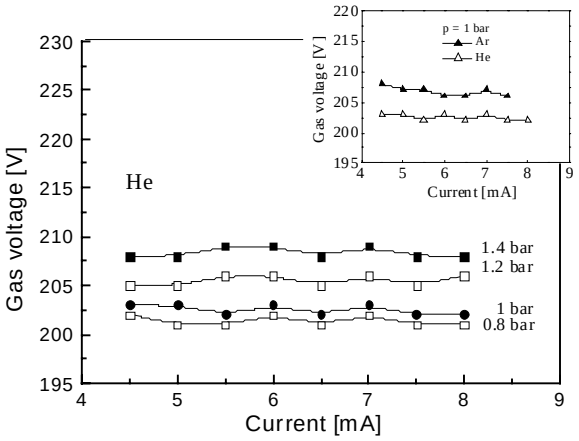


FIGURE 2 U I characteristics of the discharge operating in He and Ar

3. Detection of halogenated hydrocarbons by emission spectroscopy

Atomic emission spectroscopy was applied for the detection of chlorine and fluorine resulting from the decomposition of the molecules. The experimental arrangement consists of a very small echelle spectrometer working in the 640-970 nm range (diffraction orders 120-80) and a CCD camera with a resolution of 1024×1024 pixels [7]. The plasma emitted light is imaged 1:1 on the 20 µm × 200 µm spectrometer entrance slit through an optical fibre. The entire spectral range is recorded simultaneously with an exposure time of 50 ms. In Table 1 the measured emission lines belonging to the investigated halogens and to the buffer gas are presented.

The measurements were performed mainly in He because both Cl and F atomic lines can be recorded while in Ar fluorine could not be measured. This is due to the fact that the excited fluorine levels are higher than those of Ar.

TABLE 1 emission lines

Element	λ [nm]
Cl	912.114
Cl	894.802
Cl	837.594
Cl	754.707
F	739.868
F	733.195
F	755.223
F	742.564
He	728.134
He	667.815
H	656.358
N	868.028
O	844.675
O	794.754
O	777.194
Ar	811.531
Ar	750.386
C	965.843
C	909.483

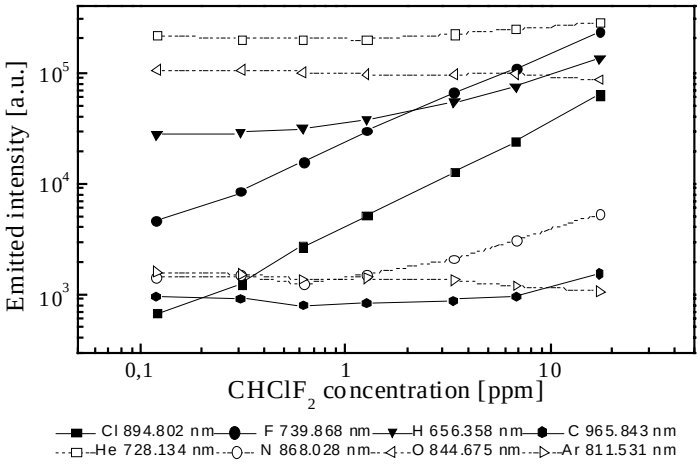


FIGURE 3 Evolution of the emitted lines with the halogenated molecule concentration in He, p=1 mbar, I = 4 mA

Fig. 3 shows the intensity of the emission lines of different elements in dependence on the $CHClF_2$ concentration in He at 1 bar and 4 mA. The intensities of the emitted lines of the buffer gas are independent of the molecule concentration. The intensities of the Cl and F lines are linearly dependent on the $CHClF_2$ concentration. Assuming the complete dissociation and atomisation of the introduced molecules, it is expected that the H and C signals are also linearly dependent on the $CHClF_2$ concentration. However this is not the case. The reason may be due to H_2O contamination of the plasma gas and the formation of parasitic species, such as CO or CO_2 in the discharge.

Fig. 4 presents calibration curves for Cl and F from CCl_2F_2 in He. For this purpose we pre-mixed the halogenated hydrocarbons with He before the gas was introduced into the plasma. The measurements started always from an initial mixture of He with 17 ppm halogenated molecules and this mixture was diluted down to a concentration when the signal was 3 times the noise. The calibration curves are linear over 3 orders of magnitude, but at small concentrations it can be noticed that the calibration curves of the F lines are not linear due to a contamination of the discharge walls by fluorine.

Nevertheless, CCl_2F_2 detection limits of 20 ppb in He were found using the Cl 912.114 nm as well as the F 739.868 nm lines. This was also obtained with other halogenated hydrocarbons, not shown in Fig. 4. The detection limits with Ar as a buffer gas are of the same order of magnitude.

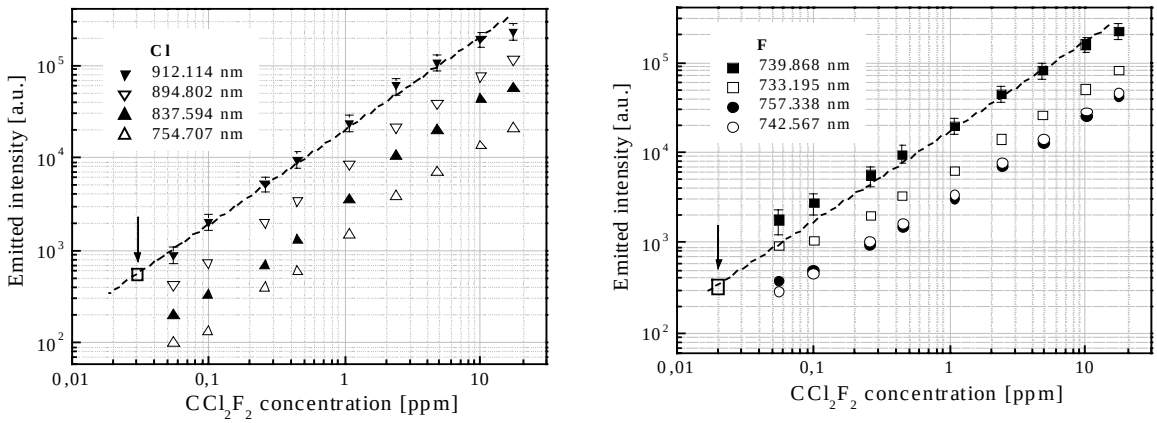


FIGURE 4 Calibration curves of Cl (left) and F (right) in He with CCl_2F_2.
The detection limit is shown by a square in every figure

In order to study the capability of complete dissociation we measured the Cl and F line intensities with CCl_2F_2 and $CHClF_2$ in the He MSE discharge, varying the species concentrations. The results are shown in Fig. 5. It can be seen that the F line intensities are independent of the species within the experimental errors. On the other hand the Cl line intesities obtained with CCl_2F_2 is a factor of two higher than with $CHClF_2$ as it is expected from the stoichiometry.

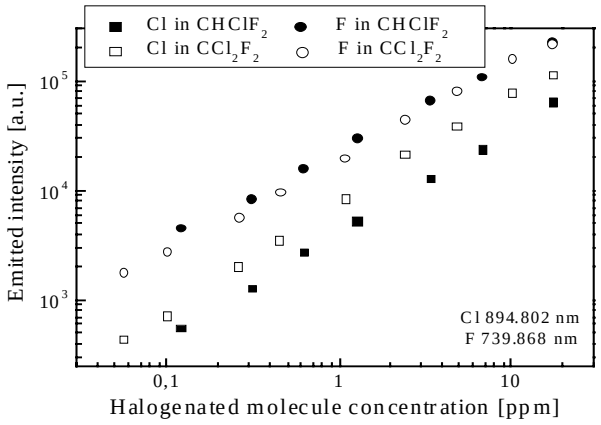


Fig. 5 Cl and F emitted signals from different halogenated molecules in He, p = 1 bar, I = 4 mA

4. Conclusions

It has been shown, that the MSE discharge can be successfully applied in analytical spectrometry. The detection limits for halogenated hydrocarbons are in the low ppb range. The efficiency of the discharge for the dissociation of halogenated hydrocarbons was demonstrated. Therefore it can be expected that the MSE discharge can be a powerfull small detector applied in gas chromatography.

5. References

[1] R. K. Marcus, E. H. Evans, J. A. Carusso, J. Anal. At. Spectrom., **15**, pp.1-5 (2000)
[2] K. H. Gericke, H. Schmidt-Böcking, German Patent DE 196 05 226 C2 (1996)
[3] M. Roth, T. Haas, M. Lock, K. H. Gericke, A. Bräuning-Demian, L. Spielberg, H. Schmidt-Böcking, Proc. of 1st Int. Conf. On Microreaction Technology, Springer Verlag Berlin, pp 62-69 (1998)
[4] W. Shi, R. H. Stark, K. H. Schoenbach, IEEE Trans. Plasma Sci. **27**, pp. 16-17 (1999)
[5] M. Moselhy, R. H. Stark, K. H. Schoenbach, U. Kogelschatz, Appl. Phys. Lett. **78** (7), pp. 880-882 (2001)
[6] C. Penache, M. Miclea, A. Bräuning-Demian, O. Hohn, S. Schössler, T. Jahnke, K. Niemax, H. Schmidt-Böcking, submitted to Plasma Sources Science and Techn. (2002)
[7] H. Becker – Ross, S. V. Florek, Spectrochimica Acta Part B, pp. 1367-1375 (1997)

INDEX

A

Abe, T. 303
Addou, A. 308
Aints, M. 83, 282
Akishev, Yu.S. 8, 99
Amirov, R.H. 337
Anikin, N.B. 73
Appleton, A.T. 313
Arnesen, A. 291

B

Baba, S. 148
Baranchuk, M.S. 93
Bartnikas, R. 124
Behnke, J. 48, 53
Behnke, J.F. 48, 53, 68, 410
Bibinov, N.K. 73
Bogaerts, A. 130
Boksha, N.S. 114
Borra, J.P. 364
Brablec, A. 68
Brandenburg, R. 13, 28, 63
Bräuning-Demian, A. 206, 390
Brisset, J.L. 308, 379
Brožek, V. 161
Burlica, R. 379

C

Calvo, S. 296
Chang, J.S. 78
Cheron, B. 379
Chéron, B.G. 308
Chikeev, E. 277
Choi, J.J. 360
Chutov, Yu.I. 88
Clark, R.J. 374
Cormier, J.-M. 176, 296
Croquesel, E. 23
Czeremuszkin, G. 124, 400

D

Datta, S. 390
Dekempeneer, E. 385
Demyanov, A.V. 8
Deniset, C. 355
Dewulf, J. 342
Dhainaut, M. 171
Djéga-Mariadassou, G. 296
Dors, M. 78, 144
Drinkenburg, A.A.H. 318
Dudemaine, M. 176
Dudziński, K. 415
Dupré, S. 355

E

Ebert, U. 33
Ehara, Y. 244
Eliáš, M. 161
Endo, Y. 217
Engemann, J. 58

F

Fateev, A. 119
Filimonova, E.A. 337
Finney, W.C. 313, 369, 374
Foest, R. 410
Francke, K.-P. 323
Franzke, J. 206

G

Gerasimov, G. 291
Gherardi, N. 23, 28
Gibalov, V.I. 153
Gijbels, R. 130
Goedheer, W.J. 88
Goldman, A. 3, 171, 355
Goldman, M. 3, 171, 355
Golubovskii, Yu.B. 48, 53
Goodwin, A. 441
Goossens, O. 385
Gorce, O. 296
Guimond, S. 400

H

Haljaste, A. 83, 282
Hallin, R. 291
Hammer, T. 196
Hayashi, N. 213, 347, 351
Hayashi, T. 264
Heesch, E.J.M. van 318
Heintze, M. 139, 166, 201
Herbert, T. 441
Hippler, R. 410
Hnatiuc, B. 379
Hnatiuc, E. 308, 379
Hohn, O. 206, 390
Hong, J. 360
Hong, S.H. 38, 104, 109, 337
Horinouchi, T. 264
Hulka, L. 259
Humpert, C. 234

I

Ignatkov, A. 58
Ihara, S. 213, 347, 351
Ishii, S. 217
Ito, T. 244

J

Jahnke, T. 206, 390
Jahołkowski, K. 239
Jalviste, E. 291
Janča, J. 161, 425
Janowska, J. 415
Janowski, T. 249
Jidenko, N. 364
Jodzis, S. 269
Joshi, P. 390
Jouve, G. 3
Jurado, H. 296

K

Kanazawa, S. 78
Kaneda, S. 213
Kang, W.S. 38, 109
Kapička, V. 68
Kappes, T. 196
Karal’nik, V.B. 8
Karimi, C. 171
Karpiński, L. 420
Kettlitz, M. 139
Khacef, A. 296

Khampan, C. 28
Kim, S. 360
Kim, Y.-H. 38, 104, 109, 337
Kim, Y.-K. 360
Kirkpatrick, M.J. 369
Kishida, H. 244
Klíma, M. 68
Kochetov, I.V. 99
Kocik, M. 78
Kogoma, M. 303, 436
Kozlov, K.V. 13, 28, 114
Kozlov, M.V. 43
Kravchenko, O.Yu. 88
Krawczyk, K. 181, 186
Kunze, K. 206

L

Laan, M. 134, 286, 405
Landing, W. 374
Langenhove, H. Van 342
Lavrov, O.A. 88
Leadley, S. 441
Lebedev, V. 410
Lee, Ke. 360
Lee, Ki. 360
Leis, F. 206
Lendresse, Y. 296
Leu, G.F. 58
Leys, C. 342
Lisitchenko, T.E. 88, 93
Lissovski, A. 277
Loboiko, A.I. 99
Locke, B.R. 313, 369, 374
Lukes, P. 313
Lunk, A. 119

M

Madani, M. 130
Magureanu, M. 139, 201
Maiorov, V.A. 48, 53
Marode, E. 18, 355
Massines, F. 23, 28
Michel, P. 13, 28, 63
Miclea, M. 206
Miessner, H. 323
Misiak, M. 415
Miyake, Y. 244
Mizeraczyk, J. 78, 144
Monich, A.E. 8
Morent, R. 342
Morozov, A.M. 114
Moussa, D. 308
Mukhopadhyay, S. 390
Murata, T. 153

N

Nair, S.A. 318
Nakajima, N. 264
Napartovich, A.P. 99
Naudé, N. 23
Navratil, Z. 63
Niemax, K. 206
Nowakowska, H. 144

O

Ochman, P. 191
Odic, E. 171
Ohkubo, T. 78
Okazaki, S. 239
Okholin, M.M. 93
Ono, S. 431
Opalinska, T. 191, 254, 420

Opalska, A. 191
Ostrikov, K. 395
Ozonek, J. 239

P

Paris, P. 405
Park, J.M. 104
Pasedag, D. 63
Paulussen, S. 385
Pawłat, J. 327
Pemen, A.J.M. 318
Penache, C. 206, 390
Penghui, G. 347
Petit, M. 364
Peyrous, R. 222
Pietruszka, B. 166
Pietsch, G.J. 153, 229, 234, 259
Plank, T. 83, 134
Podliński, J. 78
Polaczek, J. 191
Pollo, I. 239, 327
Pouvesle, J.M. 296
Protas, G.I. 88
Ptasinski, K.J. 318

R

Radu, I. 124, 400
Raud, J. 286
Repän, V. 134
Roots, L. 282
Rudolph, R. 323
Rusu, I. 176
Ruszniak, J. 181
Rutgers, W.R. 33
Rzanek-Boroch, Z. 415

S

Sahni, M. 374
Samoilovich, V.G. 114
Satoh, S. 148, 213, 347, 351
Saveliev, A.B. 229
Schiene, W. 196
Schmidt – Böcking, H. 206, 390
Schmidt-Szałowski, K. 181, 415, 420
Schössler, S. 206, 390
Schwabedissen, A. 58
Sentek, J. 181
Severac, C. 3
Shimosaki, M. 213
Šícha, M. 68
Šira, M. 73
Slavíček, P. 68
Smerechuk, A. 291
Sokolova, M.V. 43
Song, Y.-H. 38, 109, 337
Sonnenfeld, A. 410
Sťahel, P. 425
Stańco, J. 144
Steffen, H. 410
Stryczewska, H. D. 249
Subedi, D.P. 425
Swallow, F. 441
Szymańska, A. 415

T

Takayama, S. 431
Tanaka, K. 303, 436
Tardiveau, P. 18
Teii, S. 431
Temnikov, A.G. 43
Teshima, K. 332
Thomas, C. 296

Timatkov, V.V. 43
Treshchalov, A. 277, 291
Trunec, D. 63
Trushkin, N.I. 8

U

Ulejczyk, B. 420

V

Valtna, H. 405
Vangeneugden, D. 130, 385
Veis, P. 23
Veldhuizen, E.M. van 33
Vereshchagin, I.P. 43
Vertriest, R. 342
Vinogradov, I.P. 119
Vitrac, H. 308
Vladimirov, S. 395

W

Wagner, H.-E. 13, 28, 63
Wertheimer, M.R. 124, 400
Wieczorkowski, M. 186
Wiesemann, K. 73

Y

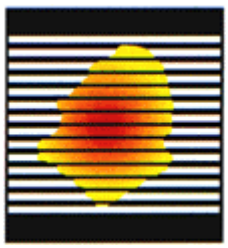
Yamabe, C. 148, 213, 327, 347, 351
Yamamoto, K. 351
Yan, K. 318
Yasuoka, K. 217
Yoshioka, Y. 332

HAKONE VIII

International Symposium on
High Pressure
Low Temperature
Plasma Chemistry

Contributed Papers

Volume 2



Pühajärve, Estonia

July 21 - 25, 2002

ORGANIZER

Institute of Experimental Physics and Technology of the University of Tartu

INTERNATIONAL SCIENTIFIC AND ORGANIZING COMMITTEE

Brisset, J.-L.	France
Herbert, T.	Ireland
Ito, T.	Japan
Janča, J.	Czech Republic
Kogelschatz, U.	Switzerland
Kozlov, K.V.	Russia
Pietsch, G.	Germany
Pollo, I.	Poland
Rea, M.	Italy
Sakai, T.	Japan
Skalný, J.D.	Slovakia
Wagner, H.-E.	Germany
Yamabe, C.	Japan

LOCAL ORGANIZING COMMITTEE

Aaviksoo, J. (Chairman)	Aints, M.
Laan, M. (Vice-chairman)	Korge, H.
Haljaste, A. (Secretary)	Paris, P.
	Plank, T.

PREFACE

The HAKONE VIII Symposium hosted by University of Tartu at Pühajärve, Estonia, is the eighth in the series originated in Hakone (Japan) in 1987. It follows along the lines of the previous meetings providing the participants with the opportunity to present the progress in high-pressure low temperature plasma chemistry and physics in recent years. As the plasma chemistry is of increasing interest to industrial technologies and environmental applications, the HAKONE symposiums are appreciated as events that bridge the gap between basic research and applications. HAKONE VIII with its high number of participants (over 110) and 87 contributions testifies to that opinion.

This two-volume set of Symposium Proceedings contains the Contributed Papers, which were accepted upon the review of abstracts by the Local Organizing Committee (LOC) by the authority of the International Scientific and Organizing Committee. About 4% of the submitted abstracts were rejected, mostly on the ground that they were outside the subject area of the symposium. The authors of the accepted papers were provided with the Preparation Guide and Sample Format of Papers describing the rules of preparation. The length of the papers was limited to five pages. One of the requirements for the inclusion of the papers in the Symposium Proceedings was that at least one of the authors had to be registered. The authors were asked to submit their papers as camera ready electronic files in the PDF format. DOC files were accepted as an exception and they were formatted and converted into the PDF format by the Symposium organizers. No editorial corrections pertaining to contents were made and therefore the authors are fully responsible for the scientific and technical contents of their contributions. The papers of unsatisfactory printing quality (especially concerning the illustrations) were returned to the authors for improvements until a satisfactory material was completed. The editors thank the authors for they efforts to comply with the unified rules of preparation.

In the HAKONE VIII Symposium as well in the Symposium Proceedings, the contributions are distributed in seven different topics. Within each topic, the papers are selected for oral and poster sessions denoted by L and P in the contents of the Symposium Proceedings. Most of the contributed papers are available on the Internet under the address http://www.ut.ee/hakone8/papers/Papers.html .

The LOC hopes that you will find these five days at HAKONE VIII to be very valuable and fruitful for discussing your results hitherto, sharing experiences and exchanging new ideas. We hope the beautiful scenery of Pühajärve will create a cozy atmosphere and help you to realize your aims.

Tartu, June 2002 The Local Organizing Committee

ACKNOWLEDGEMENTS

Hakone VIII acknowledges the sponsorship and financial support of the following institutions and companies:

- E. C. Chemical Co., Ltd. (Japan)
- Estonian Science Foundation
- International Nuclear Information System
- Matsushita Electric Works Machine & Vision, Ltd. (Japan)
- Toppan Printing Co., Ltd. (Japan)
- Trailigaz (France)
- University of Tartu

Editors: Ants Haljaste, Toomas Plank

Cover design: Peeter Paris

ISBN: **9985-4-0258-8**

Contact address:

Ants Haljaste
Institute of Experimental Physics and Technology
University of Tartu
Tähe 4
51010 Tartu
ESTONIA
Phone: +372 7 375 565; +372 7 375 564
Fax: +372 7 375 858
E-mail: haljaste@ut.ee

Aiplasma
Atmospheric-pressure
Plasma Cleaning Unit

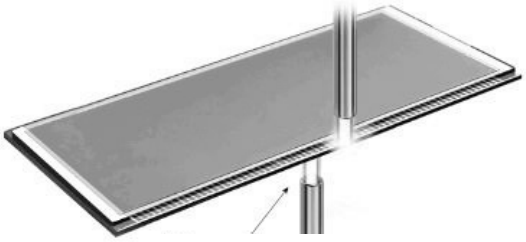
Smart Solutions by NAIS

High-speed, point-specific plasma cleaning of contacts in electronic components, under atmospheric pressure

Aiplasma **removes contaminants and improves surfaces, offering better bonding reliability, improved bonding strength, and better overall product quality**

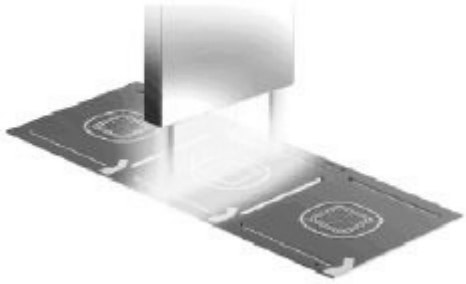
High-speed, point-specific plasma cleaning

Improves surface cleaning of organic contaminants *under atmospheric pressure*



Aiplasma nozzle

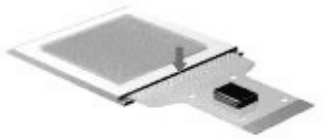
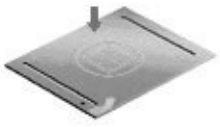
Spot: 5 to 10mm dia.



Wide: 25 to 75mm

Using propriety technology (over 60 patents pending), ***Aiplasma*** enables stable, continuous plasma flow at atmospheric pressure. Since ***Aiplasma*** works under atmospheric pressure, it can be implemented into existing manufacturing facilities for high-speed, continuous processing. With ***Aiplasma***, oxygen and hydrogen plasma are used for the removal of organic compounds on contact points of LCDs/PDPs and electronic components, and to remove surfaces and improve adhesion strength of resin substrates before sealing. These processes can all be performed in-line for improves quality, higher productivity and reduced manufacturing costs.

Applications

OLB(FOG) contact surface cleaning	BGA substrate/bonding pad cleaning	Compound chip package cleaning
		
Sections where the LCD/PDP panel bonds to the film substrate are cleaned	Cleaning the bonding pad improves the wire bonding and the peel shear strength of the sealing resin	The contact sections of compound electric components are cleaned

Matsushita Electric Works Machine & Vision, Ltd

Head Office : 1048, Kadoma, Kadoma-shi, Osaka 571-8686, Japan
http://www.aiplasma.com/
E-mail : webmaster@naismv.co.jp

Trailigaz

Ozone - Ultraviolets - Electrochloration



- **Oxidation and Disinfection technologies for Industrial and Municipal Applications**



- **Trailigaz proposes specific technical solutions well adapted to your project**



- **Compact and reliable equipments**

  Ozone generators and ancillary equipments, skids for specific applications, UV reactors, Electrochlorators…

trailigaz

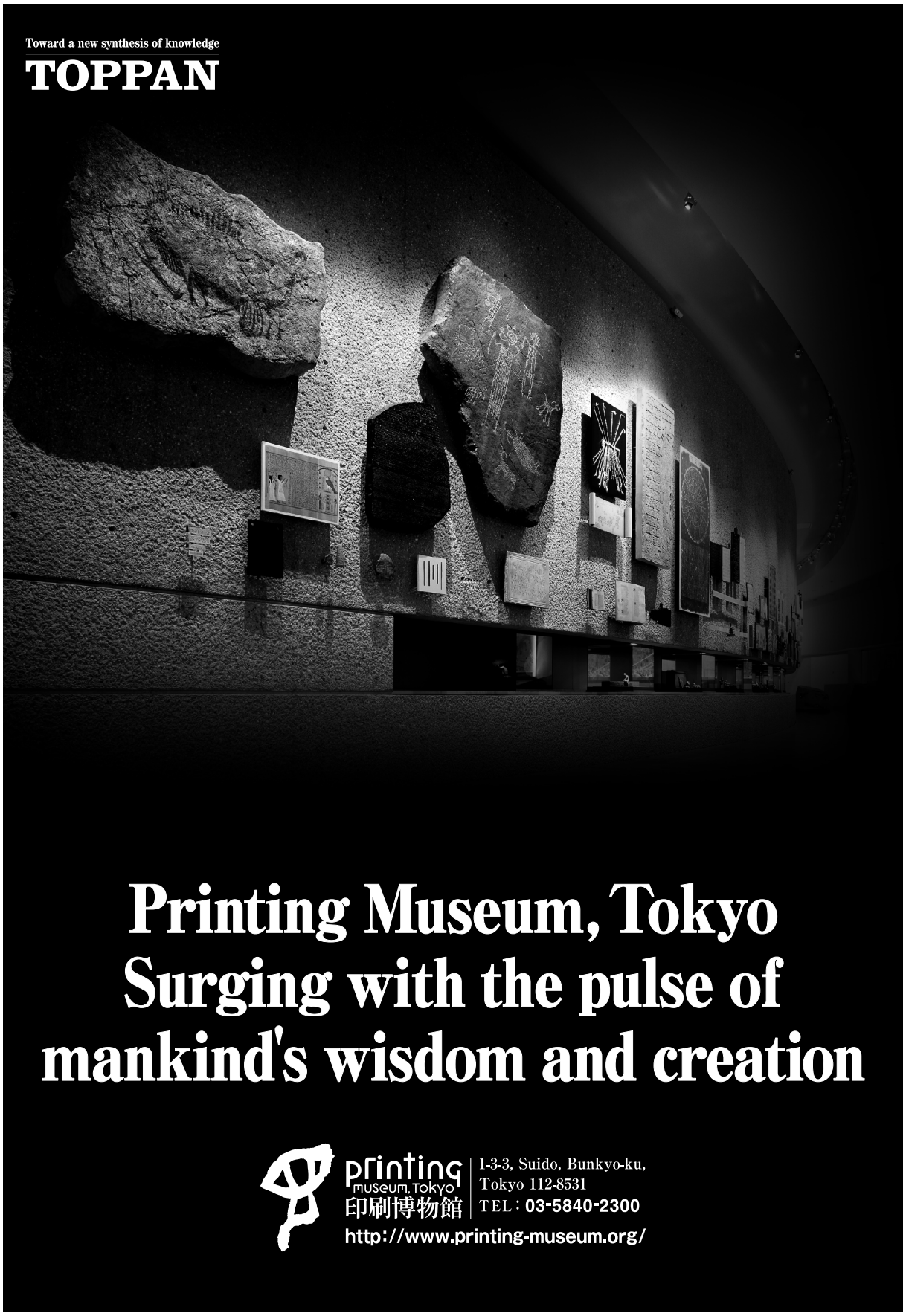
TRAILIGAZ
29-31 Boulevard de la Muette
F 95145 Garges-les-Gonesse Cedex

Tel. 33 (0)1 34 53 45 00
Fax 33 (0)1 34 53 01 96
www.trailigaz.com

VIVENDI water

Toward a new synthesis of knowledge

TOPPAN



Printing Museum, Tokyo
Surging with the pulse of mankind's wisdom and creation

printing museum, Tokyo
印刷博物館

1-3-3, Suido, Bunkyo-ku,
Tokyo 112-8531
TEL：03-5840-2300
http://www.printing-museum.org/

●ACCESS: 13 minutes walk from Iidabashi Station on the JR Chuo and Sobu lines, or the Yurakucho, Tozai, Nanboku and Ōedo Subway lines. 8 minutes walk from Edogawabashi Station.●HOURS: 10:00-18:00 (last admission 17:30) ●CLOSED: Mondays (unless Monday is a holiday, in which case it will be closed the following day); New Year period; when changing exhibitions (prior notice will be given).●ADMISSION: Adults (including junior high school students) 300 yen; Elementary school students 100 yen

E.C.

Fine Chemicals & Atomosphere Plasma Treatment

E.C.Chemical Co., Ltd.

2-28-3 Kasuganishimachi Hirakata, Osaka, JAPAN

TEL 072-850-1111

FAX 072-858-5652

E-mail : ec-chemi@rd6.so-net.ne.jp

CONTENTS

TOPIC 1:
Fundamental problems of high pressure discharges

L1.1 G. Jouve, A. Goldman, M. Goldman and C. Severac
Electrochemical phenomena at the plane electrodes of point-to-plane air corona gaps operated in glow regimes 3

L1.2 Yu.S. Akishev, A.V. Demyanov, V.B. Karal'nik, A.E. Monich and N.I. Trushkin
AC barrier pin-plane corona: similarities and distinctions to DC positive and negative coronas and dielectric barrier discharge 8

L1.3 H.-E. Wagner, K.V. Kozlov, R. Brandenburg and P. Michel
Experimental study of repetitive electrical breakdown in the barrier discharge in air 13

L1.4 P. Tardiveau and E. Marode
Effects of dielectric droplets on point-to-plane discharge dynamics and spark formation 18

L1.5 N. Gherardi, E. Croquesel, N. Naudé, P. Veis and F. Massines
Two different origins for the destabilization of a glow dielectric barrier discharge in nitrogen 23

L1.6 R. Brandenburg, K.V. Kozlov, N. Gherardi, P. Michel, C. Khampan, H.-E. Wagner and F. Massines
Spatio-temporally resolved spectroscopic diagnostics of the atmospheric pressure glow discharge in nitrogen 28

L1.7 E.M. van Veldhuizen, W.R. Rutgers and U. Ebert
Positive and negative pulsed corona in argon 33

L1.8 Y.-H. Kim, W.S. Kang, S.H. Hong and Y.-H. Song
Comparative study of pulsed corona and dielectric barrier discharges using single-streamer modeling and NO decomposition experiment 38

L1.9 M.V. Kozlov, M.V. Sokolova, A.G. Temnikov, V.V. Timatkov and I.P. Vereshchagin
Surface discharge characteristics for different types of applied voltage and different dielectric materials 43

P1.1 Yu.B. Golubovskii, V.A. Maiorov, J. Behnke and J.F. Behnke
Influence of elementary processes over an homogeneous barrier discharge in helium 48

P1.2 Yu.B. Golubovskii, V.A. Maiorov, J. Behnke and J.F. Behnke.
Townsend and glow modes of an homogeneous barrier discharge in helium 53

P1.3 A. Ignatkov, A. Schwabedissen, G.F. Leu and J. Engemann
Studies of the atmospheric pressure jet matrix plasma source: electrical properties and discharge stability 58
P1.4 D. Trunec, R. Brandenburg, P. Michel, D. Pasedag, H.-E. Wagner and Z. Navratil
Spatio-temporally resolved emission spectroscopy of the atmospheric pressure glow discharge in neon 63
P1.5 P. Slavíček, A. Brablec, M. Klíma , V. Kapička, J.F. Behnke and M. Šícha
Comparison of the barrier - torch discharge and torch discharge at atmospheric pressure 68
P1.6 N.B. Anikin, N.K. Bibinov, M. Šira and K. Wiesemann
Silent discharges in helium and helium – nitrogen mixtures 73
P1.7 J. Mizeraczyk, J. Podliński, M. Dors, M. Kocik, T. Ohkubo, S. Kanazawa and J.S. Chang
Electrohydrodynamic transport of ozone in a corona radical shower non-thermal plasma reactor 78
P1.8 T. Plank, M. Aints and A. Haljaste
Initiation probability of burst pulses 83
P1.9 Yu.I. Chutov, W.J. Goedheer, O.Yu. Kravchenko, O.A. Lavrov, T.E. Lisitchenko and G.I. Protas
Dusty RF discharges 88
P1.10 M.S. Baranchuk, T.E. Lisitchenko and M.M. Okholin
Statistical properties of electric breakdowns between glass surfaces in inert gases and their mixtures 93

TOPIC 2:
Modeling and diagnostics

L2.1 Yu.S. Akishev, I.V. Kochetov, A.I. Loboiko and A.P. Napartovich
3-dimensional model for Trichel pulses: results of numerical studies for air 99
L2.2 J.M. Park, Y.-H. Kim and S.H. Hong
Three-dimensional numerical simulations on the streamer propagation characteristics of pulsed corona discharge in a wire-cylinder reactor 104
L2.3 W.S. Kang, Y.-H. Kim, S.H. Hong and Y.-H. Song
Numerical modeling on recurrence of microdischarges in dielectric barrier discharge 109
L2.4 K.V. Kozlov, N.S. Boksha, A.M. Morozov and V.G. Samoilovich
Plasma diagnostics by cross-correlation spectroscopy in investigations of chemical activity of negative corona in air at atmospheric pressure 114
L2.5 A. Fateev, I.P. Vinogradov and A. Lunk
Dynamics of the gas temperature in dielectric barrier discharge in He/N_2 mixtures 119

L2.6 I. Radu, R. Bartnikas, G. Czeremuszkin and M.R. Wertheimer
Diagnostics of dielectric barrier discharges at atmospheric pressure in noble gases 124
P2.1 M. Madani, A. Bogaerts, R. Gijbels and D. Vangeneugden
Modelling of a dielectric barrier glow discharge at atmospheric pressure in nitrogen 130
P2.2 V. Repän, M. Laan and T. Plank
Electric field modelling for point-plane gap 134
P2.3 M. Magureanu, M. Heintze and M. Kettlitz
OES investigations of a pulsed microwave plasma used for methane conversion to C_2 hydrocarbons 139
P2.4 H. Nowakowska, J. Stańco, M. Dors and J. Mizeraczyk
Modeling of plasma chemistry in a corona streamer pulse series in air 144
P2.5 S. Baba, S. Satoh and C. Yamabe
Development of measurement equipment of ozone half life 148
P2.6 V.I. Gibalov, T. Murata and G.J. Pietsch
Parameters of barrier discharges in coplanar arrangements 153

TOPIC 3:
Molecular synthesis and decomposition

L3.1 J. Janča, M. Eliáš and V. Brožek
Low temperature reduction of tungsten precursors in RF discharge plasma reactors 161
L3.2 B. Pietruszka and M. Heintze
Plasma-promoted partial oxidation of methane to syngas over α-alumina supported nickel catalyst in dielectric-barrier discharge 166
L3.3 M. Dhainaut, E. Odic, M. Goldman, A. Goldman and C. Karimi
Dependence of the oxidation properties of a dielectric barrier discharge in air on the plasma and gas temperatures 171
P3.1 J.-M. Cormier, I. Rusu and M. Dudemaine
On a new magnetic blow out glidarc reactor 176
P3.2 K. Krawczyk, J. Ruszniak, J. Sentek and K. Schmidt-Szałowski
Acetylene from methane by gliding arc processing 181
P3.3 K. Krawczyk and M. Wieczorkowski
Studies of nitrous oxide conversion in gliding arc discharges 186
P3.4 A. Opalska, T. Opalinska, J. Polaczek and P. Ochman
Plasma-induced decomposition of chlorodifluoromethane 191
P3.5 T. Kappes, W. Schiene and T. Hammer
Energy balance of a dielectric barrier discharge reactor for hydrocarbon steam reforming 196
P3.6 M. Heintze and M. Magureanu
Efficient methane conversion to acetylene in a microwave plasma 201

P3.7 M. Miclea, K. Kunze, J. Franzke, F. Leis, K. Niemax, C. Penache, O. Hohn, S. Schössler, T. Jahnke, A. Bräuning-Demian and H. Schmidt – Böcking
Decomposition of halogenated molecules in a micro-structured electrode glow discharge at atmospheric pressure 206

TOPIC 4:
Ozone generation and applications

L4.1 S. Kaneda, M. Shimosaki, N. Hayashi, S. Ihara, S. Satoh and C. Yamabe
Ozone production by an atmospheric pulsed discharge with pre-ionization electrodes and partly covered electrode 213

L4.2 K. Yasuoka, Y. Endo and S. Ishii
Experimental study on ozone generation using DC driven micro-plasma 217

L4.3 R. Peyrous
Possibility of improvement of ozone production by using the back-corona effect 222

L4.4 A.B. Saveliev and G.J. Pietsch
On the structure of dielectric barrier surface discharges 229

L4.5 G.J. Pietsch and C. Humpert
Discharge mechanism and ozone generation by surface discharges depending on polarity 234

L4.6 J. Ozonek, K. Jahołkowski, I. Pollo and S. Okazaki
Operation conditions in an ozonizer containing a wire packing 239

P4.1 Y. Miyake, Y. Ehara, H. Kishida and T. Ito
Generation of ozonized water by surface discharge 244

P4.2 H. D. Stryczewska and T. Janowski
Reactive power of the ozone generators 249

P4.3 T. Opalinska
Cold plasma reactor with dielectric barrier discharge 254

P4.4 L. Hulka and G. J. Pietsch
On the ignition voltage and structure of coplanar barrier discharges 259

P4.5 T. Horinouchi, T. Hayashi and N. Nakajima
Development of a new type ozoniser with rotating electrode 264

P4.6 S. Jodzis
Application of surface discharges in electroplasma ozone synthesis 269

TOPIC 5:
Generation of radiation in high pressure discharges

L5.1 A. Treshchalov, A. Lissovski and E. Chikeev
Spectroscopic diagnostics of high-current discharges in UV-VUV excimer lasers 277

P5.1 M. Aints, A. Haljaste and L. Roots
Photoionizing radiation of positive corona in moist air 282
P5.2 M. Laan and J. Raud
HF capillary discharge: distribution of radiation along electrodes 286
P5.3 A. Treshchalov, E. Jalviste, A. Smerechuk, G. Gerasimov, R. Hallin and A. Arnesen
VUV emission of Kr_2 molecules under high-current sliding discharge excitation 291
P5.4 A. Khacef, J.M. Cormier, J.M. Pouvesle, O. Gorce, H. Jurado, C. Thomas, G. Djéga-Mariadassou, S. Calvo and Y. Lendresse
Plasma-catalyst system for NO_x remediation in simulated lean exhaust 296

TOPIC 6:
Environmental applications

L6.1 M. Kogoma, T. Abe and K. Tanaka
PFCs abatement system by the atmospheric pressure glow plasma 303
L6.2 D. Moussa, H. Vitrac, B.G. Chéron, E. Hnatiuc, A. Addou and J.L. Brisset
Acidity control of the oxidation reactions induced by non-thermal plasma treatment of aqueous effluents in pollutant abatement processes 308
L6.3 A.T. Appleton, P. Lukes, W.C. Finney and B.R. Locke
Study of the effectiveness of different hybrid pulsed corona reactors in degrading aqueous pollutants 313
L6.4 S.A. Nair, A.J.M. Pemen, K. Yan, E.J.M. van Heesch, K.J. Ptasinski and A.A.H. Drinkenburg
Chemical processes during biogas conditioning by pulsed corona discharges 318
L6.5 R. Rudolph, K.-P. Francke and H. Miessner
Determination of OH radical concentration in dielectric barrier discharges by CO oxidation 323
L6.6 J. Pawłat, C. Yamabe and I. Pollo
Foaming apparatus as oxidants' generator 327
L6.7 Y. Yoshioka and K. Teshima
Calculation of NO_x removal process taking pulse micro-discharge and diffusion of radicals into consideration 332
L6.8 E.A. Filimonova, R.H. Amirov, S.H. Hong, Y.H. Kim and Y.H. Song
Influence of temperature and hydrocarbons on removal of NO_x and SO_2 in a diesel exhaust gas activated by pulsed corona discharge 337
P6.1 R. Vertriest, R. Morent, J. Dewulf, C. Leys and H. Van Langenhove
Removal of trichloroethylene with a DC-excited multi-pin-to-plate plasma source 342

P6.2 G. Penghui, N. Hayashi, S. Ihara, S. Satoh and C. Yamabe
Studies on an AC/DC combination discharge mode for NO_x treatment 347
P6.3 N. Hayashi, K. Yamamoto, S. Ihara, S. Satoh and C. Yamabe
Treatment of fluorocarbon using atmospheric non-thermal plasma produced by streamer corona discharge 351
P6.4 S. Dupré, C. Deniset, A. Goldman, M. Goldman and E. Marode
Main oxidation processes and their relative contributions in the NO removal by a dielectric barrier discharge for air cleaning 355
P6.5 J. Hong, S. Kim, K. Lee, K. Lee, J.J. Choi and Y.-K. Kim
PFC decomposition with atmospheric pressure microwave plasma using resonant and non-resonant structure 360
P6.6 N. Jidenko, M. Petit and J.P. Borra
Volatile organic compounds depollution by dielectric barrier discharge in porous media 364
P6.7 M.J. Kirkpatrick, W.C. Finney and B.R. Locke
Chlorinated organic compound removal by gas phase pulsed streamer corona electrical discharge with reticulated vitreous carbon electrodes 369
P6.8 M. Sahni, W.C. Finney, R.J. Clark, W. Landing and B.R. Locke
Degradation of aqueous phase trichloroethlyene using pulsed corona discharge 374
P6.9 E. Hnatiuc, B. Cheron, B. Hnatiuc, R. Burlica and J.L. Brisset
Cold plasma electrochemical reactor with rotary discharge 379

TOPIC 7:
Surface processing and technology
(cleaning, coating, etching, modification, equipment)

L7.1 O. Goossens, D. Vangeneugden, S. Paulussen and E. Dekempeneer
Physical and chemical properties of atmospheric pressure plasma polymer films 385
L7.2 C. Penache, S. Datta, S. Mukhopadhyay, A. Bräuning-Demian, P. Joshi, O. Hohn, S. Schössler, T. Jahnke and H. Schmidt-Böcking
Large area surface modification induced by parallel operated MSE sustained glow discharges 390
L7.3 S. Vladimirov and K. Ostrikov
Nano- and micro-particles in low-temperature plasmas: occurrence, dynamic processes, and applications 395
P7.1 S. Guimond, I. Radu, G. Czeremuszkin and M.R. Wertheimer
Modification of polyolefins in nitrogen atmospheric pressure glow discharges 400
P7.2 P. Paris, M. Laan and H. Valtna
Laser ablation and aerosol particles 405

P7.3 J.F. Behnke, H. Steffen, A. Sonnenfeld, R. Foest, V. Lebedev and R. Hippler
Surface modification of aluminium by dielectric barrier discharges under atmospheric pressure 410

P7.4 Z. Rzanek-Boroch, K. Schmidt-Szałowski, J. Janowska, K.Dudziński, A. Szymańska and M. Misiak
Thin films obtained by PE-CVD method from hexamethyldisiloxane under atmospheric pressure 415

P7.5 T. Opalinska, B. Ulejczyk, L. Karpiński and K. Schmidt-Szałowski
Deposition of thin films on polycarbonates by pulse dielectric barrier discharge 420

P7.6 P. Sťahel, J. Janča and D.P. Subedi
Surface modification of non-fabricated polypropylene textile in low-temperature plasma at atmospheric pressure 425

P7.7 S. Ono, S. Teii and S. Takayama
Surface treatment of plastic film by using an atmospheric pressure corona torch 431

P7.8 K. Tanaka and M. Kogoma
Deposition of multi-layer films of hexafluoropropene - ethylene composite polymer with jet-type plasma reactor at atmospheric pressure 436

P7.9 A. Goodwin, T. Herbert, S. Leadley and F. Swallow
Atmospheric pressure liquid deposition – a new route to high performance coatings 441

Index 447

TOPIC 4:

Ozone generation and applications

OZONE PRODUCTION BY AN ATMOSPHERIC PULSED DISCHARGE WITH PRE-IONIZATION ELECTRODES AND PARTLY COVERED ELECTRODE

S. Kaneda, M. Shimosaki, N. Hayashi, S. Ihara, S. Satoh and C. Yamabe

Department of Electrical and Electronic Engineering,
School of Science and Engineering, Saga University
1 Honjo-mach, Saga, 840-8502, JAPAN

Abstract. In this Paper, results on ozone production by atmospheric pulsed discharge, are reported. In our research, two types of ozonizer (Type I and Type II) have been used to investigate improvements of ozone concentration and production efficiency. The ozonizer has plane-to-plane metal electrodes structure, and pre-ionization electrodes are placed on the high voltage electrodes (Type I). In Type II, the surface of grounded electrode with 20mm of width is covered partly by dielectric (thin rubber) with 11mm of width, while the geometry of both metal electrodes is same to Type I. In the case of Type I, maximum concentration of about 100ppm and maximum yield of 70 g/kWh were obtained at input power of 0.3 W. On the other hands, in the case of Type II, 800ppm and 100 g/kWh were obtained at input power of 1.5 W. It was found that the ozone concentration and production yield were improved by using electrode covered by dielectric.

1. INTRODUCTION

Ozone is one of the strongest oxidants and this property makes it a potent germicide as well as a strong bleaching agent. As the result, ozone is employed for the treatment of wasted water, treatment of offensive odors, disinfections and the removal of organic substance [1]. To generate ozone the discharge plasma methods such as silent discharge, surface discharge and positive streamer corona discharge have been introduced to obtain the higher efficiency and higher ozone concentration.

Atmospheric pulsed discharge has been used for efficient ozone production, and the experimental results have already been reported [2,3]. In this research, the double discharge method was employed to obtain a homogeneous pulsed discharge. This method consists of two discharges, i.e., a pre-discharge (pre-ionization) and a main discharge with short pulse duration. In previous experiments [2,3], plane-to-plane metal electrodes have been used for formation of the main discharge. However this configuration has problem that the discharge power and volume are limited by occurrence of arc discharge.

In order to revise the problem, the electrode covered by dielectric was proposed. As the results, the discharge power and volume was increased, and the ozone concentration and generation yield were improved. In this paper, the experimental results of ozone generation using pulsed discharge with pre-ionization are explained. And the improvement of ozone generation yield using the electrode partly covered by dielectric is described.

2. EXPERIMENTAL APPARAUS AND METHOD

The equivalent electrical circuit for ozone generation using the pulsed discharge with pre-ionization is shown in Fig. 1. And the configurations and dimensions of electrodes are shown in Fig. 2. The electrical system consists of trigger spark gap for triggering of circuit, ceramic type capacitor C_1, C_2 and electrodes for discharge formation. The ceramic type capacitors C_1, C_2 with capacitance of 200 pF in respective are charged at a certain high voltage. The length of the anode A and cathode K are 160 mm and 150 mm, respectively. The cathode K has grooves on its surface and copper wire

enclosed in glass tube as electrode for pre-ionization are settled in the grooves.

The circuit operation is as follows. The trigger spark gap is turned on by external pulsed high voltage after the capacitors C_1, C_2 are charged. After that the corona discharge (i.e., pre-ionization) occurs in the space between the outside surfaces of the glass tubes, which enclose the copper wire, and the cathode K. The main discharge takes place after occurrence of the pre-ionization.

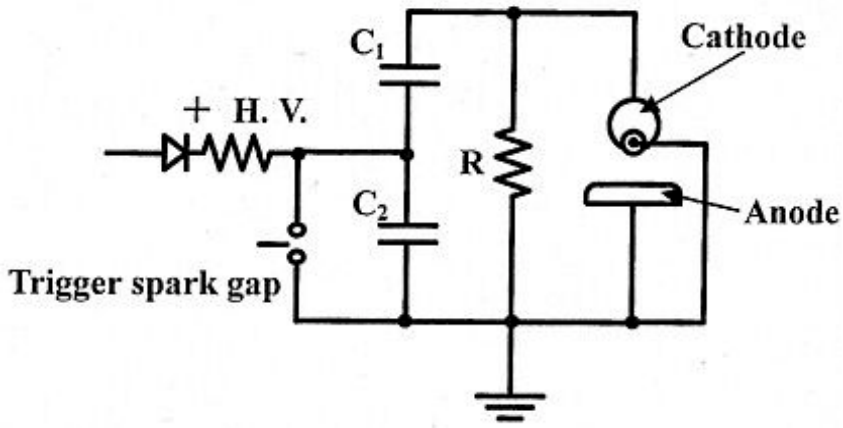


FIGURE 1. Equivalent electrical circuit for ozone generation using the pulsed discharge with pre-ionization.

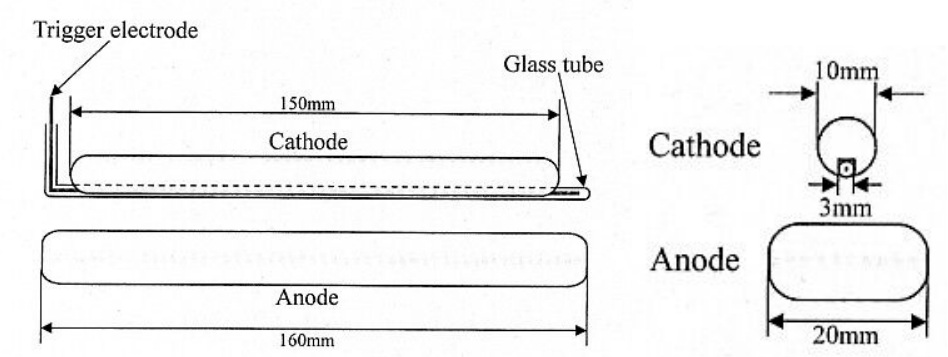
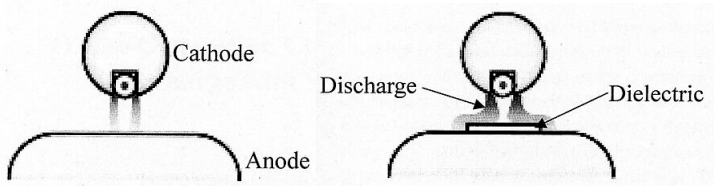


FIGURE 2. Configurations of electrodes.

The typical examples of discharge formations using electrodes with and without dielectric are illustrated in Fig. 3. Covering the electrode by dielectric can increase the discharge volume. In this experiments thin rubber was used as a dielectric, the characteristics of ozone generation was obtained for different widths of rubber.

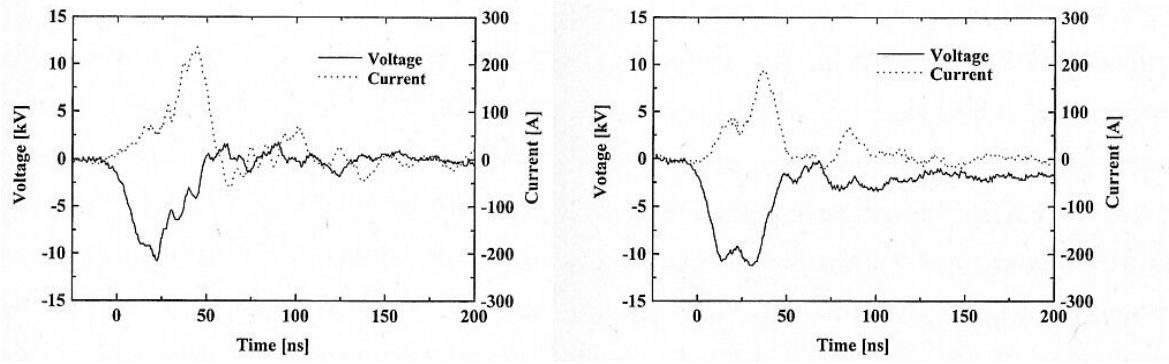


(a) without dielectric **(b) with dielectric**

FIGURE 3. Examples of discharge formation in cases of using electrodes with and without dielectric.

3. EXPERIMENTAL RESULTS AND DISCUSSIONS

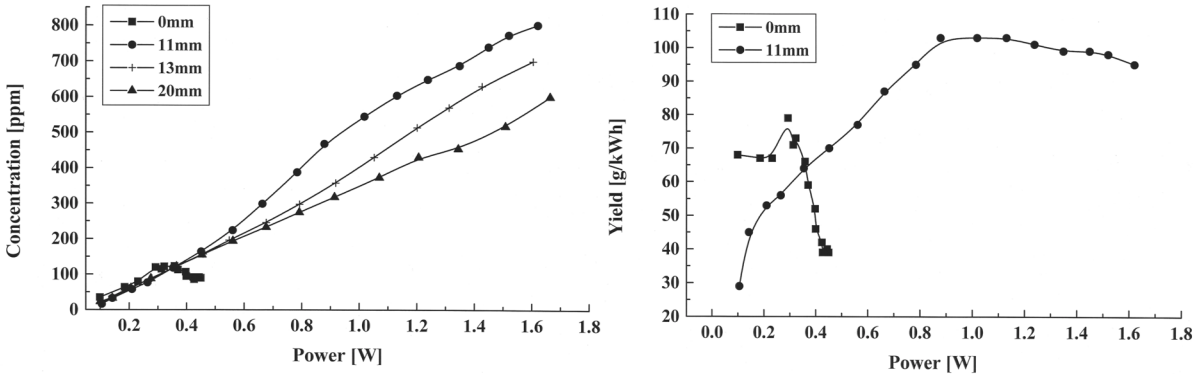
The typical waveforms of voltage across the main electrodes and main discharge current at the same charging voltage are shown in Fig. 4(a) and (b). Although the maximum voltage is about –11 kV in both cases, the maximum current are 230 A and 180 A for the electrode without and with dielectric, respectively. At the maximum current, the voltage is -3 kV, -8 kV for the electrode without and with dielectric, respectively. Thus the values of maximum discharge power are 0.7 MW and 1.4 MW, respectively. It is found that the maximum power increases by a factor of about 2 when the electrode is covered by dielectric.



(a) without dielectric **(b) with dielectric**

FIGURE 4. Waveforms of voltage across the main electrodes and main discharge current.

Figure 5(a) and (b) show the characteristics of ozone generation, concentration and yield for different widths of dielectrics. In these results the width of 0 mm means that the electrode was not covered, and the width of 20 mm means that electrode was covered entirely. In the case of 0 mm width, the maximum concentration of about 100 ppm and maximum yield of 70 g/kWh were obtained at input power of 0.3 W. In this case arc discharge occurred above 0.5 W. On the other hands, in the case of 11 mm, the homogeneous discharge was obtained up to 1.6 W, and 800 ppm and 100 g/kWh were obtained at input power of 1.5 W. It was found that the ozone concentration and production yield were improved using electrode partly covered by dielectric.



(a) Concentration **(b) Yield**

FIGURE 5. Characteristics of ozone generation.

4. CONCLUSION

The experiments of ozone production by atmospheric pulsed discharge are carried out using electrode partly covered by dielectric. In the case of electrode without dielectric, maximum concentration of about 100 ppm and maximum yield of 70 g/kWh were obtained at input power of 0.3 W. On the other hands, in the case of electrode covered by dielectric with width of 11 mm, 800 ppm and 100 g/kWh were obtained at input power of 1.5 W. It was found that the ozone concentration and production yield were improved by using partly covered electrode.

REFERENCES

[1] U. Kogelschatz , *Advanced Ozone Generation*, Plenum Press, New York, 1988, p. 87

[2] K. Hakiai, N. Taniguchi, S. Ihara, S. Satoh and C. Yamabe, Characteristics of Ozone Generation with Glow Discharge Using a Double Discharge Method, Proc. 13th Ozone World Congress, Kyoto, 1997, C2-2-4, pp.859-864.

[3] K. Hakiai, D. Takazaki, S. Ihara, S. Satoh and C. Yamabe, Spatial Distribution and Characteristics of Ozone Generation with Glow Discharge using a Double Discharge Method, Jpn. J. Appl. Phys., Vol.38, No. 1A, pp. 221-224.

EXPERIMENTAL STUDY ON OZONE GENERATION USING DC DRIVEN MICRO- PLASMA

Koichi Yasuoka, Yasunobu Endo and Shozo Ishii

Department of electrical and electronic engineering,
Tokyo Institute of Technology, 2-12-1 Meguro-ku Ookayama, Japan, 152-8552.

Abstract: A new type of ozone generator using a micro hollow cathode discharge has been developed. The electrode system consists of two thin metal cathodes and a ceramic spacer with center holes of a few100 mm diameter. The ozone generation efficiency increases up to 45 g/kWh at the ozone concentration of 7.6 g/Nm^3 without any cooling systems by feeding high- pressure oxygen. In this ozone generating system, the ozone decomposition mechanisms such as electron impacts and the heat rise of oxygen gas are effectively removed by decreasing the gas-residence time in the discharge space.

1. INTRODUCTION

The dielectric barrier discharge is widely used for ozone generation in air-fed and oxygen-fed ozone generators. Recently, high ozone concentration of 300 g/Nm^3 with the efficiency of 55 g/kWh was reported by using an extremely narrow gap discharge in an oxygen-fed ozone generator [1]. It is explained that high concentration is achieved by two effects such as the effective cooling of discharge space and the reduction in the population density of low energy electrons that has a large cross section of ozone decomposition. Another type of ozone generator that had coplanar electrodes with narrow gaps showed high concentration of over 300 g/Nm^3 in oxygen [2]. The narrow gap seems to be crucial to generate high concentration of ozone molecules.

In barrier discharge- type of ozone generators, the generation and decomposition of ozone occur simultaneously in a same discharge space. Therefore, another way of improving the efficiency is to separate these spaces [3]. Reference 4 points out the time lag of micro- second from the oxygen dissociation by electron impacts to the ozone formation in a discharge space. So the separation would be possible by using a small discharge space to reduce the interaction time between the material gas and the discharge. Recently, a micro- hollow cathode discharge with small diameter of less than 1 mm has been developed to produce stable plasmas at atmospheric pressure [5]. This plasma has notable features, such as high current density, high electron energy, stable operation in high- pressure gases. Theses characteristics are effective to produce a compact and efficient ozone generator because of separating the oxygen dissociation space from the ozone formation space. In this paper, we report a new ozone generation system using high- pressure micro- plasmas driven by a direct-current source to realize a compact and efficient ozone generator.

2. OZONE GENERATING SYSTEM USING MICRO- HOLLOW CATHODE DISCHARGE

The schematic diagram of ozone generation system is shown in Fig.1. The electrode assembly for the high-pressure micro discharge is essentially a concentric arrangement of the alumina- spacer sandwiched by two thin electrodes of molybdenum. Oxygen gas flows through the center holes of the electrodes, one of which is connected to high voltage DC source through ballast resistors. The inlet gas pressure of oxygen is changed from 1.5 to 3 atm. The flow rate of oxygen can be controlled by a mass flow controller but is influenced by the hole- diameter of electrode. The residence time is estimated to be the order of micro- second by changing both the hole- diameter of 100~400 μm and thickness of the

yasuoka@ee.titech.ac.jp

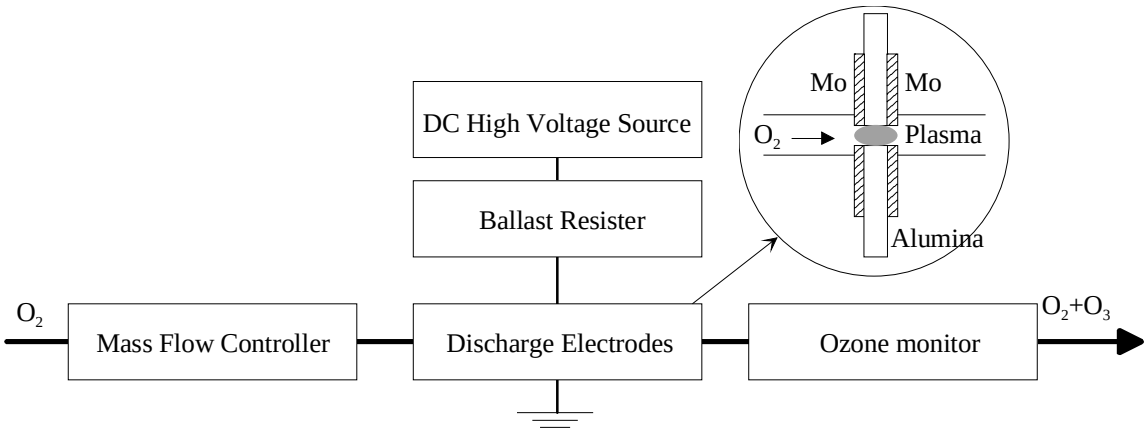


FIGURE 1. Ozone generation system with micro hollow electrodes shown inside the circle.

alumina-spacer from 300 to ~500 μm. The pressure at the outlet is atmospheric and no cooling system for the discharge space is used.

3. DISCHARGE AND OZONE GENERATING CHARACTERISTICS

The ozone generation characteristics are examined by changing the discharge parameters such as electrode hole diameter, spacer thickness, discharge current, gas flow- rate and pressure. The voltage and power relations with discharge current are shown in Fig. 2 with the electrode system of 200 μm diameter. The thickness of alumina spacer is 500 μm. The pressure at inlet is 1.5 atm. The discharge voltage that indicates the sustaining voltage of micro- discharge decreases with increasing the discharge current. The discharge is unstable under 5 mA so that the data is not obtained at low current region. The discharge power increases almost linearly with the current.

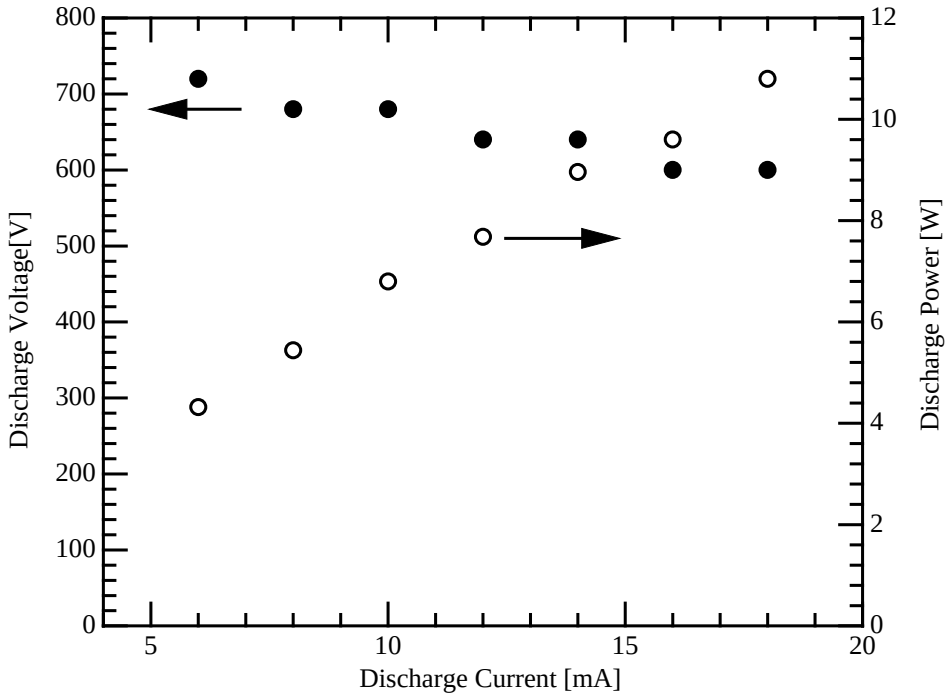


FIGURE 2. Plots of discharge voltage and power versus discharge current with the hole- diameter of 200 μm and spacer- thickness of 500 μm.

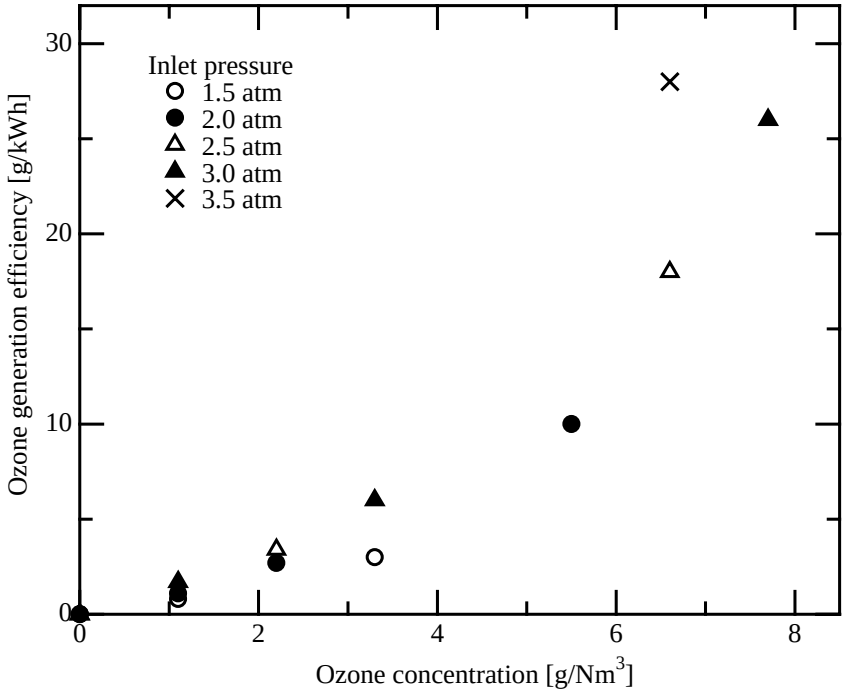


FIGURE 3. Ozone generation efficiency versus ozone concentration at different inlet gas pressure.

Figure 3 shows the ozone generation efficiency as a function of ozone concentration for different pressure of oxygen at inlet of discharge space. The characteristics of the efficiency as a function of the concentration are very different from the characteristics of a barrier discharge ozone generator where the efficiency shows the maximum value at low ozone concentration. This is because in the micro-hollow discharge, the discharge area changes with the discharge current which has a suitable value for filling the discharge space depending on the pressure and flow rate of gas. At small current values, the discharge space is not filled by plasma, so the part of oxygen passes through the hole without interacting the discharge. Similarly, the efficiency and the concentration of ozone is low with the electrode of large hole- diameter of 400 μm. The efficiency is also low with very small hole of 100 μm because the current and power density seems to be too high for ozone generation. Therefore, the characteristics of ozone generation are affected by many discharge parameters such as discharge current, hole- diameter, spacer- thickness, pressure and flow rate.

The ozone generation efficiency, however, has an obvious relation with the gas- residence time in the discharge space as shown in Fig.4 with the electrode hole diameter of 300 μm and the spacer thickness of 400 μm. The gas- residence time: t_r is estimated by the following equation, where V is the volume of discharge space and Q is the flow late of the oxygen.

$$t_r = \frac{60 \times 10^3 \times V}{Q}$$

The maximum efficiency of 45 g/kWh at ozone concentration of 7.6 g/Nm^3 is obtained when the residence time is 2.3 μsec where the suppression of the ozone decomposition and effective heat removing can be occurred. This tendency is slightly affected by the discharge current in the range of 10 mA~30 mA. The maximum efficiency was obtained with the current of 26 mA. The power density corresponding to the current of 26 mA is 200 kW/cm^3. The optimum power density for both efficiency and concentration of ozone increased to 450 kw/cm^3 with 200 μm diameter. The heat generated in the discharge space can be removed by heat conduction through the electrode. The removal of heat in a small hole is more easy than that in a large hole, so the optimum efficiency is high with the small hole.

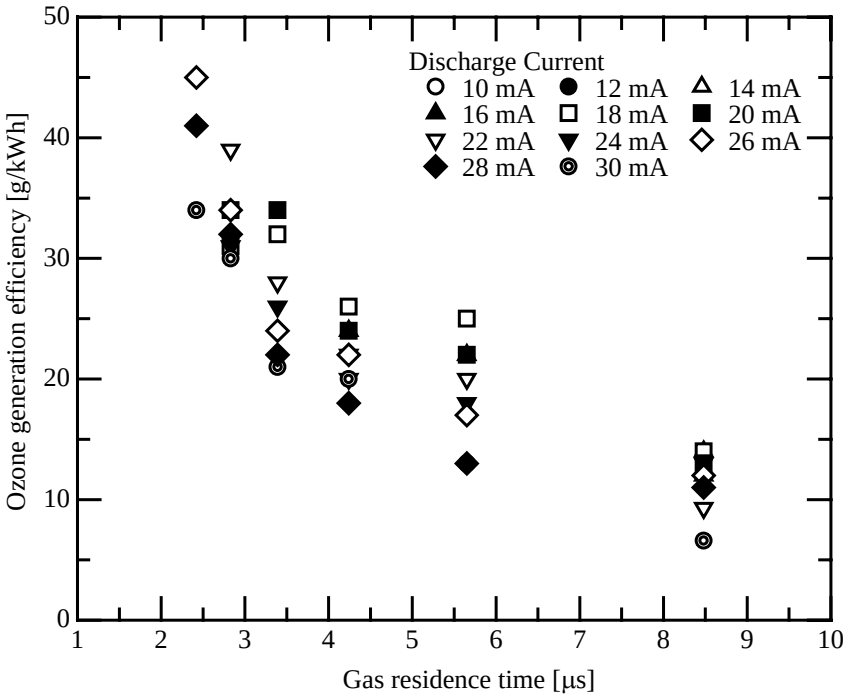


FIGURE 4. Dependence of the ozone concentration on the gas residence- time within the discharge space for different discharge current.

The average power density for the various types of discharges for ozone generation is summarized in Fig.5. The barrier discharge consists of many micro discharges, one of that is shown at the right hand side of the figure. Using a pulsed power voltage source, high power density of discharge is obtained ,

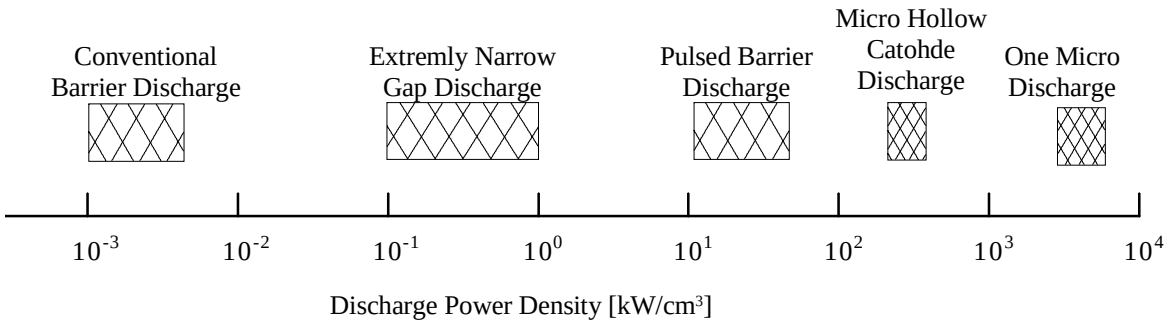


FIGURE 5. Comparison of the average discharge power densities for different types of discharge.

however, the continuous operation is difficult [6]. The power density in the micro- hollow cathode discharge is smaller than that of one micro- discharge but about 10000 times as large as that of the conventional barrier discharge. Therefore, by using of micro-hollow cathode discharge, one can make a compact ozone generation system.

4. CONCLUSIONS

The compact ozone system is proposed and evaluated by using a micro- hollow cathode discharge with gas flow of oxygen. The generation efficiency and concentration of ozone gas depend on the electrode hole- diameter and the thickness of the alumina spacer. The maxim value of 45 g/kWh at 7.6 g/Nm^3 is obtained with 300 μm hole- diameter without any cooling systems. The gas residence time in the discharge space is a crucial parameter to accomplish efficient operation of this system because the ozone molecules are not dissociated and effective cooling of gas is expected when the residence time is less than a few micro- second. From these results, we can expect of improving ozone generation efficiency comparing with that of the conventional ozone system and making a compact and cost effective system by using the micro hollow cathode discharge.

Part of this work has been supported by the Grant-in-Aid for Exploratory Research of JSPS.

REFERENCES

[1] Kitayama J. and Kuzumoto M., *J.Phys. D:Appl. Phys.*, **30**, 2453-2461 (1997)
[2] Okita Y., Noguchi M. and Murata T., Procc Int. Conf. on Phenomena in Ionized gases, **4**, 29-31 (2001)
[3] Tabata N., Tanaka M., *Proc. 13th Ozone World Congress*, **2**, pp.833-840 (1997)
[4] Eliasson B., *IEEE. Trans. Plasma. Science*, **19**, 6 (1991)
[5] Schoenbach K. H., *Plasma Sources Sci. Technol*., **6**, 468-477 (1997)
[6] Endo E., Suzuki K., Aoki T., Yasuoka K., Ishii S., *Proc. Int. Conf. on Phenomena in Ionized gases*, **4**, 157-158 (2001)

POSSIBILITY OF IMPROVEMENT OF OZONE PRODUCTION BY USING THE BACK-CORONA EFFECT

R. Peyrous[a]

a) Université de PAU & Pays de l'Adour, CURS, Laboratoire L.E.G.P., Avenue de l'Université, 64000 PAU (FRANCE)

Abstract : Previous works dealing with electro-filter problems and experimental results in point-to-plane or wire-to-cylinder systems indicate that the presence of a thin layer of porous dielectric material on the electrodes increases the current for the same applied potential. This leads generally to a lower sparking potential.

This so called **Back Corona effect** depends on the polarity of the active electrode, nature, thickness and porosity of the insulating layer and of its position on the active or passive electrode. With a dielectric porous layer on the grounded electrode the current may be many times higher than its "normal" value (clean electrodes) for which the potential applied can be lowered by 30%.

Then it appears possible to increase the yield of ozone production, for the same running conditions (gas flow, electrical circuit, etc.), in a DC negative wire-to-cylinder system where the ozone concentration depends quasi directly on the discharge current.

1. INTRODUCTION

Some previous works [1,2] dealing with electrofilter problems, indicate that the presence of a thin layer of porous dielectric material on the electrodes increases the current inside the precipitator system for a given applied potential. This current increase leads generally to a lowering of the sparking potential, which appears to depend on the dielectric layer thickness. This particular so called **Back-Corona effect**, generally considered as detrimental in electrostatic precipitators [3], led me to verify these statements with a view to increase **OZONE** production.

Some experimental results, in wire-to-cylinder [3-4] or point-to-plane systems [2, 5-9], show that the behaviour depends on the polarity of the active electrode, on the nature, thickness and porosity of the insulating layer and its position on the active or passive electrode. In a point-to-plane or wire-to-cylinder system, whatever the polarisation of the stressed electrode, with a dielectric porous layer on the grounded electrode, above a threshold potential, the current may be many times higher than its "normal" value with clean electrodes before the transition to arc.

Already in 1958 [3] it was noted that "…in cleaning air for ventilating purposes … the **OZONE** generated may be many times that of the normal discharge.", and "...with a thin layer of dust the corona current tended to be above normal.". Numerous results have shown that Ozone concentration depends quasi directly on the discharge current, in a wire-to-cylinder system, with a DC negative voltage applied to the wire [10]. Then it appears possible to increase the ozone production by covering the inner wall of the cylinder with a porous dielectric layer and, at the same time, the yield of ozone production for the same running conditions (reactor geometry, gas flow, electrical circuit). Back-corona "… operates at lower voltage than the DC streamer corona in the same geometry and for the same electrical circuit…" [7]. For the same current the potential applied can be lowered by about 30% [2, 5- 6, 9].

A few results obtained with various porous layers, presented in the following, confirm this point. A good knowledge of the **Back-Corona effect**, which is already used for the decomposition of

[a] Electronic address : rene.peyrous@univ-pau.fr

hydrocarbon gaseous contaminants [7, 8] and in NOx removal [11], could lead to various industrial applications and more particularly in OZONE production in wire-to-cylinder systems.

2. EXPERIMENTAL SET-UP AND CONDITIONS

From the previous results obtained [3, 5, 6] and remarks noted in the literature [2, 12] we have attempted to determine the various parameters acting on the current increase due to the Back Corona effect. We have taken into account numerous remarks made by various authors [1-4, 7-10, 12], on the role, on the Back Corona effect, of the thickness, resistivity and porosity of the layer deposited on the electrodes. Consequently we have used various dielectric supports (paper, coffee filter paper, nylon fabrics, PTFE film) of which we can measure the thickness, porosity and resistivity values with the aim to define the best conditions to obtain a regular and steady Back-Corona. In a wire-to-cylinder ozonizer the ozone concentration is a quasi linear function of the total mean discharge current [10], so we have attempted to use this fact to improve the ozone production and to transform a so considered detrimental effect in electrofilters into an advantageous one in wire-to-cylinder ozonizers [3, 7-8].

Firstly the experiments were made with a point-to-plane device. The conical rhodium point has a 50μm tip curvature radius and the plane, in aluminium or stainless steel, has a 60 mm diameter. The DC HV is applied to the point through a 20 or 50 MΩ HV loading resistor, by using a reversible HV power supply (DEL RHVS). The total mean current is measured at the plane through a 50 Ω resistor (Metrix 56 asycII) and the interelectrode voltage with a HV probe (Fluke 87).

Numerous results were obtained by varying:

- the polarity of the DC HV applied to the point, positive or negative,
- the point- to- plane distance : 7 mm or 10 mm,
- the nature of the dielectric porous layer deposited on the plane : printing paper, filter paper, nylon fabrics or PTFE film.

We have chosen dielectric layers in the limited thickness range from 0.09mm to 0.3mm considered as permitting to obtain a high current value without lowering of the sparking voltage [1-4, 7-10, 12]. Nylon fabrics and PTFE films have a high resistivity, in the 10^{13}-10^{15} Ω·cm range, higher than the value of 10^{11}-10^{12} Ω·cm generally admitted as the critical value [12]. When ρ_d (resistivity of the dielectric layer) was between ~ $5 \cdot 10^{10}$ and $9 \cdot 10^{10}$ ohm.cm...excessive sparking tended to occur….. But "…when $\rho_d > 10^{12}$ ohm·cm excessive sparking disappears but an abnormal increase in current occurs." [13] , which agrees with the values given in [14]. The resistivities for the classical 80 g white printing paper and paper filter are in the $1 \cdot 10^{11}$-$3 \cdot 10^{12}$ Ω.cm range but nevertheless, from the results obtained, it appears that they induce an important Back Corona effect. In this case the limitation for a possible industrial application is the chemical reactivity with the ozone produced.

To verify the assumptions of Laurent [2] on the role played by the number of holes in the dielectric we have regularly pierced a variable number of holes 200 μm in diameter, as used in [7, 8], through printing papers or PTFE films (thickness e=0.1mm) by using printed circuits with 1.27 mm (1/20'') or 2.54 mm (1/10'') grid steps. So we modify the porosity in a 4-fold ratio. As a general rule, when there is only one hole, at the good place, in the dielectric layer, there is always a Back Corona effect.

The filter paper (e=0.1 mm) have numerous randomly distributed irregularly shaped holes in the 10-100 μm diameter range but essentially lower than 80 μm. Due to their fashioning, nylon fabrics have regular rectangular holes in the 40-80 μm x 40-120 μm range sides and more generally with a dimension of 80 x 80 μm. This was measured by using a two-eyed microscope (Leitz). We have used three types of nylon fabrics in single layer (e=0.09, 0.1 or 0.125 mm) or double layers (e=0.18, 0.23 mm). "The resistivity of most dust and porous material varies with the relative humidity [4]". But hygrometry is without influence on the nylon tissue [1, 2, 9] which is not the case for paper.

The spark-over voltage depends on dust layer thickness for a medium-resistivity dust [12].

3. EXPERIMENTAL RESULTS

Keeping in mind that some interesting results in ozone production were obtained with dry air by using a very simple DC HV wire-to-cylinder system [15, 19], we will only present here the results obtained with Back-Corona in negative polarity. "Negative abnormal corona will not cause the excessively premature breakdown that positive flares will." [3].

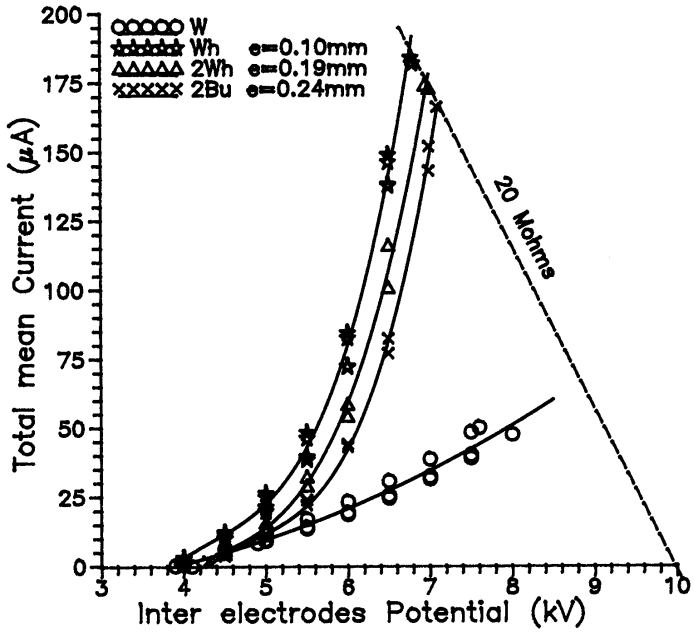


FIGURE 1. Total mean current as a function of the interelectrode negative potential applied to the point.

Gap d=7 mm, Atmospheric Air.

Back-Corona effect: comparison between various dielectrics, nylon fabrics, 1 or 2 layers.

W : without dielectric

Whatever the polarisation, in a point-to-plane system, with a dielectric porous layer on the plane, the current, with back ionisation, before the transition to arc, increases much more rapidly and can be many times higher than with clean electrodes in accordance with [3]. A hysteresis effect of the threshold potential was equally observed, but it is without interest for us. The corona onset voltage is independent of the dust layer thickness, in the 0.09-0.23 mm range, if the critical resistance is in the range of 10^{11}-10^{12} Ω·cm which is the case for the dielectric layers considered.

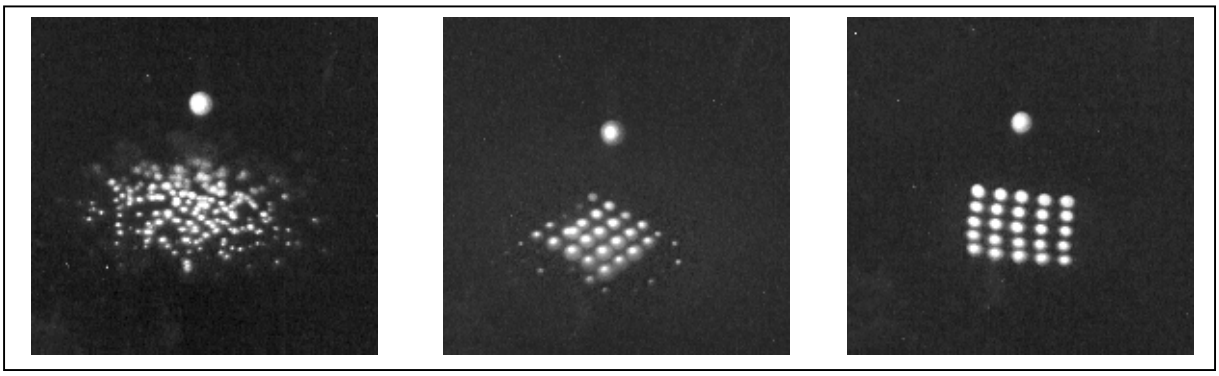
As reported in **Figure 1**, the Back-Corona effect is steadily obtained with all the various dielectric layers used from paper to PTFE film with comparable results. With a printing paper layer we have always a corona discharge when for PTFE film, without hole, we have not a current up to 10kV applied to the 7 mm interelectrode gap. The curves obtained with printing or filter paper are comprised inside the ones for nylon fabrics.

The “normal” current can be five times higher in presence of the dielectric layer for the same interelectrode applied potential. The higher steady current is reached for a 7 mm interelectrode gap and the gap voltage reduced of about 25% (at 35 μA for example) in stable conditions in complete agreement with [1, 6, 7]. These curves can be compared with the Pauthenier' results [9] who noted that : "...for a constant voltage, the appearing of back-corona well corresponds with an increase of the discharge current….(which) may be several times the "normal" current (up to 7 times).” [2, 4 - 9].

The spark-over voltage is not related to the intensity of the back-corona current but to the thickness of the dust layer *(or equivalent)* and its resistivity. This implies that, as previously noted, "there is some **optimum thickness**." [3]. " One of the unexpected characteristics of the thin layers is that even though large total back-corona flow and the back discharge is uniformly distributed over the surface**,** the spark-over is above "normal". However, as the layer thickness increases the spark-over voltage decreases…"[12].

The results presented on the **Figure 1** can lead to a misunderstanding because it could be deduced that the current decreases as a function of the dielectric layer thickness. But…by superposing two layers of nylon fabric we have modified not only the thickness of the layer but equally the number and dimension of the holes. The role played by the number of holes in the dielectric layer on the passive

electrode was approached by piercing holes of 200 μm in diameter regularly separated by using a grid of 1.27 mm or 2.54 mm step. "Each hole, becomes the seat of a flare, the secondary emission is a function of the **number of holes** up to a maximal value." [2].



Back Corona effect photographs :

A : Coffee filter paper, "natural"	**B :** white printing paper, 50 holes	**C :** PTFE film, 25 holes,
Holes in the 10-100μm range	ϕ =200μm on 1.27mm grid	ϕ =200μm on 1.27mm grid
6.8 kV, 175 μA, exp : 0.5s	7.3 kV, 147 μA, exp : 0.25s	7 kV, 160 μA, exp : 0.5s

The **photographs** presented here above are also reported in colours on an inserted sheet. One another was added to complete the information. They can be compared with the ones published by Masuda et al. [13] obtained equally in a point-to-plane geometry. Each hole looks like a glow surrounding a point and we assume that the visible halo all around the holes is contained into a limited area defined by the Warburg law were the ions can be trapped by the dielectric layer. The intensity of the light emission and its wavelength, which depend on the nature of the layer, is decreasing from the discharge axis to the surroundings. The wavelength is essentially blue for the paper filter and nylon fabric (photos **A** and **B**), when the luminosity is quasi identically distributed in the purples tones for the PTFE film (photo **C**). "As the current density is increased some individual discharges stabilise and become the source of significant current and are thus **clearly visible**." [12]. This point needs to be compared with the remarks made in [3], ("…holes (*of the dielectric*) can support flares (*or tuft*) which are produced at the edge of the layer of insulation."), and with the observation made in [7], ("Streamers originate not only from the active electrode (needle) but also from the craters in the dielectric layer.").

This behaviour and observation are also in accordance with the ones on the light emitted from the back-ionising layer made by Cross [14]. The stronger and more stable back-corona discharge points tend to be evenly distributed over the dust layer for uniform current density [12]. This can be applied to an insulating material covering the passive electrode (plate or cylinder) simulating the dust deposit.

With negative corona the flares (*tufts*) are associated with high-resistivity material on the passive electrode [4]. "Increase in ρ_d favours the tendency to the **surface-glow** mode and **space-streamers** are few. In this case many weak points broke down and the current increased readily without excessive sparking."[13]. This is also in accordance with Penney and Craig [5].

The results obtained show clearly that each hole interact with its neighbour and, with PTFE film, it is better to use a 1/10" (2.54 mm) grid step to reach more rapidly the maximum of current for the same potential applied. The number of holes is about 25 to reach 130 μA under 7 kV.

When using a paper layer of lower resistivity than PTFE the grid step does not act particularly but we need equally about 30 holes to reach the same maximal current values which remains constant up to more 50 holes. Consequently the porosity cannot be a valuable criterion because it depends on the number and area of the holes regularly distributed on a determined surface. From the results obtained, holes of about 80 μm in diameter separated by about 300 μm seems to be a reasonable compromise.

4. OZONE PRODUCTION : TEMPORARY CONCLUSION

In some recent papers dealing with ozone production in electrostatic air cleaners (wires-plate system [20]), it is pointed out that "…contamination of the electrodes does not alter corona onset voltage, but reduces sparkover voltage.". "…dusty plates rather than contamined wires cause higher current and OZONE concentration levels." And "…Ozone production with time is due to the formation of BACK CORONA."…" a 3 fold escalation in current is accompanied by a 10 fold increase in ozone."

With the point-to-plane device we have verified some parts of the assertions on the back corona discharge but we cannot obtain a very important and interesting production of ozone. To do comparisons, we need to use a well-known (for us) wire-to-cylinder system, 20 cm long cylinder as previously reported in [16, 17]. We have overlapped the internal surface of the cylinder with a dielectric porous layer (nylon fabric), and plotted the I vs. V curves and the ozone concentration as a function of the total mean current for the two wire-to-cylinder reactors (simple and back-corona).

In the range of 0-600 μA current the increase in ozone concentration for the same current and gas flow is obvious but… in the case of back-corona, we need to increase the potential applied to the gap. In the 600-1200 μA range the "standard" system appears more efficient. The external wall temperature is also enhanced for the back-corona reactor and this point can explain the decrease in ozone concentration. A cooling fan blowing on the external wall permits to increase the ozone concentration.

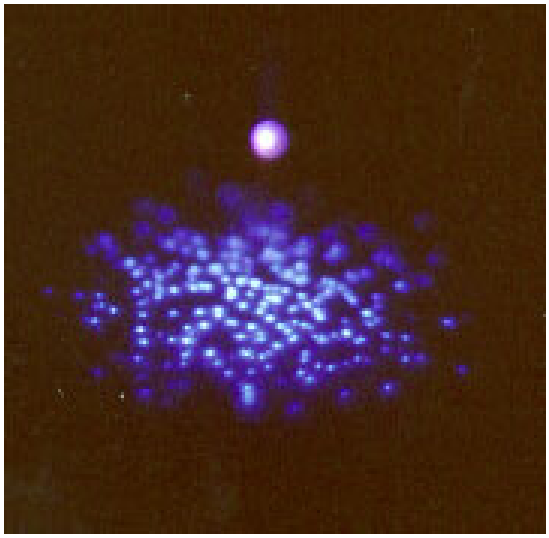
Then it does not appear evident that the back-corona system is powerful than the "standard" wire-to-cylinder one. We cannot simply modify the "standard" wire-to-cylinder reactor to increase efficiently the ozone production. All the parameters need to be reconsidered and optimised. The reactor geometry will also be modified by taking into account the role played by the dielectric porous layer, its structure, mesh, porosity, and nature on the electric field distribution inside the interelectrode gap. Consequently as some years ago an attempt to optimise the back-corona reactor is necessary. The dielectric layer is a new parameter to take into consideration.

AKNOWLEDGEMENTS

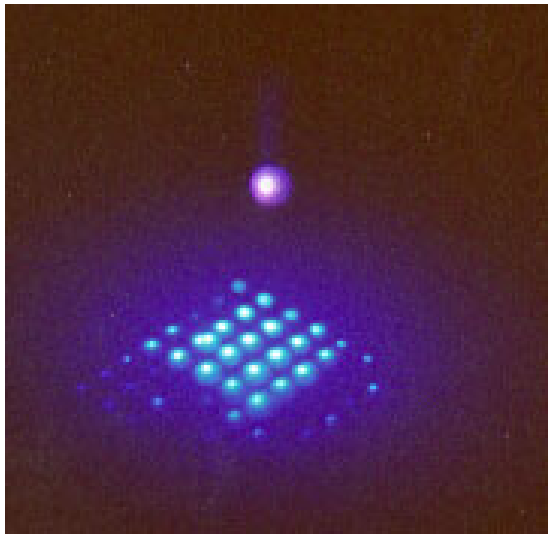
I wish to thank S. Lachaud for the photographs of the lights emitted by the back ionising dielectric layer on the plane.

REFERENCES

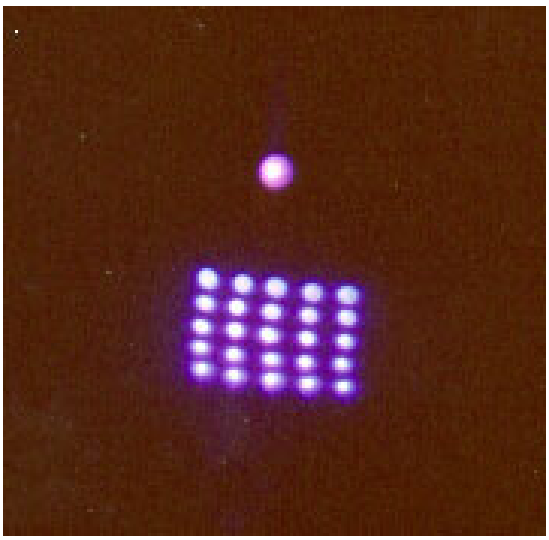
[1] Pauthenier M., Demon L., Laurent E., *C. R. Acad. Sciences*, **222**, p 1219-1220, (1946)
[2] Laurent M. E., *Rev. Gen. Elec*., **57**, p 114-116, (1948)
[3] Penney G. W., Hewitt J. G., *Trans. A.I.E.E*., pt I, **77**, p 319-327, July (1958)
[4] Penney G. W., Craig S. E., *Trans A.I.E.E*., **79**, p 112-118, May (1960)
[5] Rivière R., CNAM Eng. Thesis, Université de Pau, France, (1974)
[6] Peyrous R., CNAM Eng. Thesis, Université de Pau, France, (1974)
[7] Jaworek A., Krupa A., Czech T., *J. Phys. D : Appl. Phys.* , **29**, p 2439-2446, (1996)
[8] Jaworek A., Krupa A., Czech T., *Contrib. Plasma Phys.*, **36**, n° 5, p 619-629, (1996)
[9] Pauthenier M., *Rev. Gen. Elec*., **69**, n° 3, p 175-184, (1960)
[10] Castle G.S.P., Inculet I.I., Burgess K.I., *Trans. IEEE.*, **IGA 5**, n° 4, July-Aug. (1969)
[11] "Ozone News", **28**, n°5, p 9-10, October (2000)
[12] Mc Lean K.J., IEE proceeds., **135**, pt A, n° 6, p 347-361, July (1988)
[13] Masuda S., Mizuno A., *J. of Electrostatics*, **4**, p 35-52, (1977/1978)
[14] Cross J. A., *J. Phys. D : Appl. Phys.*, **18**, p 2463-2471, (1985)
[15] Peyrous R., Lacaze C., *Ozone Sci. & Eng.* , **8**, n° 2, p 107-128, (1986)
[16] Monge C., Peyrous R., Held B., *Ozone Sci. & Eng.* , **19**, n° 6, p 533-547, (1997)
[17], Peyrous R., Monge C., Held B., *Ozone Sci. & Eng.* , **20**, n° 4, p 317-342, (1998)
[18] Held B., Peyrous R., *Eur. Phys. J. AP*, **4**, p 73-86, (1998)
[19] Held B., Peyrous R., *Eur. Phys. J. AP*, **7**, p 151-166, (1999)
[20] Dorsey J.A., Davidson J.H., I.E.E.E. Trans. on Industry Applications, **30**, n° 2, pp 370-376, (1994).



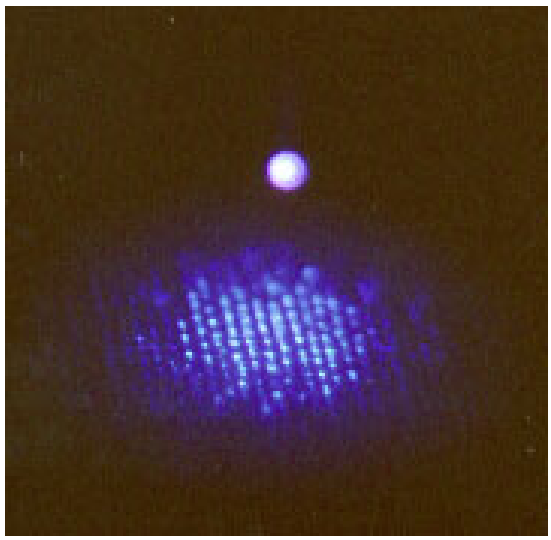
(A)



(B)



(C)



(D)

Back Corona effect photographs :

A : Coffee filter paper, "natural"
Holes in the 10-100µm range
6.8 kV, 175 µA, exp; 0.5s

B : white printing paper, 50 holes
ϕ=200µm on 1.27mm grid
7.3 kV, 147 µA, exp; 0.25s

C : PTFE film, 25 holes,
ϕ=200µm on 1.27mm grid
7 kV, 160 µA, exp; 0.5s

D : Nylon fabric, 80-100µm meshes,
6.5kV, 160 µA, exp; 0.25s

ON THE STRUCTURE OF DIELECTRIC BARRIER SURFACE DISCHARGES

A. B. Saveliev and G. J. Pietsch

Electrical Engineering and Gas Discharge Technology, Aachen University of Technology, 52056 Aachen, GERMANY

Abstract. Pure surface discharges on a dielectric layer are an efficient source for non-thermal plasmas, which can be used for e. g. surface treatment and light sources. The structure of such discharges has been investigated with an intensified CCD camera at pulsed and AC voltage. Independent on polarity a channel structure has been found. Its character depends on polarity and the level of the applied voltage to the surface electrode. The structures can be explained by field distortions resulting from surface charges.

1. INTRODUCTION

Common dielectric barrier discharges (DBDs) appear in arrangements with a gas gap (volume discharge, VD) and consist in general of numerous microdischarges. If AC voltage is applied to an arrangement with e. g. a wire electrode on the surface of a dielectric plate and an extended metallic electrode on the reverse side, surface discharges (SDs) appear. The properties of VDs and SDs differ. While the length of the discharge in VD arrangements is determined by the gas gap, the SDs propagate stepwise on the dielectric surface with rising voltage.

There exist already some information about the structure of SDs by measuring the residual charge density on the dielectric surface after the extinction of the discharge, mainly based on the dust figure method [1]. However, these results refer most often on the application of pulsed voltages and are not representative for normal AC operation.

In the following the discharge structure in dry air at atmospheric pressure is investigated with an intensified CCD camera depending on polarity, voltage amplitude and shape (pulsed and AC voltages).

2. EXPERIMENTAL SET-UP

The structure of the SDs has been examined in an arrangement depicted in Fig. 1. The grounded electrode was transparent by using salted water in between two glass plates. The capacity of a glass plate is 3.8 pF / cm^2, its thickness 2 mm and the relative permittivity ε_r = 8.6. The surface electrode has a diameter of 2 mm. If high voltage is applied to the surface electrode, SDs appear on the glass surface perpendicular to the surface electrode. The structure of the discharge is observed with a CCD-camera together with a quick triggering image amplifier in the visible wavelength range. The voltage is measured with a voltage divider 1:1000 and a digital oscillograph, the current by integrating it in a capacity of 1 µF.

If rising voltage is applied to the surface electrode, first discharge phenomena, a discharge pulse, appears at breakdown voltage. This pulse lasts about 50 to 200 ns [1]. During its activity charge is collected on the glass surface, which causes a counter-field. The discharge extinguishes by the growing counter-field in the above-mentioned time period. The surface charge distribution after the pulse influences the appearance and development of the succeeding discharge pulse.

As the detection of the discharge structure by the dust figure method has some limitations, the residual charge distribution after discharge extinction can be detected only. A sensitive CCD camera (with image amplifier) and exposure times down to the nanosecond range has been used to identify the dis-

charge structure.

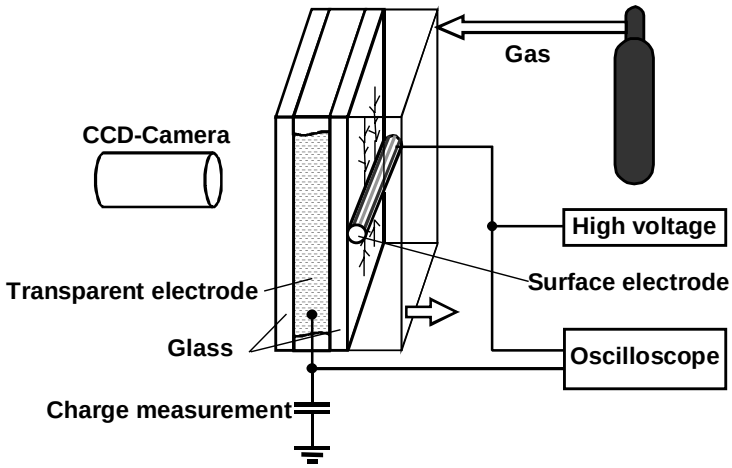


FIGURE 1. Sketch of the experimental set-up.

The discharge was investigated with supply voltages of two kinds, pulsed voltages of both polarities (peak voltage U_p = ± 20 to 25 kV, rising time ~ 150 µs) and voltage oscillation packets (U_p up to ~ 23 kV, frequency ~ 20 kHz, number of oscillations 100 to 300, repetition frequency between packets 0.5 to 10 Hz). Applying oscillation packets to the arrangement it is possible to operate with relative high voltages without overloading the device.

In order to observe the discharge structure and its development on an uncharged surface, it was cleaned with a conductive brush from residual charges before applying pulsed voltages.

3. DISCHARGE STRUCTURE AT PULSED VOLTAGE

In Fig. 2 and 3 photographs of the discharge development at positive and negative polarity at the surface electrode on the dielectric is shown. The exposure time is 10 µs in each case, significant longer than the duration of the discharge pulse (50 to 200 ns) and much shorter than the voltage rise time up to voltage peak (150 µs). The frames do not belong to a single voltage pulse; each picture belongs to a different pulse.

The dark stripe in the frames marks the position of the surface electrode. At both polarities the discharge shows a channel structure in contradiction to the findings in [1]. They propagate mainly perpendicular to the surface electrode. In general the higher the applied voltage the longer the discharge channel.

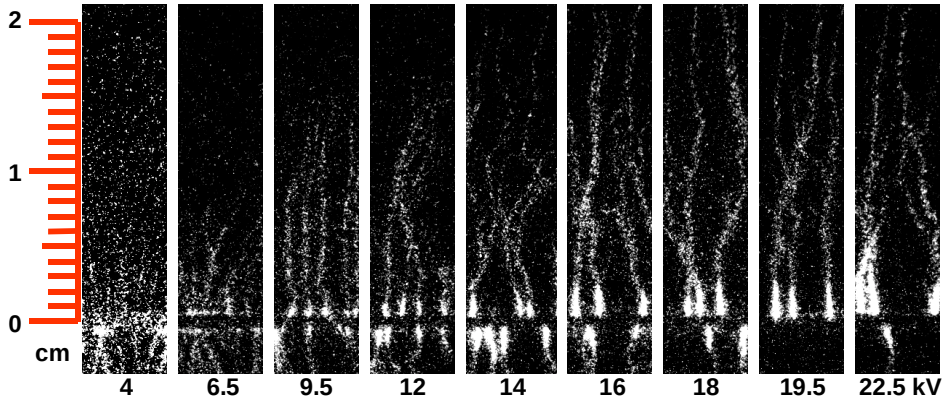


FIGURE 2. Development of the discharge structure at pulsed voltage and positive polarity of the surface electrode (dry air of atmospheric pressure, exposure time of each frame 10 µs).

At positive polarity of the surface electrode (Fig. 2) the discharge channels are rather thin. Their thickness and light intensity do not change significantly in the whole voltage range and in different distances to the electrode (except of the region nearby the electrode). The length of the more intensive radiation region near the electrode rises with voltage as well.

At negative polarity of the surface electrode (Fig. 3) the channels are shorter, much broader, more expanded at their tips and sometimes branching in comparison to the opposite polarity. They are narrow nearby the cathode (surface electrode) and get thicker with distance from the surface electrode. In general the light intensity decreases with the channel length. However, in the higher voltage region (from about 15 to 18 kV) the channel structure changes. Their number decreases and they become much stronger (see – 14 and – 21 kV) discharging a broad area far from the surface electrode (in a distance of more than 8 to 10 mm). If stronger channel appear it happens occasionally that the area nearer to the surface electrode is discharged by shorter channels (see – 17 and – 20 kV).

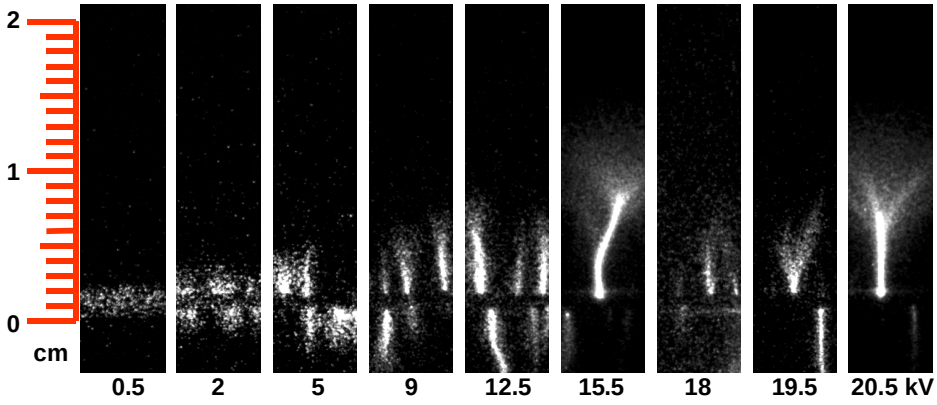


FIGURE 3. Development of the discharge structure at pulsed voltage and negative polarity of the surface electrode (dry air of atmospheric pressure, exposure time of each frame 10 µs).

In Fig. 4 the channel lengths depending on voltage are presented for voltage pulses of both polarities. Up to 15 kV their lengths at positive polarity have twice the value of those at negative polarity. In the upper voltage range a division of the lengths at negative polarity in two parts happens. The longer and stronger channels have lengths nearly comparable with the channels at positive polarity, while the shorter channels are hindered in their propagation by the stronger ones.

The longer channel length the more charge is deposited on the surface resulting in a stronger counterfield, i. e. the residual effective field strength is reduced.

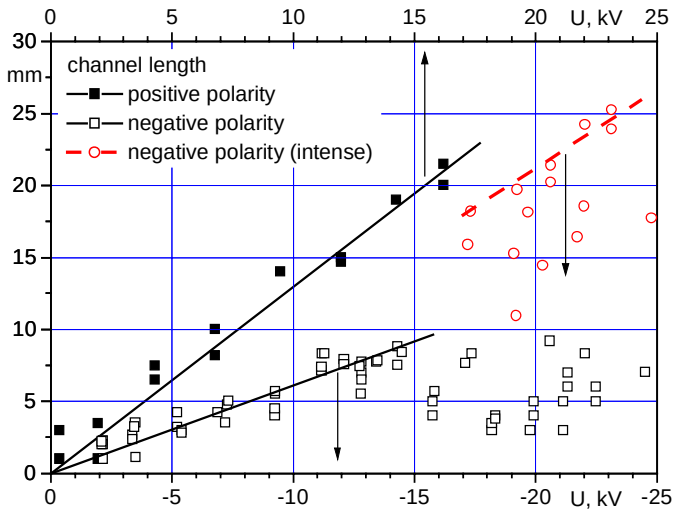


FIGURE 4. Length of the discharge channels depending on the value of the pulsed voltage for both polarities (at the surface electrode).

The mean value of the electrical field strength in the region, which is more or less dense covered by discharges, has a nearly constant value [2]. The value depends on polarity. As the (absolute) mean value of the potential at the tip of this region is much smaller than at the surface electrode (applied potential), it can be approximately estimated from the gradients in Fig. 4. For the negative polarity follows a mean field strength component in parallel to the surface of ~ 1.6 kV/mm and about half the value ~ 750 V/mm for the positive polarity at the surface electrode.

In Fig. 5 the dependence of the charge (per unit electrode length) on voltage for both polarities of voltage pulses is given. As the discharged capacity of the dielectric is proportional to the extension of the discharge area it is proportional to voltage amplitude. And as the charge is furthermore proportional to the capacity times voltage, the charge is proportional to the square of the voltage. This behaviour is confirmed by measurements (Fig. 5). For negative polarity the changing of the discharge structure disturbs this behaviour (for voltages more than 18 kV). According to the different extensions of the discharges on the surface for the voltage polarities, the charge is approximately two times larger for the positive polarity.

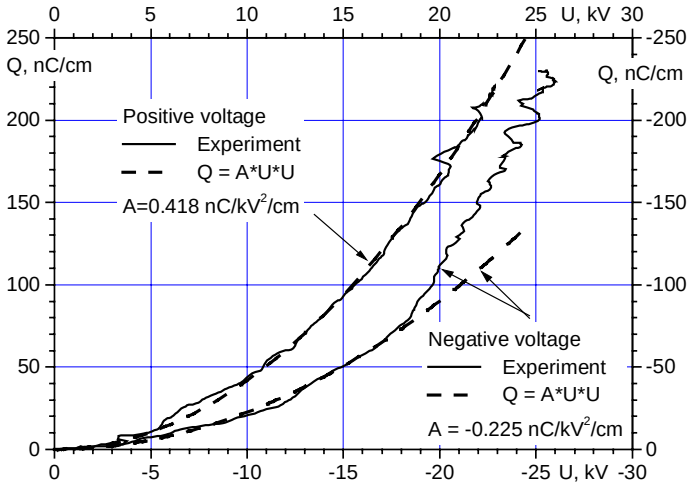


FIGURE 5. Charge-voltage behaviour of SDs in air (charge per unit electrode length, voltage pulses).

4. DISCHARGE STRUCTURE AT AC VOLTAGE

The discharge structure at AC voltage is represented in Fig. 6 and 7. Residual charges on the surface influence the propagation. In Fig. 6 the voltage amplitude is so low that no strong channels appear. For the two left frames the surface electrode is positive with respect to the surface potential, the others belong to the opposite polarity.

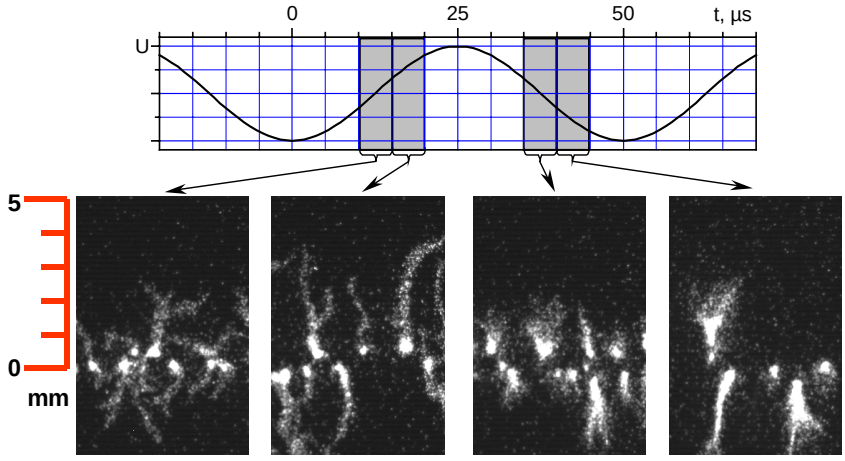


FIGURE 6. Channel structure at AC voltage of low amplitude (7.1 kV, exposure time 5 µs).

With higher voltage amplitude the appearance of strong channels determines the discharges structure (Fig. 7). Because of charges on the surface from preceding discharge activities at AC voltage, strong channels (of both polarities) appear already at voltages of 12 to 14 kV. The number of strong channels is independent on polarity. Their position is almost fixed on the surface because of the charge distribution and local heating effects.

From short-time exposures (up to 20 ns) it is found that at positive polarity most often several channels appear at the same position on the surface one after the other. At negative polarity the strong channels are continuously burning at the same position up to voltage peak. The branching of the strong channels is more homogeneous at negative polarity.

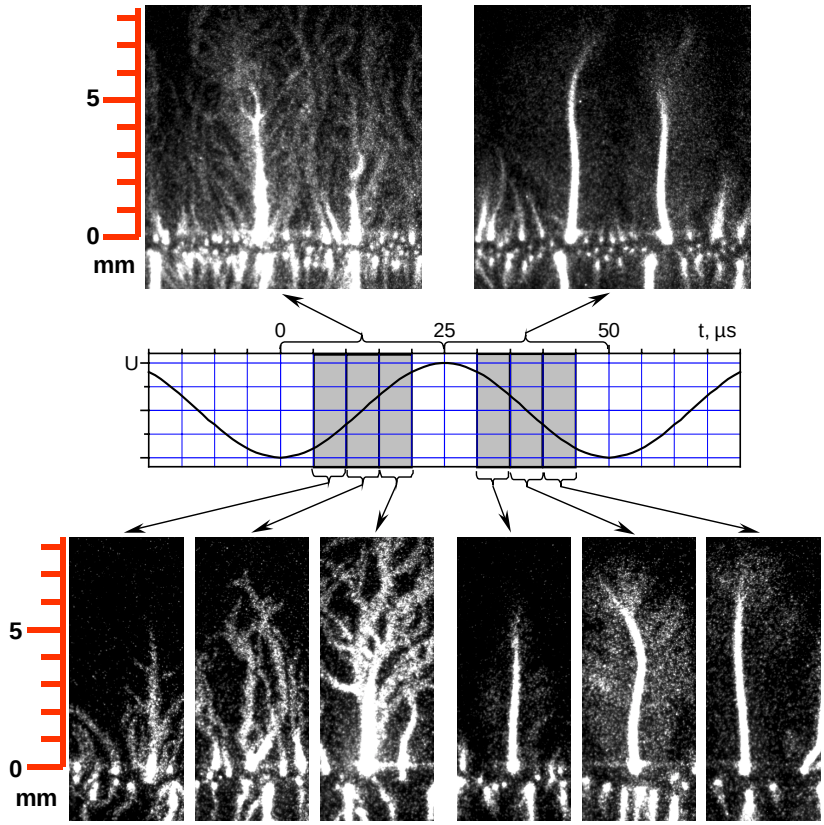


FIGURE 7. Channel structure at AC voltage of high amplitude (23 kV) for exposure times 25 and 5µs.

5. CONCLUSIONS

With the help of high speed and sensitive CCD photographs it has been found out that the discharge structure of SDs consists of channels even at negative polarity of the surface electrode. Furthermore, the character of the channels as well as the optical appearance of the discharge changes at a certain level of the applied voltage at negative polarity.

At AC voltage supply the structure is mainly determined by surface charges from preceding discharge activities. From this results strong discharge channels at both polarities at elevated applied voltages.

REFERENCES

[1] Gibalov V. I., and Pietsch G. J. , *J. Phys. D: Appl. Phys.*, **33** 2618-36 (2000)
[2] Saveliev A. B., Gibalov V. I., Pietsch G. J., and Saenko V. B., Efficiency of ozone synthesis in the surface discharge arrangements. In: *14th Int. Sym. on Plasma Chemistry*, Prague, 1999, pp. 2343-8.

DISCHARGE MECHANISM AND OZONE GENERATION BY SURFACE DISCHARGES DEPENDING ON POLARITY

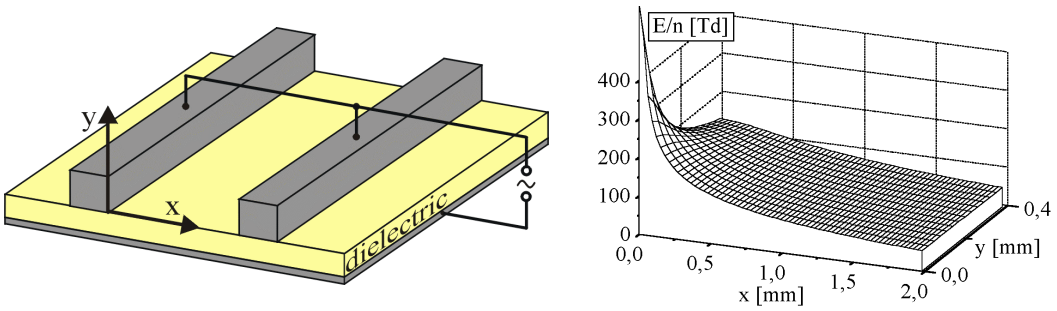
G. J. Pietsch and C. Humpert*

Electrical Engineering and Gas Discharge Technology, Aachen University of Technology
**) now with ABB Calor Emag Mittelspannung GmbH, Oberhausener Str. 33, 40472 Ratingen, Germany*

Abstract. Surface discharges are a special kind of dielectric barrier discharges, which develop in steps on the dielectric surface during increase of the applied voltage. The results of a two-dimensional simulation show that the discharge development at negative polarity is dominated by a cathode-fall mechanism at the metallic surface electrode. At positive polarity a positive streamer develops on the dielectric surface in each discharge step. A cathode fall appears near the streamer head on the dielectric surface. Because of the higher field strength at the tip of the discharge at positive polarity, ozone and nitrogen oxides are produced nearly homogenously in the whole discharge region. At negative polarity ozone and nitrogen oxides are mainly synthesized in the cathode fall region. Altogether an enhanced nitrogen oxide production is observed at positive polarity.

1. INTRODUCTION

Surface discharges (SDs), a kind of dielectric barrier discharges, are observed in arrangements e. g. with small but long high voltage electrodes in parallel (wires, bars, stripes) on one side of a dielectric layer and a plane counter electrode on its reverse side (Fig. 1, left). This arrangement is used like the well-known volume discharge (VD) arrangement with a gas gap in commercial ozone generators.



edge length of the square electrodes	3 mm	thickness of the dielectric	2 mm
distance between adjacent electrodes	12 mm	feed gas	air, 1.0 bar, 293 K
relative permittivity of the dielectric	8.4	applied ac voltage	U_0 = 12 kV, f = 10 kHz

FIGURE 1. Sketch of the SD arrangement (with boundary conditions) and initial field strength distribution near the triple junction line at 4.6 kV.

The development of SDs is determined by the inhomogeneous initial field strength distribution with a maximum at the triple junction line, where the surface electrode, the dielectric and the gas space come together (Fig. 1, right). It is known from experiments [1] as well as simulation [2] that SDs propagate in steps on the dielectric during voltage rise. During each step the accumulation of charge carriers on the dielectric leads to a reduction of the field strength and a decay of the discharge. After voltage rise a next discharge step can occur.

The ozone synthesis in oxygen- and air-fed SD ozone generators has been investigated in detail experimentally [1]. In oxygen the maximum ozone concentration and the efficiency are comparable with those of comparable VD ozone generators. In air ozone production and its efficiency is significant lower in SD arrangements. At higher energy densities a nearly complete destruction of ozone is obtained. The reasons for this behavior may be found in the discharge mechanisms of SDs, which are

different from those of VDs. To clarify this, the discharge development in air and the gas composition following the discharge, especially the ozone concentration, are investigated with the help of a self-consistent two-dimensional model for both polarities of the applied voltage.

2. SIMULATION METHOD

The continuity equations of electrons, positive and negative ions together with the Poisson equation are solved in two dimensions (Fig. 1). In the discharge region, the rate equations of ionization, recombination and attachment are solved in dependence of the local electric field strength. On surfaces, secondary electron emission by photons and positive ions is taken into account. The dielectric surface is defined as an impermeable boundary. All charged particles reaching this boundary are collected on the surface.

To obtain the source terms of the dissociation products and excited particles, the corresponding rate equations of the corresponding electron collision processes are solved in each time step of the simulation, too. Apart from this the most important chemical reactions in air are taken into account to get the spatial resolved production of the plasma-chemical components, especially ozone, in the discharge area. The reaction scheme is based on the data given in [3 to 6]. The temperature in the discharge area is determined from energy densities of electrons and ions and is included in the chemical reaction systems.

3. TEMPORAL AND SPATIAL DEVELOPMENT OF SURFACE DISCHARGES

The simulation is performed continuously during a positive and negative quarter period of the applied voltage. In both polarities three discharge pulses occur, which lead to a stepwise charging of the dielectric surface up to 3.2 mm at negative polarity and 6 mm at positive polarity of the surface electrode. The dependence of discharge extension on polarity is found experimentally as well. The total transferred charge during a quarter period and the charge of individual discharge steps are in good agreement with measurements (Fig. 2). The differences are caused on one hand by measuring errors due to the fast discharge process and on the other hand by the two-dimensional approach of the simulation.

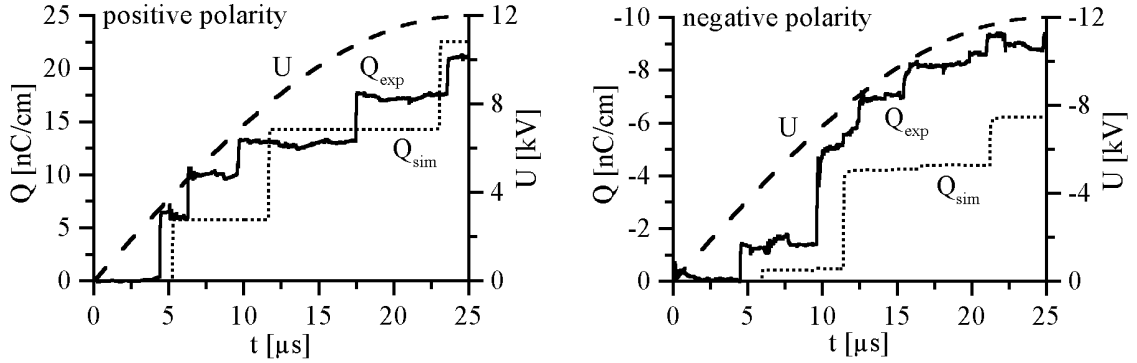


FIGURE 2. Transferred charge from experiment (Q_{exp}) and simulation (Q_{sim}) during a positive and a negative quarter period of the applied voltage.

The mechanisms of the discharge development on the dielectric surface depend on polarity of the applied voltage. At positive polarity of the surface electrode electrons are emitted from the dielectric surface by secondary effects and move towards the metallic surface electrode. In the initial phase of the discharge a maximum of the electron density arises in front of the surface electrode leading to the development of a positive streamer, which moves along the dielectric surface [2]. The streamer channel is nearly neutral resulting in rather low field strength of about 10 Td in the channel (Fig. 3). At the streamer head a positively charged area occurs, which causes maximum field strength of up to 1400 Td (Fig. 3, x = 1.44 mm). The thin positively charged area in front of the channel (Fig. 3, S) is due to the positive streamer mechanism; the broad positively charged area at the dielectric surface

(Fig. 3, C) is due to a cathode fall of 290 V with a thickness of about 12 µm (in y-direction). During the development of the discharge the streamer head and the cathode fall region move along the dielectric surface. Their properties are nearly unchanged till the decay of the discharge step.

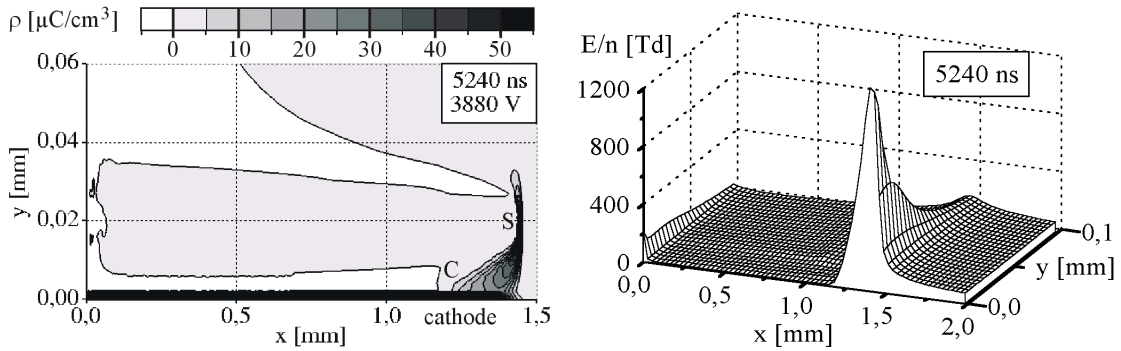


FIGURE 3. Net charge density ρ and distribution of the reduced field strength E/n during the development of the first discharge step at positive polarity.

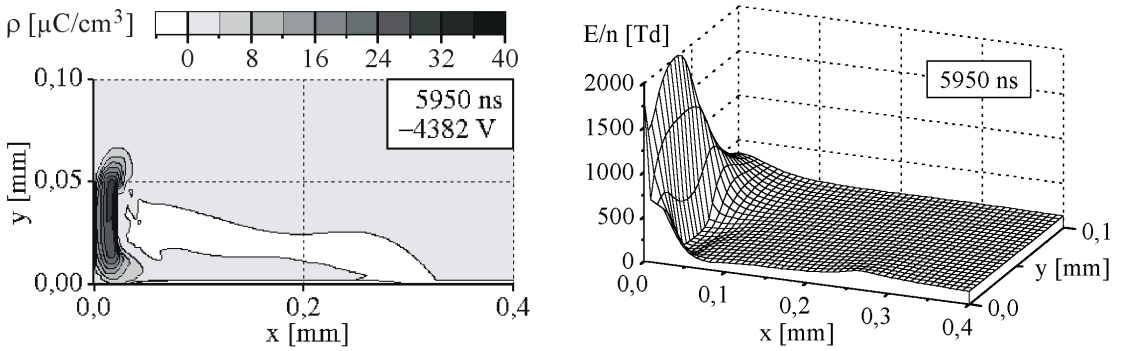


FIGURE 4. Net charge density ρ and distribution of the reduced field strength E/n during the development of the first discharge step at negative polarity at the maximum of the cathode fall.

At negative polarity electrons emitted from the cathode surface by secondary effects move towards the dielectric and are multiplied on their way. In a small distance of about 0.15 mm from the surface electrode the electron density is high enough to initiate an ionization wave, which propagates like a weak cathode-directed streamer towards the cathode [2]. When the ionization wave reaches the cathode, a cathode fall with a maximum value of 550 V establishes at the cathode surface near the triple junction line. The maximum field strength during the cathode fall reaches a value of about 1900 Td; the thickness of the cathode-fall in x-direction is about 15 µm (Fig. 4).

After formation of the cathode fall the discharge spreads out in x-direction. With the tip of the discharge a field strength maximum moves over the dielectric surface (Fig. 4, x = 0.25 mm), which decreases during the discharge development from an initial value of about 210 Td to a value of about 120 Td. Behind this maximum the accumulated charge carriers on the dielectric surface cause a reduction of the field strength to a minimum value of about 75 Td. This discharge development is comparable with the development of a weak streamer.

4. OZONE GENERATION WITH SURFACE DISCHARGES

To reveal the influence of the discharge mechanisms on the production of the plasma-chemical components, the reaction scheme is solved spatially during the discharge phase in the first quarter period of the applied voltage as well as during the following quarter period without discharge. In each discharge step oxygen and nitrogen atoms are produced, which react between and after the discharge steps mainly to ozone and nitrogen oxides (Fig. 5 and 6, left).

Because of the streamer mechanism at positive polarity oxygen molecules are dissociated and ozone is produced nearly homogenously along the dielectric surface in a layer of about 50-µm height (Fig. 5,

right). At negative polarity the main ozone concentration can be found in the cathode region and near the triple junction line to a distance of x = 0.3 mm on the dielectric. This is due to the relative low field strength at the tip of the surface discharge at negative polarity.

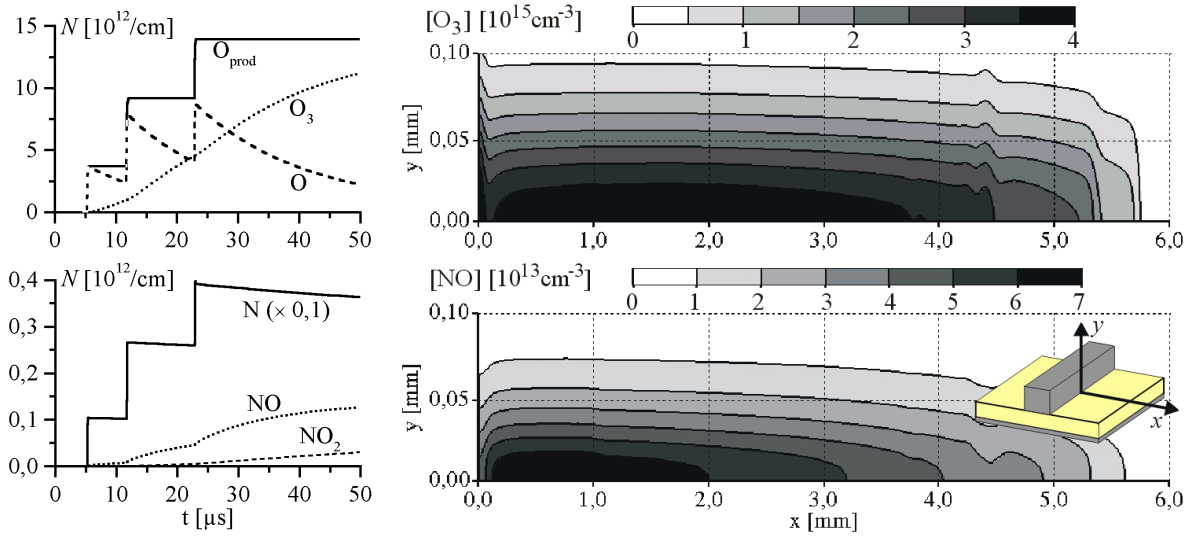


FIGURE 5. Temporal development of the total number of the most important plasma-chemical components (O_{prod} is the sum of all produced oxygen atoms, the number of N-atoms is divided by 10) and distributions of O_3 and NO at 50 µs at positive polarity.

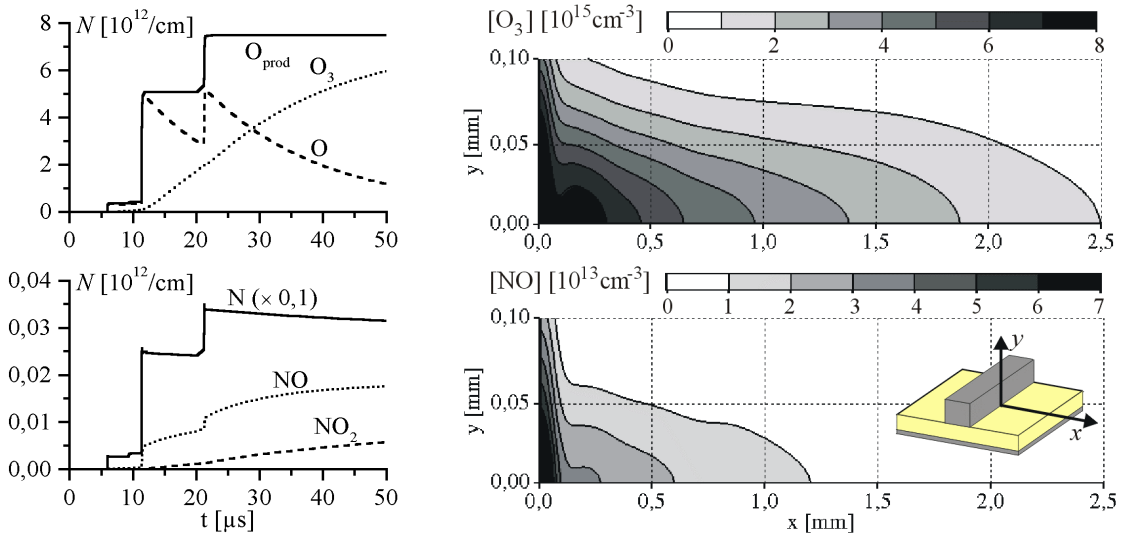


FIGURE 6. Temporal development of the total number of the most important plasma-chemical components (O_{prod} is the sum of all produced oxygen atoms, the number of N-atoms is divided by 10) and distributions of O_3 and NO at 50 µs at negative polarity.

Related to the amount of oxygen atoms the total amount of produced nitrogen atoms is about five times higher at positive polarity compared with the negative polarity (Fig. 5 and 6, left). Assuming that the complete energy density of the charged particles is converted into heat and considering the heat conductivity of the gas, the metallic surface electrodes and the dielectric, a maximum temperature increase of about 80 K near the metallic surface electrode is found after the third discharge step at both polarities (Fig. 7). This leads to a significant production of nitrogen oxides, especially of NO. As a result at positive polarity roughly one NO molecule can be found per hundred O_3 molecules after 50 µs (Fig. 5, left). At negative polarity this relation is only one per four hundred (Fig. 6, left).

The high nitrogen atom and nitrogen oxide concentration at positive polarity is caused by the high field strength at the head of the positive streamer, which leads to an increased dissociation of nitrogen and production of nitrogen oxides nearly in the whole discharge area (Fig. 5, right). At negative polarity nitrogen is dissociated and nitrogen oxides are produced only in the cathode fall region (Fig. 6,

right), because the dissociation energy of nitrogen is significant higher than that of oxygen.

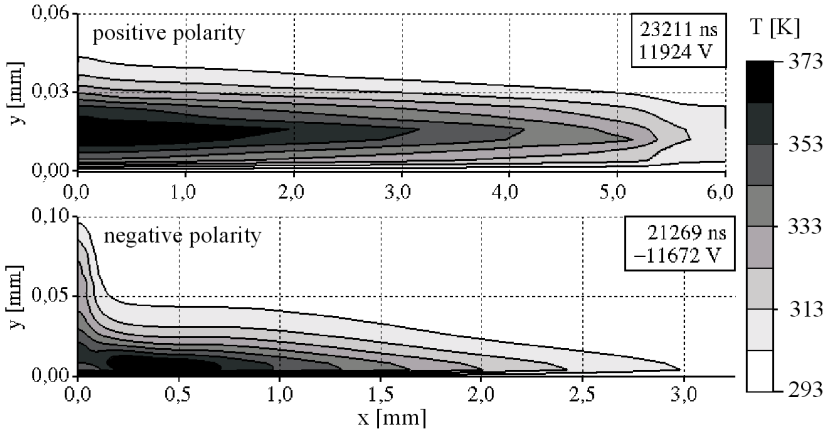


FIGURE 7. Temperature distribution after the third discharge step at positive and negative polarity.

5. CONCLUSIONS

Both polarities of the voltage applied to a SD arrangement have been simulated up to voltage peak. With respect to ozone generation the simulation results reveal that different discharge mechanisms have influence on the results. Because of the high field strength at the streamer head with positive polarity more nitrogen oxides are produced as with negative. Nevertheless the calculated efficiency of the ozone production is nearly the same at both polarities. With a value of about 56 g(O_3)/kWh it is comparable high, because destruction processes of ozone are negligible at this early stage of the discharge. Considering a multitude of succeeding cycles of the applied voltage the nitrogen oxides may be accumulated in the discharge region resulting in an effective destruction of ozone and oxygen atoms in catalytic reaction chains. Additionally, the results of the plasma-chemical simulation show that ozone is mainly synthesized directly at the dielectric and metallic surface of the discharge arrangement. Ozone molecules can be destroyed by collisions with surfaces. To avoid the accumulation of nitrogen oxides in the discharge region and the ozone destruction at surfaces optimized gas conduction is necessary, which leads to an effective mixture of the process gas.

Apart from this local over-temperatures of up to 80 K are found at both polarities especially near the surface electrodes. Succeeding discharge pulses and cycles of the applied voltage stress them. As the surface electrodes are cooled only indirectly over the dielectric barrier, it is expected, that the temperature of the surface electrodes increase during this stress. This may be avoided by a direct cooling of the surface electrodes.

REFERENCES

[1] Pietsch, G. J., Haacke, M., Parameters Influencing the Yield of Surface Discharge Ozone Generators, In: *Proc. 14th Ozone World Congress*, Michigan, 1999, vol. 1, pp. 311-323

[2] Humpert, C., Pietsch, G. J., Modelling Results of the Discharge Development and the Energy Density of Barrier Discharges on Dielectric Surfaces, In: *Proc. 15th Int. Sym. Plasma Chem. (ISPC-15)*, Orleans, France, 2001, pp. 1485-1490

[3] Eliasson, B., Kogelschatz, U., Basic Data for Modelling of Electrical Discharges in Gases: Oxygen, *Brown Boveri Research Report* KLR 86-11 C (1986)

[4] Kossyi, I. A., Kostinsky, A. Yu., Matveyev, A. A., Silakov, V. P., Kinetic Scheme of the Non-Equilibrium Discharge in Nitrogen-Oxygen Mixtures, *Plasma Sources Science and Technology*, **1**, 207-220 (1992)

[5] Lowke, J. J., Morrow, R., Theoretical Analysis of Removal of Oxides of Sulfor and Nitrogen in Pulsed Operation of Electrostatic Precipitators, *IEEE Transactions on Plasma Science*, **23**, 661-671 (1995)

[6] Guerra, V., Pinheiro, M. J., Gordiets, B. F., Loureiro, J. Ferreira, C. M., Calculated Data on Electron Transport and Excitation Rate Coefficients in N_2-O_2 and N_2-H_2 Discharges, *Plasma Sources Science and Technology*, **6**, 220-230 (1997)

OPERATION CONDITIONS IN AN OZONIZER CONTAINING A WIRE PACKING

Janusz Ozonek[a], Krzysztof Jahołkowski[b], Iwo Pollo[c,a] Satiko Okazaki[d]

a) Department of Chemical Technology, Lublin Technical University
b) Department of Electrical Machines, Lublin Technical University
c) Private University of Environmental Protection, Radom, Poland
d) Sophia University, Kioi-cho 7-l,Chiyoda-ku, Tokyo 102-8554, Japan

Abstract. Investigations into an ozone generation process in an ozonizer containing a copper wire packing in the discharge zone are presented. Electrical characteristics of such discharges have been analyzed and energy dependences that are characteristic for the ozone synthesis process in an ozonizer with a conducting packing have been determined.

1. INTRODUCTION

An increasing number of ozone applications, especially within the environment protection technologies (water treatment, sewage treatment, preventing the emission of noxious substances into the atmosphere) causes a significant growth of interest in the possibility of designing an ozone synthesis apparatus that could ensure an increase of an ozone production yield and an energy efficiency enhancement of within the ozone synthesis process.

Among a number of propositions elaborated in various research centers attempts to apply so called "mixed" discharges seem to be dominating and these are for example surface or silent discharges as well as electrical discharges coupled with other methods of creating advantageous conditions of ozone synthesis like the application of ultraviolet radiation. Some research teams have attempted to introduce a solid packing to the discharge zone that performs a role of a catalyst. Both non-conducting [1] and conducting kinds of a packing [2] have been tried and a one first applied by S. Okazaki in 1988 presently meets a growing interest. The presented work is based on experiments on the course of ozone synthesis in the mentioned kind of an apparatus [3,4]. Particular attention has been paid to the obtained ozone concentrations, and energy efficiency of the process.

Properties of the experimental apparatus with a wire packing designed by the authors have been analyzed in the course of the experiments.

2. EXPERIMENTAL SET-UP

A diagram of the experimental setup is shown in the Fig. 1. The electrical feeding system has been adapted to feed an ozonizer with a voltage of up to 15 kV and frequency of 50 Hz. The electrical measurement system is composed of a kilovoltmeter of the C-96 type, a measuring probe Tetronix P6015A, an oscilloscope Tetronix model TDS3012B, and a meter to measure a current intensity. The analytical system has been set to a continuous measurement of ozone concentration by means of a photometric method (at λ= 253.6 nm) with the application of an ozone analizer BMT 964.

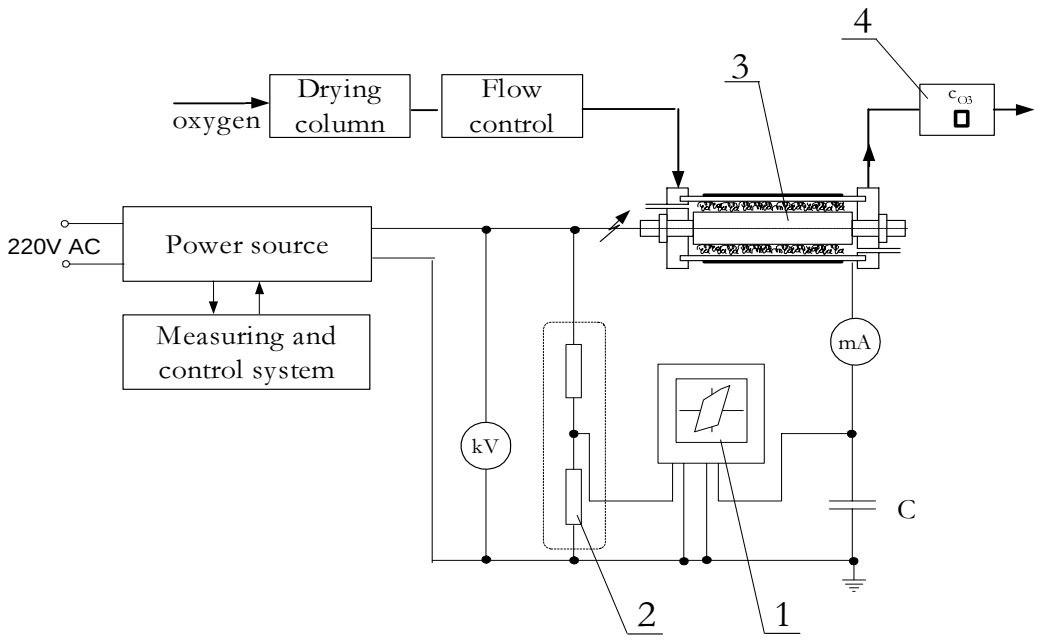


Fig. 1. The experimental setup
1- oscilloscope, 2- voltage divider, 3- ozonizer, 4- ozone concentration measurement

Tests performed to assess a conducting packing effect on the ozone synthesis process efficiency have been done with the application of an ozonizer whose diagram is presented in Fig.2. An essential element of the ozone generator is a packing made of a copper wire coil of the 1.2 mm diameter placed in the discharge zone. The tests have been performed with an ozonizer of the discharge gap size of d=6.0 mm.

In the course of the performed tests feeding voltage of the ozonizer and a current passing through the discharge gap have been measured. Active power supplied to the discharge zone has been determined from the surface area of an adequate Lissajous figure whose area is proportional to the active power absorbed by the ozonizer. The gas flow has been varied within the range of 20 - 200 Ndm^3/h. Measurements have been carried out at the temperature of the electrode liquid coolant of 18^oC.

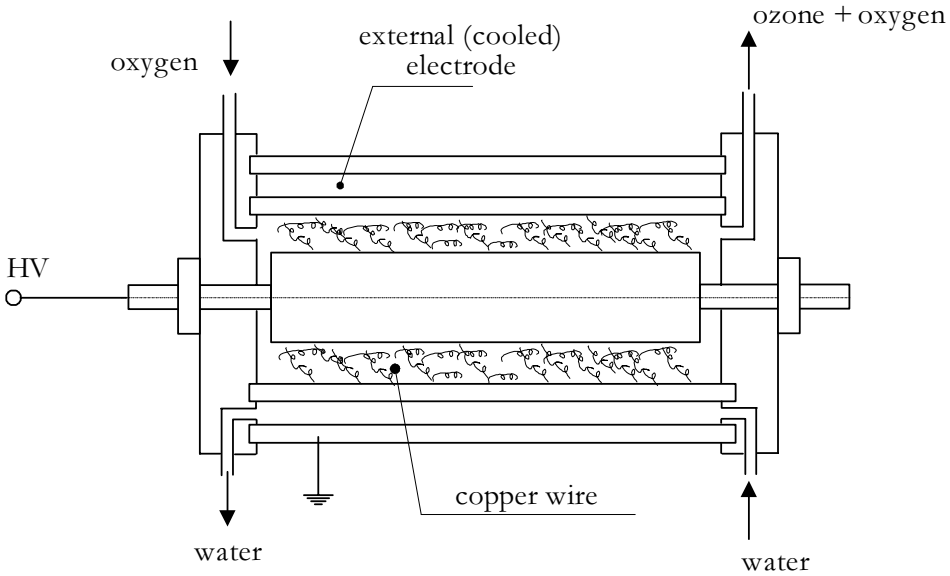


Fig. 2. An ozonizer with a wire packing

3. RESULTS AND DISCUSSION

The knowledge of electrical characteristics of an ozonizer makes possible to evaluate it as an electrical energy receiver that converts electrical energy to the energy of ozone synthesis.

A feeding voltage on the value of a current passing through the discharge zone as a function of a feeding voltage is presented in the Fig. 3. The measured total volume of the ozonizer with a wire packing is given there as well. The value of a total volume calculated for an ozonizer without a packing and with a discharge gap of d=6.0 mm is C_c=36.87pF. The presence of a packing brings about an increase of the ozonizer volume by almost 5 times and according to the Manley formula at constant values of an ozonizer feeding voltage and of a dielectric layer volume active power supplied to the discharge zone is bigger.

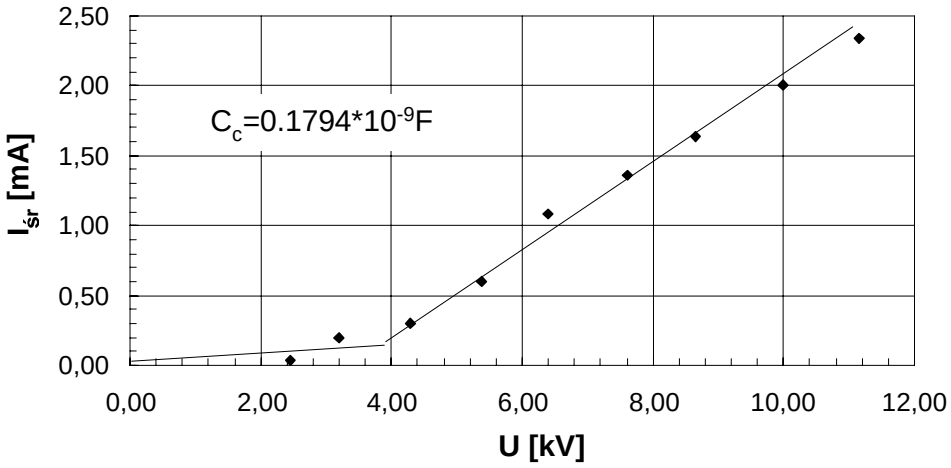


Fig. 3. Feeding voltage vs. current passing through an ozonizer with a wire packing depending on the discharge gap size (f=50Hz, substrate gas - oxygen.)

An example oscillogram obtained in the course of taking measurements for a discharge gap of 6.0 mm and a feeding voltage of U= 9 kV is presented in the Fig. 4.

It follows from an analysis of a dynamic charge-voltage characteristics that the forming discharges are of a mixed character i.e. they exhibit properties of a silent discharge as well as of a corona discharge. The obtained Lissajous curves are of a different character than those obtained in the case of ac corona discharges [5] and of classical silent discharges which proves a different operation mode of the presented apparatus.

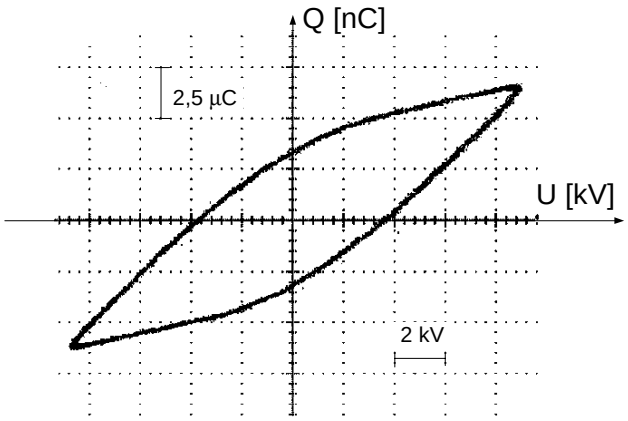


Fig. 4. Lissajous curve for an ozonizer with a conducting packing substrate gas - oxygen, F_v=90Ndm^3/h, f= 50Hz

Fig, 5 presents preliminary results illustrating changes in ozone concentration as a function of

energy density.

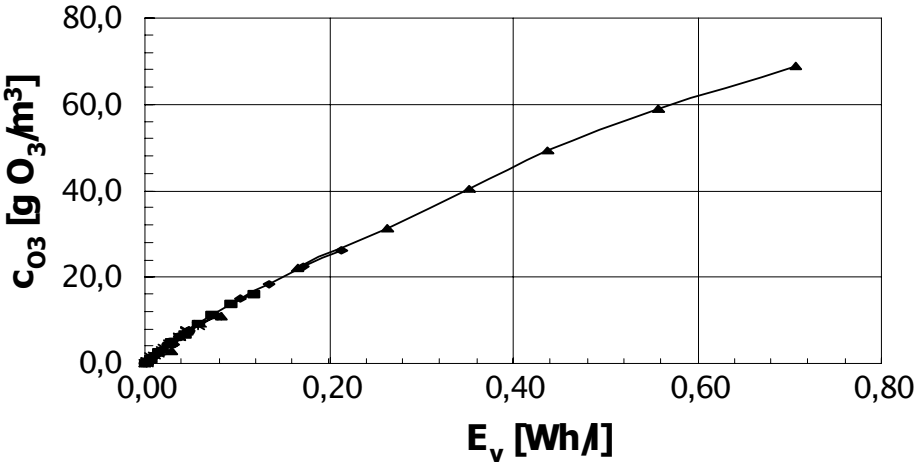


Fig. 5. Ozone concentration vs. energy density for an ozonizer with a wire packing

The introduction of a conducting packing to a discharge gap because of the developed surface should also influence the course of physical and chemical phenomena within the ozone synthesis process. Electrical characteristics, both static and dynamic ones, of ozonizers with and without a packing don not differ much, experimental data however indicate an active role a packing performs in the process [6, 7, 8].

In ozone generators containing a metal packing their discharge gap size does not influence the obtained ozone concentration so much as it is in the case of no-packing ozonizers. In traditional ozonizers that operate with a small discharge gap its size is limited by technical conditions. A conducting packing causes a formation of a strongly asymmetric electrical field and advantageous conditions for the development of streamers not only in the vicinity of the inner electrode but over the whole discharge area. Corona discharges initiate a process of a low-temperature plasma formation and an initial gas ionization while the very ozone synthesis process proceeds in a silent discharge. In tubular ozonizers of the Siemens type small discharge gaps of the 0.2-0.8 mm order are applied for to obtain high ozone concentrations at comparatively low energy consumption [9].

A discharge zone volume is of no decisive effect on the obtained ozone concentrations as it is in the case of typical ozonizers where along with the gap size growth at constant electric feeding conditions ozone concentration dramatically decreases. In such a setup hydrodynamic conditions are strongly disturbed and the course of a heat exchange between gas in the gap and the cooled electrode is more advantageous.

4. CONCLUSIONS

The obtained results of testing an ozonizer with a conducting packing in its discharge zone indicate that the application of such packing can intensify the ozone synthesis process.

The following factors contribute to the mentioned effect:

- a character of electrical discharges that form in a discharge gap;
- a change in hydrodynamic conditions (resulting from a linear velocity increase and disturbed gas flow) that brings about acceleration of heat transfer to the cooled electrode by means of a forced convection;
- a greater thermal conduction in a packing than of in a substrate gas which makes a heat transfer to the cooled electrode easier.

The obtained results show how essential is the effect of a conducting packing placed in a discharge

gap on the ozone synthesis process course and its energy efficiency and that it can make a good prospective design solution for new types of industrial ozonizers.

ACKNOWLEDGENTS

The presented research work has been sponsored by the national Committee for Scientific Research in Poland within the project No 7T09B09321

REFERENCES

[1] Schmidt-Szałowski K., Kowalczyk K., Jodzis S.; Application of silica as a catalyst for ozone synthesis; *Polish J. Appl. Chem.*, **1993**, *37*, 183-192
[2] Okazaki S., Sigimitsu H., Niwa H., Kogoma M., Moriwaki T., Inomata T., Ozone formation from the reaction of O_2-activated N_2 molecules and a new type of ozone generator with fine wire electrode, *Ozone Sci. Eng* 1988, *10*, 137-151.
[3] Okazaki S. Ando A., Kogoma M.: A new type ozonizer with fine metal wire electrode, *Proceedings of the III International Scientific Symposium: Ozone Synthesis, Properties and Applications*, Wydawnictwo Lubelskie, Lublin 2000, 69-72.
[4] Okazaki S. Ando A., Jahołkowski K., Ozonek J., Pollo I.: Effect of conducting filling on energy efficiency of ozone synthesis, *Proceedings of the III International Scientific Symposium: Ozone Synthesis, Properties and Applications*, Wydawnictwo Lubelskie, Lublin 2000, 69-72.
[5] Rzączyńska M., Pollo I., Szymański W., Ozone synthesis in all-metal generator for semi-corona discharges with a polyester dielectric, *Plasma Chemistry VI, Wydawnictwo Politechniki Lubelskiej*, Lublin 1997, 91-96
[6] Samoilovich V.G., Gibalov V.I., Kozlov K.V.: Fizicaskaja chimia bariernogo razriada. Izd. Mosk. Univ., Moskva 1989.
[7] Quederni A., Limvorapitiuk Q., Bes R., Mora J.C., Ozone decomposition on glass and silica, *Ozone Sci. Eng.*, 1996, 18, 385-415
[8] Schmidt-Szałowski K., Borucka A., Catalytic activity of silica in ozone formation in electrical discharges, *Plasma Chem. Plasma Proces.*, 1990, *10*, 443
[9] Tabata Y., Kuzumoto M., Development of a very narrow discharge gap ozone generator with 1 kg/hour production capacity, *Proc. of 13th Ozone World Congress*, Kyoto (Japan) 1997, vol. 2, 901-906

GENERATION OF OZONIZED WATER BY SURFACE DISCHARGE

Y.Miyake, Y.Ehara, H.Kishida, and T.Ito

Musashi Institute of Technology

1-28-1, Tamazutumi, Setagaya-ku, Tokyo 158-8557, Japan

g0163072@eng.musashi-tech.ac.jp

Abstract: In order to generate ozonized water, both ozonizer and reaction tub have generally been used. In this study water is introduced to the discharge space produced by surface discharge. Two devices of the ozonizer and reactional vessel were unified. As a result, dissolved ozone concentration of 0.7ppm was obtained on 3.5 Watts discharge power.

1. Introduction

Ozone has the strong oxidization power which ranks second to fluoride, and the oxidization action is called 6 times of chlorine, and has a powerful sterilization action, a virus inactive action, decolorization, a deodorization action, etc. Moreover, natural decomposition is carried out to return to oxygen. As ozone has the character which does not produce residual toxicity, and which absorbs a detrimental ultraviolet ray, it is useful for solving a health problem or earth environment protection, and it attracts attention as a disinfectant which replaces chlorine with the worries about residual toxicity. The method of using as gas and the method of using as ozone water are the common usage of ozone. We need to make a choice the proper method for using ozone. Ozone gas is used for deodorization, indoor disinfection, and semiconductor manufacture. Ozone generates OH, HO_2 and so on in water. In order to accelerate a reaction, they are used as ozonized water.

For the sake of generation of ozonized water, it needs both ozonizer and a reaction vessel in general and melting ozone in water at the reaction vessel. Therefore we propose the system that generates ozonized water by ozonizer and reactional vessel unified to one device.

2. Experimental set-up

A schematic diagram of experimental system is shown in Fig.1. Pure oxygen and water (electric conductivity < 0.1 μS/cm) are used as materials. Oxygen and water flow rate are controlled by using the flow meter and output of pump. The oxygen and water are kept at a

fixed flow rate. The ozone and dissolved ozone concentration are measured by the ozone monitor (Ebarajitugyo: EG-2001) and dissolved ozone monitor (Ebarajitugyo: PL-320) respectively.

The schematic diagram of reactor is shown in Fig.2. The experiment is carried out at a constant water flow rate of 300mL/min and a constant oxygen flow rate of 100~300mL/min. The schematic diagram of electrode is shown in Fig.3. The dielectric plate is Pyrex glass. The electrode is constructed 9 copper wires with the interval of 5 mm. Aluminum foil was attached to one side of Pyrex glass. Copper wires are connected with the GND electrode. And aluminum foil was used as high voltages electrode. Surface discharge is generated at one side of Pyrex glass. The discharge power is measured by Lissajous figure method.

In this study, the absorption efficiency is defined as follows

$$\eta = \frac{O_3 l \times L}{O_3 g \times G + O_3 l \times L} \times 100 \qquad (1)$$

η :absorption efficiency[%], O_3g:ozone concentration[mg/L], O_3l:dissolved ozone concentration[mg/L], G:oxygen flow rate[L/min], L:water flow rate[L/min]

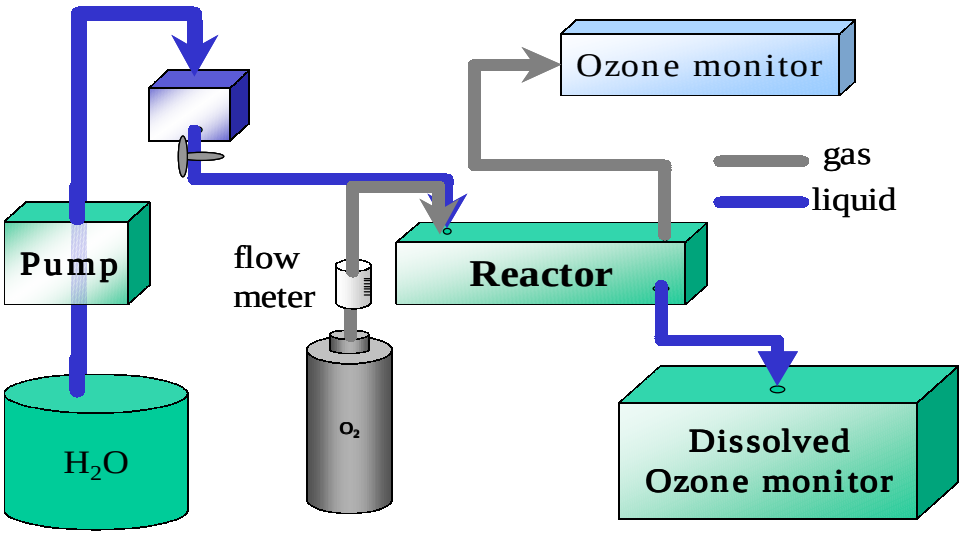


Fig.1 Schematic diagram of experimental system

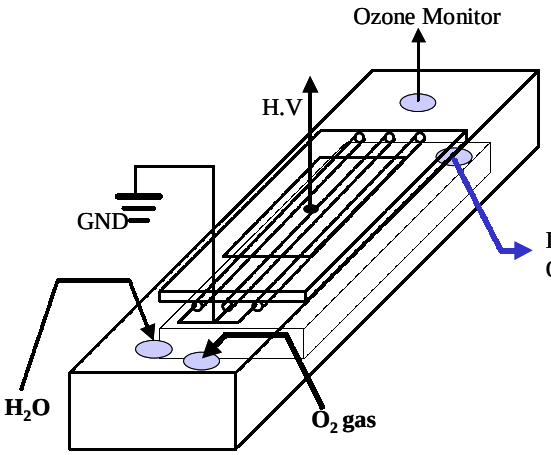


Fig.2 Schematic diagram of reactor

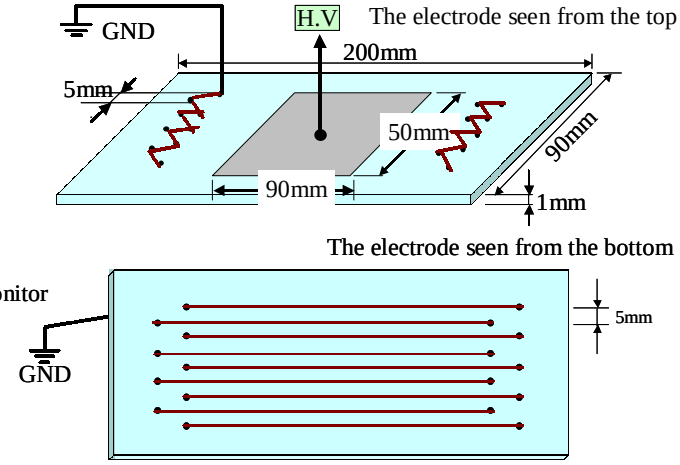


Fig.3 Schematic diagram of electrode

3. Results and Discussion

3.1 Effect of oxygen flow rate on ozonized water generation

When 9 copper wires were used as electrodes, the experimental conditions were as follows, water flow rate was 300mL/min, and oxygen flow rate was 100~300mL/min. The ozone concentration in gas and dissolved ozone concentration as a function of discharge power are shown in Fig.4 and Fig.5 respectively. Both the ozone concentration and dissolved ozone concentration increased with increasing discharge power. The ozone concentration and dissolved ozone concentration increase by reduction of oxygen flow rate at the same discharge power. This result suggests that the ozone concentration depends on the residence time of oxygen flow.

The absorption efficiency as a function of discharge power is shown in Fig.6. The absorption efficiency is almost constant regardless of electric discharge power. The absorption efficiency increases by reduction of oxygen flow rate at the same discharge power.

3.2 Effect of number of copper wire

When the number of wire electrode is 3 or 9, and water flow rate was 300mL/min, the oxygen flow rate was 100mL/min. The ozone concentration in gas and dissolved ozone concentration as a function of discharge power are shown in Fig.7 and Fig.8 respectively. The

ozone concentration and dissolved ozone concentration increased with increasing discharge power. The ozone concentration and dissolved ozone concentration were different by the number of wire electrode. When ozone concentration and dissolved ozone concentration were compared with the same discharge power, the value of the case of 9 wires is larger than that of the case of 3 wires. It is thought that discharge space increases by the increase the number of wire electrode.

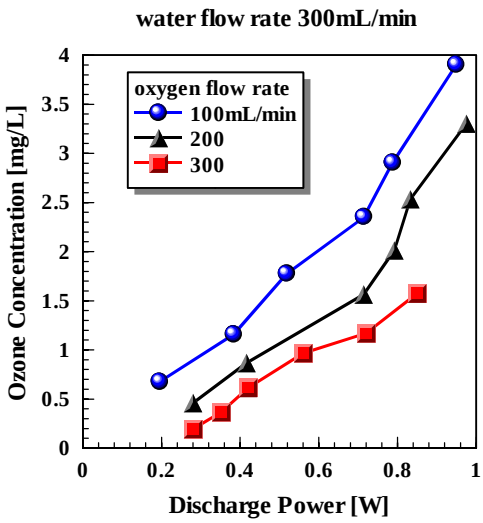


Fig.4 Ozone concentration as a function of discharge power

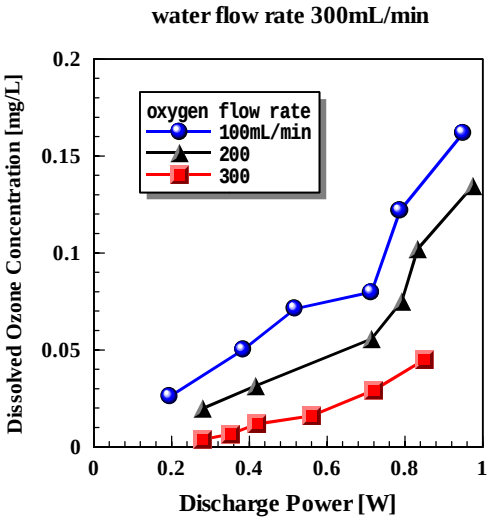


Fig.5 Dissolved ozone concentration as a function of discharge power

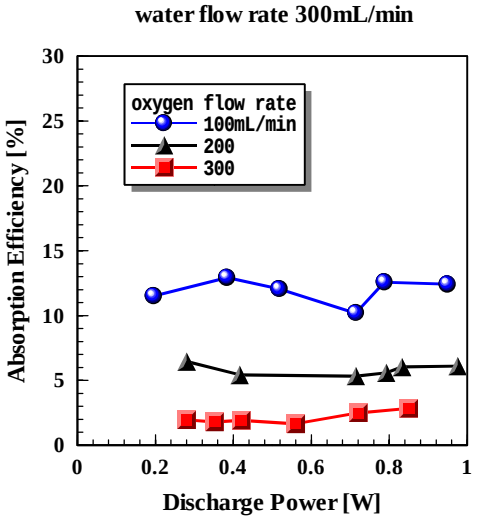


Fig.6 Absorption efficiency as a function of discharge power

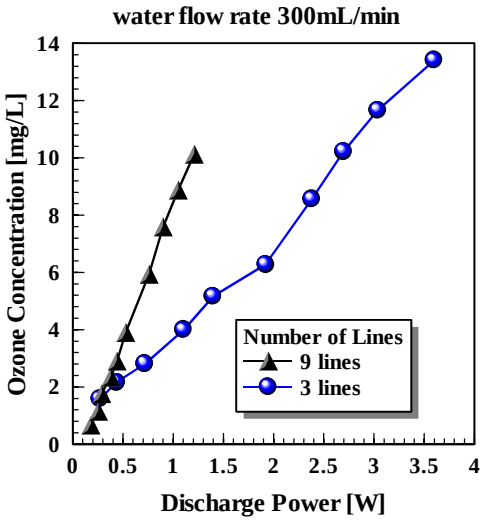


Fig.7 Ozone concentration as a function as a function of discharge power

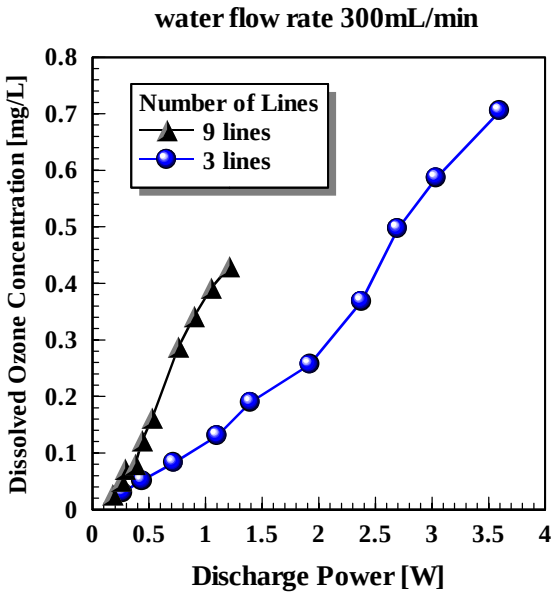


Fig.8 Dissolved ozone concentration as a function of discharge power

4. Conclusions

In this paper, a new type ozonized water generation system using water electrode was proposed. The results obtained are as follows.

(1) Ozone concentration and dissolved ozone concentration increase by reduction of oxygen flow rate at the same discharge power. This result suggests that the ozone concentration depends on the residence time of oxygen flow.

(2) Ozone concentration and dissolved ozone concentration increase with increasing the number of wire electrode. It is thought that discharge space increases by the increase in the number of wire electrode.

REFERENCES

[1] R.Tajima et al; HAKONE Ⅶ pp412-416(2000)

REACTIVE POWER OF THE OZONE GENERATORS

Henryka Danuta Stryczewska and Tadeusz Janowski

Institute of Electrical Engineering and Electrotechnology, Lublin Technical University, Nadbystrzycka 38A, 20-618 Lublin, Poland

Abstract: The paper presents the analysis of the reactive power flow in the ozone generator power system and discusses some possibilities of its minimization. Discharge elements of the ozone generator comprise strong non-linear capacitive energy receiver and supply system should provide the ozone generator with the active power *P* necessary to carry out reactions in the inter-electrode zone, the reactive capacitive power Q_C that is to generate electric field at the gap and the dielectric of the discharge elements and the distortion power Q_D due to the ozone generator non-linearity. The reactive power is provided to the circuit from the power network and the same amount is returned during every period of supply voltage resulting in the energy loss at the elements of the power system. Their minimizations in the ozone generators allow reducing power loss in the process of the ozone generation and improve overall efficiency of the system.

1. INTRODUCTION

In environment protection technologies generators are applied where low-temperature, non-equilibrium plasma has been generated in the process of electrical discharges. Discharge devices for power network of sinusoidal voltage are highly non-linear energy receivers distorting voltage and current courses. At high power value of the generators such distortion unfavorably influences the operation of the power network and decreases power efficiency of plasma generators. Electrical discharge processes in reactor chambers require the supply of energy estimated by apparent power *S* comprising active power *P* equivalent to the energy consumed in the reactor and reactive power *Q* passing between the network and the reactor. Reactive power *Q* at the sinusoidal courses is defined by the capacitance *C*, or inductance *L* and is called the displacement reactive power. The relations between the apparent power *S*, active power *P*, and the reactive power *Q* at the sinusoidal conditions of currents and voltages are expressed by known relations:

$$\begin{aligned} S &= U \cdot I = \sqrt{P^2 + Q^2} \\ P &= U \cdot I \cdot \cos\varphi \\ Q &= U \cdot I \cdot \sin\varphi \end{aligned} \quad , \tag{1}$$

where: *U* – voltage, *I* – current, φ – phase displacement angle between current and voltage.

Reactive power has been assumed as positive value for the inductive type ($Q > 0$) and as negative value for the capacitance type of the receiver ($Q < 0$). The relations (1) can be graphically presented as power triangle (Fig.1a). At the sinusoidal courses, reactive power of the reactor can be totally compensated or limited by properly selected chokes or condensers.

In case of non-sinusoidal courses of voltages and currents reactive power can be interpreted in various ways. The paper presents the most common Budeanu approach where apart from the reactive power of the displacement *Q*, also the reactive power of the distortion *D* has been introduced. Periodical courses of distorted voltage and current have been distributed into the Fourier's series. Their effective values can be expressed by its Fourier's series coefficients as follows:

$$U = \sqrt{U_0^2 + U_1^2 + U_2^2 + ... + U_k^2} = \sqrt{\sum_{k=0}^{\infty} U_k^2}$$
$$I = \sqrt{I_0^2 + I_1^2 + I_2^2 + ... + I_l^2} = \sqrt{\sum_{l=0}^{\infty} I_l^2} \quad (2)$$

where: U_0, I_0 – effective values of constant components, U_k, I_k – effective values of higher harmonics of distorted voltage and current.

Following the relation (2) previously introduced powers can be defined by:

apparent power: $S = U \cdot I = \sqrt{\sum_{k=0}^{\infty} U_k^2} \cdot \sqrt{\sum_{l=0}^{\infty} I_l^2} = \sqrt{P^2 + Q^2 + D^2}$ (3)

active power: $P = U_o \cdot I_o + \sum_{k=1}^{\infty} U_k \cdot I_k \cdot cos\varphi_k$ (4)

reactive power of the displacement: $Q = \sum_{k=1}^{\infty} U_k \cdot I_k \cdot sin\varphi_k$ (5)

distortion power: $D = \sqrt{S^2 - P^2 - Q^2}$, (6)

where: φ_1, $\varphi_{2, ...,}\varphi_k$ – harmonic displacement angles of voltage and current of *k*-harmonics

In the distorted case the graphical powers interpretation is no longer in the form of triangle and has been presented as rectangular (Fig.1b).

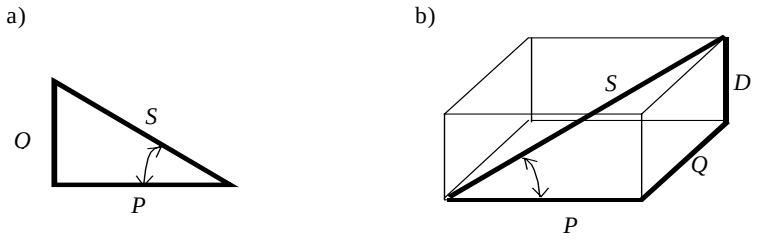


FIGURE 1. Graphical interpretation of powers for sinusoidal (a) and distorted (b) course of currents and voltages

The distortion power *D* cannot be totally compensated through the application of the chokes. It can be limited to the significant level due to the application of special LC filters and such design of the supply system that the reactive power required for the core magnetization would compensate the reactive capacitive power of the ozone generator.

2. POWER FLOW IN SUPPLY SYSTEMS OF THE OZONE GENERATORS

In case of industrial ozone generators of power frequency or higher supply voltage at electrodes of the discharge elements is practically sinusoidal whereas the passing current is significantly distorted. Voltage and current courses at the discharge gap of the discharge element at the sinusoidal voltage are presented in Fig. 2.

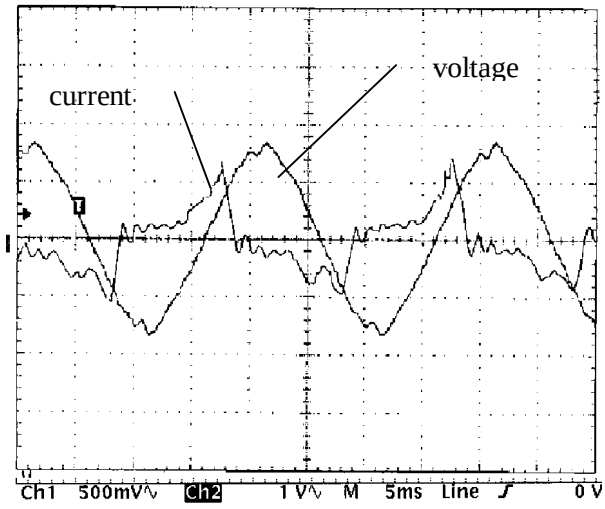


FIGURE 2. Courses of voltage and current of ozone generator at 50Hz

At instant values lower than the ignition discharge voltage, the discharge element is operating as the laminar condenser. At the moment when the voltage of the discharge gap exceeds the value of the ignition voltage, silent electric discharges are generated that break diatomic oxygen and as a consequence of the recombination and diffusion processes – ozone O_3 is generated. The discharge element is becoming the series connection of the ionized, conducting gaseous gap and the solid dielectric. The Manley's relation expresses active power consumed by the ozone generator for the process of gas ionization in the operating gap and the ozone synthesis:

$$P = 4fC_dU_i\left(U_m - \frac{C_g}{C_e}U_i\right) \tag{7}$$

in which: f – frequency, U_i – ignition voltage, U_m – supply voltage magnitude, C_e – equivalent capacity of the ozone generator discharge element, C_g – capacity of the discharge gap, C_d –capacity of the dielectric layer.

Apart from the active power contributed to the process of the ozone generation and heat losses occurred in the discharge gap, the flow of the reactive power Q between the ozone generator and the supply system will emerge as well as the distortion reactive power D caused by the non-sinusoidal current and voltage courses. Although the reactive power is required for the ozone synthesis, it could not be the measurable factor of the power conversion. The reactive power can attain the value of the apparent power and thus the value of the current passing in the supply system which leads to the energy loss of the system elements ($\Delta P = I^2 R$), reduce efficiency of the power system. Ozone generator is highly non-linear, active-capacitive energy receiver of low power factor. Power factor of discharge elements is limited to the range of 0,3 – 0,8 and is too low to connect the generator directly to power network. To ensure proper cooperation between the ozone generators and the supply network, provide proper voltage, high efficiency and reliability, as well as control and regulation of the ozone generation process – special supply systems have been designed comprising various components satisfying the mentioned above requirements.

3. POWER LOSSES AND THE EFFICIENCY OF THE OZONE GENERATOR

High power efficiency of the ozone generation process can be achieved by maximal reduction of reactive power in supply system. It would be the most favourable solution to compensate the reactive power at the place of its generation i.e. in discharge elements since the apparent power of electrical elements of the ozone generator will reach the lowest value, and thus the level of power losses is minimal. The paper presents the issue of reactive power compensation in view of three model solutions: transformer system operating at power frequency of 50Hz, thyristor system of 600Hz, and integrated system of 150 Hz [3].

The active power *P* of the ozone generator results from the required amount of the generated ozone that is assured by relevant number of discharge elements connected in parallel. Discharge elements of the tubular construction commonly used in ozone generator have active power of 350W with the efficiency of 60g of ozone from 1kWh at the frequency of 50Hz or about 800W and 50g/Wh at the frequency of 600Hz. The number of discharge elements in one generator usually oscillates between 200 to 1000 [3], therefore the active power of one industrial generator may range between 50-900 kW.

Power factor of the discharge element expressed as:

$$\lambda = \frac{P}{\sqrt{P^2 + Q^2 + D^2}}, \tag{8}$$

amounts between 0,3 – 0,8, which means that the apparent power *S* provided by the supply system has to be considerably higher than the active power *P* required for the ozone generation. In order to reduce power losses and the size of supply system elements, the capacitive power of ozone generator has been compensated by the inductive power *Q* of chokes, whereas the distortion power cannot be easily compensated.

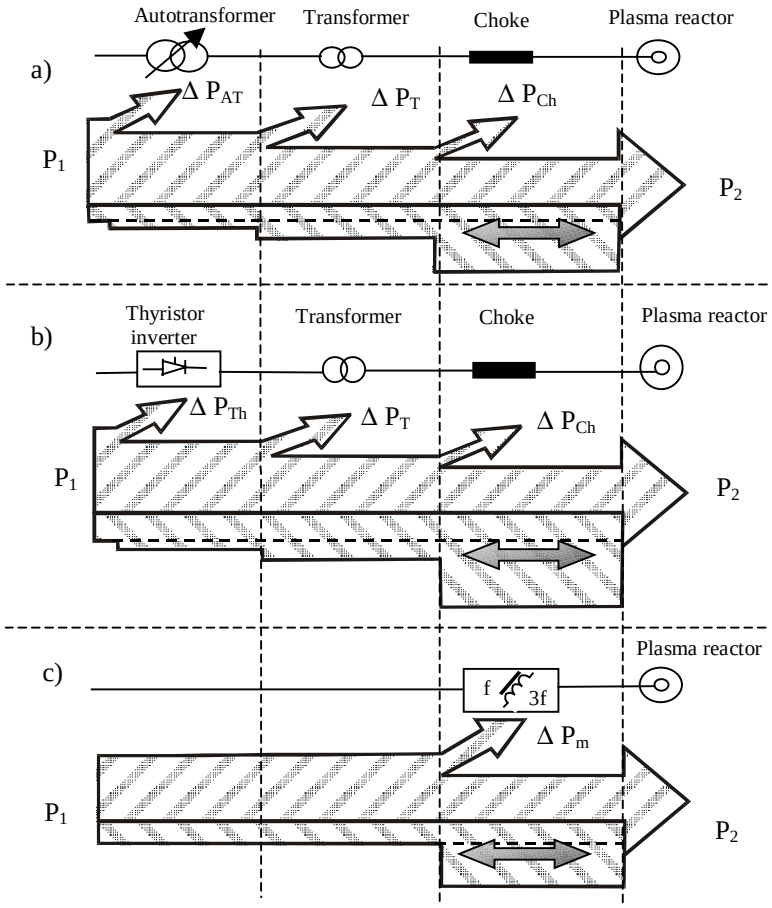


FIGURE 3. Block diagrams: supply systems of the ozone generators with the indicated active power losses in the elements of the system, a – supply system of the ozonizer with power frequency, b – supply system of the ozonizer of medium frequency with thyristor multiplier, c – integrated supply system

Power factor of the ozone generator after the compensation of the capacitance current is ranging from 0,8 – 0,9 which means, that the apparent power of the transformer in supply system S_n has to be 10 to 20% higher than the active power. The transformer has been designed for the apparent power, and its power losses ΔP_T are proportional to the apparent power. The power of the choke compensating the capacitive power of the ozonizer is equal to Q=(0,7-0,5)P. The choke is also the source of active power loss ΔP_{Ch} , the value of which is the same as the losses in the transformer. If the supply system includes control autotransformer, it also becomes the source of losses ΔP_{AT}. In supply systems of increased frequency, the choke and the transformer are smaller but total power losses are higher than in case of the system of power frequency.

The integrated system comprises only one element – magnetic frequency multiplier – with the losses comparable to transformer [1].

Block diagrams from Fig.3 compare the supply systems of the ozone generator energized from different systems. The analysis of power losses is carried out for the ozonizer of 160kW, efficiency of

10kg O_3/h from the air and the ozone concentration of 18mg/l. For active power P_a=160kW the rated power of the transformer will amount to 200kVA. Power transformer of 200kVA and voltage 30/0,4 kV has the efficiency of about 96% with the proportion of the losses in windings to the losses in coil as high as 3:1. Due to the distorted current and voltage courses of the ozonizer, power losses in the supply transformer are higher and are assumed as 5% i.e. 10kW, and the efficiency will amount to 95%. Power factor will have the value λ = 0,5 – 0,8. Assuming that λ = 0,6 - the apparent power of the ozonizer S will amount to 270 kVA, and the reactive power and the distortion power $\sqrt{Q_c^2 + D^2}$ is equal to 210 kVA. If the value of the distortion power D is assessed as 20% of P, i.e. 32kvar, the reactive capacitance power will amount to Q_C=200 kvar. The power of the control autotransformer S_{AT} depends on the control range and it can be determined at the level of 0,8 of the transformer's power S_{AT}= 0,8 S_T and power losses similarly (ΔP_{AT} = 0,8 ΔP_T). In the systems of medium frequency (600Hz) (Fig.3b) despite smaller dimension of its components, power losses are 10% higher as compared with the supply system of power frequency at the same efficiency of the ozone generation. In case of the integrated system (Fig. 3c) power losses are detected only in the magnetic multiplier ΔP_m and due to higher induction of its operation and power losses in control system, the losses are 10-20% higher than in the transformer of the same power (ΔP_m=1,1 – 1,2 ΔP_T).
Table 1 presents the results of the analysed power losses and the efficiency of the integrated system compared with commercially applied systems of mains and increased frequency [2].

Table1. Results of power losses and efficiency of the ozone generator supply systems

System / Component	**Mains frequency system 50Hz** Fig. 3 a						**SCR thyristor system 600Hz** Fig. 3 b						**Integrated system 150Hz** Fig. 3 c					
	S_n	Q	D	ΔP	ΔP	λ	S_n	Q	D	ΔP	ΔP	λ	S_n	Q	D	ΔP	ΔP	λ
	kVA	kVAr	kVAr	kW	%	-	kVA	kVAr	kVAr	kW	%	-	kVA	kVAr	kVAr	kW	%	-
Choke	160	160	-	4,8	3,0	0,03	160	180	-	5,6	7,0	-	-	-	-	-	-	-
Transformer	200	10	-	10	6,2	0,05	200	10	-	11	6,8	-	200	180	20	11	6,8	0,06
Autotransformer	200	10	-	6	3,7	0,03	-	-	-	-	-	-	-	-	-	-	-	-
SCR inverter	-	-	-	-	-	-	200	20	10	8	5,0	-	-	-	-	-	-	-
Power in the whole system	200	20	90	20,8	13	0,9	200	180	100	24,6	15,5	0,9	200	-	110	11	6,8	0,9
Power of the ozonizer P_2=160 kW	Q=160 kVAr, D= 90 kVAr						Q=180 kVAr, D= 90 kVAr						Q=160 kVAr , D= 90 kVAr					
Power from the mains P_1	180,8 kW						184,6 kW						171 kW					
Efficiency $\frac{P_2}{P_2 + \Delta P} \cdot 100\%$	88,5 %						86,7 %						93,6 %					

REFERENCES

[1] Janowski T., Stryczewska H.: Magnetic Frequency Triplers: Another Way To Supply Ozone Generators, Ozone Science & Engineering, vol. 14, (1992), 139-152
[2] Janowski T., Stryczewska H.: Electrical power losses and efficiency of ozone generators. Polish Journal of Applied Chemistry, XXXIX, z.4, (1995), 535-54
[3] Kogelschatz, U., Advanced Ozone Generation, in: Process for Water Treatment. ed. S. Stucki, Plenum Pub., 1988, 87-120
[4] Stryczewska H. D.: An analysis of integrated power supply systems of ozone generators. Lublin Technical University, (1996), p.136
[5] Stryczewska H. D.: Plasma reactor feeder. Polish Patent Application No P-339397, 2000

COLD PLASMA REACTOR WITH DIELECTRIC BARRIER DISCHARGE

T. Opalinska[a]

Industrial Chemistry Research Institute, Rydygiera 8, 01 793 Warszawa, POLAND

Abstract. A new reactor was constructed and tested to generate a cold oxidizing plasma, based on the principle of a barrier electric discharge. In contrast to conventional reactors, the discharge was generated between several parallel plates made of a high-permittivity (e > 1500) ferroelectrics ceramic material. The capacitance of the reactor decreased as the number of the ceramic plates was increased and was equal to the capacitance of one ceramic plate divided by the number of the ceramic plates provided inside the reaction chamber. The gap spacing potential had a constant value for each gap between the plates and was related to gap thickness only. As the number of ceramic plates is increased and the thickness of the gas gap is enlarged, the power in the outer circuit falls. The specific energy was a parameter used to describe the chemical process run in the new reactor.

1. INTRODUCTION

The electric barrier discharge has been used most frequently for making ozone [1]. Recently, the barrier discharge has been used to apply thin films on the surfaces of various materials like silicon [2] and plastics [3]. In this case, a low-permittivity (e = 3—15) dielectric-barrier material is used. This material can be replaced by a ferroelectric ceramics, which has a much higher permittivity (e > 500). Ceramics are advantageous in that they allow to increase power density without requiring the frequency of the supply voltage to be increased and allow considerably lower voltages to be used. The structure of the ferroelectric material and its nonlinear properties can facilitate discharge induction and give rise to self-stabilization of the properties of the material [4,5].
So far various chemical reactions, including preparation of ozone, have been studied in a small reactor equipped with double ceramic electrodes, each 5 cm^2 in surface area [5-8]. The interest for producing oxygen-containing plasma to enable new chemical processes, *e.g.* removal of organic impurities from exhaust air, to be carried out, makes it desirable to find ways to enlarge the reactor. It has been found that enlargement of the reactor should consist in increasing the number, rather than the surface area, of the ceramic electrodes placed in the reaction chamber [9].
The purpose of the present study is to construct and to test a new generator for making cold oxidizing plasma, based on the principle of the barrier electric discharge. In contrast to conventional reactors, the new generator would generate the discharge between several parallel plates made of high-permittivity ferroelectric ceramics (e > 1500).

2. EXPERIMENTAL

2.1. The reactor

A scheme of the reactor is given in **FIGURE 1**. The reactor consists of a reaction chamber equipped with parallel ceramic plates. The plates are made of ferroelectrics ceramics. Two external electrodes were coated on one side with a thin film of silver to ensure a good electric contact between the metal electrodes and the ceramic electrodes. In a given type of the reactor examined, the distance between the ceramic plates was kept constant. The plasma gas (oxygen) was introduced into the reaction chamber through a mixing zone and allowed to flow through the space between the ceramic plates. The electric discharge was generated in this space.

2.2. Experimental conditions

Two (reactor type *A*), three (reactor type *B*) or four (reactor type *C*) ceramic plates were placed in the reaction chamber. Each plate had an electric capacity of 30 nF. Barium titanate was the main

[a] Electronic adress: Teresa.Opalinska@ichp.pl

component of the ceramic material. In the experiments carried out with no electric discharge generated, the inter-plate distance (*d*) was kept equal to 0.08 mm. In the presence of discharge, the distance between the plates was kept at 0.09 mm (reactors *A* and *B*) or 0.15 mm (reactor *C*). The discharge was generated in oxygen gas under static or under steady-state flow conditions. Before the experiment, the oxygen gas was dried by passing through silica-gel columns and 4Å molecular sieve columns.

The reactor was supplied with a sinusoidal alternating current, 50 or 100 Hz in frequency, the voltage amplitude varying from 0 to 6.5 kV. During the experiment, the following parameters were measured: the maximum voltage applied to the electrodes (U_m), the charge transferred in the outer circuit (Q) (with respect to the half-period), and the real power (P) supplied to the reactor. The maximum voltage was measured with a peak probe. The charge was calculated from the drop of potential recorded across the measuring capacitor. The power supplied was calculated as the surface area of an adequate Lissajou's figure [10]. Concentration of ozone was measured in terms of UV absorption spectrophotometry at a wavelength of 254 nm.

Synthesis of ozone from oxygen was used as the test reaction to establish the reactor properties. One series of experiments was performed in reactor *A* at constant oxygen flow rate of 0.29 mol/h with the electric power varied.

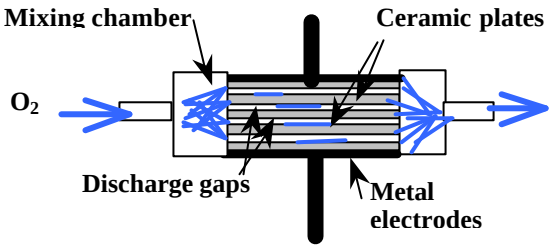


FIGURE 1. A scheme of reactor.

Two series of experiments were performed in each of the two reactors, *B* and *C*. In the first series, the oxygen flow (0.29 mol/h) was kept constant and the power of discharge was varied from 0.8 to 5.6 W. In the second series, the power supplied to the reactor was kept constant (reactor *B*, 3.3 W; reactor *C*, 4.4 W). The flow rate of oxygen gas was varied from 0.07 to 0.38 mol/h.

3. RESULT AND DISCUSSION

3.1. Electric characteristics of reactor

3.1.1. No electric discharge

The first stage of experiments was to study the behavior of reactor as an element of electric circuit. The reactor played part of ceramic-air capacitor in electric circuit. It could be represented as ceramic and air capacitors connected in series. The capacitance of this capacitor (C) is given by:

$$C = \frac{C_g \times C_d}{n \times (C_g + C_d) - C_d} \qquad (1)$$

where: C_g, and C_d - the capacities of gas layer and ceramic plate, respectively; n – number of ceramic plates.

With 1 unity taken for the gas permittivity and at a given inter-plate distance, the capacitance of the gas layer was 106 pF. The gas layer capacitance is seen to be much lower than the capacitance of ceramic plate: $C_g << C_d$. Therefore, equation (1) can be simplified:

$$C = \frac{C_g}{n-1} \qquad (2)$$

Thus, in the absence of electric discharge, the capacitance of the reactor should decrease as the number of the ceramic plates is increased and should be related only to the capacity of the gas layer between the ceramic plates. The charge-voltage characteristics for the current frequency 50 Hz are shown in **FIGURE 2.** Regression equations, $Q = f(U_m)$, of the curves presented in **FIGURE 2** are given in **TABLE 1**. This Table lists also the capacitance values calculated for the reactors on the basis of these characteristics. The values are in good agreement with those calculated from equation (2). The relationship $Q = f(U_m)$ is seen not to be related to current frequency (**FIGURE 3**), a fact confirming that the measurements were correct.

TABLE 1. The charge-voltage characteristics of reactor in the absence of discharge.

Type of reactor	Number of ceramics plates	Charge –voltage* characteristics	Capacitance of reactor [pF]		Voltage frequency [Hz]
			I **	II***	
A	2	$Q = 2.090\ U_m$	105	106	50
A	2	$Q = 2.089\ U_m$	105	106	50; 100
B	3	$Q = 1.084\ U_m$	54	53	50
C	4	$Q = 0.712\ U_m$	35	35	50

*$Q=10^{-7}$As, $U_m=10^3$V; **calculated from charge-voltage characteristics; ***calculated from equation (2)

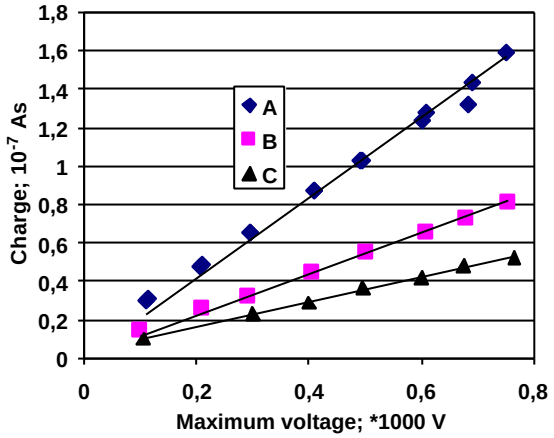


FIGURE 2. Charge voltage characteristics in the absence of discharge for rector types *A, B* and *C*.

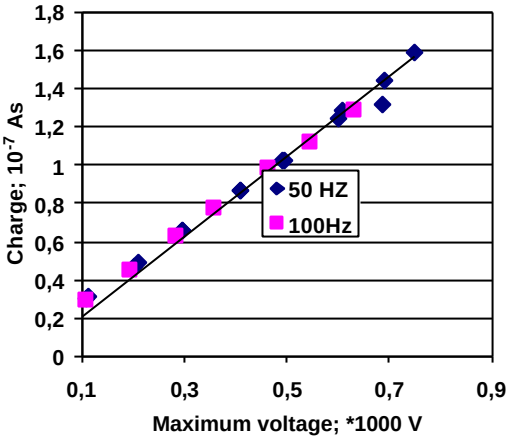
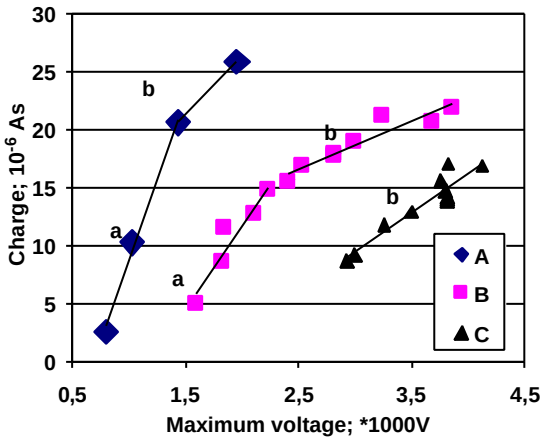


FIGURE 3. Charge - voltage characteristics in the absence of discharge at varying voltage frequencies in reactor

3.1.2. Electric characteristics of reactor in the presence of discharge

The charge-voltage characteristics established in the presence of electric discharge are complicated and include several rectilinear sections (**FIGURE 4**). Regression equations calculated for the individual straight-line sections (**TABLE 2**) show the first section to be the only one that is consistent with the theory of barrier discharge [10,11] and also with the earlier results obtained in the reactor comprising two small parallel equidistant ceramic plates (5 cm^2)[4]. The capacitances of reactor *A* and reactor *B* are compatible with the following equation:

$$C = \frac{C_d}{n} \qquad (3)$$



The gap spacing potential of reactor *B* (1.21 kV) is a multiple value of the gap spacing potential of reactor *A* (0.69 kV). The shape of the characteristic curve established for reactor *C* is different from the shapes established for reactors *A* and *B* and is difficult to explain. The increase in the number of ceramic plates resulted in a decreased capacitance of the reactor and of the charge transferred in the outer circuit. The conditions are thus favorable to the formation of atomic oxygen and ozone in the oxidizing plasma.

FIGURE 4. Charge voltage characteristics in the presence of discharge in rector types *A, B,* and *C*.

TABLE 2. Charge-voltage characteristics of reactor in the presence of discharge.

Type of reactor	Number of ceramics plates	Charge –voltage characteristics*	
		a	b
A	2	$Q = 27.57(U_m - 0.69)$	$Q = 10.07U_m + 6.05$
B	3	$Q = 14{,}82(U_m - 1.38)$	$Q = 6.70(U_m - 0.12)$
C	4	-	$Q = 6.79\ (U_m - 1.61)$

*$Q=10^{-7}$As, $U_m=10^3$V

3.2 Charge -voltage characteristics versus chemical reaction effect

As the charge transferred in the outer circuit was raised, the ozone concentration rose, *viz.*, slightly in the reactors with a small discharge gap (0.09 mm) and considerably in the reactor with the wider discharge gap (0.14 mm) equipped with four ceramic plates in the reaction chamber (**FIGURE 5**). At the charge corresponding to the one of the second section in the charge-voltage characteristics, the concentration of ozone did not increase any longer. As the mole flow rate of oxygen gas was increased, the ozone concentration slightly decreased (**FIGURE 6**).

A general parameter describing the chemical process carried out in the reactor is necessary to characterize the reactor efficiency. The specific energy can be used as such a macroscopic parameter. This parameter was used by Warburg [12] and Vasilev, Kobozev and Eromin [13] to describe the kinetics of the chemical reactions proceeding in an electric discharge. The energy was defined as the ratio of power and reactant flow rate. The specific energy characterizes the yield of ozone produced in a multi-plate reactor at a given discharge gap (**FIGURE 7**). Here, the power is calculated in relation to a single discharge gap (*P/n*).

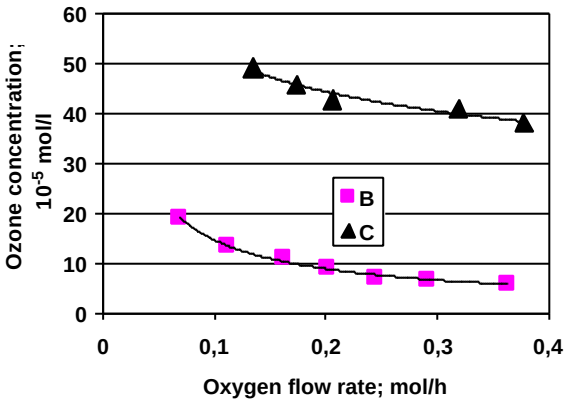


FIGURE 5. The concentration of ozone in relation to oxygen flow rate in reactors *B* and *C*

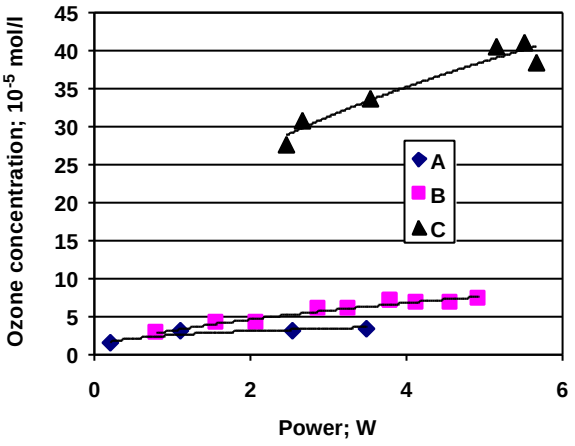


FIGURE 6. The concentration of ozone in relation to power supplied reactors *A*, *B* and *C*.

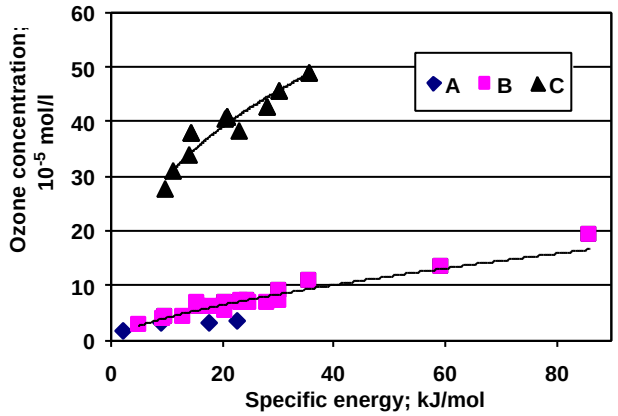


FIGURE 7. The concentration of ozone in relation to specific energy of oxygen. Reactors *A*,*B* and *C*.

The new reactor allowed to achieve higher ozone concentrations than did the small reactor comprising two 5-cm^2 parallel ceramic plates at an identical oxygen flow rate and quite similar ceramic plate properties [4]. This fact proves that the method used to enlarge the reactor was successful.

The electric and the chemical characteristics of the new reactor make it possible to modify the experimental conditions by varying the size of discharge gaps, the number of ceramic plates and the ceramics properties to suit a concrete chemical process.

4. CONCLUSIONS

1. The reaction chamber comprising several parallel equidistant ceramic plates made of a high-permittivity (e > 1500) ferroelectric ceramic material, is the main element of the new reactor to be used to generate a cold plasma
2. In the absence of electric discharge, the capacitance of the reactor decreases as the number of the ceramic plates is increased and is related to the capacity of the gas layer between the plates.
3. In the presence of discharge, the capacitance of the reactor decreases as the number of the ceramic plates is increased and corresponds to the capacitance of one ceramic plate divided by the number of ceramic plates provided in the reaction chamber. The gap spacing potential has a constant value for each gap between the plates and depends on the thickness of the gap only. The power in the outer circuit decreases as the number of the ceramic plates is increased and as the thickness of the gas gap between the plates is enlarged.
4. The specific energy is the parameter used to describe the chemical process run in the reactor. The specific energy is defined as the ratio of the power supplied to the reactant molar flow rate. The power is calculated in relation to one discharge gap.
5. The method of enlarging the reactor consists in providing more ceramic plates into the reaction chamber.
6. The electrical and chemical characteristics of the new reactor allow to modify the experimental conditions by varying the size of discharge gaps, the number of ceramic plates and the ceramics properties so as to suit the requirements of a concrete chemical process run in the reactor.

5. REFERENCES

[1] Horvath M., Bilitzki L., Hüttner J., *Ozone*, Akadèmiai Kiadó, Budapest 1985.

[2] Schmidt-Szalowski K., Rzanek-Boroch Z., Sentek J., Rymuza Z., Kusznierewicz Z. and Misiak M., *Plasmas and Polymers*, **5**, 173-190 (2000)

[3] Opalinska T., Ulejczyk B., Karpinski L. and Schmidt-Szalowski K., present Proceedings

[4] Opalinska T. and Szymanski A., *14th International Symposium on Plasma Chemistry, Prague1999, Czech Republic, Symposium Proceedings* ed. by M. Chrabowsky, M. Konrad and V. Kopecki, pp. 801-805

[5] Opalinska T., Kozlov K.V., Voblikova V.A. and Szymanski A., *Acta. Phys. Universitatis Comenianae*, **34**, 33-38 (1993)

[6] Szymanski A., Opalinska T., *Acta. Phys. Slov*. **35,** 363-368 (1985)

[7] Szymanski, A. Opalinska T., Deutsch H.and Wiener K., *Plasma Chemistry V*, Politechnika Lubelska Wydawnictwa Uczelniane 1987 ed. by I. Pollo and A. Szymanski, pp. 5-10

[8] Opalinska T., *Acta. Phys. Slov*., **39**, 83-87 (1989)

[9] Opalinska T. and Szymanski A., *Contrib. Plasma Phys.*, **36**, 63-73 (1996)

[10] Kogelschatz U., *Advanced ozone generation,* In: *Process Technologies for Water Treatment,* ed. by S. Stucki, Plenum Press, New York and London 1988, pp. 87-118

[11] Samoilovich V.G., Gibalov V.I and Kozlov K.V., Fizicheskaya khimia bariernovo razriada, IMU Moscow 1989.

[12] Warburg E., *Jahrubuch der Radioaktivität und Electronik* **, 6**, 181-229 (1909/1910),

[13] Vasiliev S.S.,. Kobozev N.J and Eremin E.N:., Zh. Fiz. Chim. **10,** 619 (1936)

[14] Opalinska T. *HAKONE VII International Symposium on High Pressure low Temperature Plasma Chemistry, Contributed Papers, Greifswald 2000, Germany*, ed. by H-E. Wagner, J.F. Behnke and G. Babucke, pp.98-102

ON THE IGNITION VOLTAGE AND STRUCTURE OF COPLANAR BARRIER DISCHARGES

L. Hulka and G. J. Pietsch

Electrical Engineering and Gas Discharge Technology, RWTH Aachen, Schinkelstr. 2, 52056 Aachen, GERMANY

Abstract. Coplanar discharges (CDs) appear in arrangements where pair(s) of electrodes are embedded in a solid dielectric. The ignition voltage of CDs is much higher than that in common dielectric barrier discharge arrangements with a gas gap comparable with the electrode distance of CD arrangements. From calculations of the initial field strength distributions the ignition voltage can be found for different electrode distances. In order to analyze the discharge structure an intensified CCD camera has been used. From highly resolved photographs follows that CDs consists of more or less parallel discharge channels on the surface similar to those in common arrangements with gas gaps.

1. INTRODUCTION

Dielectric barrier discharges (DBDs) are characterized by discharge gaps and the presence of one or more insulating layers in between the gaps. Typical operation conditions are pressures between 0.1 and 10 bar and frequencies in the range of 50 Hz to 100 kHz. There exists a broad range of applications for DBDs like ozone generation, pollution control, surface modification and light production in e. g. CO_2 lasers, UV and VUV lamps as well as in ac plasma display panels [1].

Three basic configurations to produce DBDs can be distinguished [2], the volume discharge (VD), the surface discharge (SD) and the coplanar discharge (CD) arrangement. The VD arrangement is most common. It consists in general of a gas gap between parallel electrode plates with one or both electrodes covered by a dielectric layer. The ignition voltage is mainly determined by the size of the gap, the kind of gas and its pressure.

SD arrangements consist of one or more long high voltage electrodes on the surface of a dielectric and an extended counter electrode on its reverse side. Pure SDs appear on the surface of the dielectric. The discharge ignites at Paschen minimum conditions. Its area on the surface is proportional to the amplitude of the applied voltage [3].

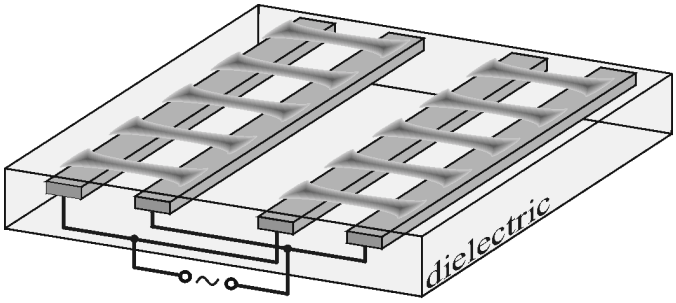


FIGURE 1. Principle of a coplanar discharge arrangement.

The CD arrangement on the other hand consists of pair(s) of extended electrodes that are embedded in a dielectric close its surface. Most often the electrode separation is in the order of 100 µm. The discharge occurs on the surface of the dielectric in between the location of the electrodes. A principal arrangement is shown in Fig. 1. The advantages of VDs (like constant electrode gap) and SDs (like direct contact with the surface) are combined in this type of discharge. In order to be able to optimize

the properties of CDs for special applications it is necessary to understand their behavior. For this purpose the ignition conditions as well as the structure of CDs has been investigated.

2. EXPERIMENTAL SETUP

In order to investigate the discharge behavior in CD arrangements, a simple model device has been developed with the possibility to change easily the electrode distance and the thickness of the dielectric layer above the electrodes. In order to facilitate optical investigations, the electrode distance was chosen in the range of a few millimeters.

The model device consists of a Teflon plate with milled deep grooves. Thin electrodes are placed in these grooves and they are poured with epoxy resin in order to improve the dielectric strength of the device (Fig. 2).

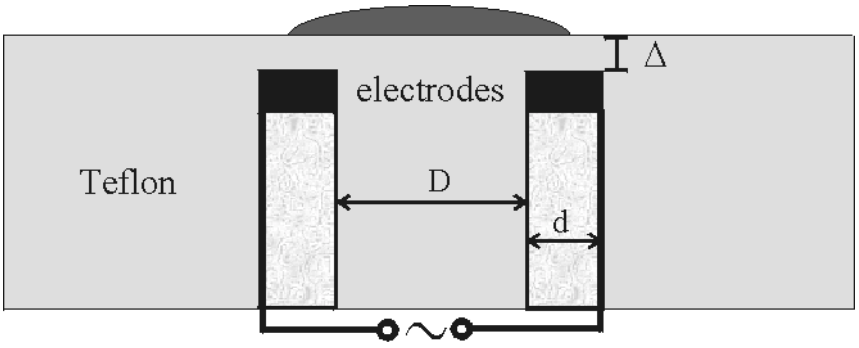


FIGURE 2. Sketch of the model coplanar discharge arrangement (D - electrode separation, d – electrode width, Δ - thickness of the Teflon layer above the electrodes).

3. IGNITION VOLTAGE

The ignition voltage of DBDs depends on the arrangement. It differs considerably. While it is comparatively low in SD arrangements (ignition at the Paschen minimum), it is rather high in CD arrangements, even much higher than in VD arrangements with a comparable electrode distance.

The reason is found in the different field strength distributions. While the field strength distribution in VD devices is rather homogeneous in the gas gap, the situation is quite different in CD devices (Fig. 3). Here the field strength maximum is in between the electrodes within the dielectric bloc. For the breakdown in the gas region the tangential component of the field strength in parallel to the surface of the dielectric is of importance.

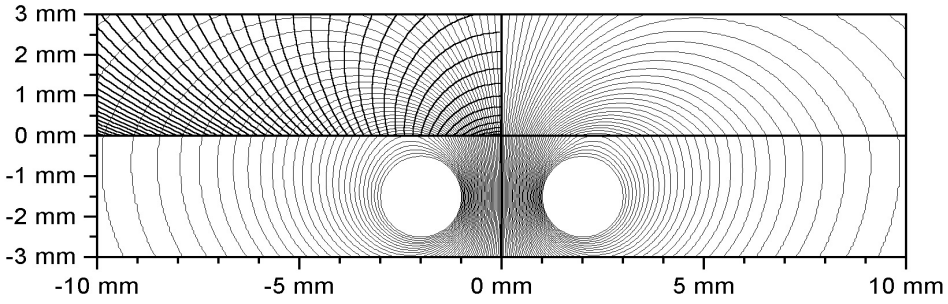


FIGURE 3. Equipotential lines of a coplanar arrangement with round electrodes and added field strength lines in the upper left part of the figure.

In Fig. 4 the absolute value of the electric field strength in the gas region above the dielectric surface is given for different electrode distances (round electrodes). The shape changes with growing electrode

distance. At 2 mm distance a single maximum appears, at the higher values two of them at the location of the electrode edges.

From the figure follows an electric field strength of 3.2 kV/cm in the gas region between the location of the electrodes with a distance of 2 mm. In a VD arrangement with a 2 mm gas gap the electric field strength is higher, 5 kV/cm, with the consequence of a remarkable lower ignition voltage.

For larger electrode distances the breakdown voltage is mainly determined by the value of the field strength minimum, which occurs in the gas space in between the location of the electrodes.

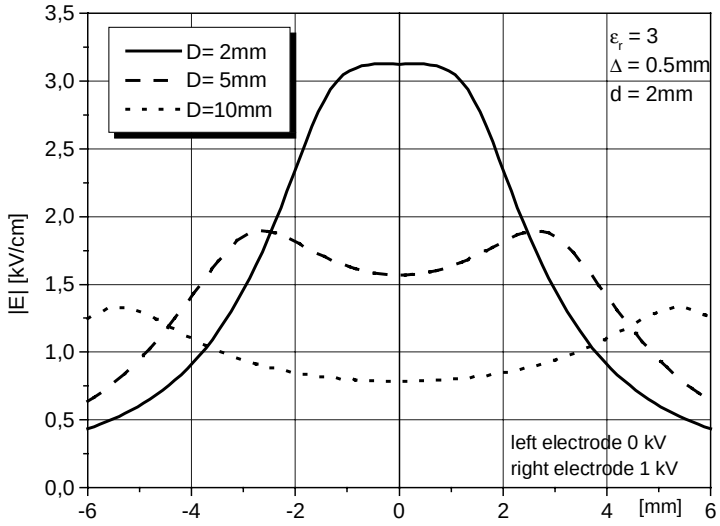


FIGURE 4. Absolute value of the electric field strength in the gas region above the dielectric surface for different electrode distances D (round electrode with a diameter of d = 2 mm).

The electric field strength in the gas region depends not only on the electrode distance, but also on the thickness of the dielectric Δ, its permittivity and the shape of the electrodes. In Fig. 5 the electric field strength distributions in the gas region above the electrodes are given for three different electrode shapes. The sharp edges of rectangular shaped electrodes cause a higher field strength than round electrodes even with a diameter of 1 mm.

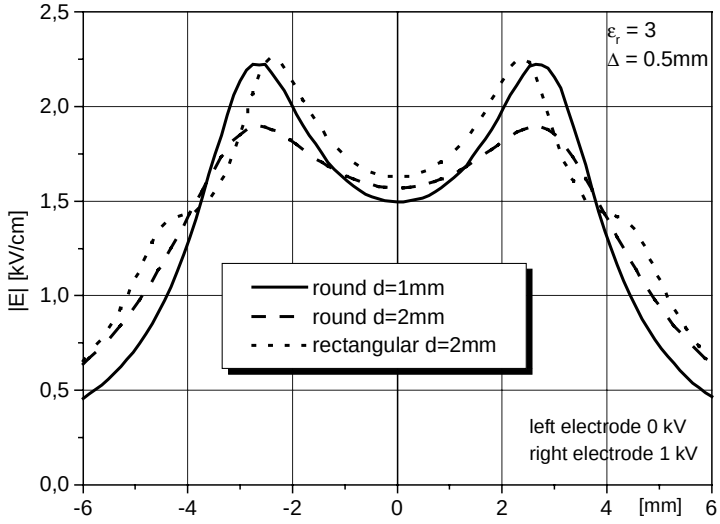


FIGURE 5. Absolute value of the electric field strength in the gas region above the dielectric surface for different shapes of the electrode (electrode distance 5 mm).

With the knowledge of the minimum field strength in the gas space at the location between the electrodes, the ignition voltage can be estimated. Dividing the critical field strength value (about

30 kV/cm for air at atmospheric pressure) by this minimum value the ignition voltage for the given arrangement results.

In Fig. 6 the ignition voltages resulting from such estimations are depicted together with measured values for different electrode distances. At small electrode distances a certain influence of the electrode shape on the ignition voltage is given. The larger the electrode distance the less is this influence. The measured values are in good agreement with those found by estimation.

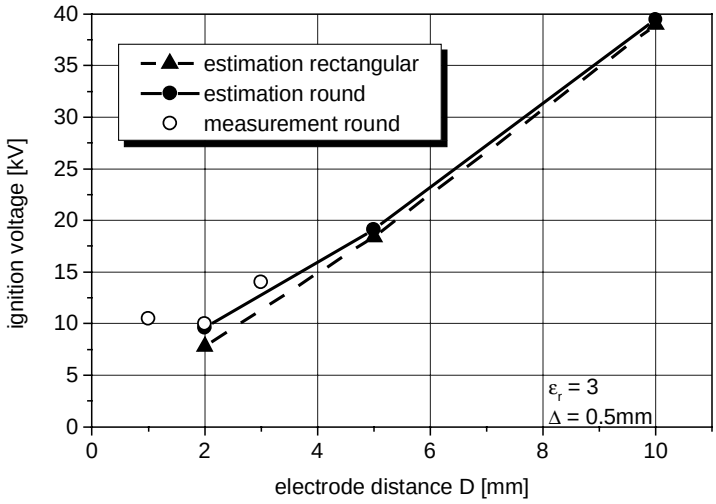


FIGURE 6. Estimated and measured values for the ignition voltage for different electrode distances D in air at atmospheric pressure.

4. OPTICAL INVESTIGATIONS

In Fig. 7 a photograph of a discharge channel in a coplanar arrangement just at ignition voltage with short exposure time is shown. The position of the two round electrodes with a diameter of 2 mm inside the Teflon plate is marked by dashed lines. On the left side is the cathode and on the right the anode. This photo was taken with an intensified CCD camera in ambient air and an electrode distance of 2 mm.

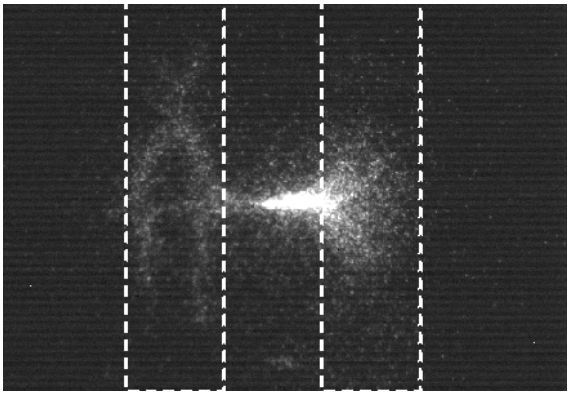


FIGURE 7. Photograph of a discharge channel on the dielectric surface from the top (CD arrangement, cathode left, 2 mm electrode diameter and distance, dielectric Teflon, ambient conditions, exposure time 200 ns).

The discharge channel in between the position of the electrodes looks quite similar to those, which are taken from VD arrangements. There exist a dark zone in front of the cathode and the channel looks a bit like cone shaped. The discharge propagates even on the area above the electrodes. The structure in these regions differ. Above the cathode weak channels can be distinguished, above the anode is a homogeneous discharge distribution. These patterns corresponds to those of the corresponding

footprints of microdischarges in VD arrangements [2, 4].

In Fig. 8 photographs of CDs are shown of an arrangement with 2 mm electrode distance, however, with electrode widths of 8 mm. The left one is taken during voltage rise, the right one nearby voltage amplitude, both with an exposure time of 5 µs (period duration 50 µs). A number of nearly parallel channels appears with almost equal distances from one another. The patterns of the channels during voltage rise corresponds to those at ignition voltage (Fig. 7), while at enlarged voltage the character changes. The channels become longer and stronger and seem to discharge larger areas above the electrodes farther from the gap midst. With SDs and high voltage values a similar phenomenon has been observed [5]. Within the exposure time some additional rather faint channels are detected. They result from discharging a limited area in between strong channels due to the rise of voltage. The far distant areas are already discharged by the strong channels so that a limited area is left.

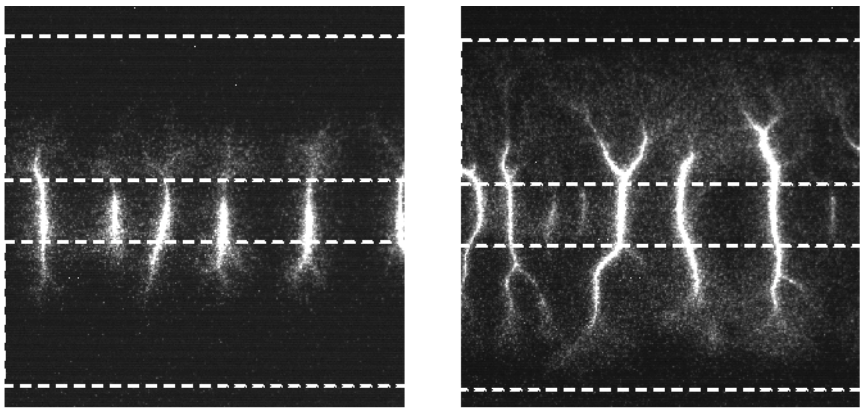


FIGURE 8. Photographs of discharge channels on the dielectric surface from the top, left during voltage rise and right at voltage maximum (exposure time 5 µs, AC of 20 kHz, voltage amplitude 30 kV, ambient air, electrode distance 2 mm, width 8 mm, cathode at the top).

5. CONCLUSIONS

Investigating the initial field strength distribution of CD arrangements it has been found that the character depends on electrode distance. At larger distances two field strength maxima appear. The value of the minimum between them allows to estimate ignition voltages, which are in good agreement with measured values. The shape of the electrodes has only a limited influence on ignition voltage. In comparison to VDs the ignition voltage of CDs is remarkable higher.

From photographs taken with an intensified CCD camera follows that the CDs consist of more or less parallel discharge channels, which discharge even the area above the full width of the electrodes at high voltage amplitudes. Their structure is similar to those of microdischarges in VD arrangements.

REFERENCES

[1] Kogelschatz U., Eliasson B., and Egli W., Dielectric-Barrier Discharges - Principle and Applications, *J. Physique **IV***, C4 47-66 (1997)

[2] Gibalov V. I., and Pietsch G. J., The Development of Dielectric Barrier Discharges in Gas Gaps and on Surfaces, *J. Phys. D: Appl. Phys.* **33**, 2618-36 (2000)

[3] Haacke M., and Pietsch G. J., Some Features of Dielectric Barrier Discharges, In: *13th Int. Conf. on Gas Discharges and Their Applications*, Glasgow, UK, 2000, pp. 267-70

[4] Heuser C., and Pietsch G., Prebreakdown phenomena between glass-glass and glass-metal electrodes, In: *6th Int. Conf. on Gas Discharges and Their Applications*, Edinburgh, IEE Conf. Publ. 189, 1980, pp 98-101

[5] Saveliev A. B., and Pietsch G. J., On the Structure of Dielectric Barrier Surface Discharges, In: *Proc., 8th Int. Symp. on High Pressure, Low Temperature Plasma Chemistry (Hakone VIII)*, Pühajärve, Estonia, 2002

DEVELOPMENT OF A NEW TYPE OZONIZER WITH ROTATING ELECTRODE

T. Horinouchi, T. Hayashi and N. Nakajima

Department of Electrical Engineering, Chiba Institute of Technology,
Tsudanuma Narashino Chiba 275-0016, JAPAN

Abstract. We propose a new type ozonizer using silent discharge in this paper. The grounded 36 pieces of tungsten wires are fixed parallel to the rotation axis on the rotating cylinder surface. Two dielectric high voltage electrode shaped thin plates are attached on the casing of ozonizer 1 mm apart from the rotating cylinder surface. The speed of the rotating electrode is varied from 0 to 1200 rpm by a variable speed motor. Obtained ozone concentration and ozone generation efficiency increases than the case of which the electrode does not rotate. The maximum generation efficiency is estimated to be 61 g/kWh at 800 rpm, and this value is twice as large as the case of no rotation.

1. INTRODUCTION

Many studies of ozone production have been conducted practically in the field of technology, for example, improvement of the human environment, especially concern with water and air treatment [l - 3]. A new type ozonizer [4, 5] is introduced using silent discharge generated between the fixed electrodes covered with thin ceramic sheet and the cylindrical rotating electrode. High voltage is applied to the fixed dielectric electrodes and the rotating electrodes are grounded. Electric current and discharge power are enhanced by the rotation of cylinder electrode, which is driven by a variable speed motor. Furthermore, ozone concentration and yield are also increased in each applied voltage. The micro discharge appeared in the gap is observed by static photographs and oscillograms. The maximum ozone generation efficiency is obtained by the value of 61 g/kWh at 800 rpm.

2. EXPERIMENTAL APPARATUS AND METHOD

The apparatus using this experiment is similar to the ones reported in the previous papers [5 - 7]. The structure of electrode unit is shown in Fig. 1. The rotating cylinder ① is made of acrylic resin. The grounded 36 pieces of tungsten wires ① are fixed parallel to the rotating axis of the cylinder on

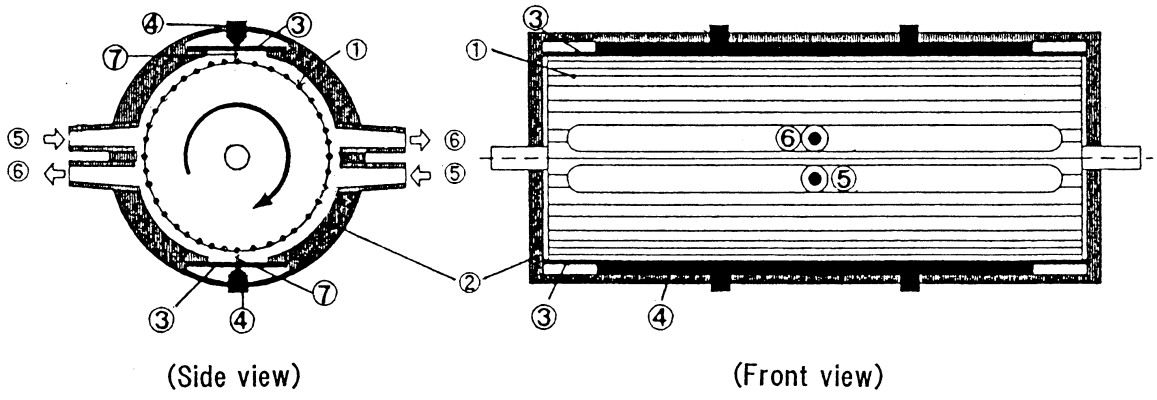


FIGURE 1. Structure of electrode

the surface of the rotating cylinder ①. The diameter of the wire is 0.5 mm. The chamber ② is made of acrylic resin. The diameter of the chamber is 12 cm and its length is 25 cm. The dielectric electrodes made of almina ceramic plate ③ fixed on the conductor ④ are high voltage electrodes and they are located on the inside of the chamber. The length of the dielectric electrode is 21.5 cm and the width is 8 cm. The length of the gap ⑦ between the rotating electrode and the fixed electrode is 1 mm. Ozone is generated in the gap. The 99.95% oxygen gas is used in this experiment. The gas flows into the electrode gap though the inlet ⑤ and flows out from the outlet ⑥. The flow rate of gas is fixed at 1.5 l/min and the temperature is kept between 18°C and 24°C. The rotation speed of the rotating electrode can be varied from 0 to 1200 rpm. AC 50 Hz high voltage is applied to the dielectric electrodes through a leakage transformer. The discharge current is detected by the resistor of 10 kΩ. Lissajous figure is observed by the capacitor of 1 μF and the potential divider. The figure is used for the measurement of the discharge power. The concentration of ozone is measured by ozone-monitor using the 254 nm photo-absorption method.

3. EXPERIMENTAL RESULTS AND DISCUSSIONS

3.1. Discharge power and rotation speed

Fig. 2 shows Lissajous figure observed by the variation of the rotation speed of the rotating electrode 0, 700 and 1200 rpm at 7 kV in applied voltage. It can be obtained from the discharge energy for one cycle as the following formula.

$F=2e_0q$ (J). F : Dissipate energy,

e_0 : Sustaining voltage of discharge,

q : Electric charge of discharge for half-cycle.

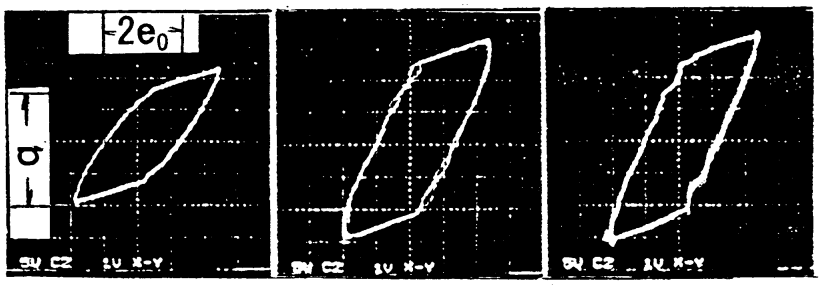


FIGURE 2. Voltage-charge Lissajous figures for 0, 700 and 1200 rpm.

The gap length of electrode is not constant owing to the rotation; nevertheless the sustaining voltage of discharge e_0 is almost constant. In Fig. 2, it can be easily know that discharge power is larger with the increasing of the rotation speed of the electrode.

Fig. 3 shows the relationship between the rotation speed and the discharge power. The discharge power has maximum about 600 rpm in each applied voltage. When the rotation speed is over more than 600 rpm, the discharge power decreases monotonically.

3.2. Ozone concentration and ozone yield versus rotation speed.

Fig. 4 shows the variation of ozone concentration and the ozone yield depended to rotation speed. The ozone concentration rapidly increases by the increasing of the rotation speed up to 800 rpm. When the rotation speed is more than 800 rpm, the ozone concentration is decreased. 8.7 g/m^3 can obtain as the

maximum ozone concentration. The maximum ozone yield of 0.79 g/h at 8 kV is estimated, as supposing that the loss of ozone from the chamber to the ozone monitor is not considered.

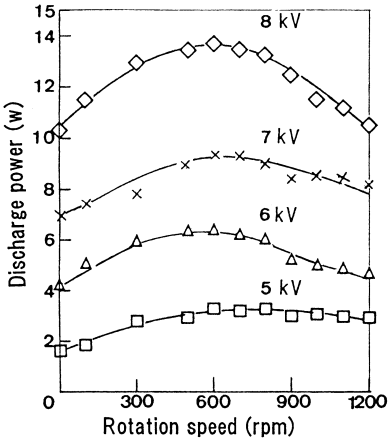


FIGURE 3. Relation of discharge power vs. rotation speed.

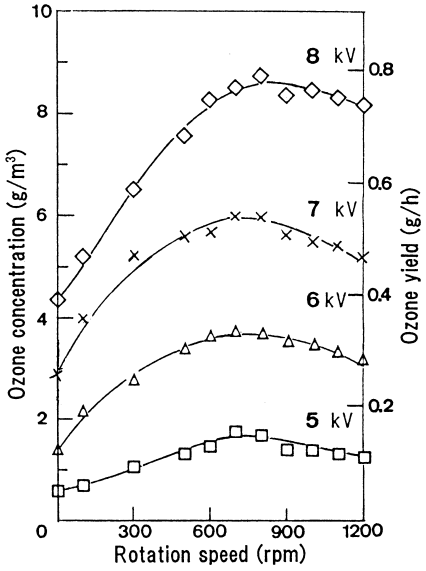


FIGURE 4. Relation of ozone yield and its concentration vs. rotation speed.

3.3. Wave forms of discharge current and discharge lights.

Fig. 5 shows the voltage and the current waveforms of discharge, and it shows the photographs in the discharge gap of ozonizer. The rotation speed is varied from 0 to 1000 rpm under constant applied voltage of 8 kV.

In the rotation speed from 0 to 400 rpm, discharge spots appeared on the rotating electrode in the front view of the photograph and the glow like column is found in the side views of the photographs. In the case of the rotation speed of 400 rpm, the glow like discharge separated into two parts. In this case, many pulses are observed in the current waveform. The pulse current enhances the increase of the discharge power and the ozone concentration as shown in Fig. 2, 3 and 4.

On the contrast, at rotation speed from 600 to 800 rpm, the discharge column spread over the gap. Furthermore, the case of 800 rpm, we can observe many intensive and fine discharge channels in the front view of the photograph. We name this "micro discharge". From the results, we consider that the micro discharge gives the increase of ozone concentration without the increase of the discharge power. The maximum ozone concentration is obtained at about 800 rpm. This 800 rpm is the optimum condition for the ozone production in this ozonizer. The pulse components of current waveform appear frequently on the oscillogram, and the pattern of discharge light shows almost dense and uniform in the gap space. If the rotation speed is over 1000 rpm, the discharge light in the discharge gap becomes weak and the micro discharge disappears.

Namely when the rotation speed becomes fast, it is assumed that the micro discharge can not maintain in the gap. At 1000 rpm, the pulse components of current waveform decrease on the oscilloscope and the discharge light change more weakly.

3.4. Ozone concentration and discharge power versus rotation speed.

Fig. 6 shows the variation of the ozone concentration and discharge power against the rotation speed at applied voltage of 8 kV.

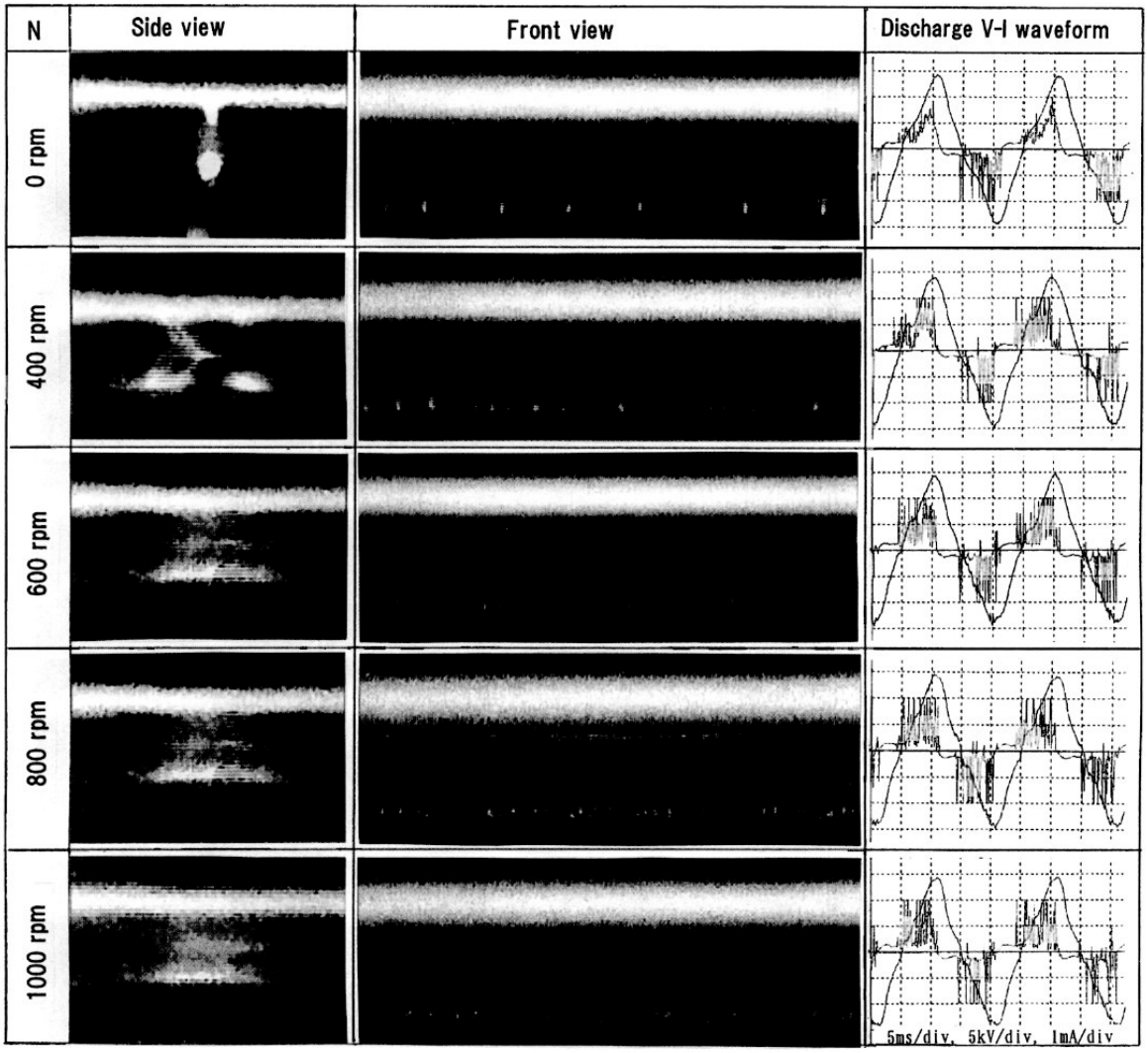


FIGURE 5. Voltage—current waveform of discharge and discharge light. (Applied voltage: 8kV)

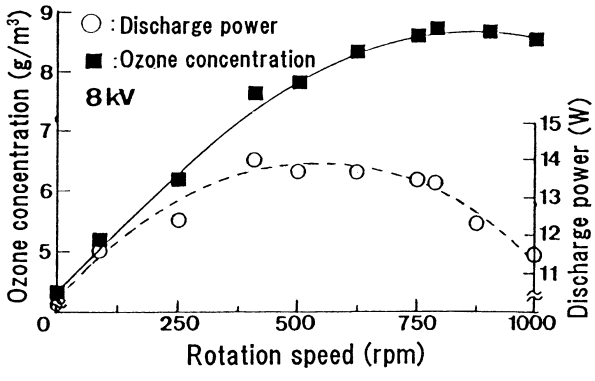


FIGURE 6. Relation of ozone concentration and discharge power vs. rotation speed.

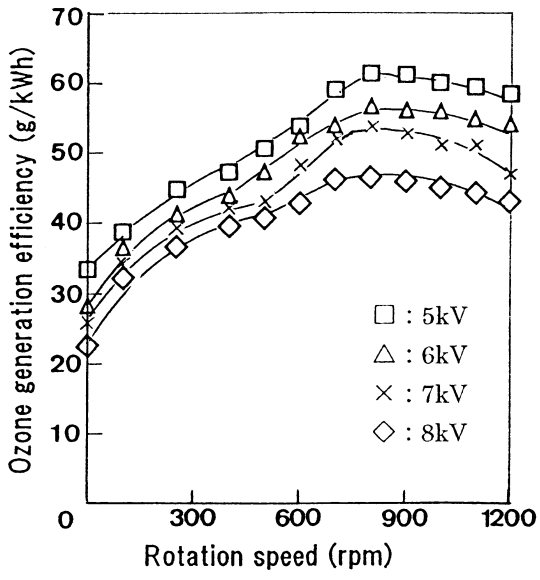


FIGURE 7. Relation of ozone generation efficiency vs. rotation speed.

Discharge power and the ozone concentration become the maximum about 600 rpm and 800 rpm, respectively. It is important to note both maxima did not show at the same rotation speed. At first, the discharge power reaches the maximum at 600 rpm. After that the value decreases with the increasing of the rotation speed, but the ozone concentration increased and reached the maximum at 800 rpm. Owing 600 ~ 800 rpm, the micro discharge is found in the photograph and current waveform. So we consider that the micro discharge is the main cause to give the peak of ozone concentration at 800 rpm.

3.5. Ozone generation efficiency and rotation speed.

Fig. 7 shows the rotation speed dependence on the ozone generation efficiency. The ozone generation efficiency increases and shows a saturation curve, but the value rapidly increases again from 600 rpm to 800 rpm. This increment is supported by the micro discharge. The ozone generation efficiencies are improved about twice as large as than the case of rotation. 61 g/kWh is obtained as the maximum ozone generation efficiency under the conditions by the speed of 800 rpm and at applied voltage of 5 kV.

4. CONCLUSION

The development of the ozonizer using a rotating electrode is described. The obtained results are shown as follows.

(1) Discharge power, ozone concentration and ozone generation efficiency are improved by using the rotating electrode.

(2) Under the same applied voltage, discharge power and ozone concentration has the maximum at 600 rpm and 800 rpm, respectively.

(3) The rotation of electrode gives the enhancement of discharge current, discharge power, ozone concentration and ozone generation efficiency.

(4) The rotation effect includes two mechanism:
i) pulsing current component increases up to 600 rpm.
ii) the stable micro discharge is observed in 600 ~ 800 rpm.

(5) The rotation effect disappeared over the 800 rpm, and discharge current, power, ozone concentration and ozone generation efficiency decrease monotonically.

(6) The optimum condition of ozone production is 800 rpm.

REFERENCES

[l] Eliasson B., Hirth M. and Kogelschatz U., *J.Phys.D: Appl. Phys*., **20**, 1421 (1987)
[2] Technical report of IEEJ (II), No. 340, (1990), pp.33-44.
[3] Tomasz C., Yamabe C., Ihara S., et al., *Ozone Sci. and Eng.*, **22**, No.6, (2000), pp.563-574.
[4] Horinouchi T., Hayashi T. et al., In: *Asia-Pacific Conf. Plasma Sci. and Tech.*, Vol. II, P-3, 1992, pp.497-500.
[5] Horinouchi T., Hayashi T., *National Convention Record, IEEJ*, pp.2-30, (1989).
[6] Hayashi T., Horinouchi T., and Nakajima N., Proc. 15th Ozone World Congress, Vol.3, (2001), pp. 76-81.
[7] Horinouchi T., Hayashi T.and Koma A., In: *Proc. of 9th Annual Conf. Ozone Sci. and Tech. Japan*, **13**, (2000), pp.40-43.

APPLICATION OF SURFACE DISCHARGES IN ELECTROPLASMA OZONE SYNTHESIS

S. Jodzis

Warsaw University of Technology, Noakowskiego 3, 00-664 Warszawa, POLAND

Abstract. The results of tests of a prototype ozonizer with forced electric charges passage over the dielectric surface and directed gas flow are presented. An improvement of the heat exchange conditions was obtained. The ozone concentrations achieved in a surface discharge type ozonizer were comparable with those obtained when silica packing is placed in the discharge gap.

1. INTRODUCTION

Electroplasma ozone synthesis is a process usually treated as completely homophase. In reality the process takes place in a narrow discharge gap (typically 1-2 mm) between electrodes of significant surface area. In such conditions the contact of the reacting substances with the electrodes walls is completely natural. The walls can among others participate in energy stabilisation of excited ozone molecules. On the other hand in the barrier discharge conditions the electrodes walls made of a dielectric material participate in dissipation and transfer of electric charges. The surface discharges (SD) are one from penetratingly examined in last years of phenomenon used in ozone synthesis [1-12]. The charge transfer over the dielectric surface is especially intensive when dielectric material joins both electrodes. This takes a place when the discharge gap is filled with fine-grained packing [12-19]. A change in the character of electric charges transfer between electrodes is the consequence of the presence of dielectric material in the discharge gap. Simultaneously, the electric field undergoes local disturbances.

The attempts of using some dielectric materials placed in the discharge gap in the form of fine-grained packing proved that the packing can cause a profitable effect of an increase in the ozone content, connected with a decrease in energy consumption, that gives an increase in the process energy efficiency [13-18]. In the presence of dielectric packing in the discharge gap the process running in it bears heterophase features. Detailed investigations led to suggesting a hypothetical mechanism of the process proceeding on the grains surface [13, 19]:

$$O_2 + e \rightarrow O + O + e \quad (1)$$

$$O_2 \rightarrow O_{2(ads)} \quad (2)$$

$$O_{2(ads)} + O \rightarrow O_{3(ads)} \rightarrow O_3. \quad (3)$$

The surface of the grains stabilises the ozone molecules by taking off the energy excess, according to reaction:

$$O_3^* + M \rightarrow O_3 + M. \quad (4)$$

The heat coming out on the surface of the grains is conducted in the direction of cooled electrodes and carrying out from discharge gap. Part of the heat is carried out also by the gas stream. The gas flow velocity enlarged in the presence of packing additionally enables an easy exchange of heat between the gas and both grains of packing and electrodes walls. As a result of the decrease in average gas temperature in the gap, the reactions in effect of which the ozone concentration decreases are inhibited (reactions 5 and 6) and the reaction of ozone synthesis is accelerated (reaction 7):

$$O + O_3 \longrightarrow O_2 + O_2 \qquad k = 1{,}8 \cdot 10^{-11} \cdot \exp(-2300/T) \quad (5)$$

$$O + O + M \longrightarrow O_2 + M \qquad k = 3{,}8 \cdot 10^{-30} \cdot 1/T \cdot \exp(-170/T) \quad (6)$$

$$O + O_2 + M \longrightarrow O_3 + M \qquad k = 6{,}4 \cdot 10^{-35} \cdot \exp(663/T) \quad (7)$$

Electronic adress: jodzis@chemix.ch.pw.edu.pl

In the classical Welsbach or Siemens type ozonizer glass pipe is the dielectric. In such a case the modification of discharges by the use of grains of packing slipping away in an accidental manner and causing the formation of tensions in the glass which can produce the breaking of glass.

An other way of forcing of surface discharges can be the use of a dielectric barrier e.g. from an organic material formed as a sleeve with a system of longitudinal grooves in which gas can flow. Such a solution permits to eliminate the cracking of glass, and also diminishes the gas flow resistance and arrange its motion (limitation of streaming effect).

2. EXPERIMENTAL

In figure 1 the construction of an ozonizer of surface discharges is presented. The dielectric's shape assured steered gas flow by channels along the electrodes. The movement of electric charges was also more ordered – it can pass through the gas space (like at non-filled gap) or over the dielectric surface like in the case of the gap operating with packing. The passage of electric charges has to a considerable degree a character of surface discharges. The appropriate selection of the dielectric material and modification of its surface conductance by means of depositing of additional coatings permits to modify the surface discharges intensity. These coatings protect also against the aggressive action of ozone. Hard PVC covered with an active layer of SiO_2 deposited from TEOS was used as a dielectric. The dielectric was double-side cooled by a stream of liquid. Favourable conditions of cooling the interelectrode space were obtained and ozone concentrations comparable with these obtained in an ozonizer of the same dimensions of the gap (Fig. 2a) filled with fine-grained silica. The ozonizer was supplied with 1 kHz A.C. (voltage up to 14.5 kV). The measurements were carried out in pure oxygen (dew point of ca. –76ºC).

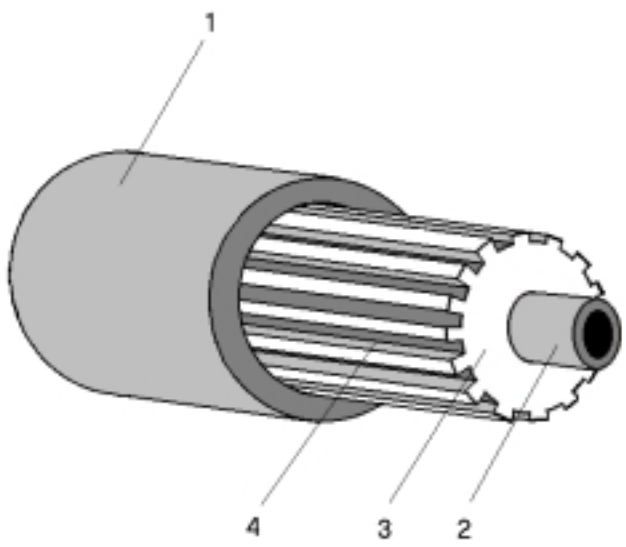


FIGURE 1. Construction of SD type ozonizer: 1 – cooled outer electrode, 2 – cooled inner electrode, 3 – dielectric, 4 – discharge gap.

3. RESULTS AND DISCUSSION

In Figure 3b the characteristics of SD type ozonizer for oxygen flow rates of 4, 32 and 100 Ndm^3/h and temperatures of thermostating liquid of 0, 25 and 50ºC vs. discharge active power is presented. When comparing it with analogous characteristics of a pipe type ozonizer from Fig. 2a operating with silica packing it can be seen, that appropriate ozone concentrations obtained in a SD type ozonizer are similar or higher.

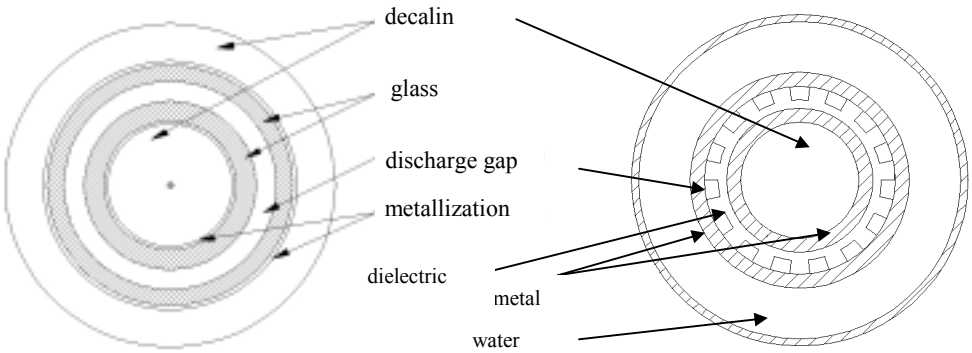


FIGURE 2. Comparison of the discharge gap construction of pipe-type ozonizer with double-side cooling system: a) Siemens type, b) SD type ozonizer.

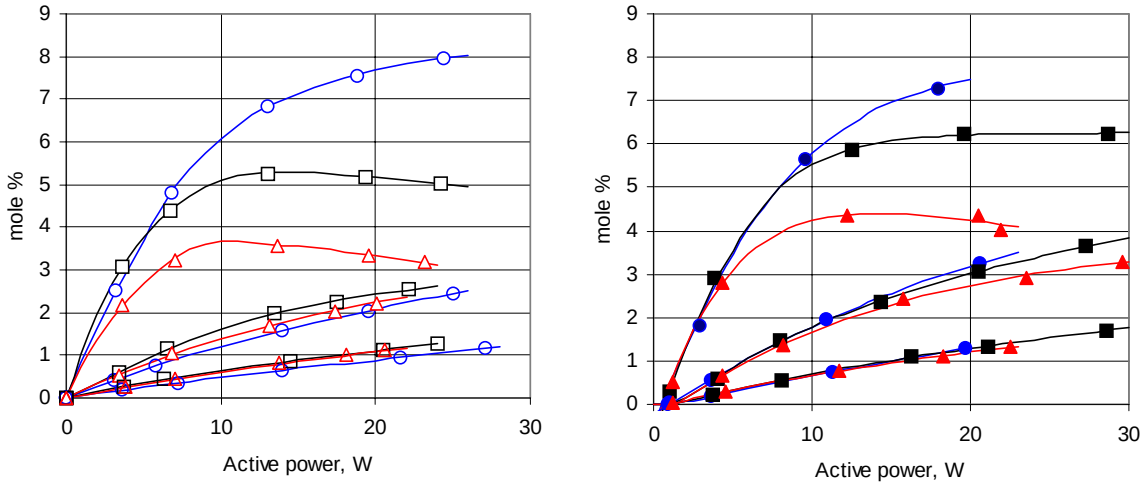


FIGURE 3. Ozone content vs. active power, a) all-glass ozonizer, b) SD type ozonizer: 4 Ndm^3/h, 32 Ndm^3/h, 100 Ndm^3/h; ○,● – 0°C, □,■ – 25°C, Δ,▲ – 50°C.

TABLE 1. Comparison of features of SD type ozonizer.

Advantages:	**Faults:**
• Ease of realisation of discharge element with needful both length and diameters, • ease of coaxial assurance of electrodes, • possibility of obtaining an equal dielectric thickness, • mechanical strength (elimination of susceptible on bursting of glass electrodes), • possibility of elimination of dielectric metalization, • increased resistance on gas moisture in relation to the ozonizer with a grain dielectric layer.	• Necessity of mechanical working of a dielectric, • necessity of coating the dielectric with protective layers, • low resistance on dielectric overheating (possibility considerable improvement in a case of ceramic dielectric usage), • still troublesome heat removing from the gap.

Characteristics of prototype ozonizer (10 cm electrode active length):

Surface energy density	0.10÷0.15 W/cm^2,
Gas flow velocity	up to 1.5 m/s (100 Ndm^3/h),
Efficiency	0.5-3 g/h O_3 (4-100 Ndm^3/h),
Unity efficiency	100-600 g/m^{2}h,
Ozone concentration	up to 120 g/m^3 (25ºC).

4. SUMMARY

The results obtained in a SD-type ozonizer and comparison of them with the characteristics of a typical pipe ozonizer indicate an advantageous influence of modification of the dielectric shape on ozone concentration obtained. It appears that effect observed to a considerable degree results from changes of discharges character in reaction zone. However, except of dielectric surface properties making possible reaching of the chemical reaction in accordance with a probable mechanism (reactions 1-3), the essential influence on concentrations attained has also the average gas temperature in the gap. This temperature depends among others from the gas flow velocity and dielectric ability to remove the heat from the reaction space. From temperature the rates of reaction 5-7 are dependent. Temperature of the gas, influencing on temperature of dielectric surface changes also its electric properties and influences on surface conductance.

1. The advantageous influence of the dielectric in the form of a profile making possible the electric charges passage over the surface joining the electrodes and of the gas flow in channels along the electrodes has been found.
2. Due to the elimination of glass elements, a considerable mechanical strength of the ozonizer was obtained, in relation to the Welsbach type construction generally used. The replacement of expensive and impermanent calibrated glass pipes by easily to form organic material can be a concurrent manner of production of discharge elements with perfect geometry. Such a solution assures an easy obtaining of concentricity of electrodes and equal distance among them, what in chemical processes reaching under electric discharge conditions is especially essential.
3. The construction proposed could be an effective concurrent device for generally used glass ozonizers, but suitable finishing up to the details (type and properties of dielectric material, section and shape of gas channels) should be determined.

REFERENCES

[1] Masuda S., Koizumi S., Inouhe J., Araki H., *IEEE Trans. on Industry Applications*, **24 (5),** 928 (1988)

[2] Humpert C., Pietsch G., Simulation of Ozone Synthesis in Oxygen- and Air-Fed Surface Discharge Arrangements. In: *Proc. 15th Ozone World Congress IOA*, London, 2001, pp. 15-29

[3] Richter R., Pietsch G.J., Discharge Phenomena on a Dielectric Surface and Ozone Concentration Distributions. In: *Proc. 4th Int. Symp. on High Pressure Low Temperature Plasma Chemistry*, Bratislava, 1993, pp. 13-18

[4] Hasegawa T., Sakiyama M., Fujioka J., Fujii S., Sugiyama K., Effect Cooling on Ozone Yield in Surface Discharge Type Ozone Generator. In: *Proc. 13th Ozone World Congress IOA*, Kyoto, 1997, P-11-4, pp. 189-92

[5] Pietsch G.J., Haacke M., Some Properties of Different Types of Dielectric Barrier Discharges for Ozone Production. In: *Proc. 7th Int. Symp. on High Pressure Low Temperature Plasma Chemistry*, ed. by H.-E. Wagner, J. F. Behnke, G. Babucke, Greifswald, 2000, pp. 299-303

[6] Humpert C., Pietsch G.J., Ozone Synthesis in Surface Discharge Arrangement During Voltage Rise. In: *Proc. 7th Int. Symp. on High Pressure Low Temperature Plasma Chemistry*, ed. by H.-E. Wagner, J. F. Behnke, G. Babucke, Greifswald, 2000, pp. 334-8

[7] Satoh S., Katsuki N., Hakiai K., Ihara S., Ishimine M., Yamabe Ch., An Effect of Superposition of Positive Streamer and Surface Discharge on Ozone Generation. In: *Proc. 13th Ozone World Congress IOA*, Kyoto, 1997, C2-2-5, pp. 865-70

[8] Murata T., Moniwa S., Okita Y., Kanemaru K., Terai K., High Concentration Ozone Generation in Surface Discharge. In: *Proc. 13th Ozone World Congress IOA*, Kyoto, 1997, C2-3-2, pp. 895-900

[9] Padmanabhan K., Ananthi S., Kirit P., Nedumaran D., Ozone Generation with Edge Discharge Electrode for Air Purifiers. In: *Proc. 13th Ozone World Congress IOA*, Kyoto, 1997, C2-4-2, pp. 939-44

[10] Pietsch G.J., Haacke M., Parameters Influencing the Yield of Surface Discharge Ozone Generators. In: *Proc. 14th Ozone World Congress, IOA*, Michigan, 1999, vol. 1, pp. 311-23
[11] Pietsch G.J., Gas Discharges in Ozone Generators. In: *Proc. Regional IOA EA3G Conf. ECWATECH-98*, Moskva, 1998, pp. 13-28
[12] Schmidt-Szałowski K., Zarębski W., *J. Chim. Phys.* **88**, 1849-63 (1991)
[13] Schmidt-Szałowski K., *Ozone Sci. & Eng*., **18**, 41-55 (1996)
[14] Schmidt-Szałowski K., Jodzis S.., Application of Silica as a Catalyst for Ozone Synthesis in Oxygen and in Air. In: *Proc. 3rd Int. Symp. on High Pressure Low Temperature Plasma Chemistry*, Strasbourg, 1991, pp. 33-40
[15] Schmidt-Szałowski K., Jodzis S., *Acta Physica Universitatis Comenianae*, **34 (1)**, 19-32 (1993)
[16] Schmidt-Szałowski K., Jodzis S., Applying the Heterogeneous Catalysis to the Ozone Generation in Silent Discharges. In: *Proc. 2nd Int. Symp. on High Pressure Low Temperature Plasma Chemistry*, ed. by Technical University Lublin, Kazimierz Dolny, 1989, pp. 51-5
[17] Schmidt-Szałowski K., Kowalczyk Z., Jodzis S., *Pol. J. Appl. Chem.*, **37 (3-4)**, 183-92 (1993)
[18] Schmidt-Szałowski K., Catalytic Properties of Silica Packing Under Ozone Synthesis Conditions. In: *Proc. Int. Ozone Symp. IOA*, „Application of ozone in water and wastewater treatment", ed. by A. K. Bień, Warsaw, 1994, pp. 243-52
[19] Schmidt-Szałowski K., Jodzis S., Kinetic-Energetic Characteristics of the Catalytic Ozone Synthesis in Electrical Discharges. In: *Proc. Europ. Ozone Conf*., Belgrade, 1990, pp. 125-35

TOPIC 5:

Generation of radiation in high pressure discharges

SPECTROSCOPIC DIAGNOSTICS OF HIGH-CURRENT DISCHARGES IN UV-VUV EXCIMER LASERS

A.Treshchalov[a], A. Lissovski and E. Chikeev

Institute of Physics, University of Tartu, Riia 142, 51014 Tartu, ESTONIA

Abstract. The aim of this work is spectroscopic diagnostics of a discharge in a new compact "sealed-off" excimer laser. Spatial-time behaviors of the main excited atomic and ionic species, gas temperature and electron density were monitored with ns-gated ICCD camera from spontaneous emission spectra of the discharge. At increased current density cathode hot spots appear after the end of the pumping pulse because of delayed explosion of overheated emission centers on the cathode surface.

1. INTRODUCTION

There have been considerable demands for the development of compact excimer lasers in the vacuum ultraviolet (VUV) spectral range. Such lasers would be applicable to various scientific and industrial fields. Ignition of a homogeneous high-current discharge in high-pressure gas mixtures with halogen additives (UV-VUV excimer lasers' active media) is a serious physical and technical problem.
The main emphasis of this work is directed to the understanding of conditions for discharge operation with enhanced stability to the constriction.

2. EXPERIMENTAL

Compact "sealed-off" excimer laser with long operation lifetime and improved efficiency, developed in close collaboration with Neweks company, is the object for our investigation. The laser has the following output parameters: pulse energy KrF (248 nm) -12 mJ, ArF (193 nm) -10 mJ, F_2 (157 nm) - 3 mJ; pulse duration 5 ns. Maximum repetition rate of the laser is restricted to 400 Hz by the development of constrictions in the discharge. Nowadays this laser with true modular design and recycling laser enclosure is the most compact commercially available excimer laser on the world market: weight - 14 kg, size - mid-tower computer case.
The laser discharge electrical driving circuit (see Fig.1.) is a simple thyratron-switched charge-transfer scheme with storage C_o and peaking C_p capacitors of 3 and 3-5 nF, respectively.

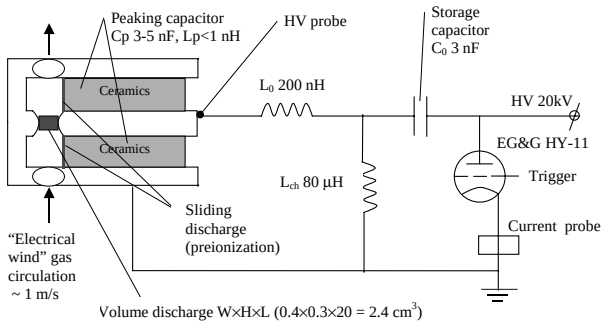


Fig. 1. Discharge excitation circuit for the excimer laser.

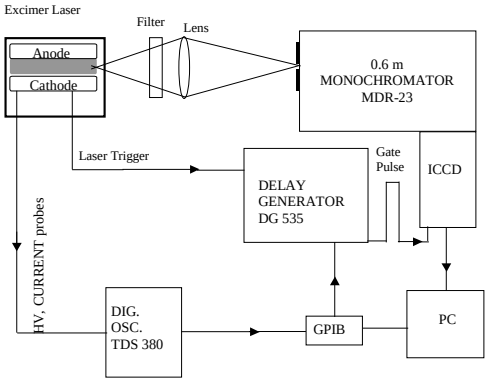


Fig.2. Schematic of the experimental apparatus

[a] Electronic address: *atr@fi.tartu.ee*

VUV automatic preionization is performed by a sliding discharge on two ceramics (sapphire) plates that are placed laterally to both sides of the cathode electrode.
Fig. 2. presents schematic of the experimental apparatus, used for the laser discharge diagnostics. Spontaneous emission from the discharge plasma is detected through the output MgF_2 laser window parallel to the discharge long axis by 0.6 m monochromator with gated ICCD camera IntraSpecV. Spectral resolution of the system is about 0.09 nm. Laser discharge and ICCD gate pulses are synchronized by a computer controlled delay generator DG-535 with a total jitter of about ± 1 ns. Signals from HV, current probes and fast vacuum photodiode are monitored by 400 MHz Tektronix-380 digitizer, connected through GPIB port with a computer.
The lens projects image of the discharge to the entrance slit of the monochromator. By adjusting the lens position it is possible to measure time evolutions of excited species from different parts of the discharge in the transverse direction of the discharge width 0.4 cm.

3. RESULTS AND DISCUSSION

3.1. Electrical characteristics

Discharges in $He/Kr/F_2$, $He/Ar/F_2$ and He/F_2 high-pressure gas mixtures are investigated in this work. Extremely low inductance of the dielectric peaking capacitor (L_p<1 nH) and uniform, intense preionization are the main peculiarities of the electric circuit used in our laser. It permits one to get a small voltage drop on this inductance and very short discharge current rise time. At this regime a large fraction of the pumping pulse duration can be utilized at a higher discharge voltage and current. The characteristic time of the first half-period of the pumping pulse (FWHM) is about 5 ns, the maximum pumping current density - about 1.5 kA/cm^2 and pumping power density - about 15 MW/cm^3.
The typical measured voltage-current characteristics are shown in Fig. 3. They are very similar for KrF, ArF and F_2 lasers with output energy-optimized gas mixtures. The minimal achieved plasma resistance is higher than 2ρ (ρ is the pumping circuit impedance, $\rho = (L_p/C_p)^{1/2} < 0.5\ \Omega$) and energy deposition into the discharge is close to a critical damped regime. At this regime the pumping takes place during the fall time of the discharge voltage and late pumping tails from a slow thyratron contour are totally absent.

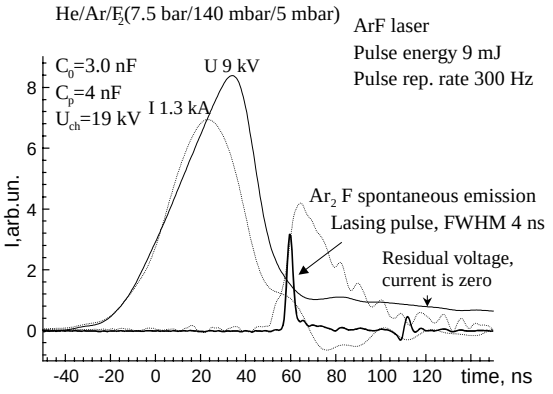


Fig.3. Voltage, current, spontaneous emission and laser pulse waveforms for ArF laser

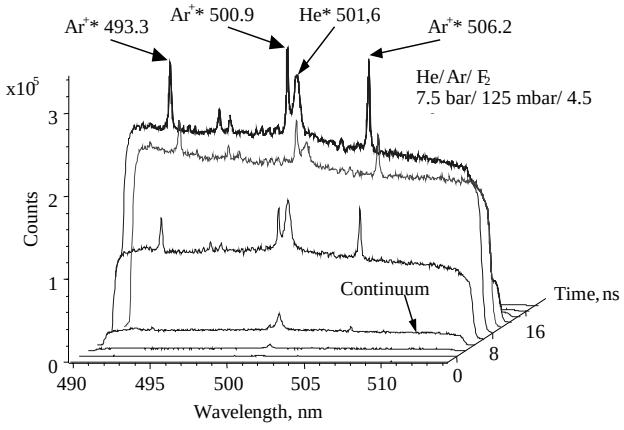


Fig. 4. Time-resolved (one step 2 ns, gate 2.2 ns) emission spectra of the bulk discharge of ArF laser.

3. 2. Time evolutions of excited species

Fig.4. presents fragment of time-resolved emission spectra from the central part of the bulk discharge plasma of ArF laser. Zero time corresponds to the beginning of the breakdown. Stark-broadened He^* and narrow Ar^{+*} lines together with strong broad continuum appear during a short discharge excitation pulse - no any long tails exist on the pumping pulse. In contrast to He^* and Ar^* so-called

primary components, excited by single-step processes, Ar^{+*} ions (as typical secondary components) appear in the discharge after obvious delay of about 4 ns, when densities of Ar^* atoms and electrons become so high that stepwise excitation-ionization processes successfully compete with direct excitation of Ar from the ground state. From this time the voltage on the discharge starts to decrease along with increase of discharge current - pumping power maximum achieves at about 8 ns.
The emission from all primary components rises exponentially in the avalanche phase of the discharge due to exponential multiplication of electrons. During this phase production of electrons is predominated by direct ionization of Ar additives. The time constant of this exponential rise is 1.2 ns. Very similar time constants were measured also for KrF and F_2 lasers with output energy-optimized gas mixtures: 1.1 and 1.4 ns respectively. In nonoptimized gas mixtures with increased helium and (or) fluorine pressures the measured time constant for multiplication of electrons exceeds 5 ns.
Electron density in the discharge was estimated from Stark broadened profiles of several helium spontaneous emission lines. Stark broadening, caused by microfields in the plasma, is well-known technique for plasma density diagnostics [1]. However, to the best of our knowledge, only few works exist where this technique is used for high-pressure discharge plasmas [2].
According to Fig. 4. at the very beginning of the discharge helium line 501.6 nm is mainly pressure broadened and has Lorentzian shape with FWHM of about 0.25 nm. At higher electron density Stark broadening adds to the pressure broadening – line becomes broader (up to about 0.6 nm) but the shape remains Lorentzian. Experimental line profiles are fitted by Lorentzian profiles and Stark broadening widths $\Delta\lambda^s$ (FWHM) are extracted. Electron density is calculated from the simple formula: $n_e = 10^{16}\Delta\lambda^s/2\omega$, where ω is a tabulated [1] Stark constant.

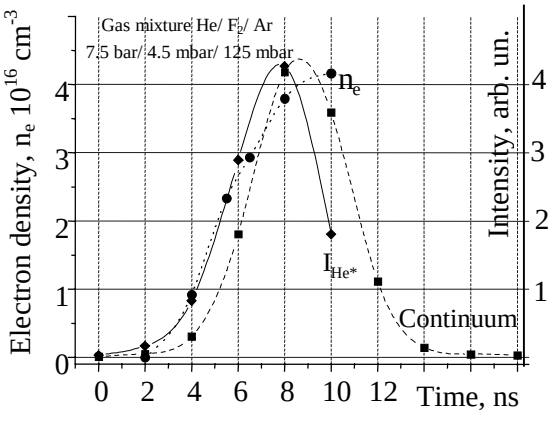


Fig. 5. Time evolutions of He^* emission line 501.6 nm, continuum and calculated density of electrons for the bulk plasma of ArF laser.

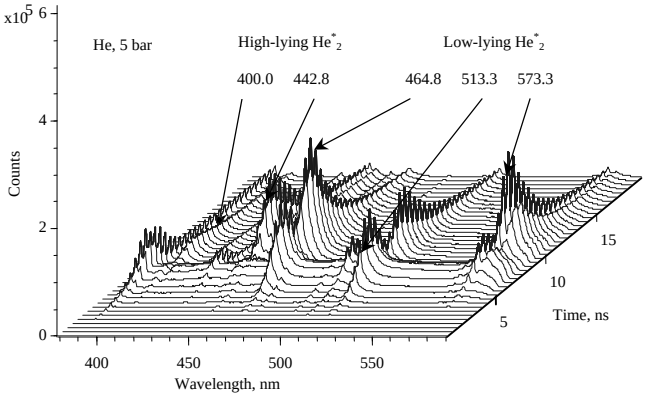


Fig. 6. Time evolution (one step 1 ns, gate 2.2 ns) of He_2^* emission bands in He discharge.

Fig. 5. shows time behaviors of emission intensity for helium line 501.6 nm, continuum and density of electrons for the discharge of ArF laser. After the maximum of the pumping pulse (t > 10 ns) electron temperature decreases and excitation of helium is terminated in the discharge. Measurements for discharges in KrF, F_2 lasers give rather similar time evolution for electron density with maximum of $7\ 10^{16}$ and $6\ 10^{16}$ cm^{-3}. We estimate the accuracy of these data as 20%. The main source of possible mistakes is poor signal-to-noise ratio for measured line profiles due to very strong continuum emission and overlapping of helium lines with emission lines from other excited species.
Together with atomic and ionic lines several well-known He_2^* molecular bands as well as a strong broad continuum are observed in our spectra (see Fig. 6.). The rise time of emission from low-lying He_2^* bands (464.8, 513.3, 573.3, 639.8 nm) and continuum is close to typical primary components (He^*, Ar^*). If we suppose that low-lying He_2^* states are populated through a three-body reaction $He^* + 2He \rightarrow He_2^* + He$, than during the excitation pulse a fraction of He^* atoms could be converted to correspondent He_2^* molecules. As vibrational relaxation of He_2^* molecules is very fast, the emission from relaxed He_2^* states practically coincides with the excitation pulse. Another mechanism which explains the first peak in emission of He_2^* molecules is direct electron impact excitation of free

collision He-He pairs to excited vibronic levels of low-lying He_2^* states. Several publications [3,4] show that at least for photoexcitation this mechanism could be dominated at high pressures.
As concerning 368.0, 400.0 and 442.8 nm He_2^* bands, emitted from high-lying molecular states, there are only weak emissions of these bands during the excitation pulse. However, both low-and high-lying He_2^* states are populated effectively during the recombination flow (see Fig.6.). The characteristic time of atomic He^+ ion conversion to molecular ions He_2^+ is very short (less than 1 ns at 5 bar of helium). So the production of He_2^+ ions mainly follows the excitation pulse. Recombination of these ions ($He_2^+ + e + He\ (e) \rightarrow He_2^* + He\ (e)$), however, occurs after definite delay. From the known rate constants [5] we estimate the characteristic recombination time of several ns (it depends strongly on the density and temperature of electrons). Our experimental data for pure helium at 5 bar shows delay between the first and second peaks of He_2^* emission as about 7 ns.
The time maximum for continuum coincides with the peak of electrons in the discharge. We conclude that this continuum is caused by free-free transitions of electrons in collisions with neutral atoms (bremsstrahlung continuum). This assignment is strongly supported by the fact that similar continuums are observed not only for He, He/F_2 but also for $He/Ar/F_2$ and $He/Kr/F_2$ gas mixtures. In later mixtures densities of $He^*(He_2^+)$, He_2^* species are small, but electron densities are very similar. The intensity of bremsstrahlung continuum is proportional to the densities of electrons and neutral particles (mainly He in our gas mixtures) [6]. Spectrum of this continuum gives also information about the temperature of electrons in the discharge.

3. 3. Spectroscopic monitoring of gas heating

Overheating of the gas during very powerful pumping is a critical factor for high efficient production of excimer molecules. For monitoring of a gas temperature with ns-time resolution during the discharge we use “internal nitrogen molecular thermometer”. Trace additives of nitrogen to the laser gas mixture have small influence to the laser output parameters and plasma-chemical kinetics. At high pressures rotational-translational relaxation is very fast, so a temperature calculated from measured rotational structure of nitrogen emission bands, is very close to a gas temperature. Time-resolved spectra in the region of N_2 ($C_0\ ^3\Pi_u \rightarrow B_0\ ^3\Pi_g$) emission band at 337.1 nm are measured for the central part of the discharge in F_2 laser. Time behavior of the space-averaged gas temperature, calculated from experimental curves, together with pumping pulse, present in Fig. 7. Good coincidence of experimental (squares) and fitted (solid curve) data is observed, so population of N_2 molecules on the rotational levels of the excited $C_0\ ^3\Pi_u$ state is well characterized by a Boltzmann distribution. The gas is heated continuously during the pumping pulse from 325 to about 380 K. After the end of the pumping there is no any extra-heating during afterglow of the discharge. Visually discharge is very homogeneous - constrictions and even tiny filaments are absent. The accuracy of this “internal nitrogen molecular thermometer” is rather good - about ± 10K.

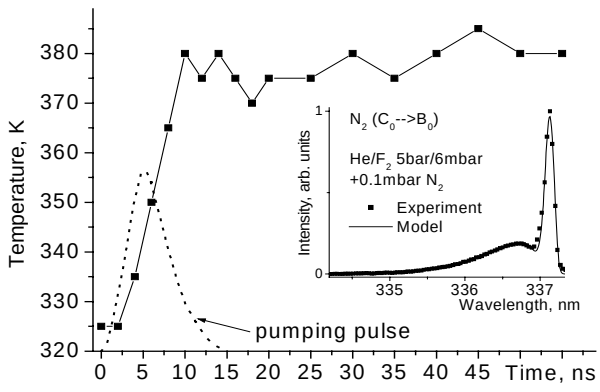


Fig. 7. Time behavior of a gas temperature for the bulk discharge plasma of F_2 laser.

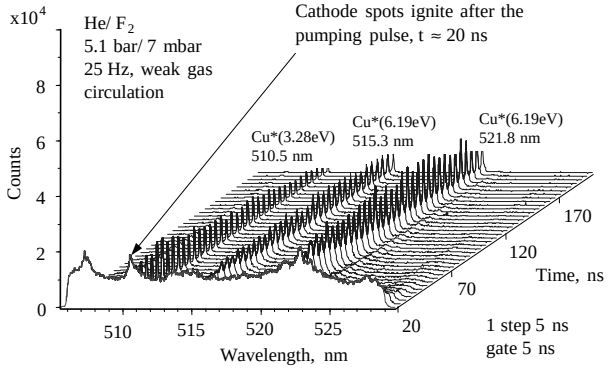


Fig. 8. Time-resolved emission spectra of the near-cathode discharge plasma of F_2 laser. Cathode hot spots (Cu^* lines) explode after the end of the pumping pulse at t ~ 20 ns.

If we suppose that 90% of the loaded energy is consumed to the heating of rectangular block of helium gas in the laser gap with volume V, we may calculate the energy deposited to the discharge during the pumping pulse: $E_d = \Delta T \rho V C_v$, where ρ and C_v are gas density and specific heat at a constant volume respectively. This estimation shows that efficiency of the pumping circuit in our laser is rather high: from 600 mJ stored in the main capacitor about 450 mJ is loaded into the plasma. Rest of the stored energy dissipates mainly in the thyratron contour and preionization discharge.

3.4. Cathode sheath and hot spots ignition

The most interesting phenomena observed in our laser are connected with ignition of cathode sheath and formation of hot cathode spots [7]. For high-current discharges with very fast current rise time (~ 1 ns) cathode sheath does not developed at all because uniform breakdown of the sheath occurs already at the beginning stage of the discharge. We did not observe any difference in time-dependent emission spectra and gas temperature measured from the bulk and sheath plasmas. It shows that there is no increased heating of the gas in the sheath layer in our laser.
Explosion of hot cathode spots is monitored in our discharge by atomic emission lines from a cathode material. With proper gas circulation hot spots and filaments are totally absent in the discharge up to pulse repetition rate of about 400 Hz. In this regime we did not observe any erosion of laser electrodes during the long-term laser operation. Fig. 8. presents fragment of time-resolved emission spectra of the near-cathode discharge plasma of F_2 laser, measured with very weak gas circulation. Copper is the material of the electrode. Cathode spots explode after the end of the pumping pulse (t ~ 20 ns) but no constrictions have been developed in the discharge from the spots because the pumping is already terminated. No copper ion lines were detected in emission spectra from hot cathode spots. Strong Stark broadening is observed for two Cu^* transitions from highly excited 6.2 eV state. We estimate the density of electrons at the moment of hot spot explosion as about $1\ 10^{18}$ cm^{-3}. Line at 510.5 nm, which belongs to transition from Cu^* low-excited 3.28 eV state, does not show strong Stark broadening and remains quite narrow during the whole ~ 300 ns period of plasma recombination in metal vapor plume. The explanation of this delayed explosion of cathode spots is the following. Due to intense ion bombardment and ohmic heating extremely high electron emissivity provides from locally heated (but not exploded!) cathode emission centers (microprotrusions) in our discharge. This behavior is very similar to superdense glow discharge phase in pseudosparks [8] and cathode spots development in vacuum explosions. As the average current for one emission center is low (about 50 mA) these superheated centers can exist rather long time (~10 ns). According to theoretical estimation in [9] these centers can accumulate the energy of the order of a few times the sublimation energy before the explosion. From this point short pumping is much more beneficial for high-current discharges which are necessary for pumping of VUV lasers.

ACKNOWLEDGMENTS

This work was supported by the Estonian Science Foundation under grant no. 5044.

REFERENCES

[1] Griem H.R., *Spectral line broadening by plasmas*, Academic, New York, 1974.
[2] Qin W., Minami K., DeSilva A., Tomimoto F. and Sato K., *Jpn. J. Appl.Phys.*, **35**, pp.4509-15 (1996)
[3] Tanaka Y., Yoshino K., Freeman D., *J. Chem. Phys.*, **59**, 5160-23 (1973)
[4] Moutard P., Laporte P., Subtil J., Damany N., Damany H., *J. Chem. Phys*., **87**, pp. 4576-12 (1987)
[5] Deloche R., Monchicourt P., Cheret M.and Lambert F., *Phys. Rev.* ***A*** **!3,** pp.1140-36 (1976)
[6] Park J., Henins I., Herrmann H. and Selwyn G., *Physics of Plasmas*, **7**, pp. 3141-4 (2000)
[7] Treshchalov A., Lissovski A., Chikeev E., High-current discharge pumping of ArF, F_2 lasers without cathode hot spots and filament instabilities, *Proceedings of SPIE*, **4747**, pp. 253-8 (2002)
[8] Korolev Y. and Frank K., *IEEE Trans. on Plasma Sci.*, **27**, pp. 1525-17 (1999)
[9] Valuev A. and Norman G., *Zh. Eksp. Teor. Fiz.*, **89**, pp. 1180-3 (1999)

PHOTOIONIZING RADIATION OF POSITIVE CORONA IN MOIST AIR

M. Aints, A. Haljaste[a] and L. Roots

Institute of Experimental Physics and Technology, University of Tartu, Tähe 4, 51010 Tartu, ESTONIA

Abstract. Absorption of photoionizing radiation generated by positive corona in the atmospheric pressure air at different moisture content is measured. Absorption coefficients for dry air and H_2O are obtained for the pressure times distance region of 400 - 750 Torr cm. Results are compared with those of earlier authors and possible reasons of discrepancies are discussed.

1. INTRODUCTION

Photoionization is an essential process when mechanisms of development and sustainment of corona discharges are considered. The photoionizing radiation of discharges has been studied in many cases. In corona, the photoionizing radiation is emitted by gas molecules or atoms excited mainly by electron impact. In air, the dominant processes leading to photoionization are the excitation of nitrogen molecules to energies of 12.1-13.6 eV, with subsequent photoionization of oxygen molecules having ionization potential of 12.1 eV [1, 2]. Data about absorption of photoionizing radiation generated by corona discharges in air, O_2, N_2 and their mixtures one can find in literature [3-9]. Air used in those experiments was dried with help of moisture absorbers or cool agents. As far as we know, air with some percent of water vapor admixture was used in few experiments only [5, 7]. Water vapor increased the absorption of photoionizing radiation significantly. However, due to difficulties in determination of water vapor concentration in the experimental chamber, only the approximate limit for the absorption coefficient K of water vapor was found ($K > 200$ cm^{-1} [5]). This result is cited in many later publications. No more attempts to determine the absorption of photoionizing radiation generated by corona discharges in moist (atmospheric) air are known for us.

Our experimental investigation is concerned with the photoionizing radiation generated by positive steady glow corona in atmospheric air. In this paper, we present the results about radiation absorption in dry and moist air.

2. EXPERIMENTAL APPARATUS

The experiments were carried out under the normal pressure and the room temperature. Laboratory air was forced by a pump (see Figure 1) through a dust filter. Thereafter a certain part of the air stream was dried by silica gel and then mixed with the non-dried part of the stream. A thermo-hygrometer measured the air temperature and humidity with accuracy of 2%. Adjusting with valves the streams of dried and humid air, the desired level of humidity was obtained in air entering the ionization chamber. Air flowed from the ionization chamber into the corona chamber through an aperture and then into environment through an opening. The point electrode (corona point in Figure 1) of the corona gap was a hemispherically capped platinum wire of 0.25 mm in diameter. The distance from the point electrode tip to the opposing endplate of the corona chamber was 3 mm. The aperture in the center of the endplate had a diameter of 2 mm. The diameter of the corona chamber was 20 mm. The corona point was fed via the series resistor $R = 10$ MΩ by the positive DC voltage about 5-6 kV ensuring the stable steady corona on the point tip. The corona chamber was grounded via a micro-ammeter measuring the

[a] Electronic address: haljaste@physic.ut.ee

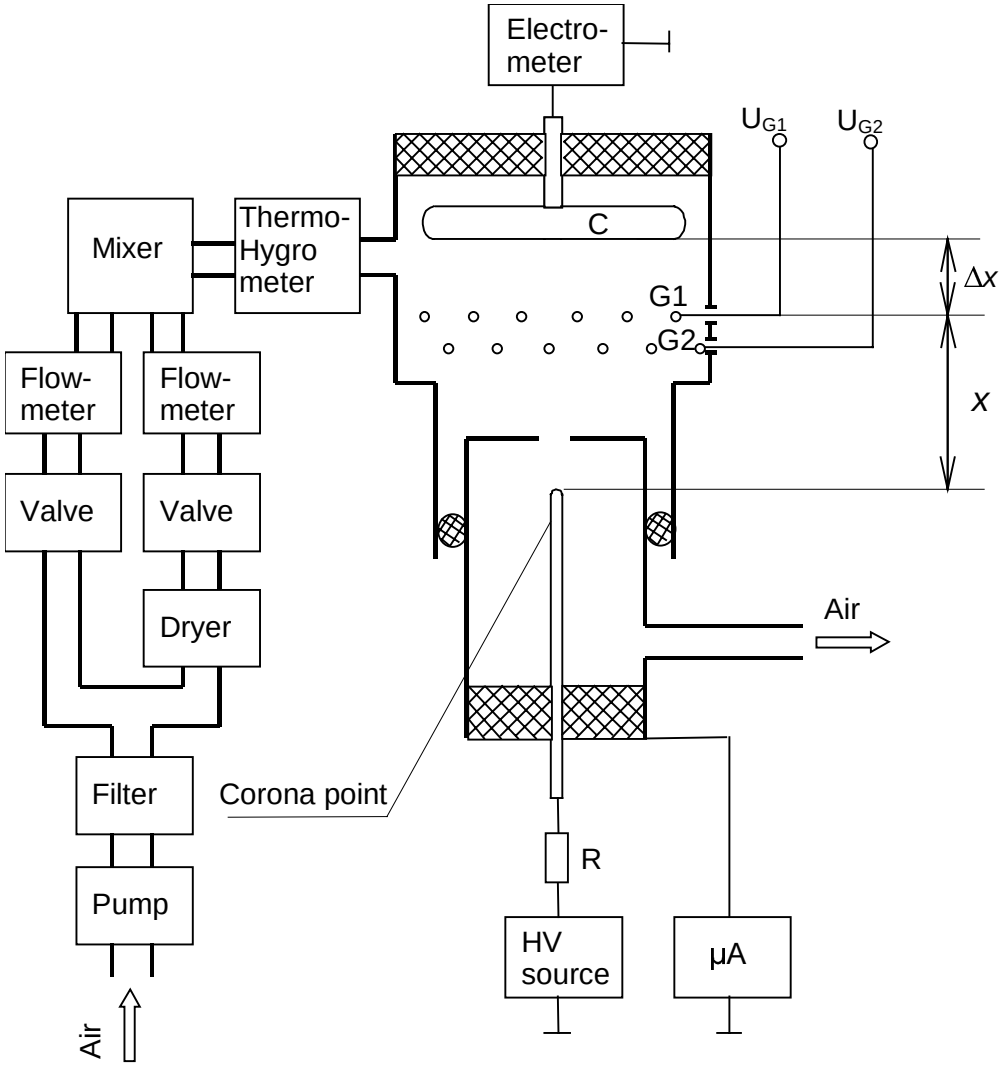


FIGURE 1. Schematic diagram of the experimental setup

corona current. Photons generated by the corona discharge passed through the aperture and, if not being absorbed by medium before, reached the ionization chamber designed to detect the photons that cause ionization.

Our ionization chamber was similar to that used by Penney and Voshall [8]. It contained a plane collector electrode C (see Figure 1) and two grids G1 and G2 parallel to the collector electrode and perpendicular to the point electrode axis. The grids were formed by parallel wires 0.07 mm in diameter. The distance between the axes of the adjacent wires was 0.4 mm in both grids. The distance between the grids was 0.4 mm. Wires of one grid were parallel to those of the other grid. The grids were shifted by the half step of the grids. The resultant optical transparency of the grids was 0.65. The distance between the collector electrode and the grid G1 Δx = 3.0 mm (see Figure 1). G1 was stressed negatively (U_{G1} = -100V), G2 - positively (U_{G2} = 50 V). Ions generated by photoionizing radiation in the space between the grid G1 and the collector electrode C caused a current in the circuit of the collector electrode. This current was measured by an electrometer with a resolution of $1 \cdot 10^{-15}$ A.

The grid G2 formed an electric field that prevented the photoelectrons, which were emitted by the grid G1, from arrival at the collector electrode. Electric field of G2 also stopped movement of positive ions from the corona discharge into the collector gap of the ionization chamber. The air stream through the orifice of the corona chamber had the same task. That airflow also removed corona products ensuring invariable medium in ionization- and corona chambers. The airflow rate was 1 l/min in our

experiments.

The corona current was varied in the range 10 - 40 μA. Under the described conditions, the steady glow corona was burning at the point electrode. No streamers were observed. The distance between the ionization chamber and the corona chamber was changeable and it was adjusted with accuracy of 0.1 mm. The distance between the tip of the corona electrode and the grid G1 is denoted by x in Figure 1. The collector current versus distance x was measured at various values of air humidity and corona current.

3. RESULTS

It turned out that the collector current was proportional to the corona current at constant humidity and distance x. The collector current fell nonlinearly off to zero with an increase in the distance x. With an increase in the air humidity, the collector current decreased as well. All these observations are in accordance with results of earlier authors referred here. An example of results of our measurements is presented in Figure 2 as a $\Psi(px)$ plot, where p is the gas pressure and Ψ is the number of photoions generated in a layer of unit thickness at distant x from the radiation source, per unit of solid angle, per one ionizing collision in the discharge, at unit pressure:

$$\Psi = \frac{I}{\Theta T\ i\ p\ \Delta x}. \qquad (1)$$

Here I is the collector current, Θ is the solid angle determined by the aperture of the corona chamber, T is the optical transparency of the grids, and i is the corona current. Partial pressure of water vapour p_{H2O} is denoted in the plot for each curve.

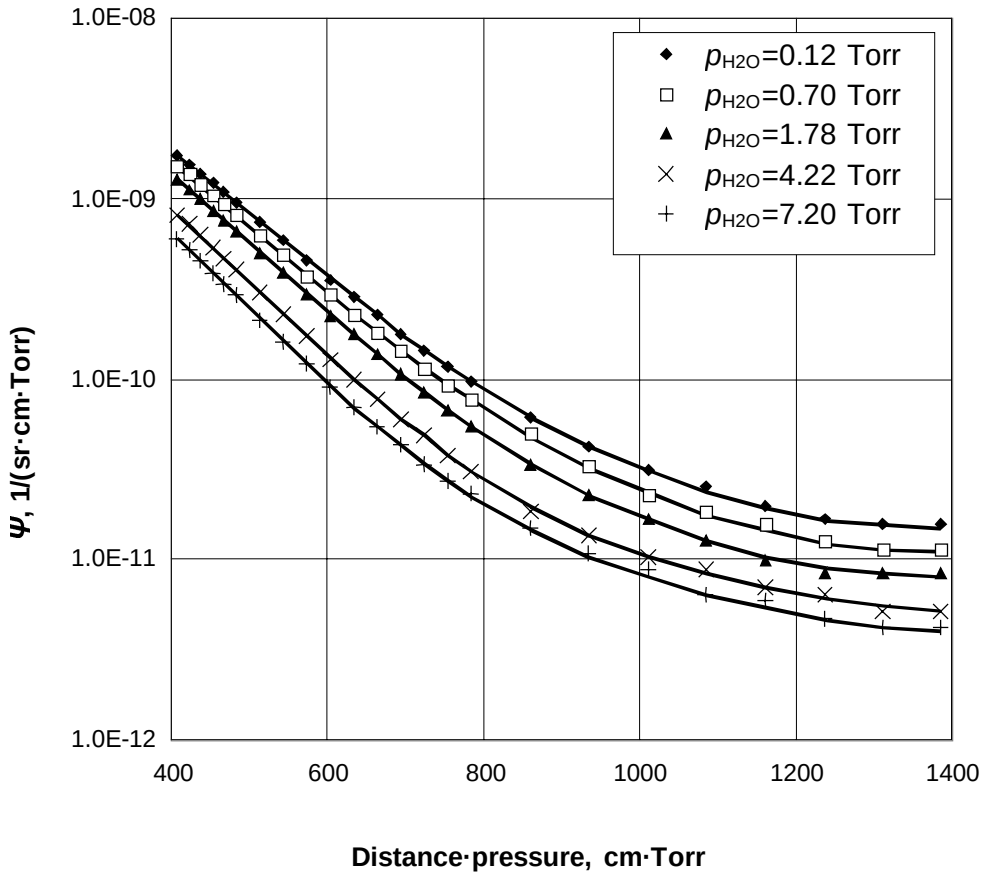


FIGURE 2. Absorption curves of corona radiation. p = 754 Torr, t = 300^{O}K.

We calculated absorption coefficients $K_{air} = \sigma_{air} n_0$ and $K_{H2O} = \sigma_{H2O} n_0$ for dry air and for water vapour in the region of $p \cdot x$ = 400-750 cm·Torr where experimental points lay on straight line in semi-logarithmic scale (see Figure 2), proceeding from the formula

$$\sigma_{air} n_{air} + \sigma_{H2O} n_{H2O} = \frac{d}{dx}(\ln I). \qquad (2)$$

Here σ_{air} is the absorption cross section of " molecules of dry air ", σ_{H2O} is that of H_2O, n_{air} is number density of "molecules of dry air" under test conditions, n_{H2O} is number density of water vapor molecules under test conditions and n_0 is number density of gas molecules at 760 Torr and 273^{O}K. The results are: K_{air}=6.88(27) cm^{-1}, K_{H2O}=107(60) cm^{-1}.

4. DISCUSSION

Comparing our values of Ψ presented in Figure 2 with those presented in literature [7, 9] it follows that our values of Ψ are lower more than one order of magnitude. The difference may be attributed to the differences in the experimental conditions. Curves of Penney and Hummert [9] were obtained at low pressures (up to 18 Torr). Teich [7]investigated absorption in dry air at pressures up to 700 Torr. As a source of ionizing radiation, he used electron avalanches developing in homogeneous electric field at E/p = 50 V/(cmTorr), not the steady corona as we did.

There is one circumstance not discussed earlier. Przybilski [5], Teich [7] and Penney and Hummert [9] made measurements in a closed chamber. It is well known that gas discharge in air produces O_3 and NO_x, which concentrations in a closed chamber can rise up to very high values. Presence of these products can change absorption properties of the gas mixture. We used flowing air free of discharge products and this may also be the reason of differences between our and cited results.

Our result K_{air}= 6.88(27) cm^{-1} is quite close to that obtained by cited authors for the px region of 400-700 Torr cm. We can compare our value K_{H2O} = 107(60) cm^{-1} only with the estimation given by Przybilski [5]: K_{H2O} > 200 cm^{-1}. The discrepancy is obvious but here the Przybilski's remark should be taken into account that determination of moisture content was inaccurate in his case.

ACKNOWLEDGEMENTS

This work was supported by the Estonian Science Foundation under grant no. 4518.

REFERENCES

[1] Meek J. M. and Craggs J. D. (eds), *Electrical Breakdown of Gases*, Wiley, Chichester etc.,1978

[2] Zheleznyak M. B., Mnatsakanian A. Kh. and Sizykh S. V. Photoionization of nitrogen and oxygen mixtures by radiation of a gas discharge, *Teplofiz. Vysokih Temp.*, **20,** No 3, 423-8 (1982) (in Russian)

[3] Przybilski A., Untersuchung über die "gasionisierende" Strahlung einer Entladung, *Z. Phys.*, **151**, 264-80 (1958)

[4] Przybilski A., Die gasionisierende Strahlung einer Entladung in N_2-O_2-Gemischen, *Z. Naturforsch.,* **16a**, 1232-7 (1961)

[5] Przybilski A., Untersuchung über die gasionisierende Strahlung einer Entladung II, *Z. Phys.*, **168**, 504-15 (1962)

[6] Teich T. H., Emission gasionisierender Strahlung aus Elektronenlawinen I. Meßanordnung und Meßverfahren. Messungen in Sauerstoff., *Z. Phys.*, **199**, 378-94 (1967)

[7] Teich T. H., Emission gasionisierender Strahlung aus Elektronenlawinen II. Messungen in O_2-He-Gemischen, Dämpfen, CO_2 und Luft; Datenzusammenstellung, *Z. Phys.*, **199**, 395-410 (1967)

[8] Penney G. W. and Voshall R. E., Ionization of a gas by radiation from a discharge, *Trans. Am. Inst. Electr. Eng., Part I, Communication and electronics*, **81**, 398-403 (1962)

[9] Penney G. W. and Hummert G. T., Photoionization measurements in air, oxygen and nitrogen, *J. Appl. Phys.*, **41**, No 2, 572-7 (1970)

HF CAPILLARY DISCHARGE: DISTRIBUTION OF RADIATION ALONG ELECTRODES

M.Laan[a] and J.Raud

Institute of Experimental Physics and Technology, University of Tartu, Tähe 4, 51010 Tartu, ESTONIA

Abstract. Medium-pressure HF discharge in the capillary is studied. The discharge is excited in He/Ar mixture. Sectioned stressed electrode is used. Both the distribution of the radiation in the capillary and spectra at different positions along electrodes as functions of discharge current are recorded. Spatial and spectral regularities of α - and γ-modes of the discharge are clarified.

1. INTRODUCTION

The high-frequency (HF) discharge is an efficient way of pumping of CO_2 laser [1]. Moreover, compared with the direct current discharge HF discharge demonstrated its advantages also in the case of Xe and metal vapor lasers [2, 3].

Depending on frequency, gas composition, pressure, input power and electrode separation HF discharge runs in α- or γ-mode. The first mode guarantees a more-or-less homogeneous medium between electrodes. For this reason α-mode of HF discharge is more suitable for lasing. Unfortunately, the existence of the α-mode is limited by a maximum input power. Simultaneous action of both modes between the electrodes allows to increase the power fed to the spatially homogeneous discharge [1].

In [4] it was found that the intensity of the radiation of HF capillary discharge increases considerably when instead of one long stressed electrode a number of short-length electrodes are used. This finding forced us to undertake a more systematic study of the phenomenon.

The purpose of the study is to find the relationship between the electrical regime of HF discharge and the efficiency of the excitation of the spectrum in different parts of the discharge.

2. EXPERIMENTAL

2.1. Set-up

A sketch of the experimental set-up is presented in Figure 1. The discharge is studied in a ceramic (Al_2O_3) capillary tube of 2-mm bore diameter. For discharge excitation a 27 MHz generator of 100 W output power is used. The length of the grounded water-cooled electrode is 195 mm. The stressed electrode consists of a number of sections. In the present study four sections are used, the length of one section is 15 mm and the distance between the sections is 40 mm. The voltage at electrodes is measured over the voltage divider and for current measurements a Rogowski coil is used.

The discharge is studied in mixture helium + 0.07 % argon (both of 99.99 % grade) at 60 Torr total pressure. As dicharges in helium are very sensitive to impurities, before every new setting of discharge parameters (e.g. a change of discharge current) the device is evacuated to the pressure $1.5 \cdot 10^{-4}$ Torr and then filled with a fresh gas. This procedure guarantees a good reproducibility of results. Energy input is not homogeneous along the capillary and it may cause substantial variations of the gas density. This effect is minimized by the fan, which creates gas circulation in the capillary.

[a] Electronic address: laan@physic.ut.ee

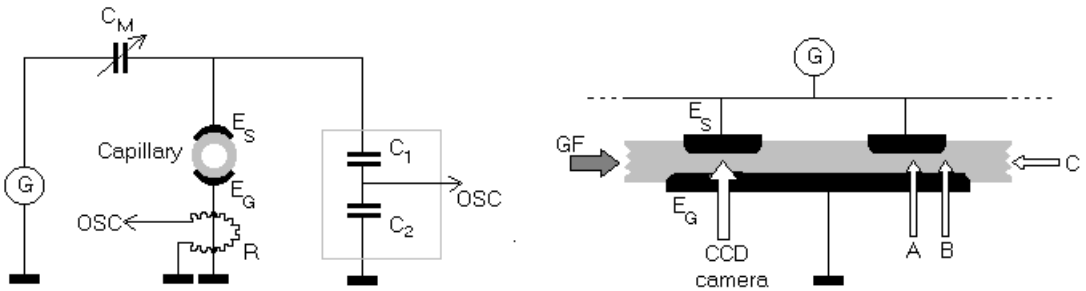


FIGURE 1. Experimental device: G - generator; C_M - matching capacitor; E_S, E_G - stressed and grounded electrodes; R - Rogowski coil; C_1/C_2 - voltage divider; GF - gas flow; **A**, **B**, **C** - positions from where spectra are recorded.

The distribution of the radiation along electrodes is recorded with CCD camera and for recording the spectrum at positions **A**, **B**, **C** (Figure 1) the spectrometer USB2000 is used. The spectrometer is sensitive in the 200-850 nm region and its resolution is 1 nm. The relative sensitivity of the spectrometer is calibrated using the tungsten FEL lamp of known spectral distribution. The walls of the capillary are opaque for wavelength $\lambda < 500$ nm; in the spectra recorded at positions **A** and **B** the transmittance of the walls is taken into account.

2.2. Results

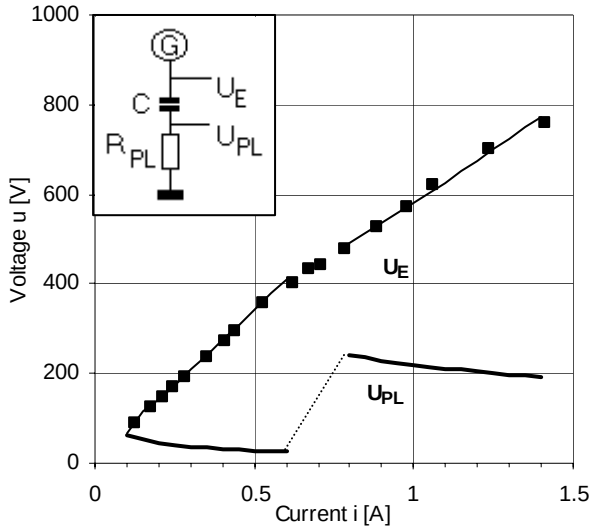


FIGURE 2. (above). Current-voltage characteristic; squares - experiment; solid lines - calculations; U_E, U_{PL} - voltages on electrodes and plasma; inset - circuit used in calculations.

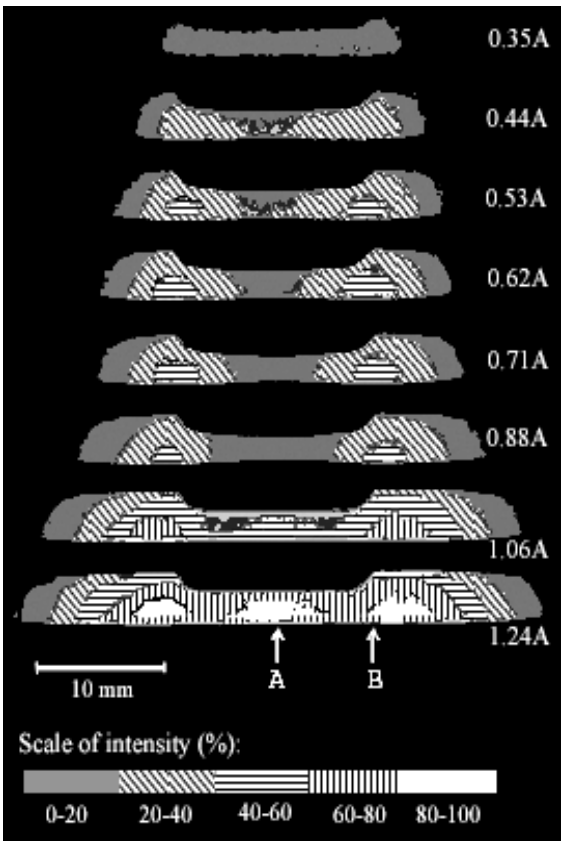


FIGURE 3. (right). Distribution of the radiation as a function of the discharge current.

Current-voltage curve of the discharge (Figure 2) has two characteristic parts ($i < 0.8$A and $i > 0.8$A) with different slopes. Figure 3 presents the distribution of the radiation near one of the stressed electrodes for different currents i. At lower currents CCD camera records a faint and spatially homogeneous luminosity with the length increasing along the capillary with the current rise. At $i \approx 0.35$A the capillary in the limits of the stressed (upper) electrode is filled with the discharge.

Further current growth causes a gradual spread of the discharge to the regions where the upper electrode is missing. The distribution of the luminosity in the capillary is not any more homogeneous: its more intensive part concentrates near the ends of the upper electrode. It is remarkable, that until the current $i \approx 0.8$ A (where the change of the slope of the current-voltage curve takes place, Figure 2) the intensity of the luminosity at the center of the electrode remains low. At higher currents the intensity grows also at the central part of the upper electrode.

Discharges starting from the neighbor electrodes approach each other with the current growth but even at the highest current there is a dark region between them. As near the end and the center of the upper electrode take place more drastic current-depending changes of the luminosity, the discharge spectra are recorded from these positions and compared with the spectrum recorded in the axial direction.

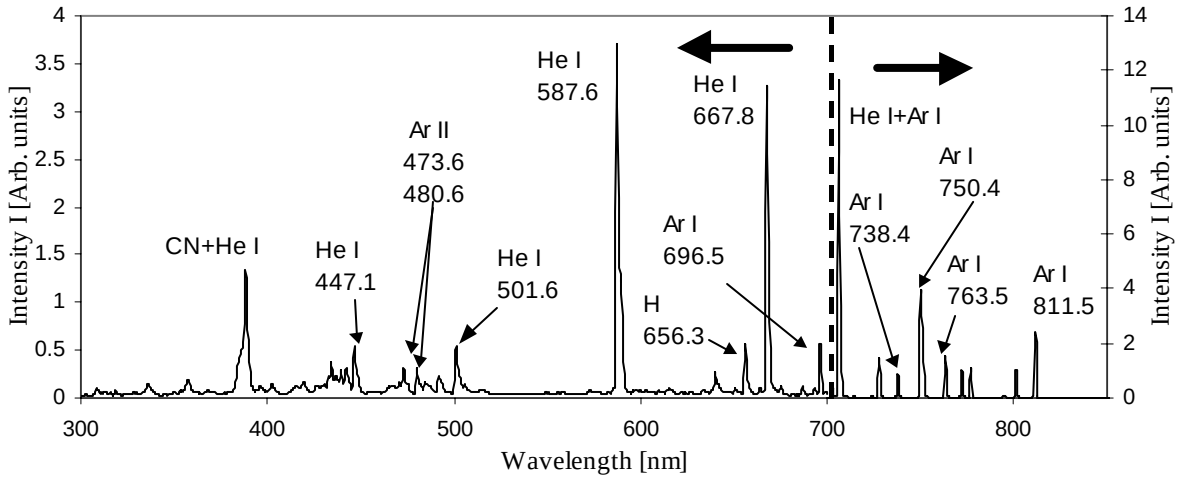


FIGURE 4. Discharge spectrum of He/Ar mixture; discharge current i = 1.24A; recording position **C**; intensity scales are different on left and right hand sides from the dashed line.

Most of the lines in the spectrum (Figure 4) recorded at the spectrometer position **C** belong to He and Ar, only at currents $i > 0.8$A the radiation of CN (bands near $\lambda = 388$ nm) and hydrogen ($\lambda = 656.3$ nm) have a considerable contribution to the spectrum. The most intensive line in the spectrum $\lambda \approx 706$ nm is the result of the overlapping of He and Ar lines. He line $\lambda = 388.9$ nm is also overlapped with CN band. For this reason lines mentioned are not used in further diagnostics. It should be pointed that among the diagnostic lines $\lambda = 501.6$ nm (He) and $\lambda = 696.5$, 763.5 and 811.5 nm (Ar) correspond to the transitions which end at the metastable states of atoms.

At the spectral regions $\lambda > 500$ nm where the capillary walls become transparent the spectra recorded at positions **A**, **B** are similar to that in Figure 4.

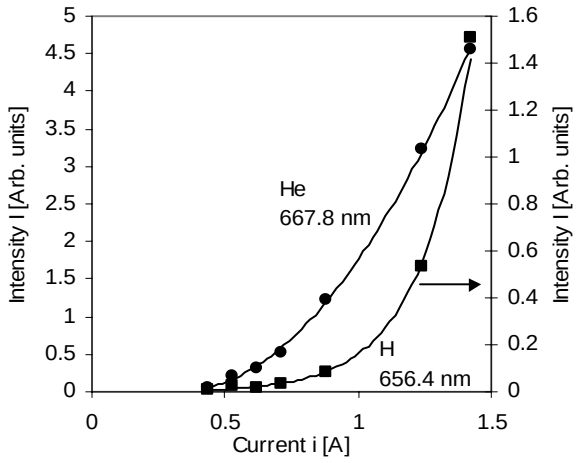


FIGURE 5. Intensity of spectral lines as functions of the current, recording position **C**.

In the axial direction all spectral lines of helium depend on the current in similar way: the intensity is a quadratic function of the current (Figure 5). In contrast, the dependence of the hydrogen line on the current is exponential, a fast growth of the intensity occurs at currents where the luminosity at the central part of the upper electrode starts to increase.

Comparison of the dependencies of the spectrum on the current recorded from the side positions **A** and **B** highlights the changes occurring with the

current growth more definitely (Figure 6). The intensity of He lines recorded at the position **B** is higher than those recorded at the position A. At higher currents their growth rate breaks and the intensity of the radiation from the position A approaches to that from the position **B**. The current where the intensity ratio I_B / I_A is maximum is close to that where the slope of the current-voltage curve changes.

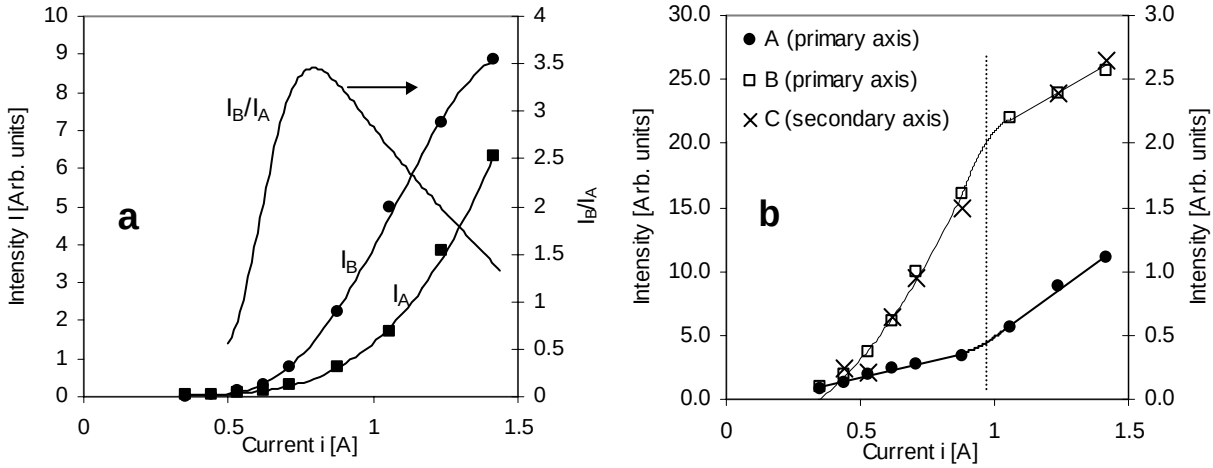


FIGURE 6. **a** - Intensity of He line λ = 587.6 nm and intensity ratio I_B/I_A as functions of the current; recording positions **A**, **B**.
b - Intensity of Ar line λ = 811.5 nm as a function of the current; recording positions **A**, **B**, **C**.

Figure 6b presents the dependencies for Ar radiation recorded at three positions. The behavior of the radiation in axial direction coincides with that recorded at the position **B** but the intensity is much lower. Again, the set of dependencies demonstrates a strong correlation with the change of the current-voltage characteristic.

3. DISCUSSION

For calculations of the voltage drop U_{PL} on plasma [1] we used a simple circuit presented at the inset in Figure 2: C is the total capacitance of the capillary walls and electrode sheaths and R_{PL} is the plasma resistance. Solid lines in the figure present results of the calculations. The jump of U_{PL} near the current 0.85 A may be related with the transition of the discharge from α-mode to γ-mode. In γ-mode the thickness of electrode sheaths is considerably smaller than it is in α-mode. Consequently the capacitance C as well as the thickness of the plasma layer length increases. The latter result leads to the growth of the voltage drop U_{PL}.

Regularities in the spectra support the interpretation presented. Indeed, in the case of γ-mode the ion bombardment of the capillary walls becomes important and an amount of impurities are liberated from the walls. The growth of the intensity of hydrogen line λ = 656.4 nm (Figure 5) results this change.

Because of the small bore diameter the space near the center of the upper electrode (position **A**) is filled only with the regions of the negative glow of HF discharge [4] and the positive column spreads to the parts of the capillary where the upper electrode is missing. In α–mode the volume filled with the positive column gradually increases with the current growth and the role of the processes between electrodes is the delivering of the column with electrons. The quadratic dependence of the intensity on the current (Figure 6a) seems to prove that in the positive column the excitation of He states has a step-wise character.

As it is mentioned already, after the transition to γ-mode thickness of electrode sheath diminishes considerably and the space at the center of the upper electrode is partially filled with plasma column (Figure 3, i > 0.9A).

In spite of the small concentration of Ar in the mixture, the intensity of its spectral lines is high. Radiation recorded at the side positions **A**, **B** is not influenced by the absorption from the lower metastable state and thus the dependencies for the intensity reflect the efficiency of the excitation in different parts and modes of the discharge. The radiation recorded in the position **A** starts to grow faster after the discharge transits to γ-mode but the total axial-direction radiation follows the radiation of the positive column as the spatial extent of it is considerably larger than the extent of the region between electrodes. The comparison of the intensities of Ar lines λ = 811.5 nm and λ = 738.4 nm gives the information about the population of Ar metastable state. The corresponding transition of the latter spectral line ends at the upper level of the Ar resonant transition. The intensity ratios of these lines recorded in the positions **B** and **C** differ ≈ 9 times, i.e. the concentration of Ar atoms in the metastable state is high.

4. CONCLUSIONS

- In HF capillary discharge in helium with the sectioned stressed electrode exist α- and γ-modes of the discharge like it is in the case of the ordinary setups. In α-mode of the discharge the region of the negative glow is concentrated in the limits of the stressed electrodes and the positive column occupies the outer regions.
- The radiation from the positive glow regions gives the main contribution to the radiation recorded in the axial direction of the capillary. The transition to γ-mode breaks the growth of the radiation intensity and impurities from the capillary walls are liberated.
- The spectral lines of argon are effectively excited. The concentration of metastable atoms of argon is high.
- The discharge type studied may be used for creation of spatially homogeneous plasma where an effective excitation of heavy trace gases takes place.

5. ACKNOWLEDGEMENT

The study is supported by Estonian Scientific Foundation, grant No 3984.

REFERENCES

[1] Raizer Y. P., Schneider M. N., and Yatsenko N. A., *Radio-Frequency Capacitive Discharges: Physics. Experimental technique. Applications*, CRC Press, London, Tokyo, 1995, pp. 270-275

[2] Udalov Y. B., Tskhai S. N., Peters P. J., Witteman W. J., Kochetov V. I. and Ochkin V. N., RF excited gas lasers- recent progress, In: *Gas Lasers-Recent Developments and Future Prospects*, ed. by W.I.Witteman and V. N. Ochkin, Kluwer Academic Publisher, Printed in the Netherlands, 1996, pp. 1-10

[3] Grozeva M., Kocik I., Mizeraczyk J. and Sabotinov N., Improvement of laser lines…, In*: ICPIG XXIV Contr. Papers*, ed. by P. Pisarczyk, T. Pisarczyk, J. Wolowski, Warssaw, 1999, pp. 161-162

[4] Raud J., *HF capillary discharge in helium*, MSC thesis, University of Tartu, Tartu, 2001, pp. 46-51

VUV EMISSION OF KR_2 MOLECULES UNDER HIGH-CURRENT SLIDING DISCHARGE EXCITATION

A.Treshchalov[a], E. Jalviste[a], A. Smerechuk[b], G. Gerasimov[c], R. Hallin[b] and A. Arnesen[b]

a) Institute of Physics, University of Tartu, Riia 142, 51014 Tartu, ESTONIA
b) Uppsala University, Department of Physics, Box 530, S-751 21 Uppsala, SWEDEN
c) Vavilov State Optical Institute, Birzhevaja Line 12, 199034 St. Petersburg, RUSSIA

Abstract. Fast-pulsed high-current sliding discharge along the surface of sapphire plate is applied for the excitation of high-pressure Kr gas. Time behavior of the VUV emission from excimer molecules and main atomic species were monitored. Kinetics of the first and second Kr_2 continua in conditions of powerful pumping and high electron density are discussed. Experimentally it is revealed the importance of direct electron impact excitation of 0_u^+ and 1_u Kr_2^* states from weakly bound Kr_2 molecules in the 0_g^+ ground state and free collision pairs of Kr atoms at high pressure conditions.

1. INTRODUCTION

A variety of applications (lithography, photochemistry, disinfections, etc) require intense light sources in vacuum ultraviolet (VUV) spectral range. Rare gas excimers have been known to be one of the most efficient VUV continuous radiation sources. For instance a dielectric barrier surface discharge in rare gas mixtures has conversion efficiency of about 60% (VUV light output from the discharge input electrical energy). Although lasing on these molecules was demonstrated long time ago, only few successful attempts to design discharge-excited lasers are reported [1]. Thus, designing and optimization of discharge-excited rare gas excimer lamps and lasers is an important and demanding task.

2. EXPERIMENTAL

Since the discharge in high-pressure inert gases tends to constrict due to ionization and thermal instabilities, specially designed fast discharge circuits should be used to avoid the constriction and to achieve high-efficient VUV emission. Figure 1 presents configuration of electrodes used in our sliding discharge. High voltage electrode (copper foil with a thickness of 0.1 mm) is placed between two grinded sapphire dielectric plates of 250×80×0.6 mm^3 (L×W×H) and pressed between two thick (10 mm) aluminum ground electrodes. This construction (a flat transmission line) plays also the role of extremely low-inductance peaking capacitor (C ≈ 3.5 nF) for the discharge.

The discharge electrical driving circuit is a thyratron-switched charge-transfer scheme with storage and peaking capacitors of 1.5 and 3.5 nF, respectively. The circuit permits a steep (~ 30 ns) voltage growth (~$3 \cdot 10^{11}$ V/s) at relatively low charging voltage (up to 20 kV). A sliding discharge is developed in two stages [2]: I - the running of direct ionization wave on the dielectric surface from the HV to the ground electrodes. This low-current prebreakdown is initiated during the rise of the voltage on the HV electrode by spatially uniform displacement currents, which are capacitively distributed along the electrode length. Stage II is a high-current back-running fast excitation wave. This stage, characterized by maximum deposition power, starts since the arrival of the excitation wave I to the ground electrode and the energy from a low-inductive peaking capacitor is deposited into the well-preionized plasma

[a] Electronic address: *atr@fi.tartu.ee*

sheet. The existence of the second stage is the main advantage of a sliding discharge over well-known surface barrier discharge, which is self-terminated after the development of the first stage.

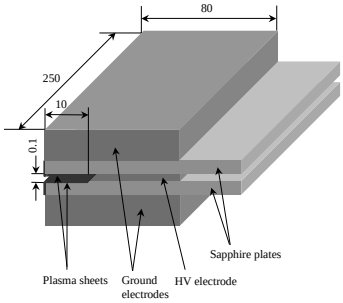


Figure 1. Schematic of the sliding discharge electrodes. Spontaneous emission from two arc-free plasma sheets (250x10x0.03 mm) is measured in the direction of the long axis.

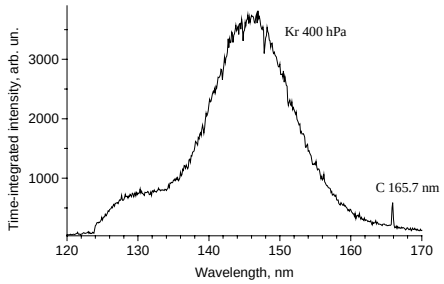


Figure 2. Time-integrated emission spectrum of a sliding discharge at a Kr pressure of 400 hPa.

Pulse repetition rate of our discharge device (up to 300 Hz) is limited mainly by the high voltage power supply. Gas mixture is effectively cooled on the surface of dielectric substrates between the excitation shots and no special gas circulation is necessary.

Spontaneous emission from the discharge plasma is detected through the output MgF_2 window by a normal-incidence 1 m vacuum monochromator with spectral resolution of 0.04 nm. Kinetics of emission were measured by the fast PMT (Hamamatsu R 1220) and the 400 MHz Tektronix 380 digitizer connected with a computer. Time-integrated emission spectra were measured by monitoring the PMT photocurrent pulse with sensitive pulse integrator. The discharge chamber (volume of ~5 l), made of stainless steel, and relevant gas handling system were evacuated by turbomolecular pumping system to 10^{-4} Pa. Kr and Xe gases with 99.998 % purity were used in our experiments.

3. RESULTS AND DISCUSSION

Figure 2. shows a typical time-integrated emission spectrum of a sliding discharge at Kr pressure of 400 hPa. The emission is known to originate from 0_u^+ and 1_u states of Kr_2 (see Figure 3.). The region of the intensity maximum (~146 nm), called the second continuum, corresponds to the low vibronic levels of Kr_2, but the blue and red shoulders, called the first continuum, originates from high vibronic levels of 0_u^+ and 1_u states.

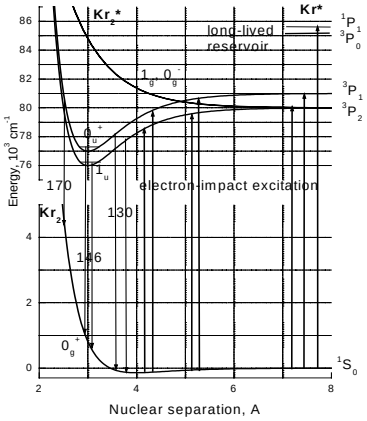


Figure 3. Kr atomic levels and simplified potential curves for Kr_2 molecules. Electron-impact excitation and spontaneous emission transitions (wavelengths in nm) are indicated.

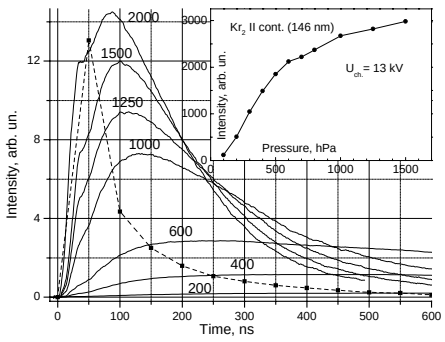


Figure 4. Time-resolved emission intensity of the second Kr_2 continuum (146 nm) in sliding discharge at different pressures (hPa). Dashed line is a time behavior of Kr^* 587 nm emission line, measured at 1250 hPa. The inset shows time-integrated intensity of the second Kr_2 continuum at different pressures at a fixed charging voltage (13 kV).

We also observed an additional broad continuum (200-400 nm) centered around 280 nm, which follows the discharge pumping pulse in its temporal behavior (see Figure 6.). We interpret this continuum as free-free transitions of electrons in collisions with neutral krypton atoms (bremsstrahlung continuum). The intensity of this continuum is proportional to densities of electrons and Kr.

Figure 4. presents time-resolved emission intensity of the second Kr_2 continuum (146 nm) in a sliding discharge at different gas pressures. Dashed line is a time behavior of Kr^* 587 nm emission line, measured at 1250 hPa. The intensity of this line follows the recombination flow in the afterglow.

The inset shows time-integrated intensity of the second Kr_2 continuum measured at different pressures at a fixed charging voltage (13 kV). The growth of the emission is caused mainly by the growth of the breakdown voltage of the discharge along with a pressure increase. Each pressure point has its specific voltage where the pumping efficiency achieves optimum. It means that maximum energy should be loaded to the sliding discharge from the fast pumping contour with low-inductance peaking capacitor and minimum energy should be dissipated into the plasma from the slow thyratron contour (storage capacitor). Figure 4. shows that even if the time-integrated intensity is close to the saturation at high pressures, the peak intensity continuously increases with pressure due to the compression of kinetics in time.

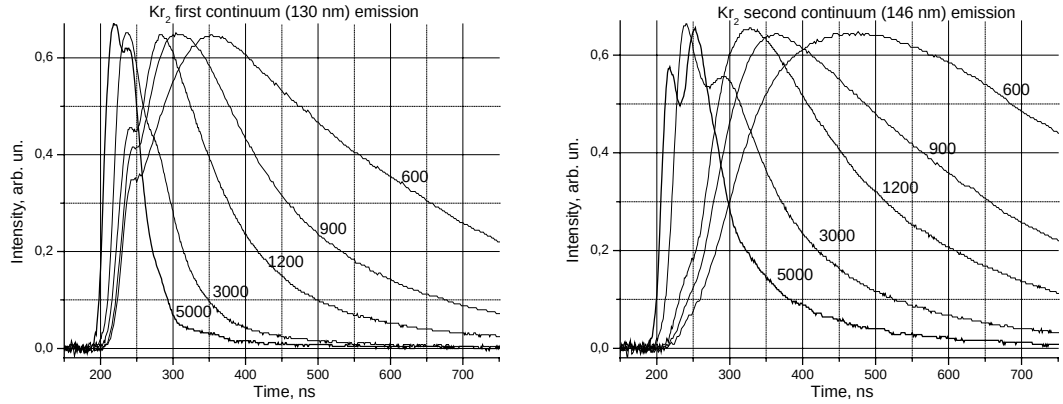


Figure 5. Time-resolved emission (normalized intensity) of the first (130 nm) and the second (146 nm) Kr_2 continua at different gas pressures (hPa). Discharge pumping pulse (FWHM) is about 20 ns.

Figure 5. presents time dependencies of the emission of the first (130 nm) and the second (146 nm) continua at different pressures of Kr. Maxima of all curves are normalized for better visualization.

The curves of these continua start with a rising edge, which becomes steeper with an increase of pressure. A small peak which is more pronounced on the curves of the first continuum appears on the rising edge of emission kinetics. Its magnitude increases with pressure (see Figure 6.). We associate the timing of the first peak with the discharge pumping pulse, whose duration is about 20 ns. The second maximum, being shallow at low pressures, and becoming sharper at higher pressures, we attribute to the population of Kr_2 0_u^+ and 1_u states via the cascade of reactions starting from recombination of Kr_2^+ ions (traditional mechanism). We also recorded the emission at 170 nm. According to [3,4] manifold of medium-high vibronic levels from 0_u^+ and 1_u Kr_2 states give their contribution to this emission. The time dependences of 170 nm emission are similar to that of 130 nm, but the first maximum is higher (see Figure 7.). Furthermore, according to [5], the radiative decay of higher vibronic levels in 1_u Kr_2 state is faster than for the lower levels. Indeed, in Figure 7. the decay time of 170 nm curve is longer than that of 130 nm. Thus, the presence of intense initial peak of the 170 nm curve indicates that corresponding intermediate vibronic levels of 0_u^+ and 1_u Kr_2^* states are effectively excited by direct electron impact of weakly bound Kr_2 molecules in the 0_g^+ ground state and free collision pairs of Kr atoms. This excitation mechanism can be used for more efficient production of VUV photons than for traditional method based on the recombination mechanism.

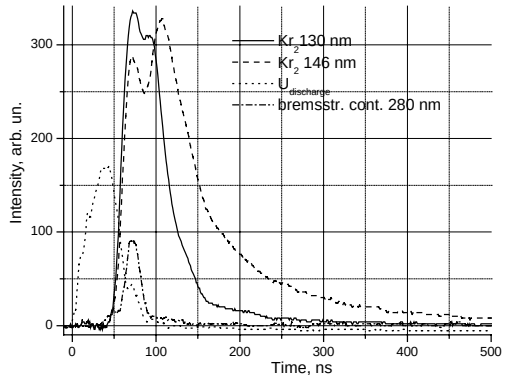


Figure 6. Time behaviors of the discharge voltage, Kr_2 the first (130 nm),the second (146 nm) and bremsstrahlung (280nm) continua at pressure of 5000 hPa.

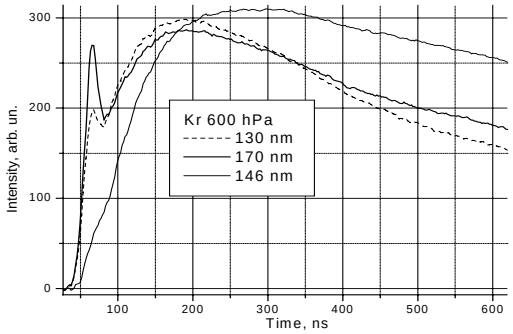


Figure 7. Time-resolved emission of the first (130, 170 nm) and the second (146 nm) Kr_2 continua at gas pressure of 600 hPa.

Rising the pressure accelerates the decay for both the first and the second continua (see Figure 5.). This pressure effect is described by two- and three-body reactions, which populate the emitting levels of Kr_2^*. Faster kinetics of the first continuum in comparison with the second continuum we explain by the fact that higher vibronic levels decay by vibrational relaxation as well as radiatively, but the lowest levels can decay only radiatively. At pressures larger that 1000 hPa the decay of both continua is non-exponential, where faster decay continuously transforms to the slower one (see Figure 5.) during the afterglow. It seems that at higher pressures the increased rate of collisional energy transfer processes is responsible for the faster component of decay in the mid-afterglow stage, but the disscociative recombination rate is responsible for the slower component in the far-afterglow.

For better understanding of the kinetics we calculated the time dependence of the second continuum using the experimental time dependence of the first continuum as a source function. This was realized by a differential equation $d[Kr_2II]/dt = [Kr_2I]/\tau_1 - [Kr_2II]/\tau_2$, where the $[Kr_2I]$ is the experimental curve of the first continuum, τ_1 is the vibrational relaxation time of higher vibronic levels and τ_2 is the effective radiative decay time of low vibronic levels. τ_2 is adjusted until the calculated and the measured time dependences of $[Kr_2II]$ are matched. The value of τ_1 almost did not affect the shape of the curves until $\tau_1 << \tau_2$ is valid.

For all the measured curves at different pressures the observed delay between the maxima of the first and the second continua as well as somewhat more rounded shape of the features of the second continuum in comparison with that of the first continuum was correctly reproduced. For pressure lower than 1000 hPa the agreement between calculated and observed $[Kr_2II]$ was good with $\tau_2 = 140$ ns. For higher pressure the modeling of the maximum intensity region required much smaller τ_2 (about 30 ns) than the tail (about 140 ns) of the $[Kr_2II]$ curve. This indicates that the effective decay rate of the emitting states of the second continuum decreases continuously with time during the afterglow. We interpret this effect by the mixing of 1_u and 0_u^+ states by electrons, whose density is decreasing in time. Complete mixing by electrons leads to the population of triplet 1_u state three times more than the population of singlet 0_u^+ state. In that case the apparent radiative lifetime, derived from known lifetimes of 1u and 0_u^+ (264 and 3.4 ns, respectively [6]), is 13 ns. Our analysis revealed that the decay time of the tail (about 140 ns) is almost pressure-independent in the range of 300-4000 hPa, but still much smaller than lifetime of 1_u (264 ns), obtained from measurements with synchrotron radiation excitation [6]. Again, the shorter lifetime we explain by partial collisional mixing with electrons in the discharge far-afterglow stage. At this final stage of the discharge the density of electrons is determined by the dissociative recombination, where the concentration of electrons and dimer ions Kr_2^+ are equalized. At electron densities between 10^{12} and 10^{13} cm^{-3} the dissociative recombination rate, being proportional to the squared density of electrons, is relatively slow and the density of electrons can be regarded as nearly constant during the time scale of few hundreds ns. This explains, why our value of

τ_2 seems to be not sensitive to the pressure.

We also interpreted the observed pressure dependence of the time behavior of the first continuum. After the fast discharge pulse the lowest $^3P_2$ and $^3P_1$ states of Kr as well as the molecular Kr_2 states emitting the first continuum, are populated by collisional energy transfer from $^1P_1$, $^3P_0$ (and higher atomic states of Kr) which can be treated as a long-lived reservoir (see Figure 3.). We found, that the two-body rate constant of collisional quenching of $^1P_1$ state in pure Kr (4×10^{-13} cm^3/s [7]), describes very well our pressure dependence of the decay rate of the first continuum in the mid-afterglow stage (the exponential decay at pressures <1000 hPa and the faster component of the non-exponential decay at pressures >1000 hPa). This rate-limiting two-body reaction simplifies significantly the kinetic modeling of fast high-pressure discharges in krypton.

ACKNOWLEDGMENTS

This work was supported by the Estonian Science Foundation under grant no. 5044 and The Royal Swedish Academy of Sciences.

REFERENCES

[1] Sasaki W. at all, *Optics Letters*, **26**, pp. 503-3 (2001)
[2] Treshchalov A. and Bashkin V., Spectroscopic diagnostics of sliding discharge as an efficient excitation source for high-pressure gas mixtures. In: *Proc. 6 th Int. Symp. On High Pressure Low Temperature Plasma Chemistry*, Cork, Ireland, 1998, pp. 298-302.
[3] Gerasimov G and Krylov B., *J. Opt. Technol.*, **62,** pp.362-4, (1995)
[4] Gerasimov G.at all, *Appl. Phys*, **B 66,** pp. 81-10 (1998)
[5] Madej A. and Stoicheff B., *Phys. Rev A*, **38**, pp.3456-9 (1988)
[6] Bonifeld T. at all, *Chem Phys. Letters*, **69,** pp. 290-7 (1980)
[7] Cook J. and Leichner P., *Phys. Rev. A*, **31,** pp. 90-9 (1985)

PLASMA-CATALYST SYSTEM FOR NO_X REMEDIATION IN SIMULATED LEAN EXHAUST

A. Khacef[a*], J.M. Cormier[a], J.M. Pouvesle[a], O. Gorce[b], H. Jurado[b], C. Thomas[b], G. Djéga-Mariadassou[b], S. Calvo[c], and Y. Lendresse[d]

a) Laboratoire GREMI, GREMI-ESPEO, 14 Rue d'Issoudun, BP6744, 45067 Orleans Cedex 2, FRANCE
b) LRS, Université Pierre et Marie Curie, 4 Place Jussieu –Case 178, 75252 Paris Cedex 05, FRANCE
c) PSA Peugeot Citroën
d) RENAULT SA

Abstract. No efficient catalyst presently exists for deNOx in lean burn conditions. Furthermore, actual catalysts generally deactivate during reaction. A cylindrical DBD non-thermal plasma reactor was coupled with a stable three-function catalyst in order to verify the nature of the effect of the plasma on the catalytic process. A mixture of $NO/O_2/C_3H_6$ in N_2 was used as a lean model exhaust. The plasma was found to perform two of the three functions: NO oxidation to NO_2 and propene activation through the partial oxidation of the hydrocarbon to aldehyde or alcohol. A complete catalyst containing the first two previous functions and the associative chemisorption of NO (third function) was used, as well as a simplified catalyst containing only the third function. Results suggest an advantageous plasma-catalyst coupling effect on NOx remediation in accordance with the proposed catalytic model.

1. INTRODUCTION

Increasingly stringent air quality standards will require future car engines to be equipped with exhaust aftertreatment systems capable of decreasing the emission of nitrogen oxides (NOx). The conventional three way catalyst (TWC) was ineffective for the NOx treatment because of the significant oxygen and water vapor levels in lean exhaust. A tremendous amount of investigation has been carried out for a couple of decades in developing catalysts for $deNO_x$ reactions in lean conditions. However, until now, no satisfactory catalyst has been found and the coupling with a non-thermal plasma discharge (NTP) can bring some new possibilities for NOx reduction as far as it is associated to a catalyst sufficiently active and stable [1-4].

Several catalytic models for the deNOx process can be encountered in the literature. They generally depend on the nature of the active site. Recently, Berger [5] has shown that three functions are necessary for a catalyst to proceed to a deNOx reaction : (i) oxidation of NO to NO_2; (ii) usage of NO_2 for partial oxidation of the hydrocarbon (reductant of NO); (iii) associative chemisorption of 2 NO molecules leading to a surface dinitrosyl intermediate species and subsequent N-O bond scissions leading to N_2 (or N_2O if the catalyst is not efficient enough); then the partial oxidized hydrocarbon (aldehyde and/or alcohol) proceeds to the cleaning of residual oxygen atoms left by NO dissociation. The two first functions can be obtained by the application of NTP discharge.

In the present work, a new catalyst -named "α"- was designed including these three functions. This catalyst is a Rh^{x+}/ CeO_2-ZrO_2 based material, as previously described elsewhere [6], to which a second and third function were added. A second catalyst -named "β"- was designed to contain only the third function assuming that the plasma would provide the first two as already suggested by Penetrante et al. [1]. This "β" material is typically Rh^{x+}/ CeO_2-ZrO_2 [6]. The catalyst support (CeO_2-ZrO_2) is not acidic and therefore does not deactivate in the presence of hydrocarbon. In addition, such a support was found to be highly stable in the presence of water.

* Electronic address : Ahmed.Khacef@univ-orleans.fr

2. EXPERIMENTAL

The experimental arrangement that was used in this work has been described in detail in reference [7]. The electrical discharge reactor used is dielectric-barrier discharge (DBD) in a wire to cylinder configuration. The DBD reactor was powered by a pulsed high-voltage generator (open circuit high voltage pulses up to 150 kV, FWHM ≈ 80 ns, voltage rise time≈40 ns, repetition rate up to 1 kHz).

The electrical energy deposition in the plasma reactor was measured with a capacitive circuit. In these experiments, the energy deposition was fixed at about 36 $J.L^{-1}$.

Reactant gases were fed from independent mass flow controllers (Brooks 5850TR) and the total flow rate was set to 150 $NL.h^{-1}$. Composition of the gas mixture (standard gas mixture) used in these experiments was : 8% O_2, 340 ppm NO, 1900 ppm C_3H_6, and, N_2 as balance.

The catalysts (weight = 5 g) were placed downstream of the plasma device in the oven as shown in figure 1 and the catalyst volume was chosen in order to obtain a space velocity (SV) of 45000 h^{-1}. The Temperature Programmed Surface Reaction (TPSR) experiments were carried out from 30°C up to 350°C with a heating rate of 1°$C.min^{-1}$.

The major gaseous components as NO, NO_2, CO, CO_2, and C_3H_6 were analyzed online and quantified using Fourier transform infrared absorption spectrometer (FTIR, Nicolet Magna 550). An electrochemical NOx analyzer (QUINTOX KM9006) was also used for monitoring continuously NO, NO_2, NOx as well as CO levels in the gas stream.

Some additional experiments (figure 7) were performed in a different experimental set up. These experiments were carried out in a U-type quartz reactor using 0.5 g of catalyst and the different flow rates were adjusted to maintain both the same reactant concentrations and space velocity as reported before. However in these cases, the heating rate was set to 10°$C.min^{-1}$. The reactor outflow was analyzed using a combination of three different detectors. A Eco Physics CLD 700 AL NO_x chemiluminescence analyzer (for NO and total NO_x (i.e. NO + NO_2)) allowed the simultaneous detection of both NO and NO_x. An Ultramat 6 IR analyzer was used to monitor N_2O and a FID detector was used to follow the propene concentration.

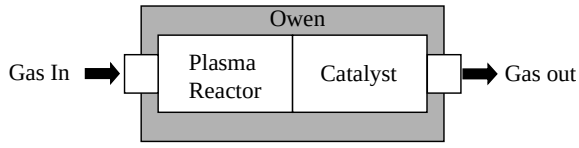


FIGURE 1. Schematic of the two-stage plasma-catalyst reactor

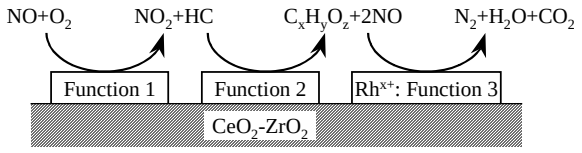


FIGURE 2. General scheme for deNOx reactions from [5], HC = Hydrocarbon, $C_xH_yO_z$ = aldehyde or alcohol.

3. RESULTS AND DISCUSSION

The aim of this paper is to show the role of plasma, taking into account both the reaction pathway already established [6] and the composition of gases at the outlet of a plasma reactor. To show that the plasma gas exhaust produces the active intermediates needed for scavenging of oxygen species left on the active site (3rd function) by $(NO)_2$ dissociation, it is convenient to develop here a general scheme for deNOx reaction.

The general scheme considers, on the 3rd function, the co-adsorption of two NO molecules, acting as ligands for Rh^{x+}. This co-adsorption is called a “associative NO adsorption” process [6]. The two NO molecules having an unpaired electron, the N-N bond is formed at this point. The associative NO adsorption is followed by subsequent N-O bond scissions and N_2 production whereas oxygen species left by this NO dissociation inhibit the Rh^{x+} site.

Activated hydrocarbon species -called $C_xH_yO_z$ and detected by Berger [5] as alcohol and aldehyde– are necessary to remove the oxygen species left by $(NO)_2$ dissociation. In the case of catalytic experiments carried out without plasma and in the presence of the complete catalyst "α", those $C_xH_yO_z$

species are formed due to a mild oxidation of HC by NO_2. This latter reaction is generally admitted by the community working on deNOx processes.

As the plasma gas exhaust contains both NO_2 and $C_xH_yO_z$ species (Figure 3), we can expect that the coupling of a plasma and a suitable catalyst provides the aldehyde and/or alcohol necessary to clean the active site from the adsorbed oxygen species allowing NO to adsorb again. Therefore the catalytic cycle could turn over. NO_2 can oxidize, over the catalyst, the HC molecules which have not been transformed to $C_xH_yO_z$ species yet.

In order to clean the adsorbed oxygen atoms left by the dissociation of two NO molecules, the three functions (Figure 2) should occur simultaneously in order to provide $C_xH_yO_z$ species, the activated form of the reducer. The support must be able to stabilize a transition metal cation, as for a zeolite support. However it must not be acidic as to avoid the hydrocarbon cracking which leads to coke formation and consequently to a strong deactivation of the catalyst. It has already shown [6] that CeO_2-ZrO_2 is able to stabilize 100% surface Rh^{x+} species.

3.1. Effect of plasma in the absence of a catalytic material

Analysis of gas composition at the outlet of the plasma reactor revealed the existence of compounds already reported in the literature [8, 9]. On figure 3, we should highlight the presence of aldehyde (CH_2O), RNOx (CH_3ONO_2), formic acid (CH_2O_2) and nitrogen dioxide (NO_2). Small amounts of nitrous acid (HNO_2) were also detected indicating the presence of moisture in the analytic system.

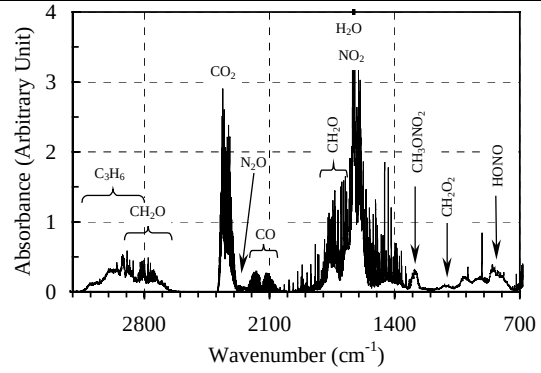


FIGURE 3. FTIR spectrum measured in the presence of plasma at room temperature – empty reactor.

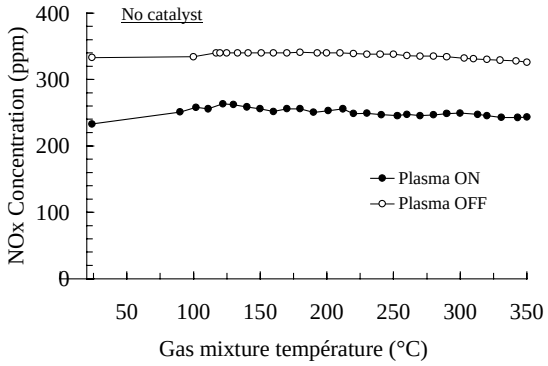


FIGURE 4 : NOx concentration versus reaction temperature (TPSR : 1°C.min^{-1}) – Empty reactor

Figure 4 shows the NOx concentration measured at the outlet of the plasma reactor in the case of empty catalytic reactor. The upper plot shows the 340 ppm NOx mixture in the absence of plasma which corresponds to the initial synthetic feed and is quite stable as the temperature rises. When the plasma was applied, it can be seen that 87 ppm of NOx were consumed. From a detailed gas chromatography analysis of the mixture at the outlet of the reactor, it appears that this NOx consumption must mainly be attributed to the formation of R-NOx species as already suggested in a previous work [9].

3.2. Plasma with CeO_2-ZrO_2 alone in the catalytic reactor

In the absence of plasma, the catalyst support (CeO_2-ZrO_2) is shown to store (chemisorption) NOx between 125 and 170°C (Figure 5), then to release NOx in two steps, from 170 to 240°C and from 240 to 320°C. If plasma is applied, storage of NOx, probably as NO, NO_2 and RNOx occurs from room temperature up to around 170°C. A loss of NOx then occurs up to 350°C probably due to a RNOx formation.

3.3. Activity of the simplified catalyst "β"

In the absence of plasma, the catalyst "β" exhibits a low deNOx activity. Figure 6 shows a NOx chemisorption at about 125°C, similar to that observed on the support alone. Then the deNOx reaction

occurs at about 280°C, with a very low conversion (about 8%).

In the presence of plasma, the NOx chemisorption observed on the support occurs up to 125°C and a global deNOx reaction is detected at around 270°C. At this latter temperature, 230 ppm of NOx are still present at the outlet of the catalytic reactor, corresponding to a 34% global consumption of NOx. Taking into account the RNOx produced by the plasma itself, the calculated deNOx conversion is equal to 13%, instead of 8% previously found in the absence of plasma. Thus, it can be assumed that the plasma provides the NO_2 (first function of the complete catalyst "α") and $C_xH_yO_z$ species (second function of the complete catalyst "α") necessary over this simplified catalyst "β" (including only the third function) to proceed to the deNOx reaction to N_2.

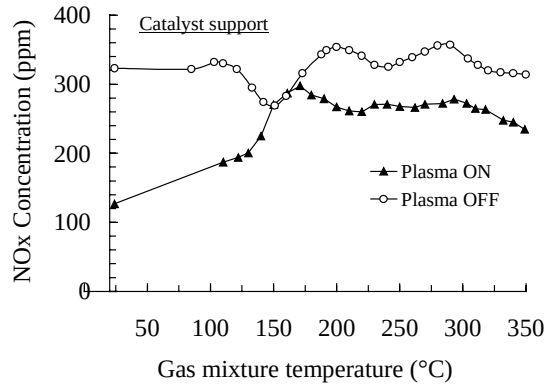


FIGURE 5 : NOx concentration versus reaction temperature (TPSR : 1°C.min^{-1}) – Catalyst Support

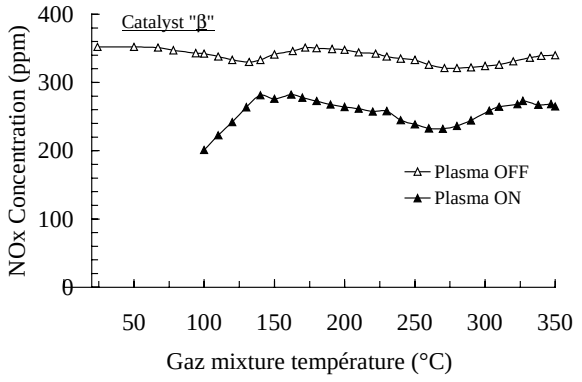


FIGURE 6 : NOx concentration versus reaction temperature (TPSR : 1°C.min^{-1}) – Catalyst "β"

3.4. DeNOx reaction over the catalyst "α"

Figure 7 shows the NOx and propene concentrations as a function of reaction temperature. After a first desorption of NO, NO_2 and N_2O around 101°C, which releases after NO adsorption during the initial reactor flushing with the feed, propene is mildly oxidized up to 225°C where the deNOx process starts. A maximum of 55% consumption of NOx, including 13% towards N_2O is observed at a temperature of 300°C. In this transient temperature programmed surface reaction (TPSR), the nitrogen balance thus corresponds to 42% deNOx to N_2 at 300°C.

Figure 8 reports the deNOx activity of catalyst "α" in the absence and in the presence of plasma. At 270°C, a 32% NOx consumption is observed. By extrapolating the data from figure 3, this NOx consumption can be attributed to a 30% N_2 formation and a 2% N_2O formation.

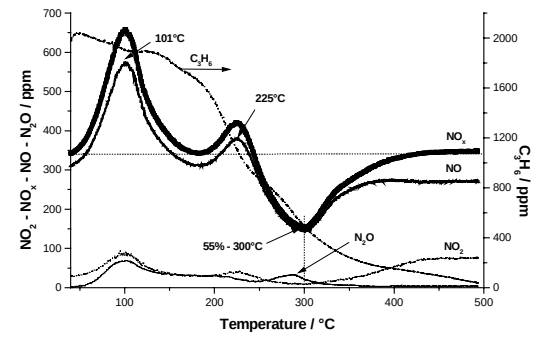


FIGURE 7 : TPSR (10°C.min^{-1}) of standard gas mixture from 30 to 500°C - Catalyst "α"

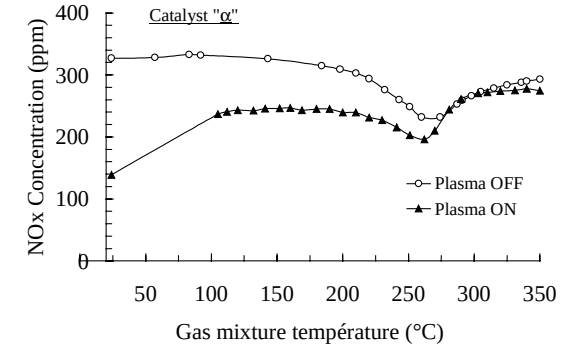


FIGURE 8 : NOx concentration versus reaction temperature (TPSR : 1°C.min^{-1}) – Catalyst "α"

If plasma is applied, the lower plot in figure 8 again shows a chemisorption of NOx or/and RNOx up to 110°C over the catalyst, then a steady-state is observed, corresponding to 250 ppm of NOx as detected over the catalyst support. At a higher temperature, the deNOx process occurs and the effect of

plasma is quite clear. Indeed, the global NOx consumption is now 40% and it occurs at a lower temperature (260°C) than that observed without plasma (270°C). Once more, the general features of the global deNOx process to N_2 are observed, as shown in figure 7 even though this experiment has been carried out in a different experimental setup.

These results shows that the deNOx conversion at about 270°C is almost the same for both catalysts and confirm the assumption that the plasma provides the first two functions (NO_2 formation and production of $C_xH_yO_z$ intermediates). The deNOx activity of catalyst "β" in the presence of plasma must be comparable to that of catalyst "α" in the absence of plasma. Nevertheless, the behavior between room temperature and 170°C is quite different, due to the probable RNOx formation in the plasma and their subsequent adsorption on the catalyst support, as evidenced by Beutel et al [10].

CONCLUSION

A general model for deNOx reaction was proposed. It assumed, that three functions are necessary for a catalyst to proceed to a deNOx reaction : (i) oxidation of NO to NO_2; (ii) usage of NO_2 for partial oxidation of the hydrocarbon (reductant of NO); (iii) associative chemisorption of 2 NO molecules leading to a surface dinitrosyl intermediate species and subsequent N-O bond scissions leading to N_2 (or N_2O if the catalyst is not efficient enough); then the partial oxidized hydrocarbon (aldehyde and/or alcohol) proceeds to the cleaning of residual oxygen atoms left by NO dissociation.

A complete catalyst "α" including the three functions and a simplified catalyst "β" including the third function were coupled to a cylindrical DBD non-thermal plasma reactor. These two kinds of catalysts were found to be stable under the experimental conditions, allowing a reliable evaluation of the effect of the plasma on the catalytic process.

It was found that the plasma leads to the formation of both NO_2 and $C_xH_yO_z$ intermediate species, permitting to substitute the first two functions of the complete catalyst "α". As a consequence, catalyst "β" in the presence of plasma was found to be equivalent to catalyst " α" in the absence of plasma. This result demonstrates what can be the role of plasma in NTP assisted catalytic NOx remediation. Furthermore, plasma is able to provide both NO_2 and $C_xH_yO_z$ intermediate species at low temperature. However, the behavior of the RNOx species formed in the plasma still remains to be studied. Indeed, in order to definitely confirm that the NOx removal leads mainly to di-nitrogen, a complete nitrogen balance would be needed.

ACKNOWLEDGMENTS

This work was performed in the frame of the French ECODEV - PREDIT program (CNRS) with financial support of the Groupement d'Intérêt Economique (GIE) PSA-Renault under contract number 97ID0024. The catalyst support was provided by Rhodia.

REFERENCES

[1] Penetrante B. M., Brusasco R. M., Merrit B. T., Pitz W. J., Vogtlin G. E., Kung M. C., Kung H. H., Wan C. Z., and Voss K. E., *SAE 982508*, (1998)
[2] Penetrante B. M., Brusasco R. M., Merrit B. T., and Vogtlin, *SAE 1999-01-3687*, (1999)
[3] Hammer T., Kishimoto T. Miessner H., and Rudolphe R., *SAE 1999-01-3632*, (1999)
[4] Balmer M. L., Tonkyn R., Yoon S., Kolwaite A., Barlow S., Maupin G., and Hoard J., *SAE 1999-01-3640*, (1999)
[5] M. Berger, *PhD Thesis*, Pierre et Marie Curie University (1999)
[6] Djéga-Mariadassou G., Fajardie F., Tempère J. F., Manoli J. M., Touret O., Blanchard G., *J. Mol. Catal. A,* **161,** 179, (2000)
[7] Khacef A., Cormier J. M., and Pouvesle J. M., *J. Phys. D : Appl. Phys* (to be published 2002)
[8] Hoard J; Balmer M. L., *SAE 982429*, (1998)
[9] Doraï R. and Kushner M. J., SAE *1999-01-3683*, (1999)
[10] Beutel T., AdelmanB., and Sachtler S., *Catal. Lett*., **37**, 125, (1998)

TOPIC 6:

Environmental applications

PFCs ABATEMENT SYSTEM BY THE ATMOSPHERIC PRESSURE GLOW PLASMA

Masuhiro Kogoma, Toshiya Abe and Kunihito Tanaka

Department of Chemistry, Faculty of Science and Technology,
7-1, Kioi-cho,Chiyoda-ku,Tokyo 102-8554, Japan

Abstract: An atmospheric pressure plasma abatement system of PFCs in the 13.56MHz cylindrical reactor is proposed. CHF_3 was destroyed completely in He-H_2O plasma. CF_4 abatement attained 96% of decomposition efficiency at 2.4kW of discharge power in the He-H_2, O_2 plasma. In the exhaust gas, CO_2, HF, H_2O and SiF_4 were found as the reaction products.

1. INTRODUCTION

In the semiconductor fabrication industry, CF_4, C_2F_6, NF_3 and CHF_3 are commonly used as the etching gases. But they have been identified as potential global warming gases. For example, CF_4 has a life time of longer than 50,000 years and it's global warming potential (GWP) is about 6,500 times higher than that of CO_2. From the point of view of the environmental protection as in the Kyoto protocol, device makers have been requested to eliminate such hard - to dissociate compounds from the exhaust gases. For most PFCs and HFCs, the conventional scrubbing systems that used the large combustion reactors have been used to achieve the abatement of such compounds. However, such a combustion system is insufficient to eliminate all of the fluorinated compounds and needs great running cost. So, a compact and more effective abatement system is strongly needed, such as a point - of - use type reactor (POU unit) in the exhaust line. Recently, a plasma abatement system that is inserted between a process turbo pump (primary pump) and a dry pump(secondary rough pump) was introduced as the POU exhaust gas treatment apparatus. The plasma abatement system, a so-called "Litmus – Blue " unit can reduce PFC and HFC emissions from dielectric etching tools in the semiconductor devices industry [1]. However, that system is available only at low pressure. A small amount of the dissociated hydrogen can easily diffuse back to the etching chamber that is kept at low pressure and will have a bad influence upon the etching. Further, because of the low-pressure, the inner surface of the pumping system must be protected from the erosion of HF molecules or F atoms. If we destroy the PFC just after the dry pump (~1atm), all of the problems should be solved. So, we will propose a new atmospheric pressure glow plasma abatement system as the post-dry pump apparatus.

2. EXPERIMENTAL

Figure 1 shows the schematics of the abatement system. We used a double cylinder-type plasma reactor. The inner electrode is a stainless steel tube cooled by water and the outer electrode is an alumina tube that is partly covered by stainless steel mesh as an outer electrode.

The outer cylinder is mainly cooled by blown air. We used He as the carrier gas to sustain the glow discharge at atmospheric pressure. The carrier gas is also to be used as the dry pump sealing gas in the exhaust system of the semiconductor etching apparatus. We used

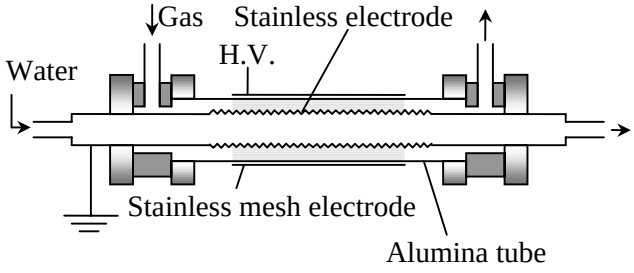


FIGURE 1 Schematic diagram of the reactor.

Table 1

Carrier gas:	He	Flow rate:	2 slm
Sample gas:	CHF_3, CF_4, H_2O, O_2 and H_2	Flow rate:	10 ~ 40sccm
Discharge power:	400~2.4kW(13.56MHz)		
Discharge electrode gap:	3~3.5mm		

fluorocarbon sample gases; CHF_3, CF_4, and we used O_2, H_2O and $H_2 + O_2$ as the de-fluorination gases which were added in the carrier gas.

The other conditions are shown in Table 1.

We used GCMS (Shimazu, QP5050) and FTIR (JASCO, FTIR7000) to analyze and to measure the concentration of the chemical products in the exhaust gas which passed through the discharge tube. A Tedler bag was used for the sampling vessel in GCMS measurements.

3. RESULTS AND DISCUSSION

3.1. CHF_3 decomposition

After discharge, quantitative analysis of the exhaust gas was done using an FTIR gas cell. In the FTIR absorption spectrum of CHF_3 treated in H_2O/He system, we found CHF_3, CF_4, H_2O, CO_2 and SiF_4. Because the FTIR gas cell is partly made of Pyrex glass, the residual HF that was produced in plasma zone has reacted with SiO_2 in the glass wall to produce SiF_4.

Figure 2 shows the concentrations of CHF_3 and CF_4 as a function of the discharge RF power when using H_2O/He system. The concentrations of CHF_3 and H_2O are 0.54% and 0.85% respectively. The above concentrations are best formation for the effective decomposition. In the case of He-H_2O discharge, CHF_3 is decreased rapidly with increasing of the RF power, and then disappeared at 700w. On the other hand, a small amount of CF_4 is increased with increasing of the RF power; after passing the maximum point, it begins to decrease. The residual CF_4 concentration is less than 0.006% at 900W of the discharge power.

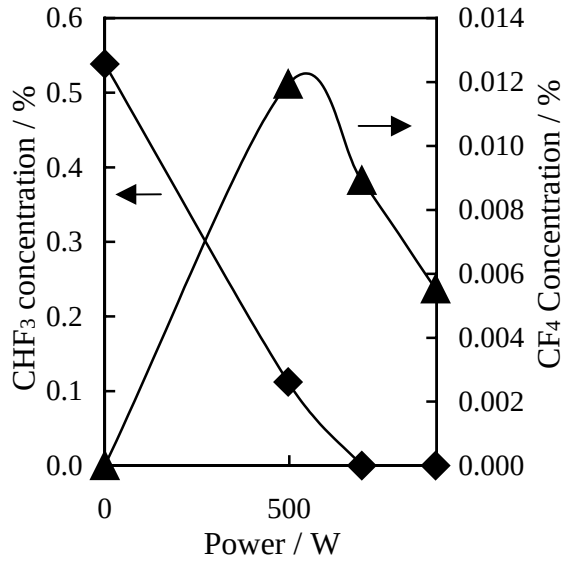


FIGURE 2 CHF_3 and CF_4 concentration as a function of discharge power.

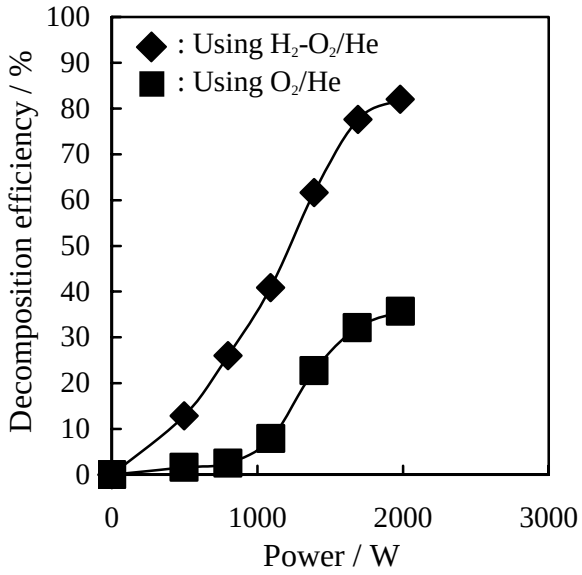


FIGURE 3 Decomposition efficiency of CF_4 as a function of discharge power, while using H_2- O_2/He or O_2/He systems.

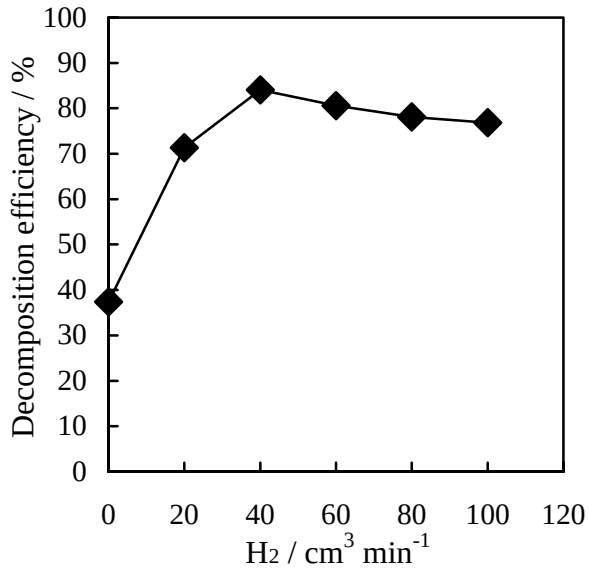


FIGURE 4 Decomposition efficiency of CF_4 as a function of H_2 flow rate.

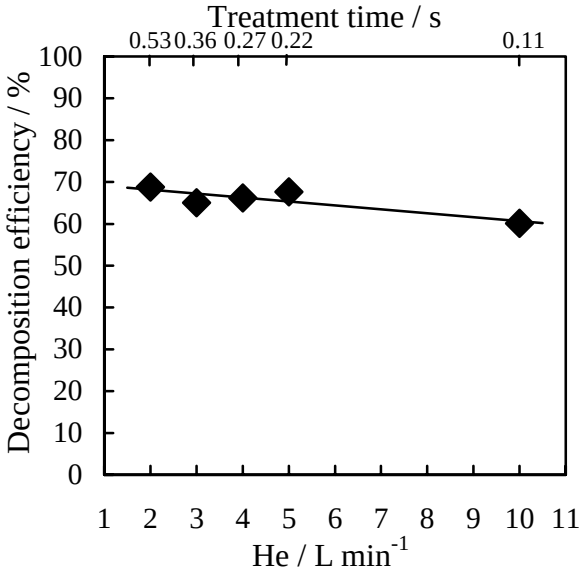


FIGURE 5 Decomposition Efficiency of CF_4 as a function of He flow rate.

3.2 CF_4 decomposition

Because of the particular stability of C-F bonds, we always found CF_4 molecules as the residual products, in the recent studies of PFCs abatement (1)(2)(3) and also in the CHF_3 abatement in this study. Owe to the difficulty of the decomposition, CF_4 is an important target of PFCs abatement. We tried to dissociate a certain amount of CF_4 (20sccm) in H_2, O_2/He system. Such a flow rate corresponds to the exhaust amount of a normal size etching apparatus.

Figure 3 shows CF_4 decomposition efficiency(DE) as a function of the discharge power in the following gas compositions; He:O_2 = 2slm:20sccm(-■-), He:H_2+O_2=2slm:40sccm+20sccm(-◆-). In the latter composition, the maximum efficiency is much better than the former. This means that the system with out of the hydrogen atoms to react with F atoms does not progress complete de-fluorination in O_2/He system.

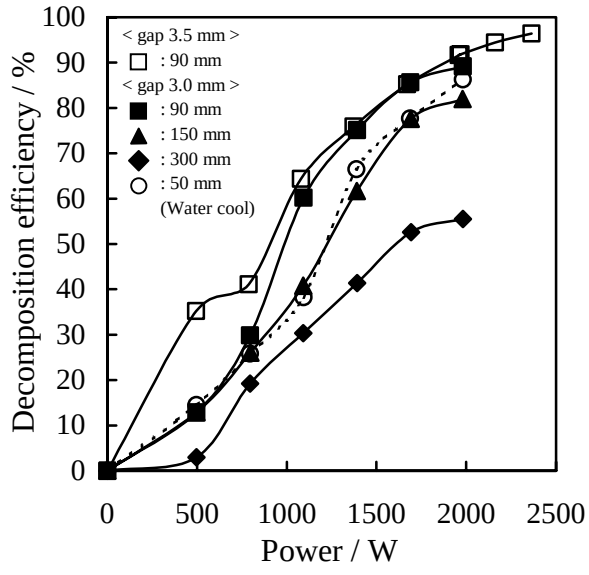


FIGURE 6 Decomposition efficiency of CF_4 as a function of discharge power.

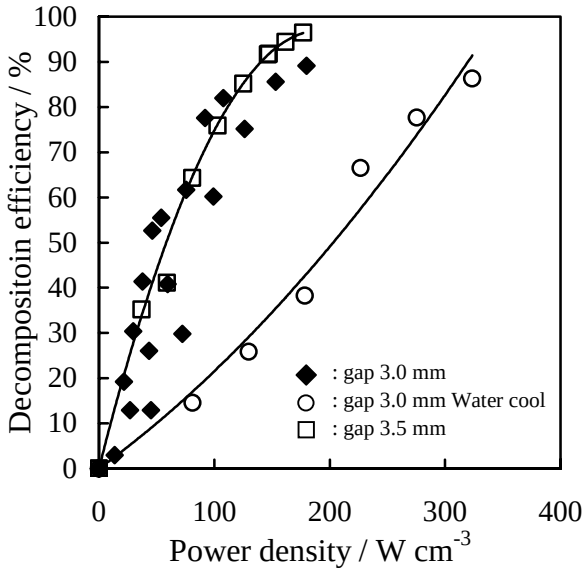


FIGURE 7 Decomposition efficiency of CF_4 as a function of power density of plasma zone.

Figure 4 shows CF_4 decomposition efficiency(DE) as a function of H_2 flow rate in the fixed flow of O_2 (20sccm). In the figure, DE increases with increasing of H_2 flow rate until 40sccm, which is a stoiciometric concentration with F atoms in CF_4, and then decreases slowly. It seems that the excessive H_2 consumes the meta-stable He atoms.

Figure 5 shows DE vs. carrier gas flow rate. If the rate-determining rate constant in the dissociation kinetics is comparable with the residence time in the discharge tube, the efficiency should be decreased with increasing of the He flow rate. But, from 2slm to 10.5slm of He flow rate changing, the efficiency shows only a small decrease. This means that the dissociation reaction initiated by electron impact reaction is much faster than the residence time.

Figure 6 shows DE vs. discharge power. The parameters are the gap length and outer electrode length. In the case of 50mm length electrode, the outer electrode is cooled by water because of the temperature increasing of the surface. In figure 6, DE curves are increased with power increasing, forming S curves. Maximum DE is 96% attained in gap: 3.5mm and the length: 90mm at 2.4kW power.

Figure 7 shows DE vs. power density deposited in the discharge space. As shown in the figure, two groups classify the curves; the first is using un-cooled outer electrode and the second is using one cooled by water. It seems that DE is strongly dependent on the situation of the plasma density and the temperature in the reaction zone. The plasma decomposition mechanism may partly include the thermal dissociation.

The related reactions of the plasma de-fluorination reaction of CHF_3 in H_2O/He and CF_4 in H_2, O_2/He, will be very complicated, but from the results of the product analysis we can suggest a possible mechanism as shown below.

<u>CHF_3, H_2O system</u>

$He + e$	→	$He^* (\sim 20eV) + e$	(0)
$CHF_3 + He^*$	→	$CF_3 + H + He$	(1)
$H_2O + He^*$	→	$H + OH + He$	(2)
	→	$H_2 + O$	(2')
$CF_3 + H$	→	$CHF_3^* \rightarrow CF_2 + HF$	(3)
$CF_2 + OH$	→	$CFO + HF$	(4)
$CFO + OH$	→	$CO_2 + HF$	(5)
$CFO + O$	→	$CO_2 + F$	(6)
$CF_3 + H_2O$	→	$CF_2 + HF + OH$	(7)
$F + H_2O$	→	$HF + OH$	(8)
$CF_3 + F$	→	CF_4	(9)
$CF_4 + He^*$	→	$CF_3 + F + He$	(10)
$4HF + SiO_2$ (glass wall)	→	$SiF_4 + 2H_2O$	(11)

<u>CF_4, H_2, O_2 system</u>

$CF_4 + He^*$	→	$CF_3 + F + He$	(10)
$CF_3 + F$	→	CF_4	(9)

$O_2 + He^*$	→	$O + O + He$	(12)
$F + H_2$	→	$HF + H$	(13)
$CF_3 + H$	→	$CHF_3^* \rightarrow CF_2 + HF$	(3)
$CF_2 + O$	→	$CFO + F$	(14)
$CFO + O$	→	$CO_2 + F$	(6)

4. CONCLUSION

We succeeded in the de-fluorination of CHF_3 with atmospheric pressure glow discharge using H_2O/He system. The de-fluorination efficiency of 20sccm CF_4 reached 96% at 2.4kW discharge power in the H_2, O_2 /He system. In the treated gas, we have only CO_2, HF and H_2O as the products that are found in GCMS and FTIR spectra.

REFERENCE

[1] SEMATECH report in 1998, International SEMATECH,Inc. USA.
[2] SELETE (Semiconductor Leading Edge Technologies, Inc. Japan) PFC Group Final Report. 2002.May 26 at Tokyo Conference Center.
[3] Steve Vitale and Herb Sawin, Study on PFC and CFC Emission and Abatement for Plasma Process, SRC Report 2001.

ACIDITY CONTROL OF THE OXIDATION REACTIONS INDUCED BY NON-THERMAL PLASMA TREATMENT OF AQUEOUS EFFLUENTS IN POLLUTANT ABATEMENT PROCESSES

D. Moussa [a], H. Vitrac [a], B.G. Chéron [b], E. Hnatiuc [c], A. Addou [d], J.L. Brisset [a]

a) Electrochimistry Laboratory (L.E.I.C.A.), University of Rouen; 76821 Mont-Saint-Aignan FRANCE
b) C.O.R.I.A., University of Rouen; 76821 Mont-Saint-Aignan FRANCE
c) Faculty of Electrotechnics; G. Asashi University,6600-Iasi ROMANIA
d) STEVA Laboratory; Mostaganem University, Mostaganem ALGERIA

Abstract. The acid properties of a non-thermal plasma in humid air (e.g., a gliding arc device) induced in an aqueous solution may deeply affect the efficiency of the matching oxidising properties, especially when the aqueous targets involve organic solutes. Hence, their oxidation rate may be strongly modified. A series of buffers is proposed to control the pH of aqueous target for at least one-hour treatments. The selected acid-base systems were selected for their inertia towards oxidation reaction, to cover a very large range of acidity.

The reported results are essential from both fundamental and applied points of view. They first allow the acute controlling of the degradation rate of organic compounds. They also enable estimating the efficiency of the gliding arc process in pollutant abatement pollutants, which is one on the main applications of the gliding arc treatments in environmental applications. Besides, they allow getting reliable data on the bactericidal effect of the plasma treatments, which are a merging application of the electric discharges.

1. INTRODUCTION

One of the major world problems of the XXI Century is related to environment, so that large efforts are devoted by many countries to promote new emerging techniques for pollution abatement. Electric discharges at atmospheric pressure and quasi-ambient temperature are carefully studied in ours Laboratories, as matching techniques to advanced oxidation processes. We focus on gliding arc discharges, which are actually quenched thermal plasmas. The chemical properties of the active species formed in the plasma are identified and quantified, in view of application to pollution abatement. The best working conditions to degrade pollutants imply a careful control of the acidity of the plasma treated targets.

2. EXPERIMENTAL SECTION

The gliding arc device used (Fig.1) for this study is close to that originally proposed by Czernichowski and Chapelle [1]. An arc, corresponding to thermal plasma, forms at the electrode "neck" (i.e., at the minimum electrode gap), moves along the electrodes, due to an air flow, then breaks when a new arc forms and gives rise to a quenched plasma. The gas flow is introduced in the reactor through a nozzle of calibrated diameter, along the axis of the reactor.

A special feeding electric device was drawn by one author (E.H.) and tested to vary the current intensity.

Magnetically stirred aqueous solutions (125 mL) are disposed as targets in front of the gas flow, so that the impinging plasma species react with the solutes at the liquid surface. The aqueous targets are analysed according to classical analytical procedures (pH-metry, UV-visible absorption spectrometry, gas chromatography).

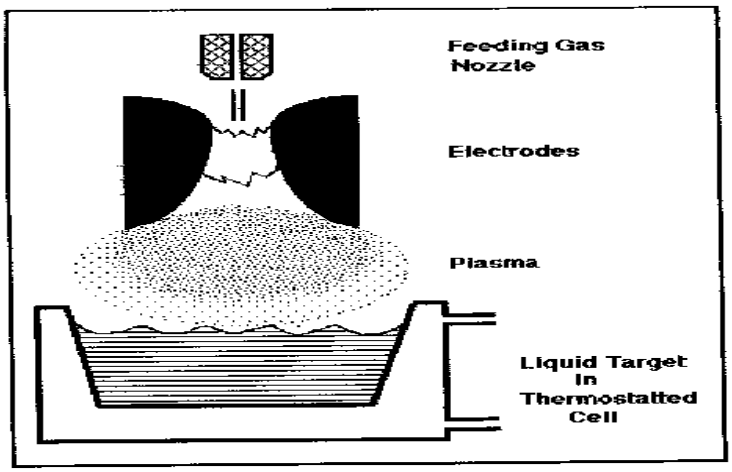


FIGURE 1. General scheme of the gliding arc device

3. RESULTS AND DISCUSSION

3.1. Chemical properties of a gliding arc plasma

Emission spectroscopy investigations show that the main active species formed in a gliding arc ("glidarc") discharge in humid air are the radicals NO and OH. These species are respectively responsible for acidifying and oxidising effects on impinging the plasma treated solution. NO gives rise to nitrous and nitric acids according to the general scheme: the relevant anions were identified and quantified according to standard procedures. Overall reactions are the followings:

$N_2 \rightarrow 2N$ and $O_2 \rightarrow 2O$

$N + O \rightarrow NO$ (or the overall reaction: $N_2 + O_2 \rightarrow 2\ NO$)

$NO + O \rightarrow NO_2$ (or the overall reaction: $NO + (1/2)\ O_2 \rightarrow NO_2$)

$NO_2 + OH \rightarrow HNO_3 \rightarrow H^+ + NO_3^-$

$NO + OH \rightarrow HNO_2 = H^+ + NO_2^-$

OH is one of the strongest oxidising agents after fluorine. Due to its high potential, the hydroxyl radical [$E°(OH°/\ H_2O) > 3$ V/NHE] is able to degrade most of the solutes. In the particular case of organic compounds, referred to as Red, oxidation of Red may be performed up to CO_2 as the ultimate product. Formally:

$Red \rightarrow \ldots \rightarrow CO_2 + qe- + r\ H^+$ $OH + e- + H^+ \rightarrow H_2O$

Oxidising degradation reactions of organic compounds often involve protons; thus, the kinetic rate very often depends on acidity. In works relevant to solution chemistry, acidity of the medium is usually fixed by using buffers, so that reaction mechanisms may be derived from kinetic data performed under controlled conditions. The lack of controlling acidity in the plasma treatment of organic solutes makes thus very difficult to estimate its efficiency.

Additionally, such a feature is of major interest for industrial applications, when organic pollutants dispersed in solution must be removed by plasma treatment.

We have just to summarise the main experimental results related to the acid effect.

3.2. Acid effects

Aqueous NaOH solutions were exposed to humid air plasmas; a steep pH lowering by more than 10 pH units for few minutes treatments results, due to the formation of nitrous and nitric acids. The pH vs

treatment time plots are thus typical titration curves of a strong base by acid (Fig. 2). These plots are characterised by the equivalent point, for pH = 7, where all the present OH^- anions initially introduced in the solution are neutralised by the impinging species, that is when the number of plasma formed acid species balance the remaining hydroxyl ions. The equivalent point, or the neutral pH (i.e., pH=7), is reached for the particular treatment time t_{eq} in given working conditions.

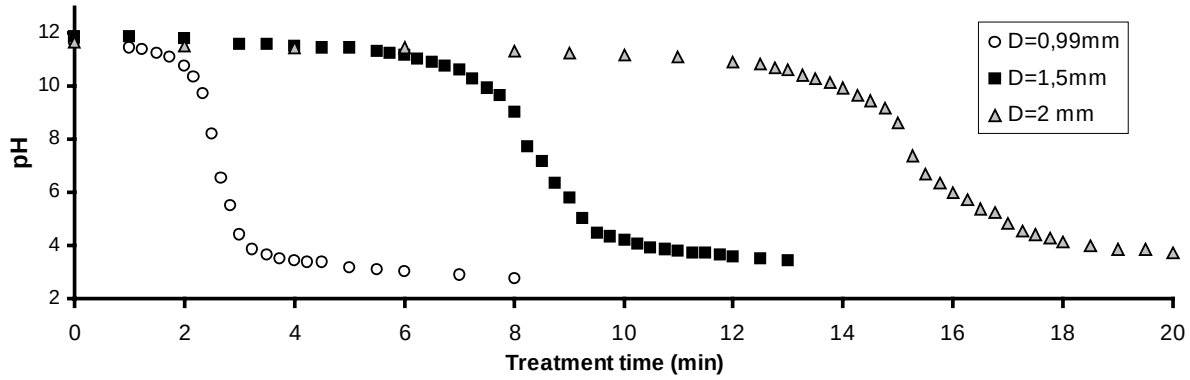


FIGURE 2. Plasma neutralisation of NaOH solutions for several electrode to liquid distances (D mm)

As previously reported [2,3], the t_{eq} values linearly depend on:

- the starting concentration C° of the NaOH solution,
- the volume of treated solution,
- the distance D between the electrodes and the liquid target (Fig.3),
- the reverse of the gas flow rate Q (Fig. 4),
- the square of the nozzle diameter Φ : teq = 4.1388 Φ^2 - 1.3243 (r^2 = 0.9987)

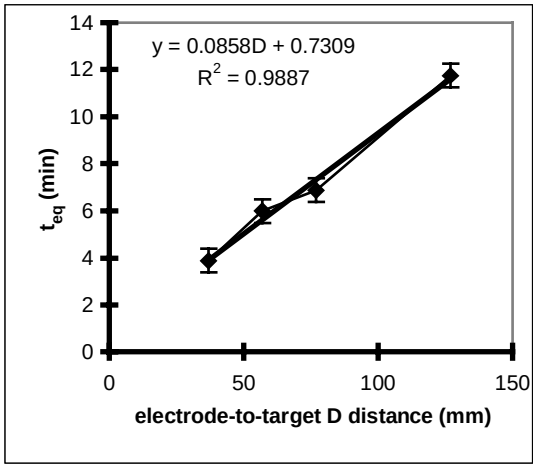


FIGURE 3. t_{eq}=f(D)

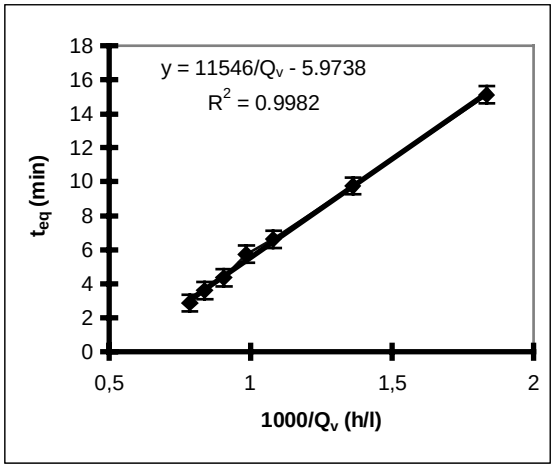


FIGURE 4. t_{eq} = f(1/Qv)

All these features easily account for the residence time of the active species formed in the plasma.

3.3. Acidity control by using selected buffers

The acid and oxidising matching effects of discharges in humid air were underlined: We wished to control acidity, so that oxidation processes could be performed in controlled conditions, which strongly suggests to use buffered media. To avoid degradation of the buffers, we had to select particular acid/base systems, which are little oxidation sensitive (5). For example, o-phosphoric acid and its conjugate bases was a suitable candidate, as were carbonic and boric acids, additionally to strong acids

and strong bases.

Table 1 gathers data relevant to selected buffered solutions exposed to the plasma for 1 hr. Emphasis is devoted to initial and final pH values, which only differ by few tenths of pH unit. This feature shows that the buffer effect actually occurs for times long enough to achieve pollution abatement by means of gliding arc treatment. Additionally, Figure 6 illustrates an example of limited and continuous pH decrease for plasma treated solution. By the way, the increasing acidity shows that the plasma treatment actually occurred.

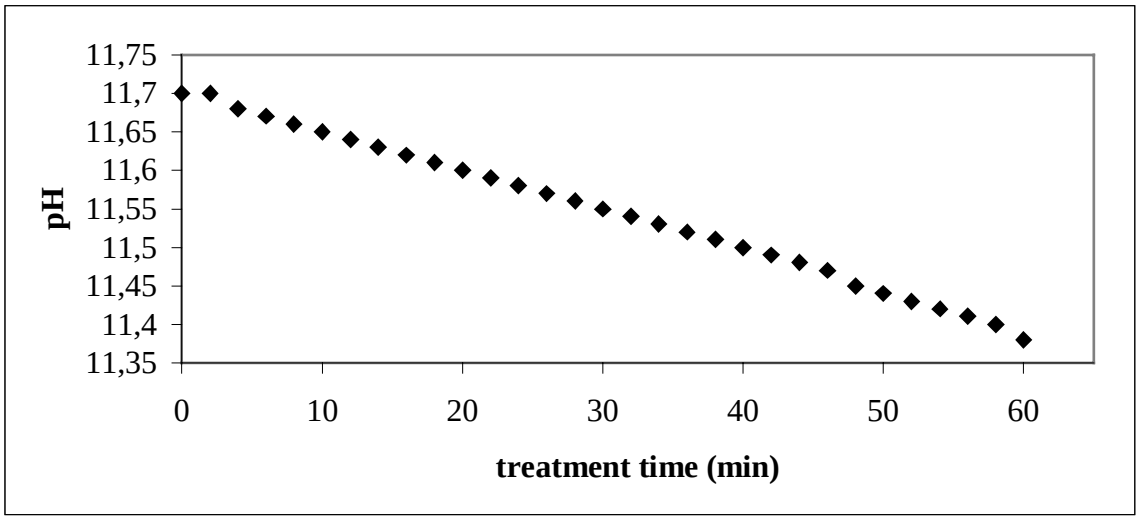


FIGURE 6. Typical behaviour of a buffered solution exposed to the gliding arc discharge. Buffer composition: Na_2HPO_4 (0.1 M) + Na_3PO_4 (0.1 M)

Table 1 also presents data relevant to buffers involving base/acid ratios different from 1:1. The limited pH evolution in this case is similar to that observed for 1:1 buffers, which confirms that the buffer effects holds again. This suggests that a large series of non-equimolar buffers can be prepared and satisfactorily used, so that the whole pH range may be now controlled.

3.4. Application to the bactericidal effect

As mentioned, numerous reactions involving organic compounds are pH-dependant. It is the case of common pollutants, such as phenols, for which the 1st oxidation step involves the formation of catechols, which are very quickly oxidised to quinones.

A matching important field of application of the plasma treatments refers to microbiology. Previous studies in ozone applications demonstrated the strong bactericidal effect of the gas (6,7). Preliminary report (8) of using a gliding arc discharge showed the bactericidal effects of the plasma treatment.

TABLE 1. pH of selected buffers exposed to the gliding arc

Composition	pH (t = 0 min)	pH (t= 60 min)
H_3PO_4 (0.1 M) + H_2PO_4Na (0.1 M)	2.16	2.0
H_2PO_4Na (0.1 M) + HPO_4Na_2 (0.1 M)	6.85	6.56
HPO_4Na_2 (0.1 M) + PO_4Na_3 (0.1 M)	11.7	11.4
H_2PO_4Na (0.15 M) + HPO_4Na_2 (0.05 M)	6.06	5.62
HPO_4Na_2 (0.15 M) + PO_4Na_3 (0.05 M)	10.73	10
HCO_3Na (0.1 M) + CO_3Na_2 (0.1 M)	9.86	9.62
HBO_2 (0.1 M) + BO_2Na (0.1 M)	9.18	8.81

Strain MG 1655 of *Escherichia Coli* were cultivated in a suitable medium (LB) and exposed to the discharge for various working conditions before numeration. The number of surviving bacteria N decreases as the exposure time increases, and the relevant plot (Figs. 7, 8) agrees with a 1st order kinetic law ($k \approx 5\ min^{-1}$). The influence of the treatment parameters was underlined from the inactivation time of the bacteria in suitable buffered solutions, according to a technique which allows to discard the acid effect of the plasma treatment on the living matter.

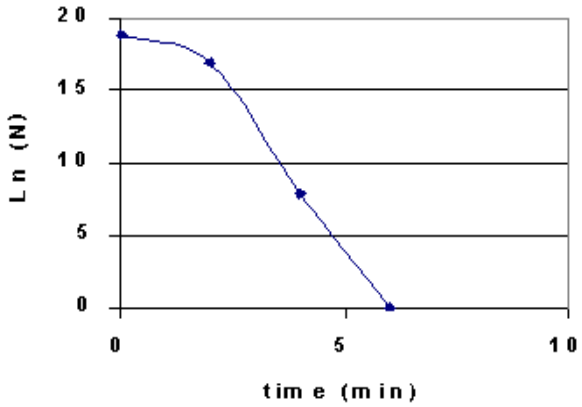


FIGURE 7. *E. Coli* abatement [d=12 cm; Q=440L/h]

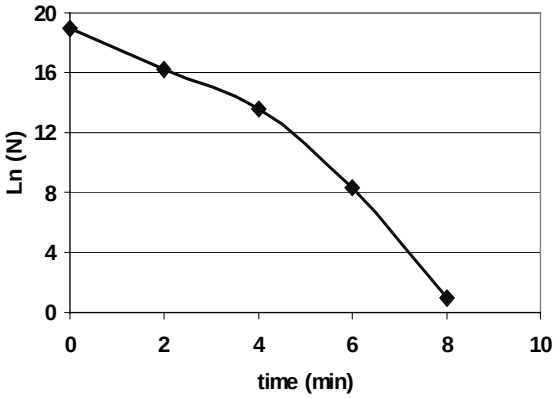


FIGURE 8. *E. Coli* abatement [d=12 cm; Q=320L/h]

4. CONCLUSION

A series of buffers, which can be used under plasma conditions, are now available. Their efficiency was tested for 1 hr plasma treatments. They enable us to control the acid effect induced by plasma exposure of aqueous solutions. As a first and direct consequence, we can now perform acute measurements of the kinetic constants of degradation reactions involving organic solutes, which are often controlled by acidity. A second consequence such is related to organic pollutants: we are now able to assess the efficiency of the gliding arc technique for pollution abatement, and even for microbiological inactivation, which appears to be an interesting and new field of application.

ACKNOWLEDGEMENTS

This work was partly performed in the frame of 2001- PAS- 23 FICU program.

REFERENCES

[1] A. Cernichowski, J. Chapelle, H. Lesueur; F. Pat. 88.14932
[2] B. Benstaali, D. Moussa, A. Addou, J.L. Brisset; Eur. Phys.J. AP 4,171-179 (1998)
[3] D. Moussa, F. Moras, J.L. Brisset; Proc. "Ozone Synthesis and Properties" (Lublin, Poland, 2000), J. Wolynska Ed., 54-58.
[4] H. Vitrac, J. Guespin-Michel, J.L. Briset; Proc."Water Air & Soil Treatment by Advanced Oxidation Technologies: Innovative and Commercial Applications" (Poitiers, France, 2001) 59
[5] F. Moras, S. Boulay, D. Moussa, A. Addou, J.L. Brisset E. Hnatiuc; Proc. "Int. Symp. Plasma Chem." ISPC-15 (Orléans, France, 2001) 3091-3095.
[6] S. Habouzit, F. Urbano, C. Monge, R. Peyrous, B. Held, P. Duroselle, J. Freney; Proc. 12th Ozone World Congress (Lille, France, 1995) Vol 1, 477-485.
[7] I. Lezcano, R. Rey, Ch. Baluja, E. Sanchez; Ozone Sci. Eng. (1999) *21*, 293-300.
[8] H. Vitrac, J. Guespin, J.L. Brisset; Proc. 7th Int. Symp. High Pressure Low Temp. Plasma Chem. "Hakone-7" (Greifswald, Germany, 2000) 393-397.

STUDY OF THE EFFECTIVENESS OF DIFFERENT HYBRID PULSED CORONA REACTORS IN DEGRADING AQUEOUS POLLUTANTS

A.T. Appleton[a], P. Lukes[b], W.C. Finney[a] and B.R. Locke[a]

a) Department of Chemical Engineering, Florida State University, FAMU-FSU College of Engineering, 2525 Pottsdamer St., Tallahassee, FL 32310 USA

b) Institute of Plasma Physics, Academy of Sciences of the Czech Republic, Za Slovankou 3, Prague 182 21, Czech Republic

Abstract: Three different types of multi-phase pulsed corona discharge reactors known as the reference reactor, the hybrid-series reactor, and the hybrid-parallel reactor were studied to remove nitrobenzene dissolved in the liquid phase. In the reference reactor, the high voltage discharge occurred only in the liquid phase while in the case of hybrid reactors the discharge was generated in both the liquid and gas phases simultaneously. Hydrogen peroxide was produced in the liquid phase and ozone in the gas phase. The highest rate of nitrobenzene removal was obtained in hybrid-parallel reactor. The major nitrobenzene oxidation byproducts were *p*- and *o*-nitrophenol.

1. INTRODUCTION

With an increased world-wide focus on environmental cleanup, new technologies are being developed to treat contaminated wastewater. Pulsed corona reactors have been shown to effectively degrade a wide variety of contaminants and have promise for further development [1, 2]. Most pulse corona reactors used to treat wastewater utilize a high voltage discharge placed in either the gas or liquid phase of the reactor. Recent studies have shown that developing a hybrid pulsed corona reactor which would combine electrical discharges in several phases enhances degradation over single phase discharge reactors [3].

In this work we present three different types of multi-phase pulsed corona reactors known as the reference reactor, the hybrid-series reactor, and the hybrid-parallel reactor. In the reference reactor, both the high voltage and ground electrodes are submerged in the solution. In the hybrid-series reactor, only the high voltage electrode is submerged while the ground is suspended above the solution. The hybrid-parallel reactor generates high voltage discharges simultaneously in both the liquid and gas phases of the reactor while the ground was placed at the gas/liquid interface. The high voltage discharge in the aqueous phase of all three types of reactors leads to the formation of hydrogen peroxide. The gas phase discharge occurring in only the hybrid reactors results in the formation of ozone thereby enhancing the rate of degradation of the contaminant in the liquid through direct ozone attack or increased hydroxyl radical formation. The effectiveness of each reactor is based upon the rate of nitrobenzene (a model nitrogen containing explosive aromatic compound) degradation, byproduct identification, the rate of hydrogen peroxide formation, and the gas phase ozone formation. Energy efficiency of nitrobenzene degradation is also determined for all reactor types.

2. EXPERIMENTAL

The three types of reactors can be seen in Figure 1. In all cases, the liquid phase electrode is made of NiChrom wire and the ground is composed of reticulated vitreous carbon (RVC), a highly conductive, macroscopically porous glassy carbon. The gas phase high voltage electrode in the parallel reactor was also made out of RVC. The high voltage electrode in the reference reactor was 5.7 cm from the ground

[a] Electronic address: locke@eng.fsu.edu

while in the parallel reactor the gas phase high voltage electrode was 5 cm from the ground. The difference between the reference and parallel configurations was only in the application of high voltage on the gas phase electrode in the parallel case. In the series configuration, the ground was suspended 5 mm above the solution surface. The high voltage pulse was provided by a pulse power supply, which was identical to that used in our previous work [4-6]. In the present study a pulsed high voltage of 45 kV with the pulse repetition rate of 60 Hz and pulse energy of 1.1 J/pulse was used.

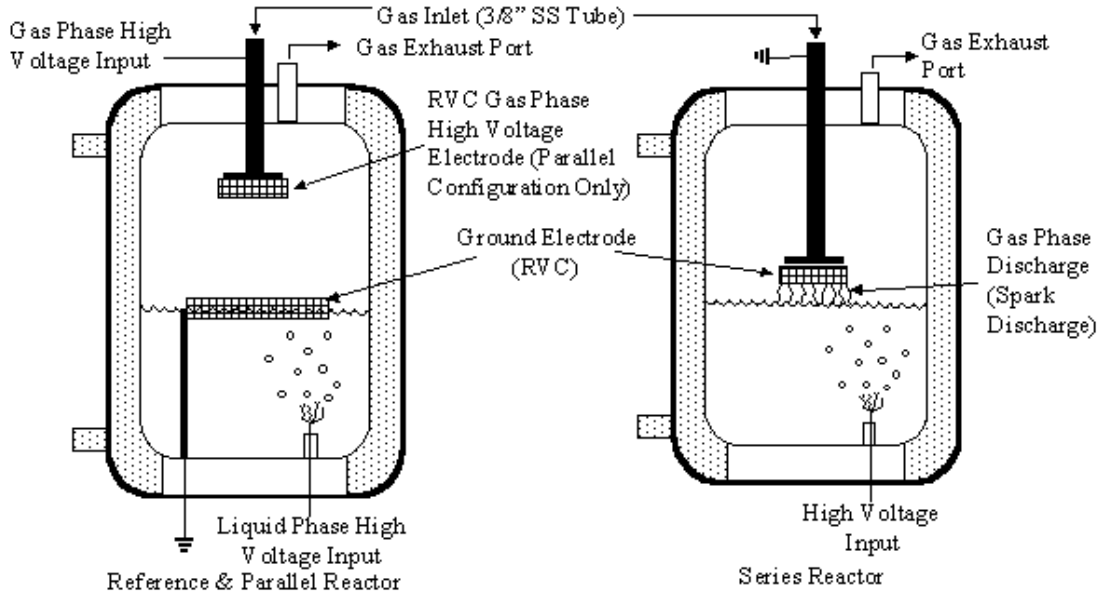


FIGURE 1. Reactor configuration.

In all reactor configurations, the same glass reactor with a capacity of approximately 1 l was used. It was surrounded by a water jacket maintained at 15 ^{o}C to prevent the reactor from overheating. The volume of 550 ml of KCl solution (0.9 mmol/l) with initial solution conductivity of 130 μS/cm was used in each case. The recirculation line used to take samples was made out of HDPE and attached to a pump moving the liquid at 400 mL/min. This reactor design is unique and was developed from earlier models [3]. The design allows the reactor to be quickly changed between the three different configurations by simply rearranging or removing components. The aqueous phase of the system, shown in Figure 1, is closed while the gas phase is open. The composition of the inlet gas stream was 200 ml/min of argon and 150 ml/min of oxygen to increase ozone production in the hybrid series and parallel reactors [7]. The inlet gas stream was pre-treated using a water filled gas wash bottle to increase gas humidity. This led to a more stable gas phase discharge although reducing the overall ozone concentration [8].

Measurements of gas phase ozone concentration were conducted using a PCI Ozone Corporation ozone monitor, model HC-1, and verified with results obtained using the iodometric method by running the reactor outlet stream through a gas wash bottle containing KI solution. The concentration of hydrogen peroxide was determined colorimetrically employing the reaction of H_2O_2 with titanyl ions. The concentrations of nitrobenzene and degradation byproducts in the solution were measured by using a Perkin Elmer high performance liquid chromatograph.

3. RESULTS AND DISCUSSION

3.1. Aqueous hydrogen peroxide formation

The results of the experiments to determine the rate of H_2O_2 formation are shown in Figure 2. The same voltage of 45 kV was applied in all three reactors. Each data set represents an average of three experiments to ensure reproducibility. The H_2O_2 concentration increased at similar rates in all three reactors. The measured rate of H_2O_2 formation in all reactors was 5.0 x 10^{-7} mol/s.

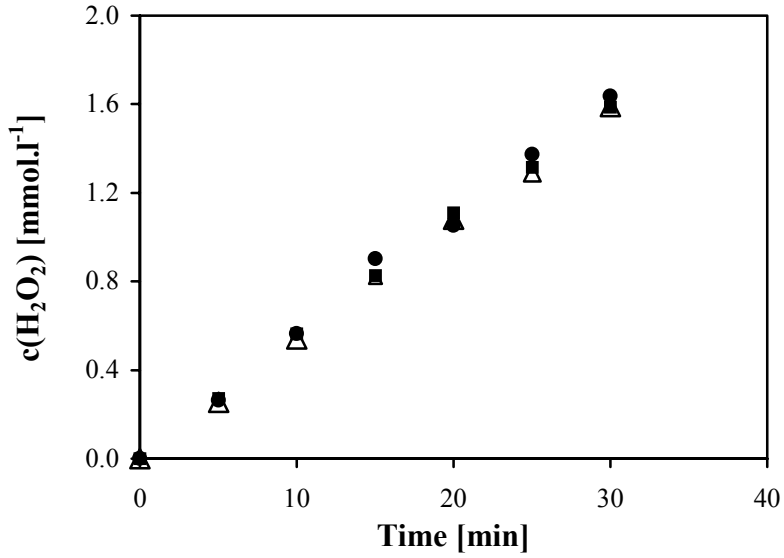


FIGURE 2. Comparison of H_2O_2 formation in reference (●), hybrid-series (▵) and hybrid-parallel (■) pulsed corona discharge reactor. Liquid phase: 0.9 mmol/l KCl solution, initial conductivity 130 µS/cm; gas phase: Ar/O_2 mixture, flow 0.35 l/min; applied voltage 45 kV, power input 66 W.

Direct reactions between H_2O_2 and dissolved O_3 had negligible effects on H_2O_2 concentration. This reaction tends to be very slow at low pH. The initial pH of the solution was 5.0 and decreased to 4.5. Since the aqueous H_2O_2 concentration in the parallel reactor is similar to the other reactors, lower applied voltage and power go to the gas phase high voltage electrode.

3.2. Gas phase ozone formation

Figure 3 shows the concentration of ozone in the gas phase of the hybrid-series and parallel reactors as a result of the gas phase discharge. No ozone was formed in the reference reactor since it is a single phase reactor. The hybrid-parallel reactor shows a substantially higher ozone concentration than that in the hybrid-series reactor. This is primarily due to the type of gas phase discharge occurring in each case.

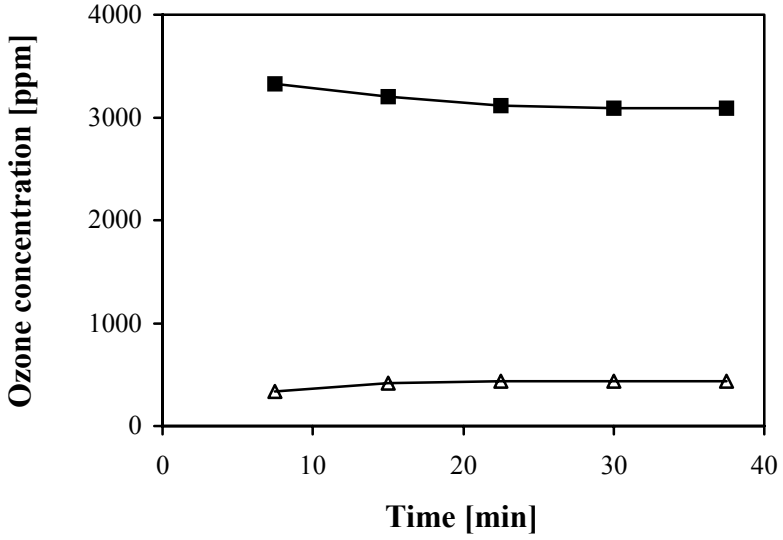


FIGURE 3. Comparison of ozone formation in hybrid parallel (■) and hybrid series (▵) pulsed corona discharge reactor. Liquid phase: 0.9 mmol/l KCl solution, initial conductivity 130 µS/cm; gas phase: Ar/O_2 mixture, flow 0.35 l/min; applied voltage 45 kV, power input 66 W.

The bright plasma channels occurring between the solution surface and ground in the series reactor have a very high electron density. Much of the ozone formed by the discharge is quickly degraded by other free electrons. The corona-like streamers formed by the gas phase discharge in the parallel reactor have a much smaller electron density. This reduces the amount of O_3 consumed by reactions with free electrons [9].

Experiments conducted in both reactors in which the gas phase discharge occurred in a pure oxygen system resulted in a minimal amount of ozone formed. As soon as the oxygen gas was mixed with argon at the specified flow rates, the ozone concentration increased rapidly thereby showing the importance of argon as a gas phase catalyst. Increasing the flow rate ratio of argon and oxygen resulted in breakdown occurring between the high voltage and ground electrodes. In this case, the RVC material making up both electrodes was damaged. Decreasing the flow rate ratio reduced the amount of ozone formed.

Although not directly measured, since the gas phase discharge occurs in a humid environment, oxidizing radicals are formed [9]. Since the radicals are formed far from the solution surface and their lifetime is short, it is expected that they do not dissolve into the solution in a large enough quantity to affect the bulk concentrations. They do bring about the possibility of treating a volatile species that may have evaporated from the solution.

3.3. Nitrobenzene removal

Figure 4 shows the results for the nitrobenzene removal experiments in all three types of reactors. The hybrid parallel reactor is the most effective in removing nitrobenzene from the solution while the reference reactor was least effective. The energy cost for nitrobenzene degradation was calculated to be 0.067, 0.042 and 0.030 g/kWhr for the parallel, series and reference reactor, respectively. This large difference can only be associated with the addition of O_3 forming in the gas phase and dissolving into the solution to enhance oxidizing radical formation. The difference is not attributed to H_2O_2 formation since all three reactors showed similar rates of formation. The difference in nitrobenzene oxidation between the parallel and series reactor is attributed to the ozone dissolving faster in the parallel reactor than the series reactor due to the higher gas phase concentration.

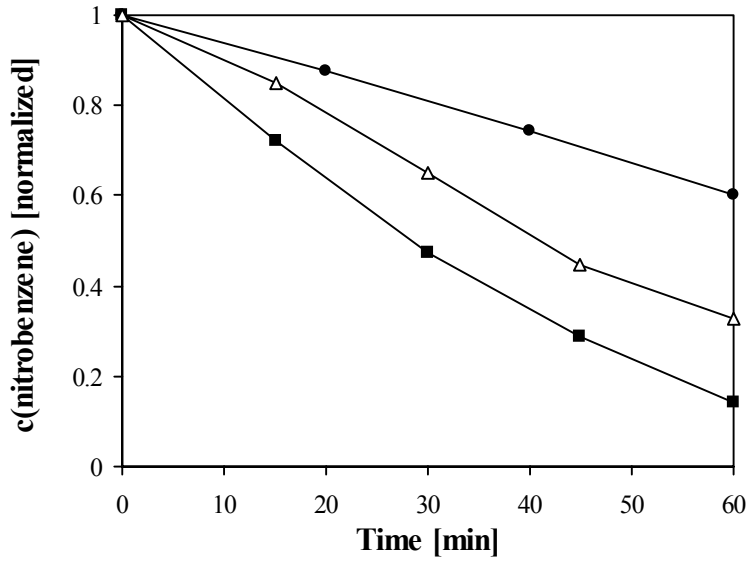


FIGURE 4. Comparison of nitrobenzene removal in reference (●), hybrid-series (△) and hybrid-parallel (■) pulsed corona discharge reactor. Liquid phase: 0.9 mmol/l KCl solution, 10 ppm nitrobenzene, initial conductivity 130 µS/cm; gas phase: Ar/O_2 mixture, flow 0.35 l/min; applied voltage 45 kV, power input 66 W.

The major intermediates and byproducts of nitrobenzene oxidation were *para*- and *ortho*-nitrophenol. A 8.5 ppm decrease in nitrobenzene concentration correspond to a final combined concentration of 3.0 ppm for the nitrophenol isomers. Often, the *ortho*-nitrophenol concentration tended to be slightly higher than *para*-nitrophenol. The remaining aqueous products were nitrate and oxalic acid.

4. CONCLUSIONS

The parallel reactor configuration proved to be the most efficient in nitrobenzene removal from solution when compared with the series and reference reactor. The reference reactor is shown to be the least effective. Since the H_2O_2 formation in all three reactors is similar, the difference in nitrobenzene oxidation must be attributed to the addition of a gas phase discharge in the hybrid reactors. This discharge resulted in the formation of ozone that dissolved into the solution, enhancing radical production.

ACKNOWLEDGEMENTS

We gratefully acknowledge partial support from the National Science Foundation, Project # INT-0086351, the Ministry of Education, Youth and Sports of the Czech Republic, Project Kontakt, the United States Army, and the Department of Chemical Engineering, FAMU-FSU College of Engineering. Discussion and assistance from Mayank Sahni, Michael Kirpatrick, and Robert Gasparik from Department of Chemical Engineering, FAMU-FSU College of Engineering and Martin Clupek from the Institute of Plasma Physics in Prague is very much appreciated.

REFERENCES

[1] Malik, M.A., Ghaffar, A., and Malik, S.A., *Plasma Sources Sci. Technol*., **10,** 82-91 (2001)
[2] Šunka, P., *Phys. Plasma*s **8,** 2587-2594 (2001)
[3] Grymonpré, D.R*., An Experimental and Theoretical Analysis of Phenol Degradation by Pulsed Corona Discharge,* Ph.D. Dissertation, Florida State University, Tallahassee, FL, 2001
[4] Sharma, A.K., Locke, B.R., Arce, P., and Finney W.C., *Hazard. Waste Hazard. Mater.,* **10,** 209-219 (1993)
[5] Joshi, A.A., Locke, B.R., Arce, P., and Finney, W.C., *J. Hazard. Mater*., **41,** 3-30 (1995)
[6] Grymonpré, D., Finney, W.C., Locke, B.R., *Chem. Eng. Sci*., **54,** 3095-3105 (1999)
[7] Manning, T.J., *Ozone Sci. Eng.* **22,** 53-64 (2000)
[8] Fouad, L., and Elhazek, S., *J. Electrostatics,* **35,** 21-30 (1995)
[9] Peyrous, R., Pignolet, P. and Held, B., *J. Phys D: Appl. Phys*., **22,** 1658-1667 (1989)

CHEMICAL PROCESSES DURING BIOGAS CONDITIONING BY PULSED CORONA DISCHARGES

S.A.Nair[a],A.J.M.Pemen[a], K.Yan[a], E.J.M. van Heesch[a], K.J.Ptasinski[b] and A.A.H.Drinkenburg[b].

a) Faculty of Electrical Engineering, b) Faculty of Chemical Engineering
Eindhoven University of Technology, P.O. Box 513, 5600 MB Eindhoven, The NETHERLANDS

ABSTRACT: Biogas conditioning or cleaning is perhaps one of the main obstacles for utilization of biomass as a source of power generation. In the present work, we try to utilize pulsed corona techniques for the mentioned application. Here we try to focus on the chemical processes that occur during pulsed corona biogas conditioning. Experimental results at 200^{o}C show that the main process for tar (heavy aromatic hydrocarbons) removal is mainly by oxidation and termination by CO. Although possibilities of cracking by H_2 exists, but experimentally not observed. In the continuing research program, experiments are also being planned at higher temperature up to 900^{o}C with the potential of reducing the energy consumption as well as satisfying the requirements of the overall process chain from gasification to power generation.

1. INTRODUCTION

Tar removal is perhaps one of the main obstacles in utilization of biomass for power generation. Gasification of biomass typically at temperatures of the order of 500-600^{o}C produces along with product gases, an undesirable stream consisting of tars (heavy aromatic hydrocarbons) , condensable hydrocarbons and solid char. Presence of this heavy hydrocarbons lead to condensation in transfer lines and causes eventual clogging resulting in regular operational interruptions. The objective of any biogas conditioning device is, thus, to provide gas stream with low dew-point. Thermodynamic analysis suggests that the high dew point of biogas is due to the high concentration of polyaromatic compounds such as naphthalene, phenanthrene, anthracene, etc. [1]. Hence the objective would be to reduce the aromatic content of the gases, as these hydrocarbons also possess calorific value which can be utilized in further stages of power generation. Presently available methods can either be primary [2] (focusing on modification of design of gasifier and its operating conditions) or secondary [3] (gas cleaning outside the gasification system, by catalytic or thermal methods). However so far, none of the available techniques have achieved success in terms of long term operation and efficiency.

Non-thermal plasma techniques have been a subject of investigation for pollution control and gas cleaning operations for the past decade. The ability to generate electrons with high energy levels (1~10eV) at normal gas temperatures allows for the decomposition of background gas molecules which otherwise is not possible. This allows for creation of a reactive atmosphere and subsequent chemical processing is possible. Plasma thus closely resembles a catalyst in terms of its operation to reduce severity of operating conditions. The same approach is used for biogas conditioning as well, here by means of pulsed corona plasma.

2. EXPERIMENTAL SET-UP

The experimental set-up consists of a pulsed power supply, and a wire-cylinder type corona reactor. The reactor is 25 cm dia. & 3m in length. This is part of a closed loop circulation system driven by a

[a] Electronic address: s.a.nair@tue.nl

fan with variable speed adjustment. The internal flow rate used for the measurement is 240 Nm^3/hr and the effective volume of the system is 300 liters. The system can handle a maximum operating temperature of 250 ^oC (*Fig.1*) Tar injection is done by means of a boiler. A weighed amount of the component can be added and vaporized into the flowing gas stream. The entire set-up is heated by means of heating tapes along with adequate temperature control. The gas temperature measurement is done at a point just at the entry of the reactor. To ensure uniform gas temperature throughout the set-up, sufficient time (60 min) is devoted to attain a steady state. Additionally, thermocouples are installed at various points, with measurement and control loops. The corona voltage, current and repetition-rate are monitored on a HP-Infinium digital oscilloscope. From the voltage and current, both the power-per-pulse and the energy- per-pulse can be determined. Tar component measurements are done by both FTIR and a GC (HP5890). Typical tar components monitored are Naphthalene (characterized as Heavy tar) and Phenol or Toluene (characterized as light tar). The GC (HP5890) is equipped with a FID and a Chrompack CP-Sil 5 CB fused silica WCOT (Wall Coated Open Tubular) column for measurement of heavy hydrocarbons (commonly 'TAR')

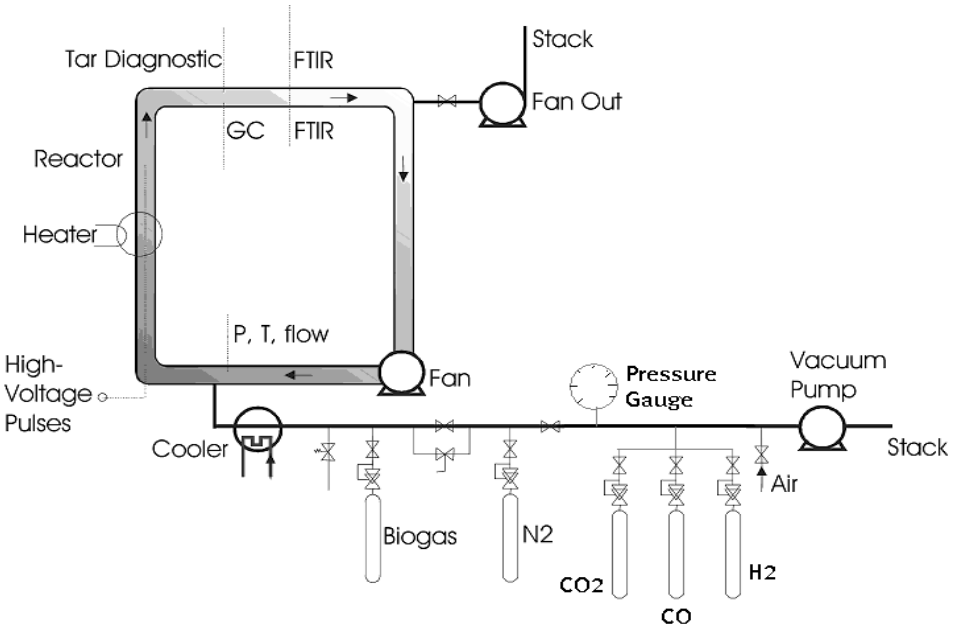


FIGURE 1. Experimental Set-up

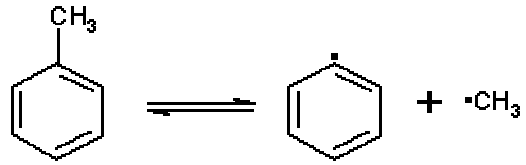
The system is filled with a synthetic biogas of composition 20 % CO, 12 % CO_2, 17 % H_2, 1 % CH_4, rest N_2 and heated up to 200 ^oC, at a pressure of 1 bar. Apart from this individual gases can be added in via separate gas injection ports. Required gas composition can be made by filling the system with each individual gas and monitoring its partial pressure. After allowing sufficient time to attain steady state, (to ensure uniform gas composition and temperature distribution) tar is vaporized into the gas stream and again allowing for the system to attain uniform concentration. This can be monitored from the FTIR spectrum. Pulsed corona discharges are then run for a particular time interval (typically 30~60 secs. at 50 pulses per seconds, with a energy of 1 J/Pulse). After every run, both GC and the FTIR analysis are done for the tar component removed. This is then plotted against the corona energy density (J/L).

3. RESULTS AND DISCUSSION

3.1. Primary Processes

Pilot scale of testing of the process on actual gasifier has shown that pulsed corona processing indeed breaks down heavy hydrocarbons to lighter ones at energy densities of the order of 160 J/L for about 60 % heavy tar removal [4]. Experimentally, typical energy costs for removal of various tar components have been determined in N_2 as well as in biogas [5]. Less energy density for removal in

N_2 as compared to biogas indicates the influence of strong radical termination reactions. It is observed that compounds containing side-chains require more energy than those without. This may be attributed to the recombination of the functional groups after radical attack.



For commercial utilization, tar removal need to be achieved at energy levels less than 200 J/L. Thus for improvement of efficiency, deeper insight into chemical processes involved is required. This can be done by determining energy requirements for removal of compounds for different gas mixtures.

a) $N_2 + H_2$ (15%)
b) $N_2 + CO_2$ (15%)
c) $N_2 + H_2O$ (17%)

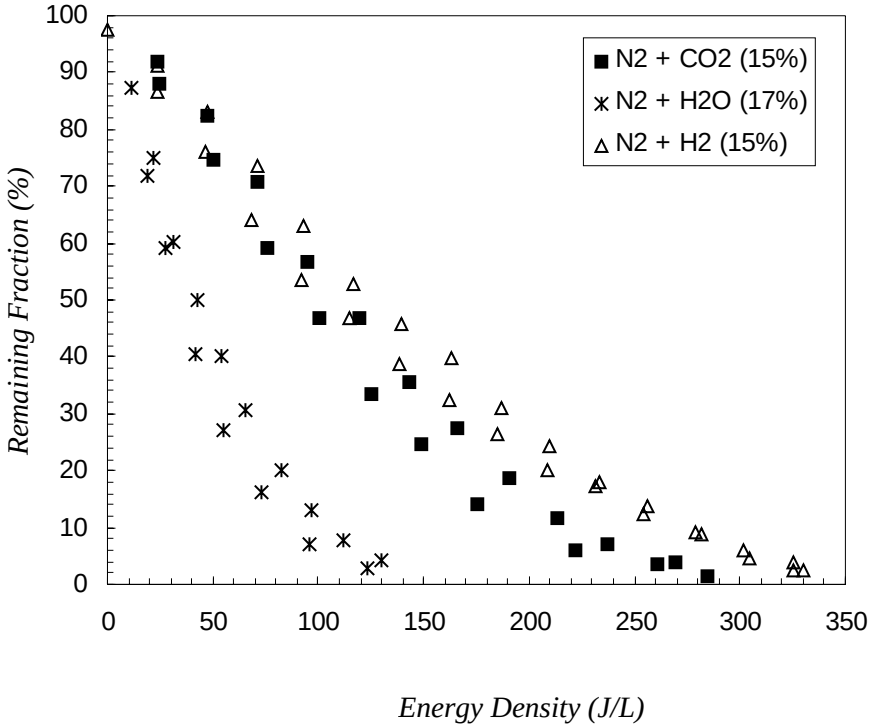


FIGURE 2: Energy consumption for Naphthalene removal (T = 200 ~ 210 ^oC) (Conc = 500 ~ 600 ppm)

Figure 2 indicates energy consumption for various gas mixtures in order to establish relative trends in energy requirement with respect to different radicals. Less energy density requirement for component removal in presence of moisture (*Fig.2*) indicates corona assisted steam reforming to be a better candidate for tar removal rather than the case of CO_2 reforming or cracking by H_2 under the conditions of experiment (T=200 ~ 210 ^oC)

From mechanistic point of view, different process can occur in each of the gas mixtures. Whereas in pure N_2, removal can occur due to presence of N radicals, the same cannot be expected to occur in presence of other gases. This can be concluded from experiments in air-like gas mixtures where no significant amount of N radical production takes place if the O_2 concentration is greater than 3.6%[6]. Similarly, in presence of CO_2 removal will mainly be governed by oxidation process (O radicals), in hydrogen, by production of H radicals, i.e. via cracking mechanism and in H_2O, may be combination of both OH and H radicals. The primary processes thus can be

$$H_2O \rightarrow H + OH \quad (1)$$

$$CO_2 \rightarrow CO + O \quad (2)$$

$$H_2 \rightarrow H + H \quad (3)$$

$$N_2 \rightarrow N + N \quad (4)$$

Energy density requirement will depend on combination of factors:

a) Energy transfer from source to reactor
b) Radical production efficiency – which will depend on the dissociation energies of individual molecules and streamer corona generation.
c) Relative reaction rates of removal and termination reactions.

With proper matching between source and reactor, the energy transfer efficiency can be as high as 90% [7]. However, this can be considered the same for all the three gas mixtures. The remaining factors will thus be largely responsible for the trend in energy density. In presence of CO_2, oxidation process dominates, but at the same time termination reactions such as

$$O + CO + M \rightarrow CO_2 + M \quad (5)$$

reduces the radical concentration leading to higher energy requirements. The same can be the case in presence of H_2, where the following terminations occurs

$$H + H + M \rightarrow H_2 + M \quad (6)$$

Thus, one possible cause for higher energy densities in H_2 would be faster termination of H radicals as opposed to that for O radicals. Tar removal in presence of moisture seems to be more effective as compared to other species so far considered. Termination reactions do play a role in presence of moisture, but the presence of more reactive OH along with H radicals makes it more efficient.

$$OH + H + M \rightarrow H2O + M \quad (7)$$

$$OH + \text{Naphthalene} \rightarrow \text{Products} \quad (8)$$

3.2. Identifying radical termination component:

Having identified the trends in energy density for the primary processes, the next step would be to analyze the reaction schemes in presence of mixture of background gases. Fundamental reactions involved for actual biogas can now be identified by comparing the energy consumption for naphthalene removal occurring in the following two cases:

a) $N_2 + CO_2$ (15%)
b) $N_2 + CO_2$ (10%) + CO (10%)

Figure 3 compares the energy consumption for naphthalene removal in presence of CO and in biogas. It thus verifies that tar removal in biogas is primarily a oxidation process and at temperatures of 200^{o}C less effect of H_2 is seen. The expected primary process to explain the above results can be similar as mentioned in Eq. 2 & 4. Here naphthalene removal can be expected to occur via

$$O + \text{Naphthalene} \rightarrow \text{Products} \quad (9)$$

Apart from the non linear terminations, O radical termination can also occur because of reaction with background CO. This further reduces O radical density.

$$CO + O + M \rightarrow CO_2 + M \quad (10)$$

This means that when CO is present more CO_2 molecules need to be dissociated for Naphthalene removal, which explains the higher energy density requirement in presence of CO. The establishment of an equilibrium between CO and CO_2 prevents further improvement in efficiency for tar removal at the conditions of the experiment. Apart from this previous experimental investigation [5] have revealed that presence of moisture has no influence on energy consumption for tar removal in biogas, although fig.2 indicates OH radicals to be more effective. This may be due to additional termination reactions involved for OH radicals, which needs to be further investigated.

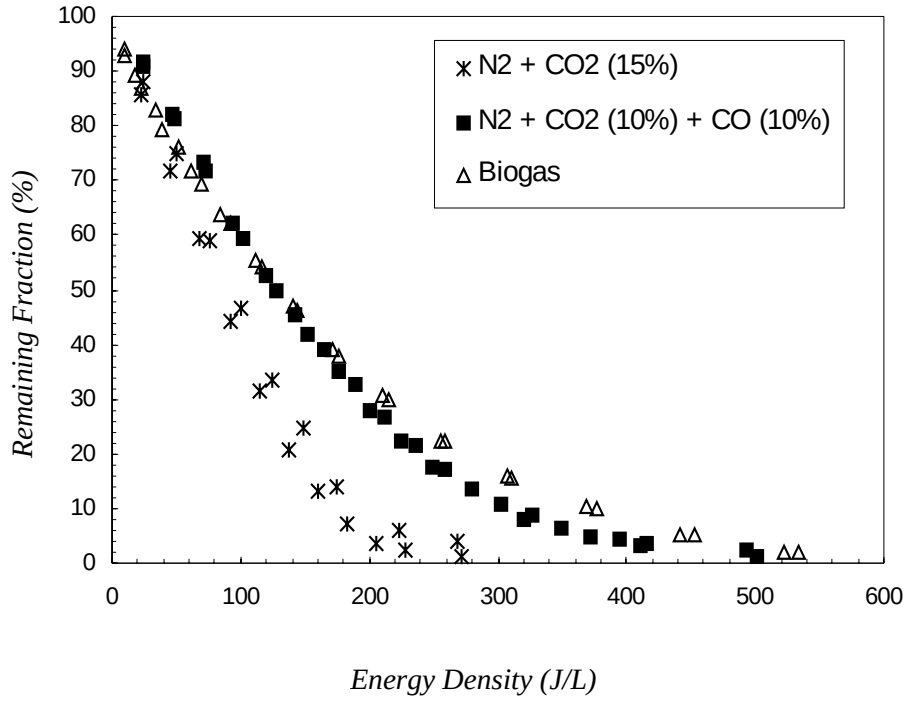


FIGURE 3: Comparison of energy consumption for Naphthalene removal in various gas compositions. T = 200 ~ 210 ^{o}C , Conc. = 500 ~ 600 ppm.

4. CONCLUSIONS

It can be stated that the primary process that occur in biogas conditioning is oxidation and that the high energy density requirement is primarily due to termination of O radicals by CO. This is in spite of the presence of components that can lead to reduction mechanisms such as H_2. Reasons may be lower concentration of H radicals or unfavorable kinetics at the experimental conditions of 200 ^{o}C. Thus, further research will focus on operation at higher temperatures where reduction can be favorable and thereby lesser energy requirements.

ACKNOWLEDGMENTS

The Dutch foundation SDE and Energy research institute, ECN are acknowledged for their support of this work.

5. REFERENCES

[1] Van Paasen.S.V.B., *Biogas treatment with pulsed electric fields*, EUT-SAI report, ISBN 90-5282-940-3, Eindhoven, April 1999.
[2] Sutton.D., Kelleher.B., Ross.J.R.H., *Fuel Processing Technology*, **73**, 155-173 (2001)
[3] Hasler.P., Nussbaumer.Th., *Biomass and Bioenergy*, **16**, 385-395 (1999).
[4] E.J.M.van Heesch, A.J.M.Pemen, K.Yan, S.V.B.van Paasen, K.J.Ptasinski, P.A.H.J. Huijbrechts: *IEEE Trans.On Plasma Science*, **28**(5), 1571-1575, (2000).
[5] Pemen A.J.M., Van Heesch E.J.M., Yan.K., Nair S.A., Ptasinski K.J., Pezzuto M.P., Conditioning of biogas by means of pulsed corona discharges, In:*15th Int. Symp. On Plasma chemistry*, ed. by Bouchoule.A., Pouvesle.J.M., Thomann.A.L., Bauchire.J.M., and Robert.E., Orleans, France, 2001, pp.3121-3127.
[6] Yan.K., Kanazawa.S., Ohkubo.T., Nomoto.Y., *Plasma chemistry & Plasma processing*, **19**, 421-443,(1999).
[7] Yan.K. *Corona Plasma Generation*, Ph.D. Thesis, Eindhoven University of Technology, 2001, pp.129-160.

DETERMINATION OF OH RADICAL CONCENTRATION IN DIELECTRIC BARRIER DISCHARGES BY CO OXIDATION

R. Rudolph[a], K.-P. Francke[a] and H. Miessner[a]

a) Institut für Umwelttechnologien, Volmerstrasse 9B, D-12489 Berlin, GERMANY

Abstract: OH radicals play an essential role in various plasma-chemical processes aimed at removal of volatile organic compounds (VOC), NO_x and SO_2 from polluted off-air flows. For the optimization of OH radical generation in non-thermal plasma discharges a simple but reliable diagnostic method is useful and necessary. We report about the oxidation of carbon monoxide as a diagnostic tool for OH radical determination in dielectric barrier discharges (DBD) at atmospheric pressure. The results are discussed in terms of a simple kinetic model allowing the determination of the average OH production efficiency (G_{OH}-value) and the OH lifetime in dependence on air flow humidity.

1. INTRODUCTION

Non-thermal plasmas are hopeful tools to treat pollution of low concentration in atmospheric gases. Such plasmas are generally produced by e-beams, DBD or corona discharges. For the oxidation of VOCs in off-air streams oxidising agents have to be produced by collisions of energetic electrons with matrix gas molecules like O_2 and H_2O.

OH radicals are one of the most important oxidising agents necessary for example for the plasma treatment of aromates and acetates in air. In discharges they are mainly generated by dissociation of water molecules by direct electron and excited atomic oxygen ($O(^1D)$) impact. At atmospheric pressure their lifetime is very low, usually in the order of some 100 µs.

OH radicals in ac or pulsed discharges have been measured by laser-induced fluorescence (LIF) [1,2] and resonant absorption spectroscopy [3]. In [4] ^{14}CO is used as a tracer for measurement of atmospheric hydroxyl radical concentrations. Su et al. [5] have applied the non-radioactive version of this method to a non-thermal argon-water plasma. In this paper we present results on OH radical concentration measurements in the humid air plasma of a DBD.

2. EXPERIMENTAL SET-UP

The laboratory scale DBD reactor consisted of a cylindrical glass barrier of 400 mm length with an inner diameter of 23 mm. An outer metallic mesh served as ground electrode and a stainless steel tube of 21.3 mm diameter as hv electrode leaving a gap of approximately 1 mm. The reactor was excited by positive pulses of 19 kV amplitude, 45 µs rise time and a pulse repetition rate of 1-107 pps.

The pulse energy was determined using the voltage-charge method. The discharge voltage and the voltage at the integrating capacitor were recorded by hv probes and a digital storage oscilloscope. The area of the Lissajous figure, representing the energy deposited during one period, was typically 50-60 mJ. At maximum repetition rate around 90 Wh/Nm^3 of plasma power per unit volume flow could be applied.

Gas flows of 1 and 2 Nl/min (STP) were prepared by means of mass flow controllers from zero air

[a] Electronic address: r.rudolph@iut-berlin.com

(21 % O_2 in N_2). Given the plasma volume of 23.7 cm^3 a gas flow of 1 Nl/min corresponds to a residence time of 1.4 s. The main part of the flow (typically 90 %) was humidified by bubbling it through distilled water of 20-22 °C and a cooling trap at 19 °C resulting in ~2 % of water vapor. The less part (typically 10 %) was mixed with carbon monoxide and added to the main flow upstream to the plasma reactor.

CO and CO_2 concentrations were measured by means of a calibrated NDIR absorption detector downstream to the plasma reactor. Because of cross interference from synthesised ozone carbon monoxide could be measured only in case of no discharge. So for the oxidative removal of CO it was necessary to follow the changes of CO_2 concentration. During several hours the stability of the CO_2 sensor was better than 1 ppm.

3. EXPERIMENTAL RESULTS

In a discharge plasma in humid air at temperature T and pressure P carbon monoxide can be oxidised in several ways:

$$CO + OH \rightarrow CO_2 + H, \qquad k_1 = 1.3\ 10^{-13}[1 + 0.6\ P_{bar}(300/T)]\ cm^3/s\ [6] \qquad (1)$$

$$CO + O + M \rightarrow CO_2 + M, \qquad k_2 = 1\ 10^{-14}\ \exp(-1630/T)\ cm^3/s\ [5][1] \qquad (2)$$

$$CO + O_3 \rightarrow CO_2 + O_2, \qquad k_3 = 4\ 10^{-25}\ cm^3/s\ [5][1] \qquad (3)$$

Furthermore carbon dioxide can be dissociated by direct electron impact:

$$CO_2 + e^- \rightarrow CO + O + e^- \qquad (4)$$

$$CO_2 + e^- \rightarrow CO + O^- \qquad (5)$$

It was confirmed experimentally that our DBD plasma with low energy density through reactions (2-5) does not influence neither the CO nor the CO_2 concentration in the ppm range. So carbon monoxide removal during plasma treatment is strongly related to the appearance of carbon dioxide: $\Delta CO = \Delta CO_2$.

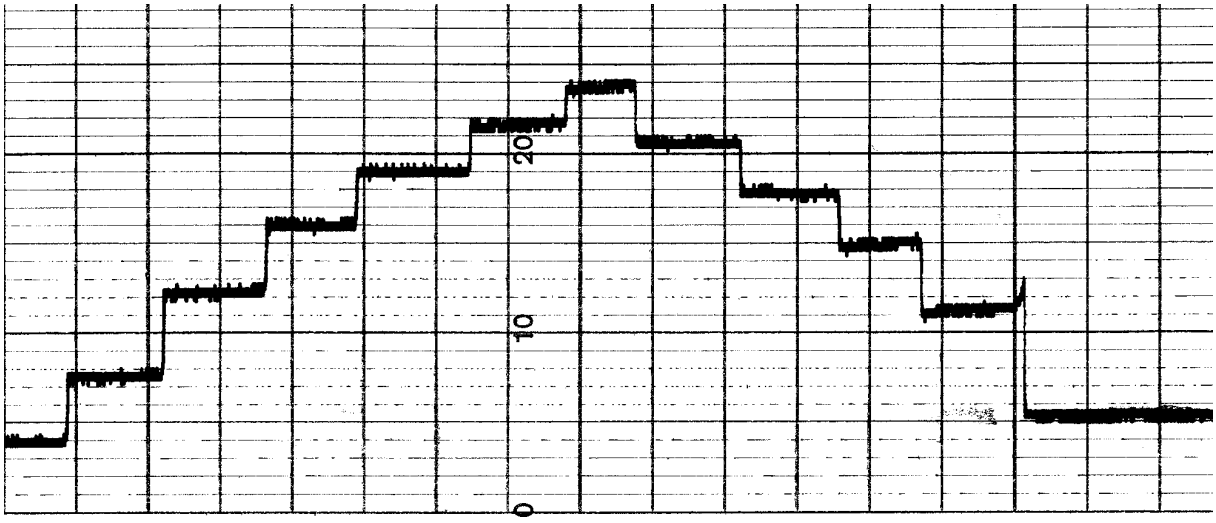


FIGURE 1. CO_2 concentration versus time (from right to left) during oxidation of 51 ppm CO in 1 Nl/min humid synthetic air (~2 % of water vapour) at different energy densities, vertically: 0,7 ppm CO_2/unit, horizontally: 10 min/unit

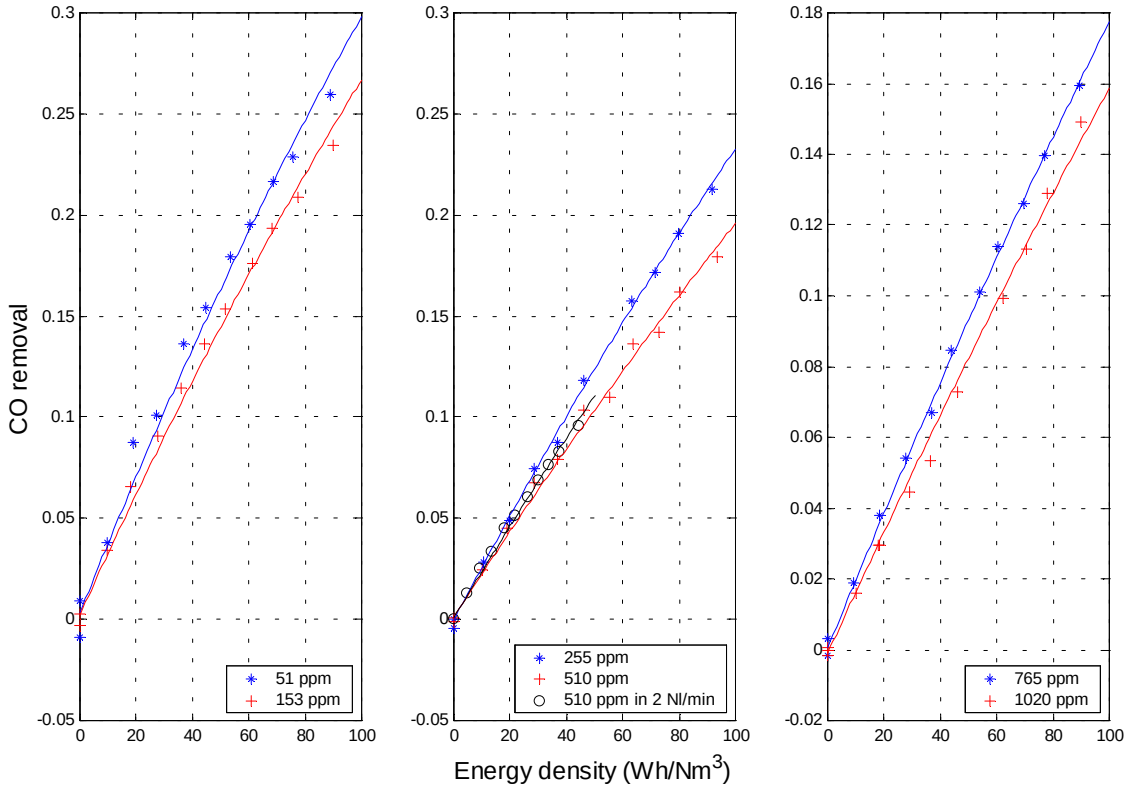
Humid air flows containing 51, 153, 255, 510, 765 and 1020 ppm CO were treated by non-thermal plasma in dependence on energy density E. Fig. 1 shows an example of a CO_2 concentration trace

[1] NIST database

versus time. The steps represent increasing and decreasing energy densities of the DBD. The initial and final CO_2 concentrations differ by 0,9 ppm. The corresponding removal rates R are shown in Fig. 2. The solid lines represent exponential fits from which, according to the relation

$$R = 1 - [CO(E)]/[CO(0)] = \exp(-E/\beta) \quad (6)$$

the β-parameter [7] for CO oxidation can be deduced. As it is suggested by Fig. 3, the β-parameter is a linear function of initial concentration CO(0). Its absolute values range from 300 to 600 Wh/Nm^3.



FIGUR 2. Oxidative removal of carbon monoxide in 1 Nl/min humid synthetic air (~2 % of water vapour) in dependence on plasma energy density

4. KINETIC MODEL FOR CO OXIDATION

Assuming that oxidative removal of CO in humid synthetic air is based on Eq. (1), the experimental results can be described by a simple model, which in addition to Eq. (1) takes into account OH formation by plasma as well as OH scavenging by "air" molecules:

$$\text{Air} + \text{Discharge} \rightarrow \text{OH} \quad (7)$$

$$\text{OH} + \text{Air} \rightarrow \text{Products}, \qquad (\text{OH lifetime } \tau_{OH}) \quad (8)$$

The corresponding rate equations for CO and OH are

$$d[CO]/dt = - k_1 [CO] [OH], \qquad d[OH]/dt = Q(E) - [OH]/\tau_{OH} - k_1 [CO] [OH] \quad (9)$$

where Q is the radical source term ($Q = G_{OH} E/\tau$), G_{OH} is the average radical production efficiency (G-value), τ is the residence time and t is time ($t = x/v$, x – reactor coordinate, v – flow velocity).

In the case of low CO removal ($R << 1$) and short living OH radicals ($\tau_{OH} << \tau$) these equations can be solved analytically

$$[CO(E)] = [CO(0)] \exp(-E/\beta), \qquad \beta = (k_1 \tau_{OH} G_{OH})^{-1} + [CO(0)] G_{OH}^{-1} \quad (10)$$

In agreement with experimental results β is a linear function of initial CO concentration. The slope of this function is inversely proportional to G_{OH}. Fitting the straight line of Fig. 3 to this relationship a G-value of 3,4 ppm/(Wh/Nm^3) and an OH radical lifetime of 200 µs are obtained. These values are in the same range as reported by Hilbert at al. [3] from resonant absorption spectroscopy studies. According to Eq. 10 they correspond to an average OH concentration

$$[OH] = Q(E)\,\tau_{OH} = G_{OH}\,E\,\tau_{OH}/\tau \qquad (11)$$

of approximately 4.9 10^{-4} E ppm/(Wh/Nm^3).

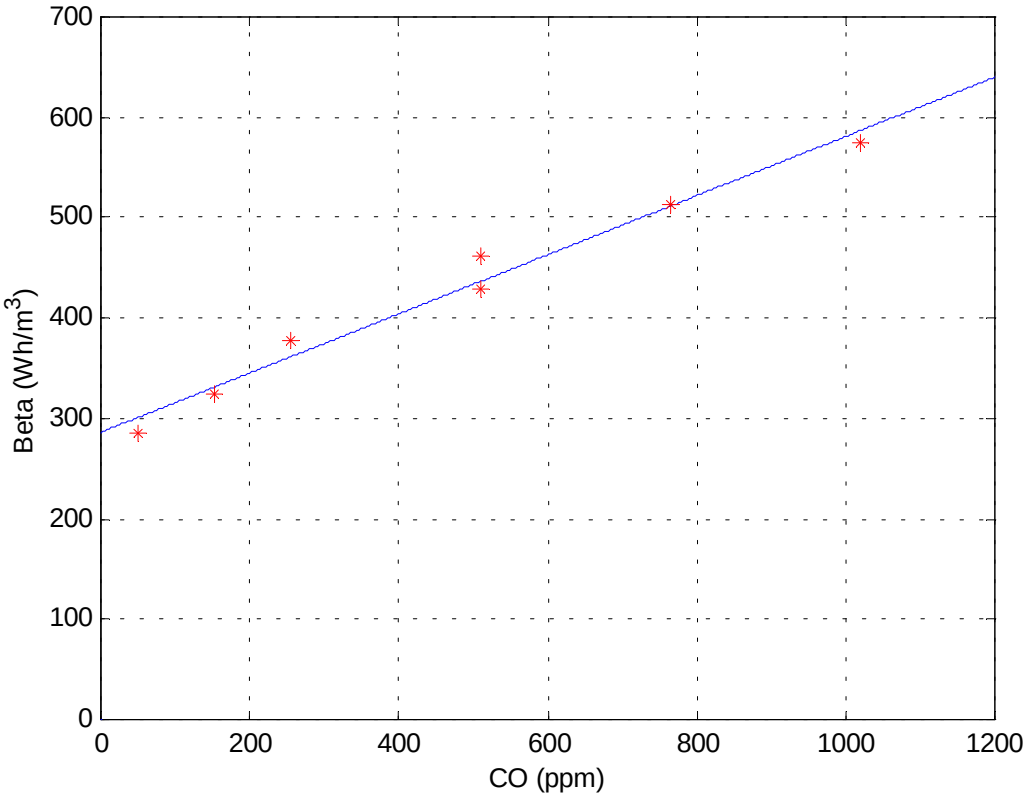


FIGURE 3. β-parameter versus initial CO concentration

ACKNOWLEDGMENTS

The financial support from Federal Minister for Education, Science, Research and Technology (BMBF) is gratefully acknowledged.

REFERENCES

[1] A. Ershov, and J. Borysow, *J. Phys. D: Appl. Phy.*, **28,** 68 (1995)
[2] R. Sankaranarayanan, B. Pashaie, and S. K. Dhali, *Appl. Phys. Letters*, **77**, 2970 (2000)
[3] C. Hilbert, I. Gaurand, O. Motret, and J. M. Pouvesie, *J. Appl. Phys.*, **85**, 7070 (1999)
[4] M. J. Campell, J. C. Farmer, C. A. Fitzner, M. N. Henry, J. C. Sheppard, R. J. Hardy, J. F. Hopper, and V. Muralidhar, *J. Atmospheric Chem.*, **4**, 413 (1986)
[5] Z. Su, H.-H. Kim, M. Tsutsui, K. Takashima, and A. Mizuno, *Thermal Science&Engineering*, **7**, 23 (1999)
[6] R. Atkinson, D. L. Baulch, R. A. Cox, R. F. Hampson, J. A. Kerr, M. J. Rossi, and J. Troe, *J. Phys. Chem. Ref. Data*, **28**, 191-393 (1999)
[7] L. A. Rosocha, and R. A. Korzekwa, *J. Adv. Oxid. Technol.*, **4**, 247 (1999)

FOAMING APPARATUS AS OXIDANTS' GENERATOR

Joanna Pawłat[a], Chobei Yamabe[a] and Iwo Pollo[b]

a) Department of Electrical and Electronic Engineering, School of Science and Engineering Saga University, Honjo-machi 1, Saga 840, Japan

b) Prywatna Wyższa Szkoła Ochrony Środowiska, ul. Zubrzyckiego 6, Radom, Poland,

Abstract. The co-current foaming column is an innovatory apparatus, allowing for generation of various active species by the electrical discharge in the dynamic foam environment. Pneumatic foam as a basic medium filling the column makes the mass transfer more efficient by assuring the extending of contact area between gas and liquid phases.

The highest concentrations of oxidants in flat column were obtained in needle-to-alumina dielectric covered plate electrode system in oxygen. At 14 kV of applied voltage and 5 dm^3/min of substrate gas flow 875 ppm of gaseous ozone, 0.5 mg/dm^3 of dissolved ozone and 62 mg/dm^3 of hydrogen peroxide were obtained. The OH radicals' presence was confirmed.

1. INTRODUCTION

Still, the widest known oxidant is chlorine and its derivates. By using this cheap method, one does not assure satisfactory treatment in some cases. Additionally the harmful secondary pollutants as trihalometanes can be formed. Ozone application for efficient treatment of various wastewaters and waters has been well known for more than 20 years and in spite of higher cost, became a treatment standard in many countries. In present days, when large amount of pollutants is discharged to the atmosphere and hydrosphere, even more sophisticated treatment procedures are necessary to preserve the natural environment. One of them is AOP (Advanced Oxidation Process), which assures increasing of oxidation power by using simultaneously several oxidative factors. Usually, oxidants as ozone and hydrogen peroxide are produced separately and dosed individually, what is the reason of transportation loses. Adding the still high energetic losses during ozone generation, total efficiency of the process decreases.

In this paper, the new attempt of simultaneous generation of various oxidants in the same reaction zone due to electrical discharge in foam is proposed. Foam was formed without an addition of surface-active substances. After further investigations this method might be potentially useful for the polluted gas treatment and for treatment of some types of wastewaters.

1.1. Properties of foam

Foam is thermodynamically unstable, colloidal system. It can be defined as highly concentrated dispersions of gas in a two-phase system with a gas phase as a dispersed phase and the liquid as continuous phase [1,2]. The amount of gas in foam ranges up to 80% of volume.

The following techniques are commonly used to create foam:

- -dispersion technique (it is not possible to control the amount of the gas),
- -orifice method (gas is passing into the liquid through an orifice, foam is generated on the top of the liquid),

[a] Electronic address: "askmik@hotmail.com"

- -shelf method (gas and liquid is passing through the perforated shelf [3]. In this case, the material of shelf plays an important role in the bubble formation [4]),
- -supersaturating the liquid with the gas (or producing the gas in situ) what causes the nucleation of the gas bubbles (method used in a gas industry),
- -co- and countercurrent multishelf foaming columns, [3,5].

Usually *homogenous, (standing)* foams are produced by vigorous agitation of solutions, and *pneumatic (dynamic)* foams are generated by bubbling of gas through the substrate solution.

It was noticed [5], that gas behaviour in liquid depends on the gas velocity. Since the critical velocity is reached, the bubbling zone is replaced successively by uniform dynamic foam zone. After onset of the foaming, at low flow rates bubbles are relatively large, with the increasing the flow rate they become smaller. Further increases in a gas flow rate causes bubbling, splashing and diameter of the bubbles increases again.

The general rules concerning the flow and apparatus-construction limits for the creation of foam environment are presented below [3]:

- Linear velocity of substrate gas for whole apparatus cross-section (V_C): 0.1-4.0 m/s,
- Gas velocity in the diffuser hole (V_D): 10-20 m/s,
- Diffuser's perforation level: 5-20% of whole shelf area.

In general, foaming leads to the intensification of the processes between gas and liquid phase.

2. EXPERIMENTAL SET-UP

The foam generation, discharge generation and data analysis sub-systems could be distinguished in the experimental apparatus.

2.1. Foam generation

Foam was generated in the polyacrylate reactor called the foaming column, which is presented in Fig. 1. The most important parts in the reactor were porous, ceramic diffusers' shelves (type IA-500 of mainly aluminium oxide) placed perpendicularly to the flow direction of media and changeable set of electrodes. Electrodes were located above the second diffuser.

Column was connected to the liquid and gas providing system. In performed investigations pure water was used as a substrate liquid and air and oxygen as substrate gases.

2.2. Discharge generation and electrical measurements

The two-stages, 5 m length Blumlein pulse power source made from RG/8-U coaxial cable as a capacitance was used for electrical discharge. Blumlein generator worked in a single shot mode or a repetition mode with 10 and 15 Hz repetition rate, regulated by an oscillator (Kenwood, AG-204D). Discharge was triggered by triggering system connected to discharge gap switch and to Blumlein serially.

The discharge voltage and current were measured by the high voltage probe (Tektronix, model P6015A) and the Rogowski coil (Pearson, model 110) with oscilloscope (Tektronix, model TDS 380), respectively. The diagram of electric power supply is shown in Fig. 2.

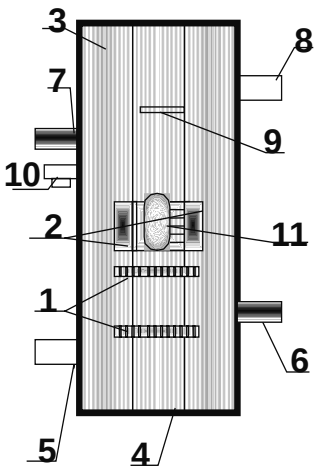


FIGURE 1. Experimental apparatus. (1-diffusers, 2-electrodes, 3-polyacrylate walls, 4-spacer, 5-gas inlet, 6-liquid inlet, 7-liquid outlet, 8-gas outlet, 9-drops' grabber, 10-overflow, 11-window).

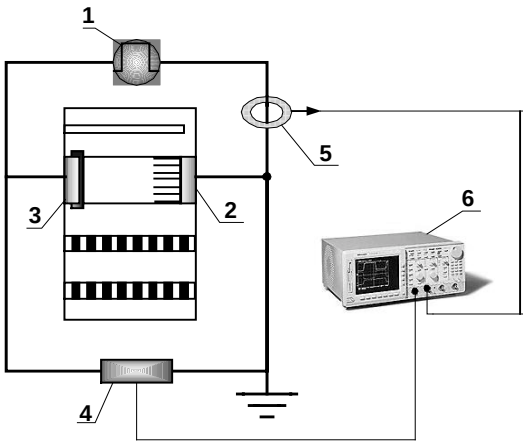


FIGURE 2. Diagram of electrical circuit. (1-power source, 2,3-electrodes, 4-voltage probe, 5-Rogowski coil, 6-oscilloscope).

2.3. Chemical measurements

Hydrogen peroxide concentration was determined using Hydrogen Peroxide Test Kit (HACH, Model HYP-1). Standard titration method was used to determine ozone concentration in the outlet gas. Dissolved ozone concentration was determined using a spectrophotometer (HACH, DR/4000) and indigo method in an acidic (pH=2.5) environment.

Spectroscopic measurements were performed to observe the generation of OH radicals.

3. RESULTS AND DISCUSSION

3.1. Foam structure in the reactor

For the most ideal condition from the foam creation point of view, the diffuser's width should be decidedly wider than 5 mm. Average diameter of single bubble in a foam ranged from 1 mm to 5 mm. The diameters of bubbles tended to be bigger (connecting to each other and then sharing their lamella) with increasing distance from the diffuser and with increasing the substrate gas flow as well.

3.2. Electrical properties of the discharge

The most common type of the discharges, appearing in above systems was named a quasi-arc discharge. With the strong light emission, the evaporation of the electrode's material from the surface and arc channel between electrodes didn't occur. Also the oscillograms didn't show the arc character. Discharge development in foam was usually very rapid: first peak of applied voltage was about 50 ns that is not enough in the case of standard arc discharge. Typical applied voltage and current waveforms with calculated power for the most frequent quasi-arc discharge in needle-to-dielectric covered metal plate electrode set-up are presented in Figs. 3 A)-C). Photo of the discharge is shown in Fig.4.

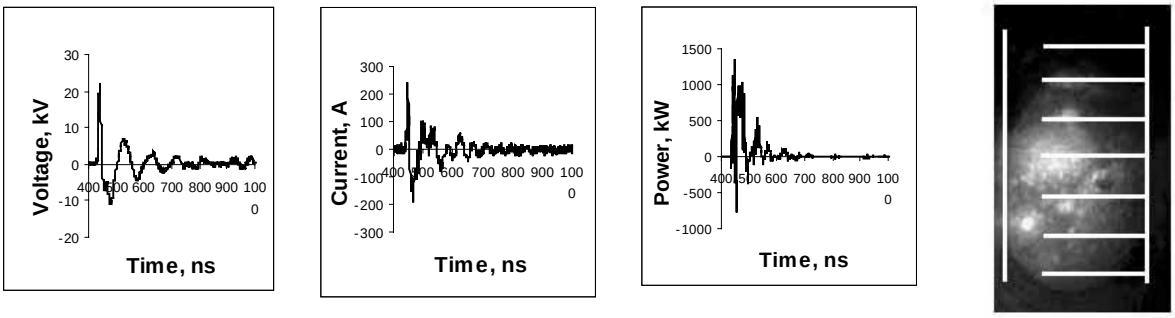


FIGURE 3. Typical applied voltage (A) and current (B) waveforms with calculated power (C) of the discharges in needle–to-dielectric covered metal electrode set-up. Airflow rate: 8 l/min, 14 kV of applied voltage.

FIGURE 4. Photo of the discharge, needle-to-dielectric plate electrode.14 kV and 10 dm^3/min air flow.

The dependence of the discharge area on applied voltage was noticed in case of metal plate-to-metal plate and needle-to-metal plate electrode. At relatively lower applied voltage, the upper parts of the foam and its surface area of the big diameter bubbles were the most preferable place for discharge occurring. The positive influence of the dielectric layer on the spatial distribution of the discharge development was observed in case of metal plate-to-dielectric plate and needle-to-dielectric plate electrodes.

3.3. Oxidants' formation

Oxidant's concentration for H_2O_2, DO_3 and O_3 in dependence on applied voltage was investigated for various electrode set-ups. The relative comparison of the maximal achieved concentrations for various electrodes is presented in the Table 1. For all types of electrodes, the presence of OH radicals was detected.

Table 1. The maximal achieved concentrations of oxidants for tested electrodes.

Qualities/ Electrodes	**Spatial uniformity of the discharge/type of the most common discharge**	**Gaseous ozone, ppm**	**Dissolved ozone, mg/dm3**	**Hydrogen peroxide, mg/dm3**
Needle-to-metal plate	Depends on applied voltage/ quasi arc	327 840	0.11 0.17	34 39
Needle-to dielectric plate	Does **not** depend on applied voltage/ quasi arc	521 875	0.36 0.5	59 62
Metal plate-to-metal plate	Depends on applied voltage/ arc	245 502	0.09 0.11	9 22
Metal plate-to-dielectric plate	Does **not** depend on applied voltage/ quasi arc	206 599	0.14 0.17	20 56

In the all analyzed cases dominance of efficiency for needle-to-dielectric covered plate electrode was easily recognized. In general, quantity of all oxidizing agents increased when applied voltage increased.

4. CONCLUSIONS

New technological solution based on the discharge in the foaming system was designed. Foam was created without addition of foaming agents, using only the kinetic energy of gas flow.

Quasi-arc discharge obtained in the foam environment was partly homogenous.

Formation of various oxidants formation such as gaseous ozone, dissolved ozone, hydroxyl radicals and hydrogen peroxide in apparatus with needle-to-metal plate, needle-to-dielectric covered plate, metal plate-to-metal plate and metal plate-to-dielectric (alumina) plate set-ups was confirmed.

The highest concentrations of all oxidants were obtained in a set-up with needle-to-dielectric electrode. The concentration increased with the voltage increasing.

Foaming system allows obtaining various species in one compact apparatus, potentially even directly in polluted medium and connects in one body the advantages of oxidants generator and reaction vessel.

ACKNOWLEDGMENT

A part of this work was supported by a Grant-in-Aid for Scientific Research (A) and (B) of the Ministry of Education, Science and Culture and by Japan Society for the Promotion of Sciences.

REFERENCES

[1] J. Patino, M. Delgado, and J. Fernandez, “Stability and mechanical strength of aqueous foams containing food proteins”, Colloids and Surfaces: A, **99**, (1995), 65-78,
[2] A. Bhakta and E. Ruckenstein, “Decay of standing foams: drainage, coalescence and colapse”, Advances in Colloid and Interfaces Science **70**, (1997), 1-124,
[3] S. Bistron, P. Sarre, and B. Szymonik, „Nowy sposob prowadzenia procesow w pianie dynamicznej”, Chemik **3,** (1978), 81-83, (in Polish),
[4] Pugh R.J „Foaming, foam films, antifoaming and defoaming” Advances in Colloid and Interface Science **64** (1996), p. 67-142,
[5] T. Hobler, ”Dyfuzyjny ruch masy i absorbery”, Warszawa, Poland: WNT, (1978), (in Polish).

CALCULATION OF NO_X REMOVAL PROCESS TAKING PULSE MICRO-DISCHARGE AND DIFFUSION OF RADICALS INTO CONSIDERTION

Yoshio Yoshioka[1], *Kentarou Teshima*

7-1 Ohgigaoka, Nonoichi-machi, Ishikawa, Japan 921-8501

Abstract.

In the NOx removal process based on silent discharge, the discharges occur in very small discharge channels and the radicals formed in the discharge channels diffuse to the surroundings and react with the pollutants. In this paper, we report a newly developed calculating program taking these mechanisms into consideration.

The calculation results show that NO concentration began to decrease at the center of a discharge channel and then the decrease spread to the surroundings. NO_2 formation is rapid at the center of micro-discharge and slow at the surroundings. Ozone formation, on the other hand, is slow even in the micro-discharge but it is increasing with a lapse of time. The effect of H_2O is also analyzed.

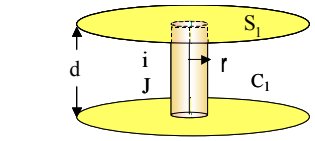
1. INTRODUCTION

NOx in exhaust gases from diesel engine can be removed by non-thermal plasma process. One of the problems of this process is known as its low energy efficiency. Various trials have been made to improve the efficiency, however in order to solve this problem completely, it is very important to know how and what chemical reactions occur in the discharge region. There are papers, which analyzed the chemical reactions in such a process by solving rate equations [1,2,3,4]. But they are assuming that the chemical reactions occur uniformly in the plasma region. In the real process based on silent discharge, the discharges occur in very small discharge channels and the radicals formed in the discharge channels diffuse to the surroundings and react with the pollutants. So in this paper, we developed a calculating program, which takes these mechanisms into consideration. Using this program, we investigated the spatial distribution and time variation of chemical species.

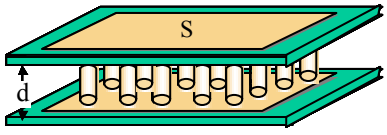
2. METHOD OF CALCULATION

2.1 Modeling of a micro-discharge

Here, we deal with the process based on the silent discharge. In order to calculate NOx removal process by chemical kinetics, the reactions by high-energy electrons must be calculated at first and radicals formed by collisions of high-energy electrons must be specified. Then we calculate the secondary reactions between these radicals and pollutants such as NO and NO_2. So far, the discharge has been dealt with spatially uniform in the reactor. Here, however, the discharge is dealt with an assembly of many micro-discharges having a column structure as shown in Fig.1. It is known that the diameter of a micro-discharge and the current density are around 0.1mm and 1kA/cm^2 respectively, the discharge period



(a) Structure of a micro-discharge



m; number of parallel discharge

(b) Overall Discharge

FIGURE 1 Model of Silent Discharge

[1] yoshioka@neptune.kanazawa-it.ac.jp

is within a few nanoseconds and the electron energy is estimated as around 4 to 5eV [2]. In the silent discharge device, once a micro-discharge takes place, electric charges move in the channel and they are accumulated on the surface of dielectric barrier. The accumulated charges cancel the electric field induced by the applied voltage. Thus, the discharge stops in a few nano-seconds. When the applied voltage rises further, the micro-discharges take place again and again until the applied voltage comes to the peak. So in order to calculate the primary reaction by high-energy electron collisions, we have to estimate the number of pulse discharge per second and per electrode surface area and also the number of electrons in a micro-discharge channel in relation to the discharge power. They are described as follows.

2.2 Description of micro-discharge and a relation to discharge power

Table 1 shows typical data of a micro-discharge, which were calculated using the equations (1) to (11) based on the silent discharge model of Fig.1. Calculations of chemical reactions were carried out on two cases of discharge power of 336 and 84 [W]. There are two values in W_1 and T, which correspond to the difference of discharge power.

(1) Electron density n_e in a micro-discharge channel

The electron density n_e in a micro-discharge with dissipating energy of Ws[W/cm^2] is written as (1) [1].

$$n_e = \kappa \cdot \frac{1}{q_e v_{de}(E/n)} \cdot \frac{Ws}{d \cdot n} \qquad (1)$$

wherein q_e; electron charge[C],
v_{de}; drift velocity of electron in electric field [cm/s]
E/n; reduced electric field, n; gas density [/cm^3],
d; gap distance[cm],
κ; dissipation factor of electrons (=0.55)

(2) Physical parameters denoting a micro discharge

Important physical parameters used in the program are as follows.

$$i = \pi \cdot r^2 \cdot J \qquad (2)$$

$$q_e = i \cdot t = C_1 \cdot V_g \qquad (3)$$

$$C_1 = \frac{\varepsilon \cdot S_1}{d} \qquad (4)$$

$$W_1 = \frac{1}{2} \cdot C_1 \cdot (V_g^2 - V_b^2) = \frac{\varepsilon \cdot S_1}{2d} \cdot (V_g^2 - V_b^2) \qquad (5)$$

$$S_1 = \frac{d \cdot C_1}{\varepsilon} = \frac{d}{\varepsilon} \cdot \frac{q_0}{V_g} = \frac{d \cdot i \cdot t}{\varepsilon \cdot V_g} \qquad (6)$$

wherein i; current of a micro-discharge [A],
r; radius of a micro-discharge channel [cm]
J; current density [A/cm^2], t; discharge duration [s], V_g; discharge initiation voltage [V],
V_b; discharge stop voltage [V], ε; dielectric constant of vacuum [F]
C_1; capacitance associated with a micro discharge [F],
S_1; small surface area associated with a micro-discharge [cm^2],

TABLE1 Micro-discharge characteristics

current of micro-discharge i [A]	0.314
electric charge per micro-discharge q_0[C]	0.942×10^{-9}
Discharge power of a micro-discharge W_1[J]	2.4×10^{-6}
Area associated with a micro-discharge S_1[cm^2]	0.47
Capacitance of a micro-discharge C_1[F]	1.04×10^{-13}
Discharge power of a micro-discharge P_1[W]	735
Number of parallel discharge area m	1596
Number of micro-discharge per second h[/s]	8.77×10^4 & 22×10^4
Time interval between successive micro-discharge T[μs]	5.7 & 22.9
Total discharge power of the discharge device P[W]	336 & 84

(3) Relation between a micro-discharge and discharge power of silent discharge device

Relation between a micro-discharge and macro discharge power is written as equation (9).

$$S = S_1 \cdot m \qquad (7)$$

$$m = \frac{S}{S_1} = \frac{\varepsilon \cdot v_g \cdot S}{d \cdot q_0} \qquad (8)$$

$$P = m \cdot W_1 \cdot h \qquad (9)$$

$$h = \frac{P}{m \cdot W_1} = \frac{2d^2 \cdot q_0 \cdot P}{\varepsilon^2 S \cdot S_1 \cdot V_g \cdot (V_g^2 - V_b^2)} \qquad (10)$$

$$T = \frac{0.5}{h} \qquad (11)$$

wherein S; area of discharge electrodes [cm^2], m; number of parallel discharge channels
h; number of discharge of a micro-discharge per second, P; macro-discharge power

T; interval of successive particular micro-discharge [s]

In the calculation, we assumed that successive micro-discharges occur in the same channel with an interval of T and a micro-discharge duration is 3 [ns].

2.2 Diffusion equation of radicals and chemical kinetics

(1)Diffusion equation and chemical reaction

Fig.2 shows a model of micro-discharge and a calculation model on diffusion of radicals. Large amount of radicals are formed in this discharge channel by high-energy electron bombardment. These radicals diffuse to the surrounding and react with pollutants. When we think of a cylindrical part located between r and r+dr, the mass balance in it is written as follows.

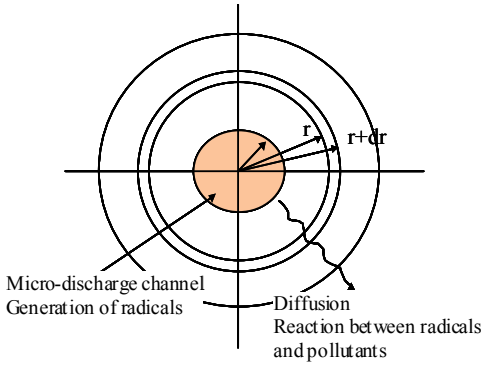


FIGURE 2 Micro-discharge and diffusion of radicals

(Molecules in cylindrical part) = (Molecules diffused from inner boundary) - (Molecules diffused to outer boundary) + (Formation of molecules by chemical reactions)

So the change of concentration A_c of a particular molecule A is written as

$$\frac{\partial A_c}{\partial t} = -\frac{1}{r}\frac{\partial F_a}{\partial r} + \Gamma \qquad (12)$$

where

$$F_a = -D \cdot (\frac{\partial A_c}{\partial r}) \qquad (13)$$

Γ denotes the formation by chemical reactions and D denotes the diffusion coefficient.

From this equation, we obtain the following diffusion equation for molecule A.

$$\frac{\partial A_c}{\partial t} = D \cdot (\frac{\partial^2 A_c}{\partial r^2}) + \frac{D}{r} \cdot \frac{\partial A_c}{\partial r} + \Gamma \qquad (14)$$

Here Γ is expressed, for example, as

$$\Gamma = -\frac{\partial A}{\partial t} = k_1 \cdot [A] \cdot [B] \qquad (15)$$

where k_1 is a rate of chemical reaction between molecules A and B. [A] and [B] are concentrations of molecules A and B respectively. These kinds of equation are valid for both electron-base reactions and radical-base reactions.

TABLE 2 Reactions Induced by Energetic Electrons

	Chemical Reactions	RateConstants [cm^3/s]
R_0	$e+O_2 \rightarrow O(^1D)+O+e$	$k_0=1.26\times10^{-9}$
R_1	$e+O_2 \rightarrow 2O+e$	$k_1=1.95\times10^{-9}$
R_2	$e+O_2 \rightarrow O+O^-$	$k_2=3.49\times10^{-11}$
R_3	$e+O_2 \rightarrow O_2(b)+e$	$k_3=1.615\times10^{-10}$
R_4	$e+O_2 \rightarrow O_2(a)+e$	$k_4=6.96\times10^{-10}$
R_5	$e+O_3 \rightarrow O(^1D)+O_2(a)+e$	$k_5=20\times k_0$
R_6	$e+N_2 \rightarrow 2N+e$	$k_6=4.6\times10^{-11}$
R_7	$e+H_2O \rightarrow H+OH+e$	$k_7=2.0\times10^{-9}$
R_8	$e+H_2 \rightarrow 2H+e$	$k_8=2.0\times10^{-9}$

(2)Primary reactions between high-energy electron and gas molecules

As is already described, the first reaction is electron-induced reactions. We used the rate constant data for 100[Td], because it is the typical reduced electric field of silent discharge. These reactions and their reaction rates are listed in Table 2. For example, in case of the reaction R_0 in Table 1,

$$\frac{d[O]}{dt} = k_0 \cdot [e] \cdot [O_2] \qquad (16)$$

where [e], [O] and $[O_2]$ are concentrations of each molecule.

Because O radical is formed by three reactions of R_0, R_1 and R_2, we can write the differential equation for O radicals as follows.

$$\frac{d[O]}{dt} = k_0[e] \cdot [O_2] + 2k_1[e] \cdot [O_2] + k_2 \cdot [e] \cdot [O_2] \qquad (17)$$

The electron-induced reactions form O, O^-, $O_2(a)$, $O_2(b)$, N, H, OH and $O(^1D)$. So differential equations for the formation of these radicals can be written in the same way. By solving these differential equations of chemical reactions and diffusion equations simultaneously, we can obtain radicals in the discharge channel. Here in the calculation, we need the electron densities n_e during micro-discharge, initial concentrations of gas component and the duration of a micro-discharge. We used equation (1) for electron densities and used 3ns as duration of a micro-discharge.

(3)Secondary reactions between radicals and pollutants

Micro-discharge is a pulse discharge and the pulse duration is very short as few nano-seconds. The radicals formed in the micro-discharge began to react with other molecules in the discharge channel, however, most of the radicals diffuse outer parts of the discharge channel and the reactions take place there for longer time until the next micro-discharge takes place. The interval of the successive micro-discharges is expressed as equation (11). Table 3 shows typical secondary reactions but we used 115 reactions in the practical calculation.

TABLE 3 Reactions with radicals and their reaction rates

NO.	Chemical Reaction	Reaction Rate[cm^3/s][cm^6/s]
R_9	$O+O_2+O_2 \rightarrow O_3+O_2$	$k_9=6.4\times10^{-35}\times(T/300)^{-2}$
R_{10}	$O+O_2+N_2 \rightarrow O_3+N_2$	$K_{10}=5.7\times10^{-34}\times(T/300)^{-2.8}$
R_{13}	$O+NO_2 \rightarrow NO+O_2$	$K_{13}=1.7\times10^{-12}\times\exp(-300/T)$
R_{15}	$N+NO \rightarrow N_2+O$	$K_{15}=3.4\times10^{-11}$
R_{20}	$N+O_3 \rightarrow NO_2+O_2$	$K_{20}=1.5\times10^{-12}\times(-1300/T)$
R_{21}	$O+NO+O_2 \rightarrow NO_2+O_2$	$K_{21}=8.6\times10^{-32}\times(T/300)^{-1.8}$
R_{22}	$O+NO+N_2 \rightarrow NO_2+N_2$	$K_{22}=1.0\times10^{-31}\times(T/300)^{-1.8}$

(4)Calculation conditions

Calculation conditions and initial conditions are shown in Table 4. We calculated two cases for H_2O concentration and two cases for discharge power.

TABLE 4 Calculation Conditions

N_2 [ppm]	780,000
O_2 [ppm]	150,000
H_2O [ppm]	0 &30000
NO [ppm]	200
NO_2 [ppm]	0
Gas pressure [Torr]	760
Gas temperature [K]	323
Radius of micro-discharge channel [cm]	0.01
Discharge area of discharge device [cm^2]	750
Discharge gap length [cm]	0.4
Discharge power [W]	84, & 336
Diffusion Coefficient[cm^2/s]	0.41
Reduced electric field [Td]	100
Electron temperature [eV]	5
Current density [kA/cm^2]	1
Discharge initiation voltage [kV]	9.08
Discharge stopping voltage [kV]	6.03
Duration of micro-discharge [ns]	3

3. RESULT OF CALCULATION

Fig.3 shows the change of NO concentrations with a lapse of time and at three positions, at the center and edge of a micro-discharge (100 μm) and at the distance of 3 times apart from the radius (300 μm) in case of discharge power of 336[W]. Fig.4 is the result of the case of 84[W]. It is seen in these figures that NO concentration decreases very fast at the center of micro-discharge but at the distance 3 times apart from the radius, NO decreases slowly and even after 1 [ms] it is still decreasing. It is seen in these figures that at the center and at edge of the micro-discharge channel, NO concentrations decrease down to around 50[ppm] and almost saturate there, however at 300[μm] apart from the edge, NO is still decreasing at 1[ms] and the concentrations are about 60% and 70% of the initial concentration respectively.

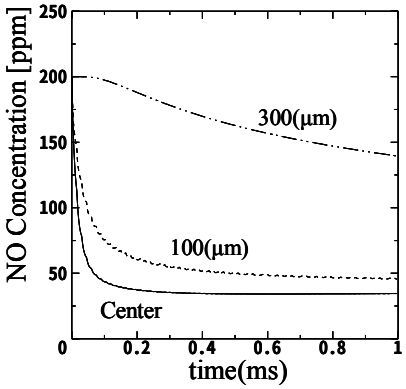


FIGURE 3 NO vs. time (P=336[W])

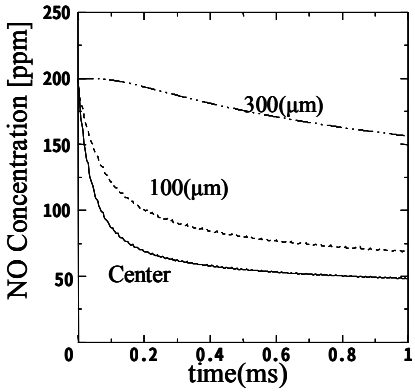


FIGURE 4 NO vs. time (P=84[W])

Next Fig.5 and 6 show the changes of NO_2 at various positions. Difference of calculation conditions is discharge power. It is seen in Fig.6 that NO_2 formation is very quick at the center and at the edge of micro-discharge and it is very slow at the 300[μm] apart from the center of micro-discharge. Fig.7 and 8 show the ozone formation. As is seen in these figures, ozone formation is slow but it is interesting to see that ozone is increasing at all positions even at 1ms. Next, the effect of H_2O(30,000[ppm]) was investigated. Fig.9 shows NO change with a lapse of time and Fig.10 shows NO_2 variation with time. NO change in Fig.9 is almost same as that in Fig.3, however, NO_2 in Fig.10 is smaller than in Fig.5. By the analysis of

reaction passage, it was found that in the case of existence of H_2O, NO decrease mainly by the reactions with OH, N and HO_2 radicals. Especially, because reactions between NO and OH form HNO_2, NO_2 generation is small in Fig.10.

It is seen that NO decrease saturates at about 40[ppm] in the micro-discharge channel. It was found that this saturation comes from NO formation reactions between N and OH. In the case without H_2O, the NO formation occurs mainly reactions between NO_2 and O radical.

4.CONCLUSION

NO removal mechanisms were investigated using a newly developed computer program in which micro-discharge and diffusion of radicals are taken into consideration. The calculation consists of electron-based 9 reactions in the micro-discharge channel and 115 radical-based reactions at the surrounding and in the micro-discharge channel. The calculation model of a micro-discharge in silent discharge is also described in detail. Calculation results show that change of NO, NO_2 and O_3 concentrations are spatially different. The influence of H_2O is also analyzed.

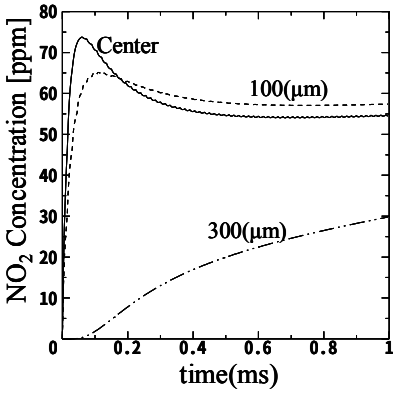


FIGURE 5 NO_2 formation (P=336[W])

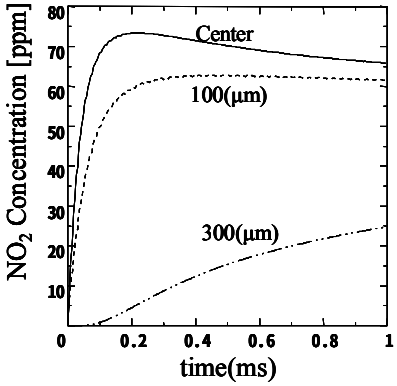


FIGURE 6 NO_2 formation (P=84[W])

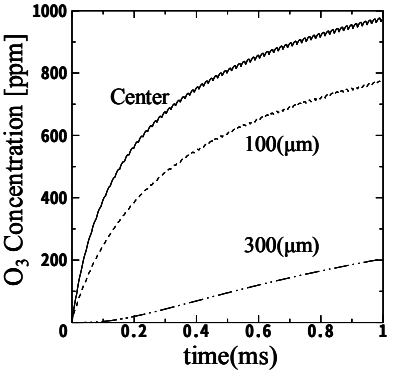


FIGURE 7 O_3 formation P=336[W])

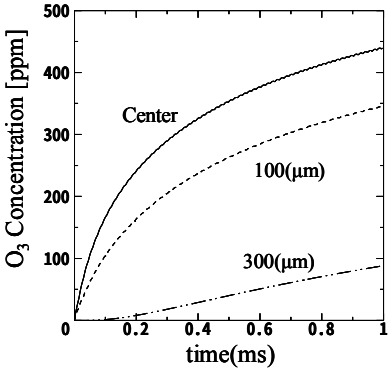


FIGURE 8 O_3 formation P=84[W])

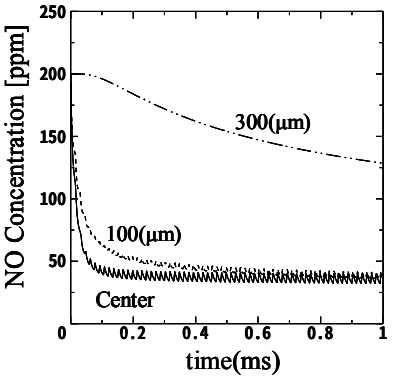


FIGURE 9 NO change when H_2O exist in gas (P=336[W])

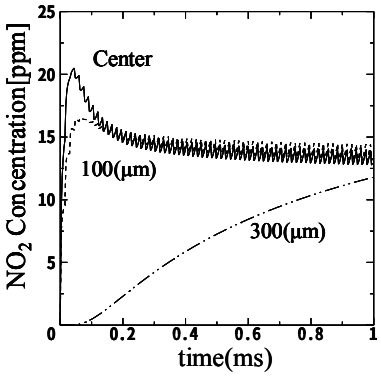


FIGURE 10 NO_2 formation when H_2O exist in gas (P=336[W])

REFERENCES

[1] N.Tabata; "A Novel Ozone Generator Converting into O_3 at Outside of Electric Discharge Space", T.IEE Japan, Vol.116-A, NO.9, pp791-797, 1996

[2] L.A.Rosocha, G.K.Anderson, L.A.bechtold, J.J.Cooagan, H.G.Heck, M.Kang, W.H.McCulla and P.J.Wantuck; "Treatment of Hazardous Organic Wastes using Silent Discharge Plasmas", Springer-Verlag, Non-theral Plasma Techniques for pollution controle", Part-B, pp281-306,1993

[3] K.Ohta, N.Wada and M.Kazumoto; "Characteristics of Ozone Generation by Both electrodes Coolong ozone Generator", T.JIEE,Japan Vol. 120-A, pp695-700,NO.6,2000

[4]B.M.penetrante; "Plasma Chemistry and Power Consumption in Non-thermal DeNOx";
Springer-Verlag, Non-theral Plasma Techniques for pollution controle", Part-A, pp65-89,1993

INFLUENCE OF TEMPERATURE AND HYDROCARBONS ON REMOVAL OF NO_X AND SO_2 IN A DIESEL EXHAUST GAS ACTIVITED BY PULSED CORONA DISCHARGE

E.A. Filimonova[a], R.H. Amirov[a], S.H. Hong[b], Y.H. Kim[b] and Y.H. Song[c]

a) Institute for High Temperatures, Izhorskaya 13/19, Moscow, 127412, Russia
b) Seoul National University, Seoul, 151-742, Korea,
c) Korea Institute of Machinery and Materials, Taejon, 305-600, Korea

Abstract: The influence of temperature and hydrocarbon additives on the NO_x removal has been studied by numerical modelling and process experiments for a synthetic gas mixture consisting of N_2, O_2, H_2O and CO_2 in a pulsed corona reactor. The NO reduction of more then 99% was achieved at the energy cost of ~14 eV per NO molecule in the presence of 550 ppm C_3H_6 additive at *T*=393 K. The simulated results agree well with the experimental data measured in the NO and NO_x removal and C_2H_4 and C_3H_6 decomposition. The C_3H_6 additive does not sufficiently suppress the conversion of SO_2 to H_2SO_4. Within a limited framework of non-uniform modelling approach, the temperature effect on the streamer nature discharge has been taken into account.

1. INTRODUCTION

One of the main problems in techniques using streamer discharges for cleaning of diesel exhaust gases is the reduction of operating power consumption. Numerous investigations have shown that the addition of hydrocarbons (HCs) to the flue gas in a cleaning process diminished the energy consumption for the conversion of NO into NO_2 [1-6]. The best NO_x conversion is resulted with propylene and ethylene. The next stage of catalytic reduction of NO_2 will be successfully working if the formation of H_2SO_4 in a sulfur containing fuel leads to no poison of catalyst agents [4,5].

Penetrante *et al* [6] investigated both experimentally and numerically a possibility of non-thermal plasma efficiently to oxidize NO to NO_2 without oxidizing SO_2 to SO_3. The rate constant for the OH + C_3H_6 reaction is much grater than that for the OH + SO_2 reaction. It is therefore expected that most of the OH radicals will be used by propylene, and the level of SO_2 oxidation will be decreased even in the presence of high levels of H_2O. The difficulties in measuring of the SO_2 concentration did not permit the experiments to show the suppression of SO_2 oxidation in the presence of C_3H_6 and H_2O, which was shown instead in the calculations, but in the absence of NO molecules. A high initial SO_2 concentration of 500 ppm was used to study this effect. In the real diesel exhaust gas it does not exceed 50 ppm.

The comparison between calculation results and experimental data is usually given for a limited number of components that are not sufficiently representative and successfully descriptive for the cleaning process. In the conventional modelling of chemical kinetics, the influence of temperature has been considered only on the change of gas density and rate constants of reactions, but not on the streamer properties. In general, this modelling makes use of the volume-averaged distribution of the chemically active species (CAS), which do not allow for getting information on the streamer nature of discharge. Since many parameters influence on the result on NO_x removal, it is important to find the respective effects of additive type, temperature, composition of matrix gas, constant rates of leading reactions, discharge parameters and so on.

In the present work, the experimental and numerical investigations on the NO_x removal process in a pulsed corona discharge have been performed in a synthetic gas like diesel exhaust gas under temperatures of 293, 393 and 493 K with and without C_2H_4 or C_3H_6 of ~550 ppm concentrations. The purpose of this study is to understand the major mechanisms, which have influence not only on the

reduction of energy consumption and by-products generation, but also on the competition between the conversion of SO_2 to H_2SO_4 and the oxidation of C_3H_6 by OH radical. The numerical modelling has mainly concentrated on the temperature effect on the streamer parameters associated with the change of gas density, such as concentrations of CAS, radius and diffusion of a streamer channel.

2. EXPERIMENTAL METHODS

The NO removal system using the pulsed corona discharge consists of a gas supply facility, a wire-cylinder reactor, a pulse power supply, and monitoring systems for the discharge and gas cleaning. In order to simulate the diesel-like exhaust gas, a mixture of pure gases, such as N_2, O_2, and CO_2, is used together with a small amount of water vapour injected by a specially designed nozzle. In the corona reactor, plasma is generated between a wire electrode of 1-mm diameter/300-mm length and a cylinder electrode of 30-mm inner diameter. A pulse power supply operated with a magnetic pulse compression switch is capable of generating a positive pulse voltage of 15 kV with a 500-ns pulse width. The repetition rates of the pulse voltage are varied up to 300 Hz, the gas flow rate is kept to be 10 l/min.

To calculate the pulse energy transferred to a flowing gas, the discharge voltage and current are measured simultaneously by using a high voltage probe (Tektronix P6015A), a pulse current transformer (Stangenes Industry) and a digital oscilloscope (LeCroy 9361). The waveform of pulse power is determined by multiplying the measured discharge voltage by the pulse current, and then it depicts the propagation of primary and secondary streamers. The delivered energy to the exhaust gas is calculated by integrating the discharge power for duration of the primary streamer propagation between two electrodes since the secondary streamer does not contribute to the formation of CAS. The electrical energy input to the gas is varied by changing the pulse repetition frequency. Specific energy deposited into the gas per pulse is $(8\text{-}15)\times10^{-5}$ J/cm^3. The outlet gas compositions are monitored with a FTIR spectrometer, which enable to detect a variety of compounds, such as CO, CO_2, C_2H_4, C_3H_6, and H_2O. A chemiluminescent NO_x analyser is used in the measurements of NO and NO_x.

3. BASIC STATEMENTS OF MODELLING

3.1. Chemical kinetics code

Simulations of NO_x removal have been carried out on the base of an approximate mathematical model developed by Zhelezniak and Filimonova [7,8] for the plasma cleaning of pollutant gas using a pulsed streamer discharge. The influence of non-uniform distribution of species arising from a great number of streamer channels in the discharge chamber is taken into account. The numerical modelling has been performed for a sequence of pulses up to 900. After each pulse, the change in the gas composition caused by chemical reactions and diffusion processes inside and outside the streamer channels was examined. The simulations have incorporated 159 components and 803 reactions.

The following experimental data are utilised in the modelling: energy deposited into the gas both per pulse W_{dc} and total W, the discharge pulse repetition rate f, reactor volume and gas flow rate Q. An initial streamer radius r_{st} is specified according to [9]. The specific energy deposited in the streamer W_{st} and its fraction q consumed for the production of CAS depends on the discharge set-up and conditions. The parameter q implicitly accounts for the deviation of the effective electric field from the theoretically acceptable one and the mutual influence of the streamers, etc. It was set so as to math the calculation results to the experimental data. The value q is assumed to be independent of the kind of additives as well as f and Q for a given gas composition. The following parameter values are used: r_{st}=0.025 cm, $W_{st}=8\times10^{-3}$ J/cm^3, q=0.4 and diffusion coefficient D_{dif} =0.3 cm^2 s^{-1} at T=293 K.

The densities of CAS generated immediately after the discharge pulse depend on the mole fraction of molecules of matrix gas, the specific energy w_{st} ($w_{st}=q\cdot W_{st}$ [8]) for the production of CAS, and the G-values representing the number of active particles produced from the molecules by electron impact per 100 eV of energy deposited in the gas. The G-values depend on the reduced electric field E/N at the

streamer head and the gas composition, where N is the total number density of the gas and E is the electric field strength. The G-values have been obtained by taking advantage of the Boltzmann equation solver, ELENDIF code [10]. This code calculates the distribution functions of electron energy using electron-molecule collision cross-sections for N_2, O_2, CO_2 and H_2O. Because calculations for E/N in the streamer head are not available for our experimental set-up as yet, it is assumed that E/N is equal to 200 Td. This value was chosen for a reasonable agreement with experimental data for NO and NO_2 without HCs at the room temperature.

3.2. Consideration of temperature influence

In reality, there has been almost no work reported in consideration of the temperature effect on streamer parameters, and most research results have been presented for normal conditions. Recently, some authors have suggested the simulated streamer dynamics in dense media [11]. Allen and Ghaffar [12] reported the measurements on the variation of positive streamer properties with temperature in air at a constant pressure. They showed that the minimum electric field for streamer propagation decreases linearly with the rise of temperature. The analysis of several authors' results revealed the divergence between temperature and pressure effects. The light emission is increased under the higher temperature, and may be explained by the growth of both radius and number of streamers or branching. The effect of temperature on the specific energy deposition at the constant input voltage and frequency was observed in experiments [5]. Apparently, it is easier to transfer the energy into the hot gas, because the minimum field for streamer propagation decreases in the high temperature gas.

In this work, an attempt has been made to find the temperature effect on the NO_x removal process by the modelling within the bounds of the present numerical approach, which takes advantage of the similarity laws in streamer propagation and the conclusions presented in Ref. [11] for dense media. According to these results, the following dependences on temperature are taken: E/N=const, $r_{st} \sim N^{-1}$ or T, $D_{dif} \sim T^{1/2}$, $n_e \sim N^2$ or T^{-2}. In the experiments it was observed that the specific energy deposited into the gas per pulse varied with temperature as $W_{dc} \sim T$. The concentrations of CAS have been changed with the rising temperature in this modelling by using the parameter q at the fixed W_{st}.

4. RESULTS AND DISCUSSIONS

4.1. Effect of temperature on NO_x removal in the presence of ethylene and propylene

The concentration of water vapour in a matrix gas at T=393 K and T=493 K is maintained with 4-5% except for an experiment with 2.3% in case of C_3H_6 additive at T=493 K. In general, the matrix gas consists of 71-73% N_2, 17-17.5% O_2, 2.3-5% H_2O, and 6.7% CO_2. Initial NO_x concentrations are introduced into the reactor ranging between 490 and 510 ppm, and the HCs additives have the following concentrations: $[C_2H_4]_0$=550 and 545 ppm, $[C_3H_6]_0$=550 and 574 ppm at T=393 and 493 K.

The gas density reduced by 25 % and 40% at T=393 and 493 K in comparison with a gas density at T=293 K. Parameters for calculations are changed in accordance with their dependences on temperature (section 3.2). A fraction q of the specific energy deposited in the streamer is accepted as 0.3 at T=393 K and 0.14 at T=493 K. Under these values, all experimental data with and without HCs additives are simulated. Thus, the concentrations of active particles decreased as $\sim T^{-1}$ at T=393 K and $\sim T^{-2}$ at T=493 K in comparison with the their concentrations at T=293 K. It is questionable for these concentrations to follow faithfully through the similarity laws because of different concentrations of water vapour at different temperatures. Water vapour remarkably influences on the NO variation.

Figure 1 shows the influence of C_2H_4 and C_3H_6 on the NO remediation process at three values of temperature. The variations of C_2H_4 and C_3H_6 concentrations are also displayed at T=393and T=493 K. The results are given in dependence on input energy in the atmospheric condition (T=293 K, p=1 atm). There is a good agreement between the experimental and calculation results for NO and HCs variation in the presence of C_2H_4. Some difference at T=493 K in the presence of propylene may be governed by experimental conditions. The energy cost of one NO removal molecule and oxidation efficiency at W=30 J/l_0 are presented in Table 1 as the common values obtained in the experiment and modelling.

Experimental results in the presence of C_3H_6 at T=493 K are given in parentheses. According to the analysis without HCs, the NO removal is most highly achieved at T=393 K and becomes worse at the higher temperature. With hydrocarbons, the NO removal decreases with increase the temperature. At the same temperature, C_3H_6 enhances NO oxidation better than C_2H_4. The NO removal efficiency with C_3H_6 reaches up almost 100% at T=393 and 493 K at the practically same cost of NO removal. The calculated concentrations of main by-products generated during the process are given in Table 2.

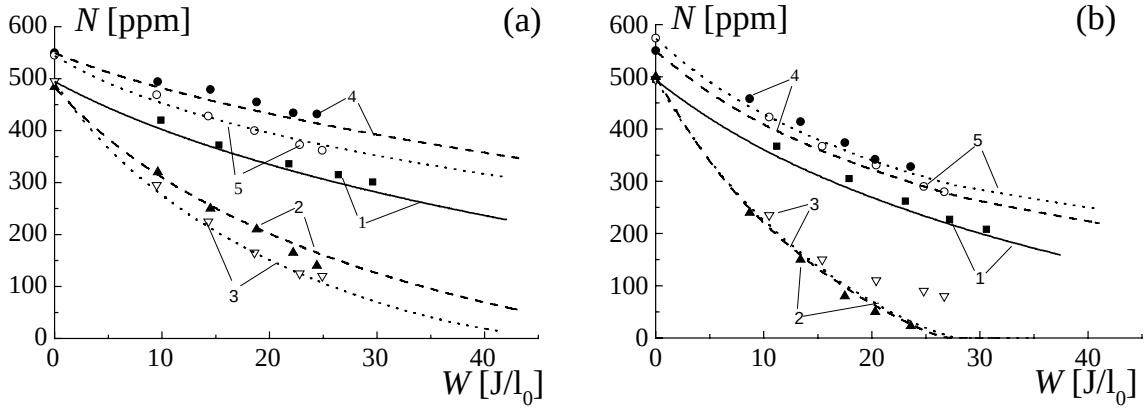


FIGURE 1. Temperature effect on concentrations of NO and HCs in dependence on input energy in the presence of (a) C_2H_4 and (b) C_3H_6. Symbols are experimental data, and the curves are the calculated results. Gas composition is given in Table1. 1: NO removal, T=293 K; 2: NO removal, T=393 K; 3: NO removal, T=493 K; 4: HCs variation, T=393 K; 5: HCs variation, T=493 K.

TABLE 1. The removal cost of one NO molecule and oxidation efficiency at the deposited energy W=30 J/l_0. Gas composition is (71-73)%N_2+(17-17.5)%O_2 +(0.8-5)%H_2O+6.7%CO_2 with $[NO]_0$ =480-500 ppm; $[C_2H_4]_0$ = 516, 550, 545 ppm; and $[C_3H_6]_0$=511, 550, 574 ppm.

Additives	T=293 K	T=393 K	T =493 K
No additives	46 eV	44 eV	62eV
	33%	36%	25%
C_2H_4	35 eV	21eV	18eV
	43%	74%	86%
C_3H_6	27 eV	14eV	14(16) eV
	60%	100%	100(84)%

TABLE 2. By-products in the NO conversion with C_3H_6 in dependence on temperature. Concentrations are given in ppm at the deposited energy W=30 J/l_0. Gas composition is appeared in Table 1.

Component	T=293 K	T=393 K	T=493 K
HNO_2	16	18	11
HNO_3	15	48	24
CH_2O	90	200	186
CH_3CHO	51	151	144
CH_3ONO_2	3	13	15
CH_2CHCHO	2	8	7
$ONCH_2CHO$	12	22	20
C_2H_5ONO	13	13	8
$C_2H_5ONO_2$	4	12	12

In the present work the total rate constant and branching of C_2H_4+O reaction were taken from Ref. [13]. The choice of reaction channels and their ratios in the C_3H_6+O reaction are based on the experimental branching ratios obtained by Koda *et al* [14]. Taking into account the measured yields of products and a pressure dependence of CH_2CHO formation, the following distribution is acceptable:

$$C_3H_6+O \Rightarrow CH_3+CH_2CHO, \quad k_a=0.2k, \quad (a)$$

$$\Rightarrow C_2H_5+CHO, \quad k_b=1.4k_a= 0.28k, \quad (b)$$

$$\Rightarrow C_2H_4+CH_2O, \quad k_c=0.52k, \quad (c)$$

where $k=4.0\times10^{-19}T^{2.56}\exp(569/T)$ cm^3 s^{-1} is a total rate constant of C_3H_6+O reaction. Reaction schemes with OH radical for C_2H_4 and C_3H_6 were constructed on the base of the data [15,16].

4.2. SO_2 conversion in the presence of propylene

Special modeling has been performed to check the influence of C_3H_6 on the SO_2 conversion. The matrix gas included 4.8% H_2O, 495 ppm NO, 50 ppm SO_2 and 545 ppm or 1500 ppm C_3H_6. The SO_2 concentration diminished by 49.3 ppm with C_3H_6 for both concentrations and by 49.4 ppm without C_3H_6 at the input energy W=30 J/l_0. In spite of the consumption of OH and O radicals by C_3H_6, an additional formation of HO_2 through the reactions O_2 + CHO=>HO_2 + CO and as a final product in the chains of interaction C_3H_6OH with NO gives a noticeable SO_3 formation through the reaction HO_2 + SO_2 => OH + SO_3. The latter reaction compensates dissipations of OH and O species in the presence of NO and C_3H_6. In dependence on catalyst, 1 ppm H_2SO_4 may be enough for its poison. If the water vapour concentration achieves 10%, suppression of H_2SO_4 formation with HCs will be problematically, and it is necessary to do a special investigation.

5. CONCLUSIONS

Numerical and experimental results on the NO_x removal using pulsed corona discharge are presented with and without C_2H_4 and C_3H_6 additives at T=293, 393, 493 K in the synthetic gas consisting of N_2, O_2, H_2O, CO_2 including 500 ppm NO. The numerical results agree well with the experiments ones for NO and NO_x removal and decomposition of HCs additives. Owing to modelling approach, taking into account of the streamer nature of discharge, the influence of temperature on the NO_x conversion has been investigated. For the same temperature, C_3H_6 is of more benefit to the cleaning process compared with C_2H_4 because of an additional formation of HCs radicals, which react with NO molecules. HO_2 radical is the main component in the NO conversion in the presence of C_2H_4 and C_3H_6. The highest NO decomposition of about 100% is expected to be obtained at the temperature of 393 and 493 K with $[C_3H_6]_0$=550 ppm, and that of 86% with $[C_2H_4]_0$=545 ppm at T=493 K with a deposited energy of 30J/l_0. The removal costs of one NO molecule are estimated as approximately 14 eV and 18 eV in the presence of C_3H_6 and C_2H_4, respectively. Without the HCs additives the best NO reduction of 36% is expected at T=393 K at an energy cost of 44 eV. A suppression of formation of sulfur acid in the diesel exhaust in the presence of HCs may not be sufficient for avoiding a poison of catalyst agents.

ACKNOWLEDGMENTS

This work was supported by the Korea Institute of Science and Technology Evaluation and Planning (KISTEP) and Seoul National University in Korea.

REFERENCES

[1] Orlandini I., and Riedel U.J,. *Phys. D: Appl. Phys.*, **33** 2467-74 (2000)
[2] Dorai R., and Kushner M.J. *J. Phys. D: Appl. Phys.*, **34** 574-83 (2001)
[3] Park K-S., Kim D-I., Lee H-S., Chun K-M., Chun B-H., *SAE paper* 2001-01-3515 (2001)
[4] Miessner H., Francke K-P., and Rudolf R., *Applied Catalysis B: Environmental* **36** 53-62 (2002)
[5] Hoard J.W., and Panov A., *SAE paper* 2001-01-3512 (2001)
[6] Penetrante B.M., Brusasco R.M., Merritt B.T., and Vogtlin G.E., *SAE paper* 1999-01-3687 (1999)
[7] Zhelezniak M.B., and Filimonova E.A., *High Temperature* **36** 352-7, 533-40 (1998)
[8] Filimonova E.A., Amirov R.H., Kim H.T., and Park I.H., *J. Phys. D: Appl. Phys.* **33** 1716-27 (2000)
[9] Babaeva N.Yu., and Naidis G.V., *J.Phys.D: Appl. Phys*. **29** 2423-21 (1996)
[10] Morgan W.L. and Penetrante B.M., *Comp. Phys. Comm.* **58** 127-52 (1990)
[11] Babaeva N.Yu., and Naidis G.V., *J. Electrostatics* **53** 123-33 (2001)
[12] Allen N.L., and Ghaffar A., *J. Phys. D: Appl. Phys.* **28** 338-43 (1995)
[13] Baulch D.L., Cobos D.J., Cox R.A. et al., *J. Phys. Chem. Ref. Data* **21** 411-734 (1992)
[14] Koda S., Endo Y., Tsuchiya S., and Hirota E., *J. Phys. Chem.* **95** 1241-4 (1991)
[15] Atkinson R., *J. Phys. Chem. Ref. Data* **26** 215-90 (1997)
[16] Atkinson R., *Int. J. Chem. Kinet*. **29** 99-111 (1997)

REMOVAL OF TRICHLOROETHYLENE WITH A DC-EXCITED MULTI-PIN-TO-PLATE PLASMA SOURCE

R. Vertriest[1], R. Morent[2], J. Dewulf[1], C. Leys[2], H. Van Langenhove[1]

[1] *Department of Organic Chemistry Faculty of Agricultural and Applied Biological Sciences, Ghent University, Coupure Links 653, B-9000 Ghent, BELGIUM*

[2] *Department of Applied Physics, Faculty of Engineering, Ghent University, Rozier 44, B-9000 Ghent, BELGIUM*

Abstract. Removal of low concentrations of volatile organic compounds in flue gases is one of many industrial applications of atmospheric non-thermal plasmas. The use of non-thermal plasmas makes it possible to achieve substantial removal efficiencies at short residence times and low energy consumption. In this paper, a DC-excited atmospheric pressure glow discharge in a multi-pin-to-plate electrode configuration is used for the removal of trichloroethylene (TCE). A removal efficiency of up to 47 % is obtained at an energy density of 35 J/l and a residence time of 0,05 s. The energy cost to destroy one molecule of TCE decreases with increasing input concentration, reaching 15 eV/molecule at 1000 ppm.

1. INTRODUCTION

Air pollution by Volatile Organic Compounds (VOC's) causes photochemical smog and enhances the greenhouse effect and the destruction of the ozone layer. Moreover, several of these VOC's are toxic or cause odour nuisance. Non-thermal plasma techniques are an economically attractive alternative for conventional removal techniques like thermal incineration, catalytic oxidation and biological oxidation methods. The essential advantage of a non-thermal plasma technique is that the available energy is added selectively to the plasma electrons. The energy in the plasma is directed preferentially to the electron-impact dissociation and ionization of the background gas to produce radicals that in turn, decompose the targeted VOC's. Due to the energy selectivity non-thermal plasma techniques are very appropriate for the treatment of gas streams with low VOC-concentrations. In addition, plasmas can be used for the simultaneous removal of different pollutants. Another possibility is the combination of a plasma technique with other VOC-abatement techniques like catalysts [1].

For the treatment of VOC-emissions plasmas are required that operate at atmospheric pressure. Among the different schemes that have been suggested to produce non-equilibrium discharges at high pressure, the DC glow discharge offers a good industrial perspective, due to its scalability and comparatively low installation cost. The plasma source that is used in the reported experiments is a DC-excited atmospheric pressure glow discharge in a multi-pin-to-plate configuration [2]. In this paper first results on the removal of low concentrations (ranging from 50 to 1200 ppm) of TCE are reported.

2. MATERIALS AND METHODS

2.1. Physical methods

The experimental set-up is shown in figure 1. A fan (Ventomatic CMT31M), with adjustable speed, drives an ambient air flow rate (relative humidity from 30 to 65%) in the 60 to 140 m^3/h range (12 m/s to 28 m/s). The fan gave a stable flow rate with a standard deviation ranging from 1.3% for the highest flow rates to 1.6% for the lowest. The residence times varied from 0.054 s

[2] Electronic address: Christophe.Leys@rug.ac.be

to 0.023 s. Temperature of the inlet gas is controlled by an electrical heater and varies between 20°C to 60°C.

The multi-pin-to-plate plasma source consists of a rectangular duct with a cross section of 16.2 cm x 1.3 cm and a length of 60 cm. The distance between the multi-pin cathode and the anode plate is 1.3 cm. Stable and uniform glow discharge operation at atmospheric pressure is ensured by a fast gas flow and by ballasting the cathode pins with a 1.5-MΩ resistor. In addition, the threshold current density for the glow-to-spark transition is increased by using an optimised electrode geometry [2].

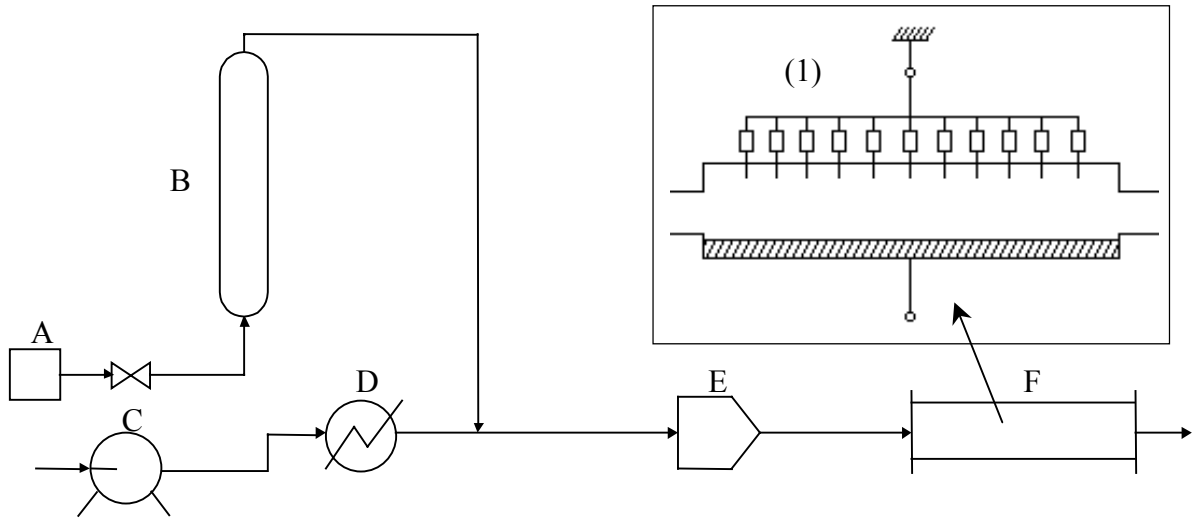


FIGURE 1. Experimental arrangement: complete set-up and detail (1) of the plasma source. Legend: A= pressurized air, B= purge column, C= fan, D= heater, E= mixing chamber, F= plasma source.

2.2. Chemical materials and methods

Trichloroethylene (Aldrich, 99.5+%) is dosed by a purge method. The air flow rate (Air Liquide, Alphagaz 1) is controlled by a mass flow controller (MKS Instruments, 1559AX-020L-SV) at a rate of 1.1 to 3.3 l/min. This air flow bubbles through a TCE column (inner diameter: 56.3 mm; height: 164.0 mm), held at 30.0±0.1°C and equipped with a frit at the inlet. This TCE enriched gas flow is mixed with the ambient air flow in a mixing chamber in front of the reactor.

Triplicate samples of gaseous TCE in front of the reactor and at the outlet of the reactor were taken by means of a 500µL Hamilton Luer Lock syringe (Type 1750 TLL). These samples were analyzed by means of a Chrompack 9002 gas chromatograph, equipped with a CP-SIL-5 CB-MS capillary column (Chrompack, 100% polydimethylsiloxane, length 50m, inner diameter 0.32 mm, film thickness 1.2µm), a flame ionization detector (FID: air feeding rate: 300 $ml.min^{-1}$, hydrogen feeding rate: 30 $ml.min^{-1}$) and a Cecil Data Control Instruments integration system (Cecil Instruments Ltd). GC oven temperature was kept at 80°C.

The overall set-up was checked to be gastight. The whole analytical procedure, including sampling and analysis, showed standard deviations between 2.8% and 9.7%. With no voltage applied, the input and output TCE-concentrations are within the standard deviations (input = 60.3 ± 5.3 ppm; output = 58.9 ± 4.2 ppm).

3. RESULTS AND DISCUSSION

3.1. Results

The stabilisation of a glow discharge at atmospheric pressure is done by an optimised point-to-plate electrode geometry, a fast gas flow and ballasting of the cathode pins with a resistance of 1,5 MΩ. The

flow velocities range from 12 to 28 m/s. The corona regime of the discharge occurs at low currents and is characterised by a linear dependence of the reduced current, I/V, on the voltage V (Fig. 2). In the corona discharge, the plasma does not fill the entire discharge gap and light is only emitted at the sharp edges of the point electrode. Increasing the current results in a gradual filling of the gap with luminous plasma. This visual observation is indicative of the transition of the discharge from corona to glow. In the glow regime the reduced current increases while the voltage stays almost constant. The average electrical field of 17 kV/cm is higher than in the corona regime. The concomitant increase in the production of active species and the higher filling factor of the electrode gap make the glow discharge the regime of choice for gas treatment applications.

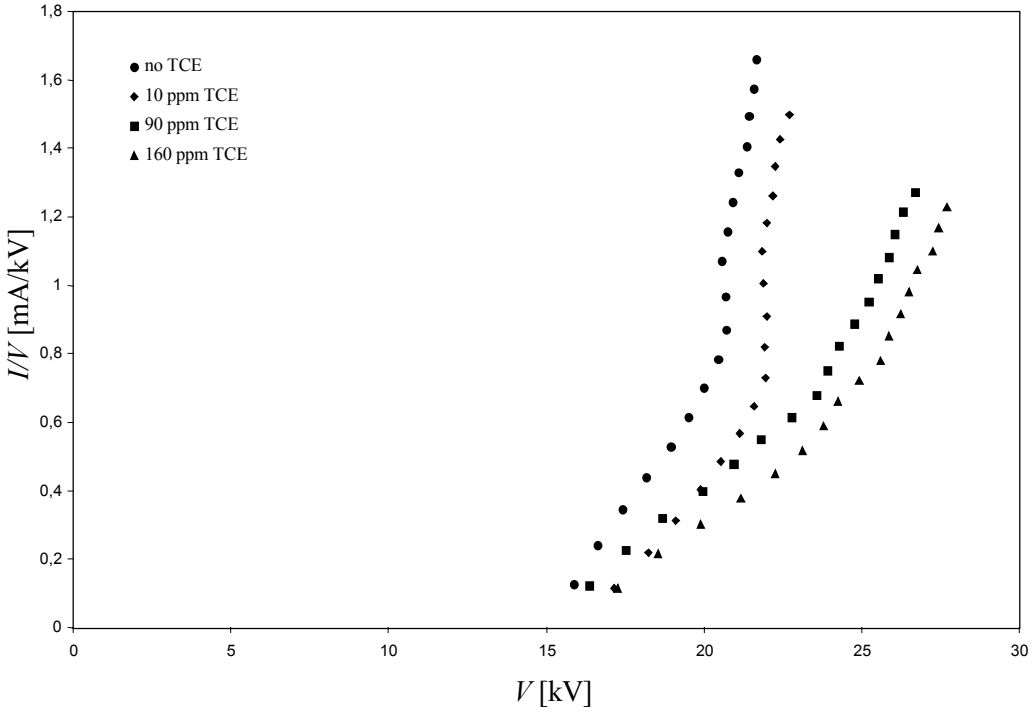


FIGURE 2. Reduced current-voltage-characteristics of the multi-pin-to-plate plasma source.

The addition of TCE gives rise to an important increase in voltage across the discharge gap (Fig.2). For a TCE concentration of 90 ppm the voltage is about 3 kV higher as in the case without TCE. A further increase of the TCE concentration has only minor effects on the voltage. The threshold current for sparking decreases with increasing TCE concentration.

Figure 3 shows the removal efficiency as a function of the energy density. The latter is varied by varying discharge current or flow rate. The apparent energy density threshold for removal at 10 J/l is due to the lower values of the reduced field strength E/N in the region of low energy densities where the glow regime is not yet fully established. A maximum removal efficiency of about 47% is obtained at an energy density of 37 J/l. Higher energy densities are difficult to reach as a result of the glow-to-spark transition.

At constant power the removal rate increases with increasing TCE influx (Figure 4). However, the removal efficiency (removal rate divided by influx) appears to be constant for a given residence time. This is in accordance with the general equation:

$$\frac{dN_{\mathrm{TCE}}}{dt} = k N_{\mathrm{TCE}} N_{\mathrm{R}} \qquad (1)$$

where N_R is the density of all particles that react with TCE. Evans *et al.* proposed a model for the removal of TCE in a silent discharge plasma [2]. In this model the ClO-radical is attributed an important role in oxidizing TCE. Ongoing research aims at elucidating the reaction kinetics of TCE removal in a glow discharge.

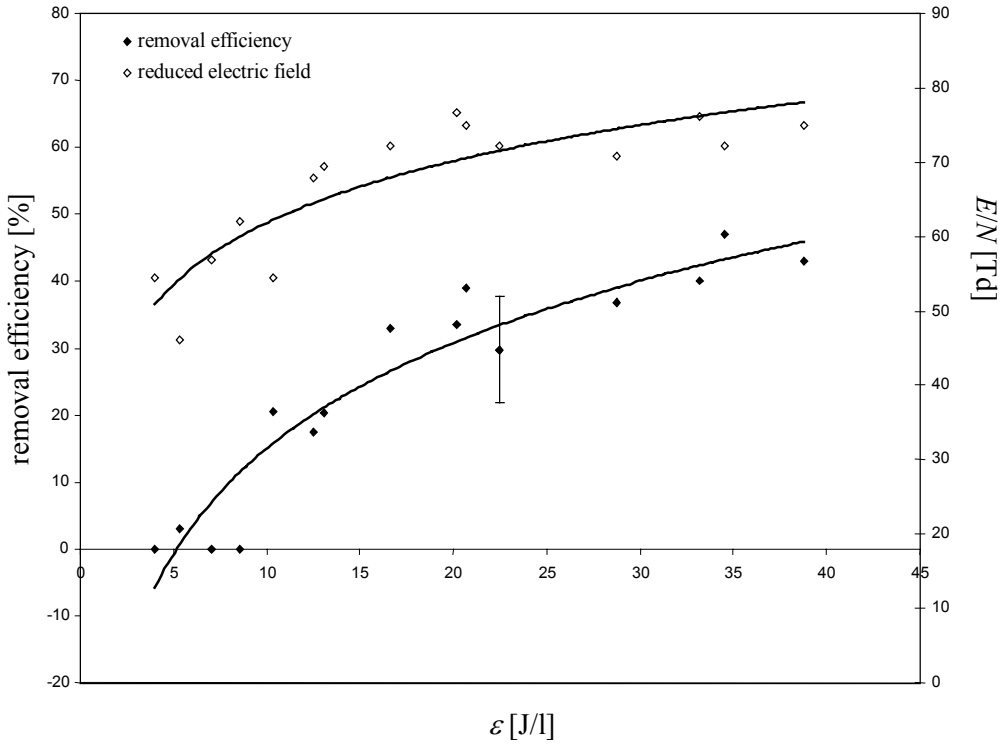


FIGURE 3. Removal efficiency versus energy density at different residence times and different currents; temperature is 25°C, relative humidity is 45 %.

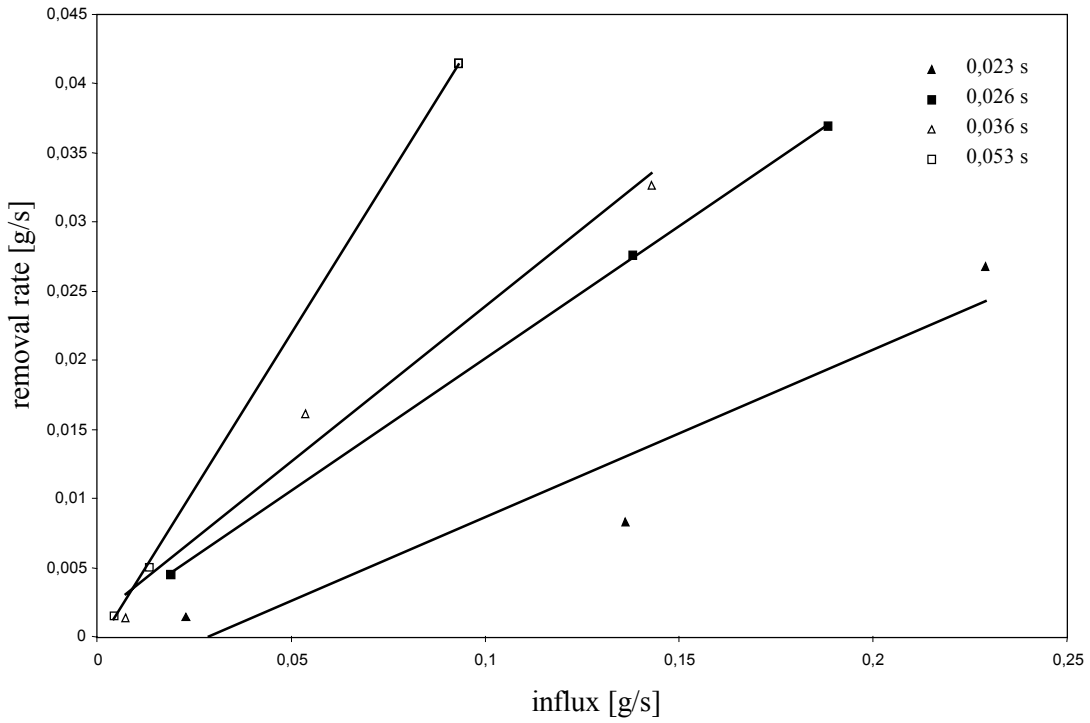


FIGURE 4. Removal rate of TCE as a function of TCE influx for different residence times.

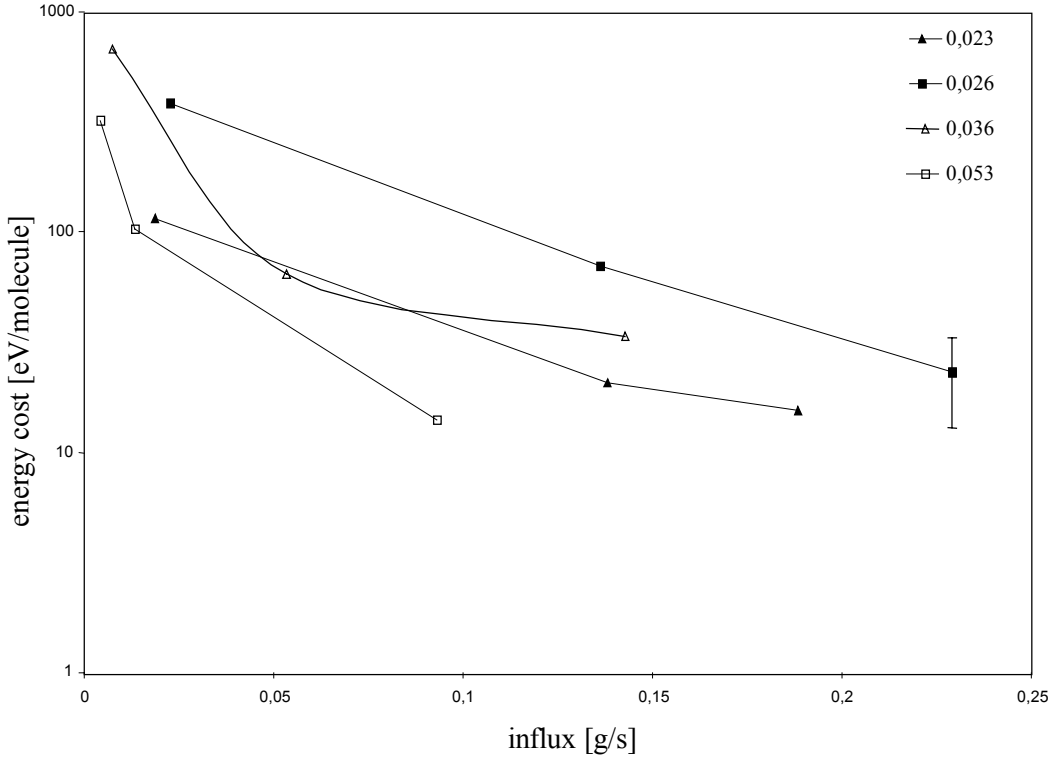


FIGURE 5. Energy cost versus TCE influx for different residence times.

The energy cost to remove one molecule of TCE is strongly dependent on the inlet concentration. With increasing input there is a sharp decrease, reaching a minimum cost at highest influx. The lowest achieved energy cost was 15 eV/molecule. In conclusion, a substantial, yet incomplete removal of TCE is observed in a plasma module based on a DC atmospheric pressure glow discharge. As the electrical power density is limited by the glow-to-spark transition, higher removal efficiencies are to be reached through longer residence times, i.e. by placing several discharge modules in series.

ACKNOWLEDGMENTS

The authors are indebted towards Prof. Yu.Akishev from TRINITI, Troitsk (RUSSIA), for providing the electrode system of the plasma source and for many stimulating discussions.

REFERENCES

[1] Oda T., Takahashi T. and Kohzuma S., *IEEE Trans.Ind.Appl.,* **37**, 965 (2001).
[2] Akishev Y., Goossens O., Callebaut T., Leys C., Napartovich A. and Trushkin N., *J. Phys. D: Appl. Phys.*, **34**, 2875-82 (2001).
[3] Evans D., Rosocha L.A., Graydon K.A, Coogan J.J. and Kushner M.J., *J. Appl. Phys.,* **74***,* 5378 (1993).

STUDIES ON AN AC/DC COMBINATION DISCHARGE MODE FOR NO_X TREATMENT

Guan Penghui*, Nobuya Hayashi, Satoshi Ihara, Saburoh Satoh, Chobei Yamabe

Department of Electrical and Electronic Engineering, School of Science and Engineering, Saga University, 1, Honjo-machi, Saga, 840-8502, JAPAN

Abstract A simplified AC/DC combination discharge mode for investigation of NOx treatment was carried out in this paper. A positive streamer corona discharge (DC) combined with a barrier discharge (AC) by an AC/DC conversion circuit. In such system, the sample gas (NO/N_2) is treated by barrier and streamer discharge serially. The NO removal rate of the system was 52%, which was 12.3% and 27.7% when only barrier or streamer discharge was used respectively.

1. INTRODUCTION

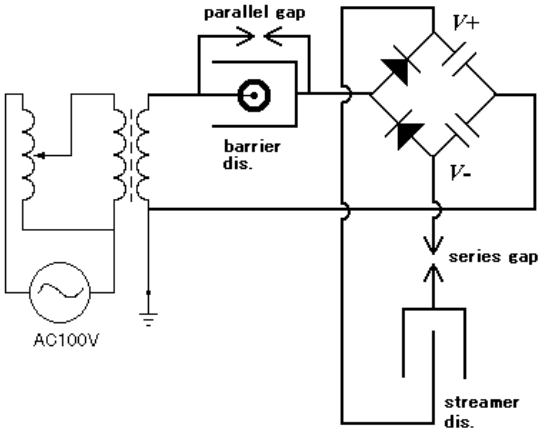
Nowadays, the affect of NOx on environment became a serious problem while humans improve their technology level. Various kind of corona-induced non-thermal plasmas have been demonstrated regarding to their technical and economical feasibility for removal of NOx from flue gas, such as pulsed streamer corona, microwave discharge, gliding arc, glow, dielectric barrier discharge and surface discharge, etc. [1]. The dielectric barrier discharge was widely used in ozone generation and gas treatment field according to such advantages as simple and commercial available power supply; spark self-quenching, etc. [2]. For the electrode arrangements with large gap spacing (>5cm), the positive DC streamer corona seems to be very suitable for inducing non-thermal plasma under high pressure [1]. This experiment was tried to cascade the positive streamer discharge with a barrier discharge. It was expected that such combination discharge system could show more efficiency than using each discharge separately.

To build such combination discharge with single power supply, an AC/DC conversion circuit was used. After barrier discharge, the AC voltage (60Hz) was transferred into DC voltage by a diode bridge for the positive streamer discharge. To solve the problem of voltage drop after barrier discharge, a 1-stage Deltatron-Greinacher circuit [3] was used for voltage conversion instead of diode-bridge, by which the AC voltage that after barrier discharge was increased two times. When input AC voltage was 8.82kV, a high DC output voltage of 16.5kV was applied on the streamer discharge reactor.

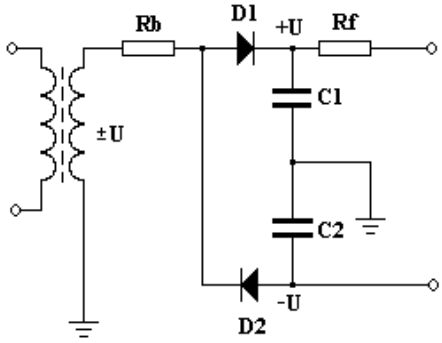
In this experiment, NO gas ($NO[450ppm]/N_2$) was treated as sample gas. The gas flows through the barrier discharge area and streamer area serially. Until now the NO removal rate of 52% was obtained.

2. EXPERIMENTAL SETUP

The experiment system includes two discharge reactors (barrier discharge reactor with a parallel gap and streamer discharge reactor with a series gap), the Deltatron-Greinacher circuit was between the two reactors as an amplifier-rectifier (See Fig.1).



FIGUER 1. Experimental setup



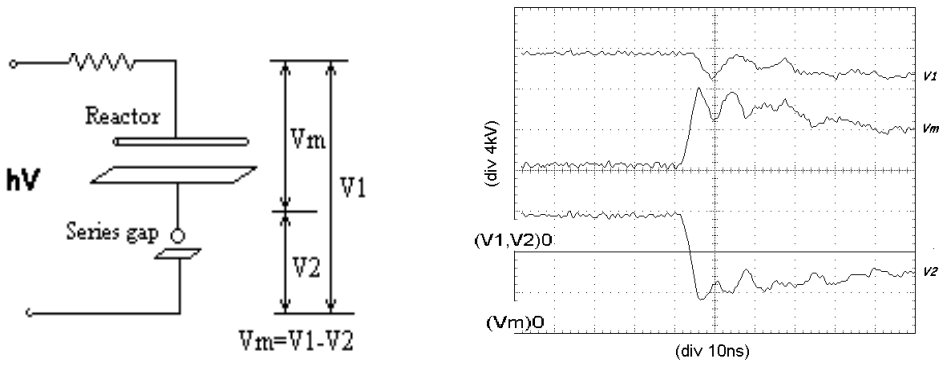
FIGUER 2. Deltatron-Greinacher circuit

The barrier discharge reactor has a wire electrode covered with glass tube and plate electrode, there were three wires (with diameter of 1mm) set inside the glass tubes in the rector as electrodes applied high voltage. The distance between the wire and the plate was 3mm. The streamer discharge reactor was wire to plate geometry. A wire whose diameter was 0.1mm was used as anode. The spacing of electrodes was 15mm.

The sample gas (NO[450ppm]/N_2) flows through the barrier discharge reactor and streamer discharge reactor with flow rate of 2L/min. the treated gas went through a water bubbling and then to a chemiluminescent NO_x analyzer (shimazu NOA-700), which measured the concentration of the NO.

Since the barrier discharge limited the total current, the streamer discharge could hardly occurred under such low current. To solve such problem, a long spacing gap (25mm) was parallelized with the barrier discharge reactor. The parallel gap operated with the barrier discharge as a trigger switch for streamer discharge.

As we know that for the gap spacing of centimeters order in air, the morphology of corona discharge may change from onset streamer to Hermstein glow, pre-breakdown streamer and then to spark breakdown by increasing the positive DC applied voltage. To produce uniform streamer discharge, a series gap was attached directly behind the main discharge reactor. The series gap was a sphere-to-plane gap with gap spacing of the order of millimeters. When series gap operated, a voltage pulse was generated and applied on the streamer discharge reactor. The series gap prevented



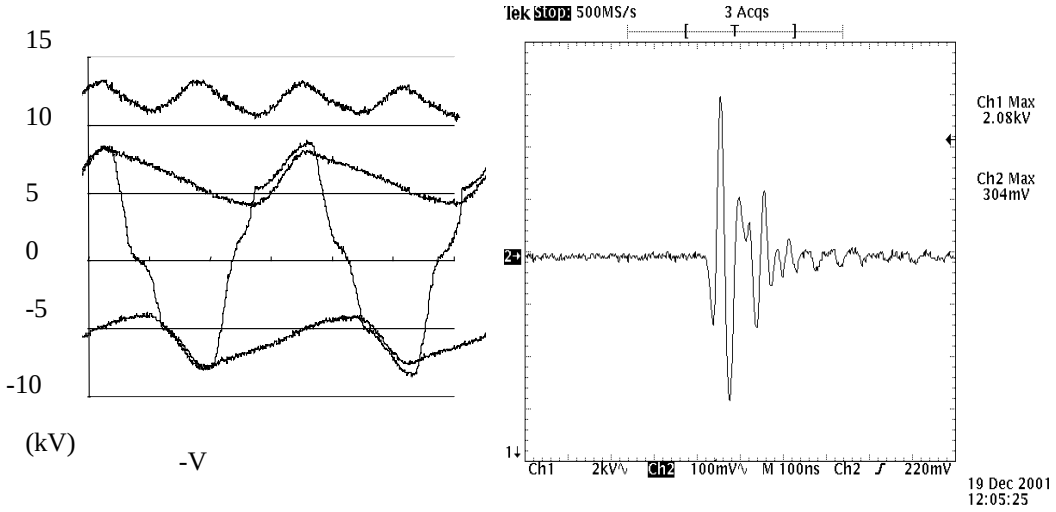
FIGUER 3. Schematic diagram of series gap and the typical voltage waveform of single pulse

the streamer discharge from changing to spark break down. The typical voltage waveform of such DC voltage pulse was shown in Fig. 3.

3. EXPERIMENTAL RESULTS

In this experiment, the applied AC voltage V_{AC}; the output DC voltage V+ and V- of amplifier-rectifier were measured by oscilloscope. The total output DC voltage of amplifier-rectifier VDC was calculated by V_{DC}=V- (-V). (See Fig.4a). When V_{Acmax}=8.7kV, we have V_{Dcmax}=13.3kV.

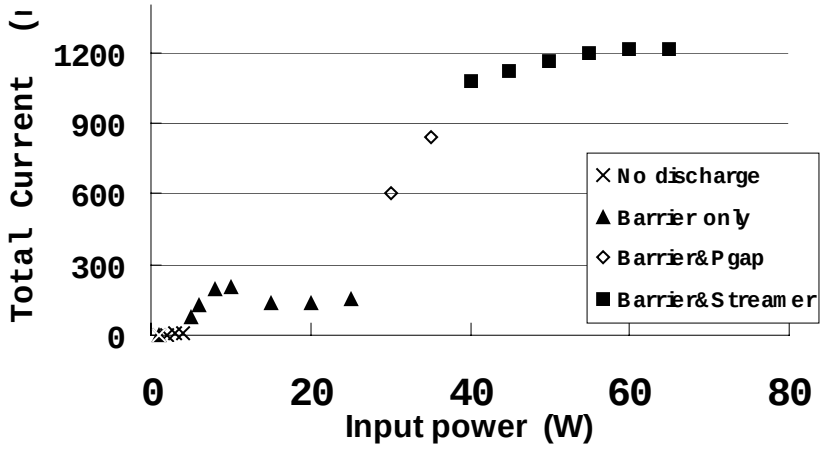
The total AC current was also measured by Rogowski Coil, typical current waveform as shown in Fig.4b.



a. Voltage waveform b. Current waveform

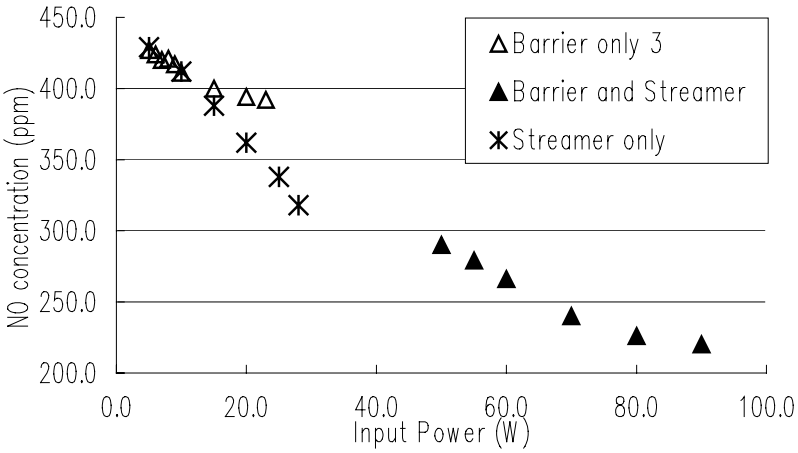
FIGUER 4. Typical current and voltage waveforms

While the applied voltage increasing, the barrier discharge appeared under AC1.5kV firstly, and then the parallel gap operated under AC3kV, finally the streamer discharge appeared under DC8kV. So both the uniform barrier and streamer discharge occurred simultaneously. Fig.5 shows change of the current in such process.



FIGUER 5. Total current as a function of input power

The Fig.6 shows the NO removal effect of the experiment, with combination discharge system, the NO concentration of barrier discharge only and barrier&streamer combination discharge was measured. It was found that with barrier discharge only, the NO removal rate was about 13%. While the input power increasing, the streamer discharge occurred and the NO removal rate increased up to 52%. As a comparison, the barrier circuit was removed and the NO concentration of streamer discharge only also been measured, which was about 28%.



FIGUER 6. NO concentration versus input power

4. CONCLUSION

This experiment showed that it's possible to occur the dielectric barrier discharge and positive streamer discharge with single power supply by the simplified amplifier-rectifier circuit. The NO treatment result shows that the combination discharge was more effective than barrier discharge only and, regarding to NO removal rate, it also showed higher effect than streamer discharge only. However, it was found that the NO treatment efficiency of single streamer discharge was rather higher than the combination discharge (see Fig.6). As further work, the experiment for increasing the NO treatment efficiency will be done, and the characteristics of different gas mixture will be studied.

REFERENCES

[1] K.Yan, S.Kanazawa, T.Ohkudo, Y.Nomoto, Trans. IEE Japan 118-A, 1998, p.948-953
[2] Sigmond R.S., in Electrical Breakdown of Gases, edited by J.M.Meek and J.D.Craggs, John Wiley&Sons, Ltd., 1978.
[3] E.Kuffel, W.S.Zaengl, High Voltage Engineering Fundamentals, ed. by P. Hammond, Publisher, Robert Maxwell, M.C., 1984, pp.13
[4] P. Guan, S. Ihara, R. Gasparik, C. Yamabe, Proc. of 1999 Joint conference of electrical and electronics engineers in Kyushu, Kitakyushu, 1999; p.67.
[5] R. Gasparik, N. Mine, S. Ihara, S. Satoh, C. Yamabe, Vacuum 59 (2000) 220-227.

TREATMENT OF FLUOROCARBON USING ATMOSPHERIC NON-THERMAL PLASMA PRODUCED BY STREAMER CORONA DISCHARGE

N. Hayashi, K. Yamamoto, S. Ihara, S. Satoh and C.Yamabe

Faculty of Science and Engineering, Saga University, 1 Honjyo-machi, Saga 840-8502, Japan

Abstract. The non-thermal plasma produced by the streamer corona discharge at atmospheric pressure was utilized for the vanishing of fluorocarbon. The effective treatment of fluorocarbon is attempted controlling discharge parameters of the plasma. The decomposition rate of fluorocarbon is investigated changing (a) discharge modes and (b) discharge characteristics i.e. applied voltage VA-K of a main discharge gap and its steepness dVA-K/dt.

1. INTRODUCTION

One of the greenhouse effect gases, hydro fluorocarbons (HFCs) and per fluorocarbons (PFCs) has been used widely in the plasma processing such as etching and cleaning of semiconductor wafer. Japan are requested for the 6% reduction of the quantified emission limitation of the greenhouse gases such as CO_2, CH_4, NO, SF_6, HFCs, PFCs according to the guideline of *Kyoto Protocol to the United Nations Framework Convention on Climate Change* (COP3, 1997) [1]. The coefficient of the greenhouse effect of fluorocarbons is significantly higher (several thousand times) than that of CO_2, CH_4, NO. Therefore, it is very important to treat fluorocarbon.

The gases used for plasma processing have been exhausted to the atmosphere after treatment by several methods, i.e., chemical filtering, catalytic reactions and baking method. Recently, treatment of fluorocarbons by a low pressure plasma has been put to practical use because of its high decomposition rate. However, the cost of these treatments is relatively expensive. Therefore, the cost reduction of the waste gas treatment and enhancement of the treatment efficiency are requested by the industry world. In this paper, the new method of fluorocarbon decomposition using non-thermal plasmas produced by atmospheric discharges was studied. The streamer corona discharge and the arc discharge were utilized for decomposition of CF_4 as PFC changing parameters such as the rise time of applied voltage pulse and peak value of the voltage.

2. EXPERIMENTAL PROCEDURE

Figure 1 shows a schematic diagram of the experimental apparatus. The chamber was made of acryl with dimensions of 100 mm length by 100 mm width and 30 mm height. A five-wires-to-double-plates electrode was set at center of the chamber. The tungsten wires with a diameter of 0.23 mm were set between two plate electrodes. The distance between the wire and plate electrode was 10 mm, and the wire-to-wire spacing was 30 mm. The series gap length was varied from 0 mm (without the gap switch) to 2.8 mm in order to change the rise time of the applied voltage pulse $dV_{A\text{-}K}/dt$. The mixture gases of CF_4 (100 ppm) diluted by oxygen and argon-oxygen mixed gas were used. The total gas flow rate was kept at 1.5 *l*/min unless stated, and the gas pressure in the reactor was kept at an atmospheric.

When a positive high voltage was applied to the tungsten wires, the pulsive plasma was produced by the positive streamer corona discharge. The series gap switch was used to stabilize the discharge and obtained a large pulse rise time of the applied voltage of discharge electrodes. The repetition frequency was determined spontaneously by the operation of series gap.

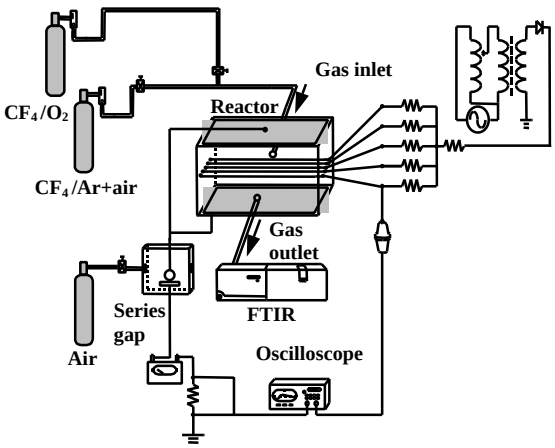


FIGURE 1. Schematic diagram of experimental setup and measurement system.

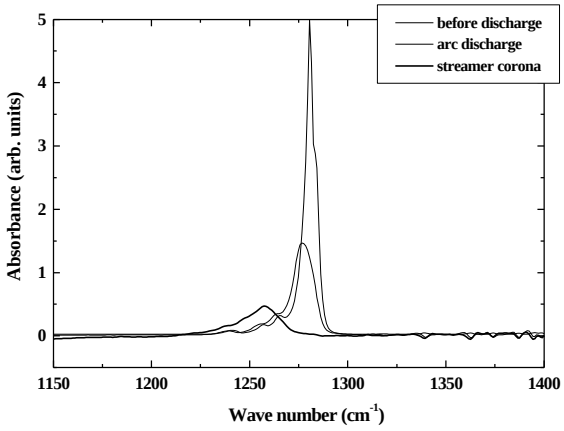


FIGURE 2. CF_4 peak height of before and after different types of discharge. CF_4 diluted by Ar+air (1.5 *l*/min).

The instantaneous waveforms of the applied voltage between the electrodes and the discharge current were measured using a high-voltage probe and Rogowski coil, respectively. The waveforms were recorded by an oscilloscope. The decomposition rate of the CF_4 gas was estimated using FTIR spectroscopy. In this experiment, the relative amount of fluorocarbon was evaluated based on the absorbance peak of 1280 cm^{-1}. The byproduct species such as CF_3, CO_2 generated by the CF_4 decomposition were identified using the FTIR absorption spectra and analysis database software.

3. RESULTS AND DISCUSSION

3.1. Decomposition of fluorocarbon using different discharge modes

The fluorocarbon, CF_4 was decomposed using two types of atmospheric discharge modes, i.e., the streamer corona discharge and the arc discharge. The discharge modes are controlled by the applied voltage between discharge electrodes. The streamer corona discharge is obtained when the applied voltage is lower ($V_{A\text{-}K}$ = 11 kV at 0.70 mm of the gap switch length), and the discharge current is several hundreds mA. The produced plasma looks spatially uniform between discharge electrodes. The arc discharge occurs at higher applied voltage of 13 kV, and the discharge current is several ten A. The plasma is produced along the discharge path and the spatial uniformity is significantly low.

Figure 2 indicates the typical FTIR spectra of low concentration CF_4 gas (100 ppm) diluted by Ar-air mixed gas for different discharge modes. Peaks of CF_4 in the FTIR spectra of different discharge modes indicate that the streamer corona discharges is suitable for the CF_4 treatment. The maximum decomposition rate using the streamer corona discharge is 92%, while that of arc discharge is 68%. This result arises from the difference of the discharge characteristics. The arc discharge has a lined discharge path and large electron energy, while the streamer corona discharge has relatively small electron energy and the large discharge volume. Therefore, the result suggests that the large discharge volume and uniformity of the plasma are essential for the efficient treatment of CF_4. Also, the lower electron energy of the streamer corona discharge than that of arc discharge is sufficient for the decomposition of fluorocarbon.

3.2. Variation of discharge characteristics

The discharge characteristics of the streamer corona depend on the rise time of the voltage pulse $dV_{A\text{-}K}/dt$ applied between discharge electrodes. Dependency of the CF_4 decomposition rate under the constant input power on the $dV_{A\text{-}K}/dt$ was investigated using the series gap switch. The $dV_{A\text{-}K}/dt$ is

considered to relate with the electron energy, that is, the electron velocity in a plasma, and was controlled by changing the length of the series gap connected with the reactor directly at downstream side [1)]. Figure 3a illustrates the typical waveforms of the discharge voltage for various series gap lengths. The shape of the applied voltage pulse changes with the gap length. In the case of large gap length, the peak voltage becomes larger than that of small gap length. However, the repetition rate of the voltage pulse becomes small in the case of large gap length. As shown in Figure 3b, the dV_{A-K}/dt was varied from 0.17 kV/ns to 0.31 kV/ns keeping the streamer corona discharge, where the gap length of series gap was changed from 0.70 mm to 2.1 mm, respectively. The number of the pulsed discharge obtained from applied voltage waveforms using the storage oscilloscope is found to decrease monotonically from 520 s^{-1} to 230 s^{-1} with the gap length of the series gap.

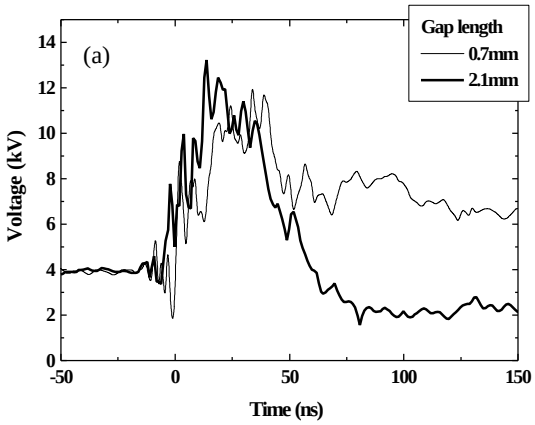


FIGURE 3 (a). Typical waveforms of applied voltage of main gap for various gap length.

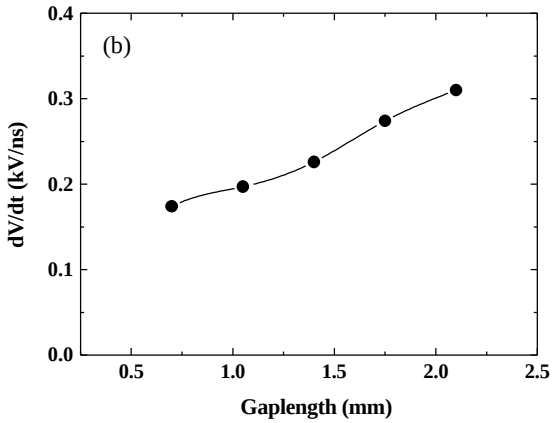


FIGURE 3 (b). Dependency of applied voltage rise time on gap length of the series gap switch.

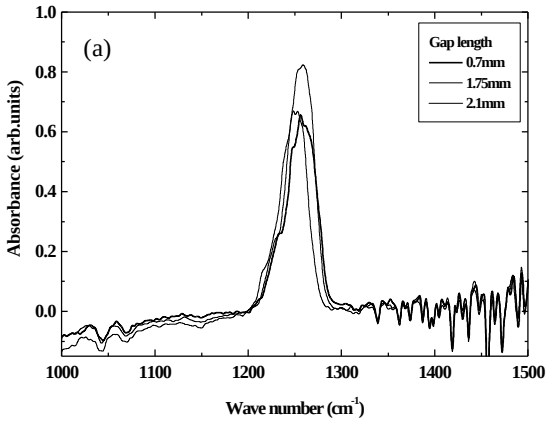


FIGURE 4 (a). CF_4 peak height of FTIR spectra varying the gap length of the series gap switch.

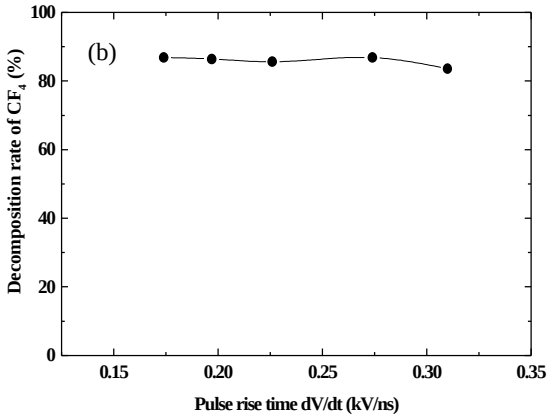


FIGURE 4 (b). Dependency of decomposition rate of CF_4 on the rise time of applied voltage.

Figure 4a shows the FTIR absorption spectra including peaks of CF_4 for different gap length of the series gap switch. The absorbance of CF_4 is found to be constant and independent on the series gap length, unlike the case of toluene decomposition [2]. Figure 4b summarizes the relationship of the decomposition rate of CF_4 with the pulse rise time dV_{A-K}/dt. The decomposition rate was found to be almost constant, 87%. This result implies the lower energy electron that corresponds to the narrow gap length 0.70 mm is sufficient for the effective treatment of fluorocarbon. Therefore, the discharge with smaller dV_{A-K}/dt and high repetition rate is preferable for CF_4 treatment [3].

The discharge characteristic is also changed by a gas composition. We determined decomposition rates of the mixture gases of CF_4 (100 ppm) diluted by oxygen and argon-oxygen mixture. Since the separated carbon atom by the discharge must be oxidized into CO_2 in order to suppress the recombination of CF_4, oxygen gas is most suitable additive gas for decomposition of CF_4. However, in the case of dilution by oxygen, the discharge current was small due to generation of negative ions of oxygen and the discharge became unstable. Also, the applied voltage increased for maintenance of the plasma. When the small amount of argon gas was introduced into the oxygen-diluted CF_4 gas, the discharge current increased and the decomposition rate of CF_4 became approximately 10% higher.

4. CONCLUSION

CF_4 decomposition rates of 92% and 82% were achieved using the streamer corona discharge when 100 ppm CF_4 gas diluted by argon and 100% CF_4 gas were used, respectively. The dependency of dilution gases (oxygen and argon-oxygen) on the decomposition rate appeared concerning the discharge characteristics. The efficiency of CF_4 treatment was enhanced using the discharge with smaller $dV_{A\text{-}K}/dt$ and high repetition rate.

REFERENCES

[1] *Kyoto Protocol to the United Nations Framework Convention on Climate Change*, COP3 (1997)

[2] N. Hayashi, H. Suganuma, M. Kamatani, S. Satoh and C. Yamabe, Jpn. J. Appl. Phys. **40**, pp. 6104.

[3] N. Hayashi, K. Yamamoto, S. Ihara, M. Kamatani, S. Satoh and C. Yamabe, Jpn. J. Appl. Phys. **41**, (in press).

MAIN OXIDATION PROCESSES AND THEIR RELATIVE CONTRIBUTIONS IN THE NO REMOVAL BY A DIELECTRIC BARRIER DISCHARGE FOR AIR CLEANING

S. Dupré*, C. Deniset, A. Goldman, M. Goldman and E. Marode

Laboratoire de Physique des Gaz et des Plasmas, Equipe Décharges Electriques et Environnement, Université Paris-Sud / CNRS, Supélec, 3 rue Joliot-Curie, 91192 Gif-sur-Yvette Cedex, FRANCE

Abstract. The NO to NO_2 removal in a Dielectric Barrier Discharge plasma reactor is experimentally investigated in dry air at ambient temperature. A modelling approach aims to evaluate the relative importance of the main reactions into play, in coherence with the experimental results.

1. INTRODUCTION

Now, it is well known that NO remediation from polluted atmospheres primarily occurs by conversion of NO to NO_2, directly or indirectly, by O atoms[1-5] according to a reactional scheme of O atoms production by the discharge and consumption of these atoms by the gas. In a first step, NO oxidation can proceed via the reactions (1) and (2):

$$NO + O + N_2 \rightarrow NO_2 + N_2 \qquad k_1=3.8\ 10^{-27}\ T^{-1.8}\ cm^6.molec^{-2}.s^{-1} \qquad (1)$$

$$NO + O + O_2 \rightarrow NO_2 + O_2 \qquad k_2=2.8\ 10^{-27}\ T^{-1.8}\ cm^6.molec^{-2}.s^{-1} \qquad (2)$$

while O_3 is produced via the reactions (3) and (4):

$$O_2 + O + N_2 \rightarrow O_3 + N_2 \qquad k_3=5.58.10^{-29}\ T^{-2}\ cm^6.molec^{-2}.s^{-1} \qquad (3)$$

$$O_2 + O + O_2 \rightarrow O_3 + O_2 \qquad k_4=8.6.10^{-31}\ T^{-1.25}\ cm^6.molec^{-2}.s^{-1} \qquad (4)$$

In a second step, O_3 so produced can convert NO to NO_2 via the reaction (5):

$$NO + O_3 \rightarrow NO_2 + O_2 \qquad k_5=3.6\ 10^{-12}\ \exp(-23400/T)\ cm^3.molec^{-1}.s^{-1} \qquad (5)$$

and the O atoms still available can via the reaction (6) destroy the NO_2 produced:

$$NO_2 + O \rightarrow NO + O_2 \qquad k_6= 17.10^{-12}\ \exp(-300/T)\ cm^3.molec^{-1}.s^{-1} \qquad (6)$$

Our aim in this work is, by experimental investigations and by a simplified modelling approach, to identify the influence of the NO initial content on the relative importance of these different reactions. Experimentally, this will be achieved by changing the injected power in order to modify the production of O atoms; in the modelling, O initial density will be arbitrarily fixed to 400 ppmv. The evolution of the exhaust species concentrations will be represented as a function of the injected power for the experiments and as a function of time for the simulation.

2. EXPERIMENTAL APPROACH

2.1 The set-up

The discharge reactor consists of a point-to-plane electrode system. The stainless steel point is connected to an 64 kHz ac high voltage supply and the plane electrode, covered with a 4 mm thickness alumina-silicate ceramics, is connected to ground. The gap length between the active electrode and the ceramics is set to 1 mm for all experiments concerned with the paper. Experiments are carried out in dry air, containing or not NO, with a total flow rate fixed to 0.3 L/min. A high voltage probe (1:1000) is used for the voltage measurements V(t), and the discharge current I(t) is determined from the

* Electronic address: sandrine.dupre@lpgp.u-psud.fr

voltage drop through a 50 Ω resistance placed between the plane electrode and the earth. Signals are stored on a 500 MHz numerical oscilloscope. The power injected in the discharge is calculated by the product of the instantaneous values of the discharge current and applied voltage. The resulting signal is integrated over 10 periods. Then, multiplying the result by the generator frequency gives the power values. The different chemical species are identified and their evolution studied by using a FTIR absorption spectrometer (Vector 22 from Bruker Instruments) which permits, with a resolution of 0.5 cm^{-1}, to quantify the nitrogen oxides (NO, NO_2, N_2O_5, N_2O), the acids (HNO_3, HNO_2) and ozone (O_3). The cell we use has an optical path length of 10 cm and CAF_2 windows (4000-1000 cm^{-1}).

2.2 The experimental results

In dry air, our discharge essentially produces an important quantity of O_3, up to 1100 ppmv, HNO_3 (due to the absorbed water in the ceramics), and smaller amounts of N_2O_5 and N_2O (<50 ppmv). When 500 ppmv of NO is added to air, O_3, HNO_3 and N_2O_5 are no more present while NO decreases and NO_2 increases showing that the NO is mainly converted to NO_2 via plasma oxidation processes. The fact that the introduction of NO induces the disappearance of O_3 should be interpreted, in a first approach, by the assumption that all NO disappeared is converted by O_3 to NO_2 via the reaction (5), but, in this case, considering the reaction molecule to molecule, ozone should be detected and NO totally removed. In reality, just 70 % of the 500 ppmv of NO are removed. An other hypothesis, which can explain that O_3 is no more observed when NO is added, is to consider the relative importance that can take reactions (1) and (2) which consume O radicals for direct NO oxidation with regard to reactions (3) and (4) which consume O radicals for the production of ozone. Then NO would be also partly removed by O radicals and ozone produced in less quantities because of the consumption of O atoms by NO. Now considering the quantity of NO introduced in comparison with the quantity of O_2 leads to consider that the four reactions of consumption of O atoms occur simultaneously but with different weights depending on the NO initial concentration.

Experimental results obtained for NO initial concentrations covering a range from 0 to 490 ppmv are plotted in Figures 1 and 2 which show, as a function of the injected power, the influence of NO initial content on the removal efficiency and on the extra O_3 appearing as a residual product when NO initial content is smaller than 400 ppmv. Two modes can so be distinguished:

- A mode 1, valid for initial NO concentrations smaller than 400 ppmv, which permits to convert the totality of NO to NO_2. In this case, increasing the power increases the removal efficiency, the power needed for a total consumption of NO increasing as the initial NO. After NO has been totally oxidized to NO_2, one can observe the extra O_3 not consumed by NO via the reaction (5), though produced in less quantity than in air without NO because of the reactions (1-2) of direct NO oxidation by O.
- A mode 2, valid for initial NO concentrations larger than 400 ppmv, where the discharge cannot produce enough oxygen atoms to oxidize the totality of NO. In this case, the input energy becomes inefficient beyond 1.5 W and ozone is no more detected.

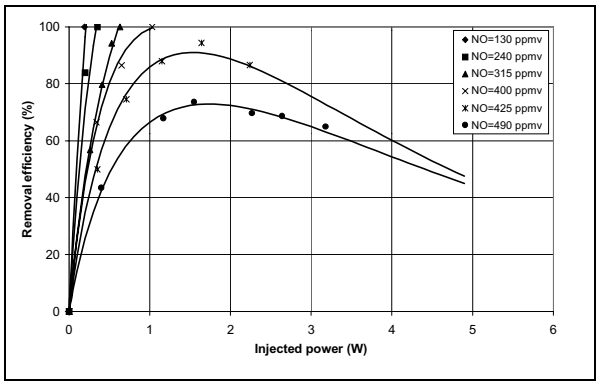


FIGURE 1. Evolution, as a function of the injected power, of the NO removal efficiency in modes 1&2.

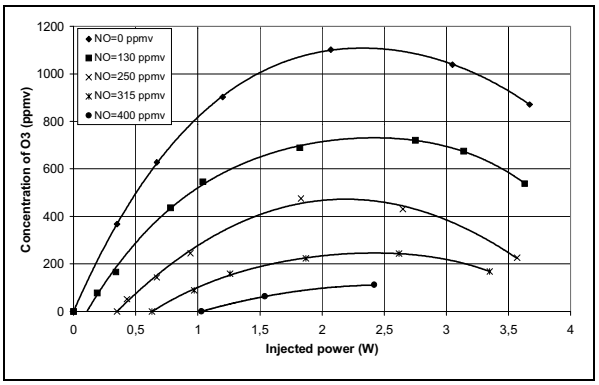


FIGURE 2. Evolution, as a function of the injected power, of the O_3 observed in mode1.

3. A SIMPLIFIED MODELLING APPROACH

3.1 The treated master equations

In order to explain the electrical, thermodynamic and chemical behaviour of the discharge, a simple 1D model of an individual streamer-filament discharge has been established, dealing with a large set of electrical and chemical reactions. Description and results given by this set of reactions have been described elsewhere[6,7]. Here, it is the equation concerning the chemical dynamics which has mainly been used. Thus we just recall here that the evolution of the local densities for a set of q species N^s is given by a system of q master equations similar to:

$$\frac{\partial N^s}{\partial t} = \sum_{n=0}^{r(s)} (-1)^{m(n,s)} k_n N_p N_q N_r$$

N^s corresponds successively to the components of: O, N, NO, NO_2, N_2O, NO_3, N_2O_5, O_3, O_2, N_2, r(s) represents the number of reactions implied in the production or destruction of the "s" species, m(n,s) is equal to 0 or 1 depending on whether the species "s" is produced or destroyed by the reaction n implying the reaction constant k_n, while N_p, N_q and N_r are the reactants of reaction n. The k_n are mainly taken from references[8-10].

3.2 Modelling results

It is obvious that the initial radical species are produced within the volume of the discharge due to electron collisions. As shown[11,12] these reactive species diffuse after some microseconds outside the discharge volume. Thus, as a first approximation we make the assumption that the chemical reactions take principally place outside the discharge channel, in a "post-discharge" state. In other words, we assume that the discharge introduces directly a given number of initial species, homogeneously, into the whole reactor volume. The following chemical reactions are then controlled by the temperature of the reactor volume supposed to be at room temperature and not at the discharge temperature.

When running the program inside the discharge volume we met the following difficulty. Normally, the discharge produces not only a given density of atomic oxygen O, but also a given density of atomic nitrogen N because the electrons dissociate N_2 as well as O_2. The resulting proportion of O and N generally predicts more produced N than O. However, the full hydrodynamic runs of the discharge showed that with the presence of N, a large proportion of NO molecules is reduced by $N+NO \rightarrow N_2+O$. However, all experimental results in the literature as well as our own experimental results suggest that the NO removal is directed towards oxidation into NO_2 and not towards reduction. We suppose thus that there is some process, acting during the diffusion process which pushes the species from inside to outside the discharge, which seems to remove N atoms, and in the following runs, concerning what happens outside the discharge, we decided to analyse what could be the action of the presence of atomic O on NO, N_2 and O_2 concentrations, if O would be added alone in the mixture air-NO by the discharge.

For the program run, the initial amount of O is thus taken equal to 400 ppmv. This value has been chosen because in pure air without addition of NO, and for a given discharge power, the produced O_3 is 400 ppmv. Thus, assuming that the recombination of O into O_2 is negligible, compared to O converted into O_3, the same amount of O must be initially present. The question is now, if NO is added what are the processes which the atomic O will undergo?

Figure 3 represents as a function of time (in a logarithmic scale) the species densities evolution for an initial NO concentration of 250 ppmv (on left) and 500 ppmv (on right). The result to be underlined is that the simulated results go towards agreement with the experiments as far as NO removal is concerned. Indeed, for 250 ppmv of NO which corresponds to mode 1, NO is totally removed and O_3 appears while for 500 ppmv, mode 2, NO is not completely removed and O_3 is no more observed. However, if the tendency between experiment and modelling is quite in the good direction, the figures are however not in a such good state. Indeed, in the simulation if the 400 ppmv of O permit to remove

70% of the 500 ppmv of NO, the same removal in the experimental case would require more than twice O concentration. More insight is needed to understand this discrepancy. Let us look closer at the modelling results, where we call partial density of a given species the part of the density of that species which has been destroyed or produced, from the beginning of the process, by one specific reaction. Figure 4, plots the partial densities of destruction of O and NO due to different reactions as a function of time for an initial NO concentration of 250 ppmv. In that case, the reaction (5) producing O_3 is the main reaction consuming O atoms. Removal of NO by reaction (2) comes in the second position with a factor 4 of reduction in comparison with O_3 formation (this factor is reduced to a factor 2 if 500 ppmv of NO is introduced). When time is flowing, the NO density decreases so that the reactions (1) and (2) become less and less important and the consumption of O with O_3 formation, by reactions (3) and (4), dominate.

As far as the sequence of NO density consumption is concerned, we see that in a first phase NO is removed by O through reaction (1) and in a second phase, when O is no more present because of its conversion towards O_3, NO is removed by O_3 through (5) with even more efficiency (by a factor 3.5).

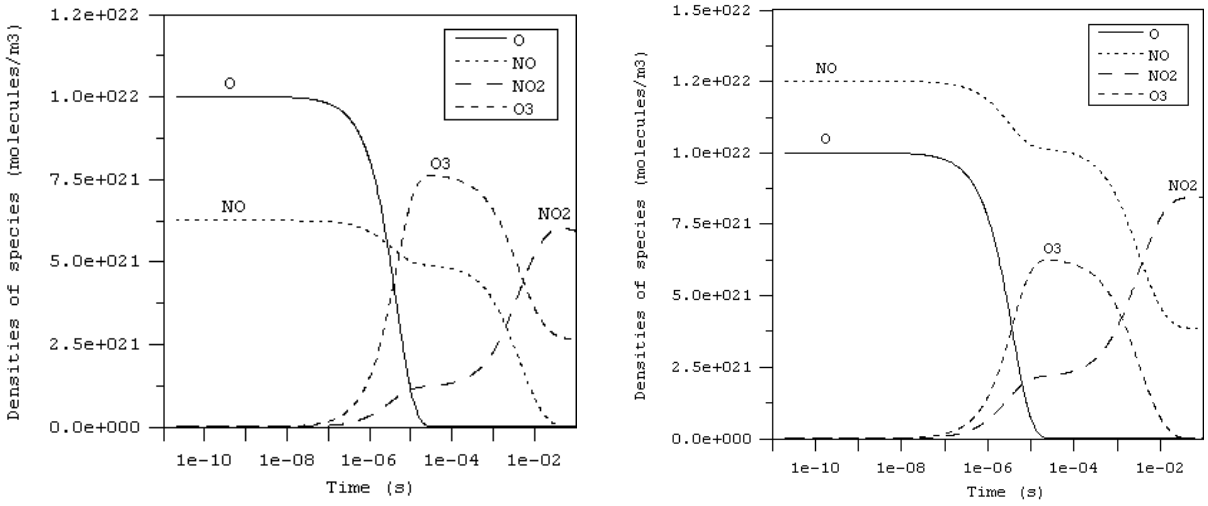


FIGURE 3. Densities of species as a function of time for NO initial concentration of 250 ppmv and 500 ppmv (time of simulation=100 ms, $[O]_{initial}$=400 ppmv, air, T=293K)

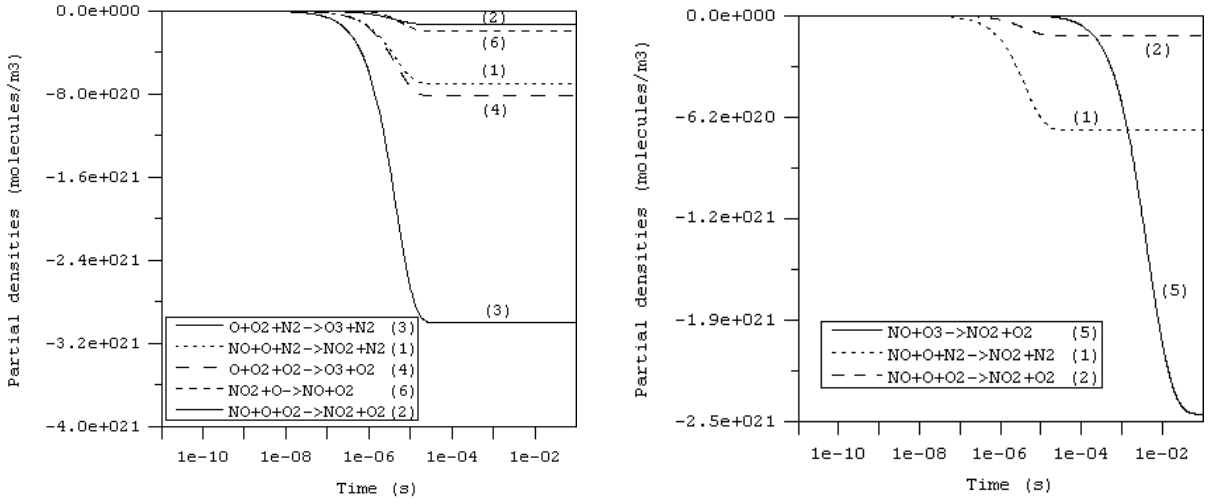


FIGURE 4. Partial densities of destruction of O and NO due to main reactions in function of time for NO initial concentration of 250 ppmv (time of simulation=100 ms, $[O]_i$=400 ppmv, air, T=293K)

4. CONCLUSION

The experiments performed for a range of initial NO values exceeding 400 ppmv have permitted to distinguish two different modes in the reactor behaviour: one for the values below, allowing a total conversion of NO in NO_2, the other allowing only a partial oxidation that diminishes when the initial NO is increased. The simplified model performed seems good enough to bring some validation to the set of reactions retained for the studies and to the hypotheses implied. It shows that in the experiments performed the oxidation by O_3 always prevails over direct oxidation by O atoms and that the limitation in initial NO at 400 ppmv for a complete removal should be pushed over by improving the ozone yield of the reactor.

ACKNOWLEDGMENTS

The authors want to acknowledge PSA PEUGEOT CITROEN, RENAULT SA and the CNRS for financial support.

REFERENCES

[1] Penetrante B.M., Bardsley J.N., Hsiao M.C., *Japanese Journal of Applied Physics*, **36**, pp. 5007-17 (1997).

[2] Krishtopa L.G., Krasnoperov L.N., NOx Destruction in Air and Nitrogen by Dielectric Barrier Corona Discharge. In: *Book of contributed papers SAE Fuel&Labs 98* (1998).

[3] Mok Y.S., Ham S.W., *Journal of Chemical Engineering Science*, **53**, pp. 1667-78 (1998).

[4] Takaki K., Jani M.A., Fujiwara T., Removal of Nitric Oxide in Flue Gases by Multipoint to Plane Dielectric Barrier Discharge. In: *IEEE Trans. On Plasma Science*, **27**, pp. 1137-45 (1999).

[5] Yan K., Kanazawa T., Ohkubo T., Nomoto Y., *Plasma Chemistry and Plasma Processing*, **19**, pp. 421-43 (1999).

[6] Marode E., Samson S., Djermoune D., Deschamps N., Touzeau M., *Journal of AOT*, **4**, (1999).

[7] Bastien F., Marode E., *Journal of Physics D: Applied Physics*, n°18, pp.377-93, (1985).

[8] Mätzing H., Chemical kinetics of flue gas cleaning by irradiation with electrons, *Advances in Chemical Physics*, ed. by Prigogine I. and Rice S. A., **LXXX**, pp. 315-402 (1991).

[9] Atkinson R., Baulch D.L., Cox R.A., Hampson R.F. Jr., Kerr J.A. and Troe J., *Journal of Physical and Chemical Reference Data*, **21**, pp. 1125 (1992).

[10] A.Kossyi, A.Yu.Kostinsky, A.A.Matveyev, V.P.Silakov, *Plasma Sources Sci. Technol.*, **1**, pp. 207 (1992).

[11] Marode E., Djermoune D., Samson S., Deniset C., Modelling of the chemical dynamics in a streamer induced discharge. In: *Proc. 11th symposium on elementary processes and chemical reactions in low temperature plasma*, Invited paper book, Tatras, Slovaquie, pp. 93 (1998).

[12] Odic E., Parissi L., Goldman A., Goldman M., Koch S., Chemical by-products in air with admixtures in correlation with the gas temperature enhanced by non equilibrium discharges. In: *2nd Intern. Symposium on Non Thermal Technology for gaseous pollution control*, pp. 107-12 (1997).

PFC DECOMPOSITION WITH ATMOSPHERIC PRESSURE MICROWAVE PLASMA USING RESONANT AND NON-RESONANT STRUCTURE

Jungmi Hong [a], Sangyoung Kim[a], Kihoon Lee[b], Keunho Lee[b],

Jin Joo Choi[c] and Yoon-Kee Kim [a]

a) Institute for Advanced Engineering, Yongin P.O.Box 25, Kyonggi-Do, 449-860, Korea
b) Plasma Systems and Materials, Yongin P.O.Box 25, Kyonggi-Do, 449-860, Korea
c) Kwangwoon University, 447-1, Wolgye-Dong, Nowon-Ku, Seoul, 139-701, Korea

Abstract : PFC(Perfluoro Carbon Compound) decomposition using resonant structure microwave plasma at atmospheric pressure has been investigated in comparison with conventional non-resonant plasma system. In the atmospheric pressure plasma abatement, the high flow rate of N_2 purging gas(>30slm) remains to be a difficult problem in obtaining the stable discharge and sufficient DRE(Destruction Removal Efficiency). In order to increase the residence time of gas molecules in discharge, we designed the resonant structure chamber with strongly coupled TE_{31}/TM_{010} mode, which generates the large area(dia.> 60mm) plasma. For the CF_4/Ar etch recipes with oxygen and water vapor, the DRE has been estimated as about 95-99% from the result measured by Fourier Transform Infrared Spectrometer(FTIR) and Quadrupole Mass Spectrometer(QMS) in detuned resonant and non-resonant system. With the coupled cavity, it is achieved to sustain the stable atmospheric pressure plasma and demonstrated the higher energy efficiency and availability than those by the conventional plasma scrubbing process under high flow rate condition.

1. INTRODUCTION

PFC emission reduction has been a big issue especially for semiconductor industries since the agreement of the 1997 Kyoto Protocol. Many research groups made significant progress in the development of PFC scrubber system using such technologies as thermal oxidations, catalytic abatements and plasma abatements. Unfortunately, “there is no one best solution that fits every fab.” [1-3] Plasma abatement is known to have much of benefits such as high efficiency, versatility and low operation cost. In spite of its high reliability through the long-term evaluation of low pressure plasma abatement systems, the industry is reluctant to adapt the scrubber for their fab because of the possibility of back streaming due to the pressure difference. Atmospheric pressure microwave plasma is widely known as one of the high efficient plasma sources with high density of radicals and high neutral gas temperature up to 3000K[4-5]. Moreover, its availability at atmospheric pressure attracts to because of no negative impact on main processes .

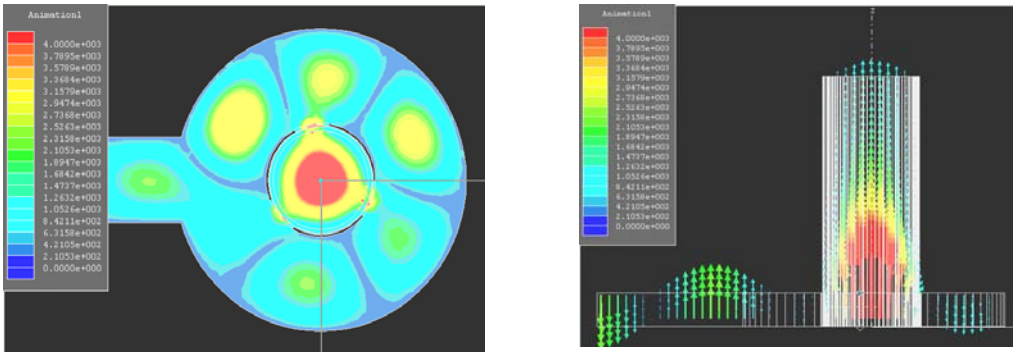
The most important problem for atmospheric pressure plasma scrubber is much of nitrogen purging gas flow over 30slm for dry pump protection, because the large amount of purging gas reduce the DRE(Destruction Removal Efficiency) and make the plasma unstable. Conventional non-resonant systems using waveguide have simple structure and are easy to manufacture but are limited in scale-up and energy coupling. Discharge diameter of typical non-resonant systems is in the range of 20-30mm which cannot meet the CF_4/Ar etch line requirement over the 30 slm of purging gas flow. On the contrary, it is possible to generate and sustain large diameter discharge, more than 80mm, at atmospheric pressure using resonant microwave systems. The electromagnetic structure of coupled cavity for resonant microwave systems was carefully designed using commercial FEM(Finite Element) Maxwell solver, HFSS(High Frequency Structure Simulator). TE_{31}/TM_{010} coupled mode was chosen for gas decomposition application to increase the residence time and reduce the linear velocity of gas molecules. The electromagnetic characteristics of the constructed two different systems were

evaluated by the cavity cold test using network analyzer to enhance the energy coupling efficiency.

The DRE has been estimated with CF_4/Ar etch recipe using Oxygen and water vapor from the results measured by Fourier Transform Infrared Spectrometry(FTIR) and Quadrupole Mass Spectrometer(QMS).

2. THE RESONANT AND NON-RESONANT PLASMA SYSTEM

The resonant cavity consists of two coupled modes (TE_{31}/TM_{010}). One is the coaxial cylindrical cavity for increasing the mode purity and improving the power coupling efficiency. The main discharge area, called central cavity has the modified TM_{010} mode. Resonance frequency of the cavity was aimed at our magnetron lasing frequency of 2.460-2.464GHz. Diameter of the discharge chamber is about 90mm and the volume is upto 1500cm^3. The residence time of PFC molecule is expected to increase 10-20 times of non-resonant system. The electric field distributions within the coupled cavity are shown in the Figure 1(a), (b)

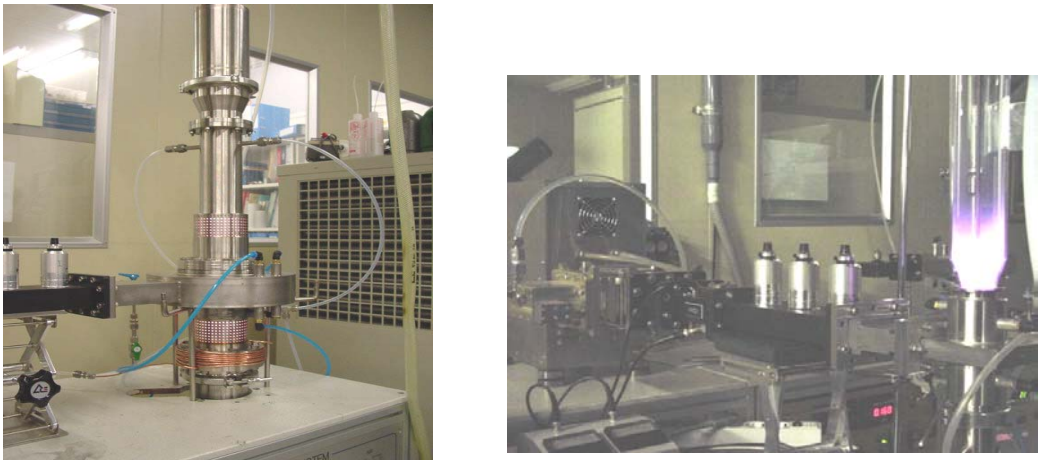


(a) (b)

FIGURE 1. : Electric field distribution within the resonant structure : (a) electric field magnitude plot at xy plane, (b) electric field vector plot at yz plane

For the non-resonant structure, the short position is detuned properly with careful EM field analysis also. The proper short position is changed from the analytically determined result due to the dielectric discharge tube and hole. In addition to careful EM analysis, the tangential guiding flow structure is adapted for both resonant and non-resonant structure systems. Furthermore, with the cold-test, we detuned finally the system with 3-stub tuner for the impedence matching and efficient power coupling.

Finally stable and uniform plasma discharge is achieved in both resonant and non-resonant systems without plasma localization or microwave leak even in high flow condition as shown in Figure 2.



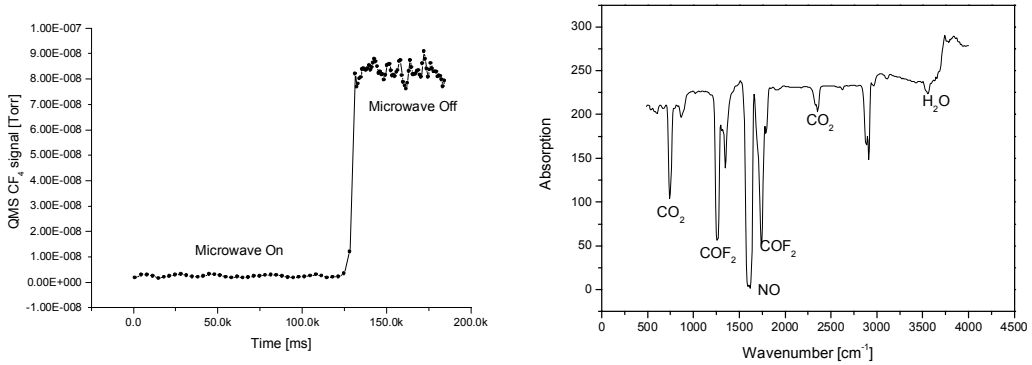
(a) (b)

FIGURE 2. microwave plasma scrubbing system : (a) resonant structure, (b)non-resonant structure

Microwave power transferred from magnetron to the plasma applicator through the isolator and tuner Plasma can interact with charged particle within the discharge and the electromagnetic field distribution will be affected. Adjustment needs continuously through the whole process according to system parameters such as pressure, power and gas flow in order to provide efficient utilization of the incident microwave energy over a wide range of discharge conditions.

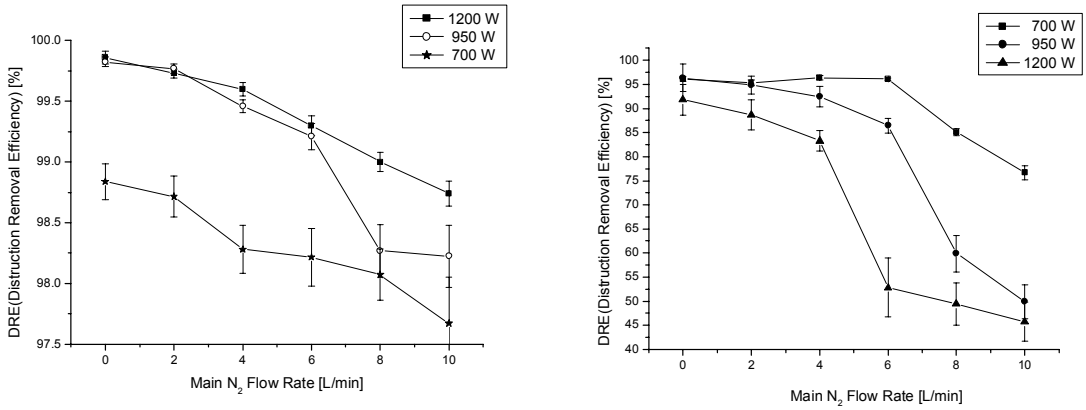
3. PFC DECOMPOSITION PROCESS

Decomposition experiments were conducted for the resonant and non-resonant plasma systems and DRE were evaluated with QMS and FTIR. Typical raw data for the abatement process are shown in Figure 3(a),(b) with the etch recipe of 10sccm CF_4 , 100sccm Ar, additive 2lpm O_2 and 10lpm support N_2 flow. Figure 3(a) shows the efficient removal of CF_4 after plasma treatment and Figure 3(b) reveals only a trace of CO_2, COF_2, H_2O and NO emitted.



(a) (b)

FIGURE 3. (a) QMS signal before and after the plasma abatement (b) FTIR emission spectra after PFC decomposition process



(a) (b)

FIGURE 4. : Effect of nitrogen flow and abatement power on CF_4 DRE (a) in non-resonant system (b) in resonant system

The resonant and non-resonant system exhibited very high DRE up to 99% with 0.7-1.2kW of microwave power as shown in Figure 4. The supporting flow was tuned to main gas flow condition for sustaining the stable discharge approximately 10 lpm. In this abatement process, gas mixture of 50sccm CF_4 , 4lpm O_2 and variable N_2 flow were introduced to the plasma applicator.

According to increasing abatement power, the DRE increases due to the increased electron energy and

lowered reaction activation energy as reported in Ref[6]. Rather low DRE in resonant cavity with increasing microwave power can be explained by contract of the plasma discharge area.

It is evaluated the effect of nitrogen flow on decomposition efficiency also as expected in many references. . According to increasing nitrogen gas flow the DRE noticeably reduced below 50% under N_2 flow of 10 lpm in resonant structure, while higher DRE has been obtained in non-resonant structure.

But for the non-resonant structure, over the 10lpm of main flow can make discharge unstable. To increase the capacity for the input gas flow is limited below 20lpm. Gas flow and input power are strongly coupled for maintaining stable plasma discharge for each discharge area and volume.

In spite of the uniform discharge over 250mm length, increased power may not transfer to discharge efficiently. In addition, higher input power is required for the increased discharge volume of resonant cavity over 10 times of non-resonant system although the resonant cavity has higher energy coupling efficiency. With the optimization of abatement process, the energetic collision between the excited species can increase the radical formation and ionization, thus drastically improved DRE can be achieved.

4. SUMMARY

We have designed and constructed two different microwave plasma system for atmospheric PFC decomposition process. CF_4 abatement has been conducted for resonant and non-resonant systems and showed high DRE. But it is revealed limitations for adapting real exhaust line due to its small discharge area and low energy coupling efficiency. We have suggested the resonant structure system as alternative for this problem. With careful electromagnetic analysis, TE_{31}/TM_{010} coupled mode cavity has been constructed and detuned. It is expected to demonstrate the higher energy efficiency and availability than those by the conventional plasma scrubbing process with the improved power coupling and the optimization of the decomposition process.

ACKNOWLEDGMENTS

This research was supported by the Ministry of Environment and Korea Institute of Environmental Science & Technology.

5. REFERENCES

[1] Water Worth , *SSA's 23rd Annual Symposium* April 12-14, (2001)

[2] V.Mohindra *MIT Dept. Chem.Eng. Ph.D. thesis*, (1996)

[3] J.E.Stevens, Y.C.Huang, R.L.Jareki, and J.L.Cecchi, *Vac.Sci.Tech.A*,**10** 1270(1992)

[4] Mizeraczyk, J., Zakrzewski, Z., Jasinski, M. Lubanski, M. *IAS Annual Meeting* v2 p881-885 (2000) IEEE Industry Applications Society

[5] E.A.H.Timmermans, J.Jonkers, I.A.J. Thomas, A.Rodero, M.C.Quintero, A.Sola, A.Gamero, J.A.M.van der Mullen *Spectrochimica Acta* Part B 1553-1566 (1998)

[6] V.Vartanian et al. *International SEMATECH, Technology transfer* #99123865B-ENG May 3, 2000

VOLATILE ORGANIC COMPOUNDS DEPOLLUTION BY DIELECTRIC BARRIER DISCHARGE IN POROUS MEDIA

N. Jidenko, M. Petit and J.P. Borra

Laboratoire de Physique des Gaz et des Plasmas
(CNRS –Univ. Paris XI) Equipe DEE, SUPELEC, France.

Abstract. In dielectric porous media (alumino-silicate: corderite ceramics), non thermal plasma at atmospheric pressure occurring in filamentary discharges is established in all the pores between the plan electrodes. A silicon paste prevents from arcs and other parasite discharges outside the pores. Current measurements have been performed to understand how discharges are controlled by surface polarisation-depolarisation and to study the micro discharges properties (charge, duration, amplitude) and their spatial and temporal repartitions. This work focuses on current measurement to highlight three different operating modes, and the influence of pores' geometry. An evaluation of the discharge efficiency for depollution of volatile organic compounds on propan-2-ol, confirm the kinetic paths previously identified. The destruction efficiencies are promising.

1. INTRODUCTION

Volatile Organic Compounds (VOC) emissions are regulated by standards, but no cheap efficient technology exists to reduce them for small and average plants. Non-thermal plasma at atmospheric pressure may be a solution. Since the last 10 years, many studies on non thermal plasma VOC's destruction at atmospheric pressure were conducted in different geometry (point to plane, plane plane, wire plane, wire cylinder) with or without dielectric barrier [1]. The dielectric barrier discharges DBD (imposing an AC voltage) are suitable for cleaning up gas stream emission [2-3] because of active chemical species. In plan to plan configuration, the discharges occur in a large number of individual parallel filaments (radius 100µm, duration 10 ns) which are identical in both polarities. In those filamentary discharges, collisions between energetic electrons (1-10 eV) and neutral species generate primary active chemical species {$N_2^*(A^3O_u^+)$, $N_2^*(B^3\Pi_g)$ O(1D), O(3P), OH…} able to oxidise pollutants or to create secondary species more stable (O_3, NO_2,…). Low costs and high operating ranges (diminution of extinction voltage and augmentation of maximum voltage by prevention from arcs, thanks to the dielectrics barriers) compared with other kind of discharges are two major advantages. To improve this process, many studies focus on oxidative effects of non thermal plasma and catalysis coupling. At the dielectric surface, the micro discharge spread into surface discharges covering a much larger area than the original channel section. Porous dielectric media increases the plasma-surface interaction because the filamentary discharges is known to "leak" dielectric walls of pores. Moreover, thermal losses heat dielectrics even better in porous medium than in classical plan to plan DBD, so that catalysis efficiency could be optimised by controlling dielectric's temperature. Two main parts will be discussed in this paper: (i) electrical characterisation related to electrical mode and geometry effects on electrical parameters (ii) chemical activity of the filamentary discharges in air and for conversion and destruction efficiencies for propan-2-ol.

2. EXPERIMENTAL SET-UP

The discharge cell is constituted by porous dielectric media between two plane electrodes. Their area is about 3 cm^2. The discharge gap in the pores measures 1mm and have three different sections: square, cylindrical and without pores (Silent discharge).

A 1 to 60 kHz signal is derived from a function generator, fed through a 2 kW audio amplifier, and

then stepped up with a high voltage transformer. This sinusoidal AC high voltage is applied across the cell electrodes and measured by high voltage probe. The current crossing the cell is measured through a 50 Ω adaptive line to prevent from deformation and reflection. Dry air (with or without VOC) flows are controlled with mass flow controllers between 0.75 and 2 L/min. Using an oscilloscope (LeCroy LC374A, 500 Mhz, 2 Gs/s) and Matlab®, both current and tension are treated as described in previous paper [4]. Gaseous species are identified and quantified by IR absorption spectroscopy (Bruker IR Vector 22).

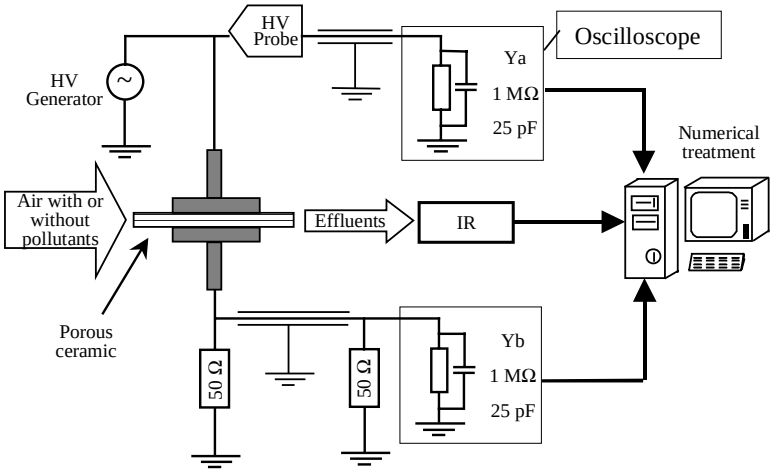


FIGURE 1. Experimental setup.

3. AVERAGE CURRENT

3.1. Difference between DC voltage and AC voltage

The current measurement presents three components: (i) a capacitive one (ii) pulses (similar in both polarities) associated to filamentary micro discharges (iii) and a pseudo-continuous current during the pulses existence phase (figure 2a). The two interesting components are separated (fig. 2b)

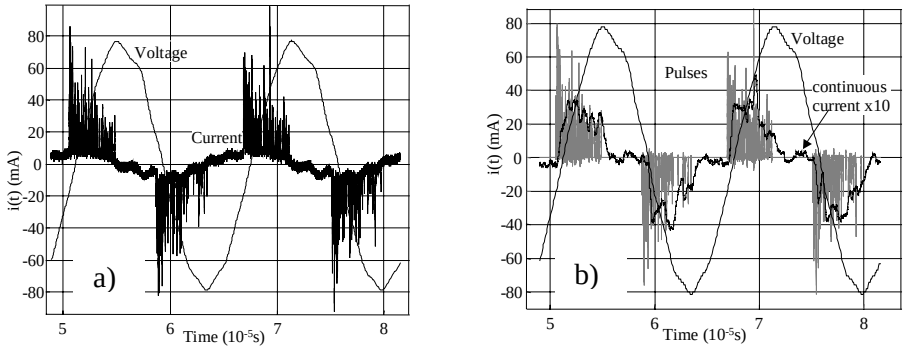


FIGURE 2. a)Voltage and instantaneous current b) Pulses and continuous currents.

The current-voltage characteristic makes the different discharge regimes identification possible. For instance, with DC high voltage discharges, the average current is used. But with AC voltage, average current is null, usually the active current I_{act} defined as P/V_{rms} (where P is the average power and V_{rms} is the effective voltage) is used [5].

3.2. Interests and drawbacks of two "average currents"

The active current I_{act} can be used to evaluate the current provided by the generator to the discharge. But it is not representative of the physico-chemical discharge activity: for high voltage, the charges laid on the dielectric during the last half period allow some pulses to occur before the voltage inversion (figure 2a). In this phase, the discharge cell becomes a generator from an electrical circuit point of view thanks to energy stored on surfaces. So instant power is negative although some discharges are efficient to produce active chemical species. Therefore, I_{act} cannot be a relevant parameter to evaluate the physico-chemical discharge activity.

A more representative regulation parameter of the physico-chemical discharge activity relies on another current I_{tot} {$I_{tot}=(|Q_{p+}|+|Q_{p-}|+|Q_{c+}|+|Q_{c-}|)/T$ (where T is the voltage signal period, Q_p and Q_c the pulses and the continuous charges during T}. I_{tot} equals I_{act} while no positive pulse or continuous charges appears for a negative applied voltage and reversibly. They diverge for higher voltages (cf. fig 3) and the difference is twice the charge amount created by discharges occurring before zero's voltage.

4. CURRENT VOLTAGE CHARACTERISTICS

4.1. Comparisons between the 2 currents highlighting different operating modes

These two current-voltage characteristics allow distinction between successive discharge operating modes related to filamentary discharges spatio-temporal repartition. To compare the current by unit surface area, the current densities J=I/S (where S is the electrode area) are plotted on figure 3.

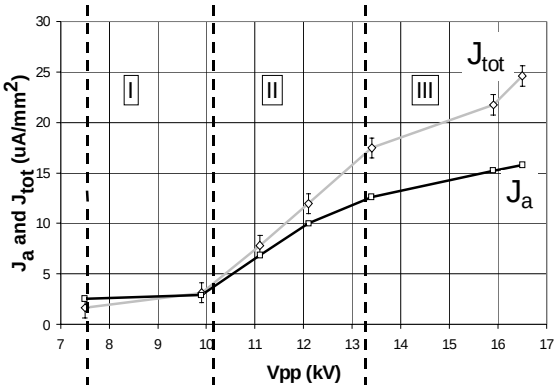


FIGURE 3. J_{tot}, J_a versus peak to peak voltage.

Three operating modes can be differentiated even if pulses have rather the same properties (same charge's quantity, duration and amplitude). From 7.5 to 10 kV (zone I), J_a and J_{tot} increase weakly, few similar filaments are created in some pores. From 10 to 13 kV (zones II), discharges occur in all the pores. The number of similar filaments and thus J_{tot} rise with voltage linearly with the number of filaments. After 13 kV (zone III), both currents rise whereas the number of filaments keeps nearly constant showing that surface polarization limits the development of supplementary filaments and that continuous current increase. In the zones II and III, pulses are homogeneously distributed.

Concerning the influence of porous media properties on current-voltage characteristics, the following conclusions can be established: the current rise with the increase of pores' volume, of surface roughness and with the diminution of dielectric constant and dielectric thickness. The most critical parameter for the current is the pores' volume.

5. CHEMICAL ACTIVITY OF DISCHARGES

The test cell has an active volume of 0.3 cm^3 allowing gas flows from 0.75 to 2L/min. The applied voltage is between 10 and 20 kV (zone II and III on figure 3: where the micro discharges are homogeneously distributed on the surface) for a 60 kHz frequency. The output concentrations depend on input power, gas flow rate (dilution and residence time), but also on surface temperature of the dielectric, gas temperature and the time between reactor output and analysis. But for one reactor with one line of measurement, the energy density J=P/q {defined as the input power P (Watt) on the gas flow q (L/s)} can be used as a chemistry indicator [6]. Before considering propan-2-ol treatment, chemical species produced by these filamentary discharges in air are presented.

5.1. Chemical species in air

There are two main chemical modes, differentiated thanks to ozone and NOx. For energy densities lower than 300 J/L (beginning of the zone II on figure 3), the major species are ozone and N_2O_5. For energy density higher than 900 J/L (middle of the zone III on figure 3), there isn't anymore ozone.

	J < 300 J/L	J > 900 J/L
O_3	1000-2000 ppmv	< 50 ppmv
N_2O_5	50-200 ppmv	< 20 ppmv
HNO_3	< 50 ppmv	< 20 ppmv
NO_2	< 20 ppmv	150-250 ppmv
N_2O	20-50 ppmv	30-60 ppmv

The transition between the two chemical modes is continuous but ozone disappearance always coincides with a reduction in HNO_3 and N_2O_5 concentrations and with an increase of NO_2. This transition with energy density can be modified by two mechanisms : (i) the time between reactor output and analysis change the final concentration of O_3, because O_3 slowly reacts with NO_2 and (ii) the temperature modifies the kinetic of ozone creation and destruction.

5.2. Conversion and destruction efficiency for propan-2-ol

Dry air with propan-2-ol (Initial concentration C_0=370 ppmv) is treated with different voltages (from 10 to 18 kV) and gas flow (from 0.75 to 2 L/min). Above all, it is wise to stress that filament volume lighten by second represents less than a few percents of the gas flow-rate. Only the diffusion of primary species from the production zone (filament) to the surrounding gas can explain the high efficiencies measured, implying that the chemical reactions mainly take place outside the plasma [5].

Two parameters are plotted on figure 4: propan-2-ol conversion efficiency {defined as $100*(C_0-C_f)/C_0$ where C_f is the final propan-2-ol concentration} and VOC destruction efficiency {which is $100*(C_0-\Sigma C_f)/C_0$ where ΣC_f is the final VOC concentrations}. Even if the conversion efficiency is rather good (more than 90 % for 400 J/L) the VOC destruction efficiency is not so good (~ 50% at 400 J/L).

The propan-2-ol concentration is linked to the energy density J as follow: $dC/dJ=-k.C$ (where C is the propan-2-ol concentration) explaining the evolution of the propan-2-ol conversion efficiency with the energy density (figure 5). This is not true for VOC destruction as it will be discussed in thc following paragraph.

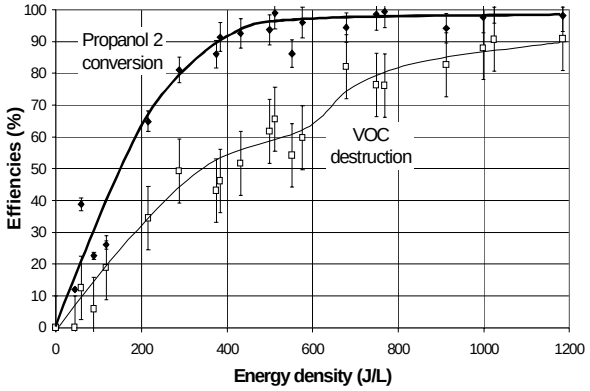


FIGURE 5. Propan-2-ol conversion and VOC destruction efficiency (%) with energy density (J/L) (initial concentration 370 ppmv).

5.3. Kinetic paths confirmation for propan-2-ol destruction

IR absorption enable us to confirm kinetic paths already identify [6]. Propan-2-ol is first convert into propanone. Then, propanone is mainly convert into CO, CO_2 and H_2O by different chemical reactions. This is a combustion like mechanism: Propan-2-ol → Propanone → … → CO, CO_2, H_2O

Comparing with the discharges in air (paragraph 5.1), the energy density related to transition between the two chemical modes highly depends on propan-2-ol concentration. Even for energy density lower than 300 J/L the ozone concentration is weaker (< 500 ppmv compared with 1500 ppmv in air) proving that either the created ozone reacts with pollutants or that the primary species leading to ozone are consumed for pollutants destruction. So that the propan-2-ol oxidation can be achieved by three mechanisms: (i) by direct electronic inelastic collisions in the filamentary discharges (for a few part: only few percent of the gas pass through the plasma) and (ii) by active species creating ozone in air or (iii) by ozone. Thus the main reaction of conversion of propa-2-ol mainly takes place outside the plasma leading to propanone and the energy density is relevant for the propan-2-ol conversion.

Propan-2-ol initial concentration doesn't have any effect on the conversion efficiency proving that the first reaction of isopropanol conversion into acetone is faster than the subsequent acetone conversion and that this reaction is slowed down by product accumulation in gas phase, leading to an equilibrium between propan-2-ol and propanone. Whatever the initial concentration of propan-2-ol is, the propan-

2-ol conversion efficiency is related to the energy density.
Nevertheless, propan-2-ol initial concentration modifies the VOC destruction efficiencies and the energy density is not anymore relevant for the efficiency of VOC destruction (different efficiencies can be measured for the same energy density and the same propan-2-ol initial concentration only by modifying input power and gas flow rate, cf. figure 5). Two hypothesis can explain this difference between propan-2-ol conversion and VOC destruction efficiencies : (i) For propan-2-ol conversion only one deshydrogenation reaction is involved and controlled by product accumulation in gas phase, whereas (ii) for VOC destruction i.e. the subsequent acetone conversion, many competitive reactions highly depending on gas temperature (thus on flow-rate as well) are simultaneously active either in gas phase only or including both gas phase and heterogeneous reactions.

European standard on VOC emission allow rejection up to 20 mg/m^3 corresponding to 96.6 % of VOC destruction for 370 ppmv of propan-2-ol. Only 91% of VOC destruction were measured with this 0.3 cm^3 reactor but better efficiencies can be reached and higher gas flows can be treated with a bigger reactor or by several small reactors association.

For complete depollution, production of suspended particles have to be investigated. In air, for stationary conditions there is no particles detected at the output of the reactor. Nevertheless, each increase of the energy density leads to an increase of particles detected at the output up to 10^3 particles by cm^3, the number of particles slowly decreases with time. Either there are no particles created by plasma surface interaction with these less energetic filamentary discharges than in centimetric gaps with DC point to plane configurations [7] or they are produced as well but collected in the reactor. With propan-2ol (respectively with toluene), the number of particles detected is much more significant up to 10^6 (respectively 10^8) particles by cm^3, confirming the gas to particle conversion and the combustion like mechanism active in the depollution plasma processes [6].

6. CONCLUSIONS

Currents measurements allow the electrical modes distinction in relation with the filaments spatial and temporal repartition. The pores' volume is a critical parameter to control currents. For propan-2-ol, standards are nearly reached in a 0.3 cm^3 reactor with promising energy cost and the kinetic paths previously identified are confirmed.

ACKNOWLEDGMENTS

We thank EDF and ADEME for the financial support and MM. Péchard and Cottet for technical works

REFERENCES

[1] Hammer T., "Application of plasma technology in environment" *Contrib. Plasma Phys*., **39** 441-462 (1999)
[2] McAdams R., "Prospects for non thermal plasma for depollution ", *J. Phys. D.*, **34**, 2810-2821, (2001)
[3] Kogelschatz U., Eliasson B. and Egli W.; "From ozone generators to flat television screens: history and future potential of dielectric-barrier discharges"; *Pure Appl. Chem*., Vol 71 , No 10; pp 1819-1828 (1999)
[4] Petit M. et al. "Electrical characterization of gas discharges using a numerical treatment. Application to dielectric barrier Discharges" review of scientific instruments; to be published.
[5] Marode E. et al., "Influence of temperature, hydrodynamic and diffusion process on chemical activity in filamentary discharge"; INSTP *2nd inter. Symp on non thermal plasma technology for gaseous pollution control*, Salvador, Bahia Brasil, 130-135 (1997)
[6] Parissi L. et al. Electrical Discharges for Environmental Purposes: Fundamentals and Applications, New york, chapter 11, pp. 279-312 (2000)
[7] Borra J.P. et al. "Electrical Discharge regimes and aerosol production in point-to-plane DC high-pressure cold plasmas:" *J Aerosol Sci* Vol **29** No5/6 pp 661-674 (1998)

CHLORINATED ORGANIC COMPOUND REMOVAL BY GAS PHASE PULSED STREAMER CORONA ELECTRICAL DISCHARGE WITH RETICULATED VITREOUS CARBON ELECTRODES

M. J. Kirkpatrick[a], W. C. Finney[a], B. R. Locke[a]

a) FAMU-FSU College of Engineering, 2525 Pottsdamer St., Tallahassee FL 32310 USA.

Abstract: Trichloroethylene (TCE) and vinyl chloride removal by pulsed corona discharge was investigated with attention to energy efficiency and byproduct identification. Approximately, 50 to 95 percent removal of TCE and vinyl chloride was observed depending on the energy density applied to the gas. Water vapor had no significant effect on TCE removal. Evidence was found for post-corona reactions leading to removal of vinyl chloride downstream of the plasma discharge. Energy efficiencies of 100-900 g/kW-hr in the case of 1000 ppm feed of TCE and efficiencies of 2-24 g/kW-hr for a 100 ppm feed of vinyl chloride were found. In TCE experiments, the formation of dichloroacetyl chloride was observed, while chloro-ethane formation was found for vinyl chloride. In both cases, Cl- was measured downstream of the pulsed corona reactor in a water trap using an ion-selective electrode, although measured amounts varied widely due to condensation in the gas lines between the reactor and the water trap. The addition of a platinum-rhodium coated electrode was found only to reduce the downstream removal of vinyl chloride at low energy density.

1. INTRODUCTION

The use of trichloroethylene (TCE) for engine degreasing over the past several decades has lead to the problem of dense non-aqueaous phase liquid (DNAPL) contamination of groundwater. Today, regulation of the use of such compounds has decreased the amount of new contamination sites, but there remain a considerable number of existing sites requiring treatment.

TCE and vinyl chloride removal by pulsed corona discharge was investigated with attention to energy efficiency and byproduct identification. This work focuses on simulated off-gas streams from TCE contaminated groundwater sites. Aerobic/anaerobic bacteria are known to break down dissolved TCE into several compounds including vinyl chloride, a known carcinogen. Previous work has shown that dilute VOCs such as ethylene and toluene are removed by pulsed corona [1,2] and previous work from the literature indicates that TCE can be removed from gas streams using non-thermal plasma reactors [3-5].

2. SPECIFICATIONS

Gas mixtures were prepared based on the assumption that a field-scale application for the removal of these compounds from groundwater contamination sites would produce gas streams which were saturated with water and containing TCE and vinyl chloride in amounts on the order of 100 ppm [6]. Some TCE experiments were performed with 1000 ppm TCE.

The gas flow system can be seen in Figure 1. Gases are mixed in a mixing stage, and thereafter flowed through the pulsed corona reactor. The gas downstream of the corona reactor was analyzed for TCE and vinyl chloride by a Perkin Elmer Autosystem gas chromatograph with FID detector. TCE and vinyl chloride experiments were performed separately. One pertinent question in the operation of such

[a] Electronic address: locke@eng.fsu.edu

a system is the fate of chlorine. Known chemical pathways result in the chlorine ending up as HCl gas. Therefore a water sparger was used to trap HCl from the gas, and a Cl^- electrode was used to determine how much of the initial chorine in the gas ended up as HCl.

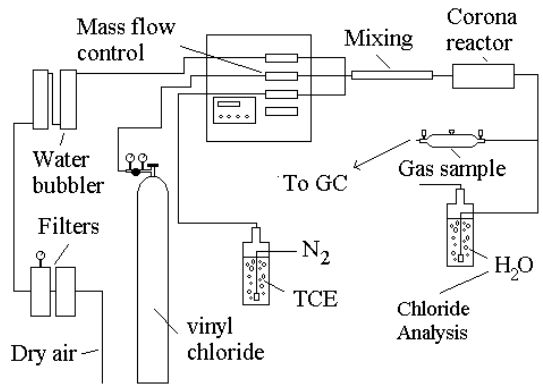


FIGURE 1. Experimental Setup

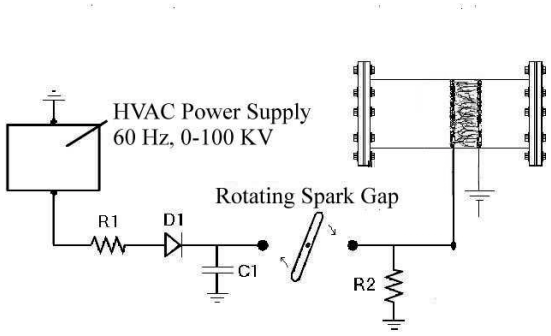


FIGURE 2. Circuit and reactor

The gas streams were treated in a pulsed corona reactor with reticulated vitreous carbon (RVC) electrodes [7]. This reactor design is unique to our lab in the field of pulsed corona reactor design. This design allows the addition of catalytic materials directly on the electrode surfaces and thereby adjacent to the plasma discharge. Hydrocarbons are known to be catalytically oxidized by platinum [8]. Therefore, TCE and vinyl chloride removal were investigated with and without platinum coated electrodes given the possibility that platinum may increase the removal of these compounds. There is also data in the literature to suggest that the combination of plasma and a catalyst may have synergistic effects [9-11], which is another rationale for the use of an electrode coated with platinum.

The system shown in Figure 1 is a continuous flow type, and measurements of TCE/vinyl chloride were made downstream of the reactor after passing through about 5 meters of 3/8" I.D. tubing. In addition to these online measurements, the question arose as to whether or not additional reactions might occur downstream of the gas sampling point, leading to an underestimation of the removal of the contaminants. Therefore, a gas sampling bottle was used to collect the gas downstream of the corona reactor, so that any continued removal by post-corona reactions could be analyzed.

The corona reactor used was made of glass, and was 46 cm long, and with a 10 cm I.D. The RVC electrodes were placed 2 cm apart, giving an active plasma volume of 160 cm^3. Gases flow through these electrodes with very low pressure drop. The system is similar to that used in our previous research [1,2]. The pulse forming circuit is shown with RVC reactor in Figure 2.

3. RESULTS AND DISCUSSION

3.1. Vinyl Chloride Removal

Data for vinyl chloride removal experiments are shown in Figure 3. Each data set represents one experiment – there were some repeats of experiments, but not enough for a full reproducibility analysis. The data for times prior to t=0 represent the steady state amount of vinyl chloride in the feed before the corona was turned on. The corona was turned on at t=0 and off at t=45 minutes. Another gas sample was taken at a specific time after the corona was turned off to make sure that the gas composition returned to the initial steady-state values observed prior to the corona operation. As may be expected, the percent of vinyl chloride removed from the gas stream decreases with increasing gas flow rate. This plot shows data for experiments with and without the platinum-rhodium coated electrodes. Each experiment, i.e. each data point, had approximately the same corona power, and so the energy deposited for a given volume of gas decreases with increasing flow rate.

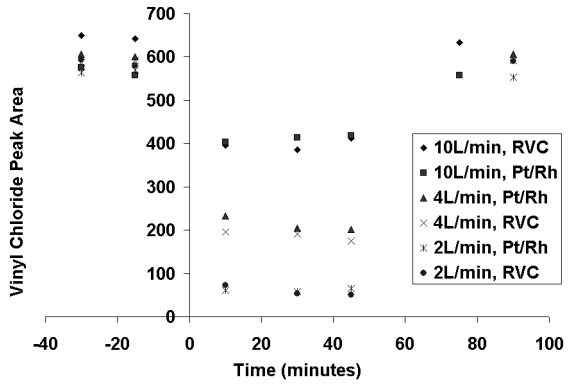


FIGURE 3. Vinyl chloride removal.

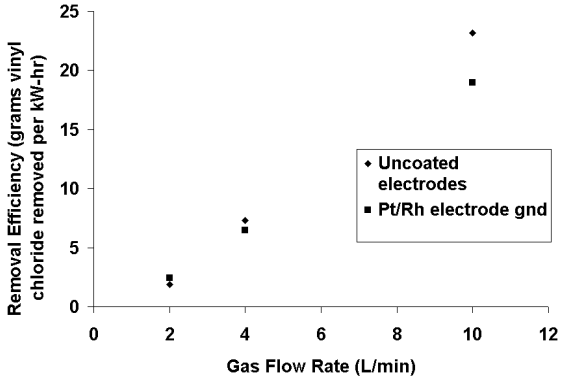


FIGURE 4. Vinyl chloride removal efficiency

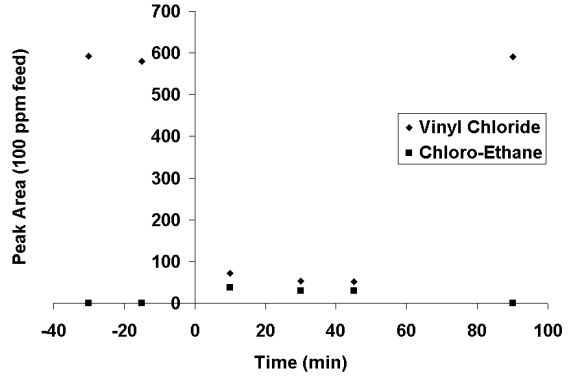


FIGURE 5. Byproduct formation

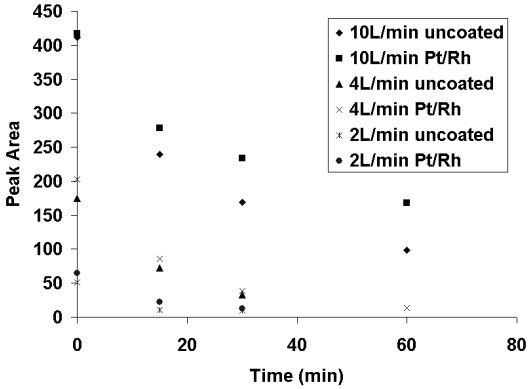


FIGURE 6. Downstream removal of VC

Figure 4 shows the energy efficiency of vinyl chloride removal vs. the gas flow rate. The energy efficiency increases with increasing flow rate even though the percent of vinyl chloride removed is less at the higher flow rates, as shown in Figure 2. This is a typical result in plasma treatment processes [4,5]. All vinyl chloride experiments were performed in humid air (~2% H_2O, 21% O_2). One byproduct was observed in small quantities. Figure 5 shows a single vinyl chloride experiment including the byproduct formation. It should be noted here that the data on the y-axis is shown in terms of peak area, the raw data given by the gas chromatograph. This was done since calibration data has not been taken for the byproduct. The byproduct shown here is most likely chloro-ethane (C_2H_5Cl). This identification has not been confirmed by further experiment, but the assumption of chloro-ethane is likely a good one since the elution time agrees with the sample chromatogram from the column manufacturer, and also because chloro-ethane is a likely byproduct of vinyl chloride degradation.

The outlet stream was also analyzed for Cl^- using the water trap. Due to deposition of HCl in condensation droplets in the reactor and in tubing downstream of the reactor, the water trap did not catch all of the Cl^- in the gas stream. Therefore, Cl^- results varied widely. However, Cl^- was detected in some experiments at levels corresponding to total conversion of chlorine from the feed vinyl chloride into Cl^-.

The work described above needs to be considered in light of the data shown in Figure 6. As described above, a gas sample bottle was closed off after 45 minutes of corona operation and allowed to stand for another hour. Samples from this bottle were analyzed on the GC. As can be seen, significant amounts of vinyl chloride were removed after the gas sample bottle was closed off. The most likely explanation for this longer-term reaction is that a long-lived species such as ozone is responsible for removing vinyl chloride downstream of the corona reactor. At the low flow rate of 2 L/min, vinyl chloride was removed below detection limits (on our GC) after 30 minutes in the gas

bottle. The lowest point on this graph corresponds to just under 2 ppm vinyl chloride, which is approaching the detection limit of the GC. At 10 L/min, there is still a significant amount of vinyl chloride after an hour in the gas bottle. One effect of the platinum coated electrode is evident from figure 6. The platinum electrode may be responsible here for ozone degradation, thereby decreasing the post-corona reactions downstream of the reactor.

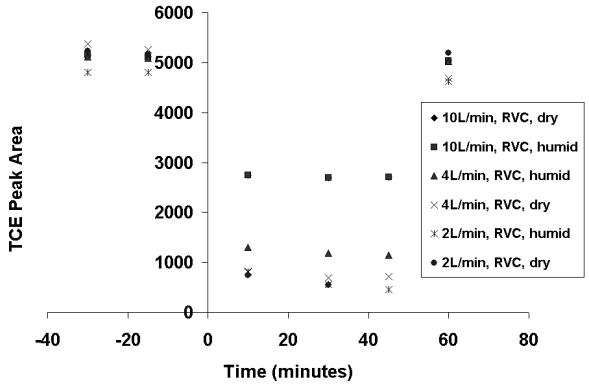


FIGURE 7. TCE removal

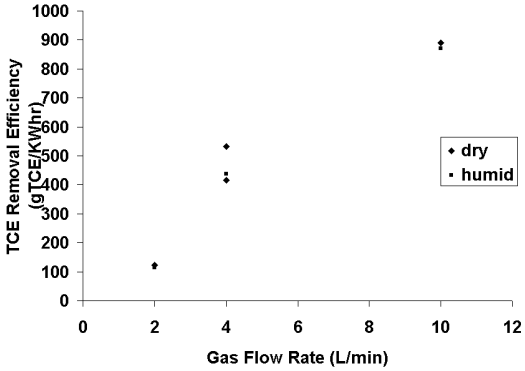


FIGURE 8. TCE removal efficiency

3.2. TCE Removal

Figure 7 shows the results for the TCE removal experiments. This data is for a feed concentration of TCE of 1000 ppm compared to the 100 ppm vinyl chloride experiments. This choice of concentration was made since data available in the literature on TCE removal from higher concentration streams could be used for comparison. These experiments were also performed with and without water present. No effect of the presence of water may be discerned from the figure.

Figure 8 shows the energy efficiency of TCE removal. The numbers are higher than those for vinyl chloride due to the higher concentration and molecular weight of TCE. Such efficiency values are functions of a number of factors, including temperature, gas composition, and discharge energy, but they are useful for comparison with other techniques. Again, efficiency improves with flow rate although there is less removal. The values of the efficiency are comparable to those reported in the literature [3]. Evans et al. used a silent discharge reactor with Ar/O_2 feed containing 500 ppm TCE. For the dry case, they found over 99% removal at an energy density of about 40 J/l. In the case of a humid gas stream, they found lower removal efficiency and could only remove about 85% at 150 J/l. Our results for TCE give 90% removal at 180 J/l (2 l/min) in the wet case and we do not find a difference between the humid and the dry cases. It is interesting to note that the removal of vinyl chloride has a similar behavior, giving 90% removal at about 180 J/l (2 l/min). A byproduct of TCE degradation was positively identified as dichloroacetyl-chloride (DCAC). A plot of DCAC formation looks very similar to Figure 5 for vinyl chloride and byproduct, and so is omitted here.

4. CONCLUSIONS AND FUTURE WORK

TCE and vinyl chloride can be removed by pulsed corona discharge and the results presented here are comparable to those given in previous literature. However, new observations from this work indicate the importance of the gas residence time downstream of the reactor. Significant post-corona reactions were observed indicating the presence of a stable reactive species, most likely ozone, formed in the discharge and leading to additional VOC degradation in the tubing downstream of the reactor. Mathematical models of the reaction system including ozone reactions can serve to assist in determining the mechanism for this effect. These post-corona reactions can lead to complete degradation of VC at the lowest flow rate or highest residence time (highest energy density). Two chlorinated byproducts have been identified, chloro-ethane and DCAC. These compounds could most

likely be removed by activated carbon, or further corona treatment.

Further work can be done to characterize the post-corona reactions that lead to the removal of vinyl chloride (and probably TCE) in order to optimize a field scale application. These reactions are 'free' with respect to electrical energy, and so it would be economically advantageous to capitalize on them. One strategy to capitalize on such reactions would be to increase the gas residence time downstream of the corona reactor. Additional lines or tanks placed downstream of the reactor would accomplish this.

One important issue for a field application of this technology is the formation of HCl. In our current system, there is some condensation on the walls of the corona reactor and HCl will likely partition into the water. This could be avoided easily by heating the reactor just above the dewpoint of the stream. HCl could then be removed from the gas by a scrubber downstream of the reactor. More work is currently being done on reactor heating and temperature effects on catalytic and plasma-catalytic oxidation of volatile organic compounds.

We are also currently developing a new corona reactor system using combined gas/liquid discharge where both gas and liquid phase contaminants can be removed. This system may be particularly useful for TCE, which is generally a problem in ground water. In addition, the so-called wet-plasma system utilizes a gas phase discharge above a water surface and has the advantage of eliminating the need for a downstream scrubber to remove such byproducts as HCl.

ACKNOWLEDGMENTS

Thanks to the Department of Chemical Engineering, FAMU-FSU College of Engineering, Florida State University and National Science Foundation, Grant INT 0086351 for financial support.

We also thank Kevin Warner, Levine-Fricke-Recon, Environmental Consultants, Tallahassee Florida for discussion and equipment support.

Thanks to Mayank Sahni, Austin Appleton, and David Grymonpré for discussion and help in the laboratory.

REFERENCES

[1] Kirkpatrick M.J., Finney W.C., Locke B.R., *IEEE Trans. Ind. Appl*., **36(2)**, 500-9 (2000).
[2] Kirkpatrick M.J., Finney W.C., Locke B.R, *SAE paper number 2000-01-2968* (2000).
[3] Evans D., Rosocha L.A., Anderson G.K., Coogan J.J., Kushner M.J., *J. Appl. Phys.* **74(9)** 5378-86 (1993).
[4] Oda T., Takahashi T., Tada K., *IEEE Trans. Ind. Appl.* **35(2)** 373-9 (1999).
[5] Futamura S., Yamamoto T., *IEEE Trans. Ind. Appl.* **33(2)** 447-53 (1997).
[6] Personal communications with Kevin Warner, Levine-Fricke Environmental Consultants.
[7] Wang J., *Electrochemica Acta*, **26(12)**, 1721-26 (1981).
[8] Heck R.M., Farrauto R.J., *Catalytic air pollution control: Commercial technology* Engelhard Corporation R&D, Van Nostrand Reinhold (1995).
[9] Francke K.P., Miessner H., Rudolf R., *Plasma Chemistry and Plasma Processing*, **20(3)** (2000).
[10] Roland U., Holzer F., Kopinke F.D., *Catalysis Today*, 2669 1-9 (2002).
[11] Ogata A., Yamanouchi K., Mizuno K., Kushiyama S., Yamamoto T., *Plasma Chem. and Plasma Proc*., **19(3)** (1999).

DEGRADATION OF AQUEOUS PHASE TRICHLOROETHYLENE USING PULSED CORONA DISCHARGE

M. Sahni[a], W. C. Finney[a], R. J. Clark[b], W. Landing[c], and B. R. Locke[a]

a) Department of Chemical Engineering, FAMU-FSU College of Engineering, 2525 Pottsdamer St., Tallahassee FL 32310 USA.
b) Department of Chemistry, Florida State University, Tallahassee FL USA
c) Department of Oceanography, Florida State University, Tallahassee FL USA

Abstract: Pulsed corona discharge has been found to be an effective method for the removal of trichloroethylene (TCE) from the aqueous phase. Almost complete degradation over one hour was observed irrespective of the electrolyte used in the solution. The degradation rates observed in these experiments are higher than those for other organic compounds such as phenol in pulsed corona reactors, thereby suggesting that hydroxyl radical attack isn't the only mechanism for organic compound degradation. This conclusion is supported by other experiments that utilized hydroxyl radical scavengers. The degradation of TCE consistently produced a byproduct that was observed in samples from both the liquid phase and the gas phase of the reactor but the identity of this by-product couldn't be established conclusively. Ion chromatography of samples from the liquid phase at the end of the experiments showed that 69% of the total chlorine present in initial TCE was released as chloride ion upon the complete degradation of TCE.

1. INTRODUCTION

Trichloroethylene (TCE) is a compound highly regulated by the environmental protection agency (EPA) due to its wide distribution in the environment and to its effects on human health. Various chemical methods (including reactions by ozone and hydrogen peroxide and dehalogenation with zero-valent iron) and biological techniques (bioremediation with aerobic and anaerobic bacteria) involving oxidation, reduction or a combination of both mechanisms have been shown to be effective in the degradation of aqueous phase trichloroethylene [1-4]. The efficacy of liquid phase pulsed corona discharge reactors for the removal of small aromatic species such as phenol by direct chemical reactions with highly reactive radicals (e.g. hydroxyl radicals), indirect reactions through radicals formed from stable molecular species (e.g. hydrogen peroxide and ozone), and direct reactions with stable molecular species (e.g. ozone) has been demonstrated by previous research [5-6]. The purpose of the present work is to determine the effectiveness of pulsed corona reactors for degrading TCE in the liquid phase.

2. SPECIFICATIONS

All experiments were conducted with solutions initially containing 100 ppm TCE. The solutions were prepared by stirring for two days in an Erlenmeyer flask. The reactor used for the experiments was a 1.5 liter vessel which consisted of a glass chamber with a cooling jacket in which water was circulated and maintained at approximately 20 ˚C. The reactor includes a glass top with openings for ground glass fittings for introduction of the electrodes and to extract the liquid and gas phase samples (Figure 1). All experiments reported here were conducted at a fixed applied voltage of 45 kV and the power supply is the same as reported in previous work [5]. The high voltage (platinum wire) and the ground electrode (reticulated vitreous carbon disk) were configured in a point to plane geometry to produce a liquid phase

[a] Electronic address: locke@eng.fsu.edu

discharge (Figure 1). The distance between the electrodes was fixed at 5 cm, which has been found in previous research to be the optimum distance for maximum hydrogen peroxide production in the reactor. Different electrolytes (including potassium chloride and ferrous sulfate) and additives (such as methanol) were used to study the degradation mechanisms responsible for TCE degradation.

The reactor was sealed after adding the 1 liter TCE stock solution. Both the gas phase and liquid phase concentrations were analyzed with gas chromatography. Experiments were conducted for 30 min or 1 hour. The liquid phase samples were collected at 0, 5, 10, 20 minutes and thereafter every 10 minutes in a Teflon-sealed vial which was stored in the refrigerator for 90 minutes and then equilibrated at room temp for 30 minutes. The gas phase samples were collected with a gas tight syringe and injected directly into the GC 2.5 minutes after starting the experiments and every subsequent 10 minutes until the end of the experiment.

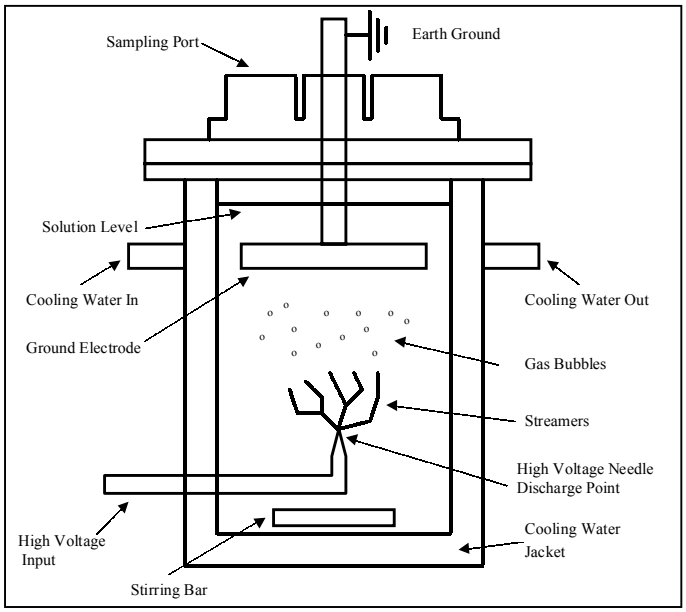


FIGURE 1. Experimental Setup

Previous research has shown the oxidation of TCE to yield a substantial amount of chlorine (as Cl^-), therefore ion chromatography was conducted on the final samples to determine the concentration of chloride and the concentration of other ions such as nitrate and nitrite. The pH and conductivity were also measured before and after each experiment.

3. RESULTS AND DISCUSSION

From the control experiments without corona (Figure 2) it is clear the TCE distributes between the liquid and gas phases although the concentration in the gas phase is relatively small during the course of the experiment. The mass balance gives a 17.2% loss of TCE from the reactor. The first series of experiments with corona discharges were conducted with potassium chloride as the electrolyte with a concentration of 805 μM to determine the rate of degradation of trichloroethylene in the absence of Fentons reactions. Figure 2 shows the trichloroethylene degradation of 56.4 % over 30 min and nearly 97% degradation over one hour. Moreover, the degradation appears to be linear (0 order).

The enhanced degradation of organic compounds due to Fentons reactions (primarily a set of chemical reactions that produce hydroxyl radicals from the reactions between iron ions and hydrogen peroxide) in solution have been well documented in literature [5,7]. Previous research has shown the efficacy of

this technique in degrading phenol in the pulsed corona reactors [5,7]. Experiments with ferrous sulfate as the electrolyte to initiate the Fentons reactions shows an enhanced degradation of TCE (Figure 3). The liquid phase trichloroethylene concentration decreased 94.7% in 30 min and degrading completely within 40 min and the data shows excellent reproducibility.
The degradation of TCE irrespective of the electrolyte used is greater than phenol but the difference in the degradation between Fentons and non-Fentons cases is smaller than observed when phenol was degraded [5]. This can be attributed to a non-hydroxyl radical mechanism responsible for some of the trichloroethylene degradation. This implies that either some oxidative species other than hydroxyl radicals, produced by the corona discharge and not incorporated into the model is responsible for this enhancement or a reductive mechanism plays a role. To verify this hypothesis experiments were conducted with methanol, a known radical quencher [8]. Experiments with methanol:TCE concentration ratios of 70:1 and higher were used. The results of the experiments (Figure 4) show that the observed 35% degradation is higher than that found in the control experiments without corona (15%). However the degradation observed with methanol in solution was less than without methanol with KCl as the electrolyte suggesting that hydroxyl radical attack is an important factor in the degradation of TCE. The purpose of conducting experiments with different concentrations of methanol was to ensure that all the hydroxyl radicals produced in the solutions were effectively quenched by the methanol. The almost equal degradation of TCE seen with 2 different concentrations (.056 and .14 M) of methanol strongly indicates that the degradation results from a non-hydroxyl radical mechanism. Identification of by-product can help in establishing the degradation mechanism since the byproducts of TCE reduction have been identified by various researchers [9-10]. A consistent by-product peak that eluted very close to the dead time peak was observed on the GC. This byproduct was present in both the gas and liquid phase samples suggesting a compound with high degree of volatility. If the byproduct is identified as ethane, ethene or other C1 to C4 hydrocarbons, the typical TCE reduction byproducts, there will be strong support for reductive processes in liquid phase pulsed corona discharges.

Ion chromatography data gives 69% of the TCE chlorine (as Cl^-) upon complete TCE degradation. This result is controversial since a few researchers have observed almost similar release of chlorine (~60-70%) [8,11] while others have observed a stoichiometric release on complete degradation of TCE [12,13].

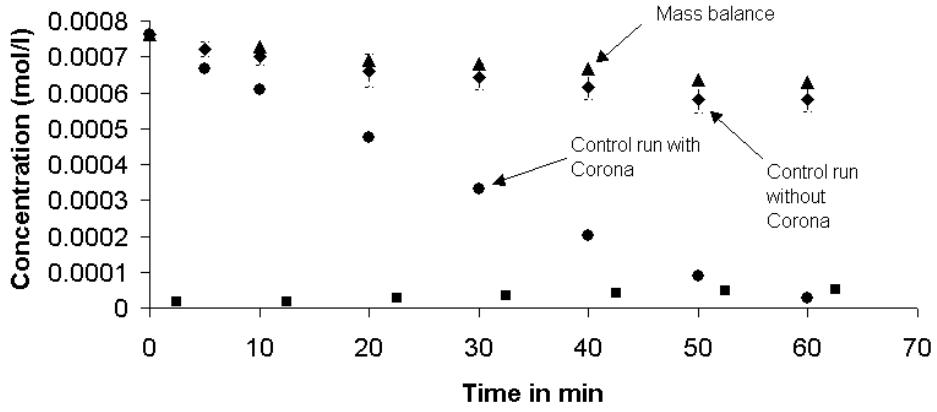


FIGURE 2. TCE concentration profiles (using KCl as electrolyte) with and without corona discharge.

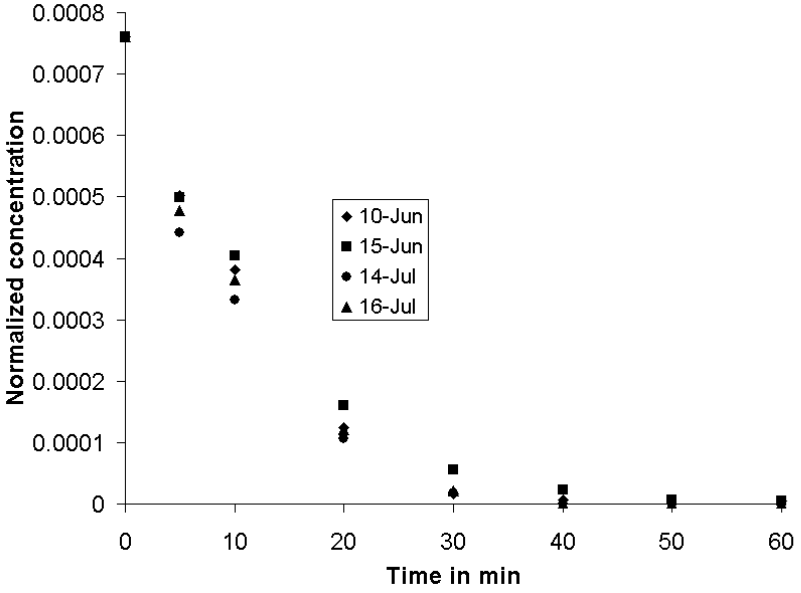


FIGURE 3. TCE degradation with ferrous sulfate as electrolyte

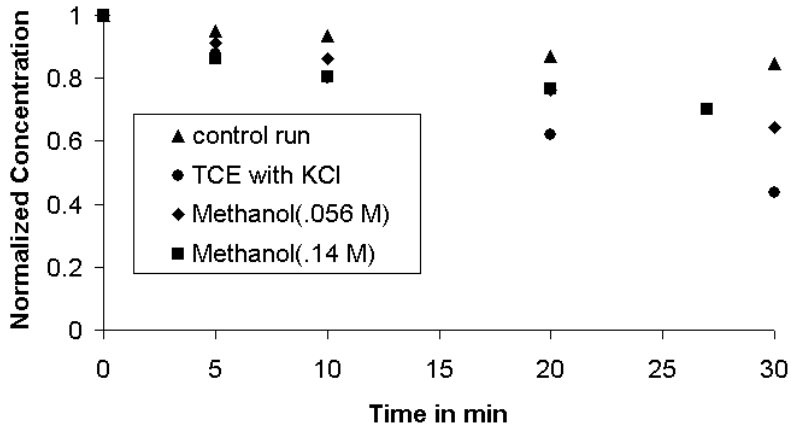


FIGURE 4. TCE degradation with hydroxyl radical scavenger

4. CONCLUSIONS AND FUTURE WORK

The effectiveness of pulsed corona discharges in degrading aqueous phase TCE is demonstrated in these experiments. Nearly complete degradation of TCE is seen within one hour for both the Fentons and non-Fentons cases. The enhanced degradation rate of TCE due to Fentons reactions is also observed. The most important conclusion from these experiments is that some of the TCE degradation results from a non-hydroxyl radical mechanism.

Further work is necessary to completely identify the degradation mechanisms and to establish the reduction pathways in liquid phase pulsed corona discharges. In addition, hybrid gas-liquid discharge reactors, that lead to combined gas and liquid phase discharges, previously studied for phenol degradation, may be particularly useful for the volatile TCE.

ACKNOWLEDGMENTS

We greatly appreciate partial support from the National Science Foundation, Grant INT 0086351, a Florida State University graduate research fellowship (for MS), and partial support from the Department of Chemical Engineering, FAMU-FSU College of Engineering, Florida State University. Discussion and advice from Mike Kirkpatrick, Austin Appleton, and Petr Lukés is also very much appreciated.

REFERENCES

[1] Smith,L.H., McCarty,P.L., *Biotechnology and Bioengineering*, **55**, 4, p. 650 (1997)
[2] Clancy, P.B., Armstrong, J., Couture, M., Lussky, R., Wheeler, K., Environmental Progress, **15**,3,187-193 (1996)
[3] Masten, S.J. and J. Hoigne, Ozone: Science and Engineering, **14**, 3, 197-214(1992)
[4] Watts, R.J., Bottenberg, B.C., Hess, T.F., Jensen, M.D. and Teel, A.L., *Environ. Sci. Technol.* **33**, p. 3432–3437(1999)
[5] Grymonpre, D. R., Sharma, A. K., Finney, W. C., and Locke, B. R.,*Chemical Engineering Journal,* **82**, p.189(2001)
[6] Sunka, P., Babicky, V., Clupek, M., Lukes, P., Simek, M., Schmidt, J., and Cernak, M., *Plasma Sources Science and Technology*, **8**, p. 258(1999)
[7] Pignatello, J. J. and Sun, Y.,*Water Res.,* **57**, 8, pp. 1837–1844(1995)
[8] Teel, A.L., Warberg, C.R., Atkinson, D.A. and Watts, R.J., *Water Res*.,**35**,4,977-984 (2001)
[9] Lowry, G.V., Reinhard, M., *Environ. Sci. Technol*., **33**,11,1905-1910 (1999)
[10] Gillham, R.W.; Orth, W.S., *Environ. Sci. Technol.*,**30**,66-71(1996)
[11] Cyr,P.J., Paraskewich, M.R., Suri, R.P.S., Water Sci. Tech.,**40**,4-5,131-136(1999)
[12] Glaze, W. H., and Kang, J. W., *Journal of the American Water Works Association*, **80**, p. 57 (1988)
[13] Sunder,M., Hempel, D.C., *Water Res.*,**31**,1,33-40(1997)

COLD PLASMA ELECTROCHEMICAL REACTOR WITH ROTARY DISCHARGE

E. Hnatiuc[a], B. Cheron[b], B. Hnatiuc[a], R. Burlica[a], J.L. Brisset[c]

a) Technical University "Gh. Asachi" Iasi, Bd. Dimitrie Mangeron , Iasi 6600 ROMANIA
b) UMR 6614 Coria, Rouen, FRANCE
c) University of Rouen, Laboratory of Electrochemistry, UFR F-76821 Mont-Saint-Aignan Cedex, FRANCE

Abstract – The paper presents a short introduction to gliding discharges technologies and a physical study of a new reactor. This new reactor is used to methane conversion. The aim of the paper is to present a simple flowing model which can be used to determine the voltage waveform of the supply and the influence of the flow on discharge resistance variations.

1. INTRODUCTION

The electrical discharges of cold plasma type (corona, dielectric-barrier discharge, glidarc, etc.) are used more and more during last years to work with active species (electrons, ions, excites atoms, etc.) in the aim to ensure, without catalysis, typically electrochemical reactions. These reactions concerned initially, the treatment by decomposition of the pollutants from air or aqueous solutions but it was proved their efficiency to obtain the syngas from methane and even for others synthesis reactions [1].

2. THE EVOLUTION OF THE ELECTROCHEMICAL REACTORS WITH PLASMA GLIDARC TYPE

The simplest electrochemical reactor with cold plasma, is presented in Figure1, and contains an electric - insulator tube, inert from chemical point of view (quartz, ceramics - *1*), two metallic electrodes placed inside it (*2*), connected to a high voltage power supply (*3)*. The air to be treated is blown after the axial direction of the tube (*1*) through the injector (*4*) ensuring the ascendant move of the electrical discharge of cold plasma type (*5)*. The ascendant evolution of the electrical discharge (*5)* is helped also by the divergent form of the metallic electrodes (*2)*. The cold character of the plasma is obtained by the limitation of the electrical current, realised with impedance Z_l.

The good results obtained with the cold plasma electrochemical reactors is based on the utilisation of the active species generated by the electrical discharge *5*. These reactors are able to produce and maintain the electrochemical reactions at the interface zone between the electrical discharge and the gas flow through the injector *(4)*. It is thus possible to obtain the depollution of the air containing SO_2, *COV*, H_2S, etc., without using supplementary catalysis.

Such a device allow to obtain the syngas, starting from the methane, by the following reaction [2]:

$$2CH_4+H_2O+\frac{1}{2}O_2\rightarrow 5H_2+2CO \qquad (1)$$

One of the most important problems for using the electrochemical rectors with cold plasma (glidarc type) is the high value of the report between the breaking voltage and the discharge voltage, that leads to a low value for the electrical efficiency (the electrical effiency is about 10%). Using a special command device in order to start the main electrical discharge, the electrical efficiency increases up to 50%, and also permit an easy adjustment of the useful electrical power injected into the electrochemical reactor.

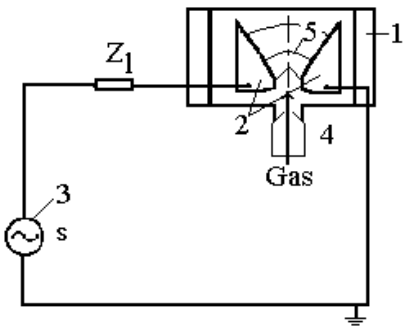


FIGURE 1. Typical gliding arc circuit

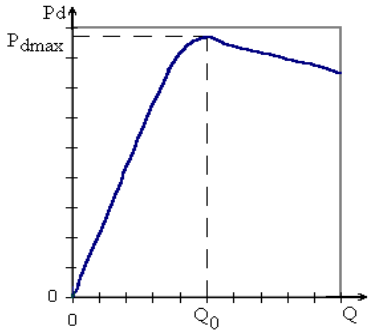


FIGURE 2. General dependence of power versus flow

Another important fact for the electrochemical reactors functioning is the influence of the gas flow on the useful electrical power of the discharge P_d (see Figure 2). The curve $P_d(Q)$, presented in Figure 2, shows an aerodynamically optimisation possibility for the construction of such devices and lead to the idea to reduce the dependence between the useful power of the discharge and the gas flow. In this aim it is preferable to adopt some technical solutions which allow obtaining a rotating electrical discharge and increasing the electrochemical efficiency using a better interface between the active species and the gas that must to be treated. The rotate electrical discharges assure better chemical effects, in rapport with electrical power of the discharge.

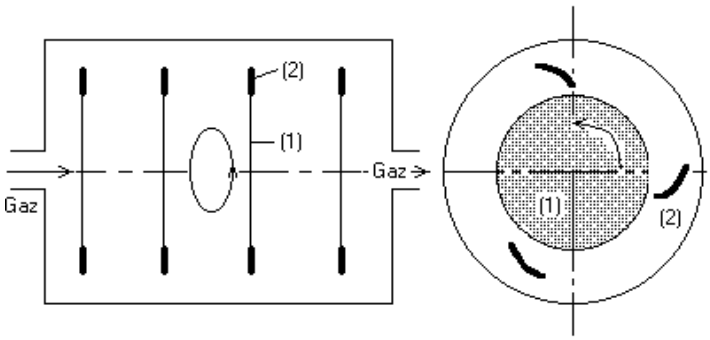


FIGURE 3. Gliding arc with a rotating electrode

The electrochemical reactors with rotating electrical discharges could be realised by a central rotating electrode (see Figure 3) or by using a local external magnetic field conveniently oriented (see Figure 4).

3. A NEW TYPE OF AN ELECTROCHEMICAL REACTOR WITH COLD PLASMA AND ROTARY ELECTRICAL DISCHARGE

Another solution for an electrochemical reactor with cold plasma and rotary electrical discharge consist in the tangential injection of the gas into the reactor.

This could be obtained by using an electrical-isolated element with a special shape (*1)* (see Figure. 5). In Figure 5 emphasises the electrical discharge (*2)* between the exterior electrode and the central electrode, a metallic cylinder (*3)* and the conical shaped inner electrode (*4)* connected to a high voltage supply (*5)*.

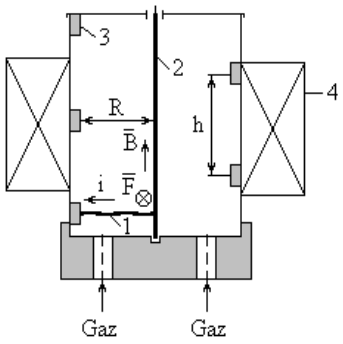


FIGURE 4. Rotating arc produced by a magnetic field

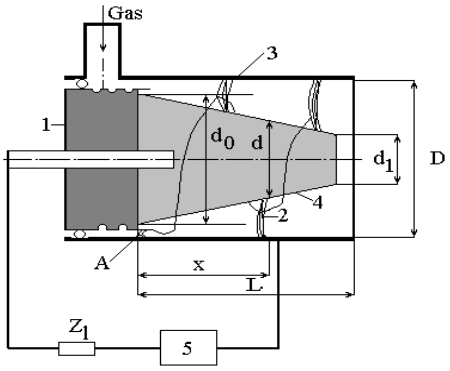


FIGURE 5. New "rotarc" arrangement

4. NUMERICAL RESULTS

The present paper proposes a model for the device behaviour, from aerodynamically and electrically points of view, with the aim to appreciate the solutions that allow materialising efficient three - phase installations.

It is necessary to use special notions to describe the aerodynamically behaviour of the reactor, like similitude criteria, fluids flowing turbulence, etc., that involves calculus difficulties and the influence of different parameters [3].

The shape of the electrochemical reactor is presented in Figure 6.

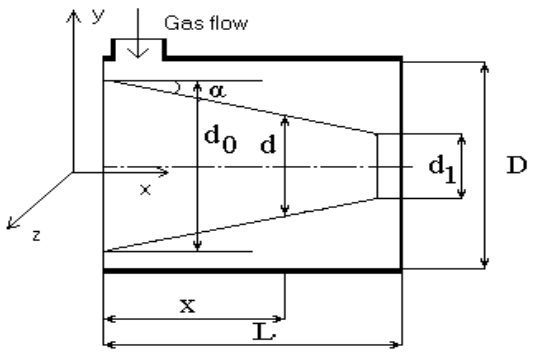


FIGURE 6. Description of the shaping of the new arc reactor

The reactor dimensions are: D=40 mm, d_0=30 mm, d_1=20 mm, L=80 mm. The airflow Q is Q=1l/sec.

For this type of the reactor the aerodynamic parameters, axial velocity of the air and the helicity, have been obtained by using the Fluent 5.4 solver. The conservation equations for mass, momentum and energy are solved, and also the compressible effect was taken into account. The turbulent kinetic energy and dissipation rate have been calculated using the standard k- ε model.

The values for the gas velocity along the reactor length v_x and the helicity, defined like:

$$H = \mathrm{rot}\vec{v} \cdot \vec{v} \qquad (2)$$

are shown in Figure 7 and Figure 8.

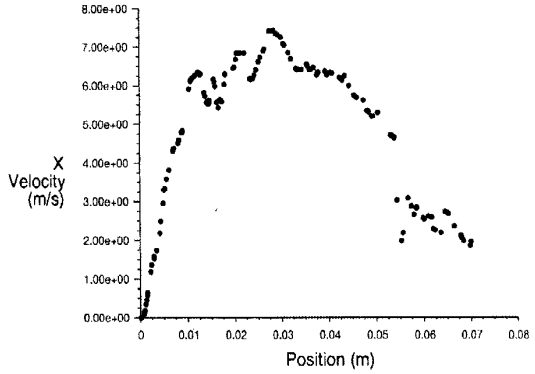


FIGURE 7. The axial component of the gas velocity

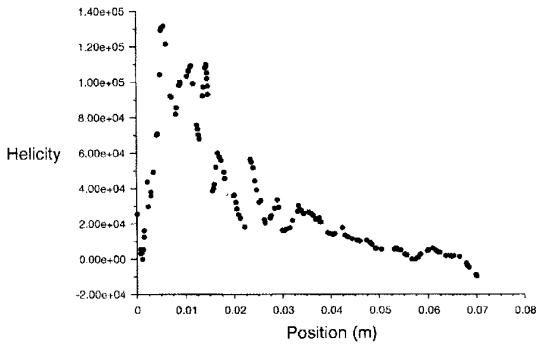


FIGURE 8. The evomution of the helicity along the x axis of the reactor

By notation v_x the axial gas velocity component of the gas velocity *v*. The calculus have been done along the x axis of the reactor and for a distance from the axis x , y=17.5 mm, constant.

The results of the numerical analyse, presented in Figure 7 and Figure 8, emphasise the rotation of the gas flow up to 35 mm along the x axis of the reactor accompanied by an important increase of the axial velocity of the gas. After this point the gas, practically, has only the axial component of the velocity. This behaviour of the gas flow has been confirmed by the experimental observations.

5. CONCLUSIONS

The present paper proposes aerodynamic and electrical descriptions of a new type of electrochemical reactor with cold plasma and rotary discharge. It is possible to get interesting information, which allow defining, by calculus, the evolution of the useful electrical power.

Our observations also define useful directions to realise a three-phase device, with three such reactors, axial disposed. However, the good working equilibrium must be optimised from the aerodynamically and electrical points of view.

The experimental results confirmed the numerical approach and also the research directions defined by theoretical analyse of the considered reactor module behaviour.

The authors would like to acknowledge the support of the European Community- Access to Research Infrastructure action of the Improving Human Potential Programme.

REFERENCES

[1] Hnatiuc B., Contributions théoriques et expérimentales à l'étude des décharges électriques de type plasma froid, *Doctoral Thesis*, Iasi, Technical University "Gh. Asachi", 2001, pp. 68-72.
[2] Cormier J-M., and Rusu I., Syngas production via methane steam reforming with oxygen: plasma reactors versus chemical reactors, *J. Phys. D: Appl. Phys.*, 34, pp. 2798-2803, 2001.
[3] Hnatiuc E., Burlica R., Hnatiuc B., Brisset J.-L., A new type of electrochemical reactor with a rotary cold plasma discharge, In *Proc. XIV-th Symposium on physics of switching arc Czech Republic*, p. 58, 2001.
[4] Cormier J.M., Martinie O., Lefaucheux P. and Hnatiuc E., Electrical study of a gliding arc discharge at 33 kHz and 50 Hz, In *Proc. OPTIM 2000 Romania*, pp. 177-180, 2000.
[5] Richard F., Cormier J.M., Pellerin S., and Chapelle J., Physical study of a gliding arc discharge, *J. Appll. Phys.*, 79 (5), pp. 2245-2250,1996.
[6] Pellerin S., Richard F., Chapelle J., Cormier J.M. and Musiol K., Heat string model of bi-dimentional dc Glidarc, *J. Phys. D: Appl. Phys.*, 33, pp. 2407-2419, 2000.

TOPIC 7:

Surface processing and technology (cleaning, coating, etching and modification equipment)

PHYSICAL AND CHEMICAL PROPERTIES OF ATMOSPHERIC PRESSURE PLASMA POLYMER FILMS

O. Goossens, D. Vangeneugden, S. Paulussen and E. Dekempeneer

VITO – Flemish Institute for Technological Research, Boeretang 200, B-2400 Mol, Belgium

Abstract: The aim of this work was to perform a detailed study of the basic properties of plasma polymers produced from ethylene, ethylene oxide and propylene. Films were deposited in an atmospheric pressure dielectric barrier discharge (DBD). Physical properties were characterized by field emission scanning electron microscopy (FESEM) and contact angle measurements. On the other hand, chemical properties were characterized by means of Fourier transformed infrared spectroscopy (FTIR), X-ray photoelectron spectroscopy (XPS), nuclear magnetic resonance (NMR) and electron spin resonance (ESR) techniques.

1. INTRODUCTION

When introducing molecular gases into a plasma, chemically active species are formed such as molecules in excited states, radicals and ions. These species can react with each other, neutral molecules or with the surface of a substrate. Depending on the nature of the molecules and the process conditions, this may result in the deposition of a thin film.

Films resulting from organic precursors are generally known as plasma polymers. The reaction chain leading to a plasma polymer film is not comparable to common polymerization reactions. For this reason, the properties of plasma polymer films can significantly differ from their classic chemical counterparts. Although widely investigated for many years, plasma polymers are still not well understood with respect to their physical and chemical properties. In particular, this is true for the more recently developed deposition technologies based on atmospheric pressure plasmas like dielectric barrier discharges (DBDs) [1, 2, 3].

When hydrocarbons are introduced in a DBD at atmospheric pressure, plasma polymerization occurs which results in the deposition of polymer-like material on the surface of the electrodes. This paper reports on a more detailed investigation of plasma polymer coatings obtained from ethylene, propylene and ethylene oxide in discharges sustained in He. The aim of this work is to gain more insight in the morphology and chemical structure of these materials. Currently, coatings obtained in Ar and N_2 discharges are also being investigated.

2. EXPERIMENTAL SETUP

Plasma polymerization is performed in the system shown in figure 1. The discharge is obtained between two disk-shaped electrodes with a diameter of 150 mm, both covered with an Al_2O_3 plate of 2 mm thickness. To ensure stable plasma operation, the gap width is typically limited to a few millimeters. The bottom electrode is connected to a variable frequency AC power source. The frequency can be varied between 1 and 30 kHz with a maximum output voltage of 20 kV. In this setup the top electrode is grounded. In order to obtain a well controlled atmosphere the configuration is mounted in a vacuum chamber. This vacuum chamber is evacuated before each run and subsequently filled with a specific process gas mixture.

Electronic address: Olivier.Goossens@vito.be

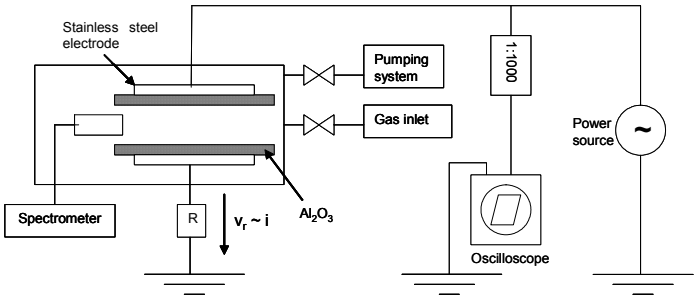


FIGURE 1. Experimental setup.

By means of mass flow controllers about 5 % of reactive gas (0.5 l/min) was added to the inert carrier gas flow (20 l/min). The deposition time was set at 10 min for deposition experiments with ethylene and propylene. In case of ethylene oxide a deposition time of 30 min was used. In order to obtain samples for the different analysis techniques, various substrates were placed between the electrodes such as glass slides, pieces of single and double polished Si wafers and polished stainless steel plates.

The optical emission spectra (OES) of the DBD are sampled through an optical fiber placed at a distance of a few centimetres from the discharge. The optical fiber is connected to a spectrometer, which has a focal length of 320 mm (Jobin Yvon, HR 320).

Plasma polymer coatings used for FESEM analysis (Jeol, JSM-6340F), FTIR analysis (Thermo Nicolet, Avatar 360 E.S.P.) and contact angle measurements (Dataphysics, OCA 15 plus) were deposited on Si-substrates placed on the bottom electrode. The plasma polymers used for NMR and ESR measurements were recovered from deposits on polished glass substrates. The plasma polymer deposition time varied from 10 to 30 min.

3. RESULTS AND DISCUSSION

Some qualitative observations are readily made. Plasma polymerization of ethylene and propylene in He results in opaque and sticky materials, this in contrast to coatings obtained from ethylene oxide which are clear and non-sticking.

In figure 2 FESEM pictures are shown that were taken from cross sections of coatings deposited on single polished Si. As such the thickness of coatings and hence the deposition rates could be evaluated. The film growth rate appears to be much higher when ethylene or propylene is used as precursor (about 100 nm/min) than when ethylene oxide is used (about 20 nm/min). Films deposited by the addition of mentioned monomers to He discharges appear to have a very smooth surface. This in contrast to coatings obtained from the same monomers in Ar discharges [3]. Under both discharge conditions coatings obtained appear homogeneous and without pinholes or structural defects.

From FTIR analysis some information can be gathered concerning the presence of functional groups in the coatings [4]. It is however quite difficult to obtain adequate information about the hydrocarbon backbone. As can be readily seen from the infrared spectra in figure 3, the ester group (C=O stretching around 1700 cm^{-1}) and the hydroxyl group (O-H stretching around 3400 cm^{-1}) are more pronounced in the plasma polymer obtained from ethylene oxide compared to that from ethylene. The presence of the latter groups in the ethylene and propylene plasma polymer originates from exposure to air after deposition. However, it has to be remarked that absorption of water vapor present in the atmosphere can also contribute to the observed O-H signal. In case of the ethylene oxide plasma polymer, oxygen already present in the monomer gives rise to more oxygen containing functionalities such as esters, ketons, ethers and alcohols. (The C-O stretching of ethers is situated around 1120 cm^{-1}). Furthermore

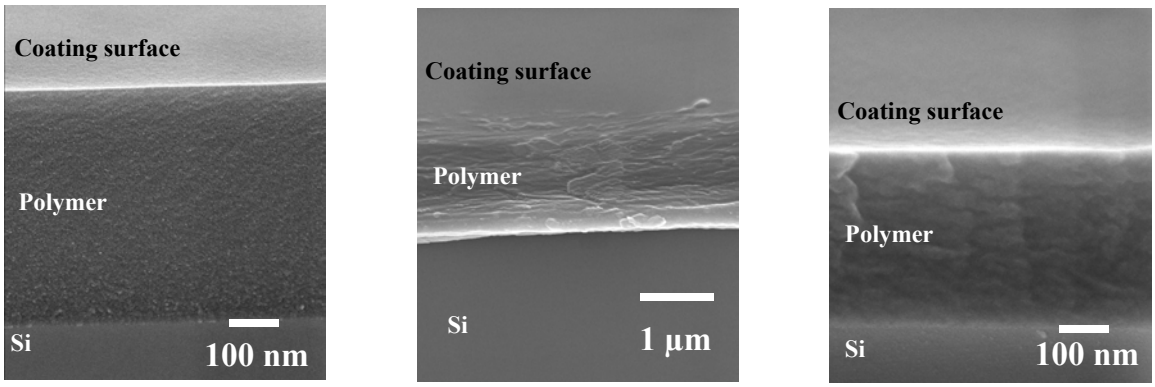


FIGURE 2. SEM cross sections of coatings obtained by plasma polymerization of respectively (from left to right) ethylene, propylene and ethylene oxide. The substrate material was Si and the deposition time was 10 minutes in case of ethylene and propylene and 30 minutes in case of ethylene oxide.

all spectra contain C-H stretching (2955 cm^{-1}) and C-H deformation (1456 cm^{-1}) bands from the obtained hydrocarbon network.

X-ray photoelectron analysis has been carried out to determine the relative amount of oxygen and carbon at the surface of the plasma polymer films. The first results correlate well with the results obtained by FTIR spectroscopy. A higher oxygen content is observed in the polymer deposited from ethylene oxide. The question whether surface properties of the plasma polymers are representative for the bulk of the material is currently being addressed. GD-OES (glow discharge optical emission spectrometry) seems to be more appropriate for this purpose than XPS.

Nuclear magnetic resonance (NMR), and in particular ^{13}C-NMR, has proven to be a powerful technique to perform detailed investigations of the hydrocarbon backbone of polymers [5, 6]. It also seemed an interesting technique to gain some more insight in the chemical structure of the obtained plasma polymers. In principle, one should be able to evaluate for instance the retention of the chemical structure of the monomers in the plasma polymers and the degree of crosslinking. Therefore, ^{13}C-NMR measurements were performed on plasma polymers from ethylene and propylene recovered from depositions on large glass plates. However, the recorded ^{13}C-NMR spectra only showed very weak signals that were strongly broadened and hence not very informative. This could be due to the presence of strong paramagnetic sites, such as remaining stable radicals.

In contrast to the ^{13}C-NMR measurements, ^{1}H-NMR analysis of the plasma polymers resulted in more useful spectra (figure 4). Although the line broadening in these spectra is also considerably higher than usual for polymers, some qualitative information can be extracted. First of all, the spectra of plasma polymers from ethylene and propylene are very similar. However, the CH_3-signal (at about 0.8 ppm) seems to be disproportionately large compared to the CH_2- and CH-groups (at about 1.2 to 1.4 ppm). As can be expected, the CH_3–signal is relatively higher for plasma polymers from propylene compared to those obtained from ethylene. Furthermore, the spectra indicate the presence of remaining C=C double bonds (signals around 4.5 to 6 ppm) and some oxygen containing unsaturated

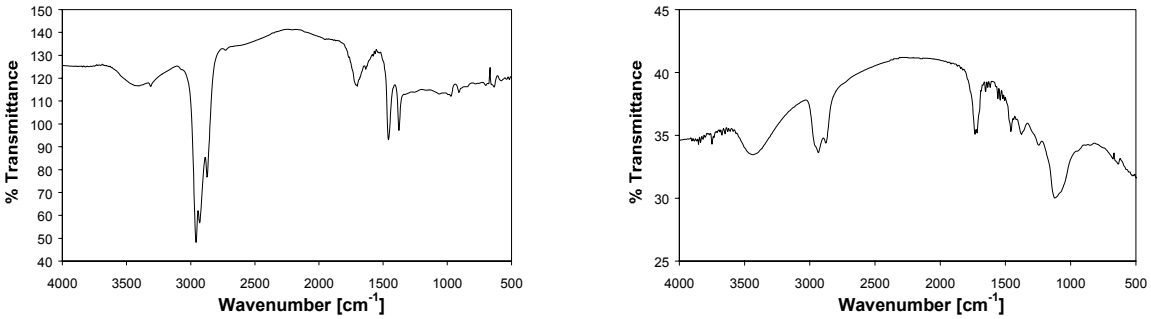


FIGURE 3. FTIR spectra of plasma polymers from ethylene (left) and ethylene oxide (right) obtained in He discharges.

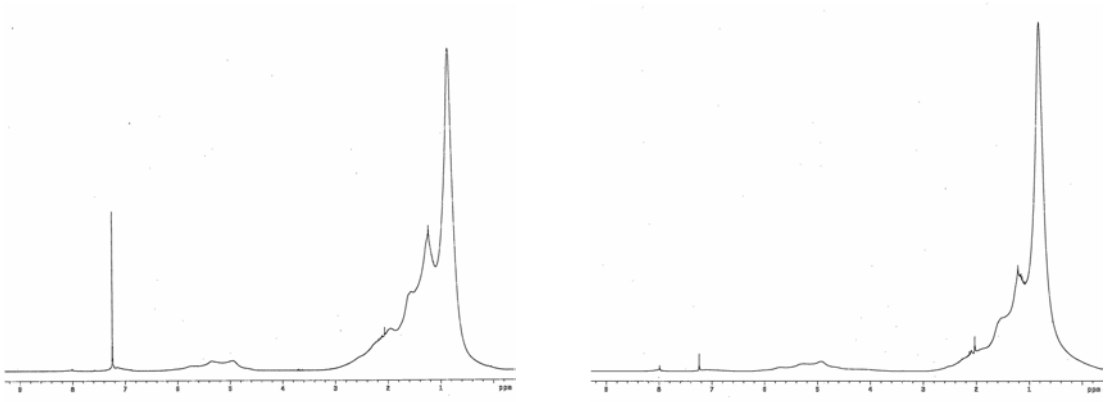


FIGURE 4. ^{1}H-NMR spectra of plasma polymers obtained from ethylene (left) and propylene (right) in He discharges.

functionalities like –OCHO or –C=CHO– (around 8 ppm). The broad signal from about 1.7 to 2.2 ppm is attributed to CH_x-groups next to double bonds.

To verify the hypothesis of remaining stable radicals in plasma polymers from ethylene, propylene and ethylene oxide, ESR measurements were performed. The ESR spectra presented in figure 5 confirm the presence of remaining radicals in plasma polymers obtained from ethylene and propylene. However, ESR measurements on plasma polymers obtained from ethylene oxide, didn't reveal any detectable signal of remaining radicals. This indicates that the monomer structure has an important impact on the formation of stable radicals. In case of plasma polymers from ethylene and propylene, the presence of remaining double bounds (as present in the monomers) is expected to have a stabilizing effect on some radical sites. By delocalization across several atoms radicals become less reactive and hence more stable. In order to substantiate this theory additional ESR experiments are being performed including the use of several ESR spectral bands (X-, Q- and W-band) and measurements under different conditions (e.g. temperature). Furthermore, plasma polymers obtained from propane and butane will be investigated.

In order to follow up the coating deposition in situ, a link between the plasma polymerization reactions and optical emission spectroscopy measurements would be very useful. It seems however quite difficult to link the physical and chemical structure of the obtained coatings to the optical emission spectra. Gathering information on plasma composition and reaction mechanisms seems rather difficult to target in this way [7]. For this purpose modeling seems to be a very powerful tool.

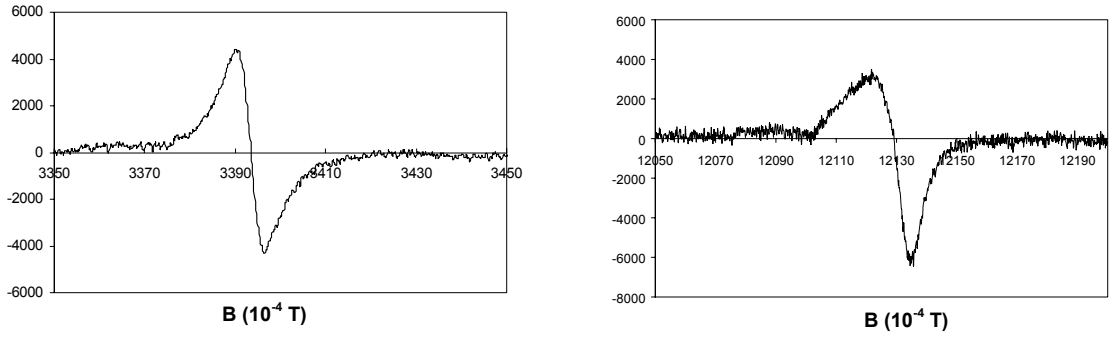


FIGURE 5. Examples of ESR measurements on plasma polymers from ethylene (left, X-band spectrum) and propylene (right, Q-band spectrum) obtained in He discharges.

4. CONCLUSIONS

Coatings were obtained by plasma polymerization of ethylene, propylene and ethylene oxide and analyzed with a broad spectrum of analysis techniques. The results presented were focused on coatings obtained in a He discharges.

The research done gives some more inside in the chemical structure of the obtained coatings. Nevertheless, it remains difficult to correlate the results of analysis on plasma polymers to plasma chemical conditions or to OES spectra taken during the deposition process.

The presented results suggest that no polymerization in the conventional sense of the word occurs. Plasma polymerization results in a network structure. In case ethylene or propylene is used as monomers, some double bounds remain present in the plasma polymers obtained. These double bonds can have a stabilizing effect on the radicals which makes them long living. The presence of such radicals was first indicated by difficulties to perform (^{13}C-)NMR measurements and later confirmed on the basis of ESR-analysis. A more elaborate investigation of the influence of the chemical structure of the monomer on the presence of stable radicals in the plasma polymer is presently ongoing.

ACKNOWLEDGMENTS

The authors would like to acknowledge Prof. E. Goovaerts from the University of Antwerp (UIA) and Prof. F. Callens from Ghent University (RUG) for the ESR measurements. The authors would also like to thank Prof P. Adriaensens from the Limburg University Centre (LUC) for the NMR measurements.

REFERENCES

[1] Prat R., Koh Y. J., Babukutty Y., Kogoma M., Okazaki S., Kodama M., *Polymer*, **41**, 7355-60 (2000)
[2] Salge J., *Surf. Coat. Technol.*, **80**, 1-7 (1996)
[3] Goossens O., Dekempeneer E., Vangeneugden D., Van de Leest R., Leys C., *Surf. Coat. Technol.*, **142-144**, 474-81 (2001)
[4] Ren W., *Colloid. Polym. Sci.*, **270**, 747-52 (1992)
[5] Randall J. C., Ruff C. J., Kelchtermans M., *Recl. Trav. Chim. Pais-Bas*, **110**, 543-52 (1991)
[6] Prasad J. V., *J. Polym. Sci.: Part A: Polym. Chem.*, **30**, 2033-36 (1992)
[7] Gherardi N., Martin S., Massines F., *J. Phys. D-Appl. Phys.*, **33**, L104-8 (2000)

LARGE AREA SURFACE MODIFICATION INDUCED BY PARALLEL OPERATED MSE SUSTAINED GLOW DISCHARGES

C. Penache[a], S. Datta[b], S. Mukhopadhyay[c], A. Bräuning-Demian[d], P. Joshi[c], O. Hohn[a],

S. Schössler[a], T. Jahnke[a], H. Schmidt-Böcking[a]

a) J.W.Goethe University, 60486 Frankfurt am Main, GERMANY.
b) The Procter & Gamble Company, West Chester, Ohio 45069, USA.
c) Wright State University, Dayton, Ohio 45435, USA.
d) Gesellschaft für Schwerionenforschung mbH, 64291 Darmstadt, GERMANY.

Abstract: A novel approach in the field of non-equilibrium plasma generation is the development of Micro Structured Electrode (MSE) arrays that can be operated at or near atmospheric pressure. The MSE-sustained discharges present a high density of electrons ($10^{15}cm^{-3}$) and metastable atoms ($10^{13}cm^{-3}$). The gas temperature immediately above the microstructure exceeds only slightly the room temperature. This study reports on the application of a microplasma array in the surface modification of plastic substrates. Detailed features of surface modification of plastics by means of MSE-sustained discharges are reported for the first time, utilizing both water contact angle and high resolution XPS analysis.

1. MSE MICROPLASMA ARRAY DESIGN

Microstructures using various types of geometry and electrode design were developed as a new and promising approach for low-cost high-pressure plasma sources [1-5]. Recent projects have explored the use of such devices for surface modification. The details of the MSE design were presented in earlier publications [6,7]. Briefly, these structures consist of a regular matrix of holes perforated in a thin composite sheet made out of two metallic foils separated by an insulator. The metal foils (electrodes) are typically 50-200 µm thick, with a dielectric layer thickness in the range of 50–250 µm. The holes, drilled through the metal-dielectric-metal composite, are typically 100-300 µm in diameter and are usually placed at a pitch (center-to-center distance) of 1.5 to 3 mm. The local electric field achieved in the vicinity of the microelectrodes is about 10^6 V/cm, strong enough for plasma generation at atmospheric pressure. Based on MSE arrays, stable direct current glow discharges were produced in noble gases (Ar, He, Ne), air and mixtures thereof, over a wide pressure range of several hundred mbar to 1 atmosphere. Discharge currents up to 20 mA per hole at moderate sustaining voltages around 200 V were measured. The MSE-sustained discharges provide non-thermal plasma that generates highly energetic electrons and free radicals without heating the gas. Therefore these devices are suitable for gas phase plasma chemistry and surface processing. Besides the ease of use, since expensive vacuum equipment is not required, these discharges offer a high density of active species. In many applications, particularly in surface modification, the free radicals generated are more important than the electrons and ions themselves.

2. SURFACE MODIFICATION OF POLYMER FILMS

Various experiments were carried out to explore the application of MSE arrays for surface modification. This paper describes the work carried out to improve the wettability of polyethylene films (PE) through surface modification induced by MSE-sustained discharges. A MSE module with

[a] penache@ist.fhg.de

40x40 mm^2 active area and consisting of 196 parallel operated holes was used to induce surface modification on the polymer films. The diameter of the holes is 300 μm and they are positioned as a 14x14 hole array with 3 mm pitch. Due to the large number of microdischarges operating in parallel, the current per hole was usually maintained relatively low at 0.05 mA/hole and the operating pressure was kept under 1 atmosphere, to prevent the onset of thermal instabilities. The discharge current, gas flow and pressure as well as the distance between the MSE array and the polymer film substrate were varied during the experiments to understand how each of these parameters affect the degree of surface modification of the PE film. A sketch of the experimental set-up is given in figure 1.

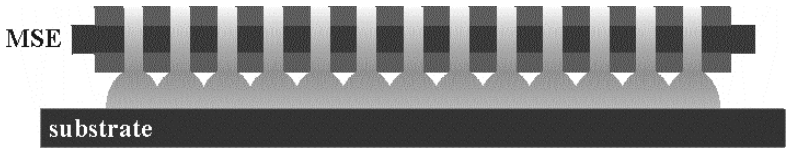


FIGURE 1. Schematic view of the experimental set-up.

Most of the measurements were done at 50 mbar using a mixture of Ar with 10% air as plasma gas. The degree of surface modification was studied using water contact angle (WCA) measurements. Chemical analysis of the surface was done using high resolution X-Ray photoelectron spectroscopy (XPS) and topographic analysis was performed using scanning white light interferometry. In addition to the data reported here, experiments were also done using a smaller array consisting of 36 holes at the same pitch, to investigate the extent of surface modification occurring in the lateral direction away from the array. In another set of experiments, surface modification of polypropylene (PP) films was studied to compare with the surface modification obtained on PE films. Results from these latter experiments will be reported in a subsequent publication elsewhere.

3. ANALYTICAL TOOLS AND METHODS

Water Contact Angle (WCA) measurements were done using a video contact angle measurement tool, Model 2500XE, made by AST Inc. 100% pure water from Baker Chemical Company was used for the measurement. Drop size was kept constant at 0.065 μl and built-in software was used to do curve fitting to accurately obtain the left and right contact angles made by the water droplet with the substrate. WCA measurements were done in several regions within the substrate area to determine uniformity of surface modification across the PE substrate directly opposing the MSE array. Untreated PE has a rather high WCA of about 110 degrees. If the surface is rendered wettable through plasma treatment, the WCA will decrease in value. WCA measurements were also done in regions of PE just outside of the MSE array position, to determine degree of lateral extension of surface modification as a function of current density, MSE-PE distance and time of treatment.

X-Ray Photoelectron Spectroscopy (XPS) measurements were done using a Kratos AXIS Ultra XPS unit. Mono-chromatized Al Ka X-ray line with a spot size of 55 μm and pass energy of 80 eV was used for enhanced spectral resolution. XPS allows to monitor and map the concentration of various elements on a surface as well as the chemical state of that element with respect to its bonding to other elements. Carbon and oxygen concentrations on treated and untreated surfaces, as measured by XPS, showed if the wettability change in PE was caused by oxygen incorporation. In addition, for each sample, XPS spectra were taken in positions on PE sample that corresponded to the location of a hole in the MSE as well as in positions on PE that fell between two adjacent holes of the MSE array, in steps of 750 μm. This allowed to obtain the detailed variation of oxygen concentration and incorporation across the PE substrate as a function of MSE hole location.

Scanning White Light Interferometry was done using a three-dimensional surface structure analyzer (Zygo, New View 5000). This measurement of surface topography indicates the presence of surface etching caused primarily by high-energy ions. The atoms on metastable states and the UV radiation are playing an important role too.

4. RESULTS

The PE films are normally hydrophobic, with a WCA value of about 110 degrees. When PE films are exposed to an oxygen containing plasma, the film is rendered hydrophilic and wettable, primarily due to oxygen incorporation leading to the formation of functional groups such as carboxyl and hydroxyl groups at the surface. For a PE film which was exposed to MSE-generated plasma at about 50 mbar pressure for 5 min, using a mixture of 10% air in Ar, the water contact angle was found to decrease from the original 110 degrees to about 40 degrees. The modification was found to be permanent whenever the substrate is placed at the anode or the cathode side.

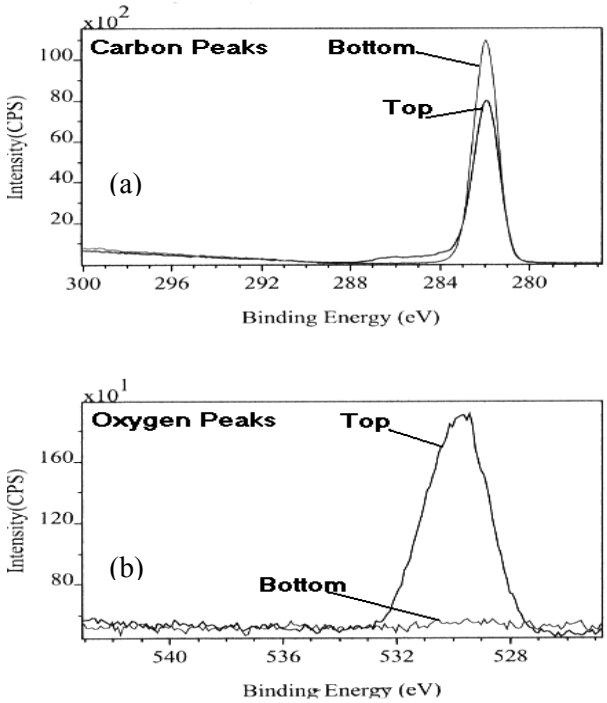


FIGURE 2: XPS Spectra of treated and untreated PE film: (a) carbon and (b) oxygen concentrations on treated (top) and untreated (bottom) surfaces. Distance MSE-PE 4 mm.

Figure 2 presents the XPS spectra of the MSE-plasma treated PE and the corresponding untreated (control) PE surface. Figure 2(a) shows the carbon concentration on the treated and untreated surface while figure 2(b) shows the oxygen concentration on the same two surfaces. Correlating the measured change in the WCA with the data from figure 2(b) it can be concluded that the increase in wettability of the PE surface after MSE-plasma treatment is due to incorporation of oxygen groups on the surface. The relatively lower concentration of carbon on the treated surface as compared to the untreated surface is due to the higher concentration of oxygen relative to carbon on this surface, after plasma treatment. It is important to note that the actual surface area of the holes in the MSE array is two to three orders of magnitude smaller than the total surface area of the PE film that was modified by the MSE-plasma. Yet, the wettability of the PE film, as measured by the WCA method, seems uniformly increased over the entire surface. The variation of WCA as a function of distance between the MSE and the PE film sample is shown in figure 3. All samples were treated for 5 min with 10% air in argon at a flow rate of 50 sccm and a total pressure of 50 mbar. In one series, the PE sample was facing the cathode surface of the MSE while in the second series, the PE sample was facing the anode surface of the MSE. As the MSE-PE distance is decreased from 11 mm to 4 mm, the WCA values of the treated surface decreases, as expected, indicating increasing wettability as the plasma source is brought closer to the substrate. However, at MSE-PE distances less than 4 mm, it was noticed that the WCA values for the PE surface facing the cathode actually increases i.e. wettability decreases, as the plasma source is brought closer to the substrate. It is also observed that for the treatment condition where the PE surface faces the cathode at a distance of 1mm, white spots are observed on the PE film corresponding

to the location of the MSE holes across the PE substrate. This was not observed for the samples facing the anode at short MSE-PE distances. Figure 4 shows the variation of WCA as a function of MSE-plasma treatment time, when the MSE-PE distance is maintained constant at 4 mm. The WCA is found to decrease as the treatment time increases from 0.5 min to 10 min and in this range of treatment time no saturation effect is observed.

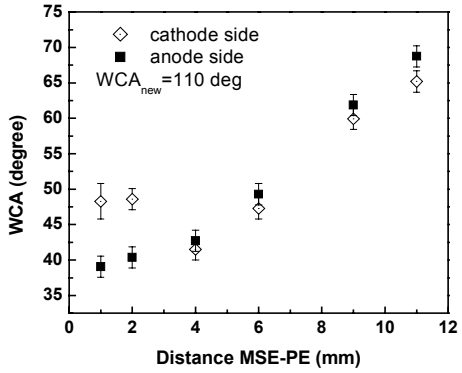


FIGURE 3. WCA variation in of plasma treated film with the MSE-PE distance.

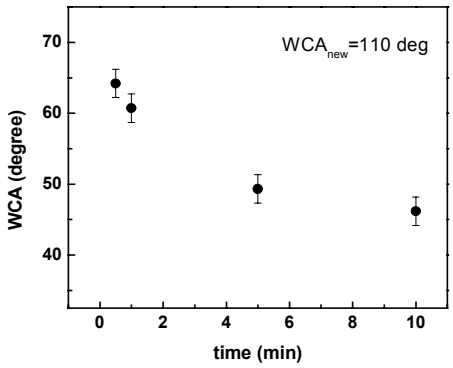


FIGURE 4. WCA variation of treated PE film surface, as function of treatment time.

Although WCA measurements indicated uniform surface modification across the PE film sample, it was expected that high resolution XPS analysis would provide more accurate data in terms of uniformity of oxygen concentration across the PE surface. In particular, this analysis is important for understanding whether the oxygen content on treated PE film varied in the region between adjacent MSE holes. To this end, extensive mapping of the oxygen content was performed using a small spot XPS unit, starting at a given hole position and moving towards the adjacent hole position while measuring the oxygen content at discrete intervals of 750 μm on the PE film.

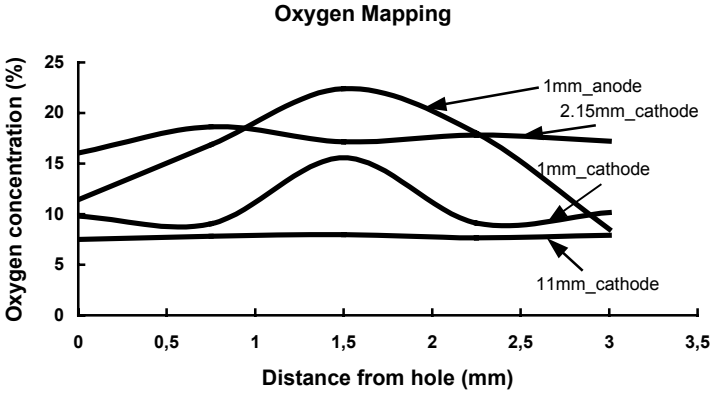
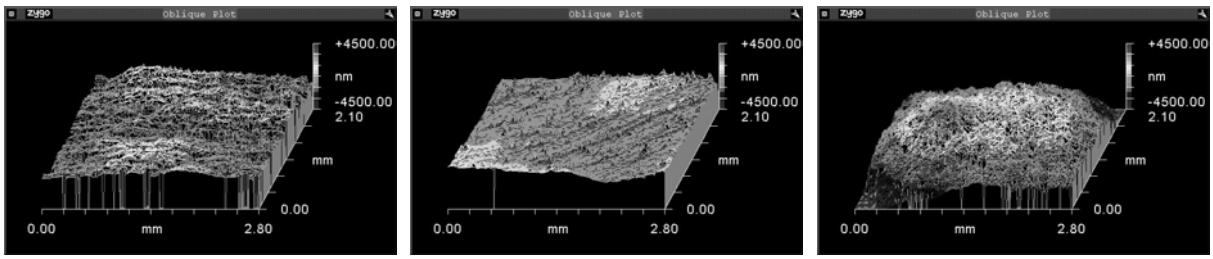


FIGURE 5. High resolution oxygen mapping on treated PE film as a function of MSE-PE distance and location between MSE hole positions.

Figure 5 shows the data of oxygen content at two adjacent hole positions (0 mm and 3 mm) and in the region between them, for MSE-PE distances of 1 mm, 2.15 mm, and 11 mm for the cathodic treatment and for MSE-PE distance of 1 mm for the anodic treatment condition. It can be seen that for MSE-PE distance of 1 mm, in both anodic and cathodic treatment, the oxygen content is actually higher in positions between the MSE holes than at the hole locations. Moreover, the concentration of oxygen is higher for anodic treatment than for cathodic treatment. In contrast, the oxygen concentrations for MSE-PE distance of 2 mm is relatively uniform at the hole positions as well as between hole positions. This indicates that, at shorter distances, there is a competition between oxygen incorporation and surface etching. Etching is more pronounced closer to the discharge location in the holes, leading to a lower oxygen concentration at the hole position compared to the region between holes.



a **b** **c**

FIGURE 6. Interferometric images showing the surface structure of a new sample (a) and of samples treated at the cathode (b) respective anode side (c).

Etching is also more pronounced for cathodic treatment than for anodic treatment. This observation is further supported by interferometric analysis of the surface which shows an extremely smooth surface for cathodic treatment while the anodic treatment retains the surface roughness of the original film sample (see figure 6). When the MSE-PE distance is increased to 11 mm, relatively little incorporation of oxygen is observed on the PE surface, explaining the very small decrease in WCA when the MSE-PE distance is increased during treatment.

5. CONCLUSIONS

The study performed here provides interesting conclusions regarding the use of MSE-arrays for surface modification of polymeric film substrates. We show that surface treatment is feasible with such electrode arrays, leading to physical and chemical modifications of the polymer surface. The degree of uniformity observed in the treatment is quite surprising, given that the area of the MSE discharge is several orders of magnitude smaller than the actual area of the surface treated. The process is non-thermal, as evidenced by the absence of any visual thermal stresses in the polymer film. The degree of surface modification is a function of the treatment time as well as the distance between the electrode array and the polymer surface. However, there is a clear competition between oxygen incorporation and surface etching that is quite pronounced at very short distances between the MSE array and the polymer substrate, especially when the polymer surface faces the cathode of the MSE array. A manuscript detailing other aspects of this study is currently under preparation.

ACKNOWLEDGMENTS

The authors like to thank Dr. M. Miclea from ISAS Dortmund, Germany for the interferometrical analysis. This work was supported by: Bundesministerium für Bildung und Forschung (BMBF), Verein Deutsche Ingenieure (VDI) and Graduiertenförderung Land Hessen. Partial support of this study by Procter and Gamble through a research grant to Wright State University is gratefully acknowledged.

REFERENCES

[1] K.-H. Gericke, H. Schmidt-Böcking, German Patent DE 196 05 226 C2, 1996.
[2] M. Roth, T. Haas, M. Lock, K.-H. Gericke, A. Bräuning-Demian, L. Spielberger, H. Schmidt-Böcking, Proc. of 1st Int. Conf. on Microreaction Technology, Springer, Berlin, 1998, pp. 62-9.
[3] K. H. Schoenbach, W. W. Byszewski, F. E. Peterkinand A. N. Dharamsi , US Patent No. 5 686 789, 1997.
[4] C. H. Kruger, T. G. Owano and C. O. Laux,, IEEE Trans. on Plasma Science, **25**(5), 1997, p. 1042.
[5] P. F. Kurunczi and K. H. Becker, Proc. of HAKONE VII, 2000, Greifswald, 2000, pp 491-5.
[6] A. Bräuning-Demian, L. Spielberger, C.Penache, H. Schmidt-Böcking, Proc. of the XIII GDA, Glasgow, 2000, pp. 426-9.
[7] C. Penache, C. Gessner, A. Bräuning-Demian, P. Scheffler, L. Spielberger, O. Hohn, S. Schössler, T. Jahnke, K.-H. Gericke and H. Schmidt-Böcking, SPIE Proc. **4460**, 2002, pp. 17-25.

NANO- AND MICRO-PARTICLES IN LOW-TEMPERATURE PLASMAS: OCCURRENCE, DYNAMIC PROCESSES, AND APPLICATIONS

S. Vladimirov[a] and K. Ostrikov[b,c]

a) School of Physics, The University of Sydney, Sydney 2006 NSW, AUSTRALIA
b) Plasma Sources and Applications Center, NIE, Nanyang Technological University, 637616, SINGAPORE
c) SOCPES, Flinders University, GPO Box 2100, Adelaide 5001 SA, AUSTRALIA

Abstract. An overview of occurrence of nano/micron-sized particles in low-temperature plasmas, associated physical phenomena, and industrial applications is presented. The most recent experimental and modeling efforts to understand the growth mechanisms of nano-clusters and micron-sized particulates in chemically active plasma environments are reviewed and the major implications of particulates in processing plasmas are discussed. Until recently, such particles were considered merely as a potential hazard for microelectronics manufacturing and a lot of effort was applied to remove them from the processing volume or suppress the gas-phase coagulation. Nowadays, fine clusters and particulates find numerous challenging applications, including production of fine metal or ceramic powders, cluster-unit thin film deposition, nanostructuring of substrates, nucleating agents in polymer and plastics synthesis, drug delivery systems, inorganic additives for sunscreens and UV-absorbers, as well as for mineral processing and environmental applications. Finally, several unique properties of the plasma-particle systems (colloid, or complex plasmas) are outlined and the most recent progress in this area is reviewed.

1. OCCURRENCE OF DUST PARTICLES IN SPACE AND LABORATORY

The complex plasma systems containing colloidal nano/microscopic particles are recently widely discussed in the physics and chemistry of plasmas, ionized gases, space physics and astrophysics, material research, etc. There are numerous reports on occurrence of small charged particles in interstellar space, planetary atmospheres, ring structures, cometary tails, etc. [1]. Under terrestrial conditions, dust particles are important parts of various colloid suspensions, charged aerosols, high-pressure ionized gas systems, nucleation catalysts, and many others [2]. Particulate powders with sizes in the micrometer range have also been detected in a number of laser light scattering experiments on low-pressure DC and RF plasmas for material synthesis and processing applications [3]. The presence of fine particles in a plasma strongly affects the fundamental properties such as distributions of electron/ion number densities, temperatures, electromagnetic fields, and plasma potentials. Under some conditions, the entire complex plasma system can self-organize into a strongly coupled Coulomb crystal-like or liquid structure, with strong electrostatic coupling between the colloidal particles [4]. Here, we discuss the most important current topics of origin and growth of nano/microscopic particles in low-pressure chemically active plasmas widely used for plasma-based synthesis and surface modification of advanced materials. We also review the role of fine powders in low-temperature processing plasmas and discuss challenging applications of nano/micron-sized particles in a number of high-tech industries. In particular, we explain why the accent in the fine particle research is now gradually shifting from the traditional view on them as not welcome process "killer" contaminants to the desired elements that dramatically improve the basic properties of plasma-made thin films. In this regard, the dynamic processes in the areas adjacent to material substrate involving dusts are of outmost importance. Some of these processes are discussed in Section 4. The outlook of major research directions in the area of complex plasma research for the coming few years is given as well.

[a] Electronic address: S.Vladimirov@physics.usyd.edu.au

2. ORIGIN AND GROWTH OF FINE PARTICLES IN CHEMICALLY ACTIVE PLASMAS

Here, we discuss the major processes involved in the generation and growth of mesoscopic dust particles in chemically active plasmas. Basically, the growth of fine powders in reactive plasmas starts with heterogeneous and homogeneous nucleation that control the formation of typically sub-nanometer/nanometer-sized protoparticles. The origin of protoparticles is followed by agglomeration and coagulation processes leading to pronounced particulate formation with a size of few tens of nanometers. Eventually, accretion of neutral or ionic monomers results in growth of sub-micron and micron-sized dusts. Large negative electric charge on larger particles appears to be a factor limiting further agglomeration/coagulation of particulates. Modern particle detection techniques (e.g. laser scattering) allow one to successfully monitor the growth and dynamics of submicron-sized particles. However, detection and diagnostics of nano-sized particles as well as investigation of the complex physical/chemical mechanisms leading to nucleation of particle precursors, appears to be a challenging problem for the coming years. At present, it is believed that the basic particle formation mechanisms are well understood in silane (SiH_4) plasmas used for advanced silicon technology applications (ULSI silicon devices, solar cells, flat displays, etc.)[5]. Few attempts to model plasma chemistry and growth of nano-sized particles in hydrocarbon (e.g. methane, CH_4 or acetylene, C_2H_2) discharges have recently been reported [6].

The recent steady-state homogeneous model [7] aims at explaining the initial particle growth in a pure silane discharge. The model assumes that the particles grow primarily from SiH_3^- anions and SiH_m radicals, first into Si_xH_m radicals. While the silicon atom number increases, large clusters, and eventually primary silicon particles are formed. Substantial experimental and theoretical efforts have been made in order to identify the fine powder precursors and the dominant gas-phase reactions leading to generation of larger particulates containing 10^4-10^6 silicon atoms. However, up to now there is yet no consensus on the question what are the dominant precursors for the nanoparticle generation. Silane neutral radicals are good candidates for such a purpose as being capable of incorporating into larger-mass saturated molecules. Positive ions can also be potential powder precursors despite high activation barriers preventing the formation of higher-mass cations. On the other hand, negative hydrosilicon ions can be efficiently trapped and levitated in the plasma sheath/presheath areas and play a key role in the plasma-enhanced polymerization. Under certain conditions, a large number of negative ions can be confined to accumulate and grow towards higher and higher masses in a similar way as the homogeneous model suggests [7]. Subsequent time-resolved mass-spectrometry data have confirmed that the negative ions are the most probable precursors of the nanoparticle generation in RF silane plasmas at low and moderate power densities [5]. Above all, it is likely that the polymerization proceeds via the negative ion clustering reaction

$$Si_nH_x^- + SiH_4 \rightarrow (Si_{n+1}H_y^-)^* + (H, H_2 \text{ products}),$$

where $(Si_{n+1}H_y^-)^*$ is the higher-mass anion in the excited state. At the second stage, the particulate formation proceeds by agglomeration (quick phase) of small clusters into larger (typically ~ 40-50nm) particles, where neutral atoms/molecules can play an important role [8]. Finally, after the rapid growth or the coagulation phase, the particle size increases only slowly and with rates comparable with the corresponding thin film growth rates. On the other hand, quickly agglomerating silicon clusters noticeably affect the plasma stability giving rise to so-called α - γ ' transitions [5,9]. It is also worth noting that nano/micron-sized particles of numerous materials (graphite, titanium, copper, aluminum, etc.) can be successfully generated in plasma-enhanced sputtering facilities [10].

3. APPLICATIONS OF NANO/MICRON-SIZED PARTICLES

Traditionally, plasma enhanced chemical vapor deposition (PECVD) systems for deposition and microstructuring of silicon films for microelectronic devices suffered from gas-phase polymerization of micron-sized and nano-sized particles. Indeed, the fallout of submicron-sized particles can be a killer effect for the microstructured wafers with the achieved feature sizes of microns to fractions of

microns. Furthermore, particle contamination can result in pinholes, delamination and interconnection shorts or opens in ULSI structures. Data storage disks are also affected by read-write errors, damaged sectors, and total failure caused by excessive dust contamination. In the last few years, there has been a notable progress in developing the efficient techniques to remove micron-sized particulates from the reactor volume or suppress nanoparticle growth processes at the initial stages [11]. Therefore, the nano-sized gas-phase nucleated silicon-based particles generated in large amounts in the prevailing sub-micron silicon plasma technologies are too small to be of any concern [12]. However, it is expected that within next ten years, the feature size of microelectronic circuit elements will shrink to 50nm, and removal/suppression of growth of nanoparticles from the reactor volume will become a critical issue.

Apart from the traditional hazardous aspect, fine particles have recently emerged as useful elements of a number of challenging applications in material engineering, optical coatings, polymer industry, mineral/ore processing and several others. In particular, nano-sized particles can be efficiently combined with polymeric/ceramic materials to form a variety of novel nano-structured materials for optoelectronic, protective coating, and fire-resistant and other applications. Furthermore, fine powders of ~10 nm-sized particles are extensively used as improved nucleating reagents for plastics, inorganic, ultra-fine UV-absorbing additives for outdoors applications. Currently, zinc-oxide nano-powders capture more than a half of Australian sunscreen market. Other applications include cosmetics, inks, pigments, textiles, wear-resistant ceramics, improved nano-crystalline materials, air and water pollution control, waste management, colloidal suspensions for mining, metallurgical, chemical, pharmaceutical industries, and food processing.

Most recently, nano-sized particles have emerged as the key elements of several technologies allowing one to manipulate the properties of the matter at nanoscales and synthesize previously unknown powder-assembled materials with unique nano-scale architectures, morphologies, as well as optical, thermal, catalytic, mechanical, structural and other properties. The quickly emerging applications of nano-sized particles include nanostructured and nanocomposite films, nanocrystalline powders and consolidated structures, nanoparticle superlattices and other 3D assemblies that represent new forms of supramolecular crystalline matter, nano-scale inorganic synthesis, dispersions and suspensions with controlled fluid dynamic properties, nano-sized single/few-electron data storage units and many others.

Plasma-based CVD methods have recently proved very efficient in fabrication of various nanostructures wherein the gas-phase grown nanoparticles play a pivotal role. Thus, the question about the controlled dynamics of fine particles in the areas adjacent to the structure being fabricated becomes critical. In the following section, we discuss several factors affecting the dynamics of dust particles in low-temperature processing plasmas.

4. DYNAMIC PROCESSES IN COMPLEX PLASMA SYSTEMS

In this section, we give a few examples of dynamic processes in complex plasma systems. Since most of the laboratory plasmas have natural boundaries such as chamber walls, internal electrodes, substrate holders, etc., a large number of experiments with plasma-particle systems involved investigation of dynamic processes in the vicinity of the boundaries. The transition area between the plasma and the boundary includes sheath and pre-sheath regions [13] where dust grains can levitate due to a dynamic balance of several forces acting on a particle. Such forces include but not limited to the force of gravity, electrostatic force, ion and neutral drag forces, etc. [14]. Since the plasma parameters vary dramatically in the sheath/pre-sheath areas, so does the equilibrium electric charge on a particle, which dynamically affects the force balance while the particle moves towards the wall. Another key feature of the plasma-wall transition areas is the presence of established supersonic ion flows directed to the walls [15] that can affect levitation and dynamics of dust particles. We thus focus here on reviewing the dynamic processes of dust levitation in the near-wall areas of argon [16] and fluorocarbon [17] plasmas, effects of ion flows on levitation of rod-like particles [18]. Self-excited vertical oscillations of dust grains in capacitively coupled RF discharge in argon [19] will be discussed as well.

Equilibrium, stability, and levitation of dust particles in collisional argon plasmas with an ionization source are investigated in Ref. [16]. Vertical motions of the dusts in the near-wall area are considered by self-consistently including the dependence of the dust charge, ion flow velocity, electron/ion number density, etc., on the local position in the sheath/pre-sheath region. It is demonstrated that an increase of the ionization rates strongly affects the equilibrium positions of the dust particles, shifting them towards the electrode as well as elevating the maximum equilibrium grain size that can be levitated in the near-electrode area. Below we briefly discuss how the change of the ionization power in the discharge can affect dust charge distributions. If the experiment is started with low input powers, which increases thereafter, the maximum size of levitating particles tends to increase. Meanwhile, the dusts become confined closer to the electrode. On the other hand, subsequent decline in the ionization power can result in diminishing of the equilibrium size of particles capable of levitating, with the heaviest grains falling down to the electrode. In this way, the charge/mass distribution of dust grains can be substantially modified, leaving only smaller (lighter) particles levitating in the sheath/pre-sheath area. For another options of control of the dynamics of nano/micron-sized particles in the near-wall areas the reader can be referred to the original article [16].

Charging and confinement of nano/micron-sized particles in near-electrode regions of octafluorocyclobutane – argon (c-C_4F_8 + Ar) etching plasmas is considered in Ref. [17]. Such chemically active plasmas often feature a very high degree of electro-negativity, with the integral number density of fluorine negative ions compared with the electron density. The model near-electrode area comprises the electronegative and electropositive pre-sheath regions as well as the sheath itself. The composition of the plasma is representative to quadruple mass spectrometry experiments in low-pressure RF inductively coupled and microwave surface-wave sustained plasmas of 10% c-C_4F_8 + 90% Ar gas mixtures for deep-micron ultra-fine selective etching of silicon [20]. It is shown that the equilibrium particle charge in the electronegative region is lower than would be in electropositive plasmas, and increases towards the electrode. In the vicinity of the wall, the ion density decreases, so does the charge on nano/micron-sized particles. The negative ions affect the particle charging and levitation through notable modification of the sheath/pre-sheath structure. Meanwhile, the particle dynamics in nearly the whole near-wall area is controlled by competition of the electrostatic and ion drag forces, whereas other forces play the role only in the electronegative plasma bulk.

The interaction of rod-like charged particles with ion flows in the near-wall region of low-temperature plasma is studied in Ref. [18]. It is well known that ion flows strongly influence formation of dust-plasma crystals as well as aligned particle structures in the direction of ion flows [4]. Physically, according to Bohm's criterion, ion flows in the plasma sheaths are supersonic, which naturally leads to excitation of wake fields that affect levitation of dust grains and self-consistently generate the attracting wake potentials between the grains of the like electric charge [15]. Article [18] reports a new step in the study of interactions of dust particles with the established ion flows by involving elongated (rod-like) particles into consideration. In many experiments, such particles typically have longitudinal size of few tens to few hundreds of microns while their transverse size is just few tens to few hundred nanometers. To a certain extent, such particles can successfully model elongated nanostructures that can be grown in the plasma bulk, like carbon/silicon nanowires, nanorods, nanotubes, etc.

Likewise, self-excited vertical oscillations in a sheath region of the RF discharge (0.5-20 Pa, 15 MHz capacitively coupled argon plasmas) dusty plasma have been observed [19]. Micron-sized carbon particles have been dispensed into the plasma. Thereafter, the dusts acquire sufficient negative electric charge for the electric force in a sheath region to compensate the forces of gravity and ion drag forces so that they can stay in equilibrium vertical positions. It was found that when the pressure decreased below a critical value, the dust particles began to oscillate spontaneously in the vertical direction, with the amplitude and frequency of few millimeters and about 10 Hz, respectively. A decrease in RF power leads to an increase of the amplitude of the oscillations. In particular, a dramatic increase in the amplitude of oscillations was observed in the pressure range below 4.5 Pa. Two possible excitation mechanisms, which treat a dust plasma layer as a static or dynamic dissipative structure [13], and account for spatial variation of the dust charge and instability of the layer of charged particles as a virtual wall (resonator), have been proposed. Naturally, the few examples considered above do not

cover the variety of dynamic phenomena in bounded complex plasma systems, and the interested reader can be referred to other publications on the subject [21].

5. OUTLOOK AND CONCLUSION

The fine particles are ubiquitous to a number of space and laboratory environments. The role of such particles in plasma processing and materials synthesis applications is rapidly increasing. The major attention they have recently attracted is due to tremendous advance in nanoscience and technology. In particular, the remarkable interest to the plasma production of nanocrystalline silicon particles is regarded as a new challenging route for fabrication of nanostructured silicon thin films [22]. This opens a new horizon of problems associated with the precise control of the size and number density of gas-phase grown silicon-based nanocrystals. Furthermore, the detailed physics and chemistry leading to particle generation and subsequent growth still remains a challenge for theoretical, computation, and experimental efforts for the next few years. The understanding of nano/micron-sized particle origin and growth should be extended to more complex reactive plasma chemistries relevant to advanced fabrication processes at nano-scale. Hence, greater modeling and computation efforts should be directed towards investigation of complex dynamic phenomena, including charging, motion, levitation of nano/micron-sized particles in near-electrode areas of chemically active plasmas. Experimentally, diagnostics of complex plasma systems with nano-sized colloid particles should include real-time, *in situ* monitoring of dynamic variations of nanoparticle size and chemical composition simultaneously with the plasma species number densities and composition.

ACKNOWLEDGMENTS

The work was partially supported by the Australian Research Council and the Agency for Science, Technology and Research (Singapore).

REFERENCES

[1] Goertz C. K., *Rev. Geophys.* **27**, 271 (1989)
[2] Garscadden A., Ganguly B. N., Haaland P. D., and Williams J., *Plasma Sources Sci. Technol.* **3**, 239-45 (1994)
[3] *Dusty Plasmas: Physics, Chemistry, and Technological Impacts in Plasma Processing,* Edited by A. Bouchoule, J. Wiley & Sons, 1999.
[4] Thomas H. M. and Morfill G. E., *Nature (London)* **379**, 806-9 (1996)
[5] Hollenstein Ch., Plasma Phys. Contr. Fusion 42, R93-101 (2000)
[6] Stoykov S., Eggs C., and Kortshagen U., *J. Phys. D: Appl. Phys.* **34**, 2160-73 (2001)
[7] Gallagher A., *Phys. Rev.* **E 62**, 2690-2706 (2000)
[8] Bingham R. and Tsytovich V. N., *IEEE Trans. Plasma Sci.*. **29**, 158-63 (2001)
[9] Fridman A. A., Boufendi L., Hbid T., Potapkin B. V., and Bouchoule A., *J. Appl. Phys.* **79**, 1303-14 (1996)
[10] Samsonov D. and Goree J., *Journ. Vac. Sci. Technol.* **A17**, 2835-44 (1999)
[11] Watanabe Y., Shiratani M., and Koga K., *Phys. Scripta* **T89**, 29-32 (2001)
[12] Bhandarkar U. V., Swihart M. T., *et. al. J. Phys. D.: Appl. Phys.* **33**, 2731-46 (2000).
[13] Tsytovich V. N., Vladimirov S. V., and Benkadda S., *Phys. Plasmas* **6**, 2972-9 (1999)
[14] Barnes M. S., Keller J. H., Forster J. C., O'Neal J. A., and Coultas D. K., *Phys. Rev. Lett.*, **68**, 313-6 (1992)
[15] Vladimirov S. V. and Nambu M., *Phys. Rev.* **E52**, 2172-77 (1995); Vladimirov S. V. and Ishihara O., *Phys. Plasmas* **3**, 444-9 (1996).
[16] Vladimirov S. V. and Cramer N. F., *Phys. Rev.* **E62**, 2754-62 (2000)
[17] Ostrikov K. N., Kumar S., and Sugai H., *Phys. Plasmas* **8**, 3490-7 (2001).
[18] Vladimirov S. V. and Nambu M., *Phys. Rev.* **E64**, 026403 (7 pages) (2001)
[19] Samaryan A. A., James B. W., Vladimirov S. V. and Cramer N. F., *Phys. Rev.* **E64**, 025402(R) (2001)
[20] Kokura H., Yoneda S., Nakamura K., *et al*, *Jpn. J. Appl. Phys.* Part 1, **36**, 3730-6 (1999).
[21] See, e.g., http://www.physics.usyd.edu.au/~vladimi/papers/
[22] Roca i Cabarrocas P., *Bull. Amer. Phys. Soc.* **46**, No.6, 49-50 (2001)

MODIFICATION OF POLYOLEFINS IN NITROGEN ATMOSPHERIC PRESSURE GLOW DISCHARGES

S. Guimond[a], I. Radu[a], G. Czeremuszkin[b] and M.R. Wertheimer[a]*

a) Groupe des Couches Minces (GCM), Department of Engineering Physics, Ecole Polytechnique, 2900 Edouard-Montpetit, C.P. 6079, Succ. Centre-Ville, Montreal (Quebec), H3C 3A7, CANADA.
b) Nova-Plasma Inc., Montreal (Quebec), CANADA.

Abstract: X-ray photoelectron spectroscopy (XPS) and contact angle measurements were used to characterize the surface modification and possible production of low molecular weight reaction products on biaxially oriented polypropylene (BOPP) and on low density polyethylene (LDPE) films treated by atmospheric pressure glow discharge (APGD) in pure nitrogen and by air corona. We have observed that surface degradation is more pronounced for air corona treatments in the case of both polymers.

1. INTRODUCTION

Polymers generally lack sufficiently high surface energy, γ_s, and the required surface chemistry for many applications that call for wettability, adhesion and biocompatibility, for example. To alleviate this problem, polymer surfaces are now routinely treated in industry using plasmas, namely corona (filamentary) discharges in air, low-pressure glow discharges, and flames. However, all of these treatments have certain characteristic drawbacks. In earlier communications [1, 2], we have shown that Atmospheric Pressure Glow Discharges (APGD) in N_2 gas, which are characterized by different physics and chemistry than the other discharge types mentioned above, can be used advantageously for the surface modification of polypropylene. N_2 APGD is a homogeneous (i.e. non-filamentary) discharge that can be obtained in a flow of very pure nitrogen, using the same dielectric barrier discharge (DBD) configuration as the one encountered in (air) corona treatment systems. We have found that N_2 APGD treatment can lead to much higher γ_s values for biaxially-oriented polypropylene (BOPP) surfaces (γ_s ~ 57 dynes/cm) than air corona treatments (γ_s ~ 40 dynes/cm). The advantages provided by APGD over the other "conventional" methods for the treatment of polymer films have lately generated much industrial interest, as illustrated by the recent marketing of APGD treating stations [3]. Besides the possibility to increase the surface energy of a film to a value required for a given application, another major concern is commonly encountered in the polymer film converting industry: the treatment-induced surface degradation of polymer surfaces (and resulting production of "Low Molecular Weight Oxidized Materials", LMWOM [4, 5]). We have investigated this aspect for the cases of corona and N_2 APGD treatments, and it is reported in the present communication. LMWOM generation on polyolefin surfaces by high energy-dose air corona treatments has been reported by several authors [4-6]. These reaction products, which mainly consist of oxidized oligomers, are believed to be generated by cleavage of C-C bonds in the polymer chains during the free-radical oxidation process [5, 7]. These light oligomers have greater mobility than intact polymer chains and they are generally observed to agglomerate as "mounds" or "nodules" on the film surface, probably owing to surface tension effects [5]. They are also quite readily removed from the surface by rinsing with polar solvents. The presence of such a low-cohesion layer can therefore potentially harm applications of the film which require good adhesion, for instance. In the present work, we extend our investigations to a second polyolefin, low-density polyethylene (LDPE), and we compare γ_s measurements of corona- and N_2 APGD-treated BOPP and LDPE films. Surface degradation and the

* Electronic address: mwertheimer@courriel.polymtl.ca

production of "LMWOM" during the treatments of these two polymers are compared, for both N_2 APGD and air corona treatments.

2. EXPERIMENTAL METHODOLOGY

2.1. Polymer characteristics

The polypropylene used in this study is a melt-extruded, isotactic, biaxially-oriented film (BOPP) obtained from the 3M Company. The film is 50 μm thick. The base resin contains approximately 200 ppm of an inorganic acid scavenger and about 1000 ppm of a high molecular-weight hindered phenolic antioxidant. It is also characterized by a melting point of 163°C, a weight-average molecular weight of 3.6 x 10^5, and a polydispersity index of 4.0. The second polymer used is a melt-extruded, low density polyethylene (LDPE) film supplied by Chevron Phillips Chemical Company; it is 35 μm thick and contains no additives. The base resin has a weight-average molecular weight of 1.2 x 10^5 and a polydispersity index of 5.3. No oxygen was detected by XPS on the untreated surfaces of either film. Using the method of Owens and Kaelble [8], surface energies (γ_s) of 27±1 dynes/cm and 28±1 dynes/cm have been measured for the untreated BOPP and LDPE, respectively.

2.2. DBD plasma treatments

The DBD experimental setup, which has been used for both N_2 APGD and corona treatments, is presented schematically in Fig. 1. The same system was used in our previous work, and its detailed description can be found elsewhere [1, 2]. Briefly, it consists of a 29 cm x 24 cm grounded Al plate electrode that can be moved at precisely controlled speed under a cylindrical, high-voltage electrode. Both electrodes are covered with a dielectric, the polymer film to be treated being placed on the top surface of a thin glass plate on the grounded electrode.

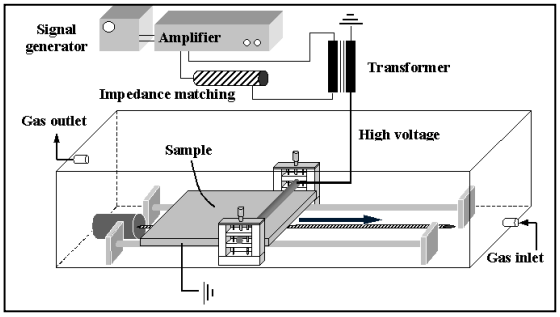


FIGURE 1. Schematic view of the DBD treatment experimental set-up.

In this study, the inter-electrode gas gap was fixed at 1 mm. The entire system is housed in a hermetic Plexiglas enclosure, which is continuously flushed with a 9 slm flow of the desired treatment gas (dry air for corona, and Air Liquide UHP-grade nitrogen for APGD). For all the treatments, the enclosure was purged for 15 minutes before igniting the discharge. In the case of N_2 APGD treatments, the very pure gas flow was then directed into a diffuser, which supplies the region of the system where the discharge is generated. This assures a very low level of impurities in the treatment zone, both from the feed gas and from a build-up of volatile products from the discharge-treated surface. This is necessary since, as shown by Miralaï *et* al [9], N_2 APGD can revert to a filamentary discharge if a small concentration (a few hundred ppm) of impurities in the gas is exceeded. To establish whether the discharge is of the glow or filamentary type, the photomultiplier signal of light emitted from the gap and the discharge current waveform have been monitored. In the case of APGD, only a single broad peak is observed per half cycle of the applied voltage; in contrast, filamentary discharges display many short (~100 ns) pulses of varying amplitude during each half cycle. For both treatment types, the energy density, E_d, has been calculated using the following formula:

$$E_d = \frac{V_{rms} \cdot I_{rms} \cdot \cos\phi}{w \cdot s} \cdot n \qquad (J/cm^2)$$

where ($V_{rms} \cdot I_{rms} \cdot \cos\phi$) is the electrical power dissipated in the gas (in W), *w* is the width of the discharge zone (24 cm), *n* is the number of passes of the film through the discharge zone, and *s* is the effective speed of movement under the electrode (in cm/s). In turn, $s = l/t$, where *l* is the "length" of the discharge zone (~1cm) and *t* is the residence time. Discharge frequencies, f, of 1 kHz and 4 kHz have been used for all corona and N_2 APGD treatments, respectively; in earlier work we found treatment results to be independent of f, for 1 kHz ≤ f ≤ 6 kHz [2].

2.3. Analytical procedures

Treated surfaces were analyzed by X-ray photoelectron spectroscopy (XPS) and by contact angle goniometry with several probe-liquids, using the method of Owens and Kaelble [8]. This latter method allows one to determine the total surface energy (γ_s), along with its polar (γ_s^p) and dispersive (γ_s^d) components, the liquids used being water, glycerol, formamide, ethylene glycol, and tricresyl phosphate. XPS analyses were performed in a VG ESCALAB 3MkII system, using non-monochromatic Mg Kα radiation. Spectra were acquired at a take-off angle normal to the sample surface, and the binding energies were referenced to the carbon (C1s) peak at 285.0 eV, to adjust for possible charging effects. To study the production of "LMWOM"* by the air corona and N_2 APGD treatments of both polymers, surface energy and XPS data were obtained in conjunction with the washing of some films following treatment at different E_d values: immediately after each treatment, a piece of every treated sample was immersed in a bath of deionized water for one minute, then dried for one hour in ambient air. Following this, contact angle measurements were made on both the washed and unwashed portions of the sample. XPS data were acquired within at most one or two days after treatments.

3. RESULTS AND DISCUSSION

The evolution of γ_s as a function of E_d for both washed (open symbols) and unwashed (full symbols) air corona treated BOPP samples is shown in Fig. 2 (b). Corresponding values of the surface oxygen concentration, [O] (at.%), determined by XPS, are shown in Fig. 2 (a). Here, only oxygen is incorporated at the surface, but no detectable nitrogen. Inspecting Fig. 2(a), we note that much of the oxidized surface material, presumably LMWOM, is removed when the sample surfaces are washed in water. Furthermore, this amount increases with increasing E_d values, beginning near $E_d \approx 0.01$ J/cm^2. Strobel *et al* [5] reported a comparable "LMWOM threshold" ($E_d \approx 0.05$ J/cm^2) for their corona treatment of a similar BOPP film. Interestingly, for E_d values above this threshold, all washed samples possess the same [O] values (≈ 4%), while Fig. 2 (b) shows that they also have the same surface energies, $\gamma_s \approx 33$ dynes/cm. A simple explanation may be proposed, based on the free radical oxidation mechanism [5, 7]: it comprises many simultaneous reaction pathways which lead to both oxidized functional groups on the polymer chains, and to chain scissions. For E_d values below the "LMWOM threshold", [O] increases rapidly by oxidation of the polymer chains, but there are few chain scissions. As E_d is further increased, however, scission reactions become more abundant, giving rise to the formation of light, water-soluble oxidized oligomers, but to no further oxidation of the macromolecular chains. It should be emphasized that the presence of LMWOM at the surface renders the validity of contact angle data or similar measurements highly questionable. Indeed, the thermodynamic interpretation of such data assumes that the probe liquid is not "contaminated" or modified by its contact with the surface. In order to compare "LMWOM" production by air corona and N_2 APGD treatments of BOPP, XPS and contact angle measurements, combined with water washing, have also been carried out following N_2 APGD treatments (see Figs. 3 (a) and (b)). Comparing Figs. 2 (b) and 3 (b), we note that, even after washing, N_2 APGD results in a significantly higher γ_s value (≈ 40 dynes/cm, versus ≈ 33 dynes/cm for corona). This is substantiated in Figs. 2 (b) and 3 (b) by the fact that the concentrations of heteroatoms ([O] and [N]) on the washed surfaces is higher following APGD treatment (8% vs 4% for corona).

---

* We use the term "LMWOM" also for N_2 APGD treated samples, even though the chemical composition of these light reaction products differs greatly from corona-generated LMWOM.

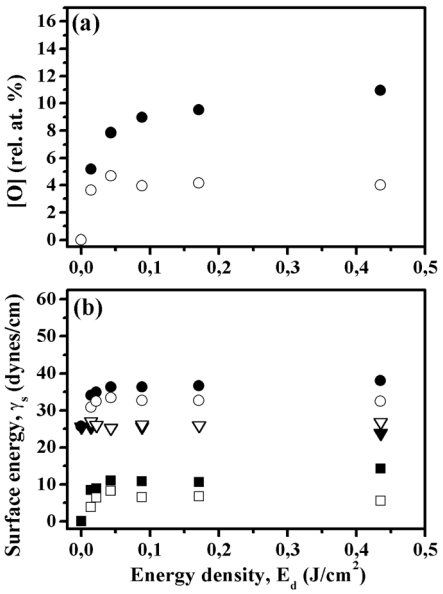


FIGURE 2. Effect of water washing on air corona-treated BOPP, as a function of the energy dose, E_d. (a): Surface concentration of oxygen, [O]. (b) Surface energy, γ_s, (●) and its polar, γ_s^p, (■) and dispersive, γ_s^d, (▼) components. Open symbols pertain to the washed samples.

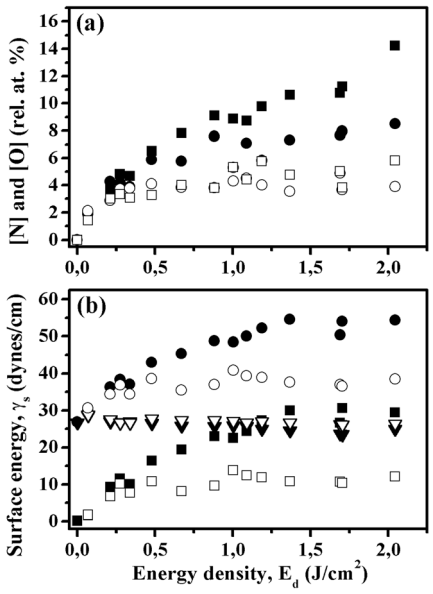


FIGURE 3. Effect of water washing on N_2 APGD-treated BOPP, as a function of the energy dose, E_d. (a): Surface concentrations of nitrogen, [N], (■) and oxygen, [O] (●). (b) Surface energy, γ_s, (●) and its polar, γ_s^p, (■) and dispersive, γ_s^p, (▼) components. Open symbols pertain to the washed samples.

The presence of bound oxygen after N_2 APGD treatment may result from some O_2 and H_2O "contaminants" present in the discharge, or from post-treatment reactions which can occur when the sample is reexposed to atmosphere [1, 2]. LMWOM generation with increasing E_d appears to follow a similar trend after N_2 APGD as was observed after corona (Fig. 2), except that the "LMWOM threshold" is now much higher ($E_d \approx 0.3$ J/cm^2, compared with 0.01 J/cm^2). The same comparative study has also been carried out for LDPE, as shown in Figs. 4 (a, b) for air corona, and in Figs. 5 (a, b) for N_2 APGD. Clearly, both treatment types result in higher γ_s values for LDPE than for BOPP. Also, comparing the "LMWOM threshold" values (Table 1), LDPE is clearly less prone to degradation than BOPP, in agreement with data from the literature [5, 6]. Finally, as in the case of BOPP, N_2 APGD treatment of LDPE leads to higher γ_s values than air corona. The higher E_d values required for N_2 APGD treatments are presumably due to the fact that molecular N_2 is quite inert, and that the energy required to generate "active nitrogen" (atomic or excited molecular species) is much higher than for the case of oxygen. All these comparisons are succinctly summarized in Table 1.

TABLE 1. "LMWOM threshold" doses, E_d*, and maximum surface energies after washing, γ_s max, for both polymers and both treatment types.

		γ_s max. (dynes/cm)	E_d* (J/cm^2)
BOPP	Air corona	33	0.01
	N_2 APGD	40	0.3
LDPE	Air corona	40	0.015
	N_2 APGD	45	0.5

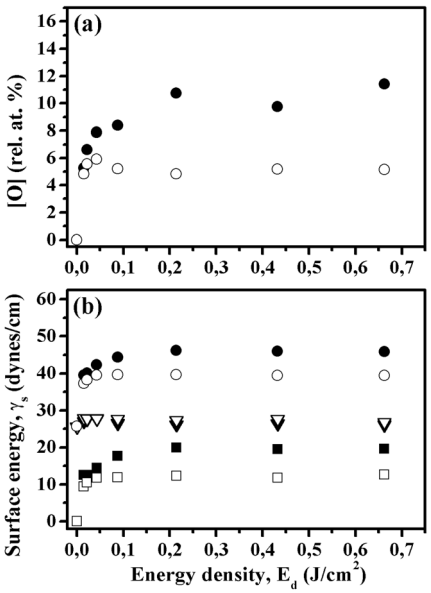


FIGURE 4. Effect of water washing on air corona-treated LDPE, as a function of the energy dose, E_d. (a): Surface concentration of oxygen, [O]. (b) Surface energy, γ_s, (●) and its polar, γ_s^p, (■) and dispersive, γ_s^p, (▼) components. Open symbols pertain to the washed samples.

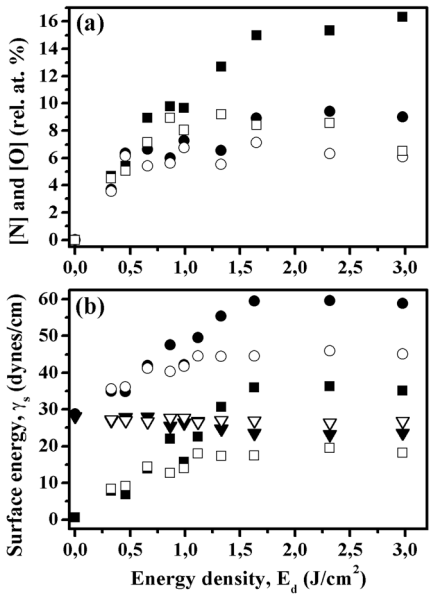


FIGURE 5. Effect of water washing on N_2 APGD-treated LDPE, as a function of the energy dose, E_d. (a): Surface concentrations of nitrogen, [N], (■) and oxygen, [O] (●). (b) Surface energy, γ_s, (●) and its polar, γ_s^p, (■) and dispersive, γ_s^d, (▼) components. Open symbols pertain to the washed samples.

4. CONCLUSION

We have shown that surface degradation occurs at higher E_d values and to a lesser extent with N_2 APGD than with air corona treatment. Related to this, we also find that N_2 APGD allows higher γ_s values to be achieved on both polyolefins.

ACKNOWLEDGEMENTS

This work constitutes part of the scientific program of the NSERC Industrial Research Chair on Plasma Processing of Materials. The authors wish to thank Dr Mark Strobel (3M Company) and Mr. Gary Jerdee (Chevron Phillips Chemical Company) for kindly providing the BOPP and the LDPE materials, respectively.

REFERENCES

[1] Guimond S., Radu I., Czeremuszkin G., Carlsson D.J. and Wertheimer M.R., SVC 44th Ann. Tech. Conf. Proc., pp 347-352 (2001).
[2] Guimond S., Radu I., Czeremuszkin G., Carlsson D.J. and Wertheimer M.R., *Plasmas and Polymers* **7**, 71 (2002).
[3] http://www.enerconind.com
[4] Kim C.Y. and Goring D.A.I., *J. Appl. Polym. Sci.* **15**, 1357 (1971).
[5] Strobel M., Dunatov C., Strobel J.M., Lyons C.S., Perron S.J. and Morgen M.C., *J. Adhesion Sci. Technol.* **3**(5), 321 (1989).
[6] Gerenser L.J., Elman J.F., Mason M.G. and Pochan J.M., *Polymer* **26**, 1162 (1985).
[7] Briggs D., Kendall C.R., Blythe A.R. and Wootton A.B., *Polymer* **24**, 47 (1983).
[8] Kaelble D.H., *Physical Chemistry of Adhesion*, ch 5 and 13, Wiley, New York (1971).
[9] Miralaï S.F., Monette E., Bartnikas R., Czeremuszkin G., Latrèche M. and Wertheimer M.R., *Plasmas and Polymers* **5**(2), 63 (2000).

LASER ABLATION AND AEROSOL PARTICLES

P. Paris[a], M. Laan and H. Valtna.

The University of Tartu, Institute of Experimental Physics and Technology.

Abstract: In the paper the electrical parameters of plasma created by laser ablation are related with the regularities of corresponding particle spectrum. An explanation of a faint dependence of laser-created particle spectrum on humidity is given.

1. INTRODUCTION

We found [1] that under certain experimental conditions the spectrum of the laser-created aerosol particles is very similar to that created by pulsed streamer corona. At the same time the regularities of particle growth with humidity for these two cases differ considerably. Corona-created particles are hygroscopic, their concentration and the mean size grow rapidly with the growth of humidity [2]. In contrast, the laser-created particle spectrum is only weakly influenced by humidity. As it was assumed in [2] and proved later [3], the different influence of the water vapor is connected with active species produced by streamer corona. Another reason for the discrepancy could be that the water vapor diminishes the concentration of precursors needed for nucleation. In the plasma plume created by the radiation-surface interaction the concentration of charged particles is high. This gives a basis to consider that the ion-induced process [4] is the most likely mechanism of the nucleation. Consequently, the correspondence between charge carriers and particle spectrum should highlight the latter assumption.

The main purpose of the study is the comparison of trends caused by the humidity on the current pulses and on the particle spectrum, both induced by the laser ablation.

2. EXPERIMENTAL

2.1. Set-up

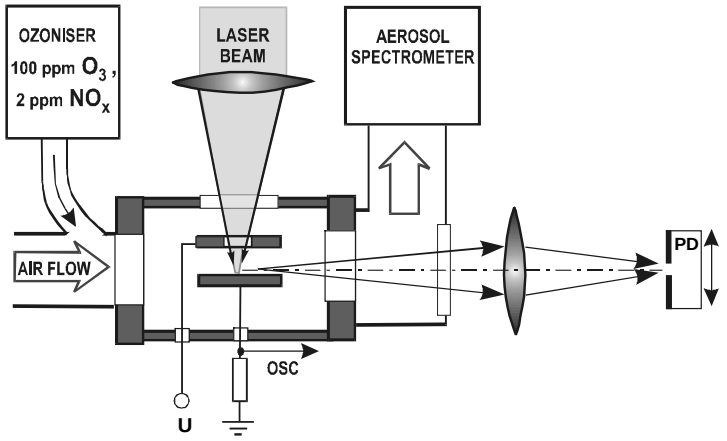


FIGURE 1. Sketch of experimental device

[a] Peeter.Paris@ut.ee.

The main parts of the experimental device are presented in Figure 1. Experiments are carried out in the flow of the filtered ambient air. Because of a high-efficiency filter the total background particle concentration is less than 10^3 cm^{-3}. The rate of the airflow is 1 l/s and it is possible to change the relative humidity RH in the limits 5 – 90 %. The temperature of the air is kept at 20 ^{0}C.

In some experiments gas from the external ozoniser is added to the main air stream; in these cases the air mixture entering the cell contains 45 ppm of O_3 and 1 ppm of NO_x.

Laser ablation is studied in a discharge cell. The distance between the cell electrodes is 6 mm. The radiation of a pulsed XeF laser (λ = 248 nm, energy per pulse 300 mJ, pulse duration 40 ns, repetition rate of pulses used is 0.5 – 5 s^{-1}) is focused on a target. In present experiments brass is used as the target material. In most of the experiments the area of the target irradiated is 3 mm^2. Using an attenuator the fluence of the laser beam at the target is changed in the limits 0.1 – 3 J·cm^{-2}. The target electrode is grounded over the resistor of 50 Ω and the voltage drop is measured by digital oscilloscope TDS-220. The opposite electrode of the cell with a hole in its center is stressed. Photodiode PD records the radiation of the plasma plume at difference distances from the target surface with 0.05-mm spatial resolution.

Aluminum pipeline of 80-cm length connects the discharge cell to the electrical aerosol spectrometer (EAS). The design and technical data of EAS are presented in [5]. The version of EAS, used in experiments, records particles starting from 3.2 nm in diameter. The measurement range is split into fractions uniformly in logarithmic scale. The noise-level of AES is ≈ 100 cm^{-3} per fraction. Recording-time of a spectrum is 10 s. In this study the averaging-time of spectra is set at 3 min.

2.2. Characteristics of laser ablation

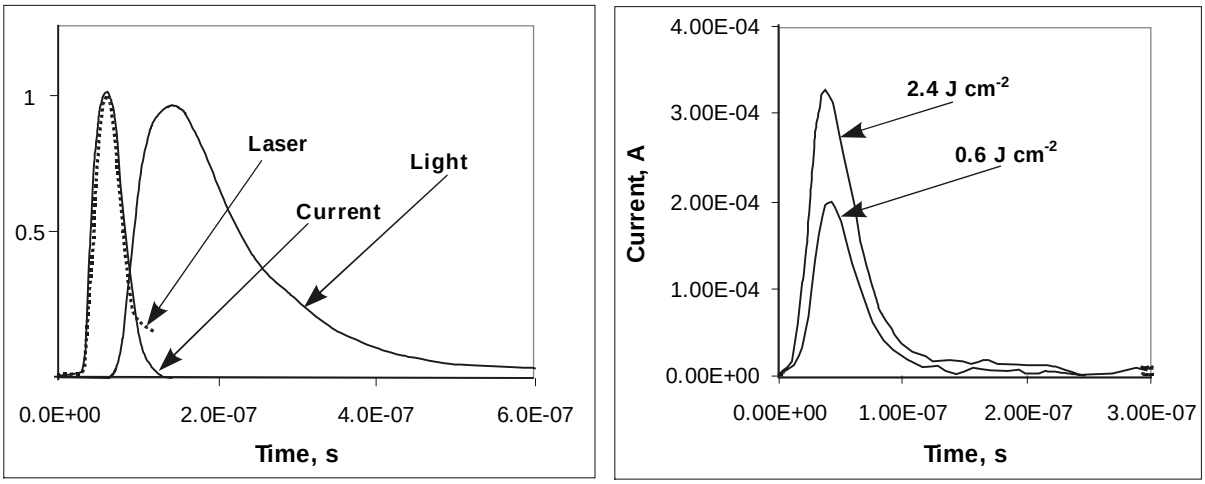


Figure 2. A - normalized temporal changes of laser pulse, current and light emitted by plasma plume at the distance 0.3 mm from target; **B -** current pulses for two different fluencies.

Figure 2A presents the time sequence of events observed in laser ablation. Independently of laser fluence and at DC bias voltages $|U| > 5$V, the waveform of the current pulse at its initial part almost follows that of the laser pulse. The half-width of the corresponding light pulse emitted by the plasma plume has a much longer duration. At the target surface the light emission starts simultaneously with the laser pulse and the larger is the distance from the target surface the later the light emission is recorded. The peak of current pulses is followed by a long tail lasting ≈ 250 ns (Figure 2B).

For all voltages used in experiment, the dependence of the peak value of the current as a function of the laser fluence (Figure 3A) demonstrates a slightly sublinear behavior. The fitting curves to the dependencies cross the X-axis at the fluence ≈ 0.1 J·cm^{-2}; the value may be treated as the onset of the laser ablation. At a certain fluence the amplitude of the current pulses is almost proportional to the bias voltage applied. From the viewpoint of the study the most striking dependencies are in Figure 3B: the

peak value of the current decreases exponentially with the relative humidity. The decay constants for all three dependencies are very close to each other.

Addition of ozone does not have any remarkable influence on current pulses.

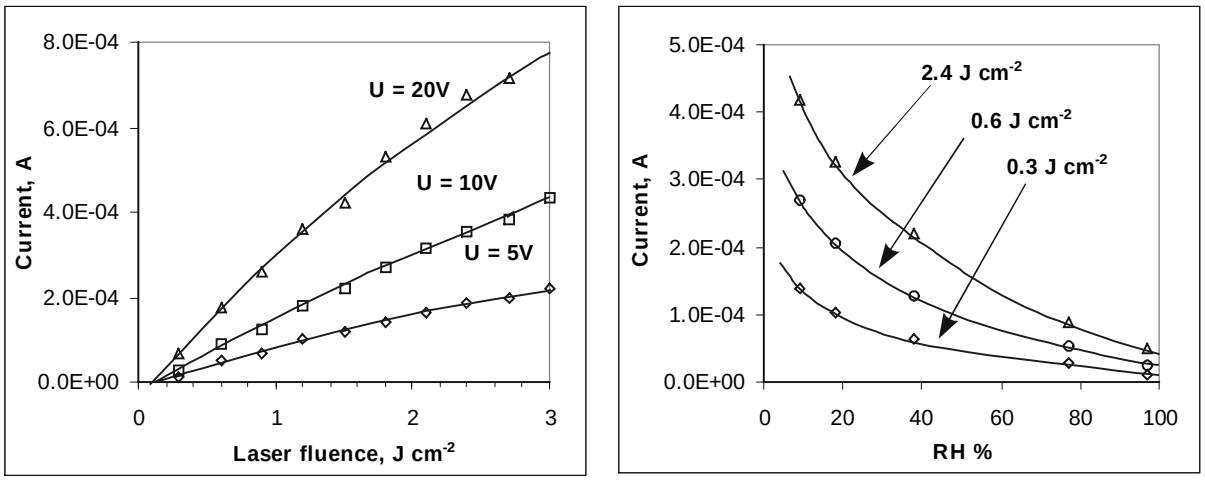


FIGURE 3. A - peak value of the current as a function of the fluence; **B -** peak value of the current as a function of relative humidity.

2.3. Aerosol spectra

The concentration of aerosol particles is proportional to the repetition rate of laser pulses. The particle spectrum has a strong dependence on the laser fluence and the addition of O_3/NO_x, but no reliable influence of the voltage applied to the discharge cell is observed. Near the ablation onset (0.1 J·cm^{-2}), the particles are recorded only at the first fractions of the spectrometer and their concentration is low (Figure 4A). A considerable part of the particles is out of the detection limit of EAS. At the fluence 0.6 J·cm^{-2} the concentration is two orders of magnitude higher, the maximum of the spectrum shifts to higher values of diameters and now the main part of particles is detectable.

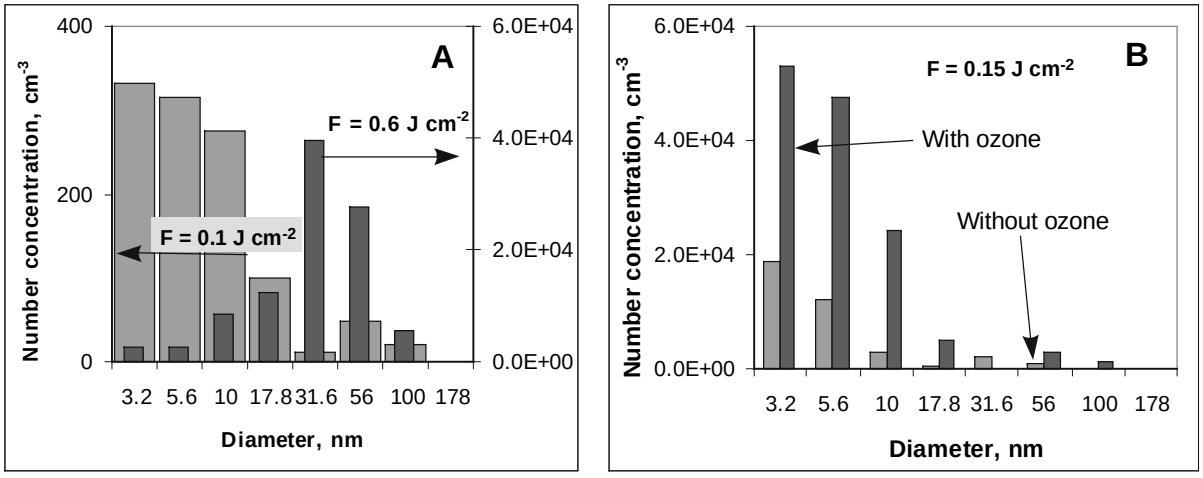


FIGURE 4. A - particle spectra for two fluence values, RH = 80 %; **B -** effect of O_3/NO_x addition; RH = 5 %

As it is found earlier [3], the addition of O_3/NO_x mixture leads to a considerable growth of particle concentration. The procedure gives a possibility to achieve more reliable/reproducible recordings near the ablation onset and especially at low values of the humidity. Figure 4B demonstrates the effect of ozone addition at a low value of the humidity: the spectral distribution remains unchanged but in every fraction of AES the concentration increases remarkably. Near the ablation threshold the growth of humidity causes a gradual increase in concentrations at the first fractions leaving the spectral

distribution unchanged (Figure 5). At higher values of the fluence the spectrum becomes more complicated and it is not presented here.

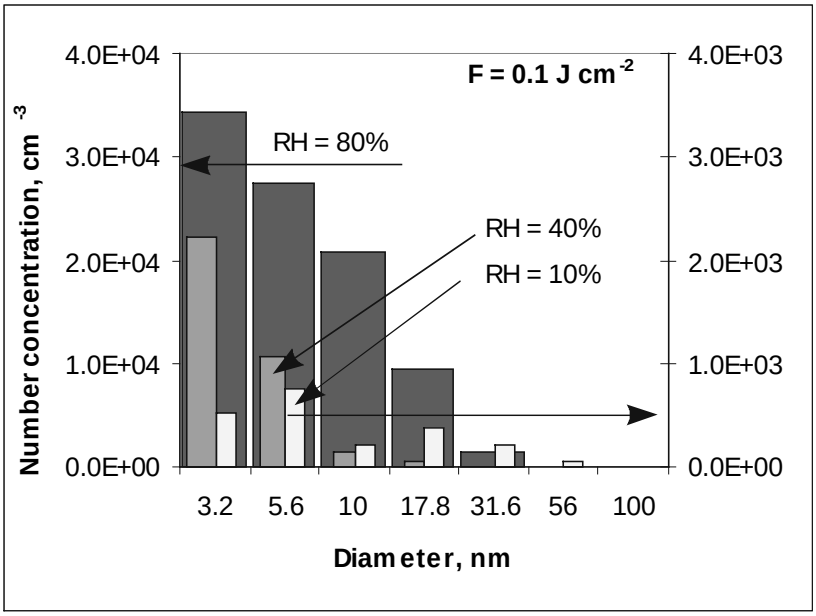


FIGURE 5. Particle spectra near the ablation onset for different relative humidities; air + O_3/NO_x mixture.

3. DISCUSSION

Starting from the ablation onset fluence ≈ 0.1 J·cm^{-2} plasma plume forms near the target surface. Because of a short laser wavelength the absorption of the radiation in plasma plume is small and the plasma current is almost a linear function of the laser fluence (Figure 3A). The current pulse recorded (Figure 2) reflects mainly the drift of electrons. As the electric field between the cell electrodes is low, during the recording times used, electrons drift a much shorter distance than the electrode separation. Consequently the duration of the current must be determined by some high-rate loss mechanism of electrons between electrodes. The time constant of the attachment to oxygen has duration of few tens of nanosecond. However, the strong dependence of the current peak on the humidity (Figure 3B) can not be explained only by this phenomenon. Another known fast loss-mechanism is the ion-ion recombination. The exponential decay of the current with humidity growth may be explained, assuming the recombination of O_2^- with some water-vapor product like hydronium ion H_3O^+ [6].

Above we assumed that the ion-induced nucleation is the dominant process leading to the aerosol particle formation. The decay of the charge carriers with the humidity means that the water vapor diminishes considerably the concentration of the main precursors of nuclei.

As it was proved earlier [2], mainly sticking of water molecules to the nuclei causes the condensation growth of the particles. It means that at certain humidity a change of the laser fluence should lead only to the growth of the particle concentration. Actually we observe (Figure 4A) that the increase of the fluence causes besides the concentration growth also a considerable increase of the mean size of the particles. Apparently it is the result of the coagulation growth mechanism.

The addition of O_3/NO_x mixture to the air remains the spectral distribution of particles unchanged (Figure 4B) but gives rise to their concentrations in the fractions. The likely reason of the effect is that the admixture enlarges the sticking ability of the water vapor to nuclei [3].

Distributions in Figure 5 demonstrate that the change of the humidity in large limits has a negligible effect on the shape of spectrum, the only remarkable effect is the growth of the particle concentrations in fractions. At the same time the mean size of the particles in the air + O_3/NO_x mixture should

effectively grow with humidity [2, 3]. The only explanation of the contradiction between our earlier and present studies is that the recombination-caused decrease of the concentration of charge carriers as precursors of the nuclei balances the increase of detectable particle concentration due to condensation.

4. CONCLUSIONS

The most important findings of the paper are:

- In the plasma plume the ion-ion recombination is the dominant loss mechanism of the charged particles. One of the components participating in the recombination is an ion formed at the basis of the water molecule.
- At higher fluencies of the laser radiation the coagulation plays an important role in the growth of particles.
- The water vapor acts in the particle evolution in two alternative directions: (i) the growth of the humidity diminishes the concentration of the nuclei; (ii) the growth of the humidity increases the mean size of particles. The independence of the particle mean size and the width of the detectable spectrum on the humidity are results of this competition.

ACKNOWLEDGMENTS

We are grateful to A. Mirme and E. Tamm from the Institute of the Environmental Physics of the University of Tartu who kindly presented us EAS and took part in lively discussions.

REFERENCES

[1] P. Paris, M. Laan, A. Mirme, The influence of corona discharge on aerosol spectra, Proc. HAKONE VII, Greifswald, **1**, 44-8 (2000)
[2] P. Paris, A. Mirme, M. Laan, *Study of corona discharge aerosol with an electrical aerosol spectrometer*, J. Aerosol. Sci. 29 (1998), Suppl. 1, S845-S846
[3] P. Paris, M. Laan, A. Mirme, E. Tamm, *Influence of active species on laser-created aerosol spectrum*, to be published
[4] F. Yu and P. Turco, *The formation and evolution of aerosols…*, J. Geophys. Research, **103,** (1998), pp. 25,915-25,934
[5] M. Laan, A. Mirme, *Aerosols and corona discharges*, In: Electrical Discharges for Environmental Purposes, ed. E. M. van Veldhuizen Nova Science Books and Jrnls. (1999), Ch. 8,193 – 220
[6] V. A. Bityurin, B. V. Potapkin, M. A. Deminski, *Chemical activity of discharges*, In: Electrical Discharges for Environmental Purposes, ed. E. M. van Veldhuizen Nova Science Books and Jrnls. (1999), Ch.4, pp. 49-118

SURFACE MODIFICATION OF ALUMINIUM BY DIELECTRIC BARRIER DISCHARGES UNDER ATMOSPHERIC PRESSURE

J.F. Behnke[a] , H. Steffen[a] A. Sonnenfeld[a,d], R. Foest[b], V. Lebedev[a,c] and R. Hippler

a) Institute of Physics, University of Greifswald, Domstr. 10a, D-17487 Greifswald, GERMANY
b)Institute for Low Temperature Plasma Physics Greifswald,F.-L. Jahn-Str.,17489 Greifswald, GERMANY
c) Faculty of Physics, St.Petersburg State University, Ulianovskaja ul., 1,198904 St.Petersburg, RUSSIA
d) Biophy Research S.A. 5 6 rue Anne Gacon, 13016 Marseille, FRANCE

Abstract. The dielectric barrier discharge (DBD) under atmospheric pressure is promising for surface modification of metallic substrates. The application of the DBD for the cleaning of hydrocarbon contaminated surfaces and for the modification of metallic surfaces by oxidation, and for deposition of organosilicon films is reported.

1. INTRODUCTION

The dielectric barrier discharge (DBD) seems to be the most promising plasma source for a plasma assisted treatment of metallic surfaces under atmospheric pressure. Investigations in the homogeneous DBD commonly known as 'atmospheric pressure glow discharge' (APGD), e. g. cf. [1], and in the filamentary or disperse DBD, e. g. cf. [2], [3], [4], proved the applicability of DBD for surface treatment techniques. The modification process for metallic surfaces consists of three steps: at first the cleaning from oil and fat contaminations, secondly, the deposition of a stable oxide layer of some tens of nm to the protecting of the metallic bulk material, and in third place, the deposition of an anticorrosive and adhesive thin film; several hundreds nm thick. In the present work, results concerning the removal of special oils (Wisura-Akamin - this oil is a typical lubricant in handling and industrial treatment of aluminium sheet metals) mainly from aluminium and silicon (ellipsometric measurements) substrates and the growth of the oxide layer of the surface bulk material by plasma treatment with a DBD in dry air under atmospheric pressure is presented. This work also deals with the deposition of SiO_x polymer films in a comparatively smooth plasma of DBD in nitrogen under atmospheric pressure with an admixture of 0.1 % of tetraethoxysilane (TEOS) as precursor. For characterisation of the surface properties of etched and deposited thin layers gravimetric and ellipsometric measurements as well as XPS, FT-IR spectroscopy and SEM have been carried out.

2. EXPERIMENTAL

The used DBD equipment consists in general of two rectangular shaped Al_2O_3 electrodes (width: 17 mm, length: 150 mm). The discharge was operated within the volume between the electrodes and the substrate (ground electrode). The electrodes could be moved over and along the substrate. A schematic view of the experimental set-up is given in Fig. 1. The typical operation conditions during plasma treatment are represented in Tab.1.

Al-plates (surface area: $80\,\text{mm} \times 150\,\text{mm}$), Si-wafers and Al-coated Si-wafers were used as substrates. For investigations of the cleaning process the substrates were contaminated with oil solved in toluene with layer thickness of 100 – 400 nm. For SiO_x deposition experiments the substrates were pre-cleaned in a supersonic alcohol bath and cleaned in a DBD in air under atmospheric pressure with a treatment time of 86 s. The time dependence of the oil mass removal and of the mass increase during the oxidation phase was measured gravimetrically by weighing the samples with a micro scale and ellipsometrically using a spectroscopic polarisation modulation ellipsometer (PME, Jobin Yvon) for characterisation of the contaminated and cleaned substrates and for quasi-in-situ monitoring of the plasma treatment process (633 nm). By using silicon wafers only the properties of the contamination layer are unknown for the optical model which makes it easier to compare the experimental

[a] Electronic address: behnke1@physik.uni-greifswald.de

ellipsometric data with the simulation. For the separation of the refractive index of the contamination the dispersion theory of Cauchy was employed.

	cleaning	**oxidation**	**deposition**
frequency /kHz	10 –25	10 -25	6.6
voltage / kV	< 15 kV_{pp}	< 15 kV_{pp}	< 15 kV_{pp}
power /W	60 - 80	80	45
power density / Wcm^{-2}	2.2 – 3,0	3	1 – 1.6
discharge gap/ mm	1.3	1.3	0.5
process gas	dry air	dry air	N_2
reactive gas	O_2 20%	O_2 20%	TEOS 0.1 %
gasflow /slm	1.6	1.6	1
treatment time /s	< 120	< 600	90
mean residence time /s	0.06	0.06	0.1

TABLE 1. Typical operation conditions during plasma treatment

The contamination was assumed to consist of one homogeneous layer. By means of the determined refractive index of the contamination film thickness as well as etching rates could be obtained not only on Si-wafers but also on Al-films and Al-plates. The etching rates are about the same on all substrates and therefore the results on Si-wafer can be generalised. Because of the low distance between electrodes and substrate for the barrier discharge the ellipsometric measurements could not be carried out in-situ.

Therefore, the substrates were treated only for a few seconds. Than the electrodes were moved away and one spectroscopic measurement was performed. This procedure was repeated until the lubricant was removed. In that way the ellipsometric measurements were carried out quasi in-situ. The ellipsometric method works well up to a layer thickness of 150 nm.
In addition, chemical composition of the surface of the substrates before and after plasma treatment was studied by XPS (Fisons MT 500). The thickness of the deposited SiO_x layer was measured gravimetrically. The chemical properties of the obtained deposits were examined by means of Fourier Transform Infrared (FTIR) spectroscopy and compared to former analyses using X-ray Photoelectron Spectroscopy.

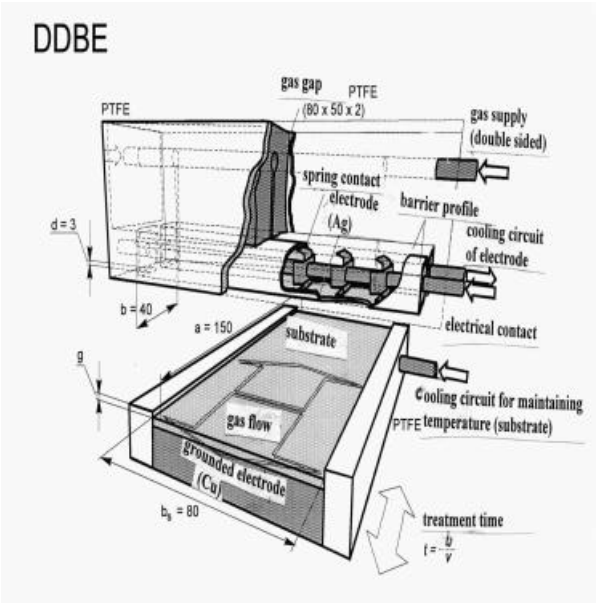


FIGURE 1. Scheme of the DBD equipment for surface modification with dynamic electrode arrangement, measures in mm.

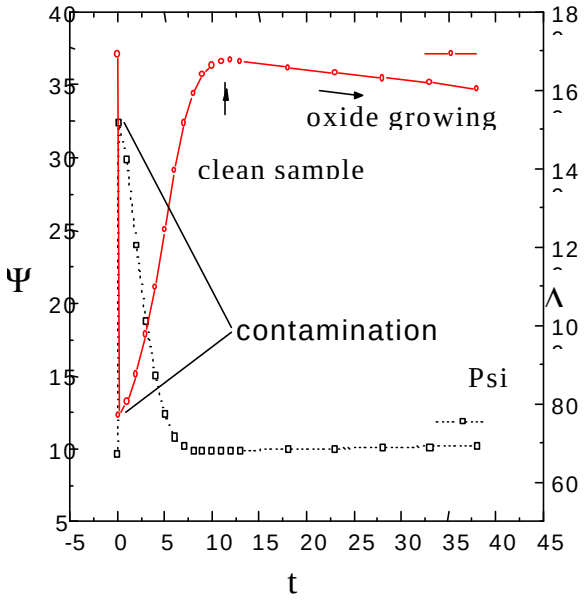


FIGURE 2. Ψ and Δ during a whole cleaning process (633 nm, 80 W) in dependence of the time in sec.

3. RESULTS AND DISCUSSION

3.1. plasma cleaning

In Fig. 2 a typical plot for the ellipsometric angles Ψ and Δ versus treatment time is given, which was monitored during the whole cleaning process (633 nm, 80 W) of a contaminated Si-wafer.

Contamination thickness and etching rate decrease approximately exponentially. The etching rate reaches values up to 40 nms^{-1} or 0.1 $nmW^{-1}s^{-1}$. It decreases linearly with the contamination thickness. An example for the exponential decay of thickness and etching rate is given in Fig. 3. The Thickness *d* and the etching rate *r* fulfil the relations:

$$\mathbf{d(t) = d_0 exp(-t/t)\ ,\ r(t) = |\P\ d(t)/\P t| = d(t) / t\ ,\ d(t)/r(t) = 1 / t = constant}$$

with τ as time constant which characterises the cleaning process in dependence of discharge power and of initial contamination d_0. One reason for such behaviour may be the statistical character of the removing process.

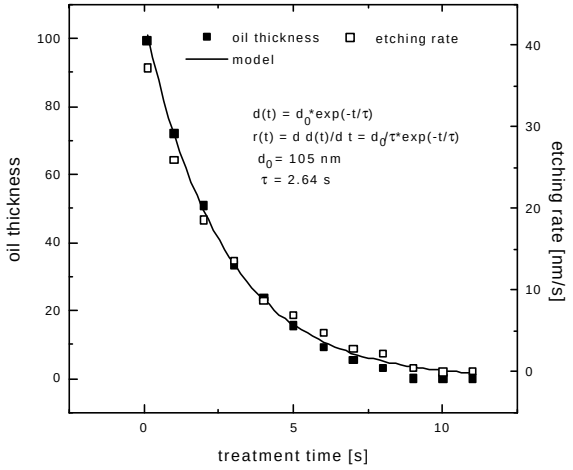


FIGURE 3. Contamination thickness **d** and deposition rate **r** vs. treatment time for the discharge power of 80W, substrate: Si-wafer.

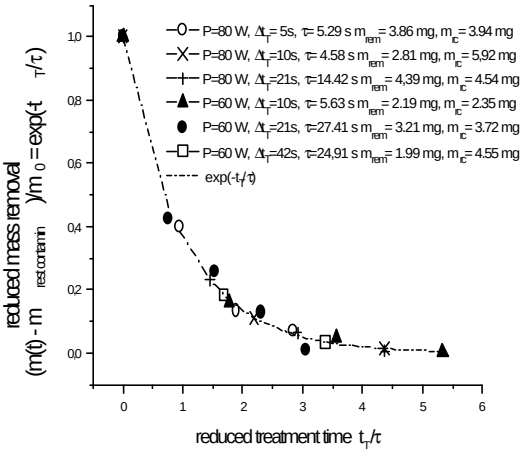


FIGURE 4. Reduced mass $(m(t)- m_{rc})/m_0$ vs. reduced treatment time t/τ, curve $exp(-t/\tau)$, parameter Δt_F : treatment interval between 2 weighting, substrate: Al plate.

A single filament removes nearly the whole contamination from the sample within the relevant area. The distribution of the filaments at the substrate surface is statistical. That means that removed mass **dm** in the time interval **dt** is proportional to the contaminated mass m,

$$\mathbf{dm = - m\ dt/t\ .}$$

The second reason is the polymerisation of the lubricant for higher initial thickness. That is clearly seen from the increase of the optical constants *n* and *k* of the layer which is related to higher layer density. To achieve a better understanding of the etching process the discharge was operated between two dielectric electrodes only. Therefore the contaminated metallic plate was not touched by filaments. Etching takes place only due to active species which were produced by the discharge. Under that conditions the etching rates are much lower and the process stops if the contamination reaches about 20% of the initial thickness. That means the filaments are essential for the cleaning process. Without filaments the polymerisation of the lubricant became the most preferred mechanism. In case of small contamination thicknesses (100-150 nm) substrates can be completely cleaned using any tested values of power. The time constants for the removal of the contamination increase approximatelly linearly with discharge power.

The behaviour of thicker contaminations was investigated by gravimetric measurements on Al substrates. The results of the gravimetric measurements can be summarised as follows. The contaminated mass decreases approximately exponentially by the law:

$$\mathbf{m(t) = m_{rc} + m_0\ exp(\ -\ t/t)\ ,}$$

with m_{rc} as remaining polymerised part of contamination and m_0 is the removed mass after treatment and τ is the etching constant. Fig. 4 shows the comparison between the model and the measurements. Time constants between 5 and 25 s are estimated. The removal of the contamination increases with power and treatment velocity (velocity of the electrodes: 0.7 ... 6 mms^{-1}). Contaminations above 6 gm^{-2} could not be removed by barrier discharge.

3.2. Plasma oxidation

In the example given in Fig. 3 the initial values of Ψ and Δ of a silicon wafer without contamination can not be reached completely after plasma treatment. Moreover Δ decreases again after reaching a maximum. The main reason is the oxide growth. This result is also based by the angle resolved XPS measurements. The XPS spectra on Al-layer were measured before and after the treatment with DBD. Before treatment the intensity of the Al 2p peak is 20% lower as the oxide peak. After the treatment the oxide peak remarkably increased and the Al 2p peak almost disappeared. By means of angle resolved measurements an increase of the oxide thickness from 3.2 to 8.6 nm was proved. Using the ellipsometry the oxidation of clean substrates was investigated. In Fig. 5 the oxidation of a Si-wafer by barrier discharge is presented. It was found that at the beginning of the treatment a decrease of the thickness ocures. The treatment starts with roughing the surface. The oxidation of surfaces by treatment with barrier discharge was investigated by the gravimetric method too. Fig. 6 shows the increase of the weight of an aluminium plate after finishing the plasma treatment. In both cases the thickness of the oxide increases approximately proportional to $\sqrt{t}$. Therefore we assume that diffusion is the reason for the growth of the oxide. By $d \approx \sqrt{4\,Dt}$ diffusion coefficients of about $2 \ldots 7 \cdot 10^{-16}$ $cm^2 s^{-1}$ are estimated. That are typical values for grain boundary diffusion [5]. The quality of this oxide depends on the treatment time. If the samples are treated continuously for some minutes the oxide layer is rough. If the samples are treated only for some seconds with breaks no roughness can be observed. For Al samples the thickness of the oxide reaches about 10 nm after several minutes

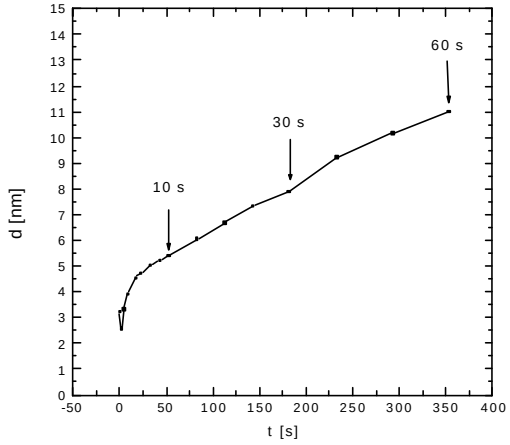


FIGURE 5. Thickness of the oxide layer vs. time on Si-wafer, parameter is the treatment time (P = 80 W)

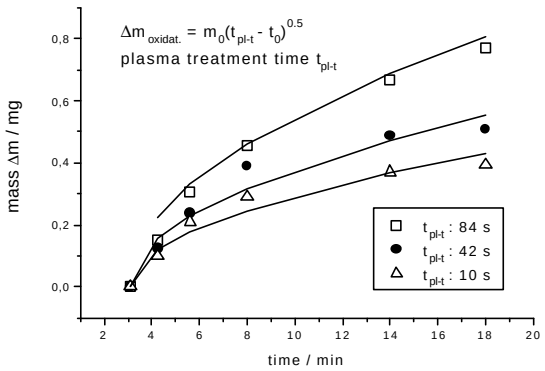


FIGURE 6. Increase of the weight after treatment with barrier discharge (P = 80 W)

3.3 Plasma deposition

The decomposition of TEOS in the plasma of DBD is controlled by electron impacts. The cleavage of the Si-O bond accounts to be main reaction path of the plasma chemical conversion of TEOS with the separation of CH_3-CH_2-O radicals [6].

The deposition occurs on the basis of small fragments of organosilicon precursor. These radical species adsorb to the substrate surface. Their unsaturated bonds initiate the polymerisation process leading to the obtained deposits. Therefore, the film is supposed to be highly cross-linked. The films are adhesive and visually uniform, transparent deposits are achieved. The films protect the substrate against corrosive liquids (NaOH, 10^{-3} $mole^{-1}$) and SEM images show that damages of the substrate surface (< 350 µm) are uniformly covered by the films.

The thickness of the deposited SiO_x polymer films are estimated from gravimetric measurements under the assumption of a film mass density of 1 g cm^{-3}. The average deposition rate depends strongly on the discharge power density and on the structure of DBD plasma (Fig. 7). Up to the maximum of the rate the DBD appears quasi-homogenous. Also in this discharge region the deposition is homogenously distributed across the substrate. Since the discharge changes to the mode of stronger

filamentation with higher power densities, the film tectonics alters to a stripe-shaped structure on the substrate, possibly due to some turbulent convection processes.
FT-IR measurements (Bruker IFS 66V) were carried out on the substrate after plasma treatment. Fig. 8 shows is a spectrum of a film produced by N_2 plasma and Ar plasma with 0.1 % TEOS admixture. The spectrum is dominated by a broad peak in the region of 1000 to 1250 cm^{-1} that indicates a large macromolecular structure of the form $(Si\text{-}O)_n$.

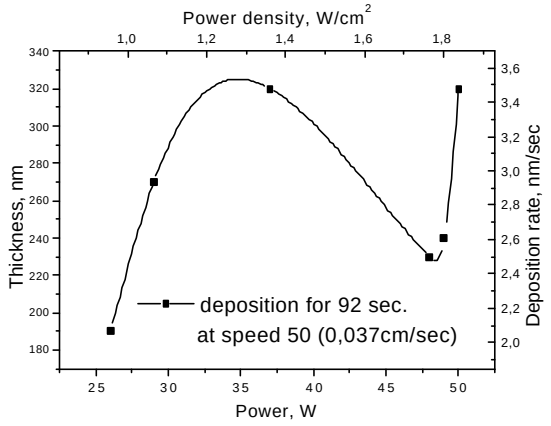


FIGURE 7. Thickness and deposition rate of SiO_x polymer films vs. discharge power, deposition time 92 s , N_2 -DBD with admixture of 0.1% TEOS.

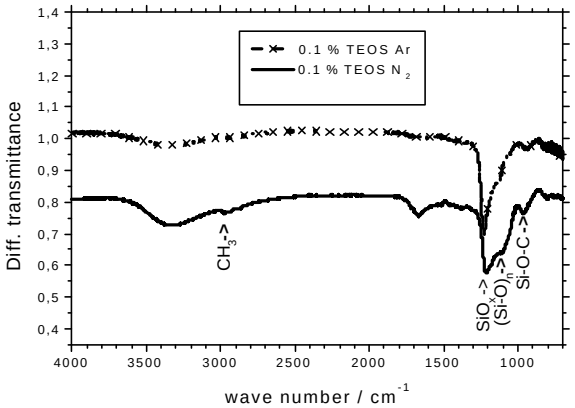


FIGURE 8. FT-IR spectra of SiO_x polymer films deposited in of N_2 -DBD with admixture of 0.1% TEOS (P = 50 W).

This structure is overlaped by the prominent SiO_x peak at 1240 cm^{-1}. The founded features together with the very low carbon content (e.g CH_3 at 2950 cm^{-1}) reveal the pronounced inorganic chemical nature of the film. That kind of film character was found also for other silicon organic precursors, e.g. HMDSO. If the specific energy per precursor molecule is large enough during the deposition, the inorganic character of the film increases, independently on the particular precursor.

CONLUSION

It could be shown that a DBD is a useful tool to modify Aluminium surfaces for cleaning and coating with anticorrosive and adhesive oxide layers of the bulk and decomposed precursor material, too.

ACKNOWLEDGMENTS

The work was supported by the BMBF Verbundprojekt ATMOSPLASMA 13N7350/0 and by the Airbus Deutschland GmbH.

REFERENCES

[1] Kogoma M., Okazaki S., Tanaka, Inomata T., Contr. Papers of HAKONE VI, Cork, Ireland, 31st.Aug. – 2nd. Sept. 1998,83-87
[2] Behnke J.F., Lange H., Michel P., Opalinski T.,Steffen H.,Wagner H.-E. *The cleaning process of metallic surfaces in barrier discharges* in: Proc. 5th Int. Symp. on High Pressure Low Temperature Plasma Chemistry (HAKONE V) ed. by J. Janca et al. , Milovy/Czech Rep., 1996, p.138-142
[3] Thyen R., Höpfner K., Kläke N., Klages C.-P., *Plasma and Polymers* 91-102
[4] Sonnenfeld A, Tun T.M., Zajickova L., Wagner H.-E., Behnke J.F., Hippler R., *The deposition process based on silicon organic compounds in two different types of an atmospheric barrier discharge in: Proc.*15th Int. Symp. on Plasma Chem. Contr. Orléans/France 9 –13 July 2001Vol V pp. 1835-40 Eds. A. Bouchoule et.al.
[5] Wulff H., Steffen H., *Characterization of thin solid films*, in: Hippler R, Pfau S., Schmidt M., SchoenbachK.H., *Low Temperature Plasma Physics* , WILEY-VCH, 2001
[6] Sonnenfeld A., Kozlov K.V., Behnke J.F., *Influence of nobel gas on the reaction of plasma chemical decomposition of silicon organic compounds in the dielectric barrier discharge in: Proc.* 15th Int. Symp. on Plasma Chem. Contr. Orléans/France 9-13 July 2001 Vol. V pp.1829-34 Eds. A. Bouchoule et.al

THIN FILMS OBTAINED BY PE-CVD METHOD FROM HEXAMETHYLDISILOXANE UNDER ATMOSPHERIC PRESSURE

Z. Rżanek-Boroch[a], K. Schmidt-Szałowski[a], J. Janowska[b], K.Dudziński[a], A. Szymańska[a], M. Misiak[b]

a) Warsaw University of Technology, Faculty of Chemistry, Noakowskiego 3, 00-664 Warsaw, POLAND
b) Warsaw University of Technology, Faculty of Mechatronics, Institute of Micromechanics and Photonics, Chodkiewicza 8, 02-525 Warsaw, POLAND

Abstract: The aim of the studies was to obtain thin films of SiO_2 from hexamethyldisiloxane (HMDSO) using discharges stabilized with a dielectric barrier (DBD) under atmospheric pressure. The process was carried out at frequency of 5 kHz. Films were deposited from the following gas mixtures: HMDSO + N_2, HMDSO + Ar + O_2, HMDSO + Ar + N_2O, HMDSO + Ar + NH_3.
The influence of the gas mixture composition on of the film properties were studied.

1. INTRODUCTION

Chemical processes occurring in non equilibrium plasmas are widely used in various branches of technology. Among the most important applications of such processes are: etching of solid surfaces and deposition (PE-CVD) of thin films of silicon compounds such as SiO_2 or Si_3N_4. Such films are widely applied as anti-reflection, corrosion-resistant, tightening, or self-lubricating coating. The studies carried out in our laboratory are focused on PE-CVD of thin films (20-600 nm) at atmospheric pressure, using organosilicon compounds as the starting materials. In the present work thin films deposited from hexamethyldisiloxane in non-homogeneous DBD were examined.

2. EXPERIMENTAL

Thin films were obtained at atmospheric pressure from HMDSO using Ar or N_2 as a carrier gas in non-homogenous DBD discharge stabilized with a dielectric barrier. The films were deposited on silicon plate (100) substrates under conditions of a frequency 5 kHz and voltage within 12.5 – 15 kV [1]. The substrate temperature was controlled in the range from the ambient temperature up to 400 ^oC. In addition to argon or nitrogen used as neutral gas carriers for HMDSO vapours other admixtures were added, such as oxygen and nitrous oxide in concentrations 0.055% to 3.4%, as well as ammonia in concentration from 10% to 40%. The admixtures diluted the input gas mixture so that the concentration of HMDSO at the reactor inlet [2] did not exceed 3700 ppm.

The following methods were applied to control the thickness, composition, hardness, and quality of the films deposited:

Film thickness was measured by ellipsometry at 632.8 nm wavelength using Ellipsometer II (Applied Materials), FT-IR absorption spectra were recorded using a Bruker IPS 113v spectrometer in the transmission mode, Atomic Force Microscope, prototype made in Łódź University, Faculty of Physics - characterisation of the surface, film nanomechanical characteristics have been measured by means of an instrument (TriboScope™ Hysitron Inc. USA) capable to make indentations at very low loads (1 μN -10 μN) and load-displacement measurements with subnanometer indentation depth sensitivity [3]

[a]*Electronic address: rzanek@ch.pw.edu.pl*

3. RESULTS

The films obtained from HMDSO at ambient temperature remained semi-liquid and their composition was very similar to that of the starting substance so further studies at that temperature have been given up. Analysis of the effect of deposition temperature on composition of the films O77, O75, O76, O44 (Table 1.) deposited from HMDSO + N_2 mixtures, on their thickness and properties has shown that:

1. The composition of all of them is similar despite of the varied deposition temperature. Their IR spectra reveal the absorption bands at wave numbers 795-802 cm^{-1}, 841 cm^{-1}, 1024-1041 cm^{-1} corresponding to Si-O-Si groups, band at 1259 cm^{-1} corresponding to residues of organic fragments $Si-CH_3$ and a band at 2962 cm^{-1} due to C-H bonds (Fig. 1.). However, the intensity of the bands due to the C-H bonds (2962 cm^{-1}) decreases with increasing deposition temperature.

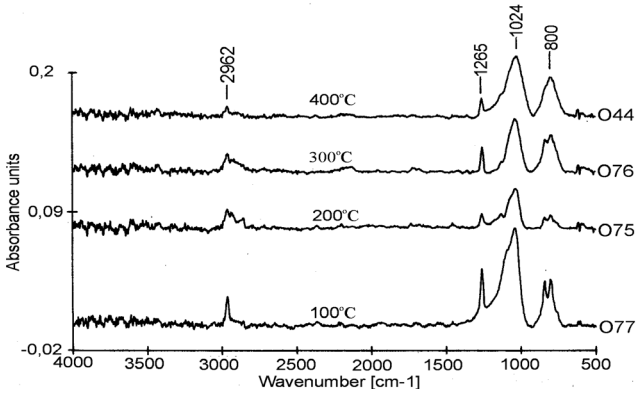


FIGURE 1. FTIR spectra of the films O77,O75,O76 and O44 deposited from the mixtures of HMDSO + N_2, at temperatures 100°C, 200°C, 300°C and 400°C (Table 1.)

2. Observation of the AFM picture (Fig. 2. and 3.) shows that the films obtained from the HMDSO + N_2 mixtures are not fully homogenous. Their surface exhibits a number of small heterogeneities and thickenings, but it becomes more homogenous as temperature is raised from 100°C (O77) to 200°C (O75)

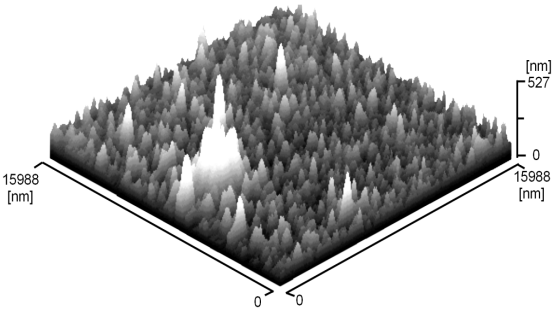


FIGURE 2. Surface of the sample O77.

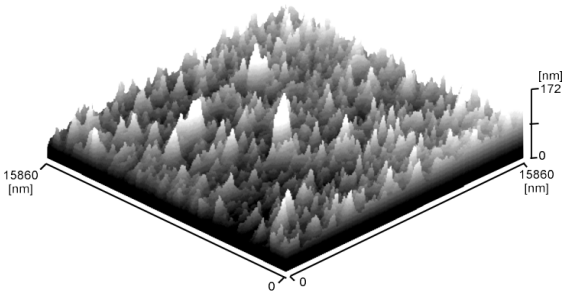


FIGURE 3. Surface of the sample O75

3. The film deposited at 400°C (O44) seems to be smooth when observed with naked eye, but under magnification it reveals a number of defects probably due to the etching of surface at the points where stronger microdischarges striked. The microhardness measurement of the O44 film gives an image of highly non-uniform surface hardness within the limits 1-6 GPa, which is characteristic to self-lubricating layers rather than to that of a hardened surface. The hardness of this film decreases evidently with increasing depth (Fig. 4.)

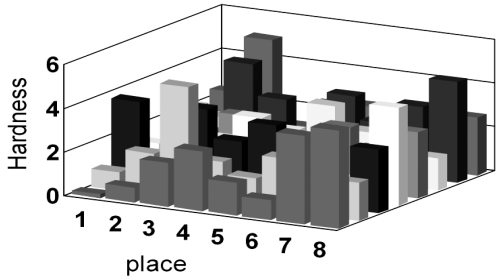


FIGURE 4. Hardness [GPa] of the sample O44 (investigated surface 8x8 μm)

.

TABLE 1. Experimental conditions and film properties Frequency 5 [kHz], Reactor B [4] with external high voltage electrode.
Gas mixtures: HMDSO + N_2, HMDSO + Ar+ O_2, HMDSO + Ar+ N_2O, HMDSO +Ar+ NH_3

Sample	O77	O75	O76	O44	O27	O54	O59	O47	O46	O43
Voltage [kV]	15	13.5	14.2	11.2	8.1	11.2	19.5	15.7	13.5	11.2
Substrate temp. [°C]	100	200	300	400	400	300	150	150	300	400
Deposition time [min]	15	15	15	15	15	15	15	15	15	15
GAS MIXTURE										
HMDSO[ppm]	3700	3700	3700	3700	3600	3600	3600	2600	2600	2600
Oxygen [%]	0	0	0	0	3.4	0	0	0	0	0
Ammonia [%]	0	0	0	0	0	0	0	40	40	40
Nitrous oxide [%]	0	0	0	0	0	3.4	3.4	0	0	0
Argon [%]	0	0	0	0	Remain	Remain	Remain	Remain	Remain	Remain
Nitrogen [%]	Remain	Remain	Remain	Remain	0	0	0	0	0	0
Thickness [nm]	103	102	280	151	137	-	105	40	63	24
Refractive index	1.33	1.42	1.37	1.55	1.2	-	1.46	1.26	1.44	1.44
Spectrum FTIR (main absorp bands)	Si-O-Si, $Si-CH_3$ C-H	Si-O-Si, $Si-CH_3$ C-H	Si-O-Si, $Si-CH_3$ C-H	Si-O-Si, $Si-CH_3$ C-H	Si-O-Si, $Si-CH_3$	Si-O-Si, $Si-CH_3$ C-H	Si-O-Si, $Si-CH_3$ C-OH	Si-O-Si $Si-CH_3$	Si-O-Si $Si-CH_3$	Si-O-Si

4. Similar properties of soft films were observed for the film O27 deposited at 400 ^{0}C from a mixture of HMDSO + Ar + 3.4% O_2 (Table 1.). Both the FTIR spectrum (Fig. 5.) and the surface hardness (Fig. 6.) are very similar to those of the film O44 discussed above, despite of different composition of the starting gas mixture.

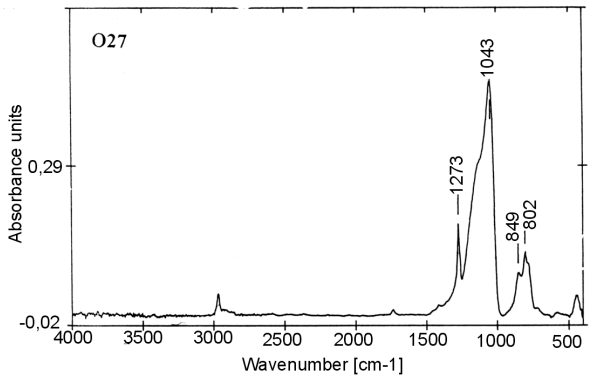


FIGURE 5. FTIR spectra of the films O27 deposited from the mixtures of HMDSO + Ar + O_2 at temperature 300, (Table 1.)

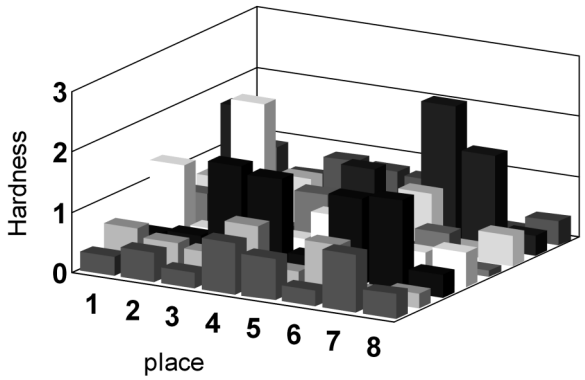


FIGURE 6. Hardness [GPa] of the sample O27 (investigated surface 8x8 μm)

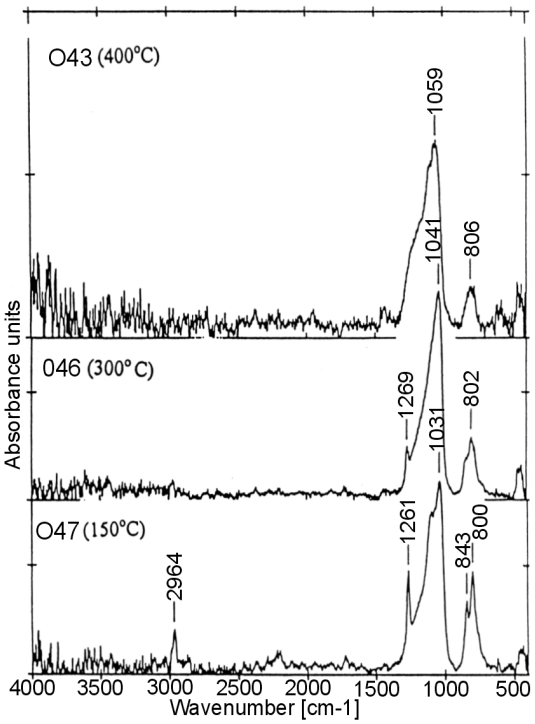


FIGURE 7. FTIR spectra of the films O47, O46 and O43 deposited from the mixtures of HMDSO+NH_3+Ar, at temperatures 150, 300, 400°C (Table 1.)

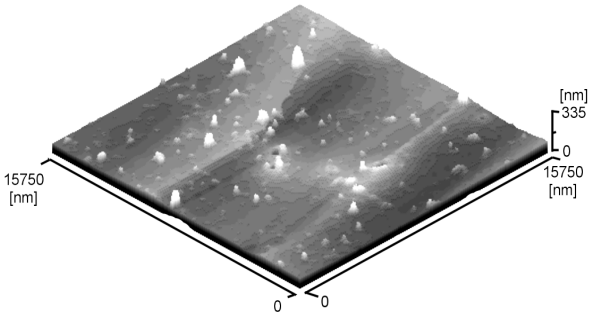


FIGURE 8. Surface of the sample O47 (Table 1.)

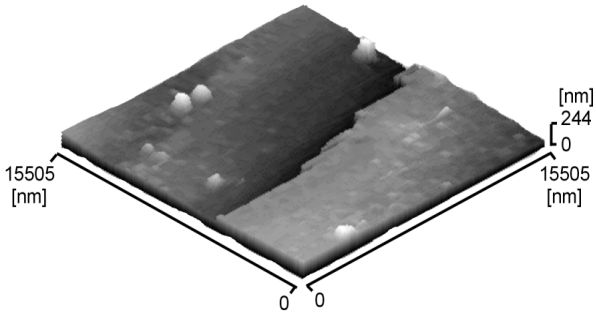


FIGURE 9. Surface of the sample O46

For the sake of comparison we show in Figure 7 a FTIR spectrum of thin films deposited from a mixture HMDSO + Ar + 40 % NH_3 at temperatures 150 - 400^{o}C (O47, O46, O43). The films contain only small amounts of organic residues which decrease with increasing deposition temperature.

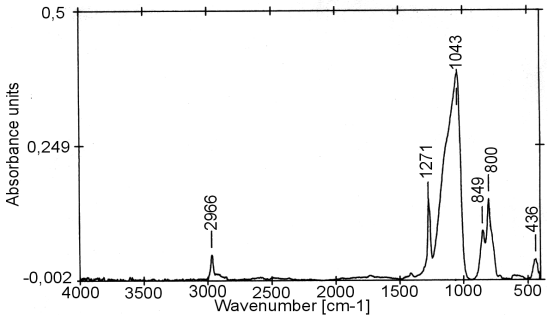


FIGURE 10. FTIR spectra of the sample O54 deposited from the mixtures of HMDSO + Ar +N_2O at the 300^oC (Table 1.)

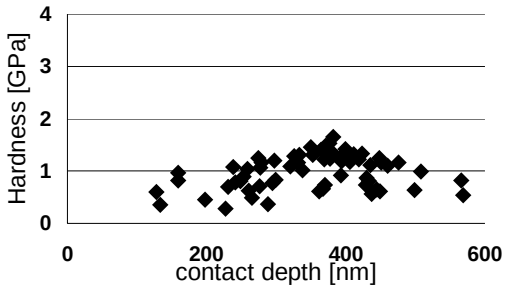


FIGURE 11. Hardness of the sample O54

For example film O46 does not reveal any more absorption band at 2964 cm^{-1} and the intensity of the band at 1269 cm^{-1} has become much less intensive. The AFM pictures of the films O47 (Fig. 8.) and O46 (Fig. 9.) obtained at temperatures 150 and 300^oC, respectively, are not homogenous and single thickenings may be seen. These films may be compared with the film O54 deposited at 300^oC from a mixture HMDSO + Ar + 3.4%N_2O (Fig. 10.). This film contains, in addition to the Si-O-Si groups represented by absorption bands at the wave numbers 436 cm^{-1}, 800 cm^{-1} and 1043 cm^{-1}, also Si-H bonds represented by the band at 849 cm^{-1}, as well as a considerable amount of organic residues represented by the band at 1271 cm^{-1} corresponding to groups CH_3 in Si-CH_3 and C-H bonds associated with the wave number 2966 cm^{-1}. The film obtained under these conditions is uniform, but its hardness is small, not higher than 2 GPa (Fig.11.). An uniform film, but of low hardness, was formerly obtained from the above gas mixture at 150 ^0C. It corresponded to the film O59.

4. CONCLUSIONS

The composition of the films obtained from the HMDSO+N_2 mixtures varies slightly and the intensity of absorption bands decreases as the deposition temperature is increased. The films obtained at 400^oC are not uniform, and their hardness falls in the region 1 - 6 GPa.

The films obtained at 400^oC from the mixture HMDSO+Ar+3.4%O_2 contain considerable amounts of organic residues, and their hardness is rather low.

The films deposited from the mixtures HMDSO+N_2,HMDSO+Ar+3.4%O_2 and HMDSO+Ar+3.4%O_2 are characterized with a small hardness. From the mixture HMDSO+Ar+ 3.4%N_2O, the smoothest film surface was obtained.

The films deposited from the HMDSO+Ar+40%NH_3 mixture at temperatures 300 and 400^oC contain only small amounts of organic residues, but their surface is not uniform.

5. REFERENCES

[1] Schmidt-Szałowski K., Rżanek-Boroch Z., Sentek J., Rymuza Z., Kusznierewicz Z., Misiak M., Thin films deposition from Hexamethyldisiloxane and Hexamethyldisilazane under dielectric-barrier discharge (DBD) conditions, *Plasmas and Polymers*, **Vol. 5, 3/4**, pp. 173-190, (2000)

[2] Schmidt-Szałowski K., Rżanek-Boroch Z., Sentek J., Rymuza Z., Kusznierewicz Z., Misiak M., Polycondensation of organo-silicon compounds under barrier-discharge conditions. In: *Proc. 7th Int. Symp. on High Pressure Low Temperature Plasma Chemistry,* ed. by H.E. Wagner, J.F. Behnke, and G.Babucke, Greifswald, 2000, pp. 434-440

[3] Rymuza Z., Misiak M., Kuhn L., Schmidt-Szałowski K., Rżanek-Boroch Z., Control tribological and mechanical properties of MEMS surfaces. Part 2: nanomechanical behaviour of self-lubricating ultrathin films. *Microsystem Technologies* **Vol. 5**. Number 4. July 1999, pp. 181-188

[4] Schmidt-Szałowski K., Fabianowski W., Rżanek-Boroch Z., Sentek J., PE CVD of SiO_2 thin films at atmospheric pressure by discharges stabilized with dielectric barrier, *Journal of Chemical Vapor Deposition*. **Vol. 6,**. pp. 183-195 (1998)

DEPOSITION OF THIN FILMS ON POLYCARBONATES BY PULSE DIELECTRIC BARRIER DISCHARGE

T. Opalińska[a], B. Ulejczyk[a], L. Karpiński[b], K. Schmidt-Szałowski[c]

a) Industrial Chemistry Research Institute, Rydygiera 8, 01 793 Warszawa, POLAND
b) Institute of Plasma Physics and Laser Microfusion, Hery 23, 01 497 Warszawa, POLAND
c) Warsaw University of Technology, Faculty of Chemistry, Noakowskiego 3, 00 664 Warszawa, POLAND

Abstract: Thin films with content of Si, C and O were deposited on polycarbonates from tetraethoxysilane by pulse dielectric barrier discharge at atmospheric pressure. Influences of plasma parameters, such as the energy of single pulse of discharge and the position PC plates on electrodes on the deposition rate, were investigated. Results shown that the deposition rate of thin film increased with increasing energy of single pulse, for example: deposition rate was 4.6 or 37 nm/min when the single pulse energy was 6.2 or 9.1 mJ. The structure of thin films was investigated using scanning electron microscopy, atomic force microscopy and infrared spectroscopy. This plasma technology can be used for successfully depositing transparent, smooth and homogeneous films.

1. INTRODUCTION

Polycarbonates (PC) have very useful properties of the bulk, such as low-density and thus reduced weight, high elasticity and transparency. They have been widely used in the industry to replace glasses in many applications, such as headlights, windscreens, lenses and compact discs. However, their use is sometimes limited by unwanted properties of the surface such as low hardness, low scratch resistance and degradation by ultraviolet. Various deposition technologies of producing thin, protective film containing silicon for remedying these limits are investigated.
Till now, the best effects were achieved by plasma methods. These methods are based on microwave plasma techniques under low pressures from 0.1 to 100 hPa. Low pressure is a practical limit of this way of depositing thin film in large scale [1-3]. For that reason, investigations about depositing of thin film containing silicon in dielectric barrier discharge (DBD) under atmospheric pressure were begun [4]. DBD is inhomogeneous and consists of many micro-discharges. The properties of the micro-discharge depend on the dielectric barrier permittivity, dielectric barrier thickness, plasma-generating gas and the others [5]. In our early studies, we observed that using a pulse power supply instead of a sinusoidal power supply made of DBD more homogenous [6].
In this work, we present the results of thin film deposition in the pulse dielectric barrier discharge (PDBD) at atmospheric pressure.

2. EXPERIMENTAL

Plasma deposition was performed in the PDBD reactor, which is showed in **FIGURE 1**. The reactor consists of two round stainless steel electrodes enclosed in Plexiglas casing. Dielectric barrier was made of a PC plate characterized by the relative electric permittivity of 2.3 (measured by a Precision LCR Meter HP 4284A). We investigated two kinds of arrangements. One arrangement: high-voltage electrode and grounded electrode were covered with PC plates. Thin films were deposited on both PC plates. Second arrangement: only the grounded electrode was covered with PC plate and the high-voltage electrode was not shielded. Thin films were deposited on PC plate and on the surface of high-voltage electrode. In all experiments PC plates of thickness 0.75 mm were used. The discharge gap distance always was 0.75 mm. All depositions were performed at the room temperature under the atmospheric pressure. The reactor was powered by a pulsed electric system with consisted of autotransformer, high-voltage transformer, high-voltage resistor, Blumlein line and spark-gap.

[a] Electronic address: Teresa.Opalinska@ichp.pl

The gas supply system is showed on **FIGURE 2**. The reactor was feded by plasma-generating gas which consisted helium (85% by vol.), oxygen (15% by vol.) and the vapor of tetraethoxysilane (TEOS - 320 ppm). Helium and oxygen were taken from gas cylinder through mass flow controllers and they were mixed. Total flow rate of the gas mixture was kept at 100 L(S.T.P.)/h in all the experiments. Next step was to pass gases through a scrubber with liquid TEOS and then let them to enter into the reactor. The concentration of TEOS in the plasma-generating gas was calculated basing on flow rates of helium and oxygen and the mass decrease of liquid TEOS in the scrubber.

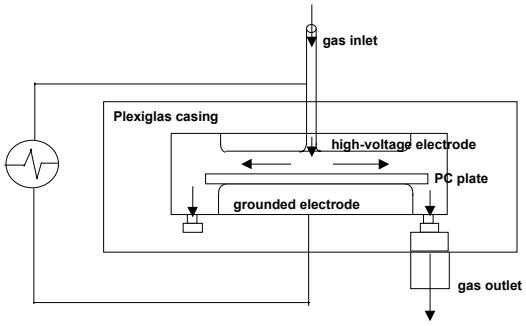


FIGURE 1. Schema of PDBD reactor.

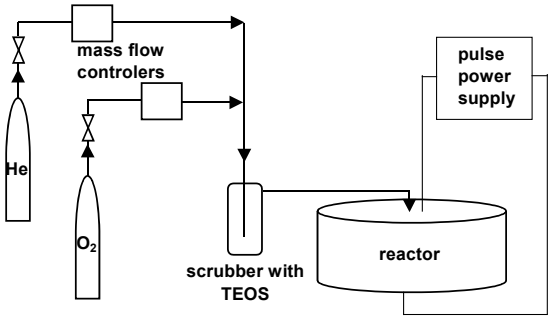


FIGURE 2. Block schema of gas supply system.

Mass deposition of the thin film was determined gravimetrically. PC plates were weighed before and after the deposition. Changes of the mass of PC plates were determined with Sartorius BP 221S balance. The thickness of the thin film was calculated from the following formula:

$$\mathbf{D=m\ (s^*\ g)^{-1}} \qquad (1)$$

where: **D** – thickness [mm], **m** – change of the mass of PC plate [mg], **s*** – arbitrary defined of PC plate' surface [cm^2], **g** – density of deposited thin film [average – 2 g/cm^3]

The morphology of films was investigated with using LEO 1530 scanning electron microscope (SEM) and Nanoscop 1030 Digital Instrument atomic force microscope (AFM/TM).

The chemical composition of the deposited films was investigated using Spectrum 2000 infrared spectrometer with Fourier transform (FTIR) and the energy disperse X-ray detector (EDX) attached to the LEO 1530.

Electric parameters, such as voltage and current, were recorded using Tektronix TDS 3054 oscilloscope. The real energy released in a single pulse was calculated from the following formula:

$$\mathbf{E}=\int_{\tau_1}^{\tau_2} \mathbf{U(t)\ I(t)}\ d\mathbf{t} \qquad (2)$$

where: **E** – real energy released in a single pulse of the discharge [J], **U** – voltage [V], **I** – current [A], **t** –time [s], τ_2-τ_1 – duration of the single pulse (**FIGURE 6**)

3. RESULT AND DISCUSSION

PC plates remained transparent after deposition of the thin film. The surfaces of the deposited films were very smooth and homogenous. All the surfaces of the PC plates were uniformly coated. PDBD did not change the surface roughness and left the original structure of the surface. The amplitude of deflection does not exceed 30 nm. The deposited films were not the pure SiO_2. EDX spectra of the thin films was exhibited Si, C and O. FTIR spectra of thin films deposited in PDBD from TEOS (upper) and original PC (down) are showed in **FIGURE 3**. The broad band in the range 3000-3700 cm^{-1} is assigned to SiOH group and COOH group and water. The peak at 1700 cm^{-1} is attributed to C=O stretching vibration, the peak at 1600 cm^{-1} is due to H_2O and the peak at 970 cm^{-1} is corresponded to Si-OH stretching vibration. Moreover, the thin films are characterized by strong absorption in the range 1000-1250 cm^{-1}. There are few peaks which are due to silylmethyl, ethoxy and aliphatic groups like: 1050 cm^{-1} C-O-C, Si-O-C and Si-O-Si symmetric deformation; 1110 cm^{-1} SiO_2 network vibration; 1170 cm^{-1} C-O-C, Si-O-C and Si-O-Si asymmetric deformation; 1200 cm^{-1} CH_3 rocking in Si-O-CH_3 and 1240 cm^{-1} CH_3 symmetric deformation in Si-$(CH_3)_x$. The peak at 800 cm^{-1} is

characterized to the symmetrical stretching of the Si-C bond. The band in the range 1350-1500 cm^{-1} is associated to the aliphatic groups vibration.

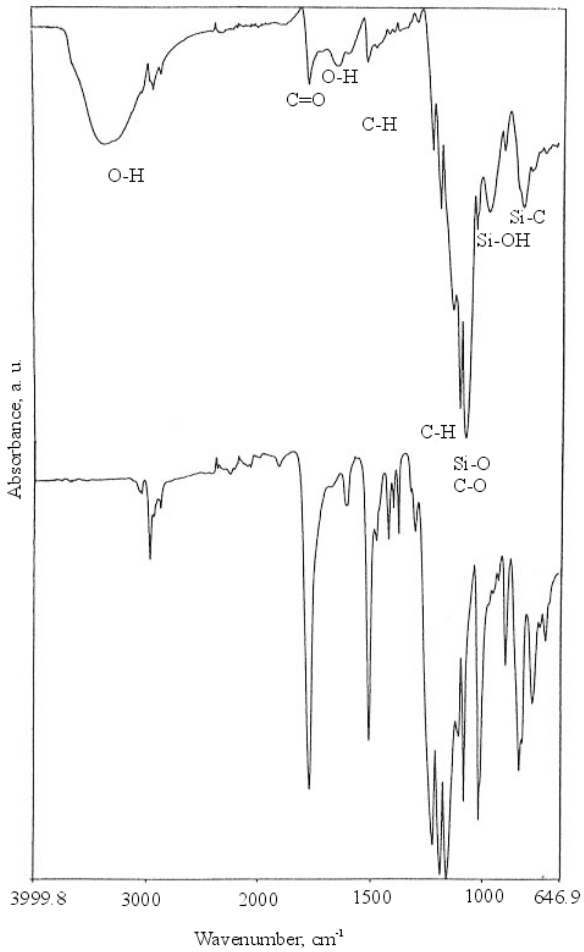


FIGURE 3. Typical FTIR spectra of the deposited thin film (upper) and original PC (under).

The deposition rate and the thickness of deposited films depended strongly on the energy of the single pulse of the discharge (**FIGURE 4, TABLE 1**) and the position PC plates on the electrodes (**FIGURE 5, TABLE 1**).

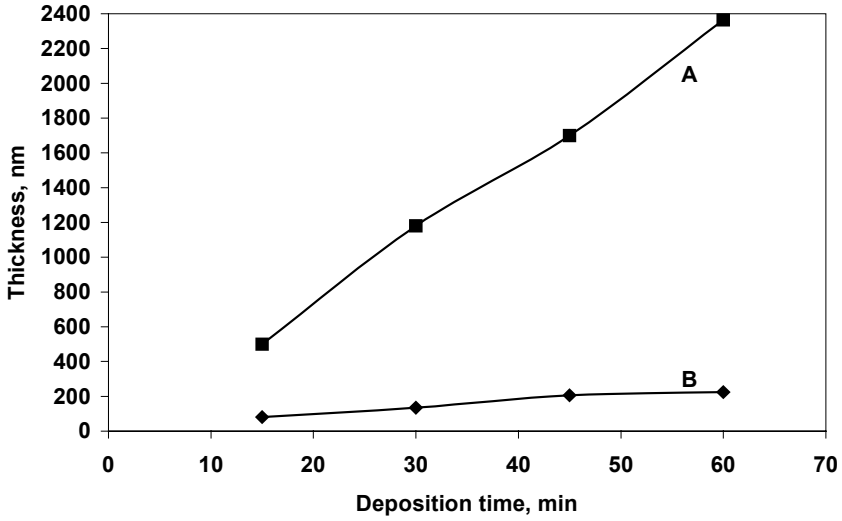


FIGURE 4. Variation of film thickness with deposition time under process conditions of: A – energy of single pulse 9.1 mJ, PC plate placed at the grounded electrode; B – energy of single pulse 6.2 mJ, PC plate placed at the grounded electrode.

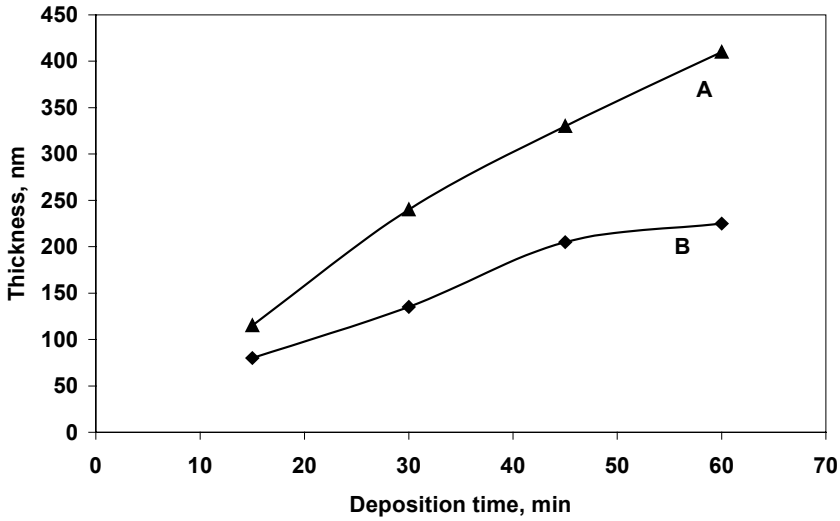


FIGURE 5. Variation of film thickness with deposition time under process conditions of: A – PC plate placed at the high-voltage electrode, energy of single pulse 6.2 mJ; B – PC plate placed at the grounded electrode, energy of single pulse 6.2 mJ.

In all the experiments the thickness of deposited films increased with increasing deposition time. It was simple and linear dependence (**FIGURES 4, 5**).

TABLE 1. Comparison of deposited rate of thin film by different parameters

Energy of single pulse, mJ	Deposition rate, nm/min.	PC plates covered electrodes
9.1	37	grounded
6.2	4.6	grounded
6.2	7.4	high-voltage

The real energy released in the single pulse of the discharge, the voltage and current depended on the arrangement of the reactor, and its electric capacity. The single pulse's current depends on the electric capacity strongly (**FIGURE 6**). We investigated two kinds of the reactor arrangement of different capacities: with single dielectric barrier and with double dielectric barriers. Runs of the voltage and current of these two kinds of the reactor arrangements are showed on **FIGURE 6**.

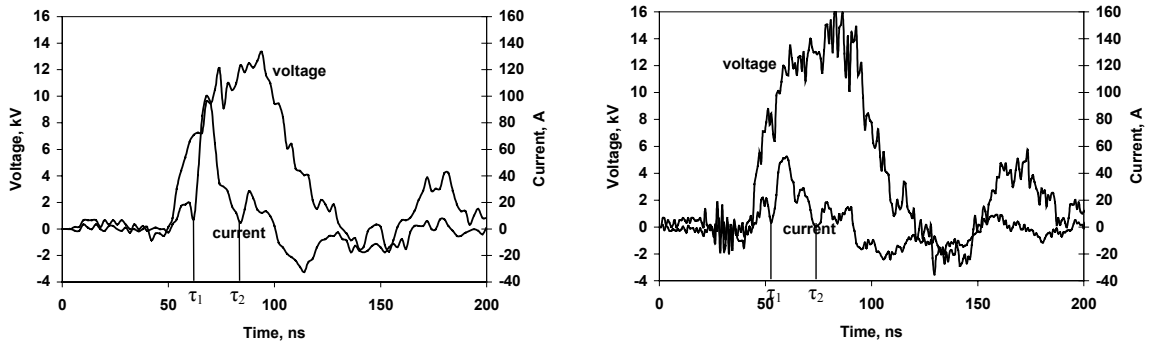


FIGURE 6. Runs of the voltage and the current of PBDB witch one PC plate (left) and two PC plates (right).

Electric capacity of the reactor with single PC plate was 23.2 pF and the value of the real energy was 9.1 mJ, calculated according the formula 2. Electric capacity of the reactor with two PC plates was 17.8 pF and the real energy was 6.2 mJ. The quite small change of the real energy released in the single pulse of the discharge (~50%) caused great increase of the thickness of the deposited film (**FIGURE 4**) and the film deposition rate (**TABLE 1**).

In the experiments, the films were deposited faster on the PC plate placed at the high-voltage electrode than at the grounded electrode (**FIGURE 5, TABLE 1**). This effect is probably depended of non-symmetric work of the electric power supply, which is showed on **FIGURE 7**. Each tooth form on the recorded voltage line is correlated to the single pulse of the discharge. This non-symmetric work of two electrodes depends on construction of the electric power supply. It is not still possible to remove it.

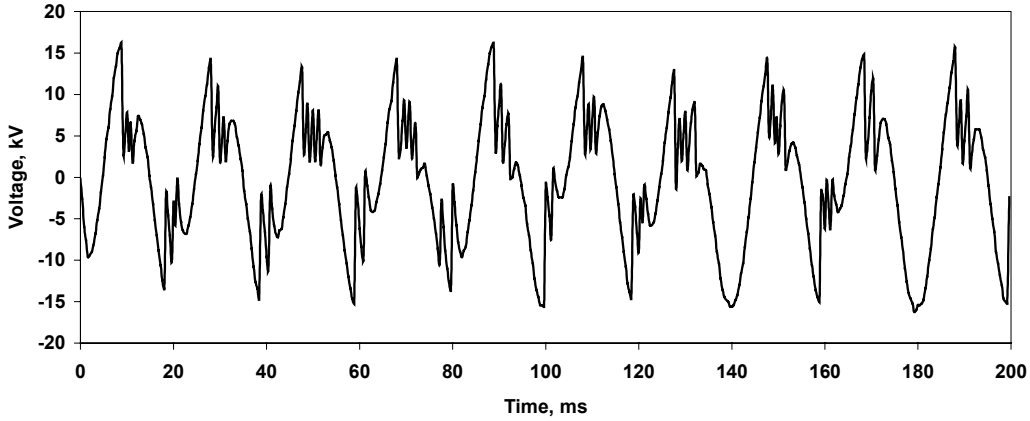


FIGURE 7. Run of the voltage, which supply the reactor with two PC plates.

4. CONCLUSION

1. Pulse dielectric barrier discharge (PDBD) can by used for thin filmsdeposition on polycarbonates (PC) under the atmospheric pressure and at the room temperature.
2. Thin films deposited by PDBD of tetraethoxysilane (TEOS) were transparent and smooth.
3. The deposition rate and the thickness of deposited film depended on the real energy released in the single pulse of the discharge and on the position PC plates on electrodes. The films were deposited faster on the PC plates, which covered high-voltage electrode than PC plates, which covered grounded electrode. The deposition rate and thickness of thin film increased with the increasing energy of single pulse.

REFERENCES

[1] Wróbel A. M., Wertheimer M. R., *Plasma Deposition, Treatment, and Ething of Polymers*, R. d'Agostino, ACADEMIC PRESS INC., San Diego, 1990, Chapter 3
[2] Hatanaka Y., Sano K., Aoki T., Wróbel A. M., *Thin Solid Films*, **368**, 287-291 (2000)
[3] Behnish J., Tyczkowski J., Gazicki M., Pela I., Holländer A., Ledzion R., *Surface and Coatings Technology*, **98**, 872-874 (1998)
[4] Schmidt-Szałowski K., Rżanek-Boroch Z., Sentek J., Rymuza Z., Kusznierewicz Z., Misiak M., *Plasmas and Polymers*, **5**, 173-190 (2000)
[5] Opalińska T., Effect of the Permittivity of Ferroelectric Electrodes on Macroscopic Characteristic of the Barrier Discharge. In: Proc. *7th Int. Symp. on High Pressure Low Temperature Plasma Chemistry*, ed. by H.-E. Wagner, J. F. Behnke and G. Babucke, Greiswald, 2000, pp. 98-102
[6] Ulejczyk B., Opalińska T., Schmidt-Szałowski K., Polaczek J., Karpiński L., Pawłowski S., *Polish Patent Appln*. P-347771

SURFACE MODIFICATION OF NON-FABRICATED POLYPROPYLENE TEXTILE IN LOW-TEMPERATURE PLASMA AT ATMOSPHERIC PRESSURE

P. Sťahel, J.Janča, D. P. Subedi

Department of Physical Electronics, Masaryk University, Kotlářská 2, 611 37 Brno, Czech Republic

Abstract: The plasma activation of polypropylene (PP) non-fabricated textile in low temperature plasma at atmospheric pressure has been studied. The aim of the present work was the study of the surface modification of non-fabricated textiles in order to improve their hydrophilic properties. The surface treatment has been provided by nonequilibrium discharges as barrier discharge and surface discharge. The surface properties have been characterized by measuring the contact angle of PP textiles with liquid, standard industrial permeability measurements and absorption tests. The degradation of treated PP samples has also been studied.

1. INTRODUCTION

Polypropylene has a very low value of the surface free energy (approximately 20-25 mJ/m^2) [1]. Due to low surface energy polypropylene has very weak hy[1]drophilic properties. In many industrial applications there is a need to modify the polymer surface with keeping their desired unchanged bulk properties. Chemical activation of the surfaces is the most often used method for their activation, however the ecological requirements force the industry to search alternative environmental safety methods. The surface modification of polymers in low-temperature plasma appears as one of the most prospective and cheap solutions.

The aim of the present work is to investigate the surface modification of non-fabricated polypropylene textiles by means of plasma treatment at atmospheric pressure to improve their hydrophilic properties. Many plasma applications in the surface modification field were made at reduced pressures in the order of 1 – 10 Pa [1, 2]. A significant increase in the hydrophilicity of low-pressure plasma treated materials was observed but the application in industry has many disadvantages, mainly problems with the need of vacuum system, long processing times and high energy consumption. This study is focused on the plasma surface activation of polypropylene non-fabricated textiles at atmospheric pressures. Interesting results were obtained using the surface discharges (SD) as well as by the application of barrier discharge (DBD). Some studies have been focused on the stabilization of surfactants [3, 4].

2. EXPERIMENTAL

In this study the plasma activation of polypropylene non-fabricated textiles were investigated. The textiles are produced by Pegas a.s. Bučovice, the main applications of these textiles are in medical, sanitary and hygienic industries. The surface weight of PP textiles varied from 20 to 50 g/m^2 in the case of spun-bond samples (in application used as a liquid transporting layer) and melt-blown type samples with surface weight varying from 50 to 200 g/m^2 (in application used as an absorption stratum). The surface activation was provided by barrier discharge (DBD) and/or surface discharges (SD) [5] at atmospheric pressure where the operation frequency varied from 50Hz to 10 kHz. The surface properties of treated and untreated samples were characterized by means of the contact angle measurement, the industrial absorption test and the water permeability measurement.

Electronic address: pstahel@physics.muni.cz

Dielectric barrier discharges (DBD) were created between two metal electrodes covered with insulating layers (glass, ceramic and polycarbonate). AC driving voltage with the amplitude of approximately 7-10 kV was used to create the discharge in DBD where the gap spacing was in the order of a few mm [8]. Many separate microdischarges are observed in DBD at these conditions. Thanks to the special shape of the metal electrodes, the microdischarges can be observed with the same density around the barrier surface. A significant disadvantage is that the DBD homogeneity considerably depends on the operating frequency and the gas mixture composition [6, 7]. Under certain specific conditions, the DBD discharge can produce so-called atmospheric pressure glow (APG) discharge [8, 9, 10], which can also be effectively used for the surface treatment [9].

Surface discharge SD was revived on the surface of the insulating plate (glass, ceramic and polycarbonate). The insulating layer was from one side fully covered with metal electrode. On the other side of the insulating plate the metal electrode consisted of 18 strips (10 cm long and 1 mm wide) with a 3 mm distance between them and connected together. The discharge appears along the insulator surface in a decreasing initial electric field from the side of the thin strips.

Dry air and partially nitrogen were used as the buffer gases. Plasma induced changes of PP textiles were indicated by the contact angle measurement and liquid permeability tests. The contact angle of liquid on solid is closely related to surface free energy and this parameter is useful in the discussion of hydrophilicity, absorbency of sample and adhesivity. The contact angle was measured directly from the observation of the solid-liquid meniscus. For the determination of total surface energy from contact angle measurement Wu's equation [11] and Owens-Wendt-Kaeble equation [12,13] can be used. Water permeability of samples before and after plasma treatment was determined measuring the time necessary for the penetration of 5 ml of the testing liquid across the sample. The absorption properties of sample were measured as a difference of the weights of the sample before and after the dipping in the testing liquid. The industrial absorption tests were measured at the Testing Textile Institute at Brno.

3. RESULTS AND DISCUSSION

The first part of our study is devoted to activation of the spun bond non-fabricated textiles with surface weight 20 g/m^2, in the second part the results of activation of melt-blown textiles are shown. The PP textiles were exposed to surface discharge and DBD in air. The degradation of spun-bond textiles is presented in the third part.

3.1. Activation of the spun-bond textiles

Plasma treatment of PP proceeds by a free-radical mechanism that introduces a wide variety of oxidized functional groups onto the surface of the treated polymer. These oxidized functional groups may include C-OH, C=O, COOH, C-O-C, epoxy, ester, or hydroperoxide [14, 15], and they are responsible for the change in the polymer surface properties.

Figure 1 shows the dependence of the water contact angle and the water permeability on the treatment time in air surface discharge. In this case the plasma was supplied with 5kHz sinus signal with amplitude 7 kV. The area of each electrode was 200 cm^2 and the power supply was 60 W. Fast increase in permeability was observed during the first 3 s, followed by a slow increase with increasing plasma exposure time. However the water contact angle linearly decreases with increasing exposure time. Figure 2 shows the dependence of the permeability on the contact angle. The permeability t_p can be described with a stretch exponential course $t_p = t_s+(t_i-t_s)*\exp(-\cos\Theta-\cos\Theta_i)/\beta$. Where t_i and Θ_i represent permeability and contact angle in initial (untreated) state, respectively t_s is permeability in (degraded) study state, and β represents dispersion parameter.

The effect of the power supply on the water contact angle and water permeability was tested and the results are shown in Figure 3. The treatment time was fixed to 2 s and the power supply was varied

The area of each electrode was 200 cm^2 and the frequency was 3 kHz. Strong influence of the power

supply to hydrophilic properties of PP textiles was observed. The permeability exponentially increases with increasing supplied power, however the water contact angle decreases linearly.

The plasma treatment of spun bond PP textiles in DBD operated at 3 kHz in air was studied (see Figure 4). The space between electrodes was 2 mm and the surface of the each electrode was 200cm^2.

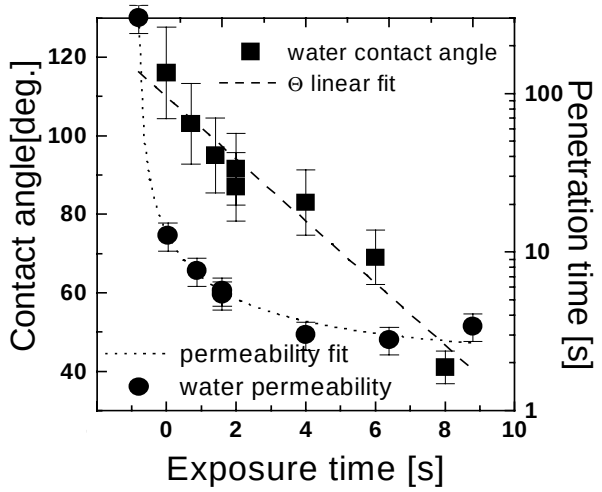


FIGURE 1. Dependence of contact angle and water permeability as a function of surface discharge exposure time.

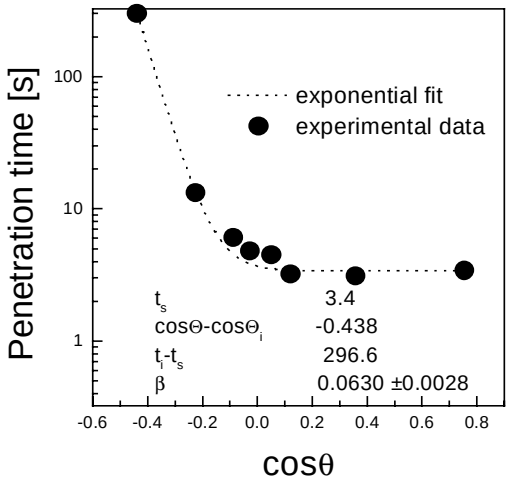


FIGURE 2. Dependence of the water permeability as a function of the cosΘ of PP sample.

The power supply was fixed to 100 W. The contact angle decreased linearly with increasing plasma treatment time. The permeability increases exponentially. The plasma treatment longer than 2 s can cause the hydrophilisation of surface of PP textile. Due to this result, the optimal plasma treatment time at this condition is 2 s. The influence of the operating frequency in range 1 kHz to 10 kHz was not registered. The higher frequency was not tested due to undesirable plasma perforations of treated material.

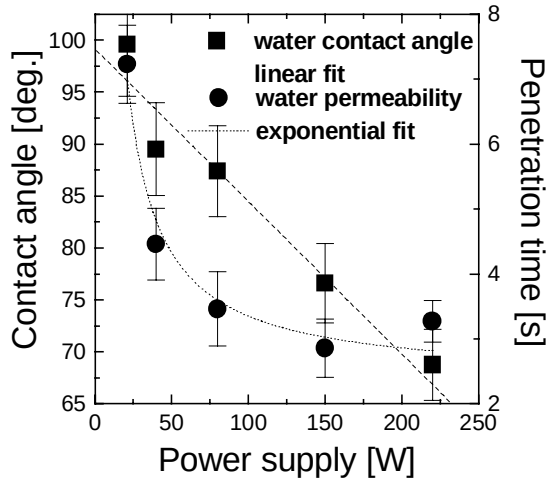


FIGURE 3. Dependence of contact angle and water permeability as a function of supplied power

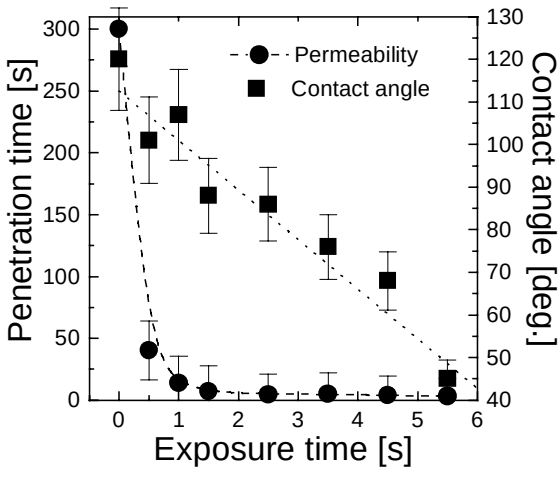


FIGURE 4. Dependence of contact angle and water permeability as a function of DBD exposure time. Dot and dash line serves as a guide of eyes.

3.2. Activation of the melt-blown textiles

In the case of melt-blown PP textiles the aim of our work was to increase the absorption capacity of the material. For the plasma surface activation, the air surface discharge operated at 5 kHz was used. For the activation of melt-blown textiles it was necessary to use higher exposure time than for spun-bond textiles. With plasma activation it is possible to reach 500% absorption improvement of polypropylene textiles with surface weight 75gm^{-2} as is shown on Figure 5. The water contact angle decreased to 70^{o}. However the samples with higher surface weight (200 gm^{-2}) treated at the same plasma conditions show only small improvement of the absorption. The plasma treatment acted only on the surface of the PP material i.e. the water contact angle decreased to 80^{o}, however the absorption increased only up to 90 % (see Figure 6).

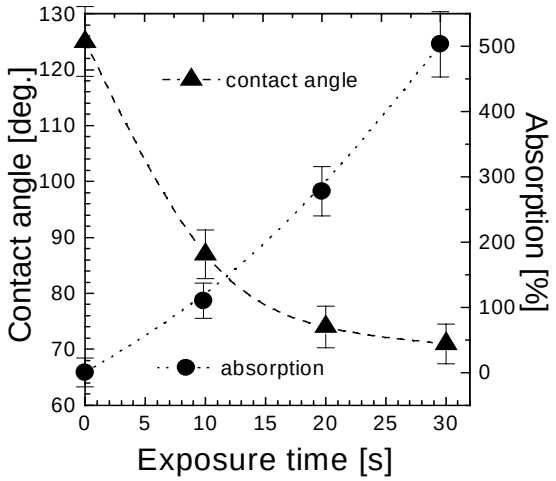


FIGURE 5. Dependence of contact angle and absorption as a function of surface discharge exposure time. Dot and dash lines serve as a guide of eyes.

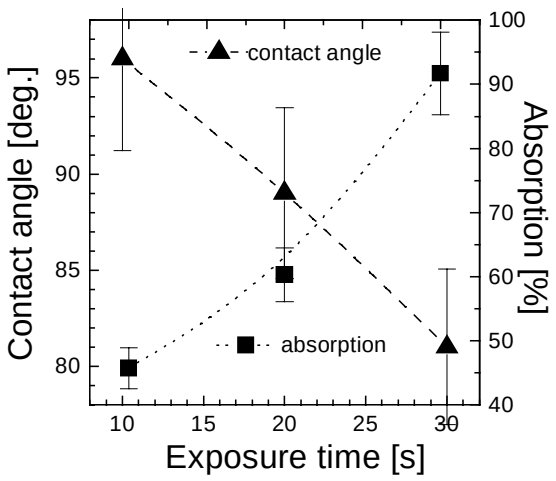


FIGURE 6. Dependence of contact angle and absorption as a function of surface discharge exposure time. Dot and dash lines serve as a guide of eyes.

3.3. Aging of spun-bond textiles

The degradation of the modified properties was studied. The metastability of the PP properties can be attributed to four effects [16]:

1. thermodynamically driven reorientation of polar species away from the surface into the subsurface

2. diffusion of mobile additives or bloomers from the polymer bulk to the surface

3. formation of low molecular weight species in subsurface during the plasma treatment and their subsequent migration to the surface

4. reaction of the residual free radicals with ambient

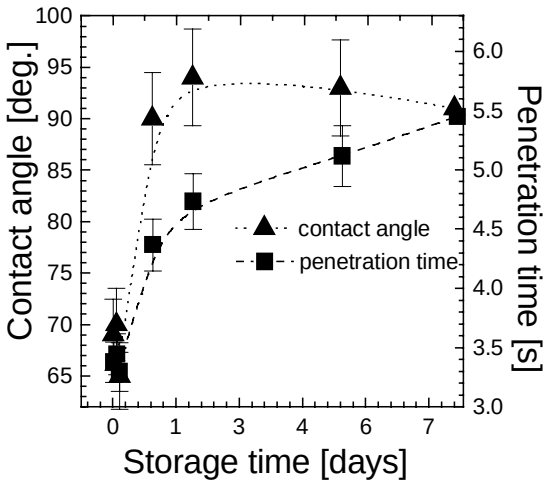


FIGURE 7. Dependence of contact angle and water permeability as a function of storage time. The plasma treatment was 3 s in air surface discharge. Dot and dash lines serve as a guide of eyes

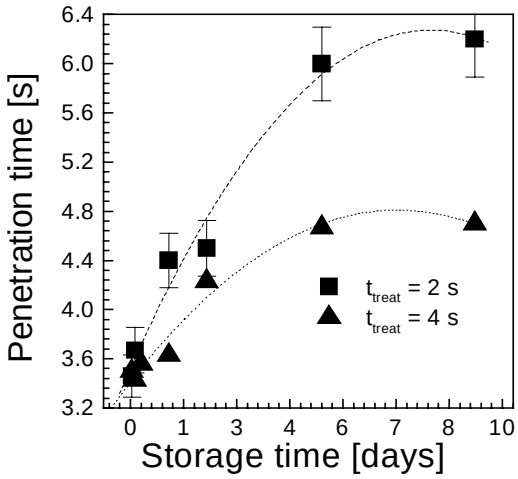


FIGURE 8. Dependence of water permeability as a function of storage time. The plasma exposure time was 2s and 4s in air surface discharge. Dot and dash lines serve as a guide of eyes.

After the plasma activation the spun-bond samples were stored in air atmosphere at 23°C. The PP samples were activated in air surface discharge. Surface area of the each electrode was 200 cm^2, power supply 60 W. The permeability and contact angle of sample were measured after the subsequent logarithmical time steps.

Figure 7 shows the kinetics of the permeability and contact angle as a function of storage time. The stretch exponential increase in water contact angle of plasma activated PP textile in the aging time was observed. The water contact angle reached the saturation 40 hours after the plasma treatment, however there was observed decrease in water permeability of sample even after 40 hours. This discrepancy can be explained with a different sensitivity region of the testing methods. The contact angle is sensitive only to surface properties however water permeability is sensitive to surface and bulk properties.

Figure 8 shows the degradation of samples treated for 2 s and 4 s at the same plasma conditions. Both samples (treated for 2 s and 4 s) reached the saturation after 10 days of the storing. Moreover, the sample treated for 4 s shows lower degradation than the sample treated for 2 s.

4. CONCLUSIONS

We made the first experiments with the plasma treatment of PP non-fabricated textiles to increase their hydrophilicity. The surface discharge was found to be more effective tool for the treatment of this type of material than the dielectric barrier discharge DBD. The barrier discharges were used at atmospheric pressure and at various operating frequencies in air. We observed that the frequency of the supplied power has no significant effect on the treatment. On the other hand, large effect of the supplied power was observed.

The plasma treatment of the PP non-fabricated textiles was characterized by different techniques. The technological and construction points of view were taken into account. The experimental results of the used techniques correspond with results obtained with other authors.

The aim of further experiments will be the optimization of the discharge conditions in order to reach the lower plasma exposure time and to increase the stability. Special attention of our work will be devoted to stabilization of surfactants namely due to grafting.

ACKNOWLEDGEMENTS

This work has been supported by Grant Agency of Czech Republic, contract No. 202/02/0880. Special thanks belong to the technical staff of Testing Textile Institute at Brno.

REFERENCES

[1] Inagaki, N., *Plasma Surface Modification and Plasma Polymerization*, Technomic Publication Company, Lancaster, 1996.
[2] France M. R. and Short , R. D. *J. Chem. Soc. Faraday Trans.*, **93,** 3173-3178**,** (1997)
[3] Favia, P., Palumbo, F., d'Agostino, R., Lamponi, S., Magnani, A. and Barbucci, R, *Plasmas and Polymers*, **3,**77-91, (1998)
[4] Dadsentan, M., Mirzadeh, H.,Sharifi-Sanjani, N., *J.of Appl. Polymer Sci.*, **76**, 401-407 (2000)
[5] Pietsch, G.J., Haacke, M., *Proc. HAKONE VII., Greifswald Germany*, (2000), 299-303
[6] Kogoma, M., Okazaki, S., *Journal of Physics D, Applied Physics*, **27** (1994) 1985
[7] Kogelschatz, U., Eliasson, B., Engli, W., *Journal de Physique IV France*, **7** (1997) C4-4
[8] Massines, F., Rabehi, A., Decomps, P. at al, *J. of Appl. Phys.*, **83** (1988) 2950
[9] Liu, C., Tsai, P. P., Roth, J. R., *Proceedings of the 20th IEEE Int. Conf. Plasma Sciences*, Vancouver 1999
[10] Kogoma, M., Prat, R., Sowa, T., at al, *Plasma Processing of Polymers, Series E: Applied Science*, ed. R. d'Agostino, P. Favia, F. Fracassi, *Kluver Academic Publishers*, **346**, (1996) 379
[11] Wu., S., *J. Colloid Interface Sci*, 71, 605, (1979)
[12] Owens, D.K., Wendt, R.C., *J. Appl.Polym.Sci. 13*, 1741-1747, (1969)
[13] Kaeble, D.H., *J.Adhesion*, 2, 50, (1970)
[14] Strobel, M., Lyons, C.S.,Strobel, J., Kapaun, R.S., *Contact Angle, Wettability and Adhesion*, 493-507, Utrecht, editor K.L.Mattal, Netherlands (1993)
[15] Pochan, J.M., Gerenser, L.J., Elman, J.F., *Polymers*, 1058-1062,(1986)
[16] Spell, H.L., Christenson, C.P., *Tappi J*., 62,77,(1979)

SURFACE TREATMENT OF PLASTIC FILM BY USING AN ATMOSPHERIC PRESSURE CORONA TORCH

Shigeru Ono[a], Shinriki Teii, Shinako Takayama

a) Department of Electrical and Electronic Engineering Musashi Institute of Technology, Tamazutsumi 1-28-1, Setagaya-ku, Tokyo 158-8557, JAPAN

Abstract: Using a simple DC discharge corona torch under atmospheric pressure has carried out surface treatments of the plastic film for improving hydrophilic property. Although the input power of the torch was very small only about 1~5W, it enables to decrease the contact angle of a ethylene glycol drop on the film surface from 50˚ to 5˚ within 1~2 minutes. The contact angle of the film after treatment recovered to approximately 20˚ in 5 days and then, kept almost unchanged thereafter. Data will be presented and discussed.

1. INTRODUCTION

Surface treatment of polymeric materials using discharge plasmas of the gases including oxygen or fluorine can improve the hydrophilic or hydrophobic properties of the materials have been reported in some low gas pressure discharges [1], [2]. These modifications of surface properties were explained by the formation of oxygen or fluorine functionalities on the material surface as the result of implantation of radicals existing in the discharge plasma.

For practical uses, however, surface modification is desirable to be done under atmospheric pressure to simplify the equipment and thus, various types of atmospheric pressure nonthermal plasma produced by pulsed or AC corona discharges for surface modification have been also reported [3], [4], [5].

In this paper, we report another experiment of surface treatment by using a simple DC type discharge corona torch at atmospheric pressure.

This small pen-like corona torch used is consisted of two coaxial cylindrical electrodes with different length and the plasma is produced by the surface discharge along the ceramic tube which is inserted between the two electrodes.

Although the input power of the torch is very small, a stationary plasma can be obtained under atmospheric pressure and it enables us to make a long time surface treatment of plastic film for improving the hydrophilic property. The time for treatment seems important with relation to the time of recovery of the hydrophilic property after treatment. All data will be presented and discussed.

2. EXPERIMENTAL APPARATUS AND METHODS

As shown in Fig.1, the stainless steel made cylindrical tube of 6.5mm diameter and 170mm length was used as the inner electrode and a 15mm length stainless steel ring was located at the distance 15mm from the tip of inner electrode as the outer electrode. A ceramic tube of 12mm diameter and 150mm length was inserted coaxially between the two electrodes for insulation. Electrical discharge was made by applying high voltage between the electrodes using a DC power supply (CS9002-30A of ULTRAVOLT Inc) which could be varied from 0~30kV. The $Ar+N_2$ gas mixture was flow through the inner electrode tube for driving the discharge and a visible plasma of approximately 5~10mm long was formed downstream of the flow because of the ionization of driving gas by the discharge. The

[a] Electronic address: ono@ee.musashi-tech.ac.jp

plastic film to be treated was put on a sample holder made of acrylic board placed downstream of the flow and the distance from the holder to the tip of inner electrode could be varied from 0~40mm.

The various particle species in the plasma were measured by the spectroscopic method and the variation of hydrophilic property was checked by measuring the contact angle using a contact angle meter.

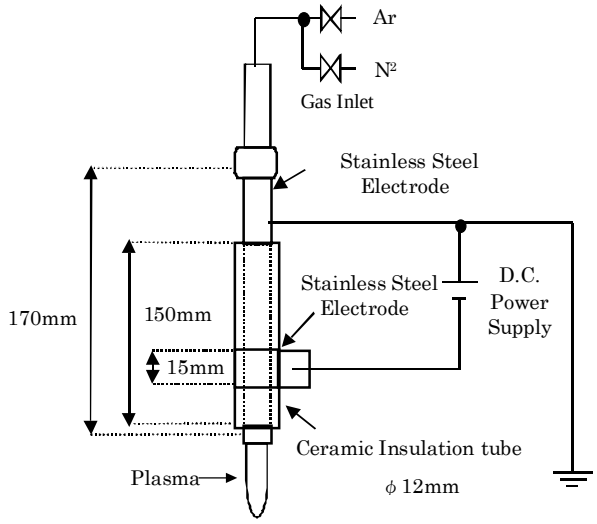


FIGURE 1 Schematic of atmospheric pressure corona torch

3. EXPERIMENTAL APPARATUS AND METHODS

Typical voltage-current characteristics of the discharges with varying Ar+N_2 gas mixture ratio are shown in Fig.2. Discharge begins approximately from the applied voltage of 10kV. The discharge current increases with increasing applied voltage and becomes approximately 250μA at the voltage of 20kV, thus it is estimated that the total input power is very small only about 1~5W.

Fig.3 shows typical spectra intensities of N_2 1^{st} positive system bands (1PSB, 673.5nm), N_2 2^{nd} positive system bands (2PSB, 380.5nm) and N_2^+ 1^{st} negative system bands (1NSB, 434.5nm) with varying gas mixture ratio. As can be seen from the figure, emission from the N_2^+ 1^{st} negative system bands is very weak because of the ionization rate is very low. All the spectra intensities are most enhanced for the gas mixture ratio of N_2 5% implies that under this condition, the highest density of N_2 radicals are existing in the discharge.

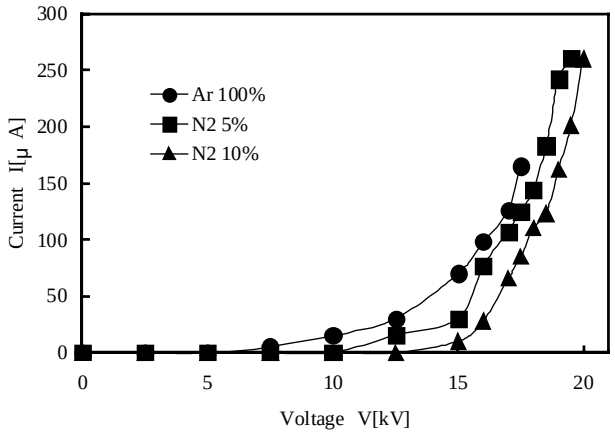


FIGURE 2 Corona torch V-I characteristics

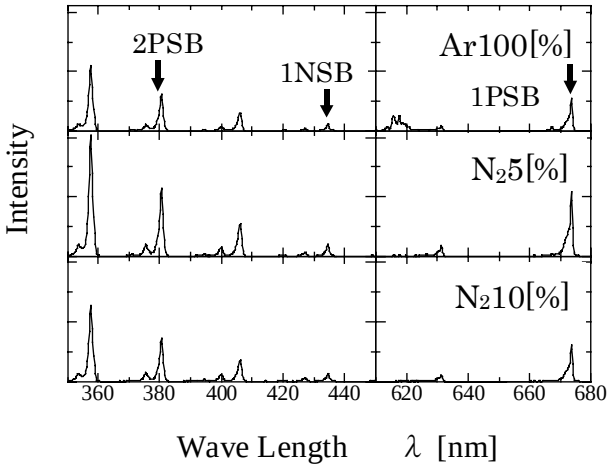


FIGURE 3 Corona torch V-I characteristics

Fig.4 shows typical results of the treatment of polyethylene terephthalate film (PET, 20×20×0.2mm) with varying the $Ar+N_2$ gas mixture ratio. Experiment was carried out under the conditions of discharge current 60μA, gas flow rate 15l/min. The sample was located 5mm below the tip of the inner electrode. Since the hydrophilic property can be expressed by contact angle, the relations between the measured contact angle using a ethylene glycol drop with the treatment time. As can be seen from the figure, the measured contact angle decreases sharply with increasing treatment time within 1~2 minutes and after this, becomes almost a constant value. Also, the treatment was most effective under the condition of 5% nitrogen gas mixture ratio in coincidence with the result of optical spectra intensity measurement as shown in Fig.3. This result implies that the excited high energy radicals existing in the plasma may play an important role for improving the hydrophilic property by enhancing the formation of oxygen functionalities on the film surface.

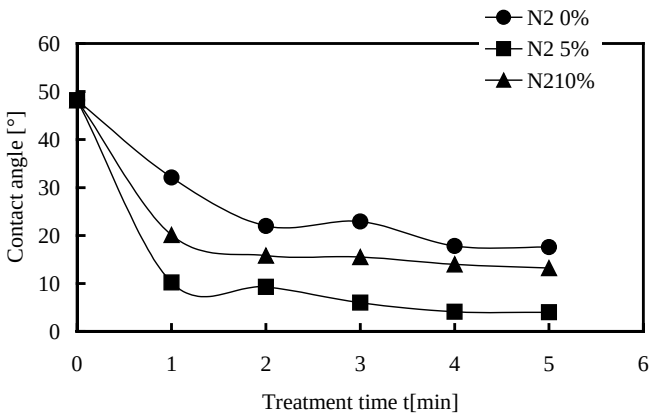


FIGURE 4 Effect of plasma treatment time on contact angle

Since the hydrophilic property of the film is related to the surface free energy which is composed of the intermolecular forces of dispersion force, dipole force and hydrogen bond force, each ingredient forces as well as the surface free energy were also measured. Typical results for the case of 5% N_2 gas mixture ratio are shown in Fig.5. As can be seen from the figure, surface free energy increases by the treatment, that is, the hydrophilic property is improved. However, as to the after forces, only the hydrogen bond force increases with increasing treatment time same as the behavior of surface free energy. These results support that, the improvement of hydrophilic property may be caused by the formation of hydroxyl group functionalities on the film surface.

Fig.6 shows typical recovery characteristics of the film using the sample treated 3 minutes in 5%

nitrogen gas mixture ratio discharge. The treated film was exposed to the air and the contact angle was measured once a day at every day's evening. As can be seen from the figure, the contact angle recovers from 5° to 20° within 5 days but after 5days, remains almost unchanged. The long durability of the hydrophilic property may be caused by the formation of sufficient thick layer of hydroxyl group functionalities on the film surface as the result of a rather long time treatment in a small input power discharge.

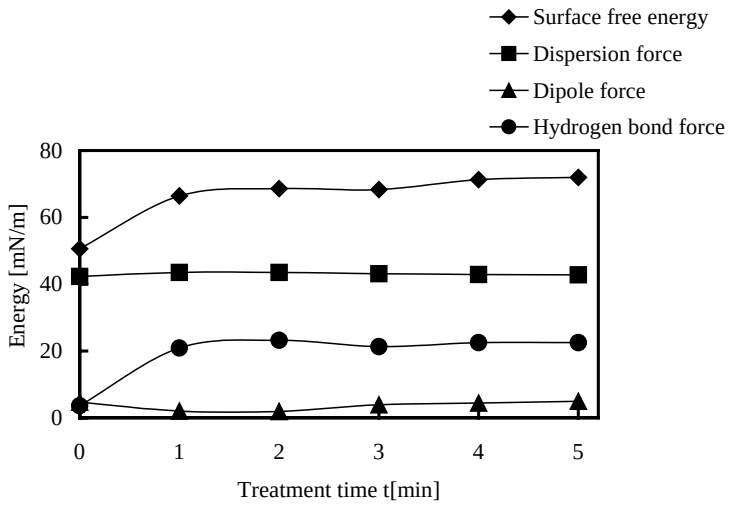


FIGURE 5 Surface free energy characteristics

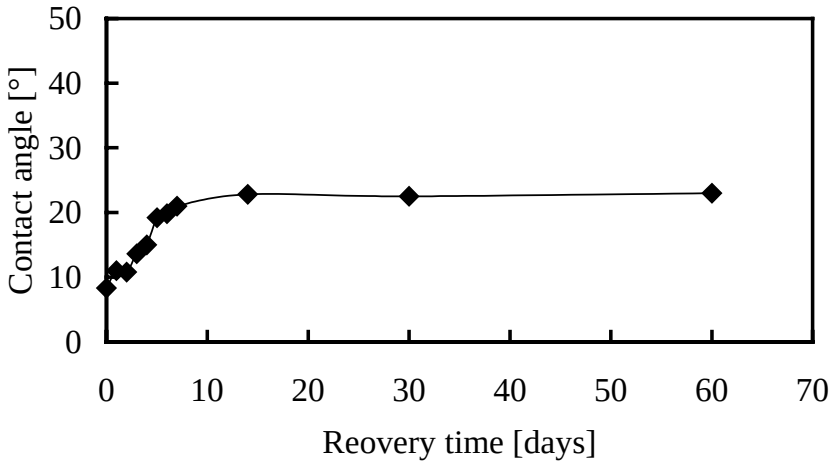


FIGURE 6 Durability test

4. SUMMARY

A simple DC discharge type atmospheric pressure corona torch with small input power of 1~5W has been developed and applied to the surface treatment of PET film for improving the hydrophilic property. Experimental results show that :

(1) The contact angle decreases within 1~2 minute treatment from 50° to below 10° for the case of 5% N_2 gas mixture ratio which is the most effective gas mixture ratio for surface treatment.

(2) The contact angle recovers from 5° to 20° within 5 days after treatment and remains almost a constant at about 20° thereafter.

(3) The measured spectra intensities and hydrogen bond force indicate the possibility of the formation

of hydroxyl group functionalities on the film surface for improving the hydrophilic property.

REFERENCES

[1] M. Strobel, S. Corn, C.S. Lyons and G.A. Korba, J. Polym. Sci., Polym. Chem. Ed., 25 (1987) 1295.
[2] M. Strobel, C.S. Lyons, P.A. Thomas, M.C. Morgan, S. Corn and G.A. Korba, J. Appl. Polym. Sci., Appl. Polym. Symp., 42 (1988) 73.
[3] T. Yamamoto, J.R. Newsome and D.S. Ensor, IEEE Trans. Ind. Appl., 31-3 (1995) 494.
[4] S. Matuda, S. Hosokawa, I. Tochizawa, K. Akutsu, K. Kuwano and A. Iwata, IEEE Trans. Ind. Appl., 30-2 (1994) 377.
[5] T. Yamamoto, M. Okubo, Y. Matsumoto, N. Imai and Y. Mori, Proc. of 4 ESA/IEJ Joint symposium in Electrostaitics, Kyoto, Japan, (Sept 2000).

DEPOSITION OF MULTI-LAYER FILMS OF HEXAFLUOROPROPENE - ETHYLENE COMPOSITE POLYMER WITH JET-TYPE PLASMA REACTOR AT ATMOSPHERIC PRESSURE

Kunihito Tanaka[a] and Masuhiro Kogoma[b]

Department of Chemistry, Faculty of Science and Technology, Sophia University
7-1 Kioi-cho, Chiyoda-ku, Tokyo 102-8554, Japan

Abstract: Multi-layer films of hexafluoropropene - ethylene composite polymer were deposited with a jet-type plasma reactor on poly (ethylene terephthalate) films, which were used as base films, at atmospheric pressure. The multi-layer films were made up by decreasing the flow rate of ethylene gas gradually and increasing that of hexafluoropropene gas simultaneously during the plasma-polymerization. Those films showed low enough peel force, whose value was near that of a Teflon sheet used as a control. Moreover, the bond strength between the multi-layer film and the base film became stronger than that between a plasma-polymerized hexafluoropropene film and the base film.

1. INTRODUCTION

Adhesive tapes are generally kept in rolls. Consequently, so that we can peel them out smoothly, the adhesive tapes consist of three layers: the adhesive layer, the base film and *the remover layer*. Some silicone polymers have been frequently used as removers of adhesive tapes because of their quite low peel force. When one uses the adhesive tape, a very small amount of the remover moves to the adhesive side. Those removers on the adhesive will desorb to the atmosphere and then adsorb somewhere again. This phenomenon may give serious damage to some electric devices such as hard disk drives.

Fluorinated polymers, such as poly tetrafluoroethylene (PTFE), have many unique characteristics: high chemical resistance, high dielectric constant, high heat resistance, low peel force and low coefficient of friction. Although they have been used as typical inert materials for many situations, they are rarely used as the remover of adhesive tapes because there is no suitable solvent for applying the fluorinated polymers on the adhesive tape films.

We have already found that APG plasma can polymerize some fluorinated polymers even at atmospheric pressure. And in our previous study, we found that a plasma-polymerized hexafluoropropene film deposited by jet-type plasma reactor had low enough peel force for practical use, and the results showed the validity of the atmospheric pressure glow discharge technique. [1] However, two problems still remained: that a large amount of the polymer was deposited inside the plasma reactor and that the bond strength between the deposited polymer layer and the base film was slightly weak. We expected that a new reactor would solve the former problem, and that some fluorocarbon - hydrocarbon composite polymer layers inserted between the deposited layer and the base film would make the bond strength stronger. Therefore, we made a new reactor and tried to deposit multi-layer films in this study.

[a] tanaka@ch.sophia.ac.jp
[b] m-kogoma@sophia.ac.jp

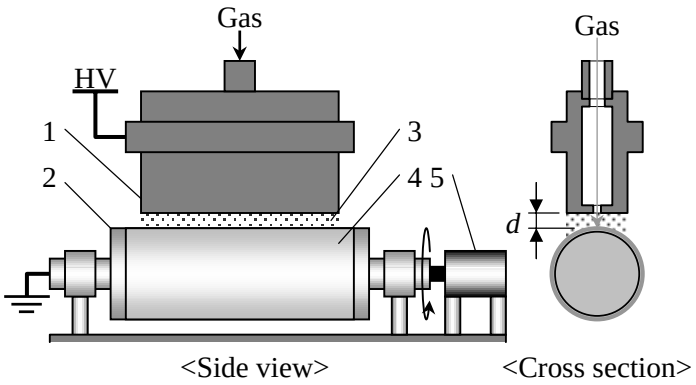


FIGURE 1 Schematic diagram of the reactor. 1, Upper aluminum electrode; 2, Lower stainless electrode (rotation drum); 3, Discharge area; 4, Sample film; 5, Motor.

Table 1 Treatment conditions.

Discharge Frequency	100 kHz
Discharge Power	20W
Monomer Flow Rate	3-20 $cm^3 \cdot min^{-1}$
He Flow Rate	5 $L \cdot min^{-1}$
Distance *1	1.5 mm

*1 The distance between the slit and the sample surface.

2. EXPERIMENTAL

The jet-type reactor used in this study is shown in Fig. 1. The entire surface of the upper high voltage electrode made of duralumin was coated with aluminum oxide by the alumite treatment. The electrode had a rectangular slit, whose size was 0.5 mm by 50 mm, at its bottom surface. The lower ground electrode was a stainless steal drum, which was wrapped with a polymer sheet during the plasma deposition. Thus this reactor was a barrier discharge system. When we used a glass plate as a substrate, a flat aluminum plate was used as the lower electrode. Of course, the deposition did not occur inside the reactor (upper electrode).

We used hexafluoropropene (C_3F_6) or ethylene (C_2H_4) as a monomer. These monomers were diluted with a large amount of helium and the mixture gas was passed through the discharge area. Then it blew over a substrate. Of course, these reactors remained in the atmosphere. Table 1 shows details of the discharge conditions in each treatment.

A poly (ethylene terephthalate) (PET) sheet or a glass plate was used as a substrate. The glass plate substrate was used only for the measurement of the deposition rate. The size of the PET sheet wrapped around the drum was 80 mm by 125 mm. The drum was rotated at a speed of 4.4 $cm \cdot s^{-1}$.

The thickness of the polymer deposited on the glass plate was measured with a surface profile measuring system (DEKTAK IIA, Sloan). This system measured the unevenness of a sample surface with a contact diamond needle. The resolution and the minimum value of the thickness were both 5 Å. The thickness of a deposited polymer film was an average of values at ten points on a sample surface. The peel force was measured with a 180° peel test: No.31B tape (Nitto Denko Co., LTD), whose width was 20 mm, was stuck on the deposited polymer and was peeled off at the speed of 300 $mm \cdot min^{-1}$. The chemical state of the deposited polymers was measured with XPS (ULVAC-Phi Co., Ltd., ESCA-5800ci). Since there was no standard energy to correct the binding energy in the C_{1s} spectra, we set the peak position of F_{1s} spectrum at 689 eV; this value was obtained from the measurement of a Teflon sheet. We fixed the interval energies between each chemical group at values observed from references 2 and 3. Then we carried out curve fitting with the XPS program of ULVAC-Phi.

3. RESULTS AND DISCUSSION

3.1. Characterization of Plasma-Polymerized Hexafluoropropene (PPHFP) and Plasma-Polymerized Ethylene (PPE)

To obtain the optimum discharge conditions, we examined how the deposition rates of PPHFP and PPE and the peel force of PPHFP depended on the monomer contents in the mixture gas. Figure 2 shows the variations of the deposition rate as a function of monomer content on PPE and PPHFP. The glass plates were used for the substrates in this measurement. Both deposition rates increased linearly until 0.12 % of ethylene and 0.06 % of HFP, respectively, and then they became slower. Especially,

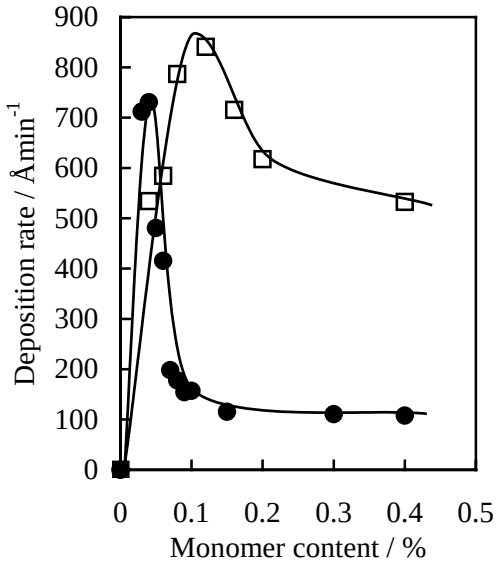


FIGURE 2 The variations of the deposition rate of □ PPE and ● PPHFP as a function of monomer content. The substrates were the glass plates.

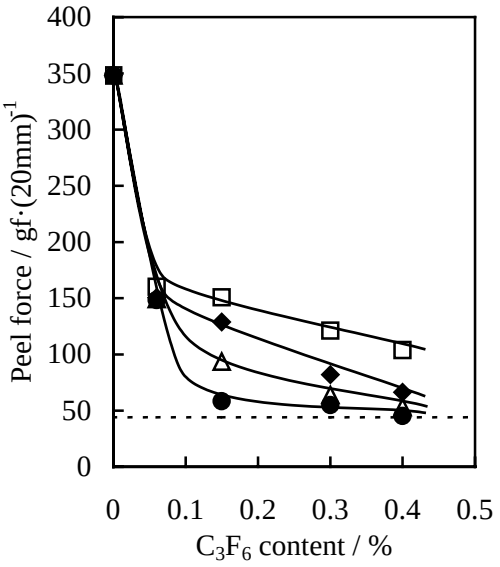


FIGURE 3 The variations of the peel force of PPHFP as a function of HFP content. The marks show different discharge times: □, 10 min; ◆, 20 min; △, 30 min; ●, 40 min.

the drop-down width of the deposition rate of PPHFP was bigger than that of PPE. The reason why the deposition rate decreased was that the discharge energy per one monomer molecule decreased as the monomer content increased. And we assumed that the deposition rate of PPHFP decreased extremely because excess HFP acted as an etchant; some fluorocarbon radicals etched PPHFP. [4] To make the treatment time shorter, the best ethylene content was 0.12 % in this study. However, for the reason described below, the best HFP content was not 0.06 %.

Figure 3 shows the variations of the peel force of PPHFP. Since we intended to use the deposited polymer for a remover, lower peel force was better. Contrary to the deposition rate result, the peel force became lower as one increased the HFP content. The PPHFP whose HFP content was 0.4 % and

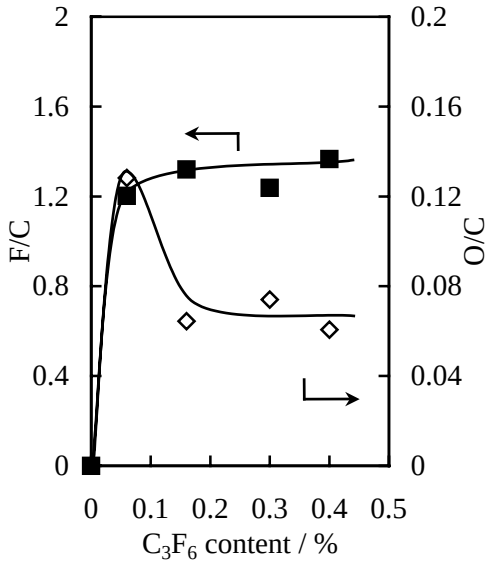


FIGURE 4 The variations of the atomic ratios of ■ F/C and ◇ O/C obtained from XPS spectra of PPHFPs whose discharge time was 20 min.

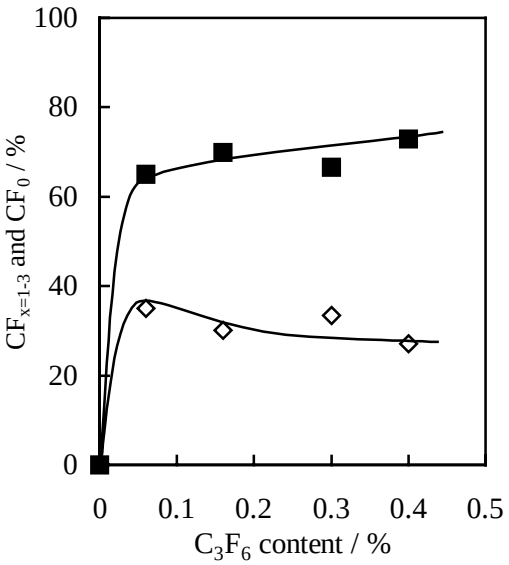


FIGURE 5 The variations of the ratio of ■ CF_x (x=1-3) and ◇ CF_0 structures in C_{1s} spectra.

for which the discharge time was 40 min had the same peel strength as the Teflon sheet, which was used as the control. Thus the best HFP content was considered to 0.4 %. The reason why 40 min discharge time was needed to make the peel force low enough was that the PET sheet was not covered with PPHFP completely for short discharge times because PPHFP was not deposited uniformly. We could expect that this problem would be solved by an improvement of the reactor. Next, the difference of the peel forces was examined via XPS spectra of PPHFPs.

Figures 4 and 5 show the atomic ratios of F/C and O/C spectra and the ratio of carbons bonding with fluorine CF_x (x=1-3) and without fluorine CF_0 (eg. -**C***(CF3)=CF-) in C_{1s} spectra obtained from XPS, respectively. According to those figures, the fluorine atom content and the ratio of CF_x structures increased with increasing HFP content. Since surface energy generally becomes lower by increasing the concentration of fluorine atoms on the surface, we considered that PPHFP deposited with high HFP content showed lower peel force. [5]

Figures 6 (a) - (d) are C_{1s} XPS spectra of the adhesive layer side of the adhesive tapes that were unused and those used for 180° peel tests of PPHFP, PPE and plasma polymerized hexafluoropropene - ethylene multi-layer film (MLF, described in the following section), respectively. Although the spectrum (a) shows that the unused adhesive tape had only C, C-O and C=O structures, some CF_x structures did exist on the adhesive layer used for the peel test of PPHFP, as shown in Fig. 6 (b). The result indicated that some part of PPHFP was peeled from the PET sheet and was pasted on the adhesive. On the other hand, since there is no difference between Fig 6 (a) and (c), it seemed that PPE was not peeled from the PET sheet; if PPE was peeled off, C-O and C=O peaks of Fig. 6 (c) would have become smaller. Moreover, we did not obtain any traces of peeled PPE on the treated PET sheets. Therefore, we expected that to insert PPE and plasma-polymerized hexafluoropropene - ethylene composite polymer (PPHE) between the PET sheet and PPHFP would make the bond strength between them stronger, and we tried a new deposition process.

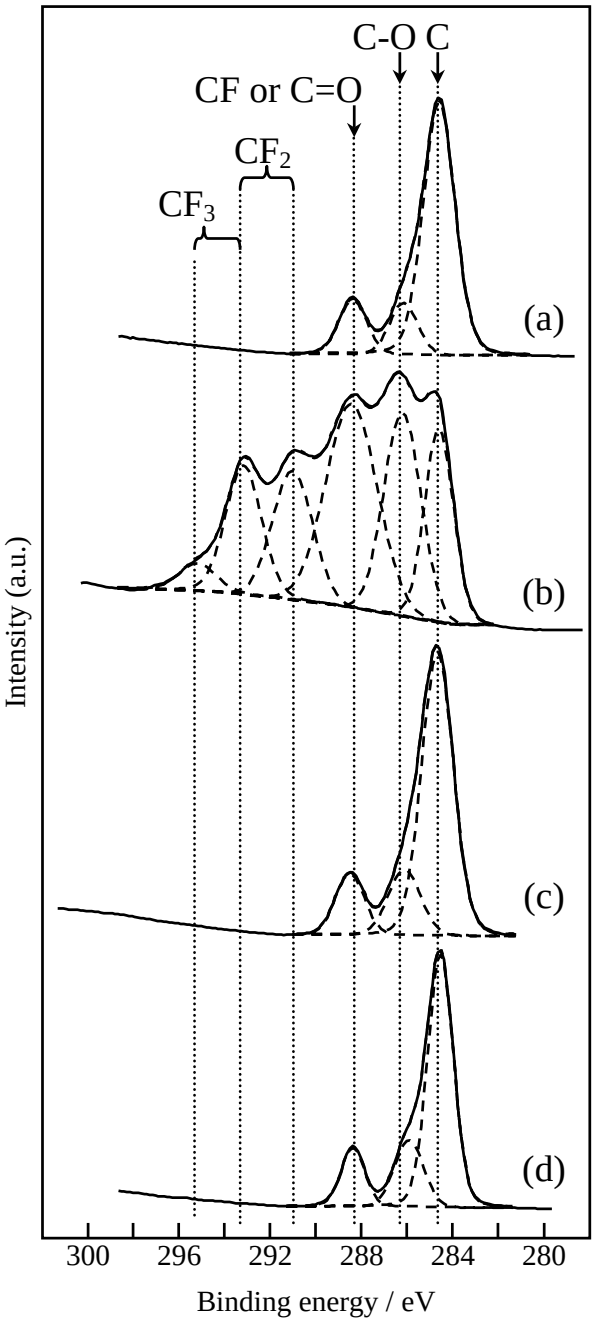


FIGURE 6 C_{1s} XPS spectra of the adhesive layer side of the adhesive tapes, which were (a) unused tape, and tapes used for the 180° peel test of (b) PPHFP, (c) PPE and (d) MLF, respectively.

3.2. Characterization of Plasma-Polymerized Hexafluoropropene - Ethylene Multi-Layer Film (MLF)

The preparation of MLF was carried out as follows: at first, PPE was deposited for 10 minutes with 0.12 % ethylene. Then PPHE was deposited with 0.09 % ethylene and 0.10 % HFP mixture gas for the

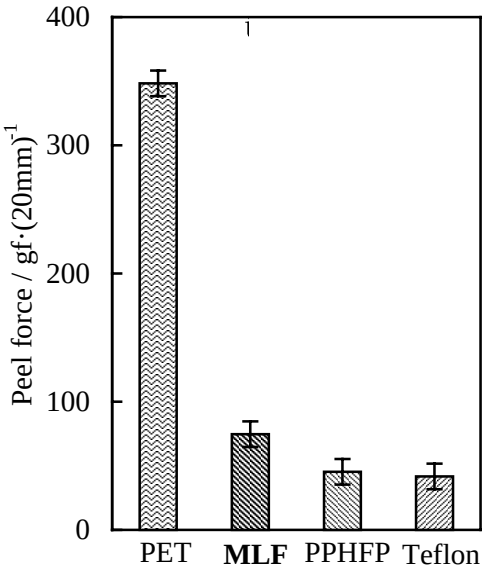


FIGURE 7 The comparison of the peel forces of PET sheet, MLF, PPHFP and Teflon.

next 10 minutes. In the same way, while PPHE was being deposited, the ethylene was decreased by 0.03 % and the HFP content was increased by 0.10 % at every 10 minutes. Finally, PPHFP was deposited for 10 minutes with 0.40 % HFP. All through the process, the discharge was being generated.

There was no difference between the C_{1s} spectra of the adhesive layer of the unused tape and that of the tape used for the peel test of MLF, as shown in Fig. 6 (a) and (d). Therefore, our conclusion was considered that our expectation was achieved. Moreover, though the peel force of MLF did not show as low value as that of Teflon sheet and PPHFP, as shown in Fig. 7, we thought that this value was low enough.

4. CONCLUSION

In this study, we could solve the bond strength problem. However, it was clear that the discharge time was too long. Thus we would have to examine the discharge time of PPHE and find some ways to deposit the polymers more uniformly.

ACKNOWLEDGMENTS

The authors wish to express their gratitude to Professor Frank Scott Howell S. J. for his valuable comments.

REFERENCES

[1] K. Tanaka, T. Inomata and M. Kogoma, *Proc. HAKONE VII*, **2**, (2000) 422.
[2] U. Gelius, P. F. Heden, J. Hedman, B. J. Lindberg, R. Manne, R. Nordberg, C. Nordling and K. Siegbahn, *Phys. Scr.*, **2** (1970) 70.
[3] D. T Llark, W. J. Feast, D. Kilcast and W. K. R. Musgrave, *J. Polym. Sci.*, **11** (1973) 389.
[4] A. Tasaka, A. Komura, Y. Uchimoto, M. Inaba and Z. Ogumi, *J. Poly. Sci. A: Polym. Chem.*, **34**, (1996) 193.
[5] P. B. Leezenberg, T. C. Reiley and G. W. Tyndall, *J. Vac. Sci. Technol. A*, **17**, 1, (1999) 275.

ATMOSPHERIC PRESSURE LIQUID DEPOSITION – A NEW ROUTE TO HIGH PERFORMANCE COATINGS

Andy Goodwin, Tony Herbert, Stuart Leadley and Frank Swallow

Dow Corning (Ireland) Ltd., Owenacurra Business Park, Midleton, Co.Cork, Republic of Ireland.

Abstract. Plasma enhanced coating processes are well known as a route to well adhered, conformal, high performance coatings. These processes deliver industrial coatings without the need for solvent, surfactant and drying ovens. However, application has often been restricted to high value opportunities as plasma processes typical operate at reduced pressure, with high capital cost and batch wise operation.

By combining Atmospheric Pressure Glow Discharge (APGD) technology with a unique precursor delivery system Dow Corning Plasma has developed a new coatings approach – Atmospheric Pressure Liquid Deposition. Operating at atmospheric pressure and ambient temperature this process allows the use of a wide range of liquid precursors delivering high coating rates onto flexible substrates. Patented APGD equipment enables the treatment of wide area substrates in true reel-to-reel conditions. Substrates can be both insulating and conducting.

The apparatus and process will be described, with a summary of unique coating chemistry that is achieved.

1. INTRODUCTION

Plasma enhanced coating processes are well known as a route to well adhered, conformal, high performance coatings. These processes deliver industrial coatings without the need for solvent, surfactant and drying ovens. However, application has often been restricted to high value opportunities as plasma processes typical operate at reduced pressure, with high capital cost and batch wise operation. As a consequence plasma enhanced coating processes such as plasma enhanced chemical vapour deposition (PE-CVD) have found wide utility in the electronics industry but are not applied on a significant scale in industries which require high volume film, fibre or textile treatment.

Industrial plasmas are typically categorised as either i) equilibrium "hot" plasmas where electrons and ions are at the same temperature reaching 1000's K in temperature or ii) non-equilibrium "cold" plasmas where the electrons and not the ions carry the kinetic energy. Hot plasmas have been widely used in industry for many years for cutting or coating metallic parts but are unsuitable for use with organic/polymeric substrates. Cold plasmas operate at ambient temperatures and are suitable for treating even low melting thermoplastics. However, cold plasmas are typically generated in conditions of high vacuum and operation is restricted to batch wise or at best pseudo-continuous processing.

Atmospheric Pressure Glow Discharge (APGD) offers an alternative homogeneous cold plasma source, which has many of the benefits of vacuum, cold plasma methods while operating at atmospheric pressure. APGD was first reported by Von Engle in the 1930's, interest was re-ignited in the late 1980's by the work of Okazaki & Kogoma[1] and subsequently other researchers [2]. More recently, Plasma Ireland Ltd. developed a series of wide area Helium APGD systems, which further refined the original APGD concept [3]. In 2001, Dow Corning S.A. purchased the APGD technology of Plasma Ireland Ltd. to launch Dow Corning Plasma.

Working in collaboration with Professor Jas Pal Badyal at the University of Durham (UK), Dow Corning has developed a new coatings process. By combining APGD technology with a unique precursor delivery system Dow Corning Plasma has developed Atmospheric Pressure Liquid Deposition [4]. Operating at atmospheric pressure and ambient temperature this process allows the use of a wide range of liquid precursors delivering high coating rates onto flexible substrates.

Patented APGD equipment enables the treatment of wide area substrates in true reel-to-reel conditions. Substrates can be both insulating (such as polymer films, non-wovens, fabrics and fibres and conducting (such as metal foils, metallised films). Dow Corning Plasma is now working collaboratively with lead customers across several industries to commercialise this exciting new coating technology.

2. PROCESS DESCRIPTION

2.1. The Equipment

Dow Corning Plasma offers wide area APGD equipment, designed specifically for plasma processing of flexible substrates, operating in reel-to-reel conditions [3, 5]. The plasma source utilizes parallel plate technology to generate a glow discharge plasma. Typical operating conditions are a voltage of 5-10 kV at a frequency of 30-50 kHz. The precursor is introduced as an atomized liquid directly into the glow discharge. Atomised liquid is generated via an ultrasonic nebuliser such as the Sono-tek, 8700-120.)[4].

2.2. Liquid Precursors

Atmospheric Pressure Liquid Deposition enables the use of a wide range of liquid precursors; not being restricted to gas or high volatility liquid precursors [4]. The precursor may be chosen from a range of polymer precursors, unsaturated organic materials such as acrylates and alkenes are particularly favoured. In oxidizing conditions, metal oxides may be produced from liquid precursors, for example organosilicon precursors will yield SiO_x coatings.

2.3. Experimental Methods

Video Contact Angle (VCA) analysis was performed using the Advanced Surface Technologies Inc., Video Contact Angle System 2000. 1ul or 2ul drops of AnalaR or HPLC grade probe liquids were applied.

X-ray photoelectron spectroscopy (XPS) was performed using the Kratos Analytical Axis Ultra spectrometer. The Axis Ultra is equipped with a monochromated aluminium (Al Ká) X-ray source, and a magnesium/zirconium (Mg Ká/Zr Lá) dual anode X-ray source. Each sample was analysed using mono-chromated Al Ká X-rays at 300 W (20mA, 15kV) power and a 90 degree take off angle.

3. RESULTS AND DISCUSSION

3.1. Hydrophobic Coatings

Polydimethylsiloxane polymer coatings are widely used [6] for their excellent hydrophobic properties, which increase water repellency, release and "handle". Tetramethylcyclotetrasiloxane and octamethylcyclo tetrasiloxane have been successfully used as precursors to produce polysiloxane coatings, which have excellent hydrophobicity. Analysis by Fourier Transform Infra-Red Spectrometry and Nuclear Magnetic Resonance Spectroscopy (not presented here) confirms the presence of D and T[7] silicone polymer units, indicating a cross-linked polymeric coating.

Scrubbed cotton substrate was coated with polydimethylsiloxane, to give a hydrophobic, water repellent material. Octamethylcyclotetrasiloxane liquid precursor was introduced into the chamber at 500 $ulmin^{-1}$ into a helium APGD with power $1Wcm^{-2}$.

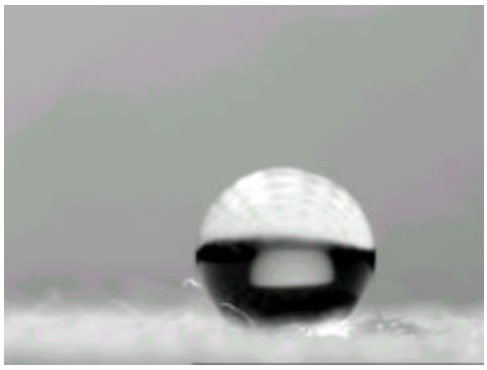


Figure 1. Scrubbed cotton coated with polydimethylsiloxane. Water droplet on cotton substrate, with water contact angle 140 degrees, non-treated cotton wets immediately.

3.2. Hydrophilic Coatings

Siloxane precursors such as tetramethylcyclotetrasiloxane and octamethylcyclotetrasiloxane may also be used to prepare hydrophilic coatings. Simply by changing to oxidising helium/oxygen APGD conditions, hydrophilic SiO_x coatings can be deposited in place of the hydrophobic coatings described earlier.

Polyacrylic acid coatings are widely used for their hydrophilic, adhesive and biocompatible properties. Many challenges exist in preparing high quality polyacrylic acid coatings via plasma polymerization, particularly in retention of –COOH functionality and coating durability. Polyacrylic acid coatings were produced by Atmospheric Pressure Liquid Deposition to give highly hydrophilic coatings with high –COOH retention. For example, polypropylene film was coated by introducing acrylic acid liquid precursor into the chamber at 30 $ulmin^{-1}$, substrate line speed of 1$mmin^{-1}$ in helium APGD with power 0.4Wcm^{-2}.

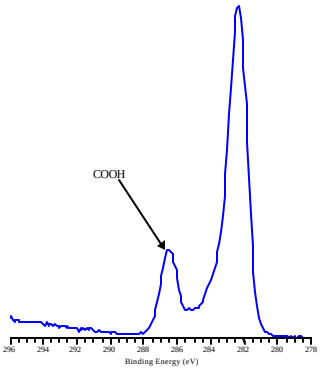


Figure 2 XPS C1s analysis Polyacrylic acid coating on polypropylene film, indicating retention of COOH.

3.3. Oleophobic Coatings

Fluorocarbon materials are well known for their low surface energy, and soil/fuel resistance. It has been previously demonstrated that low-pressure plasma can be used to generate structurally well-defined surfaces that have excellent hydrophobic and oleophobic liquid repellency behaviour [3]. Fluorocarbon coatings were produced by Atmospheric Pressure Liquid Deposition of long chain

perfluoroalkene precursors. Polypropylene film was coated with poly(heptadecafluorodecene) to give an oleophobic, fuel resistant surface. Heptadecafluorodecene liquid precursor was introduced into the chamber at 100 ulmin^{-1}, substrate line speed of 1mmin^{-1} in helium APGD with power 0.6Wcm^{-2}. The hexadecane contact angle of 61 degrees compares favourably with that of poly(tetrafluoroethylene) PTFE which has contact angle of 53 degrees when measured under identical conditions. Hexadecane wets immediately on non-treated polypropylene film. XPS analysis confirms the presence of CF_2 and CF_3 functionality upon the film surface.

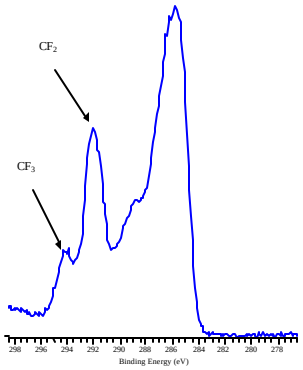


Figure 3 XPS C1s analysis of poly(heptadecafluorodece ne) on polypropylene film. Indicating retention of CF_2 and CF_3 functionality.

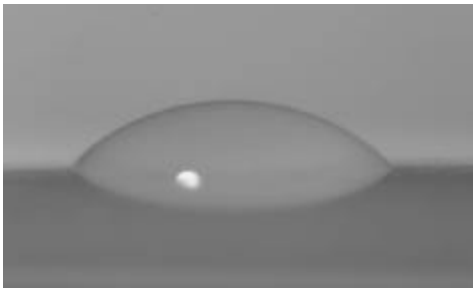


Figure 4 Polypropylene substrate with poly(heptadecafluorodecene) coating. Hexadecane droplet with contact angle of ca. 61degrees.

3.4. Controlled Chemistry

Due to the high-energy environment of plasma processes controlled polymerization chemistry is difficult to achieve. Significant advances have been made recently in low-pressure plasma processes with the introduction of pulsed PE-CVD[8,9,10]. In pulsed PE-CVD the plasma discharge is modulated in the millisecond – microsecond time scale. Polymerization may be tailored to progress via specific chemistry, fragmentation of the precursor is reduced (therefore properties maintained in coating) and deposition rates increased. This has been attributed to the increased importance of reactive neutrals over plasma ions, which in turn is due to the longer lifetime of neutrals during the off time.

In Atmospheric Pressure Liquid Deposition similar controllable chemistries can be achieved. For example, in the case of perfluoroalkene precursors, high retention of CF_2 and CF_3 functionality was observed which is similar to that reported in the literature for pulsed PE-CVD. This may be attributed to the low energy processes associated with the helium metastable species within the APGD plasma, further work is underway to investigate this effect.

4. APPLICATIONS

The current generation of APGD processing equipment is particularly suited to the coating of flexible substrates in reel-to-reel conditions. Substrates up to ca. 10mm thickness can be processed via the parallel plate configuration. The process is ideal for fabrics, non-wovens, fibres, films and papers. Control of surface energy covers many applications, from water wettable coatings on polyolefin films and non-wovens to oleophobic treatments of films, fibres and fabrics. The possibility to introduce specific functionalities to polymeric substrates is also enabled, such as barrier, adhesive, dielectric, conductivity and release.

5. CONCLUSIONS

Combining atmospheric pressure glow discharge (APGD) technology with liquid precursor delivery provides unique advantages over traditional plasma coating processes. The Dow Corning APGD equipment enables open perimeter, reel-to-reel processing of wide area flexible substrates. The combination of APGD with liquid precursor introduction opens up exciting possibilities in controlled coating chemistries.

6. ACKNOWLEDGMENTS

The authors are indebted to Professor Jas Pal Badyal and Dr. Luke Ward of Surface Innovations Ltd. at the University of Durham, UK.

REFERENCES

[1] Kanazawa S., Kogoma M., Moriwaki T., Okazaki S., *J.Phys. D: Appl. Phys.*, **21**, 838-840 (1988)

[2] Roth J.R., *Industrial Plasma Engineering Volume 2 Applications to Nonthermal Plasma Processing*, Institute of Physics Publishing, 2001, pages 37-73.

[3] Herbert A., O'Reilly F., Braddell J., Dobbyn P., PCT Patent WO 01 59809, 16th August 2001.

[4] Goodwin A.J., Merlin P.J., Badyal J.P., Ward L., PCT Patent WO 02 28548, 11th April 2002.

[5] Unpublished Dow Corning patents

[6] Owen M.J., in *Siloxane Polymers* ed. by Clarson S.J., Semlyen J.A., Prentice Hall 1993, pages 309-372.

[7] Organosilicon notation, D= $Si(Me)_2O_{2/2}$, T = $Si(Me)O_{3/2}$ or see reference 10 for more details.

[8] Coulson S.R., Woodward I.S., Badyal J.P.S., Brewer S.A., Willis C., Langmuir, **16**, 6287-6293, (2000)

[9] Qui H., Sanchez-Estrada F.S., Timmons R.B., J. of Photopolymer Science and Technology, **13**, 1, 29-32, (2000)

[10] Pryce Lewis H.G., Edell D.J., Gleason K. K., Chem. Mater., **12**, 3488-3494, (2000)

INDEX

A

Abe, T. 303
Addou, A. 308
Aints, M. 83, 282
Akishev, Yu.S. 8, 99
Amirov, R.H. 337
Anikin, N.B. 73
Appleton, A.T. 313
Arnesen, A. 291

B

Baba, S. 148
Baranchuk, M.S. 93
Bartnikas, R. 124
Behnke, J. 48, 53
Behnke, J.F. 48, 53, 68, 410
Bibinov, N.K. 73
Bogaerts, A. 130
Boksha, N.S. 114
Borra, J.P. 364
Brablec, A. 68
Brandenburg, R. 13, 28, 63
Bräuning-Demian, A. 206, 390
Brisset, J.L. 308, 379
Brožek, V. 161
Burlica, R. 379

C

Calvo, S. 296
Chang, J.S. 78
Cheron, B. 379
Chéron, B.G. 308
Chikeev, E. 277
Choi, J.J. 360
Chutov, Yu.I. 88
Clark, R.J. 374
Cormier, J.-M. 176, 296
Croquesel, E. 23
Czeremuszkin, G. 124, 400

D

Datta, S. 390
Dekempeneer, E. 385
Demyanov, A.V. 8
Deniset, C. 355
Dewulf, J. 342
Dhainaut, M. 171
Djéga-Mariadassou, G. 296
Dors, M. 78, 144
Drinkenburg, A.A.H. 318
Dudemaine, M. 176
Dudziński, K. 415
Dupré, S. 355

E

Ebert, U. 33
Ehara, Y. 244
Eliáš, M. 161
Endo, Y. 217
Engemann, J. 58

F

Fateev, A. 119
Filimonova, E.A. 337
Finney, W.C. 313, 369, 374
Foest, R. 410
Francke, K.-P. 323
Franzke, J. 206

G

Gerasimov, G. 291
Gherardi, N. 23, 28
Gibalov, V.I. 153
Gijbels, R. 130
Goedheer, W.J. 88
Goldman, A. 3, 171, 355
Goldman, M. 3, 171, 355
Golubovskii, Yu.B. 48, 53
Goodwin, A. 441
Goossens, O. 385
Gorce, O. 296
Guimond, S. 400

H

Haljaste, A. 83, 282
Hallin, R. 291
Hammer, T. 196
Hayashi, N. 213, 347, 351
Hayashi, T. 264
Heesch, E.J.M. van 318
Heintze, M. 139, 166, 201
Herbert, T. 441
Hippler, R. 410
Hnatiuc, B. 379
Hnatiuc, E. 308, 379
Hohn, O. 206, 390
Hong, J. 360
Hong, S.H. 38, 104, 109, 337
Horinouchi, T. 264
Hulka, L. 259
Humpert, C. 234

I

Ignatkov, A. 58
Ihara, S. 213, 347, 351
Ishii, S. 217
Ito, T. 244

J

Jahnke, T. 206, 390
Jahołkowski, K. 239
Jalviste, E. 291
Janča, J. 161, 425
Janowska, J. 415
Janowski, T. 249
Jidenko, N. 364
Jodzis, S. 269
Joshi, P. 390
Jouve, G. 3
Jurado, H. 296

K

Kanazawa, S. 78
Kaneda, S. 213
Kang, W.S. 38, 109
Kapička, V. 68
Kappes, T. 196
Karal’nik, V.B. 8
Karimi, C. 171
Karpiński, L. 420
Kettlitz, M. 139
Khacef, A. 296

Khampan, C. 28
Kim, S. 360
Kim, Y.-H. 38, 104, 109, 337
Kim, Y.-K. 360
Kirkpatrick, M.J. 369
Kishida, H. 244
Klíma, M. 68
Kochetov, I.V. 99
Kocik, M. 78
Kogoma, M. 303, 436
Kozlov, K.V. 13, 28, 114
Kozlov, M.V. 43
Kravchenko, O.Yu. 88
Krawczyk, K. 181, 186
Kunze, K. 206

L

Laan, M. 134, 286, 405
Landing, W. 374
Langenhove, H. Van 342
Lavrov, O.A. 88
Leadley, S. 441
Lebedev, V. 410
Lee, Ke. 360
Lee, Ki. 360
Leis, F. 206
Lendresse, Y. 296
Leu, G.F. 58
Leys, C. 342
Lisitchenko, T.E. 88, 93
Lissovski, A. 277
Loboiko, A.I. 99
Locke, B.R. 313, 369, 374
Lukes, P. 313
Lunk, A. 119

M

Madani, M. 130
Magureanu, M. 139, 201
Maiorov, V.A. 48, 53
Marode, E. 18, 355
Massines, F. 23, 28
Michel, P. 13, 28, 63
Miclea, M. 206
Miessner, H. 323
Misiak, M. 415
Miyake, Y. 244
Mizeraczyk, J. 78, 144
Monich, A.E. 8
Morent, R. 342
Morozov, A.M. 114
Moussa, D. 308
Mukhopadhyay, S. 390
Murata, T. 153

N

Nair, S.A. 318
Nakajima, N. 264
Napartovich, A.P. 99
Naudé, N. 23
Navratil, Z. 63
Niemax, K. 206
Nowakowska, H. 144

O

Ochman, P. 191
Odic, E. 171
Ohkubo, T. 78
Okazaki, S. 239
Okholin, M.M. 93
Ono, S. 431
Opalinska, T. 191, 254, 420

Opalska, A. 191
Ostrikov, K. 395
Ozonek, J. 239

P

Paris, P. 405
Park, J.M. 104
Pasedag, D. 63
Paulussen, S. 385
Pawłat, J. 327
Pemen, A.J.M. 318
Penache, C. 206, 390
Penghui, G. 347
Petit, M. 364
Peyrous, R. 222
Pietruszka, B. 166
Pietsch, G.J. 153, 229, 234, 259
Plank, T. 83, 134
Podliński, J. 78
Polaczek, J. 191
Pollo, I. 239, 327
Pouvesle, J.M. 296
Protas, G.I. 88
Ptasinski, K.J. 318

R

Radu, I. 124, 400
Raud, J. 286
Repän, V. 134
Roots, L. 282
Rudolph, R. 323
Rusu, I. 176
Ruszniak, J. 181
Rutgers, W.R. 33
Rzanek-Boroch, Z. 415

S

Sahni, M. 374
Samoilovich, V.G. 114
Satoh, S. 148, 213, 347, 351
Saveliev, A.B. 229
Schiene, W. 196
Schmidt – Böcking, H. 206, 390
Schmidt-Szałowski, K. 181, 415, 420
Schössler, S. 206, 390
Schwabedissen, A. 58
Sentek, J. 181
Severac, C. 3
Shimosaki, M. 213
Šícha, M. 68
Šira, M. 73
Slavíček, P. 68
Smerechuk, A. 291
Sokolova, M.V. 43
Song, Y.-H. 38, 109, 337
Sonnenfeld, A. 410
Sťahel, P. 425
Stańco, J. 144
Steffen, H. 410
Stryczewska, H. D. 249
Subedi, D.P. 425
Swallow, F. 441
Szymańska, A. 415

T

Takayama, S. 431
Tanaka, K. 303, 436
Tardiveau, P. 18
Teii, S. 431
Temnikov, A.G. 43
Teshima, K. 332
Thomas, C. 296

Timatkov, V.V. 43
Treshchalov, A. 277, 291
Trunec, D. 63
Trushkin, N.I. 8

U

Ulejczyk, B. 420

V

Valtna, H. 405
Vangeneugden, D. 130, 385
Veis, P. 23
Veldhuizen, E.M. van 33
Vereshchagin, I.P. 43
Vertriest, R. 342
Vinogradov, I.P. 119
Vitrac, H. 308
Vladimirov, S. 395

W

Wagner, H.-E. 13, 28, 63
Wertheimer, M.R. 124, 400
Wieczorkowski, M. 186
Wiesemann, K. 73

Y

Yamabe, C. 148, 213, 327, 347, 351
Yamamoto, K. 351
Yan, K. 318
Yasuoka, K. 217
Yoshioka, Y. 332